

Development of Enhanced Geothermal Systems (EGS) in Northern Alberta

by

Hannes Hofmann

A thesis submitted in partial fulfillment of the requirements for the degree of

Doctor of Philosophy

in

Petroleum Engineering

Department of Civil and Environmental Engineering
University of Alberta

© Hannes Hofmann, 2015

ABSTRACT

In the province of Alberta a huge amount of energy is needed for diverse applications. Specifically, the demand for heat is limited to a few locations such as the oil sands operation regions and metropolitan areas. Oil sands processing facilities near Fort McMurray and direct heat provision for different applications in the City of Edmonton are two of these major heat consumers in the province. Currently, this heat is mainly supplied by burning natural gas with significant greenhouse gas (GHG) emissions.

Geothermal energy may be an alternative heat source for these applications. While the required temperatures are reached within the sedimentary basin underneath Edmonton, wells need to be drilled deep into the granitic basement in the Fort McMurray area. Whereas high enough temperatures can be reached with sufficiently deep wells, in both cases the permeability in these deep sedimentary and granitic rocks is insufficient to produce large enough amounts of hot water.

Therefore, these rocks need to be hydraulically stimulated to improve the productivity of the wells without causing premature breakthrough of cold fluid from the injection wells. Such an enhanced geothermal system (EGS) is currently the only method that has the potential to provide heat from the earth's crust for the investigated applications. However, so far, no economically operating EGS could be developed in granitic basement rocks, which shows that earlier reservoir engineering concepts were not sufficient and parameters and processes governing the development and operation of EGS are very complex and not well enough understood.

Using a variety of numerical methods, this thesis investigates whether EGS can be an alternative low GHG emission heat source for oil sands processing in Fort McMurray and direct heating

applications in Edmonton, and how these systems should be designed to make them technically feasible and economically competitive.

It was found that the deployment of EGS can significantly reduce GHG emissions and save valuable gas resources at similar costs to burning natural gas only if the fracture network is optimally engineered. The reservoir modeling results suggested that the development of well-connected complex fracture networks between horizontal or deviated wells by multiple stimulation treatments is the most promising concept to achieve these goals. Therefore, the hydraulic stimulation process was studied numerically at the micro and giga scale and based on these results a reservoir engineering concept was proposed for the sedimentary rocks in the Edmonton area and the granitic basement rocks in Fort McMurray. Also, natural factors were identified that promote complex fracture network development in low permeability granitic basement rocks.

This thesis is dedicated to
**the research partnership between Germany and Canada,
Christin, and my family and friends.**

ACKNOWLEDGEMENT

First of all I would like to thank my supervisors Dr. Tayfun Babadagli (University of Alberta) and Dr. Günter Zimmermann (GFZ Potsdam) for their advice and support throughout the last years. I also thank my committee members Dr. Ergun Kuru, Dr. Ryosuke Okuno, Dr. Derek Apel and Dr. Doug Schmitt and the external examiner Dr. Heinz Konietzky for their service.

This study was conducted under the Helmholtz-Alberta-Initiative (HAI). I am grateful for the financial support provided by Alberta Environment's ecoTrust program and the Helmholtz Association's Initiative and Networking Fund. The memorandum of understanding between the University of Alberta and the Helmholtz Association allowed extensive collaboration with researchers from different German Universities and research centers as well as different departments at the University of Alberta. In particular I would like to thank Dr. Guido Blöcher, Dr. Harald Milsch, Dr. Jeoung Seok Yoon, Dr. Arno Zang, Dr. Simon Weides, Dr. Inga Moeck, Dr. Fiorenza Deon, Dr. Jens Mingram and Liane Liebeskind from the German Research Centre for Geosciences (GFZ), Liang Pei and Rainer Seehaus from TU Darmstadt, Dr. Thomas Frühwirth from TU Bergakademie Freiberg, Dr. Fritz Finger from TU Salzburg, Dr. Norihiro Watanabe from the Helmholtz Centre for Environmental Research (UFZ) in Leipzig, and Dr. Kayhan Develi from Istanbul Technical University. From the University of Alberta I would like to especially thank Dr. Jacek Majorowicz, Greg Nieuwenhuis, Pamela Keegan and Todd Kinnee. I appreciate the support of the team leads of HAI Theme 4, Dr. Martyn Unsworth (UofA) and Dr. Ernst Huenges (GFZ), all Theme 4 group members, and HAI administration staff. I am also thankful to my fellow HAI and EOGRRC graduate students from all over the world for sharing this experience with me. Not forgotten are the many teachers of Gymnasium Jessen, TU Berlin and University of Alberta who provided the knowledge base for this work.

I acknowledge the OpenGeoSys, Paraview and IQ-Sation communities, Meyer & Assoc., and Computer Modeling Group for free support and software licenses for research purposes.

In the end, I thank my family, old and new friends in Germany and Canada, and especially Christin for their love and support.

TABLE OF CONTENTS

CHAPTER 1: INTRODUCTION	1
1.1 BACKGROUND.....	2
1.2 NUMERICAL SIMULATION OF HYDRAULIC STIMULATION TREATMENTS	9
1.2.1 Conventional hydraulic fracturing model: MFrac	11
1.2.2 Discrete fracture network model: MShale.....	12
1.2.3 Discrete element method: Particle Flow Code	13
1.2.4 Grain-based modeling: Particle Flow Code.....	14
1.3 NUMERICAL SIMULATION OF EGS OPERATION	15
1.3.1 Finite difference model: CMG STARS	15
1.3.2 Finite element model: OpenGeoSys	16
1.4 STATEMENT OF THE PROBLEMS AND OBJECTIVES	16
1.5 SOLUTION METHODOLOGY	18
1.6 OUTLINE.....	20
 CHAPTER 2: POTENTIAL FOR ENHANCED GEOTHERMAL SYSTEMS IN ALBERTA, CANADA	 22
2.1 INTRODUCTION.....	23
2.2 MODEL DESCRIPTIONS	26
2.2.1 Geological model.....	26
2.2.2 Model parameterization.....	28
2.2.3 Hydraulic fracture development model	31
2.2.4 Thermal-hydraulic reservoir simulation model	32
2.3 SIMULATION PROCEDURE	33
2.3.1 Hydraulic fracturing simulation procedure.....	33
2.3.2 Reservoir simulation procedure.....	33
2.3.3 Economical considerations	35
2.3.4 Reductions in CO ₂ emissions	35
2.3.5 Natural gas savings.....	36
2.4 SIMULATION RESULTS.....	36
2.4.1 Hydraulic fracturing simulation results	36

2.4.2 Reservoir simulation results	44
2.4.3 Potential utilization of the extracted heat	48
2.4.4 Economical considerations	49
2.4.5 Reductions in CO ₂ emissions	52
2.4.6 Natural gas savings	53
2.5 CONCLUSIONS AND REMARKS	54
CHAPTER 3: HYDRAULIC FRACTURING SCENARIOS FOR LOW TEMPERATURE EGS HEAT GENERATION FROM THE PRECAMBRIAN BASEMENT IN NORTHERN ALBERTA.....	60
3.1 INTRODUCTION	61
3.2 MODEL PARAMETERS	63
3.3 METHODOLOGY	65
3.3.1 Fracturing simulations	65
3.3.2 Reservoir simulations	67
3.4 RESULTS.....	68
3.4.1 Sensitivity analysis	68
3.4.2 Hydraulic fracturing scenarios.....	72
3.4.3 Reservoir simulations of hydraulic fracturing scenarios	73
3.5 CONCLUSIONS AND REMAKRS	78
CHAPTER 4: HOT WATER GENERATION FOR OIL SANDS PROCESSING FROM ENHANCED GEOTHERMAL SYSTEMS: PROCESS SIMULATION FOR DIFFERENT HYDRUALIC FRACTURING SCENARIOS.....	84
4.1 INTRODUCTION.....	85
4.2 METHODOLOGY	89
4.3 DATA BASIS	90
4.3.1 Fracture systems	90
4.3.2 Stress.....	91
4.3.3 Mechanical rock properties	92
4.3.4 Reservoir leak-off parameters	93
4.3.5 Thermal properties.....	94
4.4 HYDRAULIC FRACTURING SIMULATIONS.....	95

4.4.1 General considerations	95
4.4.2 Fracturing simulator	95
4.4.3 Sensitivity analysis	96
4.4.4 Hydraulic fracturing simulation results	114
4.5 RESERVOIR SIMULATIONS.....	125
4.5.1 Reservoir simulator.....	125
4.5.2 Performance criteria	125
4.5.3 Well spacing	127
4.5.4 Number of fracturing treatments	128
4.5.5 Fracture spacing.....	129
4.6 ECONOMIC ANALYSIS.....	130
4.7 GREENHOUSE GAS EMISSION REDUCTIONS	136
4.8 SAVINGS OF NATURAL GAS RESOURCES	138
4.9 CONCLUSIONS.....	138
CHAPTER 5: NUMERICAL SIMULATION OF COMPLEX FRACTURE NETWORK DEVELOPMENT BY HYDRAULIC FRACTURING IN NATURALLY FRACTURED ULTRATIGHT FORMATIONS	144
5.1 INTRODUCTION.....	146
5.2 THE DFN FRACTURING SIMULATOR	147
5.3 MODEL PARAMETERS	149
5.4 METHODOLOGY AND THEORETICAL BACKGROUND	151
5.5 RESULTS.....	154
5.5.1 Fracture height growth containment.....	154
5.5.2 Net fracture pressure.....	158
5.5.3 Fracture area	160
5.5.4 Fairway aspect ratio.....	162
5.6 DISCUSSION	163
5.7 SUMMARY AND CONCLUSIONS.....	163

CHAPTER 6: A GRAIN-BASED MODELING STUDY OF MINERALOGICAL FACTORS AFFECTING STRENGTH, ELASTIC BEHAVIOUR AND MICRO FRACTURE DEVELOPMENT DURING COMPRESSION TESTS IN GRANITES170

6.1 INTRODUCTION.....	171
6.2 PFC2D GRAIN-BASED MODELING (GBM) OF BRITTLE FAILURE OF GRANITES	172
6.3 MODELING PROCEDURE.....	175
6.3.1 Model Setup and Calibration.....	175
6.3.2 Sensitivity Analysis	180
6.4 RESULTS.....	181
6.4.1 Model calibration.....	181
6.4.2 Sensitivity Analysis of Model Parameters.....	187
6.5 DISCUSSION	192
6.6 CONCLUSIONS	194

CHAPTER 7: PARAMETRIC ANALYSIS OF COMPLEX MICRO-SCALE FRACTURE GROWTH IN GRANITES UNDER COMPRESSION: A GRAIN-BASED MODELING STUDY199

7.1 INTRODUCTION.....	200
7.2 CALIBRATED PFC2D GRAIN-BASED MODEL OF AUE GRANITE	201
7.3 MODELING PROCEDURE.....	203
7.4 RESULTS AND DISCUSSION	204
7.4.1 Calibrated Aue granite model.....	204
7.4.2 Mineral size and randomness of mineral and particle distribution.....	206
7.4.3 Mineral and mineral boundary micro properties	209
7.4.4 Mineralogy.....	217
7.4.5 Model Size.....	219
7.5 CONCLUSIONS.....	220

CHAPTER 8: CONTINUOUS MEASUREMENT OF TIME AND PRESSURE DEPENDENT FRACTURE PERMEABILITY OF ALIGNED AND DISPLACED TENSILE FRACTURES IN GRANITIC ROCKS DURING CYCLIC LOADING224

8.1 INTRODUCTION.....	226
8.2 SAMPLE MATERIALS AND EXPERIMENTAL PROCEDURES	228
8.2.1 Sample materials.....	228
8.2.2 Fracture generation.....	229
8.2.3 Fracture displacement.....	230
8.2.4 Pressure dependent fracture permeability measurements.....	231
8.2.5 Fracture surface scanning	235
8.3 EXPERIMENTAL RESULTS	236
8.3.1 Hydraulic and strain response of an intact sample	236
8.3.2 Confining pressure dependent hydraulic and strain response of fractured samples	238
8.3.3 Confining pressure dependent hydraulic and strain response of fractured samples	244
8.3.4 Fracture surface scanning results after testing.....	249
8.4 COMPARISON WITH LITERATURE DATA AND RELEVANCE FOR EGS DEVELOPMENT	251
8.5 DISCUSSION	255
8.6 CONCLUSIONS	257
CHAPTER 9: A HYBRID DISCRETE/FINITE ELEMENT MODELING STUDY OF COMPLEX HYDRAULIC FRACTURE DEVELOPMENT FOR ENHANCED GEOTHERMAL SYSTEMS (EGS) IN GRANITIC BASEMENTS	262
9.1 INTRODUCTION.....	263
9.2 POTENTIAL FACTORS GOVERNING FRACTURE NETWORK COMPLEXITY	266
9.2.1 Natural factors	266
9.2.2 Engineering factors.....	267
9.3 DISCRETE ELEMENT FRACTURE MODEL	269
9.3.1 Particle flow code 2D	269
9.3.2 Model setup	271
9.4 FINITE ELEMENT RESERVOIR MODEL	274
9.4.1 OpenGeoSys	274
9.4.2 Model setup	274
9.5 MODELING PROCEDURE.....	277
9.6 FINITE ELEMENT RESERVOIR MODEL	277

9.6.1 Base case model.....	277
9.6.2 Effect of engineering factors on fracture pattern.....	280
9.6.3 Effect of natural factors on fracture pattern.....	287
9.7 RESERVOIR SIMULATION RESULTS	291
9.7.1 Base case model.....	291
9.7.2 Influence of engineering factors on hydraulic and thermal performance.....	292
9.7.3 Influence of natural factors on hydraulic and thermal performance	295
9.8 DISCUSSION	297
9.9 CONCLUSIONS	299
CHAPTER 10: OVERVIEW OF THE RESEARCH, CONTRIBUTIONS AND RECOMMENDATIONS	306
10.1 CRITICAL DISCUSSION OF SIMULATION APPROACHES	307
10.2 SCIENTIFIC CONTRIBUTIONS	312
10.3 PRACTICAL CONTRIBUTIONS	313
10.4 SUGGESTED FUTURE WORK.....	315
BIBLIOGRAPHY	317

LIST OF TABLES

Table 1: Summary of the main properties of the four potential target formations for geothermal energy extraction in the Edmonton Area (values from the Wabamun, Nisku and Cooking Lake formations are from the AGS database and data from the Basal Sandstone Unit are from Weides et al. [28]). ...	28
Table 2: Thermal properties of the five different rock types that are building the models.	30
Table 3: Stimulation potential for the four investigated formations based on fracture height growth confinement and other characteristics (k = permeability).	43
Table 4: Relative thermal performance and stimulation potential for different formations (1=worst, 4=best).	48
Table 5: Potential applications for heat extracted from the four formations (after [16]).	49
Table 6: Summary of the treatment parameters, advantages and disadvantages of the three main hydraulic stimulation methods (Reinicke, 2009).	62
Table 7: Summary of hydraulic and mechanical properties of granites used as input parameters for the fracturing simulations.	64
Table 8: Calculated stress states at different depths.	64
Table 9: Summary of the main parameters used for the reservoir simulation.	65
Table 10: Summary of treatment parameters of the base case and the range which has been used in the sensitivity analysis.	66
Table 11: Major observations of the sensitivity analysis performed for the treatment parameters for Scenario 1 with the auto-treatment design function with constant reservoir properties (base case). ...	69
Table 12: Results of four different treatment designs for each of the two scenarios used for the reservoir simulations.	73
Table 13: Simulated scenarios with the least number of treatments necessary to achieve a productivity index of 36 m ³ /h/MPa.	78
Table 14: Fracture properties in the three principle planes.	90
Table 15: Stress magnitudes and directions at 5 km depth.	91
Table 16: Mechanical rock properties of granites as derived from literature data.	93
Table 17: Reservoir leak-off parameters.	94
Table 18: Thermal rock and fluid (water) properties from laboratory tests and literature data.	94
Table 19: Three reservoir rock property scenarios leading to different fracture areas.	101
Table 20: Minimum stress contrast and constant stress interval requirements to confine upward and downward fracture height growth into adjacent formations.	104
Table 21: Suggested closure stress range for different proppant types [15].	114
Table 22: Fracture properties and treatment parameters for slickwater treatments without proppants for all three scenarios and different target fracture half-lengths (H = average fracture height, A = total fracture area, K = fracture conductivity, V_i = injected fluid volume, Q_i = injection rate, Slickwater = water and friction reducer).	116
Table 23: Fracture properties and treatment parameters for hybrid fracturing treatments with low proppant masses and intermediate fracturing fluid viscosity for all three scenarios and different target fracture half-lengths (H = average fracture height, A = total fracture area, K = fracture conductivity, V_i = injected fluid volume, M = proppant mass).	117

Table 24: Fracture properties and treatment parameters for gel-proppant fracturing treatments with high proppant mass and fracturing fluid viscosity for all scenarios and target fracture half-lengths (injection rate=100 l/s, proppant type=20/40 CarboHSP, fluid type=Hybor G 50lb/Mgal WG-19, H=average fracture height, A=total fracture area, K=fracture conductivity, V_i =injected fluid volume, M=proppant mass).....	118
Table 25: Comparison between optimized intact and fractured rock cases for the Base Case Scenario using conventional gel-proppant treatments with X-linked gel and high strength proppants (L = length, H = height, A = area, K = conductivity, V = injected slurry volume, M = injected proppant mass). ...	123
Table 26: Reservoir performance criteria.....	129
Table 27: Comparison of GHG emissions resulting from burning of natural gas and the production of geothermal energy.	137
Table 28: Typical rock properties of granites and shales. Bold numbers show the values used for the base case scenario and numbers in parentheses show parameter ranges.	149
Table 29: Typical fracture network properties for granites and shales. Bold numbers show the values used for the base case scenario and numbers in parentheses show parameter ranges.	150
Table 30: Calculated stress values for a 5 km deep granite and a 2.5km deep shale. Bold numbers show the values used for the base case scenario and numbers in parentheses show parameter ranges. σ_v : vertical stress, σ_H : maximum horizontal stress, σ_h : minimum horizontal stress, and P_p : pore pressure.	151
Table 31: Measured mineral content and size of all four studied granites.	179
Table 32: Overview of three scenarios with different mineral sizes to study the influence of heterogeneity on the simulation results.	180
Table 33: Laboratory test results (10x5cm specimen) compared to the GBM results for the calibrated Aue granite model (5x2.5cm model), the 10x5cm Aue granite model and the 5x2.5 cm models of the other three granites. The calibration was only done for the Aue granite.....	182
Table 34: Calibrated micro-parameters used for all four granites.....	184
Table 35: Comparison between elastic parameters (ranges taken from previous studies) ^[48-50] of minerals and their GBM micro-property equivalents (PA=particle, PB=parallel bond) used in the calibrated model.....	187
Table 36: Amount of cracks developing depending on the mineral and particle distributions with different confining pressures compared to the calibrated Aue granite base case model.....	191
Table 37: Calibrated micro-parameters for the Aue granite [16]. These parameters were used for the base case model.	202
Table 38: Laboratory test results compared to calibrated GBM results for Aue granite [16].	203
Table 39: Some properties of the four tested granitic rocks.....	229
Table 40: Ratio of total (A_T) to planar fracture surface area (A_P) and variogram fractal dimensions (D_{va}) for three samples subject to elevated confining pressure (SG, 31, 31) and one sample that was not subject to confining pressure (16).....	250
Table 41: Apertures measured with a stereo microscope before and after the experiments.	256
Table 42: Model parameters of the discrete element fracture model.	273
Table 43: Model parameters of the finite element reservoir model.	276

LIST OF FIGURES

Figure 1: Temperature map of Alberta showing the depth to drill to reach a temperature of 100°C, the depth of the Precambrian basement rocks, and the oil sands deposits (after Majorowicz and Weides, 2012). The two current research areas are shown in bold boxes. Potential future study areas are shown in dotted boxes.	4
Figure 2: Initial disk packing produced by PFC2D showing spheres (yellow circles), contacts (black lines), and internal-void centroids (red dots; left). The mineral geometry consists of polygons; one for each internal sphere, with nodes at internal-void centroids (center). The generated mesh is shown on the right (after Potyondy, 2010c).	14
Figure 3: Overview of the methodology used to identify parameters and processes that improve the efficiency of enhanced geothermal systems.	19
Figure 4: Maximum temperatures at the base of the sedimentary basins fill (top of Precambrian crystalline basement) increase from east to west with the depth of the basin. In the Edmonton area basin temperatures are below 100°C. The extent of the regional scale geological model is shown as the black rectangle around Edmonton.	24
Figure 5: Three-dimensional geological model of the study area. The model is based on stratigraphic picks from about 7000 wells and potential geothermal reservoir units are indicated by the letter “G”; from Ref. [29].	27
Figure 6: Leak-off properties of the fracturing model.	29
Figure 7: Mechanical properties and minimum horizontal stress distribution of the fracturing model.	30
Figure 8: Geometries of the three reservoir models including depths of target formations and mesh refinement around the wells and the hydraulic fractures.	32
Figure 9: Overview of the eight different well and fracture alignments as used for the stimulated reservoirs. Well spacing is 400 m for the horizontal wells and 250 m for the vertical wells. Fracture spacing is 200 m and the fracture dimensions are based on the hydraulic fracturing simulations. The horizontal well section is 1000 m open-hole and the open-hole section of the vertical wells is over the whole height of each reservoir.	34
Figure 10: Only small fractures can be created within the Wabamun Group.	36
Figure 11: Large fracturing treatments lead to unconfined fracture height growth out of the Wabamun Group.	37
Figure 12: Unconfined fracture height growth out of the Nisku formation leads to a connection from the Nisku formation to the Wabamun Group.	38
Figure 13: The possible Calmar shale stress barrier (between Wabamun Group and Nisku formation) does not lead to sufficient fracture height growth confinement, but longer fracture half-lengths can be achieved.	38
Figure 14: With a height growth confinement due to the overlying Duverney and Ireton shales, fracture development might be confined within the Cooking Lake formation and long fractures may be developed.	39
Figure 15: If the Cooking Lake formation is not confined, half-lengths of about 300 m may be achieved and the resulting fractures would be significantly higher.	39
Figure 16: “Unconfined” fracture growth from the Basal Sandstone Unit into the Precambrian basement rocks.	41

Figure 17: An increased stress confinement leads to the development of fractures with less height in the Basal Sandstone Unit.....	41
Figure 18: Slurry volume and proppant mass needed to create a fracture with 750 mDm conductivity and created average fracture area and height for different target fracture half-lengths within the Basal Sandstone Unit.	42
Figure 19: Average production rates resulting from a maximum pressure drawdown of 5 MPa in all four formations (intact and stimulated for eight different fracture and well arrangements). Because of the poor performance of the two vertical wells in the intact formations compared to the two horizontal wells, Scenarios 5 and 6 (with three vertical wells) were not simulated for the intact formations. The maximum flow rate constraint per production well is 50 l/s.	45
Figure 20: Cumulative produced heat in 30 years based on different well arrangements for the intact scenarios and different well and fracture arrangements for the stimulated scenarios.	47
Figure 21: Levelized cost of geothermal energy production from intact and stimulated reservoirs for 30 years continuous production.....	50
Figure 22: Costs of geothermal energy production vs. time for the most economic intact and stimulated reservoir scenarios.....	51
Figure 23: Potential range of CO ₂ emission reductions for the four formations assuming 53 g CO ₂ reductions per MJ (lower bound: intact rock with three horizontal wells, upper bound: most promising stimulated rock scenario).	53
Figure 24: Potential amount of natural gas saved by one geothermal system within 30 years of operation. Values range between low heating value and high heating value of natural gas.	54
Figure 25: Fracture dimensions of Scenarios 1 (left) and 2 (right), showing the different stress states in both scenarios and different resulting fracture geometries.....	65
Figure 26: 3D reservoir model including the position of the horizontal injection well (I1, blue), the horizontal production wells (P1 and P2, red) and the vertical hydraulic fractures (grey).....	67
Figure 27: Final fracture area and conductivity showing significant fracture height growth in unconfined reservoirs (Scenario 1) resulting from the use of low viscosity fluids.	70
Figure 28: Fast proppant settling due to dense high strength proppants (left) can be reduced by using ultra-light weight proppants (right).....	70
Figure 29: Relative influence of the studied reservoir and treatment parameters within their typical range on the fracture area in Scenario 2.	71
Figure 30: Relative influence of the studied reservoir and treatment parameters within their typical range on the fracture width in Scenario 2.....	71
Figure 31: Top-view of the different kinds of fracture systems (gray lines) with the horizontal injection well (blue) in the middle, flanked by two horizontal production wells (red) with changing position.	74
Figure 32: Influence of the number of fractures on the productivity index for all eight scenarios and all four fracture systems.	74
Figure 33: Influence of the number of fractures on the bottomhole temperature at the production well (left) and the cumulative heat produced (right) after 30 years of production.....	75
Figure 34: Cumulative heat produced in 30 years production (left) and final bottom hole temperature after 30 years production (right).	75
Figure 35: Number of treatments (left) and length of the horizontal section (right) to achieve the target PI of 36 m ³ /h/MPa.....	76
Figure 36: Total proppant mass needed to develop a fracture system leading to a PI of 36 m ³ /h/MPa.	77

Figure 37: Depth to a temperature of 100°C and depth to the granitic Precambrian basement. In the oil sands areas near Ft. McMurray 100°C is reached at 5 km depth within Precambrian basement rocks [10].	86
Figure 38: Calculated stress state used for the Base Case Scenario. Assuming a normal faulting regime the maximum horizontal stress σ_H is expected to be in between the minimum horizontal stress σ_h and the vertical stress σ_v . P_p is the pore pressure.	92
Figure 39: Relative influence of all studied parameters within their expected range on the fracture area.	97
Figure 40: Relative influence of all studied parameters within their expected range on the average fracture aperture.	98
Figure 41: Relative change in fracture area when changing Young's modulus, critical stress (tensile strength), and Poisson's ratio within their expected range.	98
Figure 42: Relative change in fracture aperture when changing Young's modulus, critical stress (tensile strength), and Poisson's ratio within their expected range.	99
Figure 43: Relative change in fracture area for different permeabilities (left) and critical stress values (right). Permeability is becoming to be important from values above 0.01 mD considering high critical stress (12 MPa). Without critical stress (0 MPa) permeability is important for the whole parameter range between 0.00001 and 1 mD.	100
Figure 44: The fracture grows out of the confined formation if the total height of this formation is too small leading to large fracture areas and small fracture apertures. The injection point is in the center of the confined formation.	102
Figure 45: Influence of the distance between injection point and lower stress barrier on the minimum stress contrast (left) and the minimum length of a constant stress interval (right) needed to confine the fracture height growth when injecting 20,000 m ³ slickwater at a rate of 100 l/s (for the Base Case Scenario).	103
Figure 46: Influence of stress contrasts on lower and upper fracture height for different distances between injection point and lower stress barrier (50 m, 100 m, 200 m) and for a critical stress of 12 MPa (left) and 0 MPa (right). The figures show the final geometry after injecting 20,000 m ³ slickwater at a rate of 100 l/s.	104
Figure 47: Final fracture geometries for a confined (left) and two unconfined (mid and right) formations. A stress contrast of only 1.75 MPa leads to unconfined downward fracture growth (middle) and a constant stress interval of 150 m leads to unconfined upward fracture growth (right). The treatment design (injected slickwater volume) was adapted in order to achieve the same fracture half-length of 500 m.	105
Figure 48: The total fracture area of the discrete fracture network (DFN) decreases with increasing stress difference whereas the area of the main fracture increases.	106
Figure 49: The average width of the fractures increases with increasing stress difference.	107
Figure 50: Influence of the stress difference on the volume of the main fracture, the secondary fracture network, and the total fracture network.	107
Figure 51: The aspect ratio (extent of fracture network parallel to the maximum horizontal stress divided by the extent of the fracture network parallel to the minimum horizontal stress) decreases with increasing stress difference.	108
Figure 52: The total area of the DFN and of the secondary DFN decrease with increasing fracture spacing whereas the area of the main fracture increases.	109

Figure 53: The average aperture of the main fracture, the secondary DFN, and the total DFN increases with increasing fracture spacing.	109
Figure 54: The average fracture height for low fracture spacings is high because of fracture height growth out of the formation. For higher fracture spacings the height growth is confined and the resulting height is constant.	110
Figure 55: Influence of the flow rate on the relative change in the fracture area for the Base Case Scenario with 12 MPa critical stress, 0 MPa critical stress, and 0.1 mD permeability.	112
Figure 56: Influence of the flow rate on the relative change in the average fracture aperture for the Base Case Scenario with 12 MPa critical stress, 0 MPa critical stress, and 0.1 mD permeability.	113
Figure 57: Fracture area vs. proppant mass to create a fracture conductivity of 300 mDm and 1,000 mDm for all three scenarios using gel-proppant, and hybrid fracturing treatments. The target half-lengths were 300 m, 500 m, and 700 m.	119
Figure 58: Injected fluid volume vs. fracture area for all three scenarios and all three treatment methods. The target half-lengths were 300, 500, and 700 m.	119
Figure 59: Comparison of the properties of the main fracture resulting from the same treatment (designed for intact rock) for the Base Case Scenario with intact rock (left) and with a natural fracture system of 50 m spacing (right).	121
Figure 60: Top view on the fracture network for 50 m fracture spacing (left) and 5 m fracture spacing (right).	123
Figure 61: Injected fluid volume needed to achieve a fracture half-length between 300 m and 700 m for fracture spacings between 1.5 m and 50 m.	124
Figure 62: 3-D View of an example reservoir model including initial temperature distribution.	126
Figure 63: Influence of the number of fractures (treatments) on WH temperature, extracted energy, and productivity index after 30 years of production for the Base Case Scenario (500 m fracture half-length, 400 m well spacing, 1000 mDm fracture conductivity, 100 m fracture spacing).	127
Figure 64: The minimum number of fractures (single fracturing treatments) increases with decreasing fracture conductivity.	128
Figure 65: Influence of fracture spacing on WH temperature, extracted energy, and productivity index after 30 years of production for the Base Case Scenario (500 m fracture half-length, 400 m well spacing, 1000 mDm fracture conductivity, 10 fractures).	130
Figure 66: Approximated EGS costs in % and million Canadian dollars.	131
Figure 67: Influence of well spacing, number of fractures, and fracture spacing on the geothermal energy generation costs for one example (Base Case Scenario with 500 m fracture half-length, 1000 mDm fracture conductivity, 400 m well spacing, 10 fractures, and 100 m fracture spacing). The dotted line represents the current costs of generating the same amount of energy with burning natural gas assuming 50% efficiency.	132
Figure 68: Comparison of the energy generation costs of producing geothermal energy from a 3 well EGS with a lifetime of 30 years for different stimulation types, fracture conductivities, and created fracture half-lengths for intact rock and naturally fractured rock with different in-situ fracture spacings. The presented values are for the Base Case Scenario. The error bars show the variation between all three Scenarios (Small Area, Base Case, and Large Area).	133
Figure 69: Comparison of the length of the horizontal well section and the number of stimulation treatments needed to fulfill the performance criteria for different stimulation types, fracture conductivities, and created fracture half-lengths for intact rock and naturally fractured rock with	

different in-situ fracture spacings. The presented values are for the Base Case Scenario. The error bars show the variation between all three Scenarios (Small Area, Base Case, Large Area).	134
Figure 70: Comparison of the injected proppant mass and fluid volume for different stimulation types, fracture conductivities, and created fracture half-lengths for intact rock and naturally fractured rock with different in-situ fracture spacings. The presented values are for the Base Case Scenario. The error bars show the variation between all three Scenarios (Small Area, Base Case, and Large Area).	135
Figure 71: Overview of the main parameters and processes involved in the hydraulic fracturing simulations (graphics taken from Refs. [1–3])	147
Figure 72: Critical stress for fracture propagation (redrawn from [17]).	152
Figure 73: Schematic top view of the base case scenario (two fracture sets, $\sigma_h = \sigma_H$, and 25m fracture spacing). The primary vertical fracture set is parallel to σ_H . The secondary vertical fracture set is perpendicular to the primary fracture set.	153
Figure 74: The influence of the stress variation with depth for a 2.5 km deep shale and a 5 km deep granite (1: constant stress, 2: linear stress increase, 3: stepwise stress increase, 4: low stress formation)....	155
Figure 75: Influence of the distance between injection point and the lower stress barrier on the minimum stress contrast needed for confinement and the minimum formation height (if no upper stress barrier is present).	156
Figure 76: Minimum stress contrast needed to confine fracture height growth for different fracture spacings, fracture sets, and rock types.	157
Figure 77: Influence of the differences between vertical and minimum horizontal stress and between maximum and minimum horizontal stress on the minimum stress contrast required to confine fracture height growth.	158
Figure 78: Influence of the fracture spacing on the maximum net pressure observed during stimulation for different rock types and fracture sets.	158
Figure 79: Influence of the differences between the three principle stresses on the maximum net pressure observed during stimulation for different rock types and fracture sets.	159
Figure 80: Influence of fracture spacing on the total area of the DFN for different rock types and fracture sets.	161
Figure 81: Influence of the differences between the three principle stresses on the total area of the DFN for different rock types and fracture sets.	161
Figure 82: Influence of the differences between the three principle stresses on the aspect ratio of the fracture system for different rock types and fracture sets.	162
Figure 83: Generation of a grain-based model (GBM) with different grain types based on an initial particle packing (1-4), (5) bonded particle model overlaid on the grain structure, and (6) GBM consisting of grains or minerals (parallel-bonded disks) and interfaces between the grains (smooth-joint contacts).	173
Figure 84: Parallel-bond (a) and smooth-joint contact (b) and particle movement after bond/contact breakage (c and d). ^[37]	174
Figure 85: Force-displacement behaviour for bonded particles and smooth joints: (a) normal force versus normal displacement, (b) shear force versus shear displacement, and (c) strength envelope (redrawn from Itasca) ^[18] . F_n =normal force, F_s =shear force, $-\sigma_c$ =tensile strength, U_n =normal displacement, U_s =shear displacement, k_n =normal stiffness, k_s =shear stiffness, c_b =cohesion, Φ_b =friction angle, τ_c =shear strength, A =contact area between two particles).	175

Figure 86: Photographs of the tested intact granite samples (height = 10 cm, diameter = 5 cm) ^[43] and grain-based model representation (height = 5 cm, width = 2.5 cm). Note that no photograph was available for the Aue granite that was used for calibration and the picture shown is also taken from Xin). ^[43] The colors indicate different mineral types (red=quartz, blue=plagioclase, green=orthoclase, orange=mica).....	178
Figure 87: Schematics of the three laboratory test setups.	179
Figure 88: Calibrated Aue granite and Eibenstock I, II, and Kirchberg II GBM results compared to experimental data. While the Aue granite results match the experimental values, simulated failure stresses for the other three granites are different from the experimental ones if the same mineral and mineral boundary properties are used.....	183
Figure 89: Comparison of the crack paths and AE events of the triaxial tests with the displacement vectors and micro cracks from the GBM simulations (blue=grain boundary tensile, green=grain boundary shear, red=grain tensile, black=grain shear) at different confining pressures.	186
Figure 90: Influence of the average grain diameter on number and type of cracks resulting from an unconfined compression test (left), and biaxial confined compression tests with 10 MPa (center) and 40 MPa (right) confining pressure.....	188
Figure 91: Influence of the average grain diameter on compressive strength with different confining pressures (P_c), tensile strength, and elastic properties.	188
Figure 92: Strength and elastic properties for different mineral size distribution Scenarios. Scenario 1: uniform size of all minerals; Scenario 2: multiple sizes without standard deviation; Scenario 3: multiple sizes with standard deviation.	189
Figure 93: Crack amounts and types developing in compression tests for different mineral size distributions. Scenario 1: uniform size of all minerals; Scenario 2: multiple sizes without normal distribution; Scenario 3: multiple sizes with normal distribution.....	190
Figure 94: Influence of random distribution of minerals and particles on Mohr-Coulomb failure envelope.	192
Figure 95: Bonded particles (yellow) overlaid on the grain structure (left) and parallel bonds (grey) between particles representing the intact minerals and smooth joint contacts (red) representing the grain interfaces (right).....	203
Figure 96: Evolution of vertical stress and amounts of micro cracks with 40 MPa confining pressure (calibrated Aue granite model).....	205
Figure 97: Fracture patterns resulting from compression tests with different confining pressures (P_c) at 50% below failure stress (blue = grain boundary tensile cracks, green = grain boundary shear cracks, red = grain tensile cracks, black = grain shear cracks).....	206
Figure 98: Influence of mineral size on crack patterns for different average mineral diameters (0.5 mm and 3 mm) and different mineral size distributions (Scenario 1 = all minerals have the same diameter of 1.35 mm and Scenario 3 = all minerals have different sizes: quartz = 5 ± 2.5 mm, plagioclase = 3 ± 1.5 mm, orthoclase = 2 ± 1 mm, mica = 0.5 ± 0.25 mm).....	207
Figure 99: Influence of mineral and particle random distribution on crack pattern after a confined compression test with 40 MPa confining pressure. The macroscopic rupture paths change with mineral and particle distribution, but the relative amounts of each crack type stays the same.	208
Figure 100: Influence of mineral and mineral boundary micro properties on unconfined (left) and confined strength with 10 MPa (center) and 40 MPa (right) confining pressure. Each property was set	

separately to a value of +50 % above (dark grey) and -50% below (light grey) the calibrated base case value.	209
Figure 101: Influence of mineral and mineral boundary micro properties on amount and type of micro cracks at peak load during compression tests.	210
Figure 102: Influence of mineral and mineral boundary micro properties on amount and type of micro cracks at peak load during compression tests.	211
Figure 103: Fracture patterns resulting from a confined compression test with 40 MPa confining pressure for different particle sizes.	212
Figure 104: Fracture patterns resulting from confined compression tests with 40 MPa confining pressure for increased/decreased parallel bond normal strengths and parallel bond cohesions by 50%.	213
Figure 105: Fracture patterns resulting from confined compression tests with 40 MPa confining pressure for increased/decreased values of the smooth joint cohesion and friction angle.	214
Figure 106: Fracture patterns resulting from confined compression tests with 40 MPa confining pressure for different parallel bond friction angles.	215
Figure 107: Influence of mineralogy on compressive strengths.	218
Figure 108: Influence of mineralogy on number and type of cracks at failure of an unconfined compression test.	219
Figure 109: Crack patterns resulting from a confined compression test with 40 MPa confining pressure for different model sizes (width x height). Increasing the model size gives more distinct rupture paths, but the relative amounts of micro cracks are the same.	220
Figure 110: Intact (a), aligned fractured (b) and displaced fractured (c) samples were tested in the triaxial cell. A displacement of 1 mm was maintained by putting two layers of heat shrink tube (with 0.5 mm thickness each) on half of the samples cross-sections as indicated by the black bars.	230
Figure 111: Top view of Sample 31 (left) and side view of Sample 34 (right).	231
Figure 112: Triaxial test cell with sample (left) and close-up on a sample installed in the triaxial test cell (right). The sample is equipped with one circular and two axial strain gauges. Additionally, the temperature is measured on top and bottom of the sample.	232
Figure 113: Confining pressure change with time for the Sierra granite sample.	233
Figure 114: Sample permeability over time and effective confining pressure cycles for the intact Sample 34.	237
Figure 115: Circumferential strain of the intact Sample 34 changing with effective confining pressure (left) and time (right). Only the periods with constant confining pressure (2 MPa and 50 MPa) are shown on the right.	238
Figure 116: Permeability development of samples with aligned fracture surfaces under cyclic loading conditions.	239
Figure 117: Variation of circumferential and axial strain of samples with aligned fracture surfaces with effective confining pressure.	240
Figure 118: Variation of mechanical and hydraulic apertures of samples with aligned fracture surfaces with effective confining pressure.	241
Figure 119: Permeability development of samples with displaced fracture surfaces under cyclic loading conditions.	242
Figure 120: Variation of circumferential strain with effective confining pressure for the samples with displaced fracture surfaces.	243

Figure 121: Variation of calculated mechanical and hydraulic apertures with effective confining pressure.	244
Figure 122: Fracture permeability development of samples with aligned fracture surfaces over time.	245
Figure 123: Variation of circumferential strain with time during periods of constant effective confining pressure for samples with aligned fracture surfaces.	245
Figure 124: Variation of calculated mechanical and hydraulic apertures with time for samples with aligned fracture surfaces.	246
Figure 125: Fracture permeability development of all fractured samples over time.	247
Figure 126: Variation of circumferential strain with time for samples with displaced fracture surfaces.	248
Figure 127: Variation of calculated mechanical and hydraulic apertures with time.	248
Figure 128: 3D view of the scanned fracture surfaces.	249
Figure 129: Variation of the variogram fractal dimensions (D_{va}) with the profiles parallel to the x-axis of the digitized fracture surfaces shown in Figure 128.	251
Figure 130: Comparison of measured fracture permeabilities to selected literature data from fractures in granitic rocks (Pratt <i>et al.</i> 1977; Gale 1982; Iwano <i>et al.</i> 1995; Hakami <i>et al.</i> 1996; Chen <i>et al.</i> 2000; Lee <i>et al.</i> 2002; Watanabe <i>et al.</i> 2008; Watanabe <i>et al.</i> 2009). The red lines indicate how many fractures are needed with the specific fracture permeability to achieve the design goals of an EGS project in a basement rock for a case study presented in Hofmann <i>et al.</i> (2014; data from Fig. 27).	252
Figure 131: Comparison of measured fracture permeabilities to selected literature data (Fredd <i>et al.</i> 2000; Guiterrez <i>et al.</i> 2000; Cho <i>et al.</i> 2012; Briggs <i>et al.</i> 2014; Zhang <i>et al.</i> 2014) from sedimentary rocks (sandstones and shales).	254
Figure 132: The two dimensional horizontal discrete element hydraulic fracturing model showing the particles, the principle stress directions and the injection point locations for the base case model.	272
Figure 133: Setup of an exemplary FEM model including the two horizontal wells. The FE mesh is refined around wells and fractures.	275
Figure 134: Base case completion design, treatment design, fracture permeability and stress (left) and simulated fracture network (right).	278
Figure 135: Fluid pressure at each injection domain during the treatment. In each stage 360 m ³ of water was injected at 100 l/s in one hour.	279
Figure 136: Maximum (left) and minimum (right) horizontal stress measured within a circle of 100 m radius around each injection point.	279
Figure 137: Effect of completion designs 1 - 8 on fracture pattern (blue=injection points, black=tensile fractures, red=shear fractures). For each scenario the schematic completion design and the resulting fracture pattern are shown.	281
Figure 138: Effect of completion designs 9 - 16 on fracture pattern (blue=injection points, black=tensile fractures, red=shear fractures). For each scenario the schematic completion design and the resulting fracture pattern are shown.	282
Figure 139: Effect of stage spacing on fracture pattern (black=tensile fractures, red=shear fractures).	283
Figure 140: Effect of well deviation on fracture pattern (black=tensile fractures, red=shear fractures).	284
Figure 141: Effect of well spacing on fracture pattern (black=tensile fractures, red=shear fractures).	285
Figure 142: Effect of treatment design on fracture pattern (black=tensile fractures, red=shear fractures).	286
Figure 143: Effect of fracturing fluid viscosity on the resulting fracture pattern (black=tensile fractures, red=shear fractures).	287

Figure 144: Influence of in-situ stress field on hydraulic fracture development (black=tensile fractures, red=shear fractures).....	288
Figure 145: Influence of randomly distributed natural fracture networks 1-8 on hydraulic fracture development (green=pre-existing fractures, black=tensile fractures, red=shear fractures, blue=tensile failure of pre-existing fracture, magenta=shear failure of pre-existing fracture).	289
Figure 146: Influence of randomly distributed natural fracture networks 9-12 on hydraulic fracture development (green=pre-existing fractures, black=tensile fractures, red=shear fractures, blue=tensile failure of pre-existing fracture, magenta=shear failure of pre-existing fracture).	290
Figure 147: Influence of flow channel permeability (as a function of normal stress) on hydraulic fracture development.	291
Figure 148: Pressure (left) and temperature (right) distribution of the base case model after 30 years of production.....	292
Figure 149: Influence of engineering factors on number of individual broken bonds (cracks), number of major flow paths between both wells, productivity index and production temperature after 30 years.	293
Figure 150: Influence of natural factors on number of individual broken bonds (cracks), number of major flow paths between both wells, productivity index and production temperature after 30 years.	296

CHAPTER 1: INTRODUCTION

1.1 BACKGROUND

The Athabasca oil sands located in Northern Alberta are Canada's main oil reserves and the third largest oil reserves worldwide (Government of Alberta, 2014; Hein et al., 2013). These unconventional heavy oil resources, however, are challenging and expensive to exploit and the production has a huge environmental footprint (e.g. CO₂ emissions, natural gas use, water use, and land use). On the other hand, due to the increasing energy demand and limited conventional oil resources, the price of crude oil increased significantly in the last decade making the production of oil from these unconventional resources economical. As a consequence, the exploitation of the oil sands increased significantly in recent years (Rahnama et al., 2013) and a further increase in oil sands development is expected (ERCB, 2013).

About 20 percent of Alberta's oil sands reserves are mineable from the surface (0 - 70 m), whereas the remaining 80 percent (>70 m) are recoverable only by in-situ methods (Government of Alberta, 2014; CAPP, 2014). Both processes need significant amounts of hot water/steam (i.e., about 170 million m³ per year; CAPP, 2012). For surface mining operations, water at temperatures between 40°C and 60°C is used to separate the bitumen from the sand (Long et al., 2005). The main technologies for in-situ recovery are steam assisted gravity drainage (SAGD; Butler et al., 1981) and cyclic steam stimulation (CSS; e.g. Batycky et al., 1997) requiring steam at temperatures over 200°C.

Currently, water is obtained from the Athabasca River and heated up to the desired temperatures by burning huge amounts of natural gas, which creates severe greenhouse gas (GHG) emissions. To produce 1 GJ of energy, at least 26.1 m³ of natural gas needs to be burned (BFIN, 2013). Oil sands mining, upgrading, and in-situ extraction accounted for approximately 7.8 % (about 55 Mt CO₂-eq.) of the total GHG emissions of Canada in 2011 (Environment Canada, 2013). Since GHGs are accelerating climate change, it has become a political intent to reduce GHG emissions from oil sands extraction and processing. However, even though GHG emissions per barrel of bitumen were decreased by approximately one quarter in the last 20 years (Government of Alberta, 2014), the total emissions continue to increase due to larger oil sands production every year.

Using geothermal energy, with greenhouse gas (GHG) emissions of 2-3 gCO₂-eq./MJ (Bertani and Thain, 2002), to generate the hot fluids needed for oil sands extraction and processing helps to lower GHG emissions by at least 53 gCO₂-eq./MJ compared to the combustion of natural gas, with GHG emissions of 56 gCO₂-eq./MJ (NRC, 2008).

To produce geothermal energy, the heat stored in the subsurface is commonly extracted from a permeable formation containing hot fluids by producing these fluids through one or more production well(s). On the surface, the heat is extracted from the fluid by surface heat exchangers and used either for electricity generation, different direct applications (Lindal et al., 1973) or a combination of both. The cooled fluid is re-injected into the reservoir. The heat of the rock mass is transferred to this cold fluid, which is heated up again while traveling through the fracture network to the production well(s). Alternative approaches are for example single well systems (e.g. Orzol et al., 2005). More details about different aspects of geothermal energy extraction are given, for example, in Dickson and Fanelli (2003), Tester et al. (2006), Gupta and Roy (2007), Huenges and Ledru (2010), Grant and Bixley (2011), DiPippo (2012), Stober and Bucher (2013), and Watson (2014).

Starting in 2006, the company consortium ‘GeoPos’ investigated the potential of geothermal energy for oil sands processing purposes (Majorowicz et al., 2012), but the project was discontinued in 2008 because of financial hurdles. From 2010 until 2015 a German-Canadian research partnership (Helmholtz-Alberta-Initiative, HAI) investigated the potential of geothermal energy to provide heat for oil sands processing and extraction. The presented thesis is part of these efforts.

The geology, mineralogy and temperature of the Western Canadian Sedimentary Basin (WCSB) and the underlying Precambrian basement in Alberta was investigated, for example, by Majorowicz et al. (2014), Majorowicz et al. (2010), Chan, (2013), and Walsh, (2013). **Figure 1** shows that in the vicinity of the oil sands mining areas surrounding Fort McMurray, where huge amounts of heat is currently needed, the geothermal gradient is relatively low (20 °C/km) and the granitic basement is reached at a depth of about 500 m below the surface. Here, heat for in-situ extraction cannot be provided by geothermal energy because temperatures of > 200°C are expected to be reached below 10 km depth, which is presently too deep for economic drilling. However, lower temperatures needed for oil sands processing can be found at lower depths where

heat extraction might be economical. Considering a wellbore temperature loss of 10°C from the subsurface to the surface and a temperature drawdown of 30°C in 30 years of heat production, the required subsurface temperatures are about 80 – 100°C. These temperatures are expected to be reached in a depth of 4 – 5 km. Studies on the only deep well in the region (i.e., Hunt well, 2,300 m below surface) and other granites in general show that in these depths low porosity, low permeable, and potentially fractured granitic basement rocks can be expected (Chan et al., 2012; Kalinina et al., 2012; Majorowicz et al., 2014; Majorowicz et al., 2010).

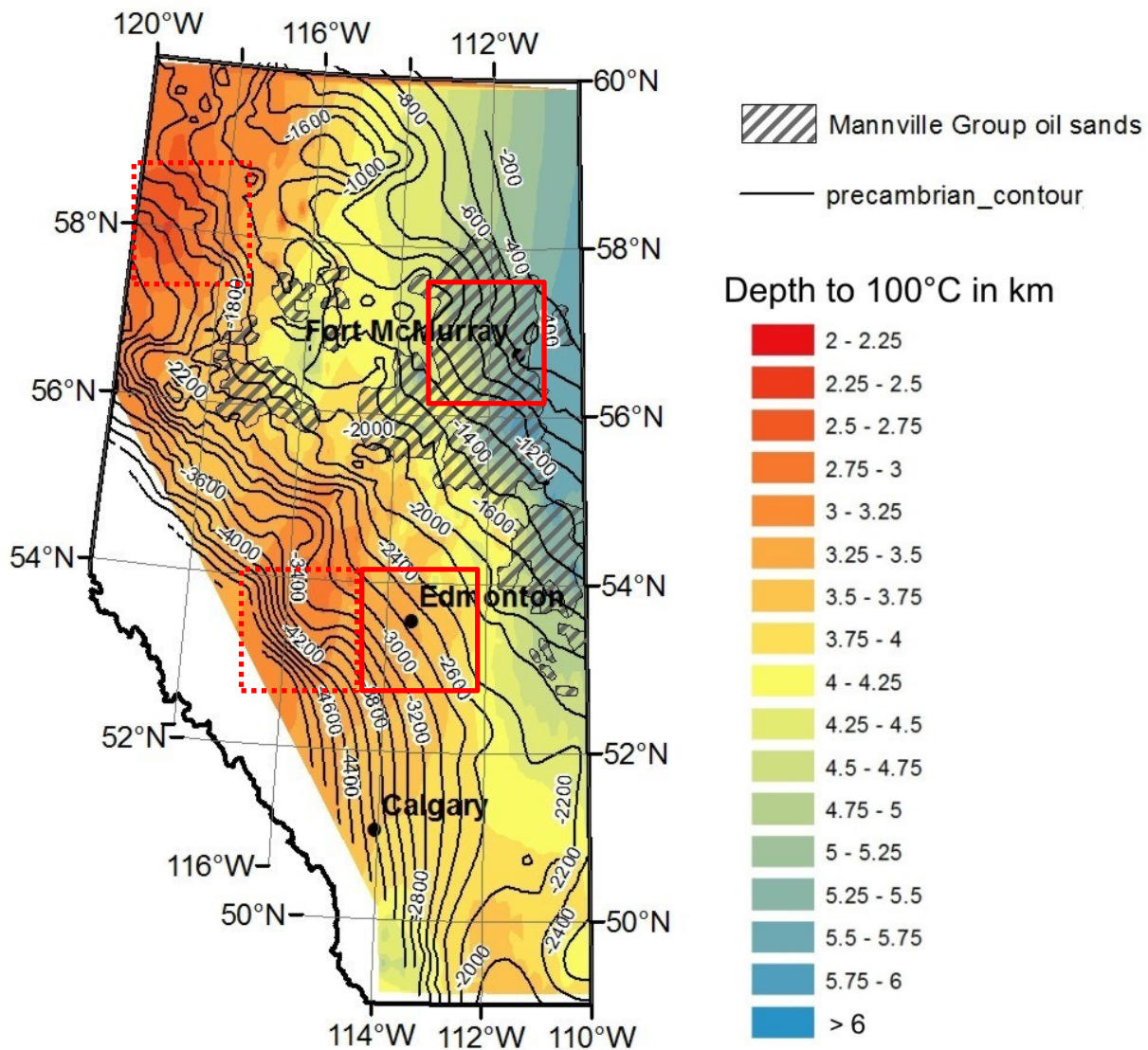


Figure 1: Temperature map of Alberta showing the depth to drill to reach a temperature of 100°C, the depth of the Precambrian basement rocks, and the oil sands deposits (after Majorowicz and Weides, 2012). The two current research areas are shown in bold boxes. Potential future study areas are shown in dotted boxes.

Since the permeability of these basement rocks is not expected to be sufficient for economic heat extraction ($10^{-15} - 10^{-20} \text{ m}^2$), stimulation treatments need to be performed to develop or improve fluid pathways and heat exchanger areas. Such an enhanced (or engineered) geothermal system is commonly referred to as EGS (e.g. Schulte et al., 2010).

As an alternative approach to lower both Alberta and Canada's GHG emissions and to provide a renewable independent base load energy source, other areas in Alberta were evaluated for their geothermal energy potential and possible applications (Hofmann et al., 2014a; Weides and Majorowicz, 2014). These alternative areas may also need to be developed as EGS (Hofmann et al., 2014a).

The required temperature of the produced water depends on the application (Lindal et al., 1973). As stated earlier, for the processing of mined oil sands, a temperature of $40 - 60^\circ\text{C}$ is needed (Long et al., 2005). Therefore, a sufficient thermal performance of a reservoir for oil sands processing purposes is a minimum production wellhead temperature of 60°C throughout the anticipated lifetime of the system.

A sufficient hydraulic performance is generally defined by a minimum productivity index (PI) or a maximum impedance (I). The PI is defined as the flow rate divided by the pressure drawdown in the production well. I is the difference between inlet pressure (bottom hole pressure of injection well) and outlet pressure (bottom hole pressure of production well) divided by the production rate. In order to be economic, EGS systems generally need a minimum PI of 10 l/s/MPa or a maximum impedance of 0.1 MPa/l/s (Baria et al., 1999; Jung, 2013).

To evaluate the efficiency of the simulated hydraulic fracturing treatments in terms of hydraulic performance, the productivity enhancement is calculated based on the productivity indices before ($PI_{\text{pre-frac}}$) and after ($PI_{\text{post-frac}}$) the fracturing treatment. One divided by the other gives the hydraulic performance increase in terms of folds of increase ($\text{FOI} = PI_{\text{post-frac}}/PI_{\text{pre-frac}}$ [Economides and Nolte, 2000]).

Depending on temperature and application, flow rates between 50 and 150 kg/s ($50 - 150 \text{ l/s}$ for pure water) are needed for an economic geothermal energy production (Tester et al., 2006), which is usually achieved by conventional hydrothermal projects. However, the highest stable

production rate achieved so far by a stimulated EGS production well in granitic rock, which was initially unproductive, is about 30 l/s in Soultz-sous-Forêts (Majorowicz and Grasby, 2010).

In order to be economically competitive to the combustion of natural gas, geothermal energy has to be less expensive than 6 \$/GJ, assuming a current natural gas price of 3 \$/GJ (Alberta Energy, 2014) and 50% efficiency. The actual reference gas price in Alberta is subject to strong variability (e.g. 11 \$/GJ in January 2001 and 1.6 \$/GJ in May 2012 [Alberta Energy, 2014]).

Different technologies are used to improve the reservoir permeability and heat exchanger areas of geothermal systems (Schulte et al., 2010). Most of which are adapted from the hydrocarbon industry where they are commonly used to develop shale gas, coal bed methane, and tight oil, and to increase the productivity of depleting conventional reservoirs (Economides and Nolte, 2000; Economides and Martin, 2007).

For the development of EGS, the most common stimulation methods are (1) hydraulic stimulations, (2) chemical stimulations, and (3) thermal stimulations (Schulte et al., 2010). Because granites are generally low reactive and a relatively low reservoir temperature of <100°C, chemical and thermal stimulation techniques are a priori expected to be inefficient for EGS development in the Fort McMurray area. The most promising technology for permeability enhancement in this region are hydraulic stimulation treatments, which can include the creation of new tensile fractures and the shear failure of critically-oriented natural fractures by the injection of large amounts of water or other fracturing fluids, which might be mixed with proppants, into the formation (e.g. McClure and Horne, 2013a).

In a hydraulic stimulation treatment fluids are injected into a formation such that a new fracture initiates in intact rock and propagates into the formation and/or pre-existing fractures jack open and/or critically stressed pre-existing fractures fail in shear.

The basics and mechanics of the hydraulic fracturing technology can be found, for example, in Economides and Nolte (2000), Economides and Martin (2007), and Yew et al. (1997). An overview of the different hydraulic fracturing methods is given in Zimmermann et al. (2011) and Schulte et al. (2010). A historic outline of hydraulic stimulation treatments and the development of stimulation parameters can be found in Montgomery and Smith (2010). Since the first

commercial hydraulic fracturing treatment in 1949, the method has been used almost 2.5 million times worldwide. For the stimulation of deep geothermal systems in different rock types, between 100 m³ (Spa Urach) and 37,000 m³ (Soultz) of water have been injected at rates between 38 l/s (Soultz) and 150 l/s (e.g., Groß Schönebeck). Wellhead pressures between 10 MPa (Soultz) and 59 MPa (Groß Schönebeck) were recorded during treatments. Commonly multiple vertical, inclined or horizontal hydraulic fractures (depending on the stress field) are developed in vertical or deviated wells (e.g. Soultz, Schindler et al., 2008; Groß Schönebeck, Zimmermann et al., 2011).

Based on fluid type and proppant mass, hydraulic stimulation treatments can be classified into conventional gel-proppant fracturing, water fracturing, and hybrid fracturing treatments (Schulte et al., 2010).

In conventional treatments, high viscosity gels are injected into the target formation together with large amounts of proppants (e.g. sand or ceramics). In water fracturing, slickwater (water with additives like friction reducers) and no or only a limited amount of proppants is commonly used to create large low conductivity fractures. This method relies on the self-propping ability of the displaced fracture surfaces (Fredd et al., 2000). Hybrid fracturing treatments combine both methods by pumping a low viscosity fluid first to initiate and develop the fracture followed by higher viscosity fluid distributing proppants in the fracture or by the injection of intermediate viscosity fluids and intermediate amounts of proppants.

One can also distinguish between tensile fracturing and shear stimulation based on the stimulation mechanism (e.g. McClure and Horne, 2012). Tensile fractures are generated due to pressures above the fracturing pressure of the formation. If fluid injection would be stopped, a tensile fracture would close again. Hence, these fractures need to be propped open by proppants to create long term permeability (Economides and Nolte, 2000). In shear stimulation fluids are pumped at pressures below the fracturing pressure inducing shear slippage on critically oriented pre-existing fractures. Water fracturing and hybrid fracturing treatments are used to exploit the self-propping mechanism, which leads to a long-term fracture permeability increase due to the aperture increase between the two rough fracture surfaces which are not aligned with each other anymore. This mechanism is typically assumed to be valid in EGS, but might not always be present (McClure and Horne, 2013a).

There are two basic design concepts of stimulated fractures for EGS reservoirs. The classic approach is to induce parallel tensile fractures in an intact rock mass (Jung, 2013). More recent developments focused on the shear stimulation of pre-existing fracture networks (Jung, 2013). A third approach is the connection of faults/fracture zones to the wells (e.g. Hofmann et al., 2014b).

Since the early 1970s, more than a dozen industrial and research projects have developed Enhanced-Geothermal-Systems (EGS), also known as Engineered-Geothermal-Systems, Hot-Dry-Rock (HDR), Hot-Wet-Rock (HWR), or Hot-Fractured-Rock (HFR) systems (Tester et al., 2006; Jung, 2013). A detailed review of and lessons learned from EGS projects in granitic basement rocks and other rock types are given by Tenzer (2001), Karner (2005), Tester et al. (2006), Jung (2013), and Breede et al. (2013). However, so far, no commercial EGS project has been successfully completed in basement rocks (Jung, 2013). The engineering concept of these projects is the development of single permeable fractures or the stimulation of an already fractured reservoir volume by a limited number of hydraulic stimulation treatments in vertical or slightly deviated wells mainly performed in open hole sections. The main problems are insufficient production rates, thermal short-circuiting, and excessive water loss (Tester et al., 2006). It is only possible to develop a successful EGS if the current reservoir engineering and stimulation approach is improved and high enough production rates can be achieved.

Part of the reason for the lack of success is the limited field experience (Tester et al., 2006). With the exception of the Habanero EGS project in the Australian Cooper Basin (e.g. Wyborn et al., 2005; Wyborn, 2011), current field work focuses on the extension of existing hydrothermal fields (e.g. Berlín Geothermal Field [Rodríguez, 2003] or the Geysers Geothermal Field [Rutqvist et al., 2015]). The reasons for the limited field experience for EGS are the high costs and risks related to drilling, stimulation, and operation. Furthermore, the interacting thermal, hydraulic, mechanical, and chemical processes governing EGS development and operation are very complex. As a result, many problems associated with hydraulic stimulation of granitic basement rocks, as well as fluid flow and heat transfer in complex fractured rock, are not yet resolved. The major question that remains unanswered is how it is possible to achieve economic flow rates of hot water/steam from an impermeable rock without producing a thermal short circuit (Tester et al., 2006).

The purpose of this thesis is to identify whether or not geothermal energy can be an alternative source of hot water for oil sands processing and other direct applications and how economic amounts of heat can be extracted from the granitic basement rocks in Northern Alberta. Additionally, the proposed research aims to improve the understanding of hydraulic stimulation treatments and EGS operation in deep granitic basement rocks. To answer these questions, different numerical simulators are used.

1.2 NUMERICAL SIMULATION OF HYDRAULIC STIMULATION TREATMENTS

A large variety of hydraulic stimulation models is available today. Reasons for this diversity are an uncertainty about the stimulation mechanism, the difficulty of validating the different model assumptions, the large number of different numerical methods, and different choices about balancing realism and computational efficiency (McClure and Horne, 2013b). First approaches to describe hydraulic stimulation treatments were the two analytical constant height-2D models KGD (Khristianovich and Zheltov, 1955; Geertsma and de Klerk, 1969) and PKN (Perkins and Kern, 1961; Nodgren, 1972) and the penny-shaped model (e.g. Yew et al., 1997).

Based on these models, several commercial pseudo 3D, planar 3D, or full 3D hydraulic fracturing simulators such as FRACPRO (Cleary, 1994), MFrac (Meyer, 2011) or GOHFER (Barree, 1983) have been developed. These are routinely used for prediction, real-time analysis, and evaluation of hydraulic stimulation treatments not only in the oil and gas industry, but also for geothermal applications (Warpinski et al., 1994; Weijers et al., 2005; Adachi et al., 2007). These models commonly assume hydraulic fracture development as a single planar fracture opening in tensile mode.

However, since it was understood that hydraulic fracture growth might be more complex in some cases (e.g. if pre-existing fractures are present [e.g. Cipolla et al., 2008]), more complex models have been developed to investigate different aspects of hydraulic stimulation treatments. The following summary of some of these models is based on McClure and Horne (2013b). These models include effective continuum (finite element method or finite difference method) models that average flow from multiple fractures into effective continuum properties (e.g. Lee and

Ghassemi, 2011; Vassilellis et al., 2011; Kelkar et al., 2012), hybrid models that combine aspects of continuum models and discrete fracture network (DFN) models (e.g. Palmer et al., 2007; Xu et al., 2010; Meyer and Bazan, 2011), and pure DFN models (e.g. Bruel, 2007; Sausse et al., 2008; Dershowitz et al., 2010).

Some DFN models neglect stress interaction to reduce complexity and improve efficiency and either upscale the DFN to an effective continuum model (e.g. Willis-Richards et al., 1996; Jing et al., 2000; Kohl and Mégel, 2007; Wang and Ghassemi, 2012) or use the DFN directly without upscaling (e.g. Bruel, 2007; Sausse et al., 2008; Dershowitz et al., 2010). Other models include stresses induced by deformation. These numerical methods include finite element methods (e.g. Rahman and Rahman, 2009; Lee and Ghassemi, 2011; Fu et al., 2013; Kelkar et al., 2012), finite difference methods (e.g. Hicks et al., 1996; Taron and Elsworth, 2009; Roussel and Sharma, 2011), boundary element methods (e.g. Cheng, 2009; Weng et al., 2011; Jeffrey et al., 2012; Sesetty and Ghassemi, 2012), block-spring models (e.g. Baisch et al., 2010), extended finite element methods (e.g. Dahi-Taleghani and Olson, 2011; Keshavarzi and Mohammadi, 2012), distinct element methods (e.g. Pine and Cundall, 1985; Last and Harper, 1990; Rachez and Gentier, 2010; Nagel et al., 2011), hybrid finite element/discrete element methods (e.g. Rogers et al., 2010), and particle-based discrete element methods (e.g. Min et al., 2010; Damjanac et al., 2010; Deng et al., 2011; Zhao and Young, 2011).

The majority of published results of coupled geomechanical-fluid flow models in DFNs, however, are limited to a small number of fractures (McClure and Horne, 2013b). This is because most of these methods have problems with large complex fracture networks. Finite element (FEM) and finite difference (FDM) methods require refined discretization around the fractures, which leads to a very large number of elements. The boundary element methods (BEM) do not need refinement around fractures, but if applied directly to large models, require the solution of dense matrices or iterative and approximate methods to improve efficiency. Also, the BEM have the disadvantage that they typically cannot handle arbitrary rock properties, heterogeneity, and low angle fracture intersections. Extended finite element methods (XFEM, e.g. Shakib and Jalalifar, 2013) are a promising technique for hydraulic stimulation modeling but this relatively new technique has not yet been demonstrated on complex fracture networks (McClure and Horne, 2013b).

Particle-based distinct element methods have the advantage of being able to handle arbitrary rock properties and avoid discretization around fractures. Also, the grain-based modeling (GBM) approach (Potyondy, 2010a) has the potential to model complex fracture development on mineral scale. The macroscopic properties (e.g. Young's modulus and Poisson's ratio) are emergent properties of the model. The model input (e.g. bond strengths and coarseness of the discretization) has to be calibrated with trial and error to match the observed behavior (Cundall, 2001; McClure and Horne, 2013b).

DEM codes like UDEC (Itasca, 2011)/3DEC (Itasca, 2013) and PFC2D (Itasca, 2008)/PFC3D (Itasca, 2014) have been increasingly used in the past years to investigate water fracturing treatments performed in geothermal settings in two and three dimensions including coupled fluid-mechanical behavior, fracture initiation and propagation of new fractures, and slip and opening along joints in a pre-existing DFN (e.g. Riahi and Damjanac, 2013; Riahi et al., 2014; Hazzard et al., 2002; Yoon et al., 2013; Yoon et al., 2014).

Jing (2003) gives an overview about numerical methods used in rock mechanics in general, which include the methods described above.

From this great variety of methods, the conventional pseudo 3D hydraulic fracturing model MFrac, the DFN model MShale, and the particle based DEM model Particle Flow Code in 2D (PFC2D) were used in this study and are briefly described in the following sections.

1.2.1 Conventional hydraulic fracturing model: MFrac

The hydraulic fracturing simulator MFrac (Meyer, 2011) is formulated between a pseudo-3D and a full 3D model. For decades, this software has been routinely used to model hydraulic fracturing treatments in the hydrocarbon industry (e.g. Warpinski et al., 1994) and was also previously applied to model the stimulation of geothermal reservoirs (e.g. Van der Hoorn et al., 2012). The model comes with an extensive material database that makes it possible to test different fracturing fluids and proppants. In MFrac fractures initiate and develop in tensile mode only. A fracture initiates or propagates if the net fracture pressure is above the critical stress, which can be specified as a constant value ($\sigma_{c|min}$, tensile strength) or calculated based on the fracture

toughness leading to a decrease in critical stress with increasing fracture length. Calculations are based on mass conservation, momentum conservation, continuity and a width-opening pressure equation. Proppant transport and heat transport are fully coupled with fracture propagation. Theoretical background of the software is provided by Meyer (2011). The modeling results can be directly compared to the DFN simulator MShale, which may be seen as an extension of MFrac which includes natural fractures and multiple fracture planes.

1.2.2 Discrete fracture network model: MShale

MShale is the DFN version of the conventional hydraulic fracturing simulator MFrac described before (**Section 1.2.1**), which is specifically designed for hydraulic fracturing treatments in tight and naturally fractured formations. Such as MFrac, the semi-analytical simulator is formulated between a pseudo-3D and full 3D model, including a coupling between fracture propagation and proppant transport (Meyer, 2011). The main reasons for this choice are the 3D modeling capabilities, an extensive material database, and the possibility to directly compare the conventional fracturing simulator MFrac with the DFN simulator MShale.

Fracture initiation and development is based on tensile opening of new or natural fractures within intact or fractured rock. The influence of thermal stresses is neglected. Other major assumptions are that fractures can only develop in the three principle planes, interfacial joint dilatancy is ignored, primary and secondary fractures have an elliptical shape and the stimulated reservoir volume has an ellipsoidal shape.

MShale accounts for the primary hydraulic fracture, which is connected to the wellbore and a network of fractures connected to it that can be activated and opened. Different proppant transport options are available to model the proppant transport in such a network. The fluid flow may be altered by changing fracture friction model parameters and a wall roughness coefficient. Tip effects may be included as well.

The model is based on a methodology similar to that presented by Warren and Root (1963). The simulator is based on a network grid system. Secondary fractures are opened if the net fracture pressure overcomes the value of the stress difference between the maximum and minimum

horizontal stresses (to open vertical secondary fractures) or between the vertical and minimum horizontal stresses (to open horizontal secondary fractures). The fundamental first-order DFN mass and momentum conservation equations and the width-opening pressure equation are based on a self-similar solution methodology utilizing a pseudo-3D ellipsoidal approach (Meyer and Bazan, 2011). Further details are described in Meyer (2011) and Meyer and Bazan (2011).

1.2.3 Discrete element method: Particle Flow Code

In the two dimensional discrete element method (DEM) model Particle Flow Code 2D (PFC2D; Itasca, 2008), the 3D rock mass is represented in 2D by an aggregate of circular or cylindrical particles with finite height which are bonded together at their contact points with finite strength and a finite volume of cementation to resist Mode I (tensile), Mode II (shear) and rotational loadings (Yoon et al., 2015). These parallel bonds (Potyondy and Cundall, 2004) can break according to the Mohr-Coulomb failure criterion in Mode I and Mode II under an applied load. Discrete pre-existing fractures are represented by the smooth joint contact model (Mas Ivars et al., 2008). In PFC2D the law of motion is applied to each particle and a force-displacement law is applied to each contact at each time step. Shear and normal displacements and forces are related by shear and normal stiffness.

The flow of a viscous fluid is simulated by assuming that each bonded particle contact is a flow channel, which connects two fluid reservoirs that can store fluid. The fluid flow rate is governed by the cubic law assuming laminar flow between two smooth parallel plates. It is possible to implement functions that relate the effective normal stress on a contact to the aperture of the corresponding flow channel (Yoon et al., 2015).

More details about PFC2D are given by Potyondy and Cundall (2004). Detailed descriptions of the fluid flow algorithm and the representation of discrete in-situ joints are given by Yoon et al. (2014).

1.2.4 Grain-based modeling: Particle Flow Code

In earlier studies, the particle model (e.g. PFC2D and PFC3D) was used directly to simulate geomechanical experiments (e.g. Potyondy, 2007; Potyondy and Hazzard, 2008). However, it became apparent that the ratio between tensile strength and compressive strength is significantly greater in the model than observed in experiments, and the failure envelope of the particle model is linear and gives a much lower friction angle as compared to laboratory results (Cho et al., 2007). These deficiencies can be reduced by introducing a clumped particle model, where several particles are clumped together to any arbitrary shape. These models already result in a better calibration of tensile vs. compressional strength, stress-strain behavior, non-linear failure envelope, as well as crack distribution and rupture path (Cho et al., 2007; Yoon et al., 2012). These clumped particles, representing the minerals, cannot break. However, in laboratory studies, it was found that fractures follow not only mineral boundaries, but also intersect minerals and grain crushing occurs (e.g. Mosher et al., 1975; Haimson, 2005; Erarsalan and Williams, 2012). Hence, the grain-based modeling (GBM) approach was developed that extends the bonded-particle model (BPM, Potyondy and Cundall, 2004) by using the smooth-joint logic (Mas Ivars et al., 2008) to mimic a grain-based material (Potyondy, 2010a).

PFC2D GBMs simulate deformable, breakable, polygonal grains. This mimics the real microstructure of crystalline rocks more closely and enables matching the ratio between unconfined-compressive strength and direct-tensile strength more closely (Potyondy, 2010a). A GBM modeling approach also exists for UDEC where the grains cannot break (Lan et al., 2010).

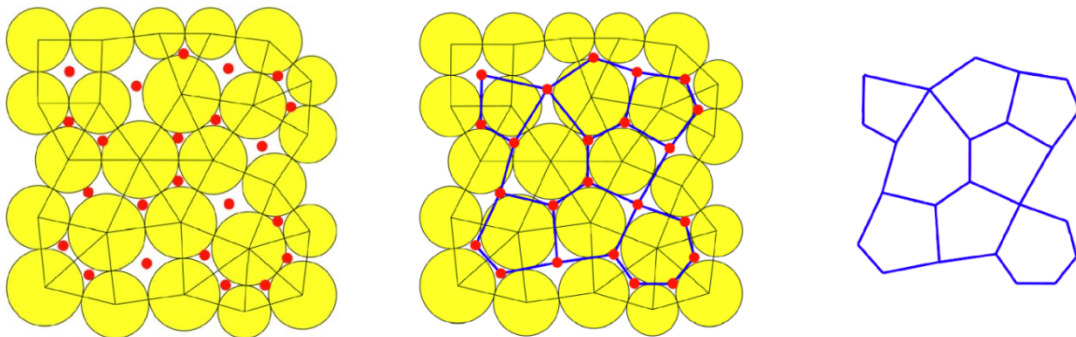


Figure 2: Initial disk packing produced by PFC2D showing spheres (yellow circles), contacts (black lines), and internal-void centroids (red dots; left). The mineral geometry consists of polygons; one for each internal sphere, with nodes at internal-void centroids (center). The generated mesh is shown on the right (after Potyondy, 2010c).

PFC2D Grain-based models are constructed by (1) generating a polygonal mineral structure that has similar statistical properties as real rock using a disk-packing scheme within PFC2D (**Figure 2**), (2) constructing the parallel-bonded material using the procedure described in Potyondy and Cundall (2004), (3) overlaying the mineral structure on the base material and modifying particles and contact properties to correspond with the minerals, and (4) associating each polygon edge with an interface consisting of smooth-joint contacts. The mineral structure generation procedure and the grain-based modeling procedure are described in detail in Potyondy (2010a-c).

1.3 NUMERICAL SIMULATION OF EGS OPERATION

There are four main approaches for reservoir simulation. (1) The most common way to model temperature and fluid flow in conventional hydrocarbon reservoirs and hydrothermal reservoirs is the Finite Difference Method (FDM, e.g. ECLIPSE – Schlumberger, 2008; TOUGH2 – Pruess, 1991; CMG STARS – CMG, 2011). (2) Specifically for large, multiwell, heterogeneous, multiphase simulations, the streamline method may be used (e.g. Thiele et al., 1997; Johansen et al., 2013). (3) If mechanical effects also need to be considered and complex geometries need to be included, the Finite Element Method (FEM) can be used (e.g. TOUGH-FLAC; Rutqvist and Tsang, 2003). (4) A relatively new approach used mainly for computational fluid dynamics computations is the Finite Volume Method (FVM). A review of numerical models for EGS is given by Sanyal et al. (2000). To model the coupled hydro-thermal reservoir behavior of complex fractured EGS reservoirs the FDM code CMG STARS and the FEM code OpenGeoSys (Kolditz et al., 2012) are used and described in more detail in the following sections.

1.3.1 Finite difference model: CMG STARS

Coupled multi-phase fluid flow and heat transport can be modeled using the commercial finite difference reservoir simulator CMG STARS (CMG, 2011). The model can additionally include mechanical effects. Fluid viscosity and density change depend on pressure and temperature. Fractures can be represented in multiple ways using single or dual porosity/permeability approaches. For the single porosity approach high conductivity fracture cells representing the fractures are located within low permeability rock matrix cells. In the vicinity of fractures and

wells the grid has to be locally refined to account for the high pressure and temperature gradients. Additionally, a wellbore model can be included.

1.3.2 Finite element model: OpenGeoSys

For the evaluation of the coupled thermal, hydraulic, mechanical, and chemical reservoir behavior resulting from the stimulation treatments the open source 3D finite element simulator OpenGeoSys (Wang and Kolditz, 2007, Kolditz et al., 2012) can be used. OpenGeoSys (OGS) uses a hybrid approach combining discrete fracture and continuum modeling for simulating fluid flow, heat transport, stress dependent fracture closure and chemical precipitation and dissolution in fractured and faulted rocks (Cherubini et al., 2013). Two-dimensional and three-dimensional permeable discrete fractures are superimposed on a continuous volume representing the porous rock matrix (Cacace et al., 2013). Fracture elements and porous media elements share the same nodes. However, this approach is only applicable when the 2D elements represent a preferential flow path, e.g. a dominant flow path along the fractures and faults (Segura and Carol, 2004; Dietrich et al., 2005). Fluid flow and heat transport in fractured porous media are described by partial differential equations that are solved based on initial and boundary conditions. Further details about governing equations and numerical schemes in OGS are given, for example, by Watanabe et al. (2010) and Watanabe et al. (2012).

1.4 STATEMENT OF THE PROBLEMS AND OBJECTIVES

As pointed out in **Section 1.1**, there are two main heat consumers in Northern Alberta: (1) oil sands extraction, processing and upgrading facilities near Fort McMurray and (2) private, commercial, institutional, and industrial buildings in the metropolitan area of Edmonton. The required heat is currently produced by burning natural gas with significant GHG emissions and costs.

To reduce GHG emissions and save valuable gas resources, government (Helmholtz-Alberta-Initiative, www.helmholtzalberta.ca) and industry (industry consortium –“GeoPos” – GeoPower in the oil sands from 2004 – 2008, Majorowicz et al., 2010) are looking for an alternative heat

source that is able to reduce GHG emissions and save natural gas resources at competitive costs. As shown before, geothermal energy is a potential renewable energy source with very low CO₂ emissions that can potentially be utilized for oil sands processing and other direct applications by using stimulation technologies to develop enhanced geothermal systems (EGS).

An initial rough estimation about the potential of geothermal energy for oil sands processing and other purposes in Alberta has already been documented (Majorowicz et al., 2010 and Majorowicz and Grasby, 2014) and a first reservoir simulation study about EGS for oil sands production was carried out by Pathak et al. (2014). However, a detailed numerical simulation study of hydraulic stimulation treatments and thermal and hydraulic performance of the developed fracture network to estimate the potential heat output of EGS for oil sands processing and other direct applications in Alberta including economic and environmental aspects is missing.

The main objective of this thesis is to respond to the question whether and how low enthalpy enhanced geothermal systems can be utilized, as an alternative heat source to burning natural gas, for oil sands processing in the Fort McMurray area and direct heating applications in the metropolitan area of Edmonton in terms of (1) technical feasibility, (2) economic viability, and (3) environmental benefits (CO₂ emission reduction and natural gas savings potential).

The following questions, which arise from this major objective, are investigated:

- Which natural and engineering factors govern fracture development in granites at micro and field scale, how can they be utilized and how can they be simulated numerically?
- Which processes and parameters govern and improve the hydraulic and thermal performance of an EGS in granites and sediments during operation (water circulation and heat extraction), how can they be utilized and how can they be simulated numerically?
- What are the requirements for a suitable EGS project to generate heat needed for both applications (well design, fracture network structure, operating conditions)?
- What are suitable reservoir engineering concepts to develop EGS projects for the proposed applications?
- What are the conditions to develop highly branched and well-connected fracture networks for efficient heating of the injected cold water?
- How permeable are hydraulic fractures subject to elevated stresses within deep reservoirs?

As mentioned above, there is a vast amount of heat stored in the earth's crust. However, the amount of heat that can actually be recovered economically largely depends on the understanding of the processes and parameters that enhance fluid flow. Therefore, the focus of the study is on the investigation of the fracture development during stimulation and operation. An improved understanding of the relative importance of processes governing the stimulation treatment and the reservoir operation are the key to develop suitable reservoir engineering concepts that need to be proposed for heat extraction from the deep low enthalpy and low permeability granitic basement rock in Northern Alberta. This would also support development of EGS in other areas in the world with similar conditions.

1.5 SOLUTION METHODOLOGY

To answer the questions stated in **Section 1.4**, the solution methodology presented in **Figure 3** was used. As shown in this figure, the work was divided into three distinct phases. In each phase, different numerical models were used that are able to model different processes, but the general workflow remains the same. First, conventional, well established methods were used and their constraints were explored. In later phases the model complexity increases to capture additional processes.

The general workflow for each stage is as follows. First, hydraulic stimulation treatments are simulated for the expected range of reservoir properties and different treatment parameters. The resulting stimulated fracture networks are then imported to a reservoir simulator. For different fracture networks and well arrangements, the thermal and hydraulic behavior of the reservoir is then modeled to evaluate the treatment efficiency in terms of hydraulic performance (productivity index, injectivity index, impedance) and thermal performance (temperature drawdown in the production well and cumulative produced thermal energy). Based on the produced thermal energy, the GHG emission reductions, natural gas savings and costs are calculated to see which natural and engineering factors improve thermal and hydraulic performance, and thereby improve economics and environmental benefits.

In Phase I, a conventional (planar 3D) fracturing simulator (MFrac) was used to model hydraulic stimulation treatments assuming the development of a single elliptical tensile fracture (Mode I

failure) in a homogeneous and intact rock mass. Fluid circulation through and heat extraction from these parallel fractures was subsequently modeled using the FDM simulator CMG STARS. The focus of this first phase was on the investigation of the influence of reservoir and treatment parameters on single tensile fracture development and the potential of conventional stimulation treatments with relatively simple assumptions.

In Phase II, the same reservoir simulator was used, but the hydraulic stimulation treatments were modeled with the DFN model MShale. MShale is based on MFract (tensile failure, homogeneous rock mass, elliptical fracture shapes) but takes additionally into account pre-existing fracture networks. Fractures can develop only parallel to the direction of the three principle stresses and the stimulated fracture network consists of a maximum of 3 individual fracture sets and has an ellipsoidal shape.

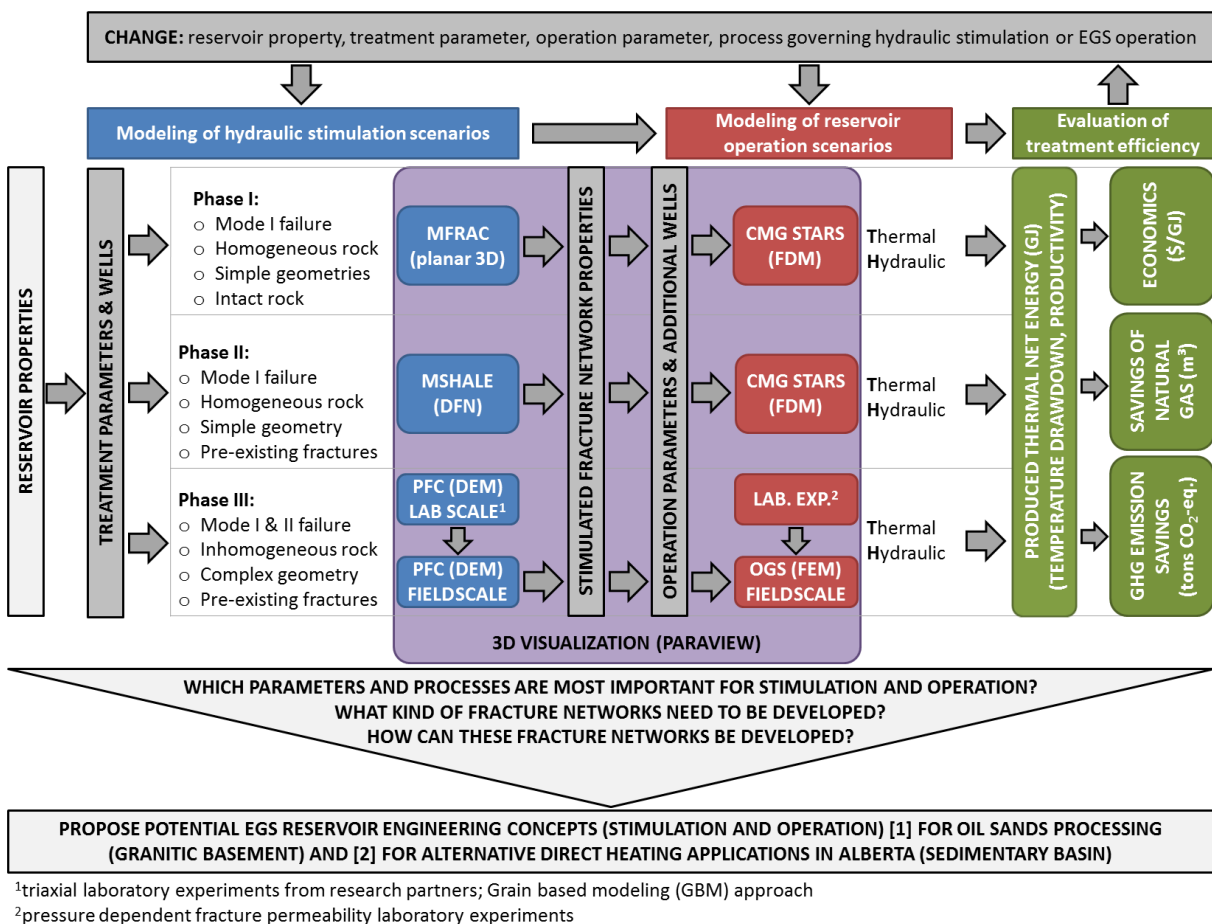


Figure 3: Overview of the methodology used to identify parameters and processes that improve the efficiency of enhanced geothermal systems.

In Phase III, the DEM model Particle Flow Code (PFC2D) was used for the hydraulic stimulation modeling part. This approach models the development of arbitrary shaped and oriented tensile and shear fractures in a discontinuous (pre-existing fractures) and inhomogeneous rock mass with a complex geometry. This study focused on the interaction between several fracturing stages and methods to increase fracture network complexity. An interface was developed to export the complex fracture geometries and their properties to the open source FEM simulator OpenGeoSys (OGS), which was used to model the thermal and hydraulic reservoir behavior. Grain-based modeling (GBM) simulations of laboratory experiments were performed to investigate the fracturing process at micro scale. For model calibration, results of geomechanical laboratory experiments from research partners were used. To investigate the pressure dependent fracture conductivity of fractures in granites, new laboratory experiments were performed. The results were used for the final field scale simulations.

For the investigation and presentation of hydraulic stimulation and reservoir modeling results, an immersive interactive 3D visualization environment was built to stimulate discussions in large interdisciplinary research groups and to make the investigated topics more approachable to non-specialists.

1.6 OUTLINE

The results of this research are published in peer reviewed journals (Hofmann et al., 2014b-d) and conference proceedings (Hofmann et al., 2012a, 2013a-b, 2015a; Majorowicz et al., 2013; Zimmermann et al., 2015), and submitted to peer reviewed journals (Hofmann et al., 2015b-e). Additionally, the results were presented in the form of one poster presentation (Hofmann et al., 2012b) and three oral presentations (Hofmann et al., 2012c, 2013c, 2014e) at the Helmholtz-Alberta-Initiative (HAI) annual meetings and HAI Science forums.

This thesis follows the solution methodology outlined in **Section 1.5**. First, a study about the environmental benefits, economics and reservoir engineering concepts of EGS development in sedimentary rocks in the Edmonton area is presented (**Chapter 2**). In **Chapters 3 and 4** results from a similar study on the granitic basement rocks in the Fort McMurray area are shown. **Chapter 5** is a follow-up study on this which compares fracture development in 5 km deep

granitic rocks with 2.5 km deep shale formations using the DFN model. In the same study, model properties are identified that increase fracture network complexity. In **Chapters 6 and 7** the grain-based modeling approach was used to study the influence of different parameters on micro scale fracture development in granitic rocks. Thereafter, the results of pressure dependent fracture permeability laboratory experiments are presented in **Chapter 8**. In the end, complex fracture network development was studied using the particle based DEM code PFC2D, the newly developed interface between DEM and FEM, and the FEM software OpenGeoSys (**Chapter 9**).

Each chapter contains its own abstract, literature survey, methodology, results, discussions, conclusions, and references. At the end, the presented simulation approaches are critically discussed and the scientific and practical contributions resulting from the presented studies are given. Additionally, areas of future research and model improvements are suggested (**Chapter 10**).

CHAPTER 2: POTENTIAL FOR ENHANCED GEOTHERMAL SYSTEMS IN ALBERTA, CANADA

A version of this chapter was published in *Energy* (2014) **69**: 578-591.

The province of Alberta has a high demand of thermal energy for both industrial and residential applications. Currently, the vast majority of the heat used in these applications is obtained by burning natural gas. Geothermal energy production from deep aquifer systems in the sedimentary basin could provide an alternative sustainable source of heat that would significantly reduce greenhouse gas emissions.

To date there has been no geothermal field development in Alberta because the average geothermal gradient was considered to be too low for economic geothermal energy generation. However, with new technologies for Enhanced Geothermal Systems (EGS), it may be possible to develop geothermal resources from the sedimentary rocks in the Western Canadian Sedimentary Basin (WCSB). A numerical feasibility study based on a regional geological model and existing and newly gained data was conducted to identify scenarios for geothermal energy production in the region.

In central Alberta, three Devonian carbonate formations (Cooking Lake, Nisku, Wabamun) and the Cambrian Basal Sandstone Unit were identified as the highest geothermal potential zones. Thermal-hydraulic reservoir simulations for a 5 km x 5 km site in the city of Edmonton were performed to evaluate reservoir development concepts for these four potential target formations; therefore, hydraulic fracturing treatments were also simulated. Different utilization concepts are presented for possible applications of geothermal energy generation in residential, industrial and agricultural areas.

The Cooking Lake formation and the Basal Sandstone Unit are potentially the most promising reservoirs because the most heat can be extracted and the applications for the heat are widespread although the costs are higher than utilizing the shallower formations. Reservoir stimulation considerably improves the economics in all formations.

2.1 INTRODUCTION

The province of Alberta (Canada) has a high demand of energy for industrial and residential applications. This demand is concentrated in urban areas. The two major metropolitan areas in Alberta are Calgary and Edmonton. From the total population of 3.65 million Albertans, around 1.16 million live in the Edmonton area [24]. Besides residential buildings (27% of Edmonton's total energy consumption in 2009), commercial, institutional and industrial buildings (48% of Edmonton's total energy consumption in 2009) are the main energy consumers in the Edmonton area [23], with a huge part of this energy being used for heating (e.g. 85% of the energy demand of residential homes is for space heating and water heating) [21].

While most of the electricity is produced by coal-fired power plants, currently, the vast majority (45% in 2009) of (mainly heat) energy used in Edmonton is obtained by burning natural gas with severe environmental and economic impacts [23]. For example, 95% of space heating demand and 90% of water heating demand are covered by natural gas [7] mainly due to the low gas price and the huge gas reserves in Alberta.

However, natural gas reserves are limited and greenhouse gas emissions from burning natural gas are significant (56 gCO₂/MJ) [22]. These are the two main reasons why alternative energy sources are needed. One alternative renewable and sustainable source of base load energy (heat and electricity) with a smaller environmental footprint (2-3 gCO₂-eq/MJ) [2] could be geothermal energy. Geothermal energy has the potential to reduce greenhouse gas emissions and save valuable natural gas reserves. Areas in the western part of the Western Canadian Sedimentary Basin (WCSB) with temperatures above 100°C within the sedimentary rocks may be feasible for electricity generation [18] (**Figure 4**).

However, there are diverse applications other than electricity generation for this low enthalpy geothermal energy such as space heating, warm water provision and balneological baths [16]. For direct utilization, geothermal wells and the consumers using the heat energy need to be in close proximity to one another to avoid heat losses during transportation. In central Alberta (Edmonton), where the energy demand is high, geothermal energy could play a role in replacing some fossil-fuel generated heat energy used for district heating, commercial and institutional buildings, and industrial applications [29]. To date, there has been no geothermal field

development in Alberta because the average geothermal gradient was considered to be too low for economic geothermal energy generation. But with new technologies for Enhanced Geothermal Systems (EGS) [25], it may be feasible to develop geothermal resources from the granitic basement [17] or from sedimentary rocks in the Western Canadian Sedimentary Basin (WCSB).

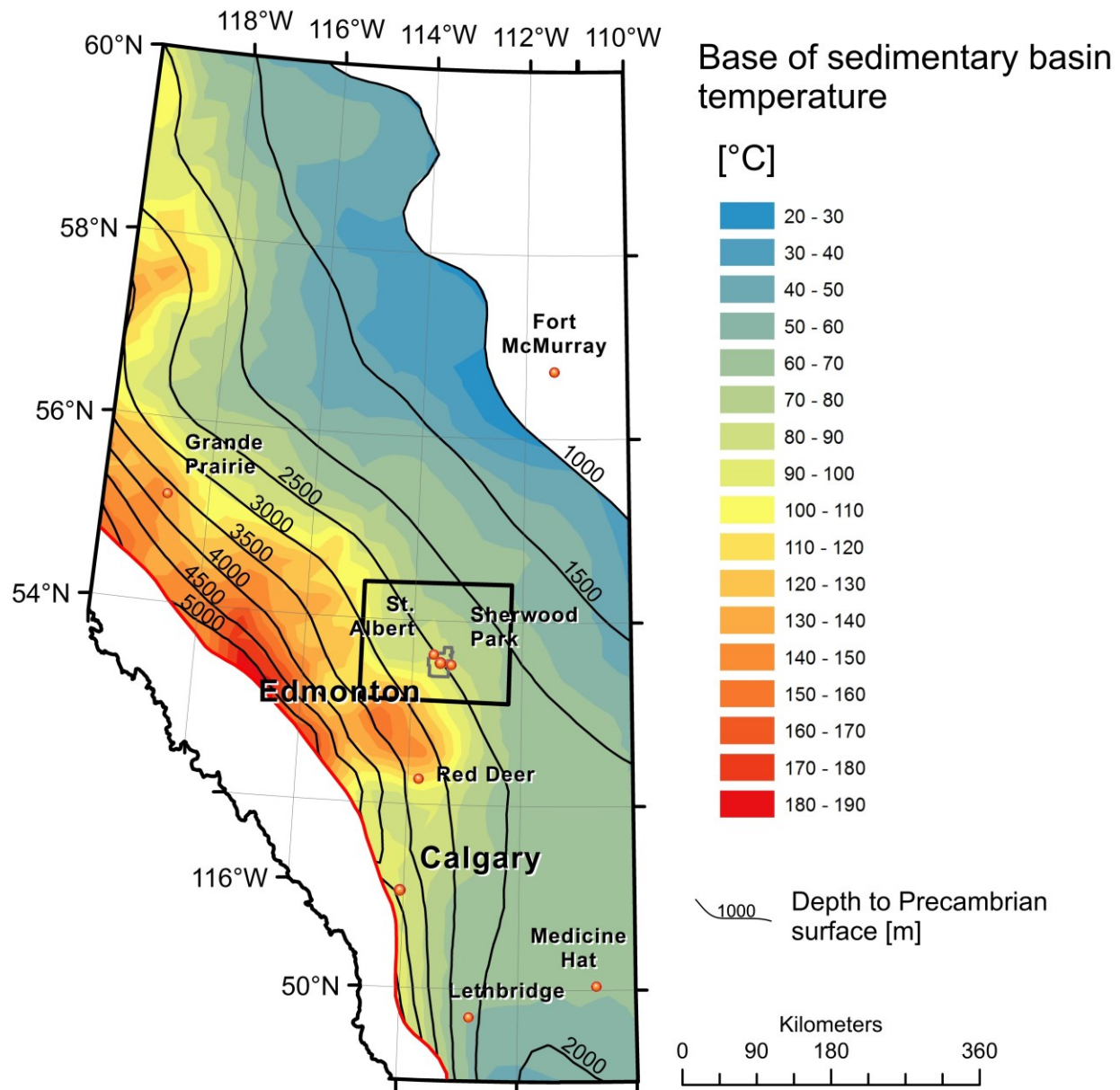


Figure 4: Maximum temperatures at the base of the sedimentary basins fill (top of Precambrian crystalline basement) increase from east to west with the depth of the basin. In the Edmonton area basin temperatures are below 100°C. The extent of the regional scale geological model is shown as the black rectangle around Edmonton.

These techniques are mainly hydraulic (gel-proppant fracturing, hybrid fracturing and water fracturing), chemical (matrix acidizing and acid stimulation), and thermal stimulation methods that can be utilized to enhance the reservoir permeability by stimulating existing fracture networks and/or creating new fractures [12].

In this study we focus on the application of conventional gel-proppant treatments because they are commonly used to stimulate sedimentary rocks (sandstones as well as carbonates). Thereby, first, a pad (fracturing fluid without proppants) is pumped into the formation to open existing fractures and/or create new ones and furthermore propagate these fractures into the formation. Then the slurry (fracturing fluid mixed with proppants) is pumped to transport and distribute the proppants in the fracture, and finally the wellbore is flushed, ideally leaving a proppant filled conductive fracture [6].

Weides et al. [29] identified formations with the largest potential for geothermal energy extraction in the Edmonton area by analyzing hydraulic parameters, depth, thickness and extension of different Paleozoic formations. In this study, we present subsequent hydraulic fracturing and reservoir simulations evaluating (1) which formations are most suitable for geothermal energy extraction; (2) which of the formations need additional engineering in order to be productive; (3) what are suitable reservoir engineering concepts for each formation; (4) how much heat can be extracted; (5) what can the heat be used for; (6) how much CO₂ emissions can be reduced; (7) how much natural gas can be saved; (8) what are the costs, and (9) what is the most economical way to extract the heat.

To answer the questions stated above, we first parameterized the geological model based on the available data and new laboratory experiments. Then, we simulated hydraulic fracturing treatments in all four potential target formations to evaluate what fracture dimensions can be achieved by one single treatment. Subsequently, the hydraulic and thermal performances of the intact and stimulated reservoirs were simulated for a lifetime of 30 years (with different fracture and well arrangements). In the end, based on the thermal output of the system, the economics, CO₂ emission savings, and natural gas savings of the intact and stimulated reservoirs were calculated. This integrated approach gives insight into which formation is most suitable for heat generation for specific applications in the vicinity of the city of Edmonton.

The paper is organized as follows: (1) the geological model, the fracturing model and the reservoir model are described, followed by (2) an explanation of the modeling procedure, and (3) finally, the results of the fracturing and reservoir simulations and subsequent economic and environmental considerations are presented.

2.2 MODEL DESCRIPTIONS

2.2.1 Geological model

A 3D geological model was developed for an area in central Alberta, located around the city of Edmonton [29]. This area is approx. 160 km x 200 km in size, and the thickness of the sedimentary succession from ground surface to the top of the Precambrian crystalline basement is between 1.8 km and 3.5 km.

The model is based on the stratigraphy identified by numerous well logs from the Alberta Geological Survey (AGS) database. In total, stratigraphic tops from 6916 wells were used to build the model. While this database is extensive, it is also biased towards hydrocarbon-rich strata and areas since most of the data comes from hydrocarbon exploration and production wells. A high amount of data exists for the Mesozoic succession (>6500 wells in the Lower Cretaceous) and hydrocarbon-bearing Upper Paleozoic strata (>2000 wells in the Upper Devonian). In contrast, only a small number of wells have been drilled in the strata below the Upper Devonian carbonates. In the central Alberta study area, 72 wells have reached the top of the Middle Devonian Elk Point Group, of which 16 wells were drilled into the Cambrian strata, with 13 penetrating the top of the Precambrian basement in a depth between 1769 m and 3533 m.

No seismic information was used in the development of the 3D model; therefore, no information on faults was integrated into the model.

Due to the large scale of the model (the study area is approx. 160 km x 200 km) only regionally extensive formations have been modelled. The lithostratigraphic 3D model comprises 20 different geological units, of which 14 are in the Paleozoic strata and 6 are in the Mesozoic- and Cenozoic-aged strata (**Figure 5**).

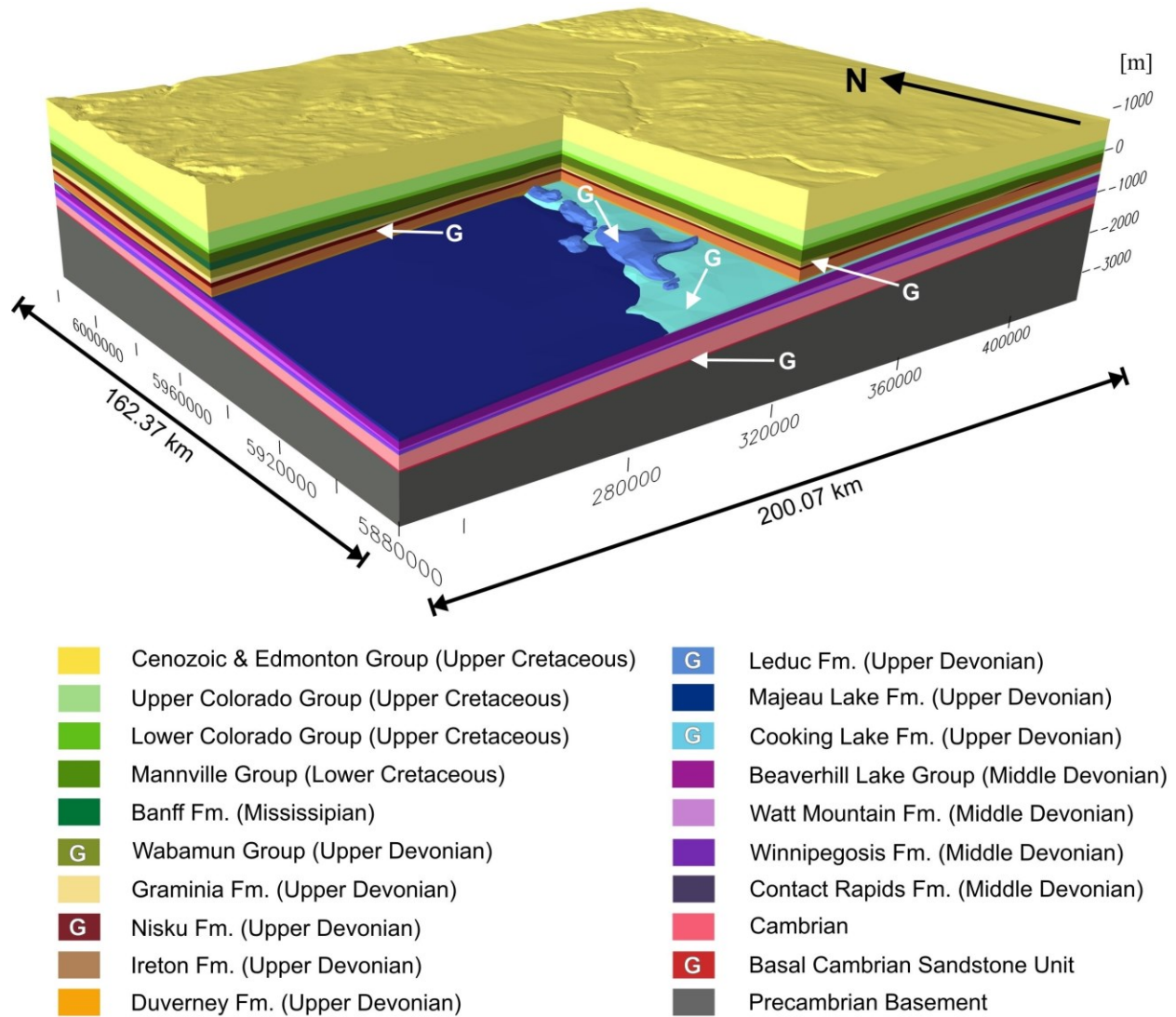


Figure 5: Three-dimensional geological model of the study area. The model is based on stratigraphic picks from about 7000 wells and potential geothermal reservoir units are indicated by the letter “G”; from Ref. [29].

Potential target formations that are present in the Edmonton area are the three Devonian carbonate formations and the Cambrian Basal Sandstone Unit. A summary of their most important properties is presented in **Table 1**. Depths are given in true vertical depth (TVD).

Table 1: Summary of the main properties of the four potential target formations for geothermal energy extraction in the Edmonton Area (values from the Wabamun, Nisku and Cooking Lake formations are from the AGS database and data from the Basal Sandstone Unit are from Weides et al. [28]).

Formation	Wabamun	Nisku	Cooking Lake	Basal Sandstone
Rock Type	Carbonate	Carbonate	Carbonate	Sandstone
TVD (center of formation) [m]	1193	1312	1615	2427
Thickness [m]	106	56	81	33
Horizontal permeability [mD]	2.8	9.7	10.4	1.6
Vertical permeability [mD]	0.5	1.3	0.4	0.6
Porosity [%]	8.0	8.0	8.2	8.9
Temperature [°C]	45	49	60	91

2.2.2 Model parameterization

The parameterization of both of the models is based on the data from the closest wells from geological databases, literature and new laboratory measurements. The data from all these different sources was integrated to build the models.

The reservoir pressure P_p at depth z was calculated based on the reservoir fluid densities ρ from Ref. [5] and the acceleration of gravity g using (**Equation 1**):

$$P_p = \rho_{water} g z \quad (1)$$

The total compressibility c_t was calculated by **Equation 2**:

$$c_t = S_w c_w + S_g c_g + c_r \quad (2)$$

where S_w is the water saturation, S_g is the gas saturation, c_w is the water compressibility, c_g is the gas compressibility and c_r is the bulk rock compressibility. Leak-off properties and mechanical rock properties of the hydraulic fracturing model are given in **Figures 6 and 7**, respectively. The

fluid viscosity for the different pressures and temperatures at different depths was taken from Ref. [15].

Porosity and permeability data were obtained from core tests reported in the Alberta general well data file and new laboratory measurements (for the Cambrian Basal Sandstone Unit; from Weides et al. [28]). These plug-scale values were first scaled-up to the well scale and then the well scale values were scaled-up to average values representing the regional scale. Data of the Devonian target formations came from wells within a 25 km x 25 km square area around the center of the model. Below the Cooking Lake formation, data from the whole basin was taken due to the lack of data in the Edmonton area.

The average temperature gradient as derived from the closest wells with thermal information is 37.3°C/km. Thermal fluid properties for pure water were also taken from Ref. [15]. Thermal rock properties were approximated for the different rock types and are summarized in **Table 2**.

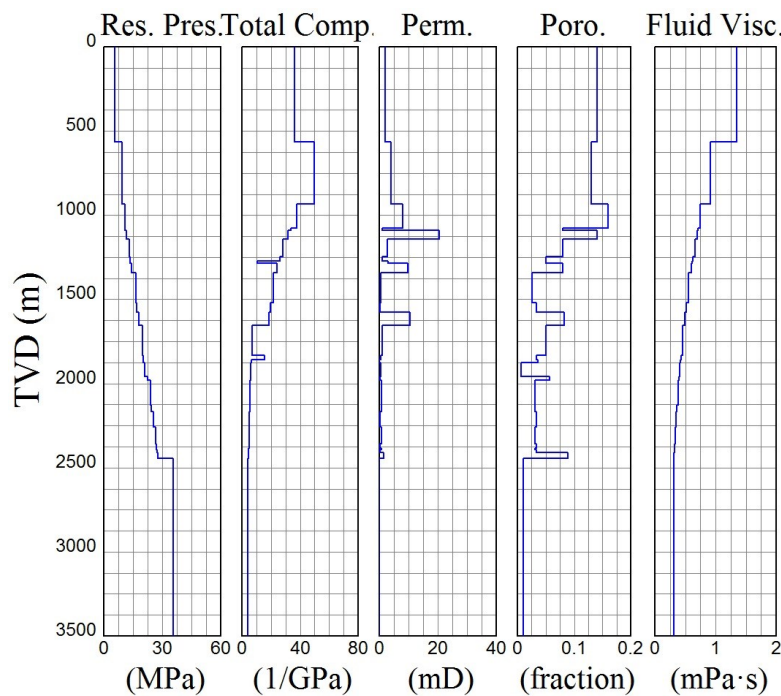


Figure 6: Leak-off properties of the fracturing model.

Table 2: Thermal properties of the five different rock types that are building the models.

Rock Type	Thermal conductivity [W/m/K]	Heat capacity [kJ/m ³ /K]
Clastics	3.10	2,300
Shales	1.38	2,392
Carbonates	2.42	2,270
Evaporites	1.38	2,392
Granites	2.70	2,385

For deep formations within the WCSB, a normal stress regime with vertical stress (σ_v) > maximum horizontal stress (σ_H) > minimum horizontal stress (σ_h) can be expected. The average gradient of σ_v is 23.8 MPa/km and the average gradient of σ_h is 16.6 MPa/km. The fracture pressure gradient (pressure at which a new fracture within the formation is opened) is about 19 MPa/km averaged over the whole WCSB. All stress gradients are taken from Ref. [9].

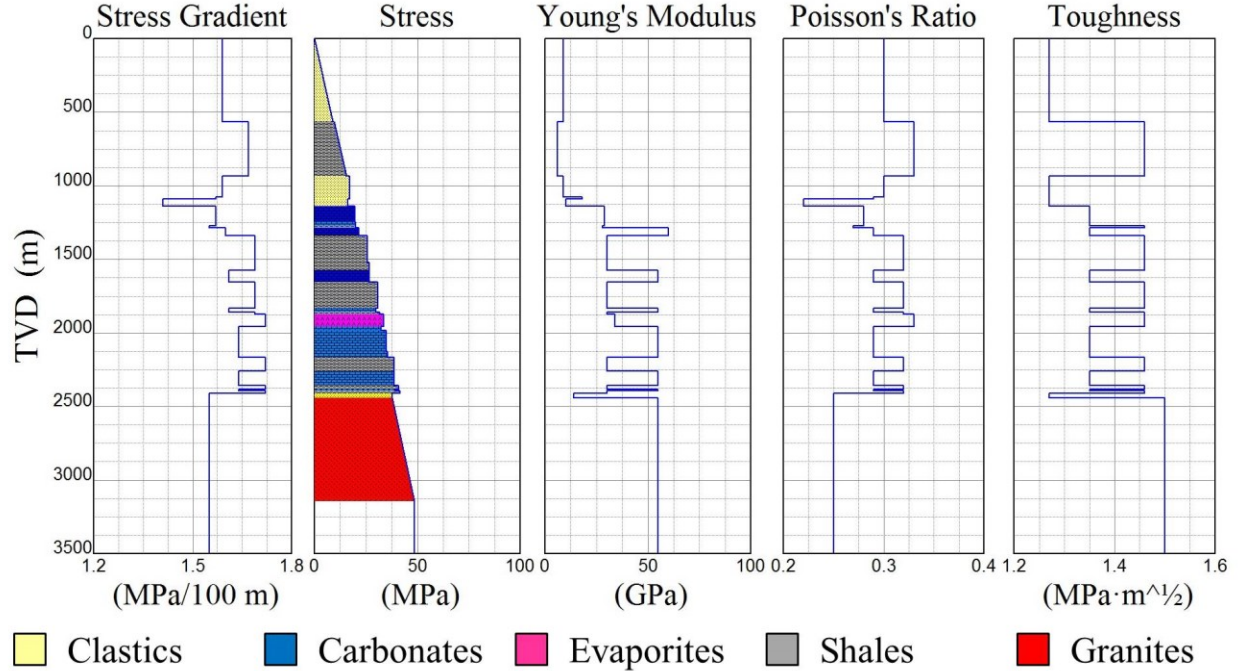


Figure 7: Mechanical properties and minimum horizontal stress distribution of the fracturing model.

Keeping these average values in mind, we calculated the minimum horizontal stress gradient based on Poisson's ratio, ν and the vertical stress using **Equations 3 and 4** [31].

$$\sigma_v = \rho_{rock} g z \quad (3)$$

$$\sigma_h = \frac{\nu}{1 - \nu} (\sigma_v - P_p) + P_p \quad (4)$$

Data from the world stress map [10] suggests the direction of the maximum horizontal stress to be approximately 45° and hydraulic fractures will tend to develop perpendicular to this direction [30].

Mechanical data for the Devonian carbonate formations was derived from the literature and new laboratory measurements were conducted on rock samples from the Basal Sandstone Unit (Weides et al., in prep.). From Ref. [8], the static Young's modulus was calculated based on UCS measurements and the dynamic Poisson's ratio was taken. For the fracture toughness, typical values for the five different rock types were chosen. The properties of deeper formations without measurements were derived based on the rock type and the properties of shallower formations. In general, for deeper formations, less information was available from close wells and therefore the information was less reliable. The mechanical parameters as well as the magnitude of the minimum horizontal stress are shown in **Figure 7**.

2.2.3 Hydraulic fracture development model

Fracturing simulations were performed for all four potential target formations with the fracturing simulator MFrac [19], which is formulated between a pseudo-3D and a full 3D model. For decades, this software is routinely used to model hydraulic fracturing treatments for application in the hydrocarbon industry (e.g. Ref. [27]) and was also previously applied to model the stimulation of geothermal reservoirs (e.g. Ref. [26] or [14]).

In this model, fractures initiate and develop in tensile mode only. Calculations are based on mass conservation, momentum conservation, continuity and a width-opening pressure equation. Proppant transport and heat transport are fully coupled with fracture propagation. Theoretical background of the software is provided by Ref. [19].

2.2.4 Thermal-hydraulic reservoir simulation model

The thermal and hydraulic behavior of the intact and stimulated reservoirs was evaluated with the CMG STARS finite difference thermal reservoir simulator [4]. A 5 km x 5 km square area around the Edmonton city airport was cut out of the regional scale geological model to build a local scale reservoir model. Some layers of the geological model were split into finer formations where more detail was necessary. The thickness of those formations was estimated based on boreholes within a 25 km x 25 km square around the center of the reservoir model. In order to reduce computation times and increase accuracy, the reservoir model was divided into three separate models in different depth ranges around the target formations (**Figure 8**). In this single porosity model, fractures are implemented as refined higher permeability cells within a low permeability matrix for the stimulated scenarios.

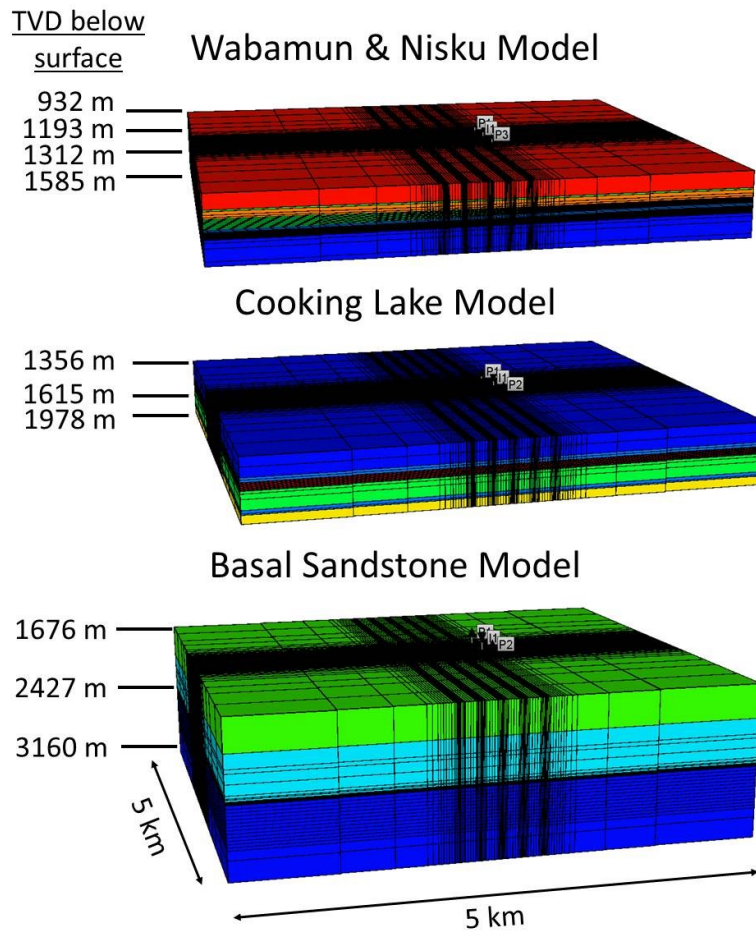


Figure 8: Geometries of the three reservoir models including depths of target formations and mesh refinement around the wells and the hydraulic fractures.

2.3 SIMULATION PROCEDURE

2.3.1 Hydraulic fracturing simulation procedure

First, hydraulic fracturing simulations were performed for all four potential target formations. To show the range of possible fracture extensions, two cases were simulated: (1) a confined case where the stress of the overlaying layer is higher than the stress in the target formation, and (2) an unconfined case where the stress in the overlaying layer is lower or equals the stress in the target formation. The fluid injection was stopped as soon as no further significant increase in fracture length was observed (due to severe fracture height growth or large fluid leak-off) or when the target fracture half-length of 600 m was achieved. For all simulations, a binary fracturing fluid was injected at a constant flow rate of 100 l/s. An intermediate viscosity fluid (65% binary with 60# gel with linearly decreasing viscosity from 302 mPa s at 38°C to 174 mPa s at 93°C) was chosen to ensure sufficient proppant transport (high viscosity needed) and to reduce fracture height growth out of target formations with low stress barriers (low viscosity needed). To keep the fractures open, 16/30 CarboLite proppants were chosen because they revealed sufficient proppant transport and fracture conductivity.

2.3.2 Reservoir simulation procedure

The major performance criteria for the reservoir simulations were a maximum pressure drawdown/buildup of 500 m (5 MPa), a maximum production rate of 50 l/s per well, a maximum injection rate of 100 l/s, and a re-injection temperature of 20°C below the initial reservoir temperature. Even though lower re-injection temperatures would increase the extracted amount of heat, we used only 20°C temperature difference to make the results of all four formations comparable. We investigated how much heat can be extracted from each target formation within these boundary conditions over a period of 30 years. First, the intact reservoirs were simulated with different well arrangements (two vertical wells with 250 m spacing, two horizontal wells with 400 m spacing, and three horizontal wells with 400 m spacing), and then the stimulated reservoirs were simulated with different well and fracture arrangements, which are given in **Figure 9**. Cases 1 and 3 consist of five fractures with a spacing of 200 m. In Cases 1, 3, 5 and 7,

the fluid flow between the wells is through the fractures. In Cases 2, 4, 6 and 8, the fluid flows from the fractures through the matrix.

The fracture half-lengths were based on the fracturing simulations: 125 m for Wabamun Group & Nisku formation; 300 m for Cooking Lake formation, and 500 m for the Basal Sandstone Unit. The average fracture heights were also based on the fracturing simulations. The fractures in the Nisku formation range up to the Wabamun Group. The average fracture conductivities were set to 750 mDm. A simulation of the stimulated Wabamun Group alone was not done because of the potential severe fracture height growth out of this formation.

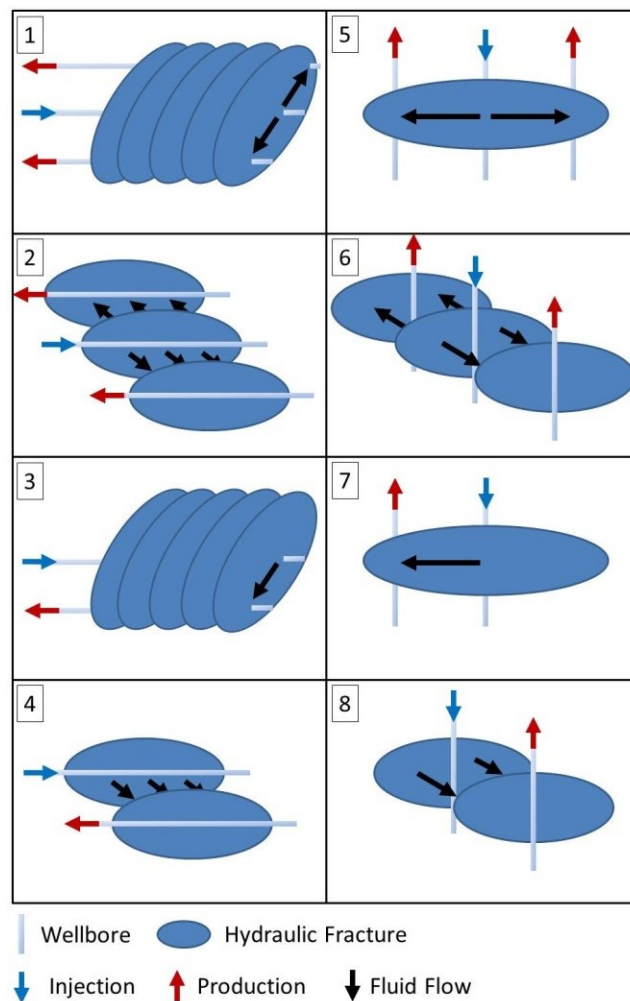


Figure 9: Overview of the eight different well and fracture alignments as used for the stimulated reservoirs. Well spacing is 400 m for the horizontal wells and 250 m for the vertical wells. Fracture spacing is 200 m and the fracture dimensions are based on the hydraulic fracturing simulations. The horizontal well section is 1000 m open-hole and the open-hole section of the vertical wells is over the whole height of each reservoir.

2.3.3 Economical considerations

The economics of geothermal energy production from intact rock and stimulated rock was approximated in terms of \$/GJ. Fixed costs for all scenarios were approximated as \$2.5 million for pumps and surface installations and \$1 million for other operational costs. The cost of one stimulation treatment was assumed as \$0.5 million [25].

A major cost factor arises from the power needed to produce and inject the fluid, which was calculated by multiplying the total required pump power (based on flow rate and well design) with the cost of 0.08 \$/kWh.

The other major cost factor is the cost of drilling, which was approximated based on the experience from hydrothermal wells. Data from Ref. [1] was fitted by **Equation 5**, which was used for cost c (million \$) estimation for the vertical wells based on the depth z (km).

$$c = 0.7108e^{0.4288z} \quad (5)$$

Horizontal wells may be up to three times more expensive than vertical wells [11]; hence, for the cost calculation for horizontal wells, the costs for the vertical wells were multiplied by a factor of 3. In the end, the total costs were divided by the cumulative produced heat after 1, 5, 10, 20 and 30 years to calculate the economics of geothermal energy production in terms of \$/GJ.

2.3.4 Reductions in CO₂ emissions

The amount of potential reductions in CO₂ emissions and the amount of natural gas that can be substituted by geothermal energy was calculated based on the extracted thermal energy in 30 years for the most economic intact and stimulated scenarios for all four formations. The combustion of natural gas emits 56 gCO₂/MJ [22]. Geothermal energy, on the other hand, emits only 2-3 gCO₂/MJ [2]. With the higher bound of 3 gCO₂/MJ, using geothermal energy can reduce CO₂ emissions by 53 gCO₂/MJ.

2.3.5 Natural gas savings

To calculate the amount of natural gas that can be saved by the use of geothermal energy, the total extracted heat from the most economic scenarios was multiplied with the volume of natural gas that needs to be combusted to produce 1 GJ of energy. This volume depends among other things on the heating value and ranges typically between 26.1 m³ and 28.9 m³ [3].

2.4 SIMULATION RESULTS

2.4.1 Hydraulic fracturing simulation results

2.4.1.1 Wabamun Group

The Wabamun Group is the shallowest unit of all four and is characterized by a relatively low permeability of 2.8 mD; hence, hydraulic stimulation may be needed. However, due to the lack of an upper stress barrier, a controlled fracture development within the target formation can only lead to relatively low maximum fracture half-lengths of about 50 m (**Figure 10**). If longer half-lengths are anticipated, the fracture grows unimpeded upwards as shown in **Figure 11**. Therefore, no hydraulic stimulation treatment should be performed within this formation.

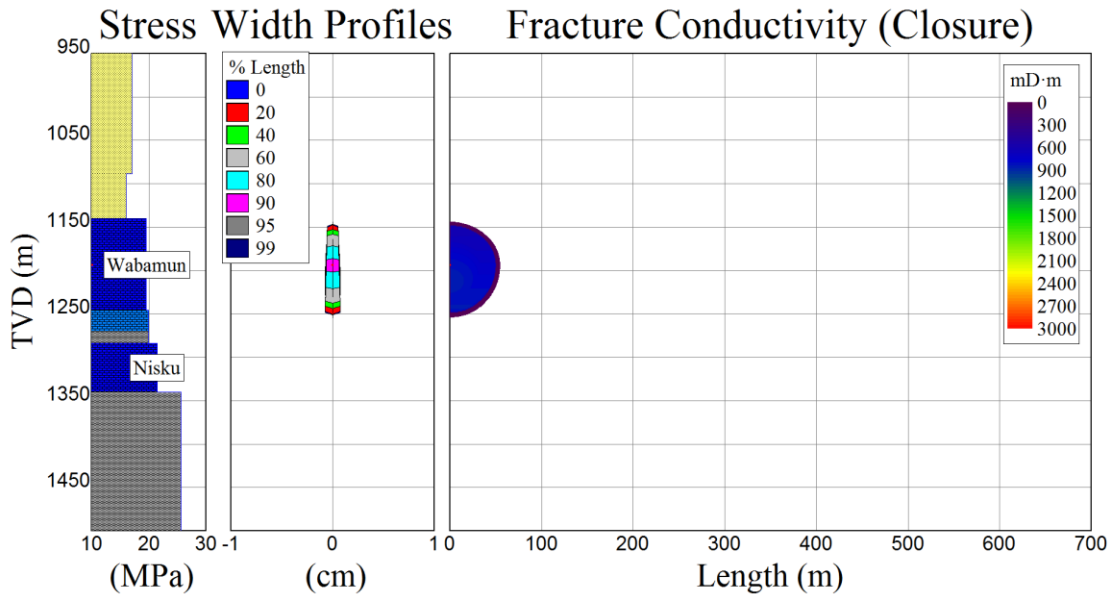


Figure 10: Only small fractures can be created within the Wabamun Group.

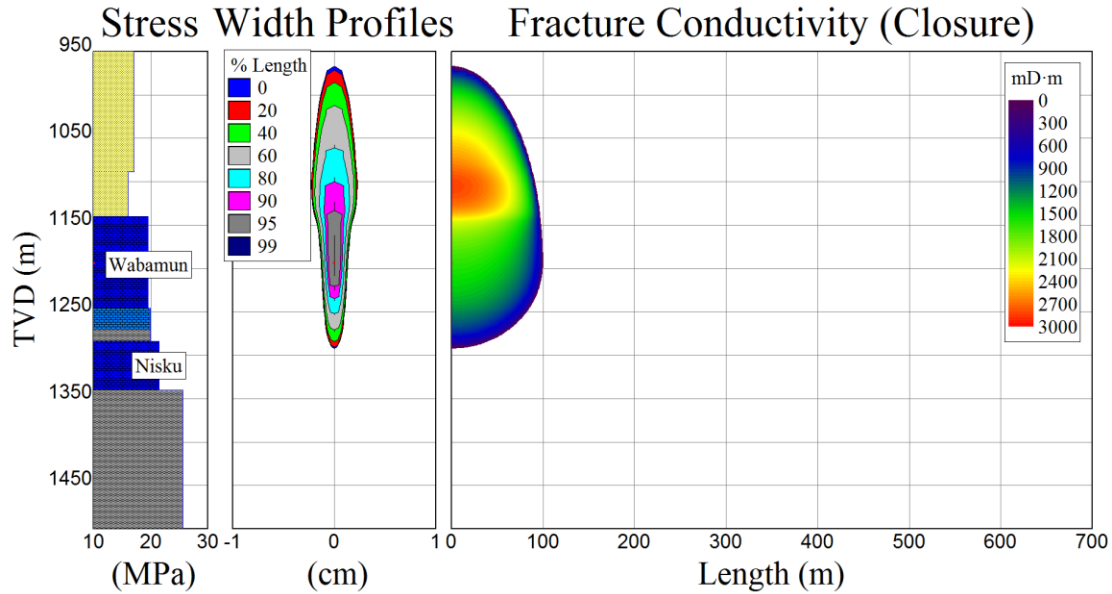


Figure 11: Large fracturing treatments lead to unconfined fracture height growth out of the Wabamun Group.

2.4.1.2 Nisku formation

Hydraulic fracturing may not be the appropriate technology to enhance the permeability of the Nisku formation because of the high fluid leak-off (and hence significant amounts of fluid needed) due to the relatively high permeability of 9.7 mD, and the unrestricted upward fracture height growth due to the lack of an upper stress barrier. Maximum half-lengths between 100 and 200 m can be achieved depending on the actual stress state (**Figures 12 and 13**).

The Calmar shale could potentially reduce fracture height growth and increase the achievable fracture length, but, due to its low thickness, fracture growth out of the Nisku formation will most likely not be prevented (**Figure 13**). Hence, the Wabamun Group and the Nisku formation may be connected through hydraulically induced fractures leading to a relatively large reservoir. However, long fractures connecting two or more wellbores separated more than 400 m cannot be created.

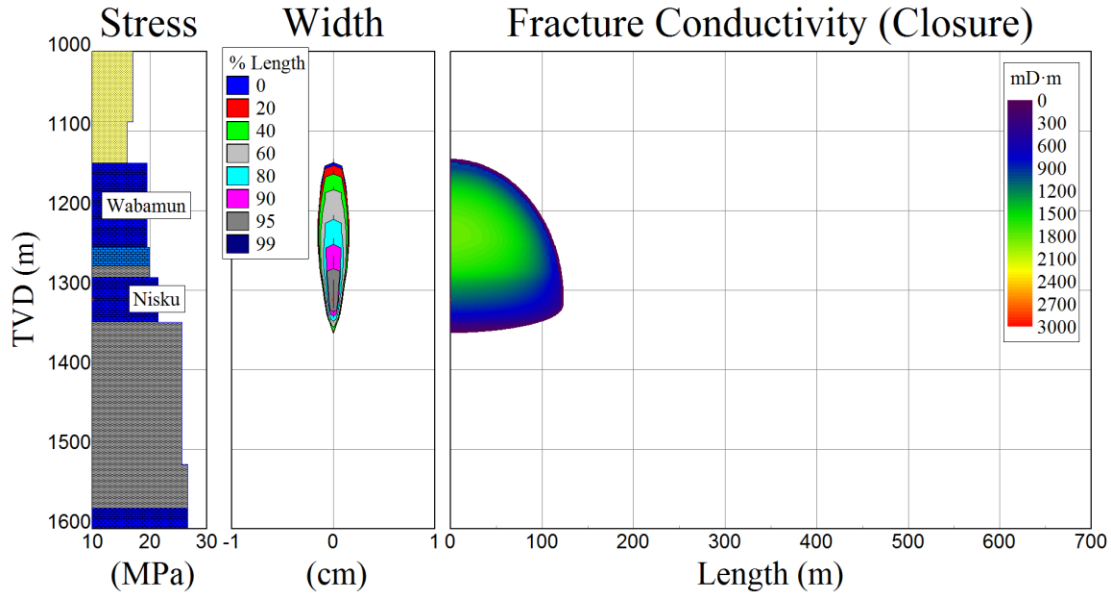


Figure 12: Unconfined fracture height growth out of the Nisku formation leads to a connection from the Nisku formation to the Wabamun Group.

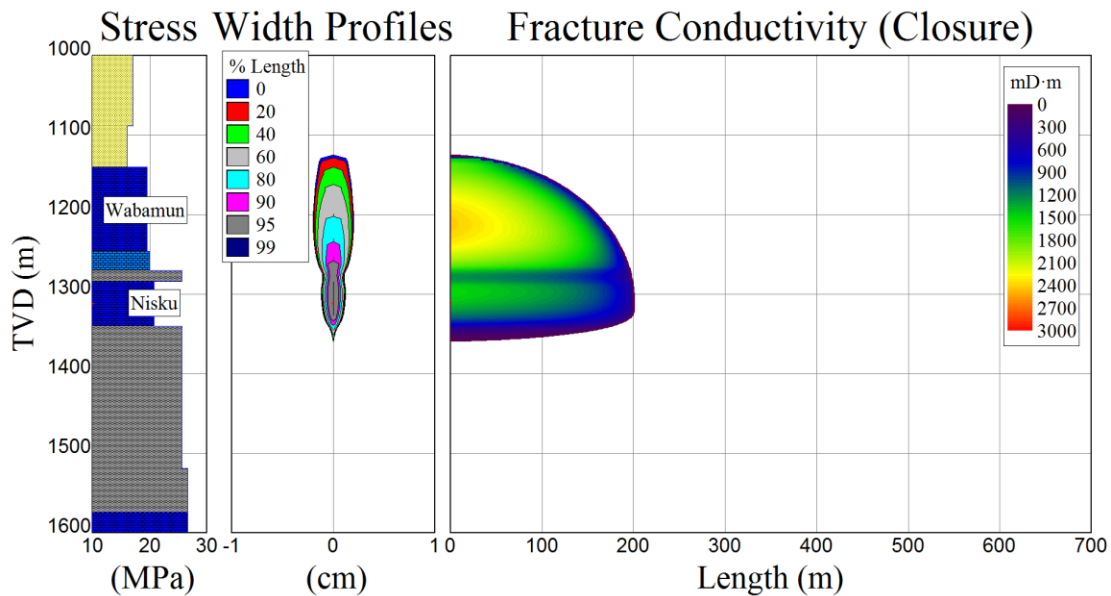


Figure 13: The possible Calmar shale stress barrier (between Wabamun Group and Nisku formation) does not lead to sufficient fracture height growth confinement, but longer fracture half-lengths can be achieved.

2.4.1.3 Cooking Lake formation

Whether or not the fracture height growth in the Cooking Lake formation is confined cannot be determined at this stage. Further investigations are needed to clarify the stress gradients within

the Cooking Lake and adjacent formations. However, the thick shale formations overlaying the Cooking Lake may have the potential to confine fracture height growth (**Figure 14**). **Figure 15** shows the simulated fracture geometry for the unconfined case where the overlying shale formation has the same stress as the Cooking Lake formation.

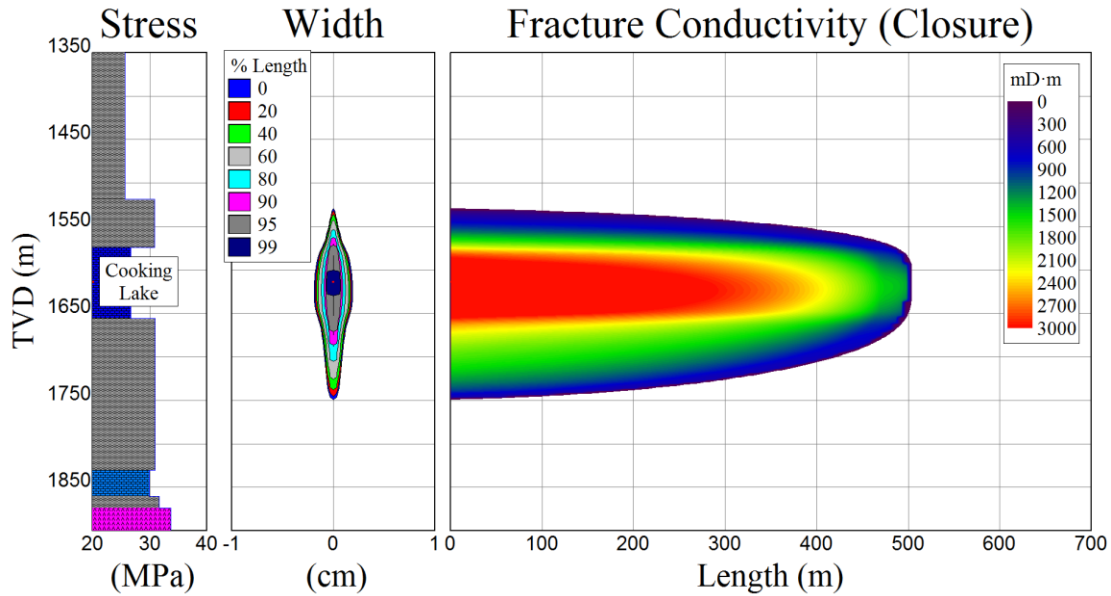


Figure 14: With a height growth confinement due to the overlying Duverney and Ireton shales, fracture development might be confined within the Cooking Lake formation and long fractures may be developed.

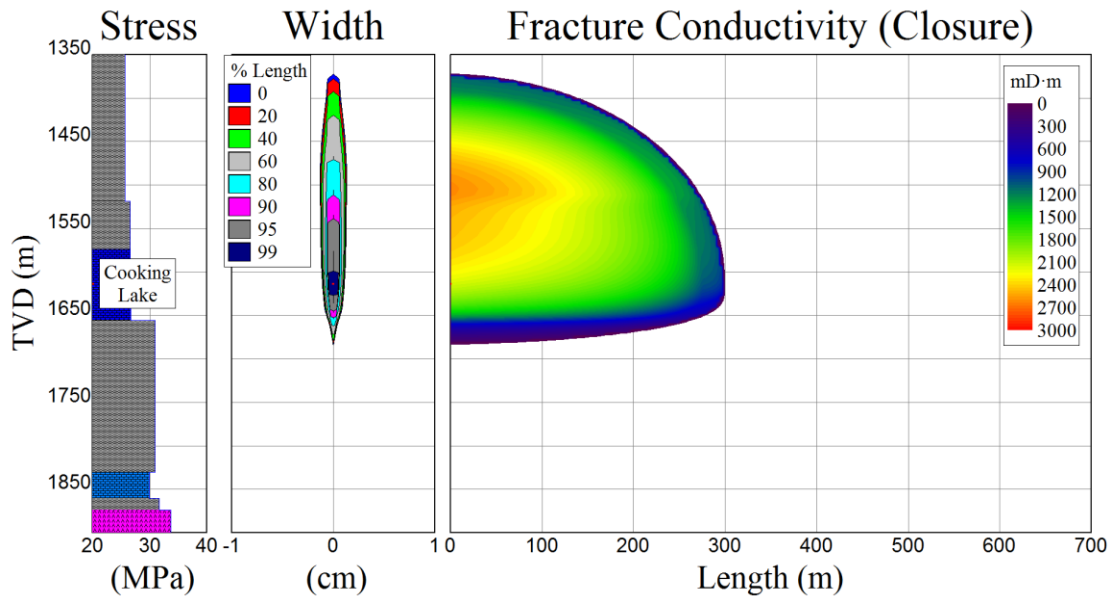


Figure 15: If the Cooking Lake formation is not confined, half-lengths of about 300 m may be achieved and the resulting fractures would be significantly higher.

Due to the relatively large initial permeability (10.4 mD), significant amounts of water would be needed to create new fractures due to the high fluid leak-off. Further investigations are needed to clarify whether or not this formation is suitable for hydraulic stimulation treatments.

2.4.1.4 Basal Sandstone Unit

The Basal Sandstone Unit is the deepest formation of the four investigated target horizons. Core tests from the wells around Edmonton result in an average regional scale permeability of 1.6 mD. This low expected permeability makes stimulation treatments imperative for efficient heat production.

The stress gradient within the sandstone formation is expected to be relatively low. The overlying shale and carbonate formations act as upper fracture height growth barrier due to their larger expected stress gradients. The increasing stress with depth within the underlying Precambrian basement rocks serves as lower stress barrier (**Figures 16 and 17**). Since the Basal Sandstone Unit has an average thickness of only 33 m, the fracture will grow into the basement rocks. Depending on the actual stress within the Basal Sandstone Unit and the actual stress gradient within the Precambrian basement, fractures will grow more or less into the basement rocks (**Figures 16 and 17**). Fracture growth into the basement can be desired because of the potential increase in the heat exchanger area.

Figure 18 shows for the less and better confined cases the increased amount of injected slurry volume (fracturing fluid and proppant) and the increased proppant mass needed to create a fracture with 750 mDm conductivity and 300 m, 400 m, 500 m and 600 m half-length within the Basal Sandstone Unit. Depending on the actual fluid leak-off, the necessary fluid volume could change significantly. Additionally, the fracture area and the average fracture height increases with increasing target fracture half-length (**Figure 18**). For the better-confined case, smaller fractures are generated (smaller area and less height) and hence less fracturing fluid and proppant are needed to create a fracture with a certain half-length.

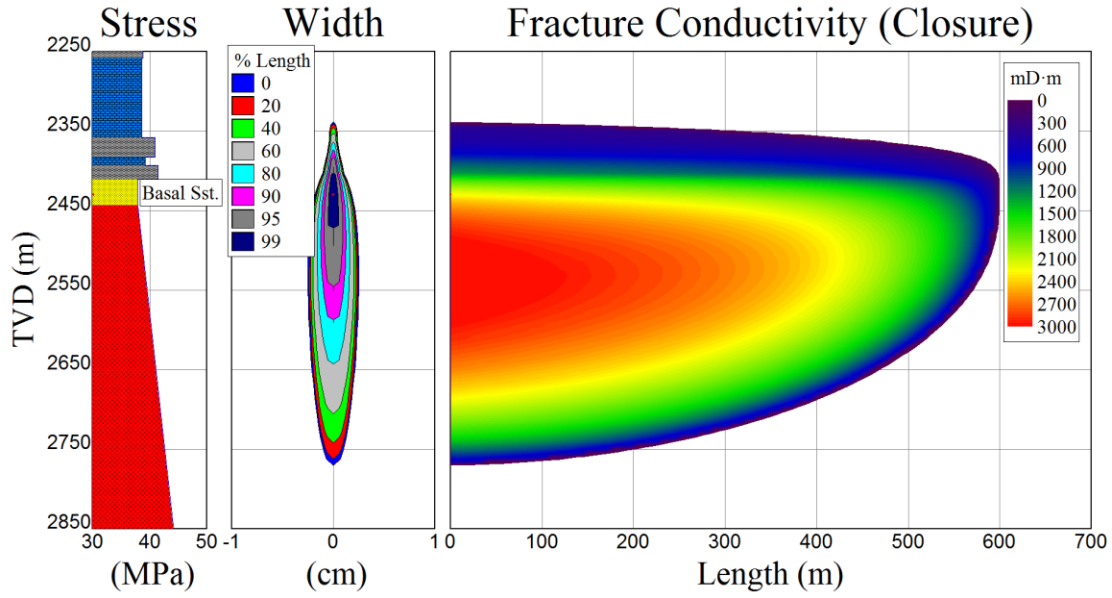


Figure 16: “Unconfined” fracture growth from the Basal Sandstone Unit into the Precambrian basement rocks.

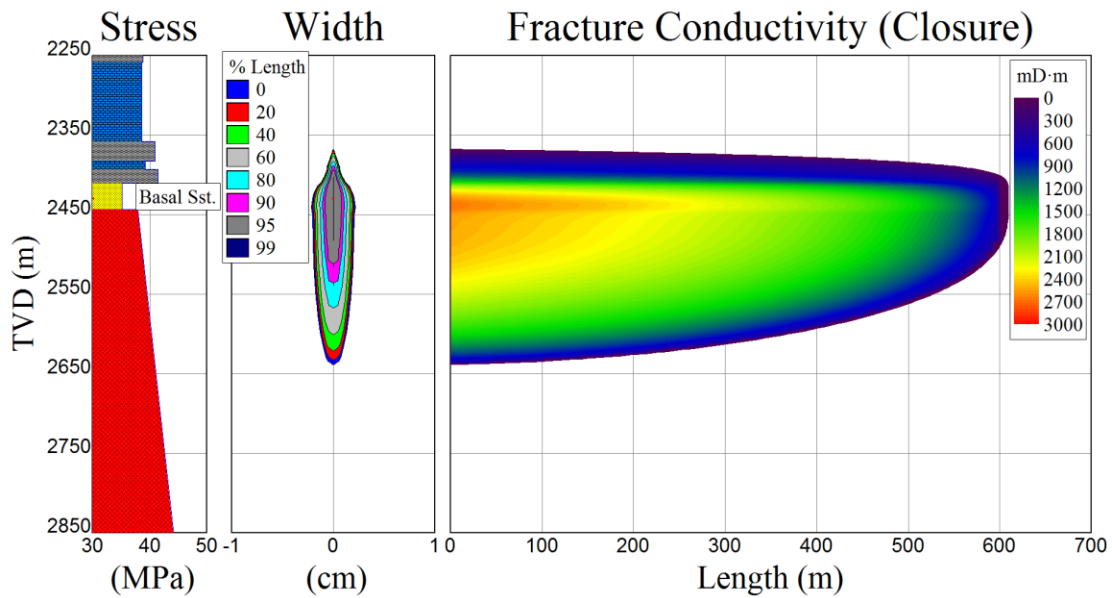


Figure 17: An increased stress confinement leads to the development of fractures with less height in the Basal Sandstone Unit.

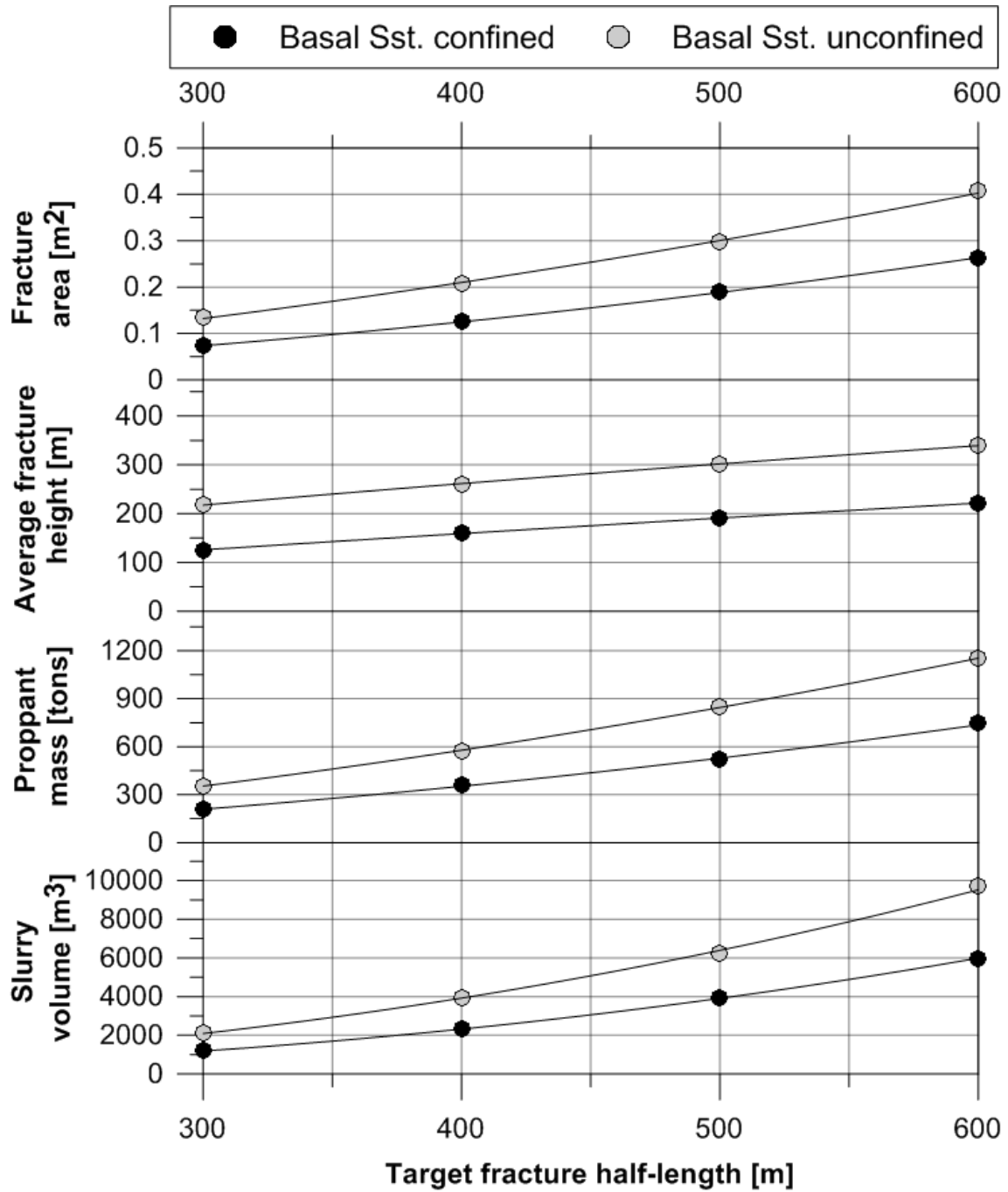


Figure 18: Slurry volume and proppant mass needed to create a fracture with 750 mDm conductivity and created average fracture area and height for different target fracture half-lengths within the Basal Sandstone Unit.

2.4.1.5 Summary of hydraulic fracturing simulation results

The stimulation potential was investigated for all four target formations. Important findings based on potential fracture height growth confinement and important reservoir characteristics are summarized in **Table 3**. We found that not all of the formations are suitable for massive stimulation treatments and the following were observed:

- The Wabamun Group should not be hydraulically fractured due to its lack of a sufficient upper stress barrier.
- For the Nisku and the Cooking Lake formations, a more detailed exploration work is needed to evaluate their confinement potential. Large fluid leak-off may be an additional challenge. While stimulating the Nisku formation, a hydraulic connection to the Wabamun Group may be developed.
- The Basal Sandstone Unit is well confined and has the lowest initial permeability. Therefore, this formation is best suited for permeability enhancements by conventional gel-proppant fracturing treatments.

Table 3: Stimulation potential for the four investigated formations based on fracture height growth confinement and other characteristics (k = permeability).

Formation	Confinement	Characteristics	Conclusions
Wabamun	Unconfined	Thickest formation, low initial k	No stimulation suggested
Nisku	Unconfined	High initial k	Potential connection to Wabamun
Cooking Lake	Possibly confined	High initial k	Short or long fractures
Basal Sandstone	Confined	Lowest initial k, thinnest formation	Long fractures, potential connection to basement

2.4.2 Reservoir simulation results

2.4.2.1 Hydraulic performance (production rates at constant bottom hole pressure)

Figure 19 shows the average production rate for the intact reservoirs (dark colors) and for the eight different stimulated scenarios (brighter colors; varying well and fracture arrangements given in **Figure 9**). A relatively poor hydraulic performance can be observed for all four formations if they are not hydraulically stimulated. Vertical wells in intact formations produce a maximum of 6 l/s (from the Cooking Lake formation, because it has the highest horizontal permeability). With three horizontal wells, up to 26 l/s can be produced in total from both wells in the intact Nisku formation (because it has the highest vertical permeability). From the Cooking Lake formation, slightly less (about 22 l/s) can be produced by the same well system due to the lower vertical permeability. The lowest production rates can be achieved in the Basal Sandstone Unit due to its low horizontal and vertical permeabilities (<1 l/s from two vertical wells and about 9 l/s from three horizontal wells).

Hydraulic stimulation treatments significantly improve the achievable production rates in all four formations. The difference between the confined and unconfined scenarios is relatively low in all formations (<7 l/s). In Scenarios 2 and 4, no difference was observed in the connected Wabamun and Nisku formation and in the Cooking Lake formation. Again, for all scenarios, with horizontal wells the highest production rates could be achieved (around 50 l/s in all formations). In the connected Wabamun and Nisku formation, the highest flow rate can be achieved by vertical hydraulic fractures parallel to the wellbore axes due to the relatively high permeability in the Nisku formation. In the similarly high permeability Cooking Lake formation, production rates of 50 l/s or more were achieved by vertical fractures parallel or perpendicular to the wellbore axes (Scenarios 1, 2 and 4). From the low permeable Basal Sandstone Unit, similar flowrates can only be achieved if the vertical hydraulic fractures are connecting the three horizontal wells (Scenario 1).

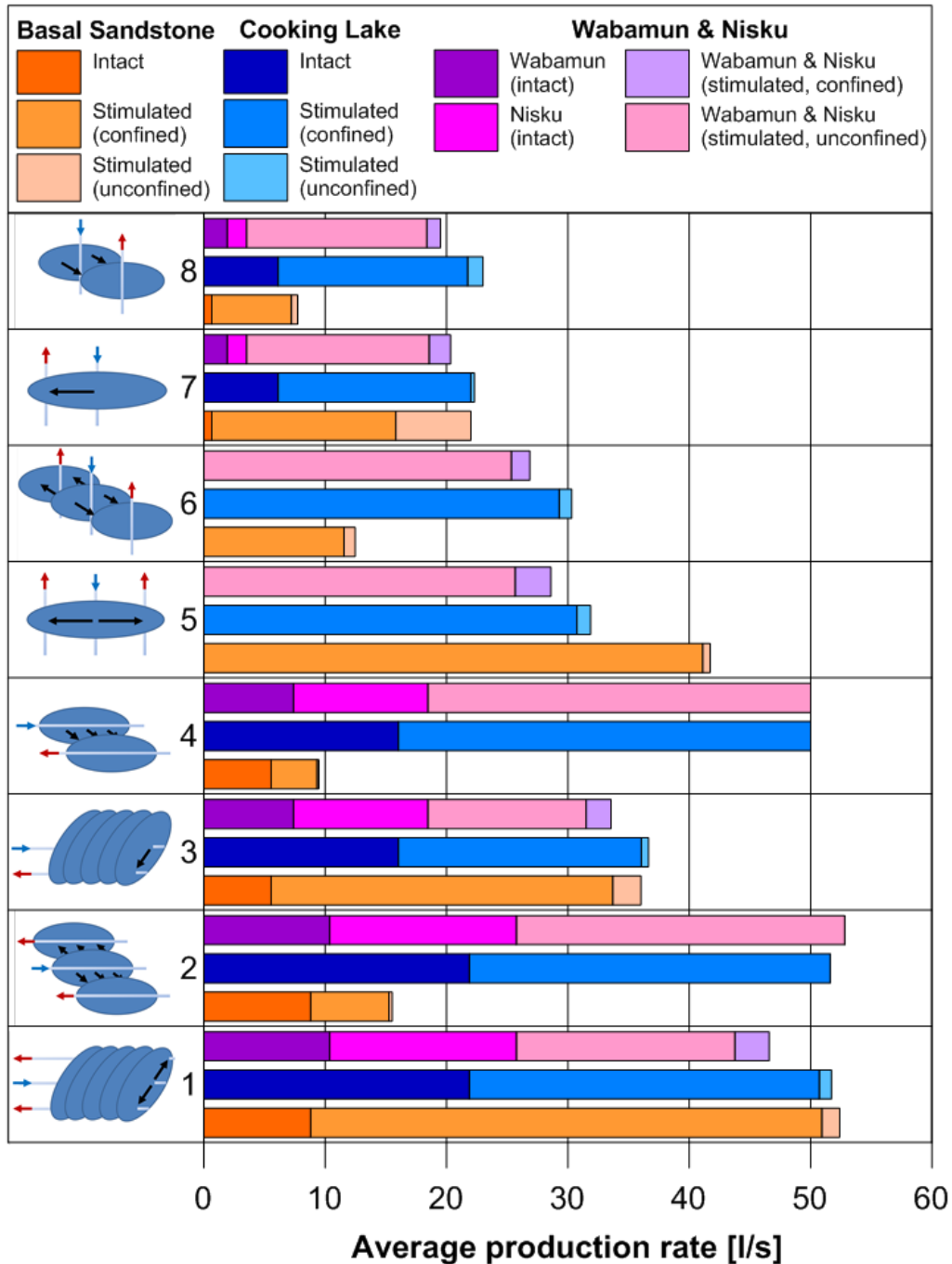


Figure 19: Average production rates resulting from a maximum pressure drawdown of 5 MPa in all four formations (intact and stimulated for eight different fracture and well arrangements). Because of the poor performance of the two vertical wells in the intact formations compared to the two horizontal wells, Scenarios 5 and 6 (with three vertical wells) were not simulated for the intact formations. The maximum flow rate constraint per production well is 50 l/s.

2.4.2.2 Thermal performance (produced heat)

The flow rate significantly influences the produced heat. The low flow rates in the intact formations lead to relatively low amounts of extracted heat from the intact formations of maximum 2.06 PJ from the Nisku formation. **Figure 20** shows the cumulative produced thermal energy in 30 years. For the intact cases, the most heat can be extracted from the Nisku formation followed by the Cooking Lake formation and the Basal Sandstone Unit. From the Wabamun Group, the lowest amount of heat can be extracted due to its low permeability and lowest initial reservoir temperature. In all intact and stimulated formations, the maximum amount of heat was extracted by three horizontal wells.

Similar to the hydraulic performance, the produced heat increased significantly when hydraulic stimulation treatments were performed. And again, the difference between the confined and unconfined scenarios is relatively low (<0.5 PJ). Even though the Basal Sandstone Unit has the lowest permeability, most heat can be extracted from the deepest formations with the highest temperatures: Cooking Lake (4.09 PJ) and Basal Sandstone (4.10 PJ). This was achieved by applying the reservoir engineering concept 1 (three horizontal wells and flow through five fractures perpendicular to the wells) to the Basal Sandstone Unit and the reservoir engineering concept 2 (three horizontal wells and flow from the three fractures, which are parallel to the wells, through the matrix) to the Cooking Lake formation. Up to 3.8 PJ can be extracted in 30 years from the connected Wabamun & Nisku formation using the reservoir engineering concept 2. A maximum of 4.10 PJ can be extracted (from the Basal Sandstone Unit) with the given maximum flow rate of 50 l/s per well and a re-injection temperature of 20°C below the initial reservoir temperature. That means 136,666 GJ of energy can be provided by 1 three-well EGS per year. From a total energy use of 126,271,000 GJ (excluding heavy industrial processes), the energy use for residential buildings (excluding electricity generation) was 27,704,000 GJ and the energy use for industrial, commercial and institutional buildings (excluding electricity generation) was 42,840,000 GJ in Edmonton in 2009 [23]. To provide the required energy (space heating and warm water provision) for residential buildings, about 203 three-well EGS need to be developed (609 horizontal wells drilled into the Basal Sandstone Unit and stimulated) and to additionally provide the energy for industrial, commercial and institutional buildings (excluding electricity) another 314 three-well EGS systems would need to be developed in the Basal

Sandstone Unit (another 942 wells). For comparison, in Alberta more than 300,000 wells were drilled already for oil and gas production.

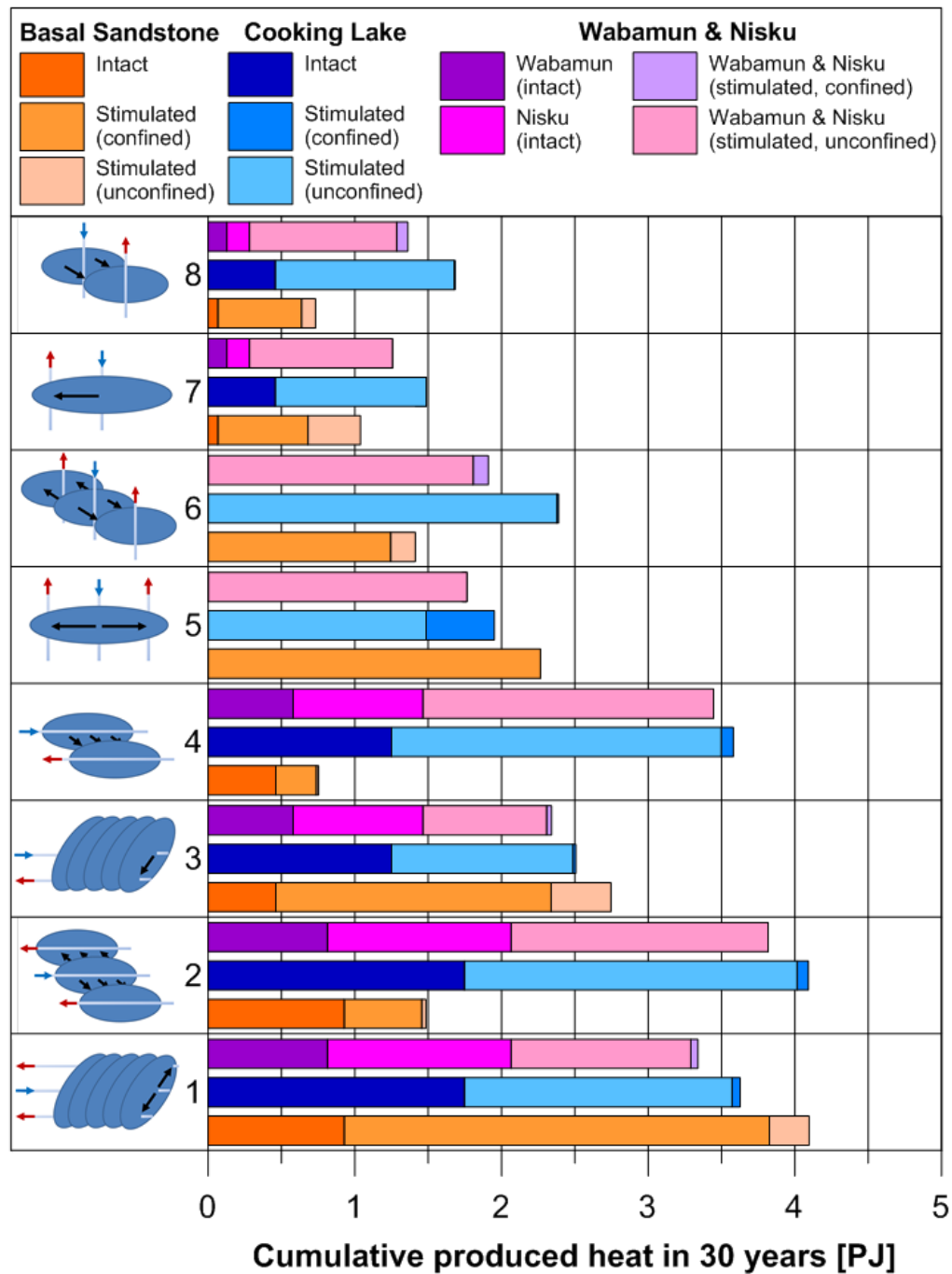


Figure 20: Cumulative produced heat in 30 years based on different well arrangements for the intact scenarios and different well and fracture arrangements for the stimulated scenarios.

2.4.2.3 Summary of reservoir simulations

To summarize the outcome of the reservoir simulations, **Table 4** shows the relative thermal performance of the four formations for intact and stimulated rock cases as well as vertical and horizontal wells. In general, horizontal wells outperform vertical wells. All formations show a much better hydraulic performance when they are stimulated, resulting in much higher flow rates and larger amounts of extracted heat. However, the Basal Sandstone Unit in particular needs to be stimulated in order to be productive.

Table 4: Relative thermal performance and stimulation potential for different formations (1=worst, 4=best).

Formation	Wabamun	Nisku	Cooking Lake	Basal Sandstone
Stimulation potential	1	2	3	4
Intact rock vertical wells	2	3	4	1
Intact rock horizontal wells	1	4	3	2
Stimulated rock vertical wells	1	2	4	3
Stimulated rock horizontal wells	1	2	3	4

2.4.3 Potential utilization of the extracted heat

The extracted heat can be used for different applications based on the fluid temperature (**Table 5**). Only in the Basal Sandstone Unit are temperatures high enough for district heating and refrigeration. Temperatures would be sufficient for domestic warm water provision in the Basal Sandstone Unit and the Cooking Lake formation. The two shallower formations can be used mainly for agricultural purposes, balneology and pre-heating in industrial processes.

As mentioned earlier, 85% of the energy demand of residential homes in Alberta is for space and water heating [21]. An average home in Alberta (140 m²) has a space-heating load of about 80 GJ per year and a water-heating load of about 40 GJ per year [7]. With the generated thermal energy from extracting water at 91°C from the Basal Sandstone Unit and re-injection at 71°C, up to 1140 houses can be heated over a period of at least 30 years from a stimulated horizontal three-well system with five hydraulic fractures. From the intact Basal Sandstone reservoir rock, a maximum of about 260 homes could be heated from three horizontal wells or about 18 houses from two vertical wells. To achieve these numbers, the system has to run without interruptions. Potentially significantly more energy could be extracted by using a lower re-injection temperature (e.g. 40°C), higher production rates (>50 l/s) and by using the heat for a combination of different applications (e.g. space heating and domestic warm water provision).

Table 5: Potential applications for heat extracted from the four formations (after [16]).

Formation	Temperature [°C]	Potential applications and minimum temperature needed
Basal Sandstone	91 - 71	70°C: Space heating (building and greenhouses), domestic warm water, refrigeration.
Cooking Lake	60 - 40	60°C: domestic warm water, Animal husbandry, greenhouses by combined space and hotbed heating.
Nisku	49 - 29	50°C: Mushroom growing, balneological baths.
Wabamun	45 - 25	40°C: Soil warming; 30°C: Swimming pools, biodegradation, fermentations, warm water for year-round mining in cold climates, de-icing; 20°C: Hatching of fish, fish farming.

2.4.4 Economical considerations

For intact rock, the most cost effective cases are the Nisku formation (6.9 \$/GJ over 30 years) and the Cooking Lake formation (8.4 \$/GJ over 30 years) which are both accessed with three horizontal wells (**Figure 21**). Energy extraction costs from the shallowest formation (Wabamun) and from the deepest formation (Basal Sandstone Unit) are significantly higher (11.8 \$/GJ and

15.1 \$/GJ, respectively) due to the low temperature and the low permeability, respectively. For all formations, energy extraction is more cost effective when using horizontal wells instead of vertical wells and when using three wells instead of two.

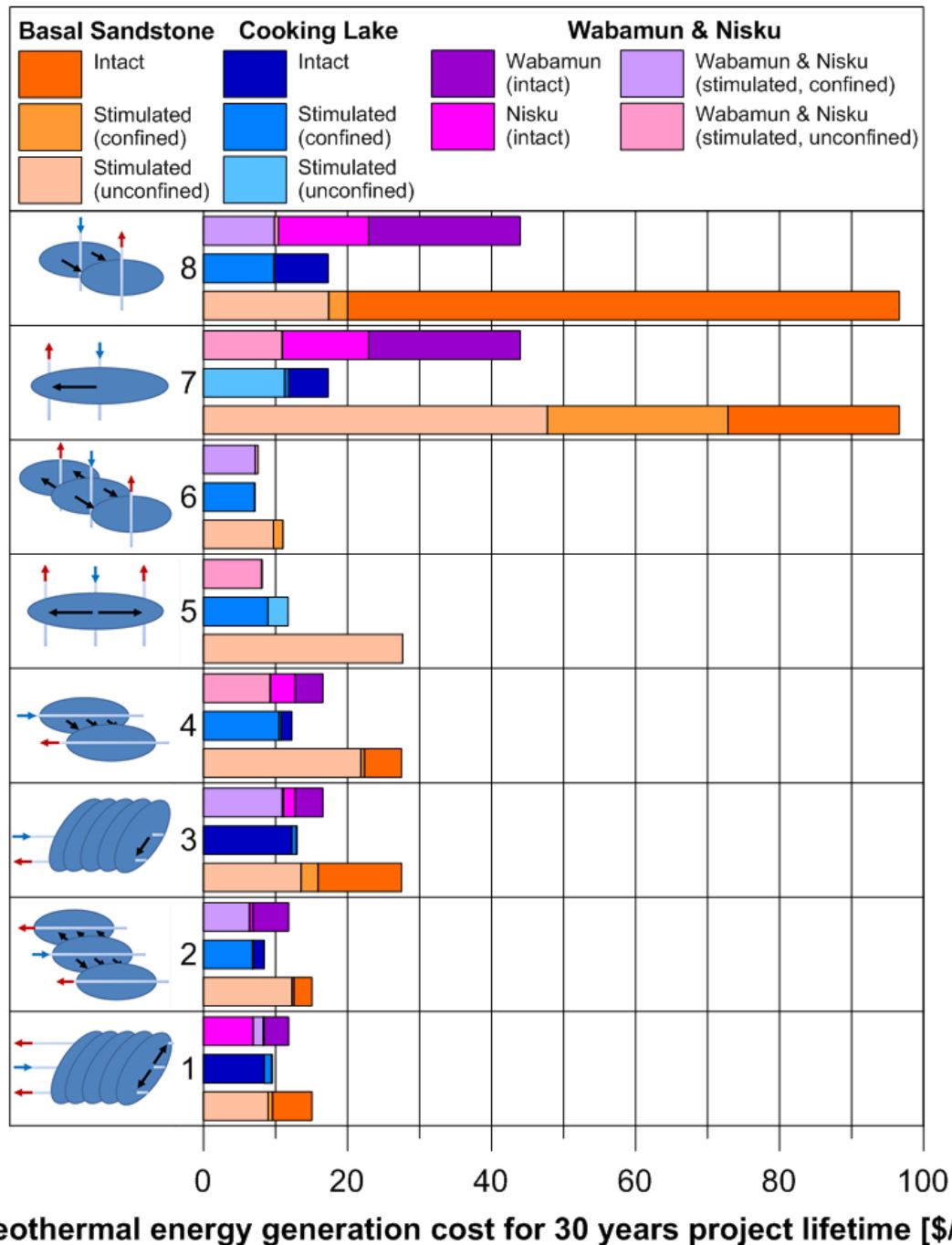


Figure 21: Levelized cost of geothermal energy production from intact and stimulated reservoirs for 30 years continuous production.

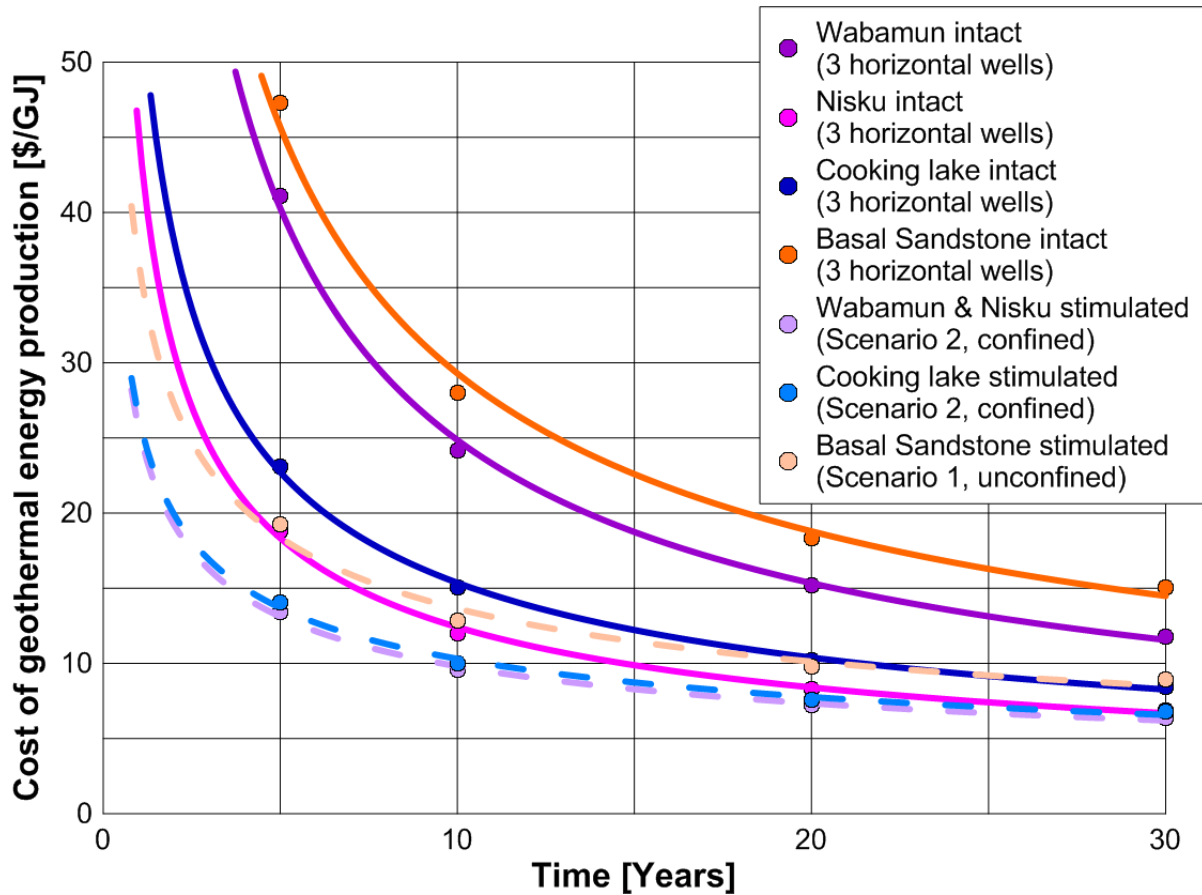


Figure 22: Costs of geothermal energy production vs. time for the most economic intact and stimulated reservoir scenarios.

For all formations, reservoir stimulation is more economic than producing heat from the intact formation when the most economic reservoir engineering concept (well and fracture arrangement) is used. For the connected Wabamun and Nisku formations costs would decrease to 6.4 \$/GJ if three horizontal wells would be stimulated along the well axes (Scenario 2) and the formation is assumed to be confined. In the Cooking Lake formation, costs could be decreased to 6.8 \$/GJ if the same well and fracture system is used (Scenario 2) and again the formation is assumed to be confined. In the Basal Sandstone Unit, stimulation leads to the most significant decrease in cost, but compared to the other stimulated formations, costs are still the highest (8.9 \$/GJ) even for the most economic scenario (Scenario 1) where three horizontal wells are connected by hydraulic fractures perpendicular to the well axes.

Figure 22 shows the cost development of geothermal energy production over time for the most economic energy production from the intact and stimulated scenarios for all four formations.

Costs are initially very high due to high initial investments but decrease significantly with time of operation. After 1 year, the costs for all simulated scenarios are higher than 30 \$/GJ. After 10 years, for all scenarios, costs range between 10 and 30 \$/GJ, and after 30 years, costs range roughly between 5 and 15 \$/GJ.

Energy can be extracted most economically by stimulating the shallower formations of Nisku/Wabamun and Cooking Lake with three horizontal wells and fractures parallel to the wells. From the Basal Sandstone Unit, heat (which can be used for space heating) can be extracted at a cost of about 9 \$/GJ from three horizontal wells with five perpendicular fractures. Lower costs may be possible if higher flow rates are used and the number of fractures, well spacing, and fracture spacing is optimized. For comparison, the price of natural gas in Alberta was 3.5 \$/GJ in April 2013 [20].

2.4.5 Reductions in CO₂ emissions

Figure 23 shows the potential amount of CO₂ emissions that can be saved by the use of geothermal energy compared to the burning of natural gas assuming a possible reduction of 53 gCO₂/MJ. For the three horizontal well intact rock cases, the highest amount of CO₂ can be saved by utilizing the Nisku formation (115,564 tons) followed by the Cooking Lake formation (97,756 tons). CO₂ savings from the intact Wabamun formation (45,528 tons) and the Basal Sandstone Unit (51,910 tons) are significantly less.

Overall, the stimulated Basal Sandstone Unit leads to the largest reductions in CO₂ emissions (229,437 tons in 30 years or 7,648 tons per year). Similar savings can be achieved for the Cooking Lake formation (229,110 tons in 30 years). For comparison, the annual greenhouse gas emissions from residential buildings in Edmonton were 2,949,000 tons CO₂-eq. in 2009 and for industrial, commercial and institutional buildings in Edmonton greenhouse gas emissions were 6,665,000 tons CO₂-eq. in 2009 [23]. By substituting natural gas with geothermal energy (203 EGS for residential and 314 EGS for industrial, commercial and institutional buildings) about 53% of the annual greenhouse gas emissions from residential areas and approximately 36% of the annual greenhouse gas emissions from industrial, commercial and institutional buildings can be reduced.

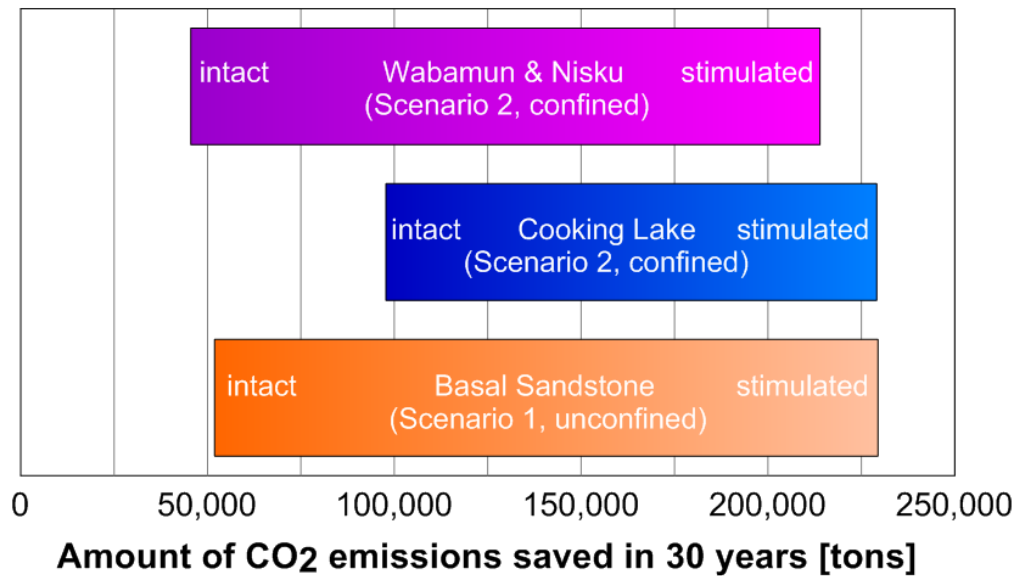


Figure 23: Potential range of CO₂ emission reductions for the four formations assuming 53 g CO₂ reductions per MJ (lower bound: intact rock with three horizontal wells, upper bound: most promising stimulated rock scenario).

2.4.6 Natural gas savings

Depending on the heating value, between 26.1 m³ and 28.9 m³ of natural gas can be saved by producing 1 GJ geothermal energy [3]. For the intact rock cases, between 21.2e6 m³ (lower boundary value of Wabamun) and 59.6e6 m³ (upper boundary value of Nisku) natural gas can be saved. The gas savings for the intact Cooking Lake formation is a maximum of 50.4e6 m³, and for the intact Basal Sandstone Unit, 26.8e6 m³. If the reservoirs are going to be stimulated, savings in 30 years are up to 118.4e6 m³ for the Basal Sandstone Unit, 118.2e6 m³ for the Cooking Lake Formation, and 110.3e6 m³ for the Nisku formation/Wabamun Group (**Figure 24**). In one year up to 3.95e6 m³ of natural gas can be saved by one EGS in the Basal Sandstone Unit.

In Alberta, about 1.0e11 m³ of natural gas were produced (70% of Canada's gas production) in 2012 from which 44% were consumed within the province itself (about 4.6e10 m³). That means the 517 stimulated horizontal three-well systems in the Basal Sandstone Unit could potentially save 4.4% of Alberta's annual natural gas consumption.

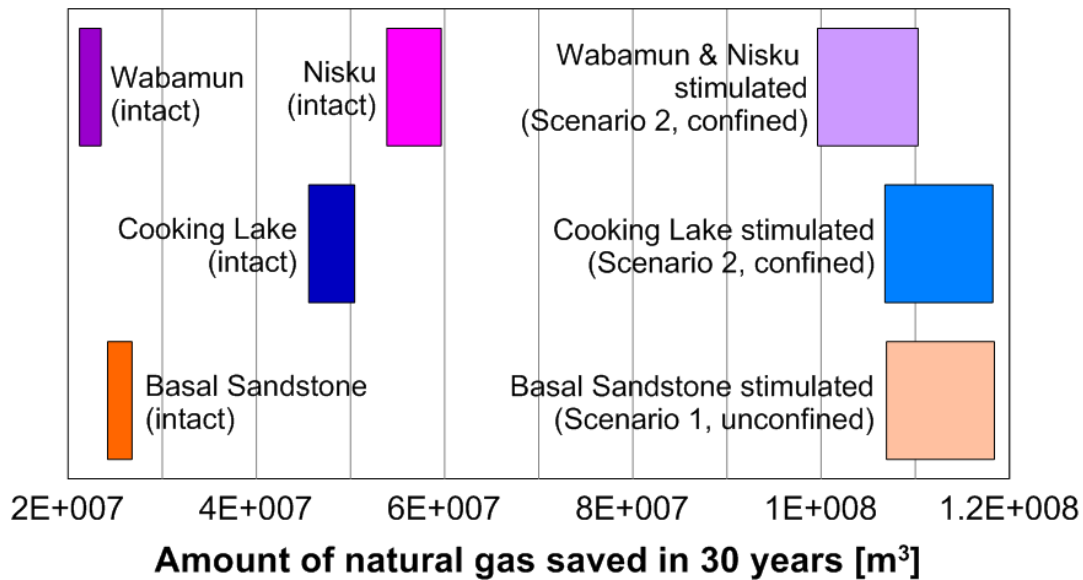


Figure 24: Potential amount of natural gas saved by one geothermal system within 30 years of operation. Values range between low heating value and high heating value of natural gas.

2.5 CONCLUSIONS AND REMARKS

The integrated geological, reservoir and stimulation modeling approach leads to the following conclusions and remarks:

- (1) The Basal Sandstone Unit is potentially the most promising EGS reservoir out of the four investigated formations due to the highest temperatures that are suitable for district heating, but reservoir stimulation is imperative for this formation and costs are the highest. Gel-proppant fracturing could be a suitable stimulation method. The fracture development is most likely well confined by the overlying shale formations. Fracture development into the Precambrian basement is likely and could increase the reservoir volume significantly; however, the data basis for this formation is very poor. Additional investigations are needed to clarify rock properties.
- (2) From the Cooking Lake formation and the Basal Sandstone Unit the highest amount of heat can be extracted. The energy generation costs for the Cooking Lake formation would be lower as for the Basal Sandstone Unit. However, because of the lower temperatures, the energy from the Cooking Lake formation may only be used for heating greenhouses and other agricultural and industrial pre-heating purposes.

- (3) Stimulation treatments may connect the Nisku formation and the Wabamun Group, which would lead to the lowest cost out of all formations, but the produced water temperatures are only applicable for agricultural and balneological purposes.
- (4) The Wabamun Group is not viable for geothermal heat extraction because temperatures and permeability are too low and productivity enhancement due to stimulation is not advised because of missing fracture height growth confinement.
- (5) For all four formations, stimulation treatments significantly improve the production rates, the amount of the produced heat and the economics. Horizontal wells outperform vertical wells and a three-well system is more economic than a two-well system.
- (6) In low permeability formations (Basal Sandstone Unit) fractures should connect the wells. In higher permeability formations (Cooking Lake, Nisku) fractures should be parallel to the wells.
- (7) Geothermal energy generation can be economically feasible if the most economic simulated systems can be realized and/or if the natural gas price increases. Costs range between 6.4 and 15.1 \$/GJ and can be further reduced by optimization.
- (8) Up to 1140 houses can be heated (space and water heating) with geothermal energy from the most promising simulated three-well system in the Basal Sandstone Unit with a reinjection temperature of 70°C.
- (9) A total of 203 of these EGS need to be developed to replace energy from natural gas with geothermal energy for residential buildings and 314 EGS need to be developed to replace energy from natural gas with geothermal energy for industrial, commercial and institutional buildings (total of 517 EGS or 1551 wells).
- (10) Large amounts of CO₂ emissions can be reduced (up to 0.23 Mt in 30 years) and natural gas can be saved (up to 118e6 m³ in 30 years) by substituting natural gas with geothermal energy from a three-well system in the Basal Sandstone Unit. Greenhouse gas (GHG) emissions from residential buildings can be reduced by approximately 53% with 203 EGS and GHG emissions from industrial, commercial and institutional buildings can be reduced by about 36% with 314 EGS. These 517 EGS would save 4.4% of Alberta's annual natural gas consumption.
- (11) Potentially, significantly more energy could be extracted, more CO₂ emissions could be reduced and larger amounts of natural gas could be saved at lower costs by using a lower

reinjection temperature (e.g. 40°C), using the heat for a combination of different applications (e.g. space heating and domestic warm water provision) and optimizing the hydraulic fracture network. This optimization would be the subject of further study.

REFERENCES

- [1] Augustine C, Tester JW, Anderson B. A comparison of geothermal with oil and gas well drilling costs. In: Thirty-first workshop on geothermal reservoir engineering. Stanford, California: Stanford University; 2006. SGP-TR-179.
- [2] Bertani R, Thain I. Geothermal power generating plant CO₂ emission survey. IGA News 2002;49:1-3.
- [3] Bioenergy Feedstock Information Network. Quick-reference list of conversion factors used by the bioenergy feedstock development programs at ORNL; 2013. Available from: https://bioenergy.ornl.gov/papers/misc/energy_conv.html [retrieved October 12, 2013].
- [4] User's guide STARS advanced process and thermal reservoir simulator 2009. Computer Modeling Group Ltd.; 2011. p. 1120.
- [5] Conolly CA, Walter LM, Baadsgaard H, Longstaffe FJ. Origin and evolution of formation waters, Alberta Basin, western Canada sedimentary basin. I. Chemistry. Appl Geochem 1990;5:375-95.
- [6] Economides MJ, Nolte KG. Reservoir stimulation. 3rd ed. Wiley; 2000. p. 856.
- [7] Hanova J, Dowlatabadi H, Mueller L. Ground source heat pump systems in Canada: economics and GHG reduction potential. Discussion paper, RFF DP 07-18, Resources for the future; 2007. Available from: http://www.green-erg.com/documents/Canada_GSHP.pdf [retrieved November 15, 2013].
- [8] Haug K, Nygaard R, Keith D. Evaluation of stress and geomechanical characteristics of a potential site for CO₂ geological storage in Central Alberta, Canada; 2007. Available from: <http://www.keith.seas.harvard.edu/papers/109.Haug.2007.EvalofStress&GeomChar.e.pdf>.
- [9] Hawkes CD, Bachu S, Haug K, Thompson AW. Analysis of in-situ stress regime in the Alberta Basin, Canada, for performance assessment of CO₂ geological sequestration sites. In: Fourth annual conference on carbon capture and sequestration; May 2-5, 2005. p. 22.
- [10] Heidbach O, Tingay M, Barth A, Reinecker J, Kurfess D, Mueller, B. The world stress map database release 2008; 2008. doi: 10.1594/GFZ.WSM.Rel2008.
- [11] Helms L. Horizontal drilling. North Dak Dep Miner Resour (DMR) News l 2008;35:1-3.

- [12] Hofmann H, Babadagli T, Zimmermann G. Hot water generation for oil sands processing from enhanced geothermal systems: process simulation for different hydraulic fracturing scenarios. *Appl Energy*; 2014:524-47.
- [13] Hofmann H, Weides S, Babadagli T, Zimmermann G, Moeck I, Majorowicz J, et al. Integrated reservoir modeling for enhanced geothermal energy systems in Central Alberta, Canada. In: *Proceedings of the 38th workshop on geothermal reservoir engineering*. Stanford, California: Stanford University; February 11-13, 2013. SGP-TR-198.
- [14] Hofmann H, Babadagli T, Zimmermann G. Hydraulic fracturing scenarios for low temperature EGS heat generation from the precambrian basement in Northern Alberta. *GRC Trans* 2012;36:459-67.
- [15] Lemmon EW, Huber ML, McLinden MO. NIST standard reference database 23: reference fluid thermodynamic and transport properties-REFPROP, version 9.0. Gaithersburg: Standard Reference Data Program; 2010.
- [16] Lindal B. Industrial and other applications of geothermal energy (except power production and district heating). In: *Geothermal energy: review of research and development*. Paris: UNESCO; 1973. pp. 135-48. LC No. 72-97138.
- [17] Majorowicz, J., Hofmann, H., Babadagli, T. Deep geothermal heat storage under oilsands. Can we use it to help oilsands industry? New EGS concept proposed. In: *Proceedings of the 37th geothermal resources council annual meeting*, Las Vegas, NV; Sept. 29-Oct. 2, 2013.
- [18] Majorowicz J, Weides S. Is it feasible to use engineered geothermal systems to produce electrical energy in Alberta Basin? *CanGRC Rev* 2012;3:2-3.
- [19] User's guide meyer fracturing simulators. 9th ed. Meyer & Associates; 2011.
- [20] National Energy Board; 2013. Available from: <http://www.neb-one.gc.ca/clf-nsi/rnrgynfntn/nrgyrprt/nrgytlk/tlksmmr2013/ntrlgs-eng.html#s2> [retrieved September 25, 2013].
- [21] Comprehensive energy use database, 1990 to 2010. Natural Resources Canada; 2010. Available from: http://oee.nrcan.gc.ca/corporate/statistics/neud/dpa/comprehensive_tables/index.cfm [retrieved January 28, 2013].

- [22] CO₂ emission factors. Natural Resources Canada; 2008. Available from: <http://oee.nrcan.gc.ca/industrial/technical-info/benchmarking/canadian-steelindustry/6602> [retrieved November 19, 2013].
- [23] Edmonton's energy transition. Discussion paper. Pembina Institute; 2013. Available from: <http://www.pembina.org/pub/2391> [retrieved October 9, 2013].
- [24] Statistics Canada. The Canadian population in 2011: population counts and growth. Ottawa: Ministry of Industry; 2012. Catalogue no. 98-310-X2011001.
- [25] Tester JW, Anderson BJ, Batchelor AS, Blackwell DD, DiPippo R, Drake EM, et al. The future of geothermal energy impact of enhanced geothermal systems (EGS) on the United States in the 21st century. Massachusetts Institute of Technology; 2006.
- [26] Van der Hoorn K, Heijnen LJ, Gankema ME, Nitters G. Hydraulic fracturing in limestone: a case study of two EGS projects in the Netherlands. In: Proceedings of the 37th workshop on geothermal reservoir engineering. Stanford, California: Stanford University; January 30-February 1, 2012.
- [27] Warpinski NR, Moschovidis ZA, Parker CD, Abou-Sayed IS. "Comparison study of hydraulic fracturing models e test case: GRI staged field experiment no. 3. SPE Product Facilities; 1994:7-16.
- [28] Weides S, Moeck I, Majorowicz J, Grobe M. The Cambrian Basal Sandstone Unit in Central Alberta – an investigation of temperature distribution, petrography, and hydraulic and geomechanical properties of a deep saline aquifer. *Can J Earth Sci* 2014;51(8):783-96.
- [29] Weides S, Moeck I, Majorowicz J, Palombi D, Grobe M. Geothermal exploration of Paleozoic formations in Central Alberta. *Can J Earth Sci* 2013;50(5):519-34.
- [30] Yew CH. Mechanics of hydraulic fracturing. Houston, TX: Gulf Publishing Company; 1997. p. 183.
- [31] Zoback MD. Reservoir geomechanics. Cambridge, UK and New York, NY, USA: Cambridge University Press; 2007. p. 464.

CHAPTER 3: HYDRAULIC FRACTURING SCENARIOS FOR LOW TEMPERATURE EGS HEAT GENERATION FROM THE PRECAMBRIAN BASEMENT IN NORTHERN ALBERTA

A version of this chapter was published in *GRC Transactions* (2012) **36**:459-467.

Previous computer simulations identified the characteristics of a fracture network that would allow sufficient heat and fluid transfer for the sustainable and economic use of geothermal heat for oil sands extraction and processing in Northern Alberta (Pathak et al., 2014). Since this type of fracture system does not occur naturally in the region, hydraulic fracturing treatments are needed. In this paper, different hydraulic fracturing scenarios are modeled with a commercial fracturing simulator to examine the dimensions of fracture systems that could be obtained artificially by conventional gel-proppant, water- or hybrid-fracture treatments. The primary objective is to evaluate different treatment approaches for these applications to the conditions existing in Northern Alberta. Additionally, a sensitivity analysis is conducted to evaluate the influence of reservoir and treatment parameters on fracture properties.

Subsequent reservoir simulations show whether these fracture systems could make a sustainable and economical heat extraction possible. Overall, the integration of the results of both models leads to proposed hydraulic fracturing strategies suitable for the conditions expected in Northern Alberta.

3.1 INTRODUCTION

Production and processing of the Athabasca oil sands in Fort McMurray in Northern Alberta, Canada, requires a considerable amount of hot water. Currently, river water is heated by burning huge amounts of natural gas. The question is whether the required hot water could alternatively be supplied by geothermal energy.

Geothermal heat is already produced on a large scale in regions with favorable conditions, where huge amounts of hot water are extracted from permeable formations at relatively shallow depths (e.g., Ragnarsson, 2005). However, in the Athabasca region, the conditions are more challenging. The temperature at a depth of 5000 m is expected to be between 70 and 120 °C (Marjorowicz and Moore, 2008), and the rocks at these depths are anticipated to be low permeability Precambrian granites.

Previous computer simulations identified the characteristics of the fracture network that would be needed for the sustainable and economical use of geothermal energy for oil sands extraction in Northern Alberta (Pathak et al., 2014). Since this type of fracture system does not occur naturally, we examine in this study the type of fracture systems that could be developed by hydraulic fracturing, using commercial fracture modeling software.

To create such an “Enhanced Geothermal System” (EGS), three main stimulation approaches exist: (1) conventional gel-proppant stimulation, (2) water stimulation, and (3) hybrid stimulation. In the past, water fracturing has been used, almost exclusively, to create EGS in low permeability basement rocks (e.g., Soultz-sous-Forêts (Schindler et al., 2008) and Cooper Basin (Wyborn et al., 2005)). Exceptions are gel-proppant stimulations of a granite in Rosemanowes (Parker, 1999) and of a sandstone formation in Groß Schönebeck (Zimmermann & Reinicke, 2010). However, Rushing & Sullivan (2003) observed that, compared to conventional waterfracs, longer effective fracture half-lengths and higher effective fracture conductivities could be achieved by the hybrid waterfrac technique used in the Bossier Tight Gas Sand Play. The basic parameters, advantages and disadvantages of the three methods, summarized by Reinicke (2009), are given in **Table 6**.

Table 6: Summary of the treatment parameters, advantages and disadvantages of the three main hydraulic stimulation methods (Reinicke, 2009).

Treatment Parameters	Gel-Proppant fracs	Water fracs	Hybrid fracs
Frac fluid viscosity	≥ 100 mPas	1 – 10 mPas	≈ 100 mPas
Proppant concentration	200 – 2,000 g/l	0 – 200 g/l	200 – 500 g/l
Fracture half-length	≤ 150 m	≤ 1000 m	≤ 250 m
Fracture width	1 – 25 mm	≤ 1 mm	1 – 2 mm
Fracture permeability	10 – 1000 D	10 – 1000 D	10 – 100 D
Fracture conductivity	0.01 – 25 Dm	0.0001 – 1 Dm	0.01 – 1 Dm
Reservoir permeability	1 – 1000 mD	≤ 0.1 mD	0.01 – 1 mD
Advantages	<p>Good control of stimulation results</p> <p>Special designs allow large fracture width</p> <p>Good control of fluid leak-off</p>	<p>Creates long fractures</p> <p>Connects to natural joint networks</p> <p>Reduced costs</p> <p>Avoids fluid incompatibilities</p>	<p>Good control of stimulation results</p> <p>Increases effective propped fracture length</p> <p>Reduced chemical loading of fluids</p>
Disadvantages	<p>Incompatibility of reservoir fluid with complex frac fluid chemistry</p> <p>Ineffective clean-up</p> <p>Screen-out of proppant in the wellbore due to high proppant loads</p>	<p>Stimulation success is difficult to predict</p> <p>Proppant placement problems</p> <p>Screen-out due to weak proppant transport</p> <p>Rapid fracture closure</p>	<p>Incompatibility of reservoir fluids with frac fluid chemistry</p> <p>Ineffective clean-up</p> <p>Screen-out of proppant in the wellbore due to high proppant loads</p>

A sensitivity analysis of the hydraulic and mechanical parameters on the fracture properties was conducted, within the typical parameter range, for 5 km deep granites, to understand the relative importance of the different parameters and to identify further data acquisition needs. Additionally, the influence of the treatment parameters was investigated to identify the

appropriate size and design of the treatments. Subsequently, eight different stimulation strategies were tested to determine the most suitable treatment design for two possible scenarios. The resulting fractures were used as input data for a thermal-hydraulic reservoir model to evaluate their effect on reservoir performance in terms of productivity, heat extraction and the sustainability of the produced water temperature.

In summary, the main goals of this study were to assess the typical range of fracture properties expected in the Precambrian basement rock in Northern Alberta, to identify the reservoir and treatment parameters with the most significant impact on the fracture characteristics, to investigate whether the desired EGS may be obtained by hydraulic fracturing and which fracturing strategy would be most appropriate, and to improve our understanding of how hydraulic stimulations should be undertaken to develop a sustainable source of geothermal energy in this particular depth and formation.

3.2 MODEL PARAMETERS

All input parameters were taken from literature since no data is available for the Precambrian basement rocks at these great depths. The rock properties and stress parameters used for the fracturing simulation and the sensitivity analysis are summarized in **Tables 7 and 8**. The data used for the hydrothermal reservoir simulation is shown in **Table 9**. Most of the data were obtained from the European EGS research site in Soultz-sous-Fôrets. A permeability of 10^{-3} mD represents fractured granite, and 10^{-8} mD is the value taken for fresh granite (e.g., Geraud, 2010).

It is assumed that the vertical stress σ_v [MPa] is the maximum principle stress in a normal stress regime. Therefore, the resulting fractures will be vertical. The magnitude of the minimum horizontal stress σ_{min} [MPa] was calculated using the following equation (Zoback, 2007):

$\sigma_{min} = \frac{\nu}{1-\nu} (\sigma_v - P_p) + P_p$, with Poisson's ratio $\nu = \frac{V_p^2 - V_s^2}{2(V_p^2 + V_s^2)}$ and the vertical stress σ_v [MPa] = $\rho_{rock} g z$, where ρ [kg/m³] is the density of the overburden rocks, g [m/s²] is the gravity acceleration and z [m] is the thickness of the overburden.

Table 7: Summary of hydraulic and mechanical properties of granites used as input parameters for the fracturing simulations.

Parameter	Base Case	Range	Source
Permeability	$5 \cdot 10^{-5}$ mD	$10^{-3} - 10^{-8}$ mD	Geraud, 2010
Porosity	0.5 %	0.1 – 1 %	Geraud, 2010
Young's Modulus	55 GPa	40 – 70 GPa	Valley & Evans, 2006
Poisson's Ratio	0.25	0.2 – 0.3	Kumar (1976)
Fracture Toughness	$1.5 \text{ MPa m}^{0.5}$	$1.3 - 1.7 \text{ MPa m}^{0.5}$	Sun & Ouchterlony (1986)

V_p [m/s] and V_s [m/s] are the compressional and shear wave velocities, respectively. Pore pressure P_p [MPa] is assumed to be equal to the hydrostatic pressure ($P_p = \rho_{water}gz$). Maximum and minimum values of σ_{min} were obtained by different Poisson ratios between 0.2 and 0.3 (**Table 8**). The direction of the induced fractures is perpendicular to σ_{min} and parallel to σ_{max} , which is presumably NE-SW, as obtained from the world stress map (Heidbach et al., 2008).

Two scenarios were considered. Permeability, porosity, Young's modulus, Poisson's ratio and fracture toughness were kept constant over the whole reservoir in both scenarios.

However, in Scenario 1 pressures and stresses increase linearly with depth (**Figure 25**, left), and in Scenario 2 the stress increases stepwise (**Figure 25**, right). In both cases the reservoir is assumed to be infinite and homogeneous in the horizontal plane. The initiation depth for both cases is 5000 m, and the initial temperature is 100 °C.

Table 8: Calculated stress states at different depths.

Depth	4000 m	5000 m	6000 m
Min. horizontal stress	55 – 61 – 67 MPa	69 – 76 – 84 MPa	83 – 91 – 100 MPa
Vertical stress	104 MPa	130 MPa	156 MPa
Pore pressure	39 MPa	49 MPa	59 MPa

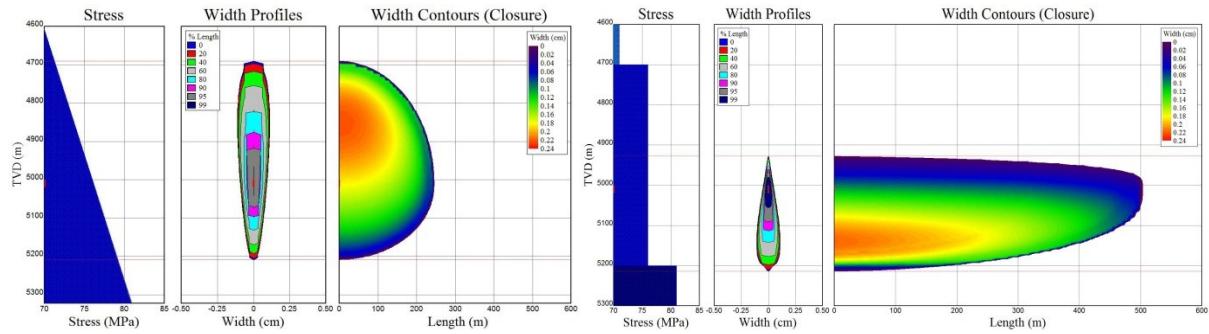


Figure 25: Fracture dimensions of Scenarios 1 (left) and 2 (right), showing the different stress states in both scenarios and different resulting fracture geometries.

Table 9: Summary of the main parameters used for the reservoir simulation.

Permeability	Porosity	Initial pressure	Initial temperature	Rock heat capacity	Rock thermal conductivity
5e-5 mD	0.5 %	48,000 kPa @ 5000 m	100 °C	2170 kJ/m/K	2.7 W/m/K

3.3 METHODOLOGY

3.3.1 Fracturing simulations

For the fracturing simulations, the software package MFrac was selected. The simulator is formulated between a pseudo-3D and full 3D model, including a coupling between fracture propagation and proppant transport (Meyer, 2011). The main reasons for this choice are the 3D modeling capabilities, an extensive material database, and the possibility to use the discrete fracture network (DFN) simulator MShale, which may be subject of future studies.

3.3.1.1 Sensitivity analysis

MFrac supports an auto-treatment design function which calculates a treatment schedule based on input parameters like fluid type, proppant type, and proppant concentration and a target parameter like a desired fracture half-length. The treatment schedules for the base cases of Scenarios 1 and

2 were derived by this auto-design function for target fracture half-lengths of 250 m for Scenario 1 and 500 m for Scenario 2. This function was also used for the sensitivity analysis of the treatment parameters to investigate which parameters should be used to most efficiently reach the target fracture size of 250 m in Scenario 1. The parameter range used for this analysis is given in **Table 10**.

The influence of the reservoir and the treatment parameters on the fracture area A_f [m²] and width w_f [m] at the end of the treatment job was studied without consideration of proppants for Scenario 2. The fracture area was calculated from the fracture half-length l_f [m] and the average fracture height h_f [m]: $A_f = 2l_fh_f$. The fracture width is the average width integrated over the whole fracture area. The studied parameter ranges are given in **Tables 7, 8 and 10**.

Table 10: Summary of treatment parameters of the base case and the range which has been used in the sensitivity analysis.

Parameter	Base Case	Range	Source
Fluid flow rate	6 m ³ /min	3 – 9 m ³ /min	Evans et al. (2012)
Fluid volume	11,500 m ³	10 – 40,000 m ³	Evans et al. (2012)
Fluid type	Cross-linked gel	Water-based fluids, linear gels, cross-linked gels	MFrac database
Proppant mass	1,536 t	222 – 2,520 t	-
Proppant type	High strength ceramic proppants (HSP)	Sand, HSP, bauxite, light weight proppants (LWP)	MFrac database
Mesh size	20/40	12/20 - 40/70	MFrac database

3.3.1.2 Treatment designs for reservoir simulations

For Scenario 1, four gel-proppant treatment designs with different proppant concentrations, but the same flow rates and fluid volumes, were simulated to show the effect of different conductivities on the thermal and hydraulic behavior of the system.

For Scenario 2, three treatment designs were simulated (**Table 10**): (1) a gel-proppant design with high proppant concentrations and high viscosity cross-linked gel; (2) one waterfrac with a high flow rate of 9 m³/min, low proppant concentrations (100 kg/m³), light weight proppants (1.25 g/cm³) and a low viscous fluid (5 mPas); and (3) two hybrid fracturing treatments with high (1,000 kg/m³) and average proppant concentrations (350 kg/m³) and water-based low viscosity (5 mPas) fluid followed by high viscosity cross-linked gel (1000 mPas).

The reservoir simulator input parameters from the fracturing designs are the propped fracture area A [km²] that acts as the heat exchanger and the fracture conductivity K_f [mDm] that enhances the flow. The fracture conductivity is the product of propped fracture width (w [m]) and fracture permeability (k_f [mD]): $K_f = k_f w$.

3.3.2 Reservoir simulations

The thermal and hydraulic behavior of the reservoir was modeled using the thermo-hydraulic finite-difference reservoir simulator CMG STARS (CMG, 2012).

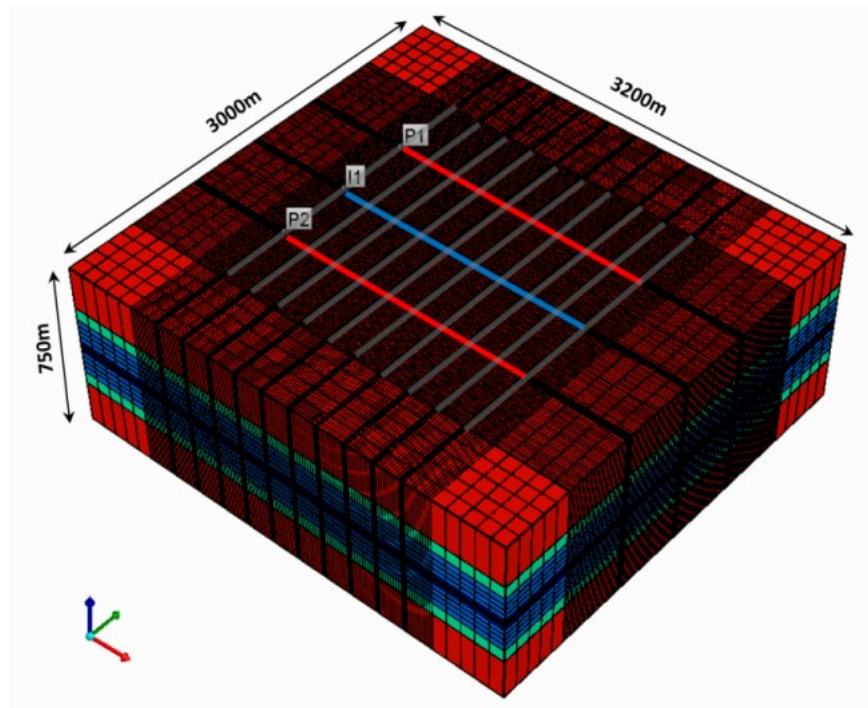


Figure 26: 3D reservoir model including the position of the horizontal injection well (I1, blue), the horizontal production wells (P1 and P2, red) and the vertical hydraulic fractures (grey).

A single porosity model was created, including one horizontal injection well (injection rate: 5,000 m³/d) at the center of the model, flanked by two horizontal production wells (production rate: 2,500 m³/d each) intersected by vertical fractures. This approach has not yet been executed in EGS applications, but is commonly used in shale gas production (e.g., Waters, 2009). The promising advantage is that more fractures can be developed in the same formation compared to vertical and inclined wells, which can greatly increase the size of the reservoir. The spacing between the fractures is 200 m to avoid significant thermal interference. To reduce boundary effects, a 3,200 m x 3,000 m x 750 m reservoir model was created, with a maximum size of the fractured volume of 2,000 m x 2,000 m x 443 m (**Figure 26**). The first fracture is located at the beginning of the open-hole section of the parallel horizontal wells, and the last fracture is located at the end of it. All fractures are perpendicular to the azimuth of the wells.

The thermal performance of the system was evaluated by the total heat produced from the reservoir and the bottomhole temperature (BHT) at production wells. The hydraulic performance was studied by the productivity index PI [m³/h/MPa] of the production wells, which was calculated by dividing the flow rate (Q [m³]) of the well by the pressure drawdown (ΔP) of the bottomhole pressure after 30 years.

For each scenario, the number of fractures was increased from 4 to 10, in steps of 2, to extrapolate the influence of the number of fractures on the performance parameters. This makes it possible to determine the number of fractures needed to achieve the targeted results, which are a PI of 1 l/s/bar or 36 m³/h/MPa, and a BHT at the production well of 70°C after 30 years of production and injection.

3.4 RESULTS

3.4.1 Sensitivity analysis

3.4.1.1 Treatment parameters

First, the influence of the treatment parameters fluid type, proppant type, and proppant mass on the fracture properties has been studied using the auto-treatment design function of MFrac for

Scenario 1. The major observations are summarized in **Table 11**. Thereafter, for Scenario 2, a sensitivity analysis for all other treatment and reservoir parameters has been performed using manual treatment designs.

Table 11: Major observations of the sensitivity analysis performed for the treatment parameters for Scenario 1 with the auto-treatment design function with constant reservoir properties (base case).

Parameter	Major observations
Fluid type	Higher viscosities more appropriate for unconfined formations (Scenario 1) Lower viscosities more appropriate for confined formations (Scenario 2) Highest influence on fracture width
Proppant type	HSP recommended because of high closure stress LWP recommended for waterfracs because of better proppant distribution
Proppant mass	Linear relation between proppant concentration and mass, width, permeability and conductivity

The simulations showed that higher gel concentrations (higher viscosities) are more appropriate for Scenario 1 since this leads to a lower height growth. Low viscosity water-based fluids that are used for waterfrac treatments, and the first pumping stage of hybridfrac treatments, lead to a significant height growth (**Figure 27**) of up to six times the fracture half-length. Another drawback of low viscosity fluids is that the fracture is not uniformly propped because of the fast settling of the proppants. With time, the horizontal and downward fracture growth slows, and the vertical upper fracture half growth increases significantly.

If the stress was constant over a depth of a couple of hundred meters (Scenario 2), a different fracturing fluid would be more appropriate, because this heavy fluid would lead to a more severe growth of the lower half of the fracture wing.

Performing waterfrac treatments with low viscosity fluids leads to a fast settling of the proppants (**Figure 28, left**). The heavier the proppant, the faster is the settling and the lower is the final propped area. That is why, for waterfracs, high strength, light weight proppants with densities of about 1.25 g/cm³ are more appropriate (**Figure 28, right**).

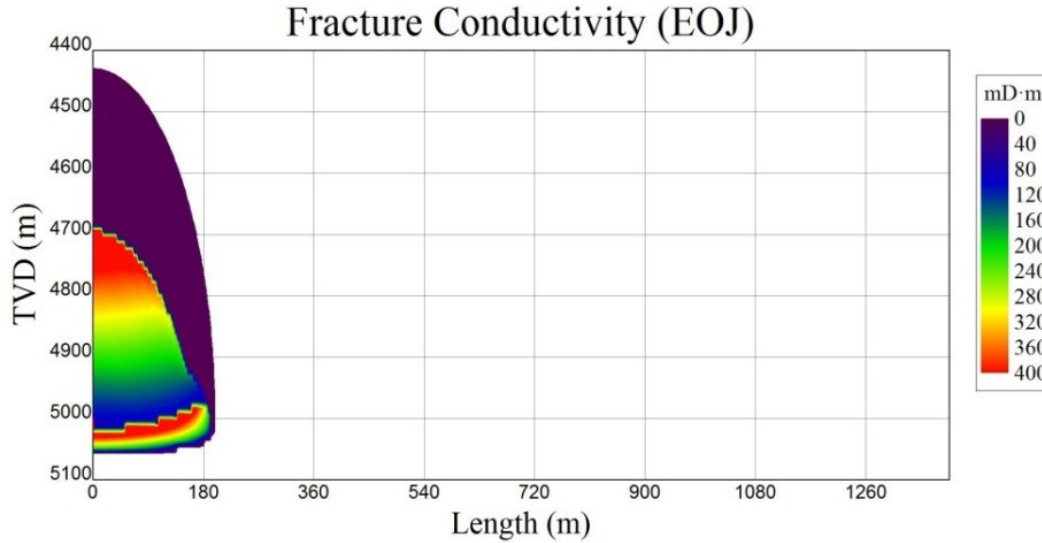


Figure 27: Final fracture area and conductivity showing significant fracture height growth in unconfined reservoirs (Scenario 1) resulting from the use of low viscosity fluids.

It was observed that the treatment parameters are very important for both fracture area and fracture width (**Figures 29 and 30**). For the area, the injected fluid volume is one of the main parameters that can be increased to increase the surface area of the fracture. Fracture width is mainly influenced by the fluid type. Higher fluid viscosities lead to an increase in fracture width of up to 166 %. This would also lead to a decrease in fracture area of 11 %. High flow rates are favorable to increase both fracture area and width. The depth has more influence on the fracture area than on the width. A 20 % bigger fracture area could be achieved with the same treatment design when stimulating at a depth of 4000 m as compared to 6000 m.

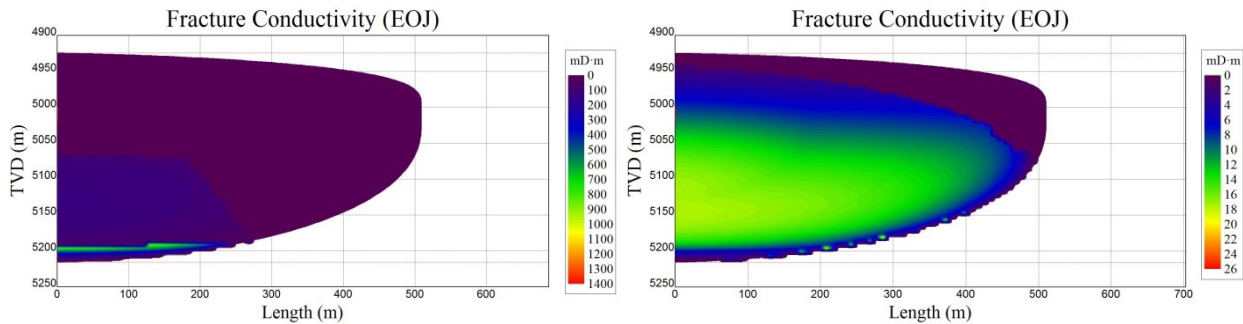


Figure 28: Fast proppant settling due to dense high strength proppants (left) can be reduced by using ultra-light weight proppants (right).

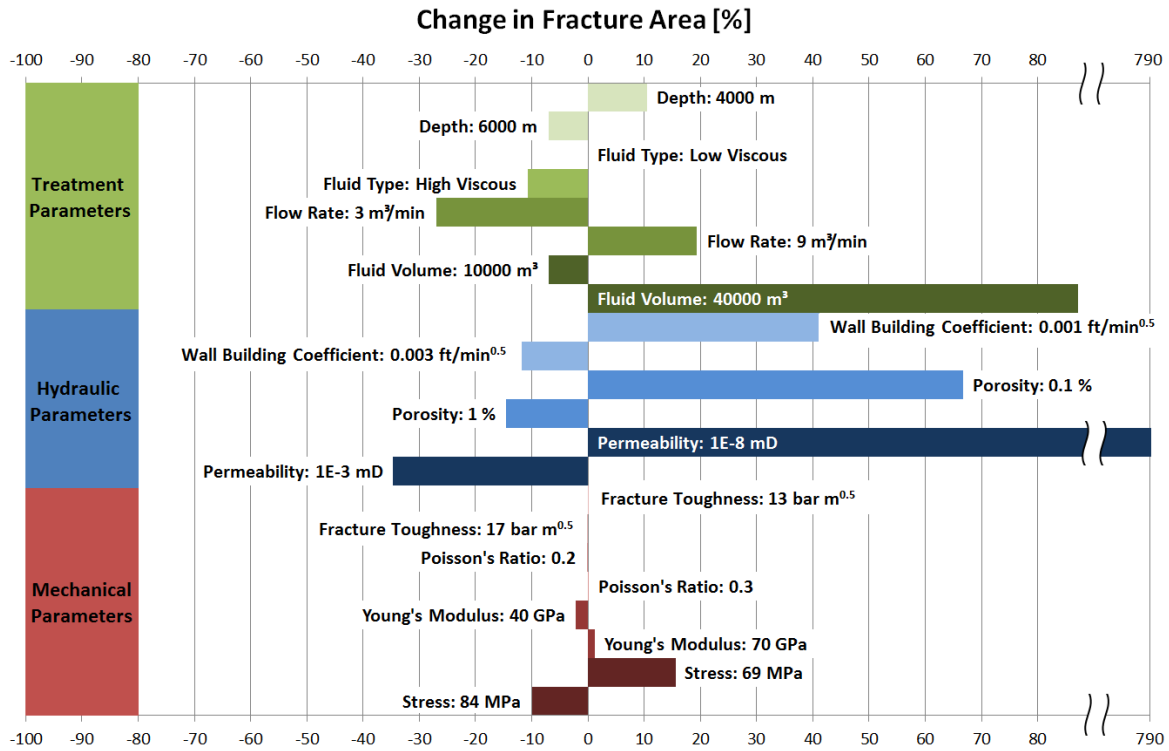


Figure 29: Relative influence of the studied reservoir and treatment parameters within their typical range on the fracture area in Scenario 2.

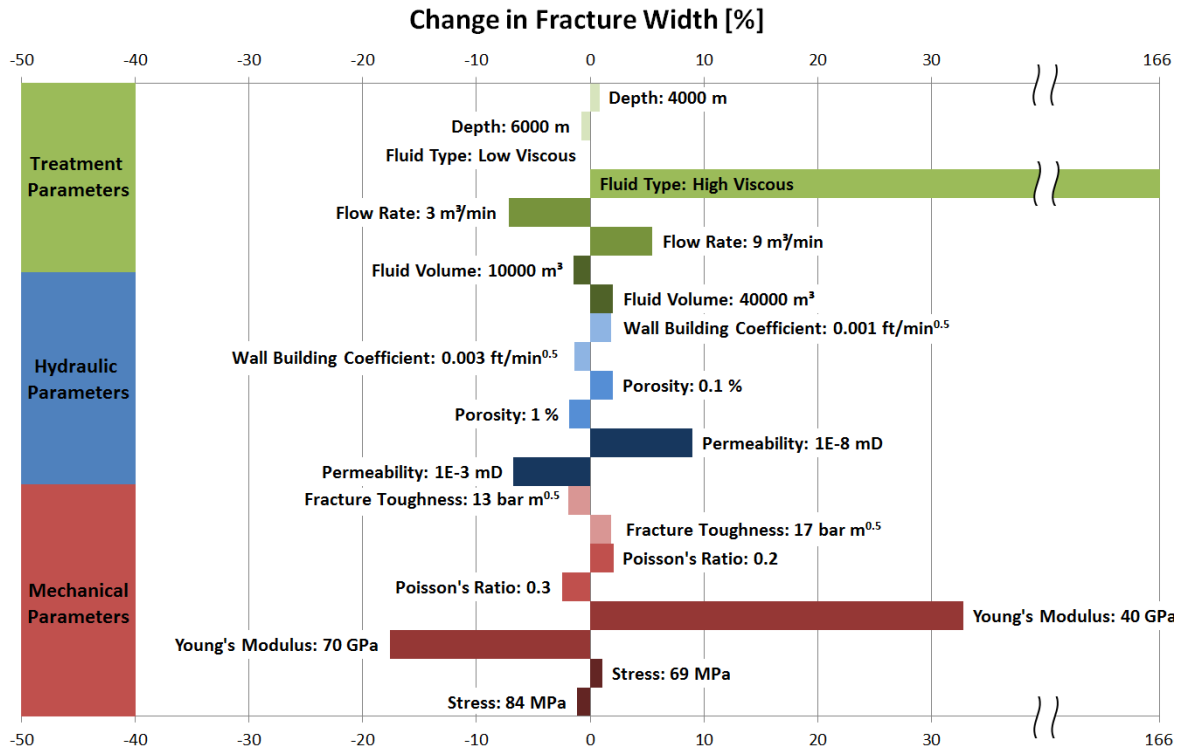


Figure 30: Relative influence of the studied reservoir and treatment parameters within their typical range on the fracture width in Scenario 2.

3.4.1.2 Reservoir parameters

The fracture area is mainly controlled by the fluid leak-off behavior (**Figure 29**). Consequently, the hydraulic parameters which directly influence the fluid leak-off have the biggest influence on the fracture area. If the leak-off is high, a wall-building fluid should be used and high fluid volumes are needed. The influence of the hydraulic parameters on the fracture widths is smaller than on the fracture area (**Figure 30**). For the width, the mechanical parameters, especially Young's modulus, are more important.

The growth of fracture height is of particular interest because the goal is to induce a fracture which is long enough that the water pumped through this fracture from the injection to the production well has enough time to extract the heat from the rock. Several different simulations show that the growth of the upper half is unconfined if the stress increases linearly with depth (Scenario 1) and the growth of the lower half is unconfined if the stress is constant. Height growth confinement is obtained if the stress is lower within the target formation than on top and at the bottom of the target formation. A stress difference of 5 MPa is a sufficient confinement for a low viscosity fluid in our simulations. This observation is independent of all reservoir parameters within their studied range. Only higher viscosity fluids have been able to overcome these height growth barriers. For them, a stronger confinement would be necessary.

3.4.2 Hydraulic fracturing scenarios

Eight different fractures derived from different treatment designs were used for the reservoir simulations (**Table 12**). In the first four gel-proppant treatments, which were simulated in Scenario 1, only the fracture conductivity is different because of the different proppant masses used. The next four treatments were derived from different treatment types used in Scenario 2, resulting in different fracture conductivities and geometries.

Table 12: Results of four different treatment designs for each of the two scenarios used for the reservoir simulations.

Scenario	Treatment type	Proppant mass [t]	Half-length [m]	Height [m]	Fracture conductivity [mDm]
1a	Gel	2520	250	400	986
1b	Gel	1536	250	400	581
1c	Gel	678	250	400	208
1d	Gel	222	250	400	96
2a	Gel	4600	500	443	783
2b	Hybrid	2630	500	208	933
2c	Hybrid	621	500	234	161
2d	Water	141	500	208	7.6

3.4.3 Reservoir simulations of hydraulic fracturing scenarios

These fractures were implemented in four different ways, as shown in **Figure 31**. In the first fracture system, the fractures of Scenario 1 were implemented with the production wells at the end of each fracture wing. In the fracture system 2, the fractures of Scenario 1 (250 m half-length) and 2 (500 m half-length) were implemented assuming that for Scenario 1 all three wells were fractured with the same treatment, and for Scenario 2 that only the injection well was fractured and the production wells are located in the middle of each fracture wing. Fracture system 3 was derived by implementing Scenario 2 fractures of the injection well, with the production wells located at the border of each fracture wing. For fracture system 4, Scenario 2 fracture treatments were implemented for injection and production wells.

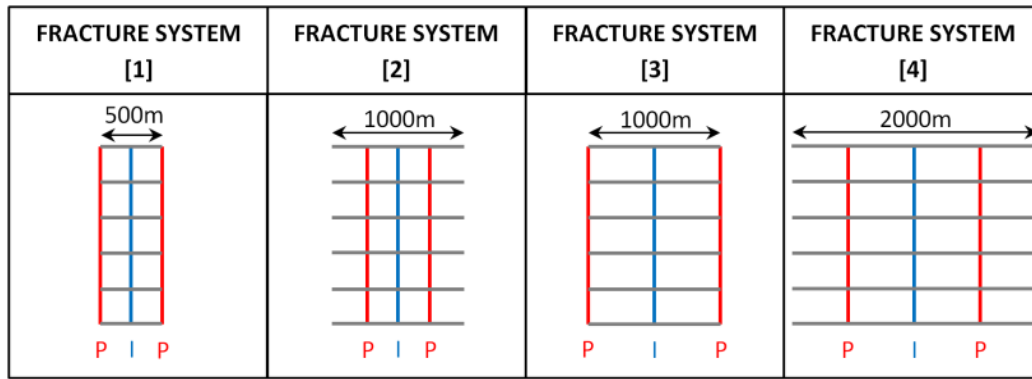


Figure 31: Top-view of the different kinds of fracture systems (gray lines) with the horizontal injection well (blue) in the middle, flanked by two horizontal production wells (red) with changing position.

In all scenarios, the productivity index (PI) increases linearly with the number of fractures (**Figure 32**). Higher permeability fractures increase the productivity and a lower number of fractures is needed. However, with only four fractures, the PI is lower than 30 m³/h/MPa for all cases. The fracture conductivity obtained by the water fracturing treatment (Scenario 2d) is too low to maintain a reasonable productivity. Therefore, this scenario was omitted from further investigation.

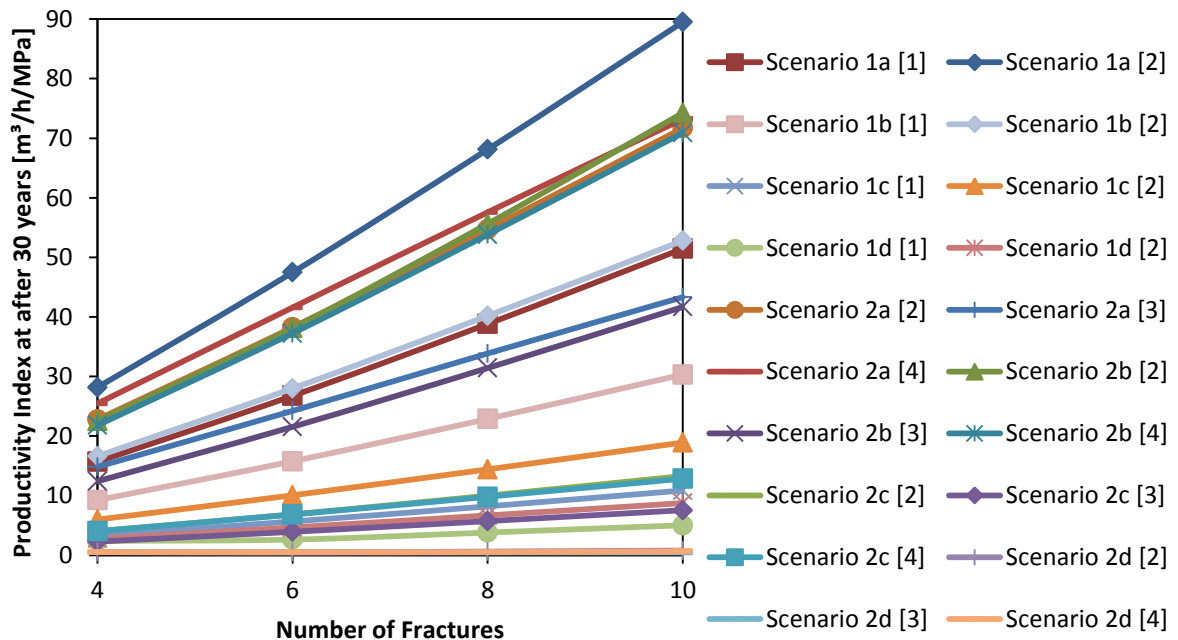


Figure 32: Influence of the number of fractures on the productivity index for all eight scenarios and all four fracture systems.

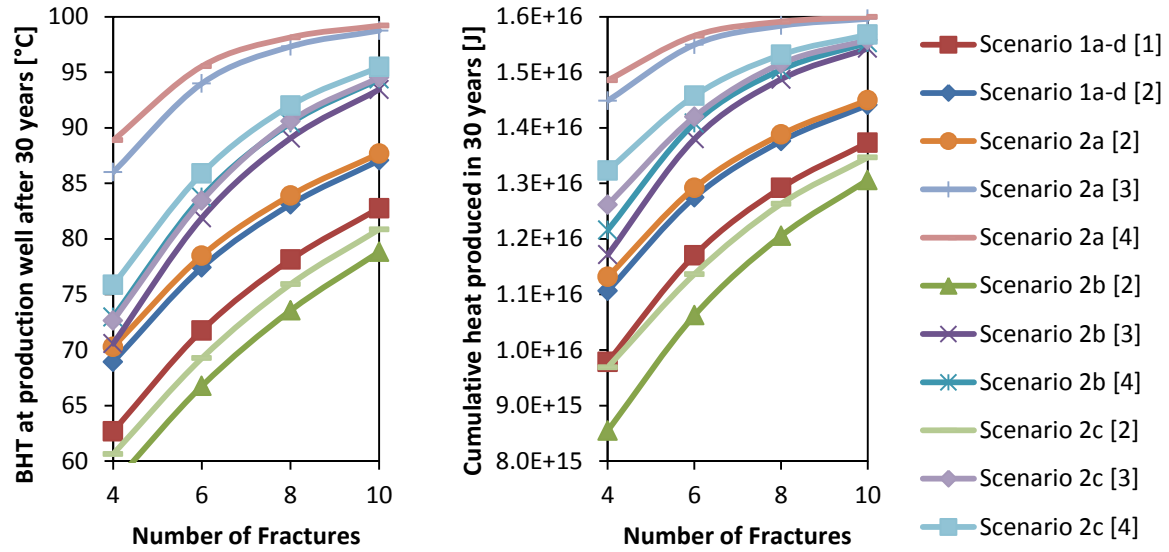


Figure 33: Influence of the number of fractures on the bottomhole temperature at the production well (left) and the cumulative heat produced (right) after 30 years of production.

The final BHT at the production well and the cumulative produced heat increase when the heat exchanger area and fluid residence time are increased by increasing the number of fractures, the fracture height or the fracture length (**Figure 33**). It was also observed that lower flow rates and higher well separations increase the final BHT significantly.

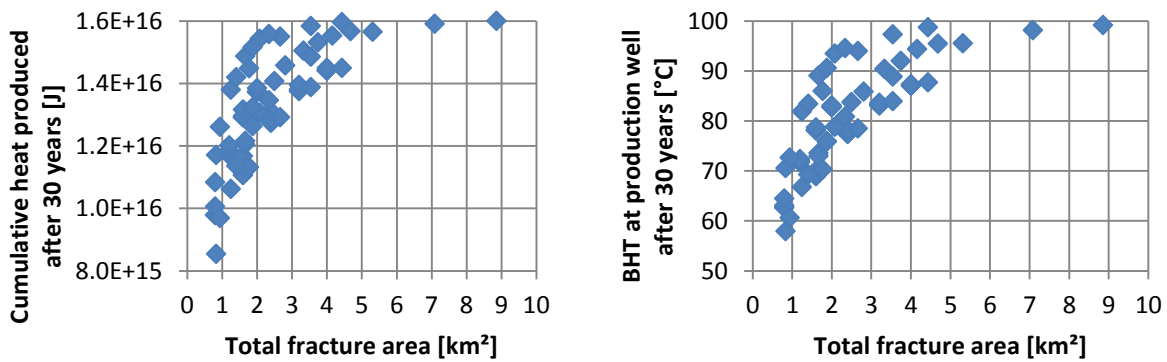


Figure 34: Cumulative heat produced in 30 years production (left) and final bottom hole temperature after 30 years production (right).

The relationship between the total fracture area and the BHT, as well as the cumulative heat produced after 30 years, is shown in **Figure 34**. Most of the scenarios achieve a final BHT of more than 70°C. A significant increase in fracture area above 5 km² does not change the

cumulative produced heat much more. The upper limit as constrained by the production rates is 1.6×10^{16} J.

With the linear relationships between the number of fractures and the PI as shown in **Figure 32**, the number of fracture treatments which are needed to achieve a PI of $36 \text{ m}^3/\text{h}/\text{MPa}$ was calculated for each scenario (**Figure 35, left**).

To create fracture system [2], obviously the least number of treatments is needed for Scenario 2. For fracture system [1] the least treatments are necessary for Scenarios 1a and 1b. The number of fractures needed increases significantly with decreasing conductivity. Scenario 2a is an exception because here the fracture height is almost twice the size of Scenario 2b, reducing the number of fractures needed. The upper boundary of fracturing treatments that can actually be performed strongly depends on the possible length of the horizontal section and the spacing between multiple fracturing stages.

Because horizontal drilling is expensive, the length of the horizontal section as shown in **Figure 35 (right)** was calculated by multiplying the number of treatments with the distance between two fractures (200 m). All cases with a length below 2,500 m (Scenarios 1a, 1b, 2a, and 2b) are assumed to be favorable.

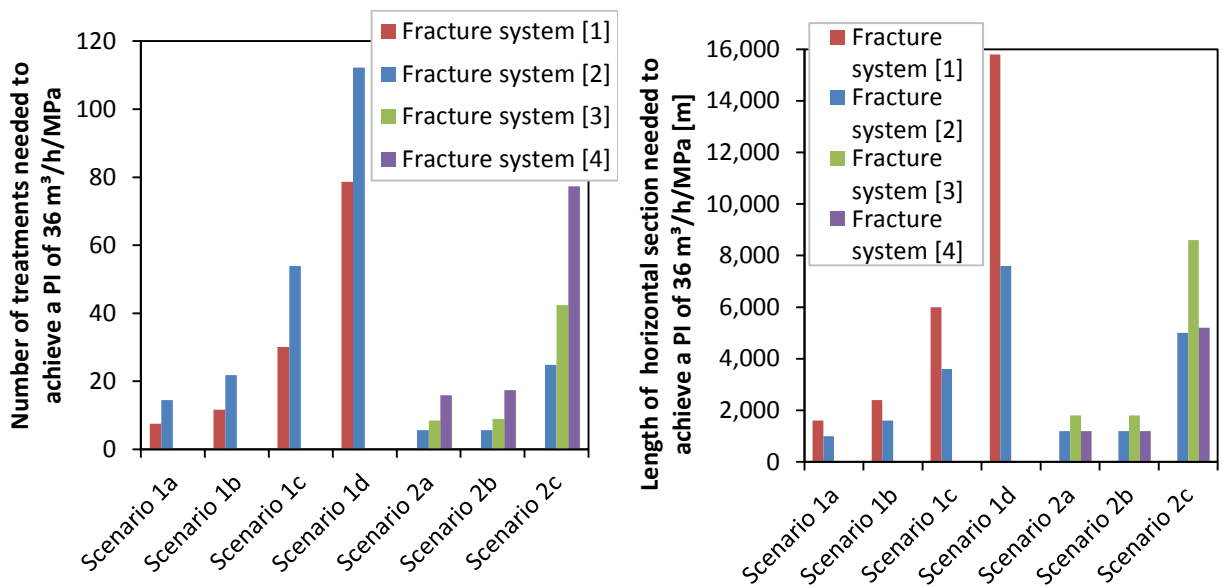


Figure 35: Number of treatments (left) and length of the horizontal section (right) to achieve the target PI of $36 \text{ m}^3/\text{h}/\text{MPa}$.

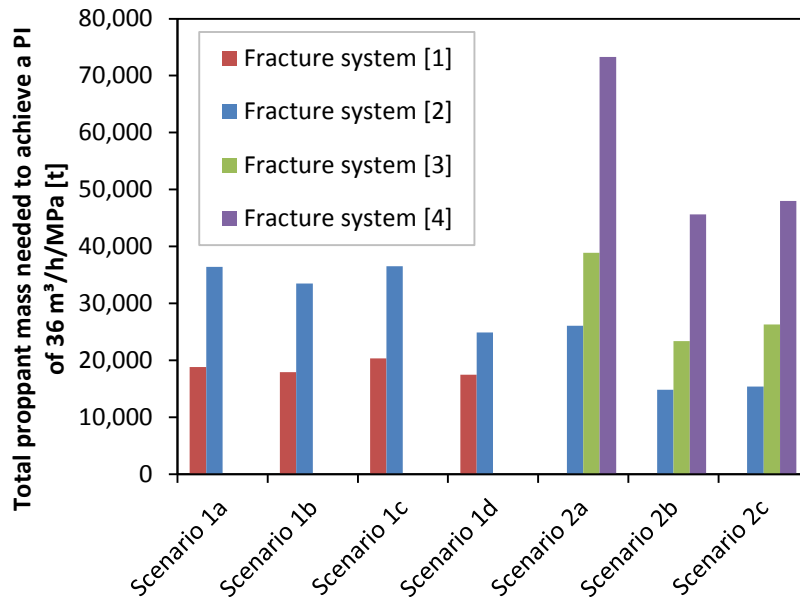


Figure 36: Total proppant mass needed to develop a fracture system leading to a PI of 36 m³/h/MPa.

Because the high strength proppants used in these scenarios are very expensive, the total amount of proppants needed was calculated as well (**Figure 36**). From this diagram, one may observe that, for the fracture system [1], the least amount of proppants is needed for Scenario 1. For Scenario 2, on the other hand, the least amount is necessary to create system [2]. System [2] (Scenario 1) and system [4] (Scenario 2) include the fracturing of all three wells, which results in much higher amounts of proppants.

The lowest number of treatments needed to achieve the desired PI were found for Scenario 2a and 2b to develop fracture system [2], and for Scenario 1a and 1b to develop fracture system [1] (**Table 13**). However, since the heat exchanger area is lowest in these scenarios due to the least amount of fractures and the flow rate through each fracture is higher than for scenarios with more fractures, the total produced heat as well as the final BHT at the production well are less than for most other cases. For Scenario 2a [2], almost twice as much proppants were used to obtain an area which is about twice as big as in Scenario 2b [2]. This leads to a significantly higher final temperature above 70°C. For Scenario 1 and fracture system [1] treatment design 1b may be preferred because less proppants are needed and more heat can be produced, as compared to design 1a, even though the horizontal section has to be at least 600 m longer.

Table 13: Simulated scenarios with the least number of treatments necessary to achieve a productivity index of 36 m³/h/MPa.

Scenario [fracture system]	Number of treatments	Total proppant mass [t]	Length of horizontal section [m]	Total heat produced [x 10 ¹⁶ J]	Final BHT at production well [°C]
2b [2]	5 - 6	13,150 - 15,780	1,000 - 1,200	0.96 - 1.06	63 - 67
2a [2]	5 - 6	23,000 – 27,600	1,000 - 1,200	1.21 - 1.29	74 - 78
1a [1]	7 - 8	17,640 - 20,160	1,400 - 1,600	1.23 - 1.29	75 - 78
1b [1]	11 - 12	16,896 - 18,432	2,200 - 2,400	1.41 - 1.44	84 - 86

3.5 CONCLUSIONS AND REMAKRS

The aim of this study was to investigate the influence of treatment and reservoir parameters on the fracturing performance, and to propose stimulation concepts, for the existing conditions in Northern Alberta. Based on the sensitivity analysis and the reservoir simulations of eight different scenarios and four different fracture systems, some conclusions can be drawn with respect to the three main treatment types.

The following conclusions with impact on gel-proppant treatments were derived:

- Gel-proppant fracs are not recommended for confined reservoirs, because high viscosity fluids are more likely to overcome stress confinements.
- On the other hand, if the target formation is not confined, gel-proppant fracs should be used because of the lower height growth compared to the other treatment types.
- If short fracture lengths are sufficient (<250 m), gel proppant fracs may be suitable.
- Main advantages are a good control of the fracture growth and a good proppant distribution.
- The main disadvantage is the lower possible fracture area as compared to the other treatment types.

The following conclusions with impact on waterfrac treatments were derived:

- For waterfracs, light-weight (e.g., 1.25 g/cm³) high strength proppants are recommended to achieve a better proppant distribution within the fracture due to a reduction in proppant settling velocity.
- The fracture conductivity derived from the simulated waterfracs is too low to maintain high enough flow rates through the reservoir. This may be caused by a lack of an adequate modeling approach.
- It may be reasonable to use waterfracs if the reservoir is critically stressed and failure in shear is more important than tensile failure, and a self-propping is likely to occur.

The following conclusions on hybrid stimulation treatments were derived:

- Hybrid fracturing treatments are the recommended method to stimulate confined formations.
- Similar fracture areas, as developed by water fracturing and fracture conductivities from gel-proppant fracturing, can be developed by pumping low viscosity fluid first to create the fracture and high viscosity fluid with proppants afterwards to widen the fracture and transport the proppants.

Also the fracture development based on different stress scenarios was studied and the following observations on fracture development were made:

- The influence of stress barriers and leakoff-zones is very important for the fracture geometry.
- With constant stress, the fracture develops downwards because of the high density of the fluid-proppant mixture. To reduce this effect low viscosity fluids and light weight proppants may be used.
- If the stress increases linearly with depth the fracture develops upwards because of the lower stress at lower depth. To reduce this effect high density proppants and fluids may be used.
- If the fracture height growth is constrained by stress barriers or leakoff zones, the fracture will develop horizontally and high half-lengths can be obtained.
- Only the treatment fluid changed the influence of the stress barrier. All other parameters don't change it significantly.

The reservoir performance was studied using a commercial three-dimensional thermal-hydraulic reservoir simulator. Based on the simulations of different fracture types and systems, the following observations on reservoir performance were made:

- For the temperature of the produced fluid the fracture surface area, flow rates and well separations are the most important variables; fracture conductivity has no influence.
- For the pressure development and therefore the productivity of the wells, the fracture conductivity is the crucial parameter. Fracture area has less influence here.
- Productivity index and injectivity index increase linearly with the number of fractures.
- Sustainable EGS triplets could be simulated for 30 years with the following minimum parameters: 5 separate treatments, 250 m half-length and well spacing, 500 mDm fracture conductivity, 10,000 t total proppant mass, 1.6 km² fracture surface area, 1,000 m horizontal well section, 200 m fracture separation, 5,000 m³/d injection and 2,500 m³/d production rate per well.
- The productivity of the two production wells should be enhanced by smaller treatments to improve the near wellbore permeability rather than conducting the same treatments for all three wells.
- It is most efficient if first the injection well is drilled and fractured, and afterwards the two production wells are drilled near the borders of the induced fractures.
- The simulations show that it is possible to design a fracture system which leads to a sustainable heat production applicable for oil sands processing in Northern Alberta.

It was shown that a detailed knowledge about the stress state is most important for planning stimulation treatments in Northern Alberta basement rocks. Without a more detailed knowledge about the stress state no particular treatment design can be suggested. Additionally, information about natural fractures, permeability, porosity and the Young's modulus have to be collected by surface geophysical methods (seismic, MT), geophysical logs, hydraulic well tests and core measurements for a detailed planning of a stimulation treatment since these parameters showed the highest sensitivities on the fracture geometry within their proposed range. The influence of the treatment parameters on the final fracture properties is high enough that unfavorable reservoir conditions can be handled efficiently by choosing different treatment parameters if the main properties of the reservoir are known in sufficient detail.

Three different treatment concepts were tested. The results of the waterfrac treatments showed that not enough fracture conductivity can be obtained considering only tensile opening of new fractures. Because this kind of treatment has already provided very good results in the geothermal and gas industry, the self-propping effect of sheared fractures seems to be significant and that is the reason why the fracturing simulator used is not appropriate to model water fracturing treatments. Therefore, future studies will focus on the influence of natural fractures, self-propping and waterfrac treatments for Precambrian basement rocks in the Athabasca region using a different approach.

REFERENCES

- T.M. Aggour and M.J. Economides, 1999. "Impact of fluid selection on high-permeability fracturing." SPE 54536.
- R. Beckwith, 2010. "Hydraulic Fracturing: The Fuss, The Facts, The Future." Journal of Petroleum Technology, v. 62, p. 34-41.
- D.W. Brown, 2009. "Hot Dry Rock Geothermal Energy: Important Lessons From Fenton Hill." Proceedings, Thirty-Fourth Workshop on Geothermal Reservoir Engineering, Stanford University, Stanford, California, February 9-11.
- Computer Modelling Group Ltd., 2011. "User's Guide STARS Advanced Process and Thermal Reservoir Simulator."
- M.J. Economides and K.G. Nolte, 2000. "Reservoir Stimulation, 3rd edition." Wiley, p. 856.
- K.F. Evans, A. Zappone, T. Kraft, N. Deichmann, and F. Moia, 2012. „A survey of the induced seismic response to fluid injection in geothermal and CO2 reservoirs in europe." Geothermics, vol. 41, p. 30-54.
- Y. Geraud, M. Rosener, F. Surma, J. Place, E. Le Garzic, and M. Diraison, 2010. "Physical properties of fault zones within a granite body: Example of the Soultz-sous-Forêts geothermal site." Geoscience, vol. 342, p. 566-574.
- O. Heidbach, M. Tingay, A. Barth, J. Reinecker, D. Kurfess, and B. Müller, 2008. „The World Stress Map database release 2008."
- J. Kumar, 1976. "The Effect of Poisson's Ratio on Rock Properties." SPE 6094.
- J. Majorowicz and M.C. Moore, 2008. "Enhanced Geothermal Systems (EGS) Potential in the Alberta Basin." ISEEE Research Paper, University of Calgary.
- Meyer & Associates, 2011. "User's Guide Meyer Fracturing Simulators, 9th edition."
- C.T. Montgomery and M.B. Smith, 2010. "Hydraulic Fracturing: History of an Enduring Technology." Journal of Petroleum Technology, vol. 62, p. 26-32.
- R. Parker, 1999. "The Rosemanowes HDR project 1983-1991." Geothermics, vol. 28, p. 603-615.
- V. Pathak, T. Babadagli, J. Majorowicz, and M.J. Unsworth, 2014. "Evaluation of engineered geothermal systems as a heat source for oilsands production in Northern Alberta." Natural Resources Research, vol. 23, p. 247-265.
- A. Ragnarsson, 2005. "Geothermal Development in Iceland 2000-2004." Proceedings, World Geothermal Congress, Antalya, Turkey, April 24-29.
- A. Reinicke, 2009. "Mechanical and Hydraulic Aspects of Rock-Proppant Systems: Laboratory Experiments and Modelling Approaches." University of Potsdam, Dissertation.

- J.A. Rushing and R.B. Sullivan, 2003. "Evaluation of a Hybrid Water-Frac Stimulation Technology in the Bossier Tight Gas Sand Play." SPE 84394.
- M. Schindler, P. Nami, R. Schellschmidt, D. Teza, and T. Tischner, 2008. „Summary of hydraulic stimulation operations in the 5 km deep crystalline HDR/EGS reservoir at Soultz-Sous-Forêts." Proceedings, 33rd Workshop on Geothermal Res. Eng., Stanford Univ, Stanford, California, Jan. 28-30.
- T. Schulte, G. Zimmermann, F. Vuataz, S. Portier, T. Tischner, R. Junker, R. Jatho, and E. Huenges, 2010. „Enhancing Geothermal Reservoirs." In: E. Huenges (ed.). "Geothermal Energy Systems: Exploration, Development, and Utilization." WILEY-VCH, Weinheim, p. 173-244.
- Z. Sun and F. Ouchterlony, 1986. "Fracture Toughness of Stripa Granite Cores." International Journal of Rock Mechanics, Mining Science & Geomechanics, vol. 23, p. 399-409.
- B. Valley and K.F. Evans, 2006. "Strength and elastic properties of the soultz granite." 2nd year report, http://www.mirarco.org/files/publications/1292527243valley_06_strength_585283.
- N.R. Warpinski, Z.A. Moschovidis, C.D. Parker, and I.S. Abou-Sayed, 1994. "Comparison Study of Hydraulic Fracturing Models – Test Case: GRI Staged Field Experiment No. 3." SPE Production & Facilities.
- N.R. Warpinski, 2009. "Stress amplification and arch dimension in proppant beds deposited by waterfracs." SPE 11935.
- G. Waters, B. Dean, and R. Downie, 2009. "Simultaneous hydraulic fracturing of adjacent horizontal wells in the woodford shale." SPE 119635-MS.
- D. Wyborn, L. de Graaf, S. Davidson, and S. Hann, 2005. "Development of Australia's First Hot Fractured Rock (HFR) Underground Heat Exchanger, Cooper Basin, South Australia." Proceedings, World Geothermal Congress, Antalya, Turkey, April 24-29.
- G. Zimmermann, and A. Reinicke, 2010. „Hydraulic Stimulation of a deep sandstone reservoir to develop an Enhanced Geothermal System: Laboratory and field experiments." Geothermics, vol. 39, p. 70-77.
- G. Zimmermann, G. Blöcher, A. Reinicke, and W. Brandt, 2011. „Rock specific hydraulic fracturing and matrix acidizing to enhance a geothermal system – concepts and field results." Tectonophysics, vol. 503, p. 146-154.
- M.D. Zoback, 2007. "Reservoir Geomechanics." Cambridge University Press.

CHAPTER 4: HOT WATER GENERATION FOR OIL SANDS PROCESSING FROM ENHANCED GEOTHERMAL SYSTEMS: PROCESS SIMULATION FOR DIFFERENT HYDRAULIC FRACTURING SCENARIOS

A version of this chapter was published in *Applied Energy* (2014) **113**: 524-547.

The oil sands in northern Alberta, Canada are home to one of the largest hydrocarbon deposits on earth. Huge amounts of hot water - around 50 – 60°C - are needed for the current extraction procedure and processing technology. The current practice of obtaining water from the Athabasca River and heating it by the burning of natural gas creates severe economic and environmental costs. In fact, 6% of Canada's gas consumption is used for this purpose. As seen, the generation of huge amounts of fossil energy through oil sands extraction requires a substantial amount of fossil energy consumption (natural gas). Geothermal energy has the potential to significantly reduce natural gas consumption and greenhouse gas emissions at competitive costs.

In this paper, we investigate how and whether or not the required hot water can be generated from the granitic basement rocks beneath the oil sands mining areas near Fort (Ft.) McMurray, located in the north east of Alberta. Hydraulic fracturing and resulting reservoir scenarios were simulated for different expected conditions in the region in order to find suitable fracturing strategies and conditions for an Enhanced Geothermal System (EGS). The simulations show that suitable fracturing treatments can increase the hydraulic performance of the system and that EGS heat generation can significantly reduce the environmental impact at comparable costs associated with the current processing technology. With this effort, significant reductions in greenhouse gas emissions and natural gas consumption can be achieved.

4.1 INTRODUCTION

The oil sands of northern Alberta are Canada's main oil reserves and one of the major oil deposits on earth. Due to the recent increase in oil prices, the production of oil from these challenging sources became economical. 20% of these oil sands are mineable from the surface whereas 80% are producible only in situ [1]. Both processes need a significant amount of water with temperatures ranging between 40°C and 50°C for surface mining [2] and more than 200°C for in situ recovery (SAGD process). Currently, the water is obtained from the Athabasca River and heated up to the desired temperatures by burning huge amounts of natural gas (6% of Canada's gas consumption [3]) creating severe greenhouse gas (GHG) emissions (8% of Canada's greenhouse gas emissions [4]). Potential technologies to significantly reduce these GHG emissions and save natural gas resources are carbon capture and storage (CCS), nuclear power (including waste disposal) and geothermal energy [5–7]. Besides the direct heating of the water for oil sands processing low enthalpy geothermal energy can be used for air conditioning [8] and electricity generation [9]. In this study, the feasibility of engineered geothermal energy generation to supply the oil sands mining operations in the Ft. McMurray area with the necessary hot water is investigated.

Assuming a 10°C temperature loss at the surface from the well to the application area, hot water at a temperature of 60°C needs to be produced at the wellhead. Additionally, the assumption of a temperature loss of another 10°C through the production well(s) (from formation to the wellhead) and a temperature drawdown of 30°C within a lifetime of the geothermal system over 30 years, leads to a formation target temperature of about 100°C. Presented in **Figure 37**, this temperature is reached at about 5 km depth near Ft. McMurray due to the low geothermal gradient of approximately 20°C/km.

Since the sedimentary cover has only a thickness of about 400 m in this region, 4600 m of the wells need to be drilled through granitic basement rocks (**Figure 37**). The granitic rocks that form the geothermal (heat) reservoir are expected to have a very low permeability and porosity. Even though natural fracture systems, which could act as fluid pathways, may be present in that region, it is crucial to enhance the permeability of the rock in order to develop a sustainable and economical geothermal system. Without this technology, no energy production would be

possible. Such an artificially altered geothermal system is commonly called Enhanced Geothermal System (EGS) or Hot-Dry-Rock (HDR) system [11]. Even though mostly hot sedimentary aquifers or high temperature EGS are considered to be economical [12] the direct use of the heat for oil sands processing represents a potential economic application of low temperature EGS.

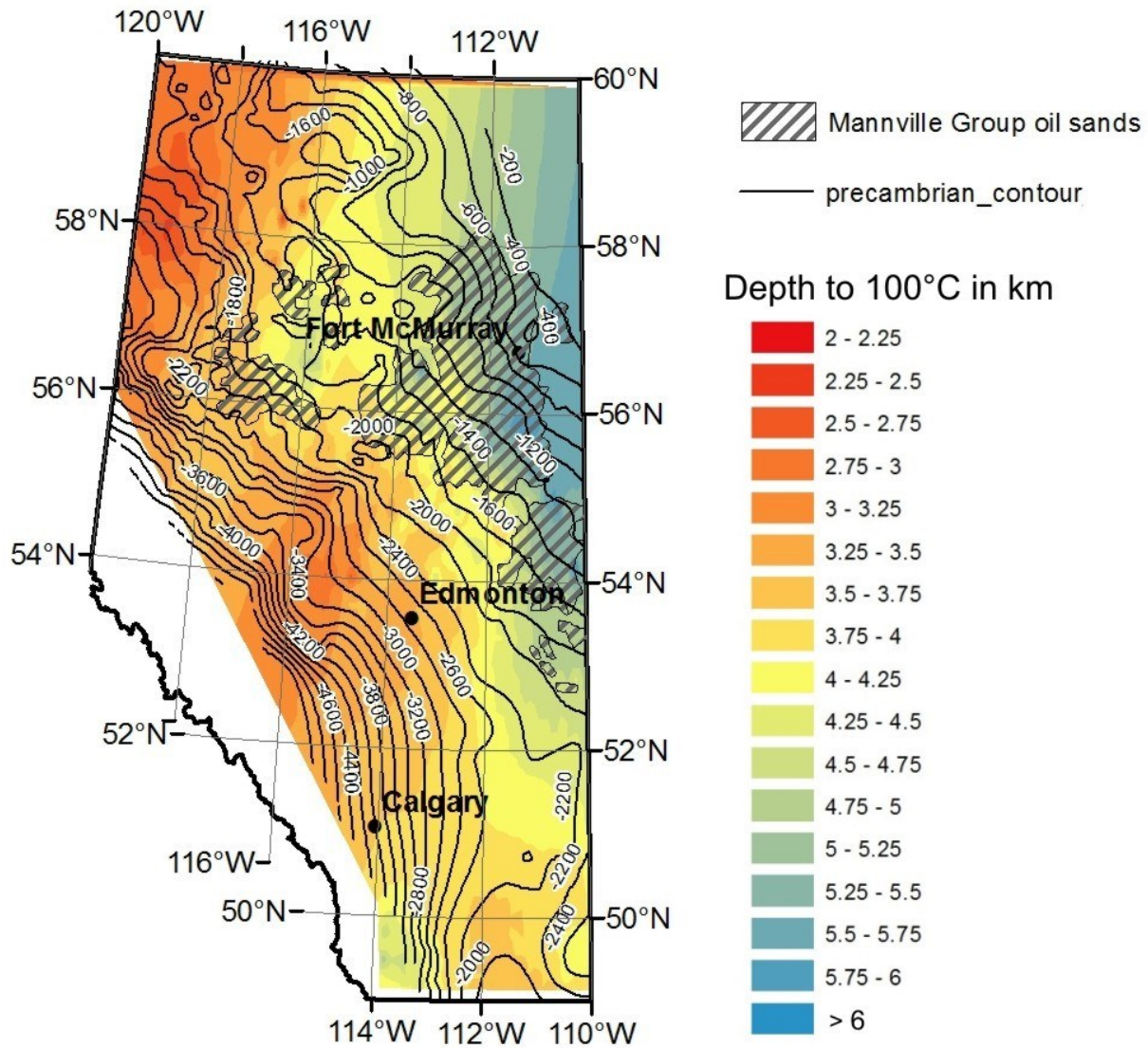


Figure 37: Depth to a temperature of 100°C and depth to the granitic Precambrian basement. In the oil sands areas near Ft. McMurray 100°C is reached at 5 km depth within Precambrian basement rocks [10].

The original concept of HDR systems was introduced in the 1970s by scientists of the Los Alamos Scientific Laboratory [13]. Our conceptual model of a pilot HDR project near Ft. McMurray consists of one injection well flanked by two production wells drilled parallel to the

maximum horizontal stress. All wells are deviated (or horizontal) to allow the creation of multiple fractures perpendicular to the well paths. Only the injection well is stimulated to create different kinds of fractures or fracture networks.

The most commonly used methods to enhance rock permeabilities are hydraulic, chemical, and thermal stimulation techniques [14, 15]. Because of its relatively low temperatures, thermal stimulation is expected to be inefficient in northern Alberta. Chemical stimulation is also not promising because of the in-reactive behavior of granites. Therefore, hydraulic stimulation seems to be the most promising technology. Hydraulic stimulation was and is used to develop HDR systems in granites worldwide with varying success - e.g. Los Alamos, Ogachi, Horijiri, Rosemanowes, Soultz, Newberry, and Cooper Basin [11].

Hydraulic stimulation treatments may be divided according to the stimulation mechanism into tensile fracturing and shear stimulation [16]. Tensile fractures develop if the bottom hole pressure overcomes the fracturing pressure of the formation. In order to achieve long term fracture conductivity during production proppants (e.g. sand) are injected into the fracture together with the fracturing fluid [15]. Shear stimulation treatments are operated below the fracturing pressure of the formation. Critically oriented natural fractures fail in shear and the natural fracture conductivity is increased by self-propping of the displaced fracture surfaces. Often the latter mechanism is assumed to be valid in EGS environments, but tensile fractures may form additionally [17].

Hydraulic stimulation techniques can also be subdivided into the three major fracturing approaches: (1) Water fracturing, (2) hybrid fracturing, and (3) conventional gel-proppant fracturing. In water fracturing treatments, large amounts of slickwater (water and additions like friction reducers and inhibitors) are pumped into the wellbore at relatively low flow rates without proppants or with only a small amount of proppants.

Different definitions of hybrid fracturing treatments exist. They include the injection of intermediate viscosity, linear or waterbased gels, or the injection of slickwater to create the fracture followed by stages of gel to transport and distribute the proppant within the fracture. The proppant concentrations pumped here are relatively low.

In conventional gel-proppant treatments, high viscosity fluids and large amounts of proppants are used.

For the conditions in northern Alberta, slickwater and hybrid fracturing treatments seem to be the most promising. The main reason for this is the low permeability of the reservoir rock and the relatively high cost of conventional treatments. Conventional gel-proppant fracturing treatments are generally more applicable for higher permeability formations; however, all three treatment approaches are simulated and compared to each other in this study.

From 2006 to 2008 a consortium of oil sands producing companies (GeoPos) started to investigate the possibilities of using geothermal energy for oil sands extraction and processing. However, the project was closed due to economic reasons and no final conclusion was given. Now the question is revisited by a German–Canadian research collaboration (Helmholtz-Alberta-Initiative). First numerical studies showed that, in general, geothermal energy systems can be created and used for the oil sands energy demand [18, 19].

In the present study, fracturing simulations, reservoir simulations, economical, and greenhouse gas emission calculations are integrated to propose the most promising stimulation and reservoir engineering approaches for conditions expected in northern Alberta. Additionally, an improved reservoir simulation including wellbore modeling and an improved fracturing simulation using the discrete fracture network (DFN) model (MShale software) is included. Van der Hoorn et al. [20] conducted a similar study using hydraulic fracturing treatments for two limestone EGS projects in the Netherlands.

We begin with the parameter ranges for the simulations, which are mainly based on literature data. Then the methodology is described in detail and the results of the hydraulic fracturing sensitivity analysis, the hydraulic fracturing simulations, and the reservoir simulations are described. An integrated analysis of the stimulation design, reservoir performance, economical, and environmental aspects then leads to the proposed reservoir engineering concepts.

4.2 METHODOLOGY

Since no well has been drilled below 2.4 km in the Ft. McMurray area a sensitivity analysis of the reservoir parameters was performed using the commercial discrete fracture network hydraulic fracturing simulator MShale [21]. Synthetic data was used to simulate as closely as possible the expected conditions at a given depth of the basement rock. First, the stress confinement barriers necessary to prevent severe fracture height growth was studied. Second, the influence of each reservoir parameter was investigated by changing the parameter in its expected range to identify which parameters were most important and how they alter the stimulation results. Based on this, three reservoir scenarios were set up leading to the largest area (Large Area Scenario), the most likely area (Base Case Scenario), and the smallest area (Small Area Scenario) created by the same fracturing treatment. Additionally, the influence of natural fracture network properties and stimulation treatment parameters on the fracture development was studied.

Subsequently, for all three reservoir scenarios, water, hybrid, and gel-proppant fracturing treatments were designed to achieve certain target fracture half-lengths (300 m, 500 m, and 700 m) and certain target fracture conductivities (300 mDm and 1000 mDm). For the water fracturing treatments, a fracture conductivity of 10 mDm and 100 mDm was assumed. The same simulations were performed for both intact rock and naturally fractured formations with different fracture spacings and differential stresses.

The resulting hydraulic fractures were imported into the commercial thermal–hydraulic reservoir simulator CMG STARS [22]. A target productivity index of 10 l/s/MPa [23] and a target minimum well head temperature after 30 years of production of 60°C [2] had to be met by the simulations. Therefore, the number of fractures, the well spacing, and the fracture spacing were changed and optimized to minimize temperature drawdown and optimize the productivity.

After the comparison of the hydraulic and thermal performance of the optimized reservoir engineering concepts, a comparison of the economics as well as the greenhouse gas emissions followed.

This integrative approach finally led to proposed preliminary reservoir engineering concepts for the development of a HDR pilot project in the Ft. McMurray area.

4.3 DATA BASIS

As mentioned earlier, since little information is available about Precambrian basement rocks in the region of Ft. McMurray, most of the input parameters used for the simulations were typical values for granites as derived from the literature. Other input parameters were obtained from laboratory experiments on cores from the Hunt Well near Ft. McMurray (depth = 2400 m) - the only well deeper than others drilled for oil production purposes in the upper sedimentary layers [3]. Hence, the simulated cases show possible reservoir scenarios, which can be expected in the Ft. McMurray area.

4.3.1 Fracture systems

There is no information about fracture systems and their properties available from the Precambrian basement rocks at 5 km depth beneath Ft. McMurray. However, Kalinina et al. [24] performed an extensive literature study about typical natural fracture properties found in granitic Enhanced Geothermal Systems (EGS) worldwide. Despite the influence of stress distribution, tectonic history, lithology, etc. on the natural fracture distribution they found similar properties for all the investigated granites with two perpendicular sub-vertical fracture systems dominate in most of the sites (**Table 14**). Due to restrictions of the simulator, we used two perpendicular and vertical fracture systems with one fracture set parallel to the minimum horizontal stress direction and one set perpendicular to it. (Sub-)Horizontal fractures are not expected in great depths according to Kalinina et al. [24]. Since these fractures intersect with one another, an infinitesimal natural fracture length was assumed. More than 90% of the fractures have spacings between 0.3 m and 4 m. Because it was observed that not all of these fractures take the water that was pumped into the formation, but the flow focused on some major fractures [11] we used a fracture spacing of up to 200 m for the simulations.

Table 14: Fracture properties in the three principle planes.

Parameter	Base Case	Range	Source
Fracture spacing (m)	1.5	0.3 - 200	[24]
In-Situ aperture (mm)	0.5	0.1 - 1	[24]

4.3.2 Stress

A first idea about the stress magnitude at 5 km depth was achieved by preliminary stress calculations performed considering linear elasticity [25]. Because of the great depth of 5 km, a normal stress regime with $\sigma_V > \sigma_H > \sigma_h$ was assumed.

The vertical stress was calculated by $\sigma_V = \rho g z$ for the whole depth (z) interval (0 - 5 km) with the density of the overburden rock ρ and the acceleration of gravity g . The density of the granite was determined to be 2650 kg/m³ by laboratory experiments on borehole samples from the Hunt Well. Due to the fact that only a small sedimentary cover was present in that region (**Figure 37**), this density was assumed for the whole rock column. The range given for σ_V in **Table 15** resulted from a density range between 2600 kg/m³ and 2700 kg/m³.

The minimum horizontal stress magnitude $\sigma_h = \nu/(1 - \nu)(\sigma_V - P_P) + P_P$ was calculated by the vertical stress, Poisson's ratio $\nu = -(d\epsilon_{trans}/d\epsilon_{axial})$ and the pore pressure P_P . The range given in **Table 15** is due to different Poisson ratios (0.1 leads to the lowest, 0.2 to the Base Case, and 0.3 to the highest stress). ϵ_{trans} and ϵ_{axial} are the strains in transversal and axial direction.

Pore pressure $P_P = \rho_{water} g z$ is assumed to be equal to the hydrostatic pressure with $\rho_{water} = 1000$ kg/m³ and $g = 9.81$ m/s².

In a normal pressure regime, this varies between 49 MPa and 56 MPa for assumed densities of 1000 kg/m³ and 1150 kg/m³. Pore pressure values are given in **Table 17**.

Table 15: Stress magnitudes and directions at 5 km depth.

Parameter	Base Case	Range	Source
σ_V @ 5 km depth (MPa)	130	128 - 132	calculated
σ_H @ 5 km depth (MPa)	105	69 - 130	assumed
σ_h @ 5 km depth (MPa)	69	58 - 84	calculated
Direction of σ_H (-)	NE-SW	-	[26]

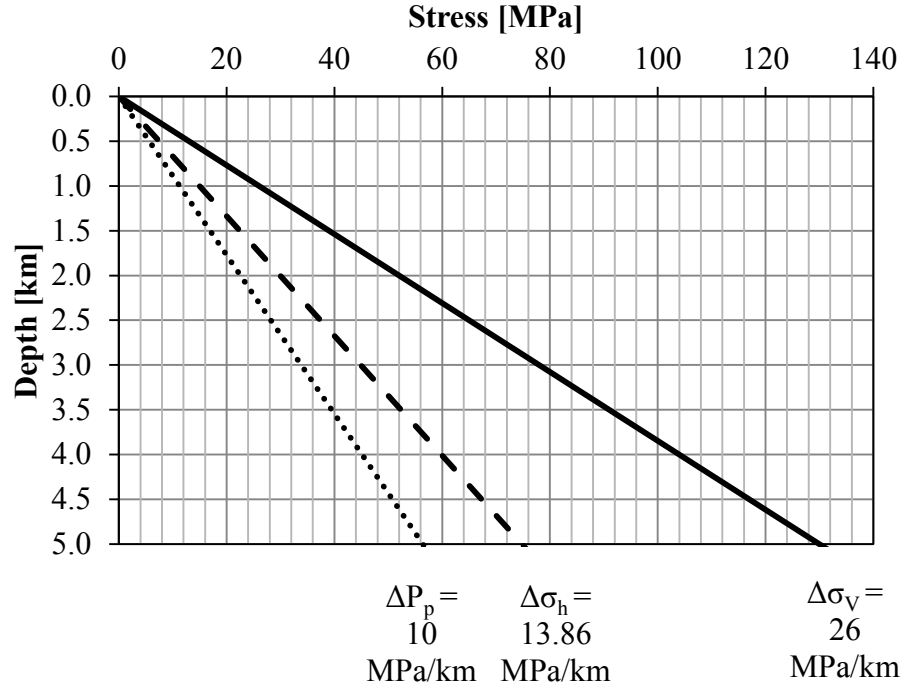


Figure 38: Calculated stress state used for the Base Case Scenario. Assuming a normal faulting regime the maximum horizontal stress σ_H is expected to be in between the minimum horizontal stress σ_h and the vertical stress σ_V . P_p is the pore pressure.

The maximum horizontal stress gradient $\Delta \sigma_H$ lies between the stress gradient of σ_V and σ_h for the expected normal stress regime. The stress gradients are shown in **Figure 38**. The stress magnitudes at 5 km depth and the direction of σ_h are summarized in **Table 15**.

σ_h is used for the fracturing simulation of all fracturing scenarios. σ_V and σ_H only influence the simulation of naturally fractured rock scenarios.

From the World Stress Map [26], it can be derived that the general strike direction of the maximum horizontal stress can be expected to be NE–SW.

4.3.3 Mechanical rock properties

Due to the lack of laboratory data, the mechanical rock properties are derived from literature data about granites, in general. The mechanical rock properties are summarized in **Table 16**. The critical stress value used by the simulator MShale is equal to the tensile strength of a rock. The critical stress values are given for intact rock. Naturally fractured rock masses, however, may

have negligible tensile strength (critical stress = 0 MPa) because discontinuities have negligible tensile strength.

Table 16: Mechanical rock properties of granites as derived from literature data.

Parameter	Base Case	Range	Source
Young's modulus (GPa)	55	40 – 70	[27]
Poisson's ratio (-)	0.2	0.1 – 0.3	[28, 29]
Fracture toughness (MPa m ^{1/2})	1.5	1.3 – 1.7	[30]
Critical stress (Tensile strength) (MPa)	12	9 – 15	[31, 32]

4.3.4 Reservoir leak-off parameters

The values of all leak-off parameters are summarized in **Table 17**. The calculation of the pore pressure is given in **Section 4.3.2**. Values for permeability and porosity were derived from literature. The given range is for intact granites measured in the laboratory [29]. Field measurements can vary significantly and values of up to 100 μ D (0.1 mD) were measured [33]. For the porosity, additionally laboratory data of granite from the Hunt Well exist which were measured together with the density. For the base case a porosity of 1% was chosen. The wall building coefficient for slickwater treatments is very high, because no or only a small filter cake is expected to develop [32]. The total compressibility C is the sum of the bulk rock compressibility and the water compressibility C_w . The bulk rock compressibility C_r is the reciprocal of the drained bulk modulus K_r . The drained bulk moduli were calculated from Young's moduli E and Poisson's ratios ν (**Table 16**) using the following expression: $K_r = E/(3(1 - 2\nu))$ [37].

The compressibility of water at 100°C and 49 MPa is 0.403 1/GPa [36]. Possible spurt loss e.g. due to natural fracture networks was neglected in the simulations.

Table 17: Reservoir leak-off parameters.

Parameter	Base Case	Range	Source
Permeability (μD)	0.5	0.1 – 1 (100)	[29, 33 - 35]
Porosity (%)	1	0.5 – 1.5	[34], Lab measurements
Pore pressure @ 5 km depth (MPa)	49	49 - 56	Calculated
Wall building coefficient ($\text{m/s}^{1/2}$)	35	-	[21], No wall building
Total compressibility ($1/\text{GPa}$)	0.43	0.32 - 0.54	Calculated, $\pm 25\%$
Reservoir fluid viscosity (mPa s)	0.29	0.22 - 0.36	[36], $\pm 25\%$

4.3.5 Thermal properties

According to Majorowicz and Weides [10] the average reservoir temperature at 5 km depth is 100°C in the Ft. McMurray area (**Figure 37**). Thermal conductivity and heat capacity data of the rock were measured in the laboratory and the same data for the reservoir fluid was derived from Lemmon et al. [36], assuming pure water as a reservoir fluid. The thermal properties given in **Table 18** are important for the reservoir simulations. Temperature is critical for the fracturing simulations because the viscosity of the fracturing fluids is strongly temperature-dependent.

Table 18: Thermal rock and fluid (water) properties from laboratory tests and literature data.

Parameter	Value	Source
Reservoir temperature (@ 5km depth) ($^\circ\text{C}$)	100	[10]
Temperature gradient ($^\circ\text{C}/\text{km}$)	20	[10]
Thermal conductivity (granite) ($\text{W}/\text{m}/\text{K}$)	2.7	[3]
Thermal conductivity (water) ($\text{W}/\text{m}/\text{K}$)	0.7	[36]
Volumetric heat capacity (granite) ($\text{kJ}/\text{m}^3/\text{K}$)	2385	[35]
Volumetric heat capacity (water) ($\text{kJ}/\text{m}^3/\text{K}$)	4186	[36]

4.4 HYDRAULIC FRACTURING SIMULATIONS

4.4.1 General considerations

Since fractures develop perpendicular to σ_h and parallel to σ_H [38], hydraulic fractures will develop approximately in the NE–SW direction as inferred from the World Stress Map [26]. Because of the low natural permeability of the granite hydraulic fractures should connect the production and injection wells if the stimulation target is to create a geothermal loop. Additionally, earlier studies showed that more than one single hydraulic fracturing treatment needs to be conducted [19]; hence, deviated or horizontal wellbores need to be drilled to avoid interference between subsequent fracturing treatments. The direction of the well deviation should be NW–SE to allow fracture development perpendicular to the wellbores. In the oil and gas industry, horizontal sections up to 3000 m are common [39], although longer sections are possible. However, due to the greater depth and the lithology (granite), we expect 5000 m as the maximum horizontal section possible to drill. This length restricts the maximum number of fracture stages and the spacing between fractures.

Earlier reservoir simulations showed that fracture conductivities of 500 mDm and fracture half-lengths of 250 m could be sufficient [19]. The fracture conductivity of water fracturing treatments without proppants or with a low amount of proppants and assuming a displaced (self-propping) fracture cannot be simulated with MShale. However, to consider shear stimulation as well, we assume a fracture conductivity of 10 mDm (no proppant) and 100 mDm (low amount of proppant) for the water fracturing treatments (see **Section 4.4.4**).

4.4.2 Fracturing simulator

For the fracturing simulations, the discrete fracture network (DFN) simulator MShale was selected. The semi-analytical simulator is formulated between a pseudo-3D and full 3D model, including a coupling between fracture propagation and proppant transport [21]. The main reasons for this choice was the 3D modeling capabilities, an extensive material database, the wide acceptance in the industry, and the possibility to directly compare the conventional fracturing

simulator MFrac with the discrete fracture network (DFN) simulator MShale. The software was specifically designed for unconventional low-permeability fractured reservoirs.

Fracture initiation and development is based on tensile opening of new or natural fractures within intact or fractured rock. The influence of thermal stresses was neglected because of the relatively low temperature gradients (max. $\Delta T = 70^{\circ}\text{C}$). Other major assumptions are that fractures can only develop in the three principle planes, interfacial joint dilatancy is ignored, primary and secondary fractures are elliptical and the stimulated reservoir volume has an ellipsoidal shape. The calculations are based on mass and momentum conservation, the continuity equation and the width-opening pressure equation which are described in detail in [21, 40].

4.4.3 Sensitivity analysis

A sensitivity analysis of the basic mechanical and leak-off parameters was already performed with the software MFrac neglecting critical stress [19]. However, the values taken for the new analysis were updated and more parameters were included. The new sensitivity analysis was performed for intact rock and for a fractured rock mass. Fracture network properties, and stress confinement were studied and are presented in detail.

4.4.3.1 Reservoir rock properties

The influence of the reservoir rock properties was studied for a 300 m high confined formation with the above given base case parameters and a 5 MPa stress contrast to adjacent formations. The treatments were performed with 5000 m³ of slickwater at a constant injection rate of 100 l/s. The mechanical, leak-off, and treatment parameters were changed within their expected ranges (**Figures 16 and 17**) and the relative changes (from the results of the Base Case Scenario) in the resulting fracture area and fracture aperture are shown in **Figures 39 and 40**.

Fracture area and aperture are influenced mainly by the mechanical parameters critical stress and the Young's modulus. The Poisson's ratio is also important. Fluid volume and fracturing fluid viscosity are the most important treatment parameters and will be discussed later in detail. In this study, the critical stress is considered the tensile strength of a material. As soon as the net

pressure in the fracture (minimum horizontal stress minus fluid pressure) reaches this value, the fracture is propagating further. Fracture initiation is governed by the fracture toughness which has no significant influence on the fracture area and aperture at the end of the treatment. An increase in the critical stress (tensile strength) from 12 to 15 MPa leads to a decrease in fracture area by 38% and an increase in fracture aperture by 27%. A decrease in the critical stress (tensile strength) from 12 to 9 MPa leads to an increase in fracture area by 21% and a decrease in aperture by 28%.

The Young's modulus is a measure of the stiffness of the rock. The influence of the Young's modulus is antagonistic to the critical stress. Increasing Young's modulus (increasing stiffness) from 55 to 70 MPa results in a 26% increase in fracture area and a 35% decrease in aperture. Decreasing Young's modulus (decreasing stiffness) from 55 to 40 MPa decreases the fracture area by 25% and increases the aperture by 28%.

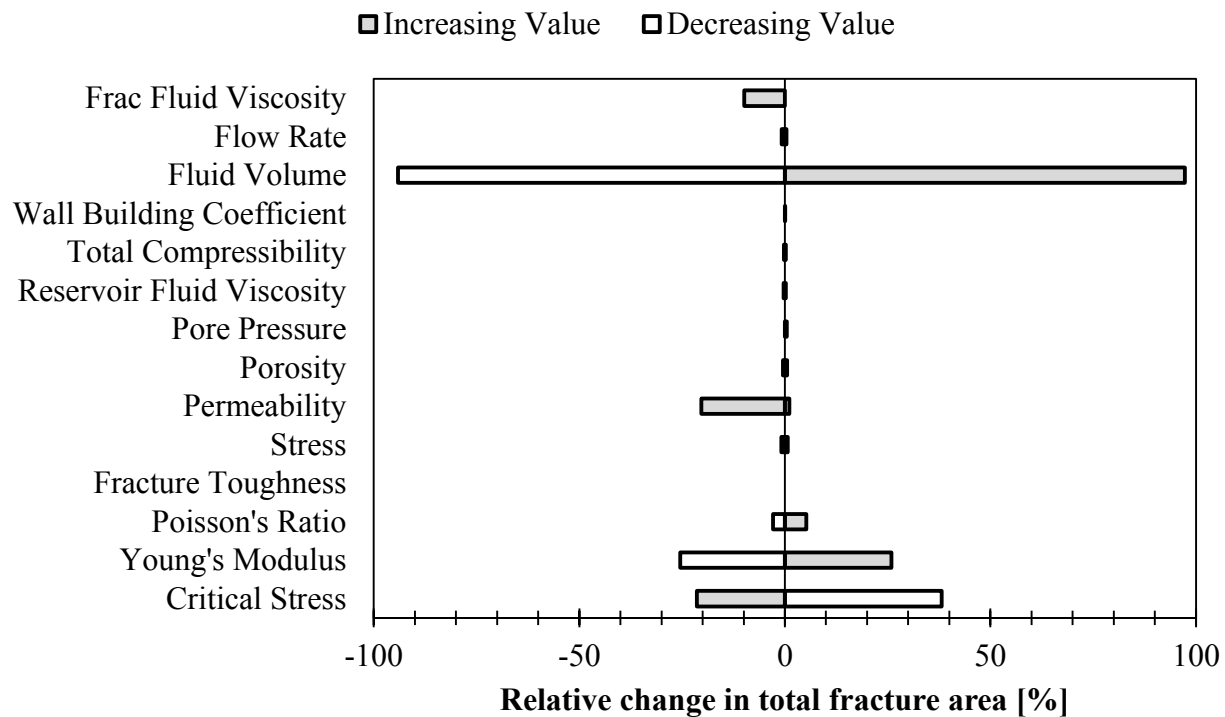


Figure 39: Relative influence of all studied parameters within their expected range on the fracture area.

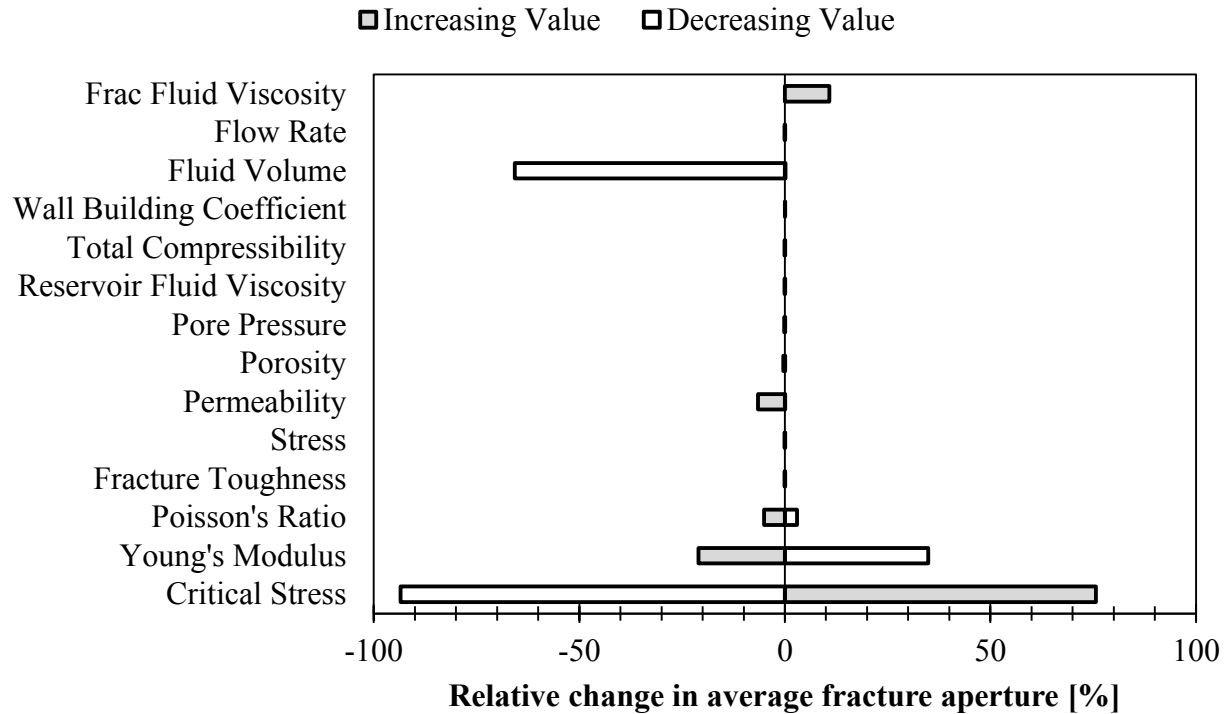


Figure 40: Relative influence of all studied parameters within their expected range on the average fracture aperture.

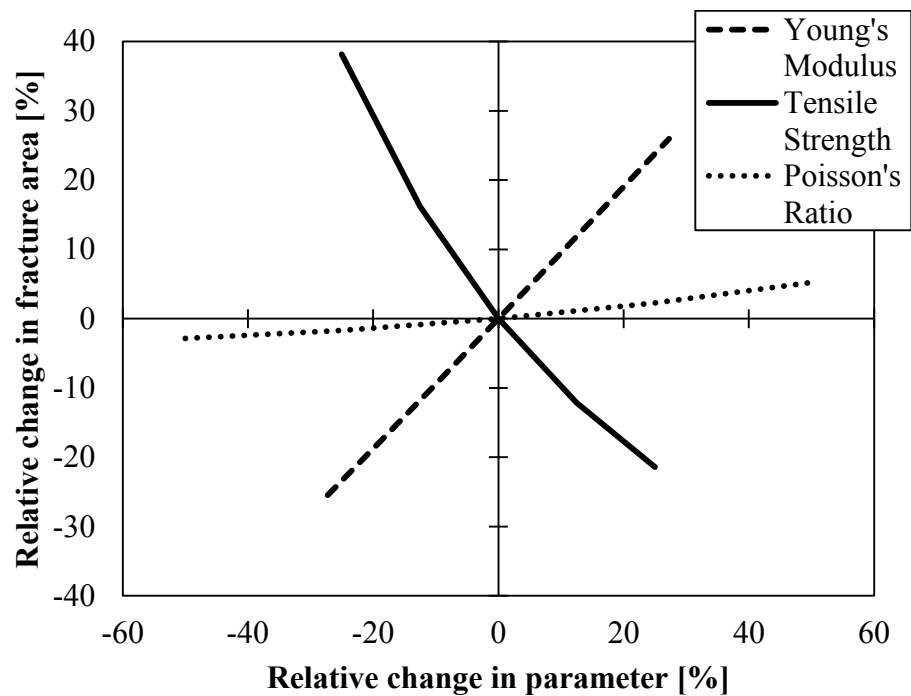


Figure 41: Relative change in fracture area when changing Young's modulus, critical stress (tensile strength), and Poisson's ratio within their expected range.

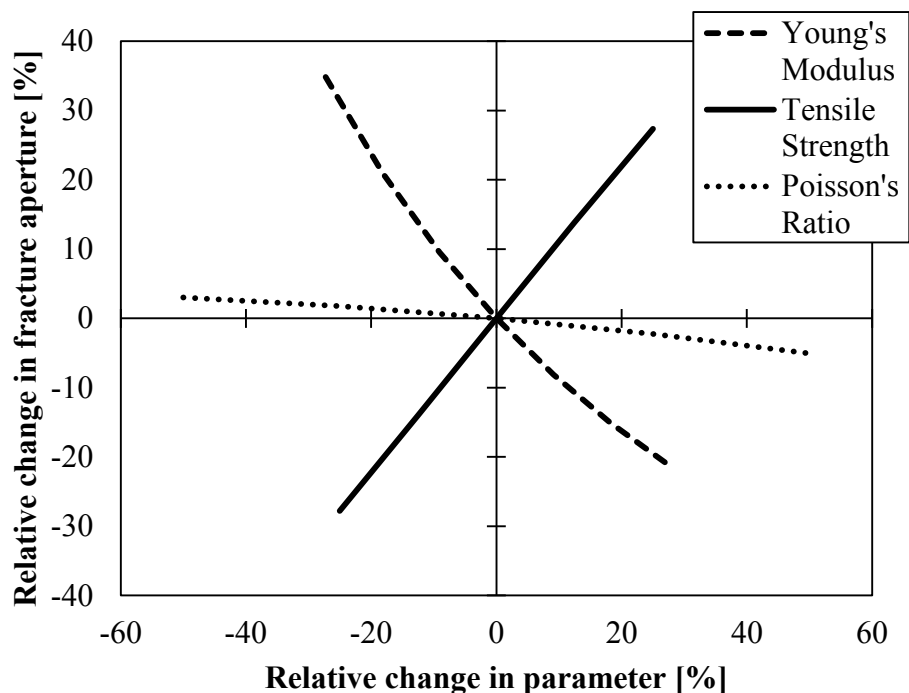


Figure 42: Relative change in fracture aperture when changing Young's modulus, critical stress (tensile strength), and Poisson's ratio within their expected range.

The Poisson's ratio (the ratio of transverse to axial strain) is less important than the other two parameters. An increase in Poisson's ratio from 0.2 to 0.3 leads to an increase in fracture area of 5% and a decrease in fracture aperture by 5%. A lower Poisson's ratio (0.1 instead of 0.2) results in a 3% smaller fracture area and a 3% wider fracture. **Figure 41 - Figure 43** give a more detailed view of the influence the three parameters have on area and aperture, showing the relative change in one of the mechanical parameters versus relative change in fracture area/aperture.

The most important leak-off parameter is permeability. A change of all other investigated mechanical and leak-off parameters within their expected range results in a relative change in fracture area and width of less than 1%. This is only true for a relatively high closure stress (12 MPa) and a very low permeability (0.0005 mD), which are typical for intact granites. Fractured granites could have a lower (or no) tensile strength with a higher permeability (e.g. 0.1 mD). In this case, other parameters are important as well. A sensitivity analysis of this type (no tensile strength with slightly higher permeability) is presented in Hofmann et al. [19]. Higher permeability leads to an increase in the importance of the other leak-off parameters (porosity, pore pressure, reservoir fluid viscosity, and total compressibility) as well as the flow rate.

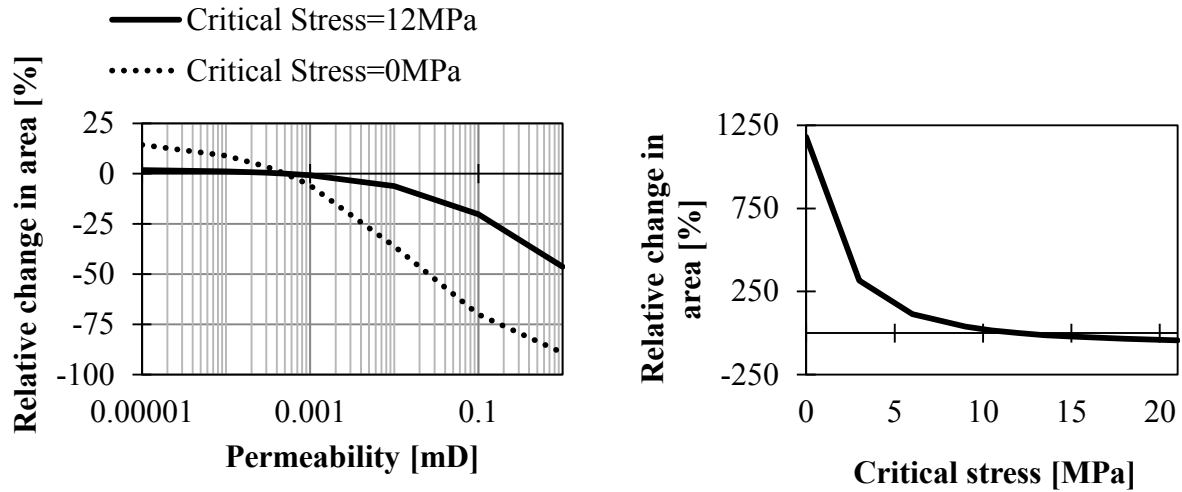


Figure 43: Relative change in fracture area for different permeabilities (left) and critical stress values (right). Permeability is becoming to be important from values above 0.01 mD considering high critical stress (12 MPa). Without critical stress (0 MPa) permeability is important for the whole parameter range between 0.00001 and 1 mD.

If no critical stress is considered, in addition fracturing fluid viscosity, flow rate, permeability, porosity, stress, and Young's modulus are of major importance to the fracture area. Fracture width is influenced additionally by the fracturing fluid viscosity, the fluid volume, Young's modulus, and the flow rate.

Critical stress values higher than 12 MPa result in a reduction of 43% in fracture area; however, lower values lead to a significant increase in fracture area of up to 317% for 3 MPa and 1181% for 0 MPa (**Figure 43**).

4.4.3.2 Resulting reservoir scenarios

In addition to the Base Case Scenario, two more reservoir matrix property scenarios were set up based on the sensitivity analysis. The parameters that showed the highest sensitivity for the fracture area were adapted for these scenarios. The parameters were chosen in such a way that one scenario resulted in the smallest fracture area (Small Area Scenario) and the other in the largest area (Large Area Scenario). **Table 19** summarizes the input parameters for all three scenarios.

Larger fractures can be achieved if the reservoir rock consists of a high Poisson's ratio, is stiff (high Young's modulus), weak (low critical stress), and impermeable (low permeability). In contrast, the Small Area Scenario consists of a less stiff (low Young's modulus) yet stronger (high critical stress) and higher permeability rock with a low Poisson's ratio.

Correlations between the four parameters are not considered. Even though there is evidence that stronger granites (higher tensile strength) also have a larger stiffness (high Young's modulus) [41], it was more important to focus on an overview of minimum and maximum possible fracture areas.

Table 19: Three reservoir rock property scenarios leading to different fracture areas.

Parameter	Small Area Scenario	Base Case Scenario	Large Area Scenario
Young's modulus [GPa]	40	55	70
Critical stress [MPa]	15	12	9
Poisson's ratio [-]	0.1	0.2	0.3
Permeability [mD]	0.1	0.0005	0.0001

4.4.3.3 Stress state

Stress confinement is critical for fracture height and length growth. A linear increase of the minimum horizontal stress within the stimulated formation leads to severe upward-directed fracture height growth. Therefore, a controlled hydraulic fracturing treatment would not be possible in this case [19].

The effect of the stress was modeled without proppants using 20,000 m³ of slickwater injected at a rate of 100 l/s. The influence of the height of a confined formation (50 m – 750 m) on the resulting fracture area and width was studied for the Base Case Scenario. The injection point was in the center of the confined formation and the stress was kept constant within the formation and confined by a stress contrast of 10 MPa.

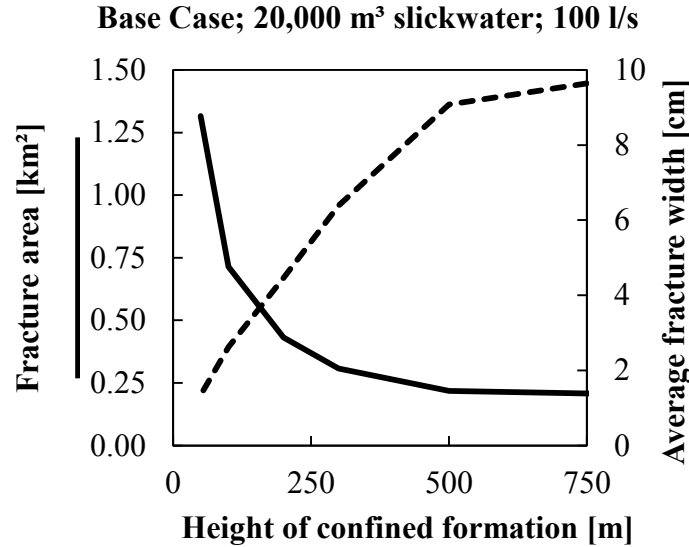


Figure 44: The fracture grows out of the confined formation if the total height of this formation is too small leading to large fracture areas and small fracture apertures. The injection point is in the center of the confined formation.

The height of a confined formation has a significant influence on the resulting fracture area and average fracture width (**Figure 44**). The fracture area decreases with increasing height of the confined formation whereas the average fracture aperture increases. Small areas indicate a well-confined fracture while high areas are the result of an unconfined fracture growth. It can be observed that a good confinement can be achieved with heights of more than 500 m while smaller heights, down to 250 m, are still sufficiently confined and will not lead to severe fracture height growth.

However, the minimum necessary height of a constant stress interval within the stimulated formation depends on the distance between the injection point and the lower stress barrier, as shown in **Figure 45**.

An approximate linear relationship between confinement height and distance between injection point and lower stress barrier can be observed for the Base Case Scenario. Higher distances lead to larger minimum confinement heights necessary to confine the fracture. For a 50 m distance, a minimum height of 100 m is necessary and for 200 m distance, a minimum height of 300 m is necessary to confine the fracture height growth. Therefore, by choosing the injection point (with respect to a lower stress barrier) the fracture height can be altered and fracture height growth can

be confined. For example, if the constant stress interval is relatively short, a short distance between injection point and stress barrier should be chosen in order to confine the fracture height growth. In the case of longer constant stress intervals, higher fracture heights and hence larger fracture areas can be achieved by choosing an injection point further up from the lower stress barrier.

How the stress contrast affects the lower and upper fracture height growth for different lengths of the constant stress interval (and injection point in the center of this interval) is shown in **Figure 46** for a 12 MPa (left) and a 0 MPa (right) critical stress. Large fracture heights indicate unconfined fracture height growth. Larger distances between injection point and lower stress barrier leads to higher stress contrast requirements in order to confine fracture height growth.

Figure 47 demonstrates the impact of the lower stress barrier (middle) and the length of the constant stress interval (right) on the fracture height growth confinement and the resulting fracture geometry. The same stress confinement sensitivity study was conducted for the Small and Large Area Scenarios. For all three scenarios, the minimum stress confinement criteria, assuming an injection point 100 m above the lower stress barrier, is summarized in **Table 20**.

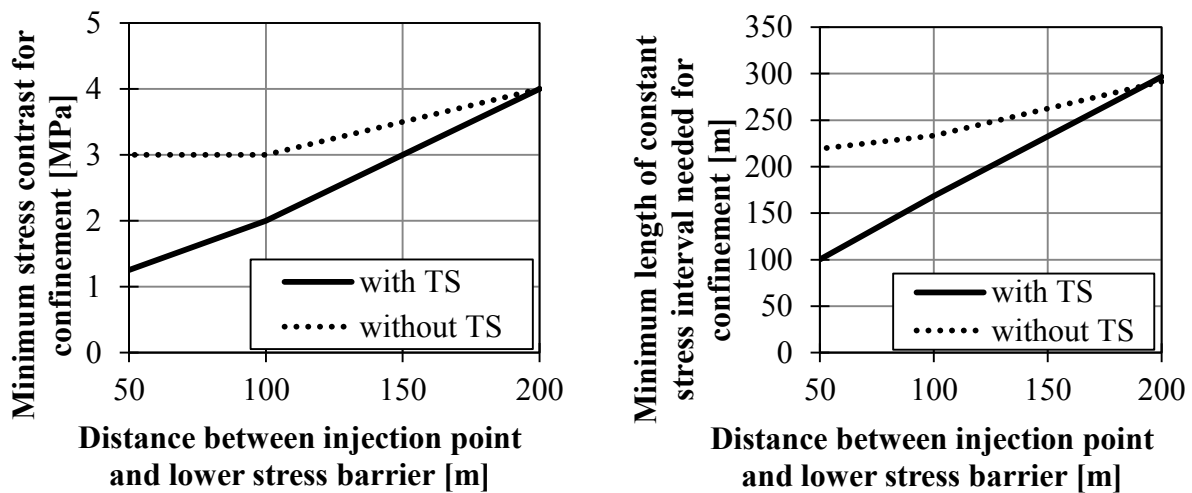


Figure 45: Influence of the distance between injection point and lower stress barrier on the minimum stress contrast (left) and the minimum length of a constant stress interval (right) needed to confine the fracture height growth when injecting 20,000 m³ slickwater at a rate of 100 l/s (for the Base Case Scenario).

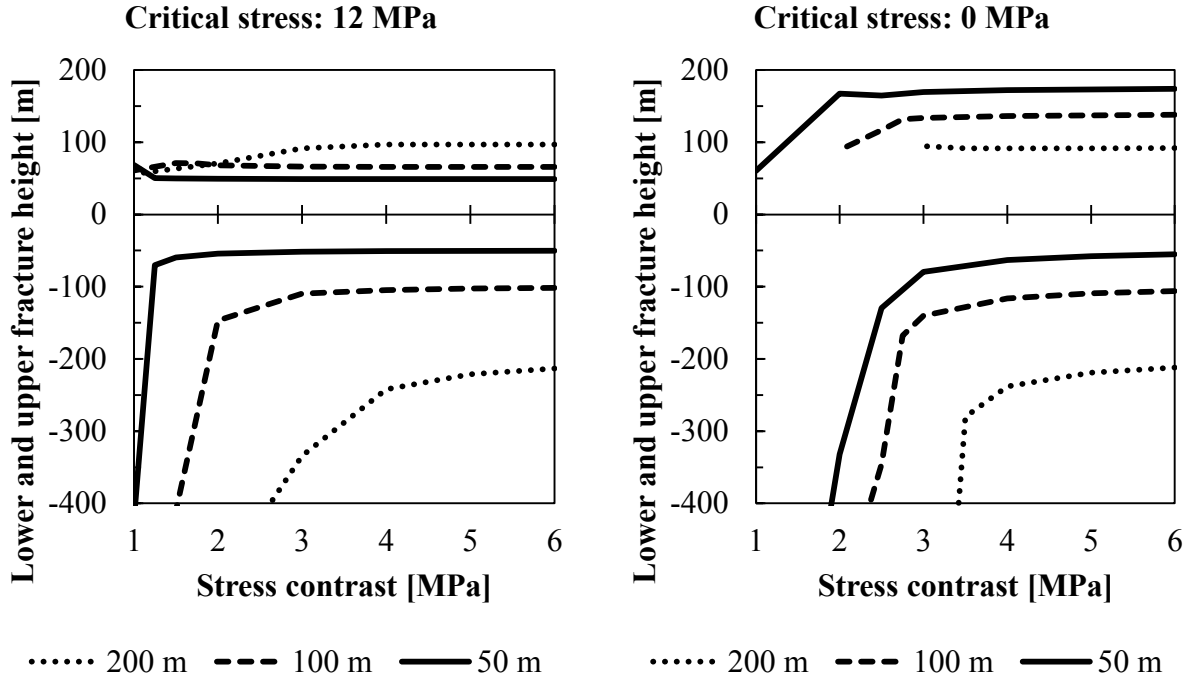


Figure 46: Influence of stress contrasts on lower and upper fracture height for different distances between injection point and lower stress barrier (50 m, 100 m, 200 m) and for a critical stress of 12 MPa (left) and 0 MPa (right). The figures show the final geometry after injecting 20,000 m³ slickwater at a rate of 100 l/s.

For all three scenarios, the minimum stress contrast at the lower stress barrier was 2 MPa. Also the length of the constant stress interval was relatively similar (between 160 m and 175 m). Hence, for all three scenarios the following simulations were performed using a stress contrast of 2.3 MPa between the target formation and the deeper adjacent formation. The total height of the formation (constant stress interval) was 200 m. Both values were derived by adding a safety margin of 15% to 2 MPa and 175 m respectively.

Table 20: Minimum stress contrast and constant stress interval requirements to confine upward and downward fracture height growth into adjacent formations.

Scenario	Minimum stress contrast	Minimum constant stress interval
Small area	2.0 MPa	175 m
Base case	2.0 MPa	170 m
Large area	2.0 MPa	160 m
All scenarios	2.3 MPa	200 m

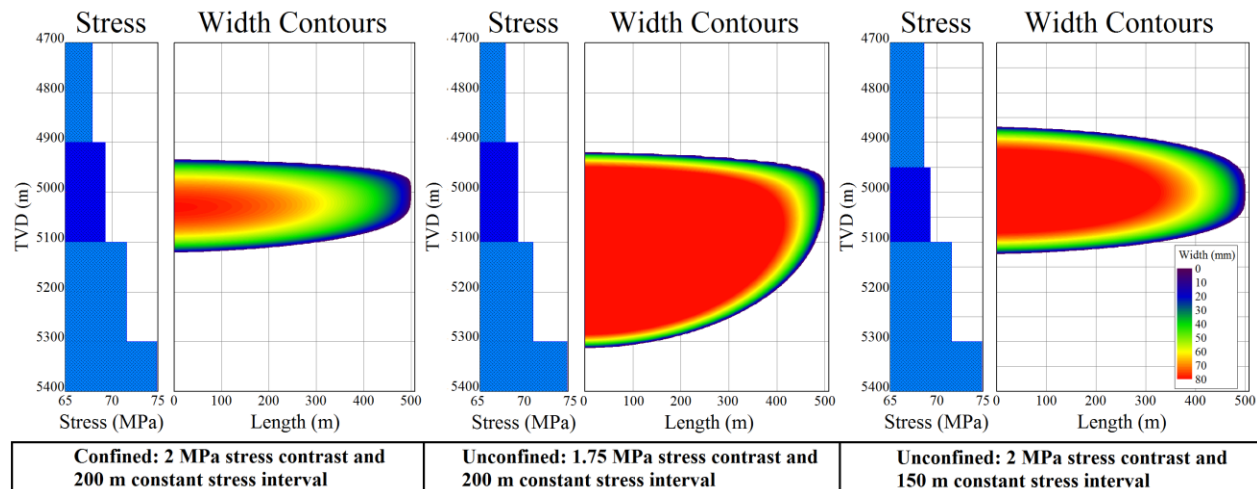


Figure 47: Final fracture geometries for a confined (left) and two unconfined (mid and right) formations. A stress contrast of only 1.75 MPa leads to unconfined downward fracture growth (middle) and a constant stress interval of 150 m leads to unconfined upward fracture growth (right). The treatment design (injected slickwater volume) was adapted in order to achieve the same fracture half-length of 500 m.

Stronger confinement criteria are necessary if natural fracture systems are present, as shown in the following section. The difference between the three principle stresses is most important for the opening and/or widening of secondary fractures (natural fracture systems) during the stimulation. The study of this effect is also presented in the following section.

4.4.3.4 Natural fracture systems

For this part of the sensitivity analysis, 10,000 m³ of slickwater was injected at a constant rate of 100 l/s. The main purpose of studying different fracture systems is to point out what kind of natural fracture systems would be suitable stimulation targets.

In order to open secondary fractures in MShale, the difference between σ_H and σ_h (to open vertical secondary fractures) or σ_V and σ_h (to open horizontal secondary fractures) should be less than the fracture net pressure, which is 9 MPa for the Large Area Scenario, 12 MPa for the Base Case Scenario, and 15 MPa for the Small Area Scenario.

In the presented Base Case, Small Area, and Large Area Scenarios, secondary natural fracture systems do not open because, in a depth of 5 km, $\sigma_H - \sigma_h = 105 \text{ MPa} - 69.3 \text{ MPa} = 35.7 \text{ MPa}$, and $\sigma_V - \sigma_h = 130 \text{ MPa} - 69.3 \text{ MPa} = 60.7 \text{ MPa}$, which are both larger than the maximum expected net

fracture pressure of 15 MPa. However, σ_H was only assumed. Therefore, in the expected normal stress regime ($\sigma_V > \sigma_H > \sigma_h$) [23], the magnitude of σ_H can vary between σ_V and σ_h . In order to investigate the influence of vertical natural fracture systems on the resulting fracture network geometry, $\sigma_H - \sigma_h$ was changed between 0 and 15 MPa for the Base Case Scenario. Horizontal fracture systems are not expected to occur. A more detailed sensitivity analysis showing the effect of different fracture sets, fracture spacings, and differential stresses on the fracture height growth confinement, the net fracture pressure, the fracture area, the stimulated reservoir volume and the fairway aspect ratio for the same reservoir as described in this paper is given in Hofmann et al. [42].

Stress difference

The total area of the discrete fracture network (DFN) decreases when the difference between σ_H and σ_h increases whereas the area of the main fracture increases (**Figure 48**). However, the average aperture of the fractures (main fractures, secondary fractures, and total DFN) increases with increasing stress difference (**Figure 49**). The largest change in fracture aperture and area is observed between 9 and 12 MPa stress difference.

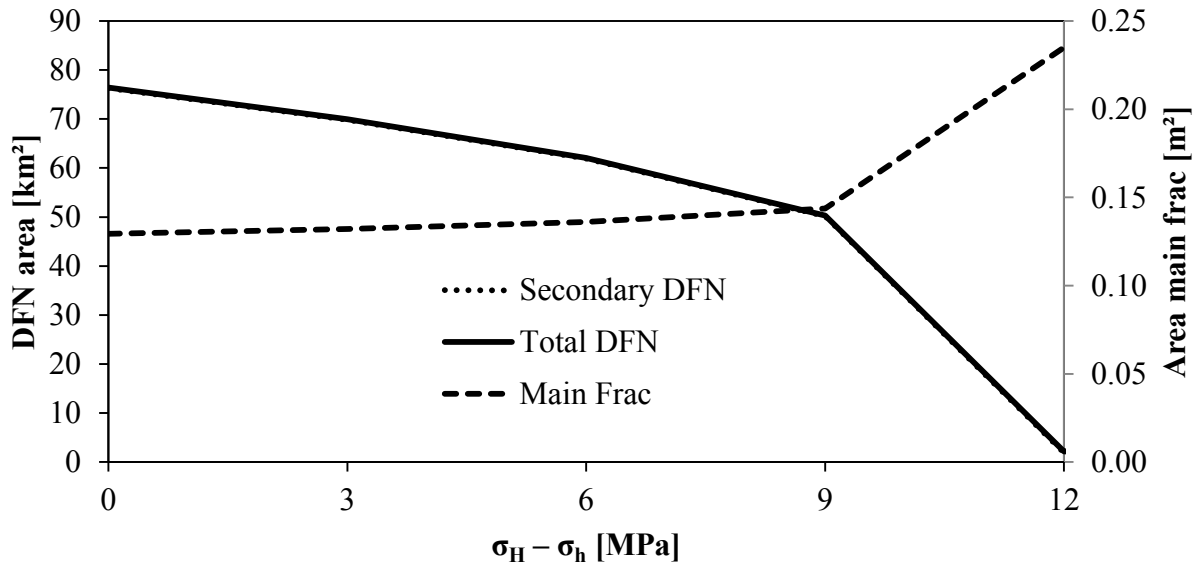


Figure 48: The total fracture area of the discrete fracture network (DFN) decreases with increasing stress difference whereas the area of the main fracture increases.

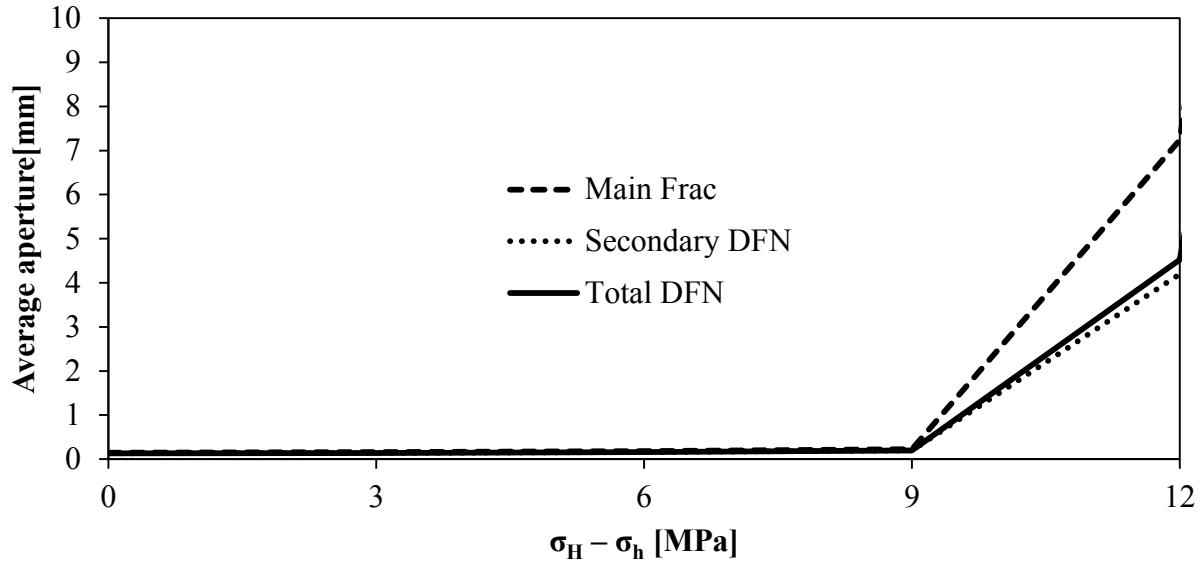


Figure 49: The average width of the fractures increases with increasing stress difference.

The fracture volume of the total DFN is independent of the stress difference. Between 9 and 15 MPa the volume of the main fracture increases while the volume of the secondary fracture network decreases significantly with increasing stress difference. At 15 MPa the volume of the main fracture is equal to the total volume of the fracture network and at 9 MPa the volume of the secondary fracture network is approximately equal to the volume of the total DFN (**Figure 50**).

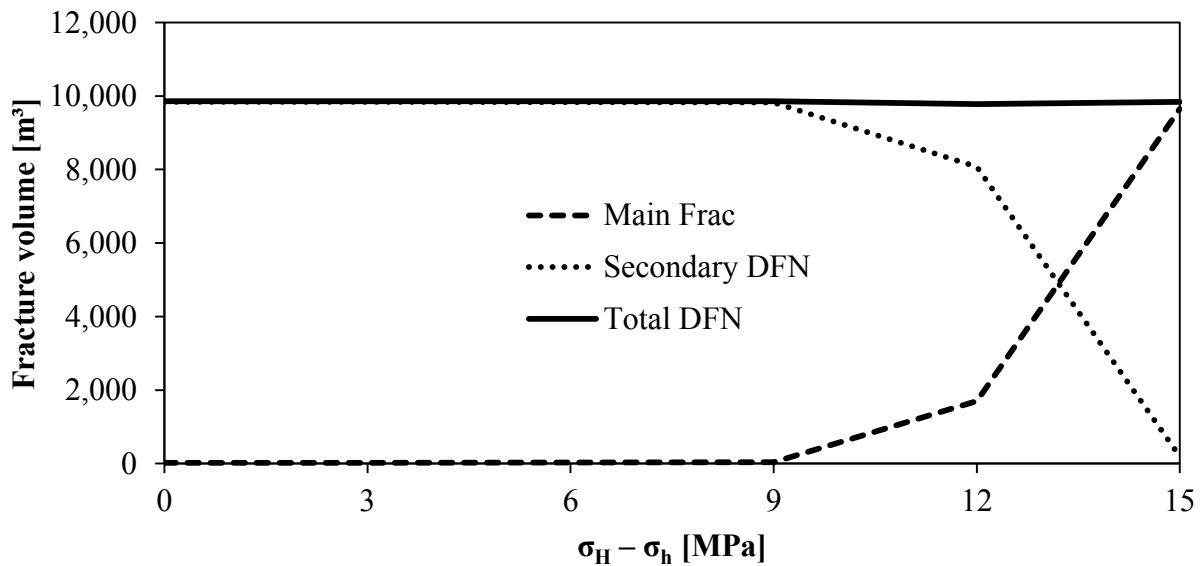


Figure 50: Influence of the stress difference on the volume of the main fracture, the secondary fracture network, and the total fracture network.

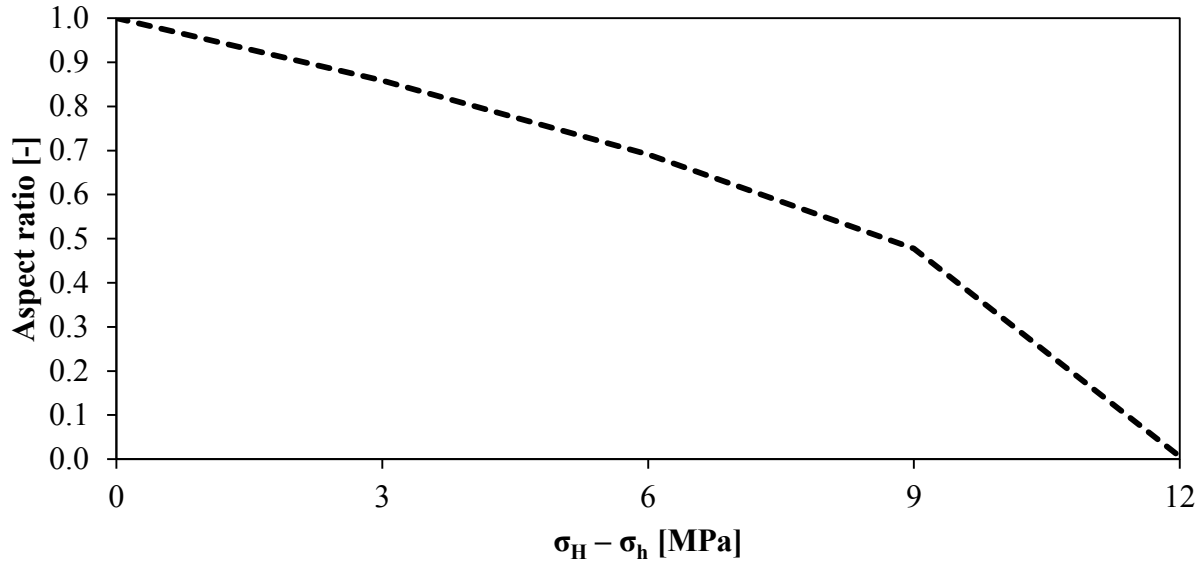


Figure 51: The aspect ratio (extent of fracture network parallel to the maximum horizontal stress divided by the extent of the fracture network parallel to the minimum horizontal stress) decreases with increasing stress difference.

Additionally, the influence of the stress difference on the aspect ratio was studied. We defined the aspect ratio as the extent of the DFN parallel to σ_h divided by the extent of the DFN parallel to σ_H . Higher aspect ratios indicate a wider fracture network, and lower aspect ratios indicate narrower fracture systems. Increasing stress differences lead to narrower fracture networks leading to a single fracture at 12 MPa (**Figure 51**).

Fracture spacing

Another important parameter is the spacing between natural fractures. We investigated the effect of the spacing for a range between 0.3 m and 200 m with a 0 MPa stress difference between the minimum and maximum horizontal stress. The total area of the DFN and of the secondary DFN decreased and the area of the main fracture increased with increasing fracture spacing (**Figure 52**). The most significant changes were observed between 0.3 and 75 m. The area of the main fracture reaches a maximum value at a fracture spacing of 25 m. This coincides also with the maximum in the length of the main fracture.

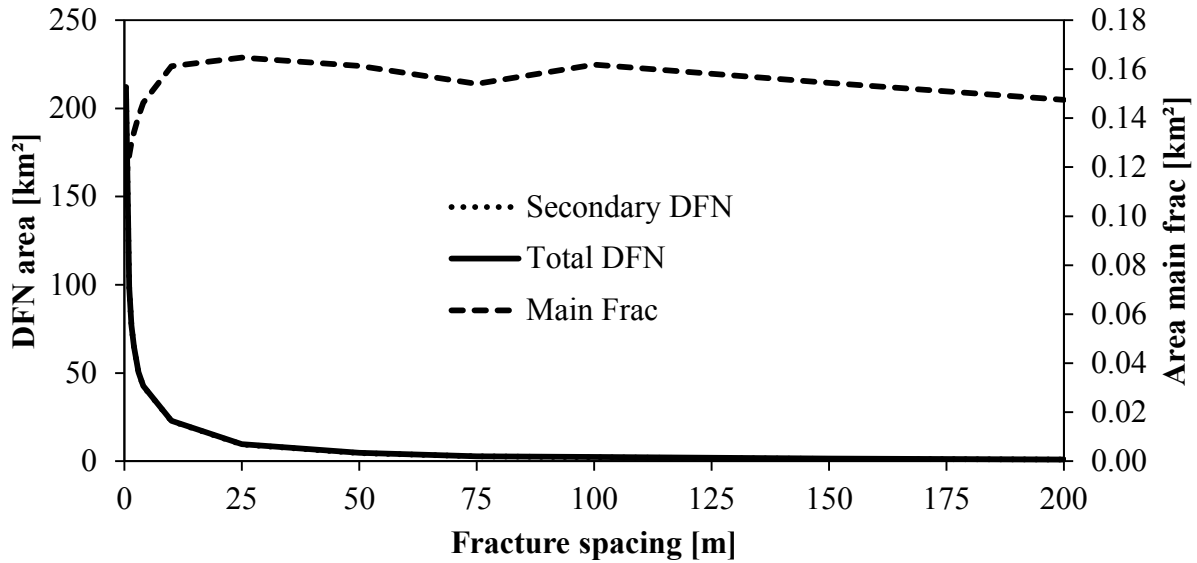


Figure 52: The total area of the DFN and of the secondary DFN decrease with increasing fracture spacing whereas the area of the main fracture increases.

The average aperture of the main fracture, the secondary fracture network, and the total DFN increase approximately linearly with increasing fracture spacing (**Figure 53**). Low fracture spacings lead to very large fracture areas, low fracture apertures, and complex fracture systems.

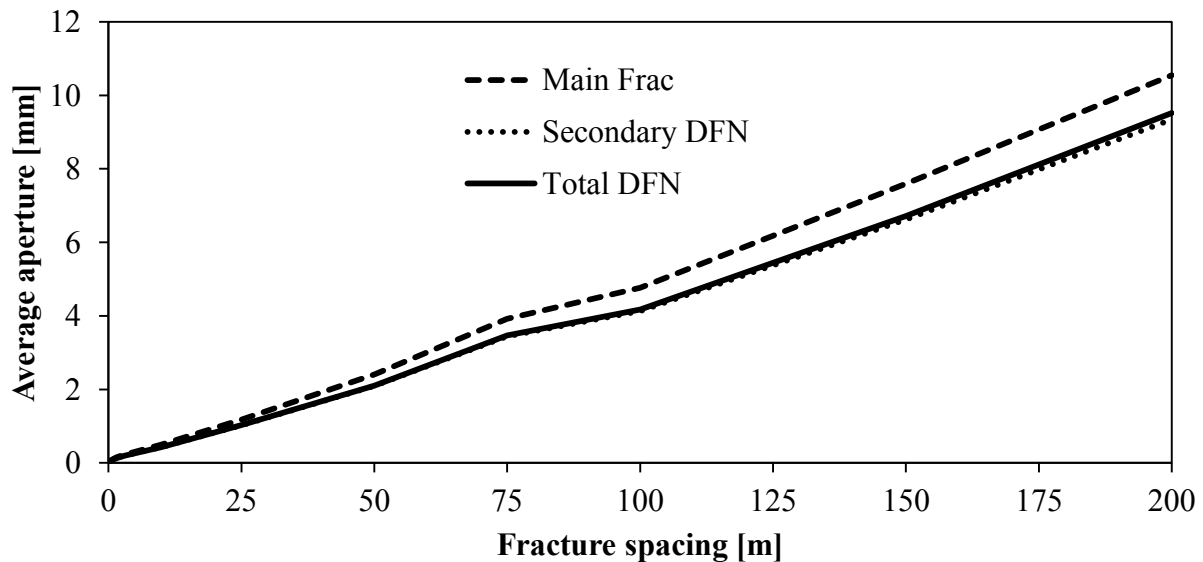


Figure 53: The average aperture of the main fracture, the secondary DFN, and the total DFN increases with increasing fracture spacing.

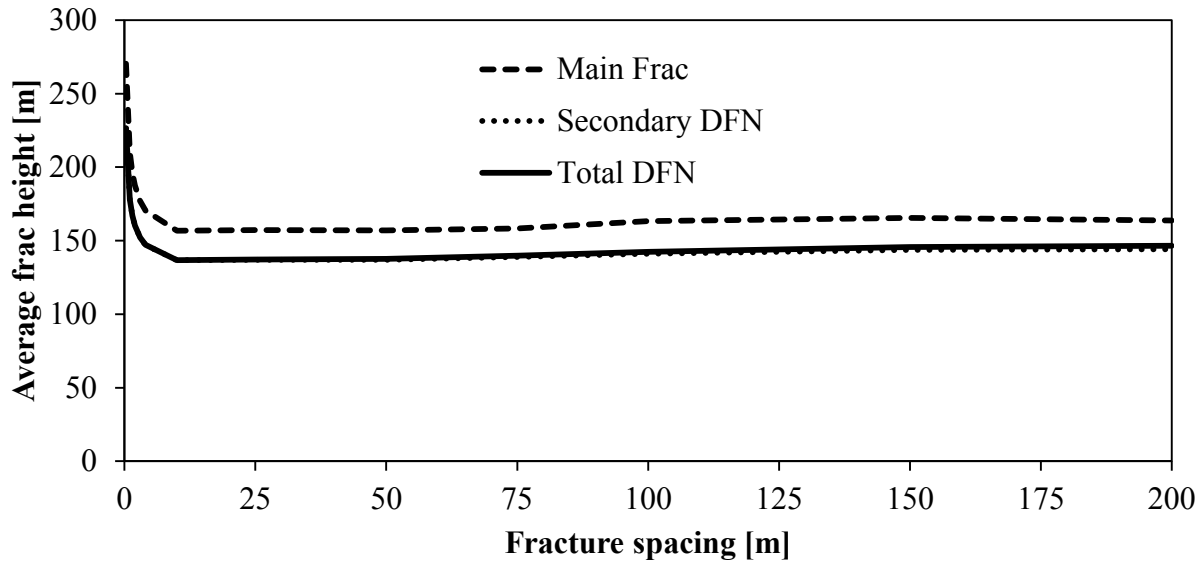


Figure 54: The average fracture height for low fracture spacings is high because of fracture height growth out of the formation. For higher fracture spacings the height growth is confined and the resulting height is constant.

Below a fracture spacing of 10 m, the total fracture height is significantly higher as compared to larger fracture spacings (**Figure 54**). This indicates unconfined fracture height growth and larger fracture height growth confinement requirements for complex fracture systems with very low fracture spacings. For larger spacings, the average fracture height is approximately constant.

Fracture aperture

Finally, the in situ aperture of the natural fractures was studied. The aperture was changed between 0 and 10 mm. Compared to the other two DFN properties spacing and stress difference, the aperture is of minor influence on the properties of the resulting stimulated fracture network. The area and the total length of the main fracture, the secondary fracture network, and the total DFN decrease with increasing in situ fracture aperture. The average resulting fracture aperture increases with increasing in situ aperture. Height and volume of the main fracture, secondary fracture network, and total DFN stay approximately the same.

3.4.3.5 Treatment parameters

Proppant type, fracturing fluid, and injection rate need to be coordinated to achieve the desired fracture properties (dimensions and conductivity) in a given formation. To find the optimum treatment design for all three scenarios, proppant mass and fluid volume are calculated by the fracturing simulator based on the given target fracture properties (conductivity and half-length). Flow rate, proppant type, and fluid type are manual input parameters.

Obviously, the more fluid is injected, the larger the fracture area. Proppant mass is adapted depending on the created fracture dimensions and the targeted conductivity. Proppant type, fluid type, and flow rate can change the fracture geometry and conductivity significantly.

Fluid type, volume, and flow rate

The fluid type is very important for the resulting fracture aperture, fracture area, wellhead pressure, stress barriers, and proppant transport. Higher viscosity fluids can create wide fractures with a smaller fracture area. On the other hand, lower viscosity fluids can create thin fractures with a large fracture area (**Figures 39 and 40**). However, the proppant transport capability of high viscosity fluids is much better compared to low viscosity fluids such as slickwater because it significantly reduces the proppant settling velocity. Because a large area is more important than a wide fracture to develop large heat exchanger areas and long fluid residence times, slickwater treatments may be more suitable for EGS.

The flow rate is important for the amount of fluid needed to be injected to achieve a certain half-length, pumping power (and energy) requirements, duration of the treatment, proppant transport, stress barriers, and wellhead pressures. The flow rate was changed between 25 l/s and 300 l/s for the Base Case Scenario with (1) 12 MPa critical stress, (2) 0 MPa critical stress, and (3) 0.1 mD permeability (**Figure 55**). With a 0 MPa critical stress the fracture area increases between 25 l/s and 50 l/s and decreases thereafter. For a 12 MPa critical stress and for 0.1 mD permeability, the fracture area increases insignificantly with an increasing flow rate. Hence, the simulations suggest using low to intermediate flow rates (50–100 l/s) for low permeability (0.0005 mD) reservoirs with high critical stress (12–15 MPa), and high flow rates (>100 l/s) for higher

permeability reservoirs (0.1 mD) or reservoirs with a high critical stress to achieve large fracture areas.

Higher flow rates generally lead to an increase in fracture aperture. However, the fracture aperture is only significantly influenced by the flow rate for low (or zero) critical stress values (**Figure 56**).

Higher flow rates lead to a better proppant distribution because the proppant settling will be less severe. This is more important for lower viscosity fluids. Higher flow rates also cause higher wellhead pressures. The maximum possible flow rate depends on the maximum pressure the wellhead, the casing or the installed fracturing string can withstand, the pump capacity, and the availability of water.

Taking into account these restrictions and the relatively low influence on low permeability, high critical stress cases, we used an intermediate injection rate of 100 l/s for our simulations. High fluid volumes are essential to create large fractures or fracture networks (**Figure 39**) but are relatively unimportant for the fracture aperture (**Figure 40**).

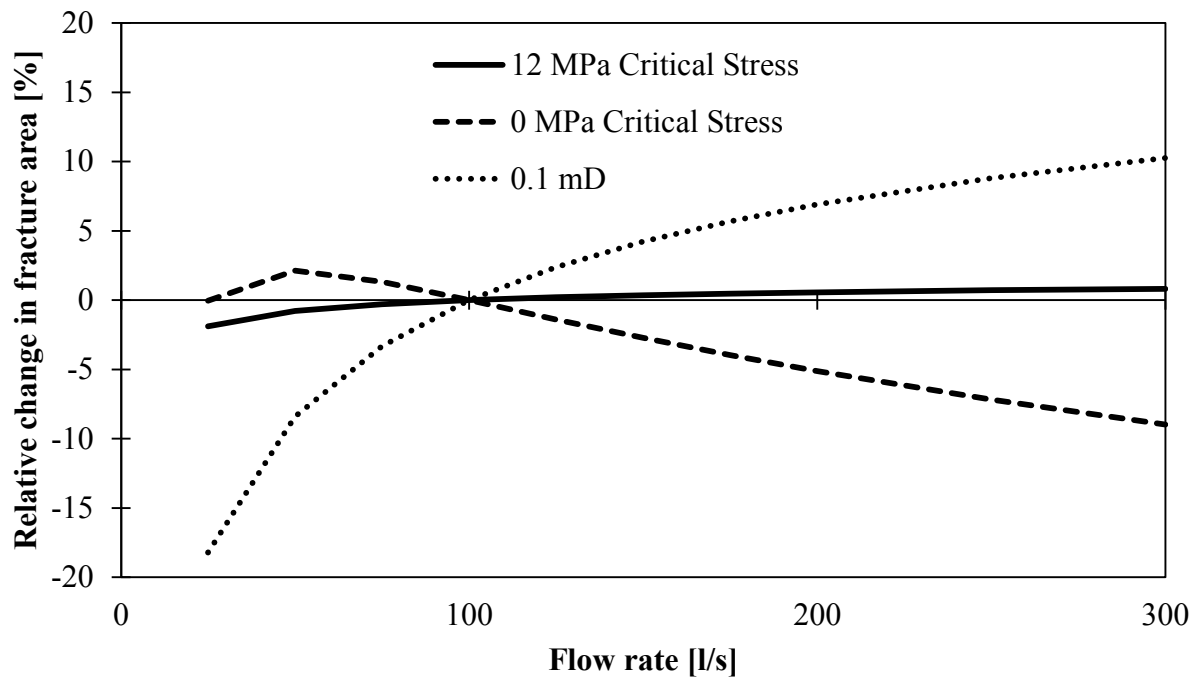


Figure 55: Influence of the flow rate on the relative change in the fracture area for the Base Case Scenario with 12 MPa critical stress, 0 MPa critical stress, and 0.1 mD permeability.

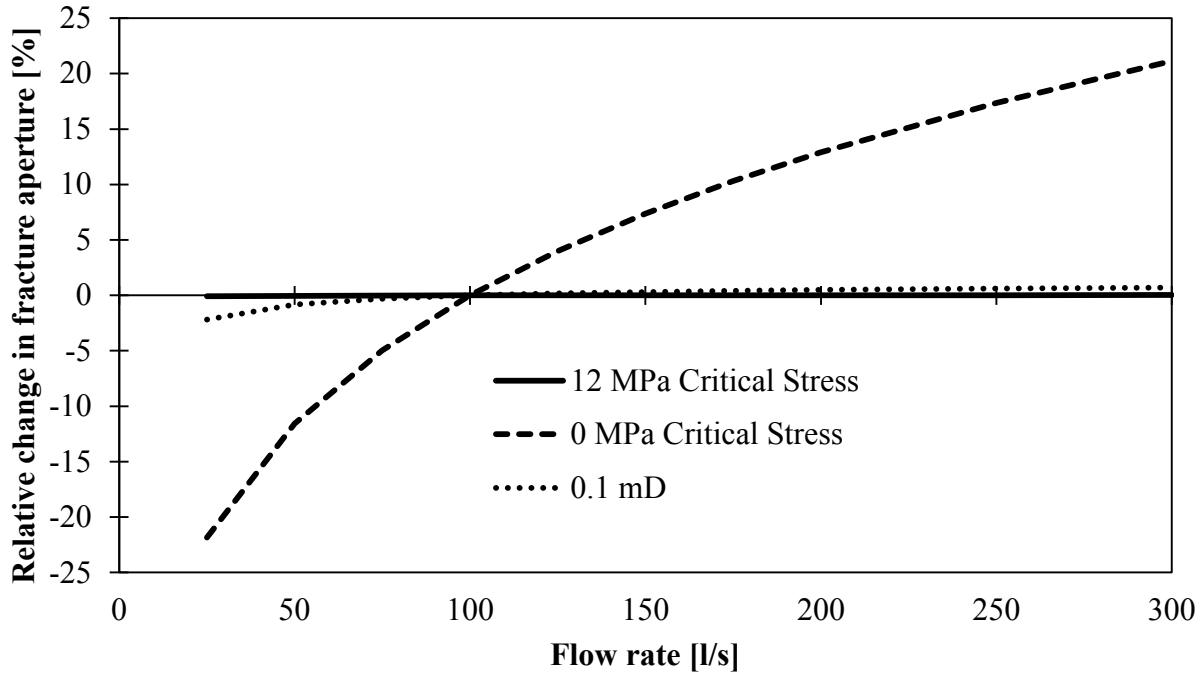


Figure 56: Influence of the flow rate on the relative change in the average fracture aperture for the Base Case Scenario with 12 MPa critical stress, 0 MPa critical stress, and 0.1 mD permeability.

Proppant type, mass, and concentration

The recommended proppant type depends on the closure stress of the reservoir rock on the proppant in the fracture. A general guideline is given in **Table 21**.

The expected minimum horizontal stress (closure stress) range in the target formation at 5 km depth is between 58 and 84 MPa. Consequently, high-strength proppants (HSP) should be used to keep the generated fractures open. HSP generally have a high density. This results in an increased settling rate with a poor proppant transport and distribution within the fracture. To improve the proppant transport, higher flow rates and higher viscosity gels can be used [15]. Ultra-light weight proppants would be needed for sufficient proppant distribution for slickwater fracturing treatments. The proppant size is also an important parameter. Large diameter proppants lead to higher fracture conductivities, but their transport is more difficult and larger fracture widths need to be generated and proppant crushing under high closure pressures is more severe [15]. In our simulations, the proppant size was selected according to stress, fracture width, and transport criteria.

Table 21: Suggested closure stress range for different proppant types [15].

Proppant type	Applicable closure stress range
Sand	< 41 MPa
Resin-coated proppant (RCP)	< 55 MPa
Intermediate-strength proppant (ISP)	34 – 69 MPa
High-strength proppant (HSP)	> 69 MPa

In the simulations, 20/40 CARBO-HSP which have a high density and strength, were used for the gel-proppant treatments. These proppants need to be transported by high viscosity gels. For the hybrid fracturing treatments, 20/40 ULWP 1.75 (ultra-light weight proppants) [43] with a low density were used.

It is not known whether the proppants would be distributed uniformly in fracture systems or if the proppants would be dominantly accumulated in the main fracture. Hence, we simulated both cases.

4.4.4 Hydraulic fracturing simulation results

Water fracturing, hybrid fracturing, and gel-proppant fracturing treatments were performed for the Small Area, the Base Case, and the Large Area Scenario for the two cases with (1) no natural fracture network, and (2) natural fracture network with different fracture spacings (1.5–50 m).

The target parameters for the simulations were a fracture half-length (of the main fracture) of 300 m, 500 m, and 700 m, and a fracture conductivity of 300 mDm and 1000 mDm. For the water fracturing simulations no fracture conductivity was calculated. A conductivity of 10 mDm and 100 mDm was assumed here for self-propped fractures with and without a very low proppant concentration.

For all these cases, a treatment design is proposed and the influence of natural fracture systems on the treatment design is shown.

4.4.4.1 Intact rock

The resulting fracture geometries and the major treatment parameters of the water fracturing simulations for all three scenarios are summarized in **Table 22**. For the Small Area Scenario, the largest slickwater volumes are needed and the widest fractures are developed. The fracture aperture for the Large Area Scenario is the smallest and the least amount of slickwater is injected here. Proppants were not used for these simulations.

Overall, to achieve a fracture half-length of 300 m, between 1875 and 8500 m³ of slickwater needs to be injected at an injection rate of 100 l/s to create a fracture with an area between 0.079 and 0.085 km² and an average total height between 130 and 142 m.

To develop a fracture half-length of 500 m, between 3280 and 16000 m³ of slickwater needs to be injected at an injection rate of 100 l/s to create a fracture with an area of 0.135–0.147 km² and an average height of 134.5–147 m.

Fracture half-lengths of 700 m can be achieved by injecting 4675 m³ (intact rock with a permeability of 0.0005 mD) – 24100 m³ (higher permeability of 0.1 mD). The resulting total fracture area is between 0.191 and 0.210 km² and the height is 137–143 m.

For the hybrid fracturing treatments, either linear or water-based gel was injected during the entire treatment or a small amount of slickwater was injected first, followed by a large amount of X-linked gel and proppant (20/40 ULWP 1.75 was used). The target fracture conductivity for all hybrid fracturing treatments was 300 mDm. The injection rate was 100 l/s for all treatments. The treatment parameters and resulting fracture geometries for all hybrid fracturing treatments are summarized in **Table 23**.

A fracture with a half-length of 300 m could be developed using a slurry volume of 1907–8490 m³, and a proppant mass between 276 and 326 t resulting in a fracture area of 0.077–0.084 km² and a total fracture height of 124–139 m.

Fracture half-lengths of 500 m were developed using a slurry volume of 4811–15952 m³ and a proppant mass of 498–559 t resulting in a fracture area of 0.143–0.157 km² and a total fracture height of 134–145 m.

Table 22: Fracture properties and treatment parameters for slickwater treatments without proppants for all three scenarios and different target fracture half-lengths (H = average fracture height, A = total fracture area, K = fracture conductivity, V_i = injected fluid volume, Q_i = injection rate, Slickwater = water and friction reducer).

	Half-length: 300 m			Half-length: 500 m			Half-length: 700 m		
	Large Area Scenario			Base Case Scenario			Small Area Scenario		
	H=130.5m	A=0.079 km ²	K=100mDm	H=136m	A=0.082km ²	K=100mDm	H=142m	A=0.085km ²	K=100mDm
	V_i =1875m ³	Q_i =100l/s	Slickwater	V_i =3670m ³	Q_i =100l/s	Slickwater	V_i =8500m ³	Q_i =100l/s	Slickwater
	H=134.5m	A=0.135 km ²	K=100mDm	H=141m	A=0.141km ²	K=100mDm	H=147m	A=0.147km ²	K=100mDm
	V_i =3280m ³	Q_i =100l/s	Slickwater	V_i =6500m ³	Q_i =100l/s	Slickwater	V_i =16000m ³	Q_i =100l/s	Slickwater
	H=137m	A=0.191km ²	K=100mDm	H=143m	A=0.200km ²	K=100mDm	H=150m	A=0.210km ²	K=100mDm
	V_i =4675m ³	Q_i =100l/s	Slickwater	V_i =9300m ³	Q_i =100l/s	Slickwater	V_i =24100m ³	Q_i =100l/s	Slickwater

Table 23: Fracture properties and treatment parameters for hybrid fracturing treatments with low proppant masses and intermediate fracturing fluid viscosity for all three scenarios and different target fracture half-lengths (H = average fracture height, A = total fracture area, K = fracture conductivity, V_i = injected fluid volume, M = proppant mass).

Small Area Scenario			Base Case Scenario			Large Area Scenario					
Half-length: 300 m			Half-length: 500 m			Half-length: 700 m					
$H=139\text{m}$	$A=0.084\text{km}^2$	$M=326\text{tons}$	$K=300\text{mDm}$	$H=128\text{m}$	$A=0.077\text{km}^2$	$M=294\text{tons}$	$K=300\text{mDm}$	$H=124\text{m}$	$A=0.077\text{km}^2$	$M=276\text{tons}$	$K=300\text{mDm}$
$V_i=8490\text{m}^3$			Linear Gel	$V_i=3661\text{m}^3$			Water based	$V_i=1907\text{m}^3$			Water based
$H=141\text{m}$	$A=0.143\text{km}^2$	$M=498\text{tons}$	$K=300\text{mDm}$	$H=134\text{m}$	$A=0.134\text{km}^2$	$M=489\text{tons}$	$K=300\text{mDm}$	$H=145\text{m}$	$A=0.157\text{km}^2$	$M=559\text{tons}$	$K=300\text{mDm}$
$V_i=15952\text{m}^3$			Linear Gel	$V_i=6591\text{m}^3$			X-Linked Gel	$V_i=4811\text{m}^3$			X-Linked Gel
$H=144\text{m}$	$A=0.201\text{km}^2$	$M=733\text{tons}$	$K=300\text{mDm}$	$H=148\text{m}$	$A=0.208\text{km}^2$	$M=733\text{tons}$	$K=300\text{mDm}$	$H=175\text{m}$	$A=0.246\text{km}^2$	$M=860\text{tons}$	$K=300\text{mDm}$
$V_i=23929\text{m}^3$			Linear Gel	$V_i=10643\text{m}^3$			X-Linked Gel	$V_i=8602\text{m}^3$			X-Linked Gel

Table 24: Fracture properties and treatment parameters for gel-proppant fracturing treatments with high proppant mass and fracturing fluid viscosity for all scenarios and target fracture half-lengths (injection rate=100 l/s, proppant type=20/40 CarboHSP, fluid type=Hybor G 50lb/Mgal WG-19, H=average fracture height, A=total fracture area, K=fracture conductivity, V_i =injected fluid volume, M=proppant mass).

Half-length: 300 m			Half-length: 500 m			Half-length: 700 m			
Large Area Scenario									
Base Case Scenario									
Small Area Scenario									
Large Area Scenario									
Base Case Scenario									
Small Area Scenario									
Large Area Scenario									
Base Case Scenario									
Small Area Scenario									
Large Area Scenario									
Base Case Scenario									
Small Area Scenario									
Large Area Scenario									
Base Case Scenario									
Small Area Scenario									
Large Area Scenario									
Base Case Scenario									
Small Area Scenario									
Large Area Scenario									
Base Case Scenario									
Small Area Scenario									
Large Area Scenario									
Base Case Scenario									
Small Area Scenario									

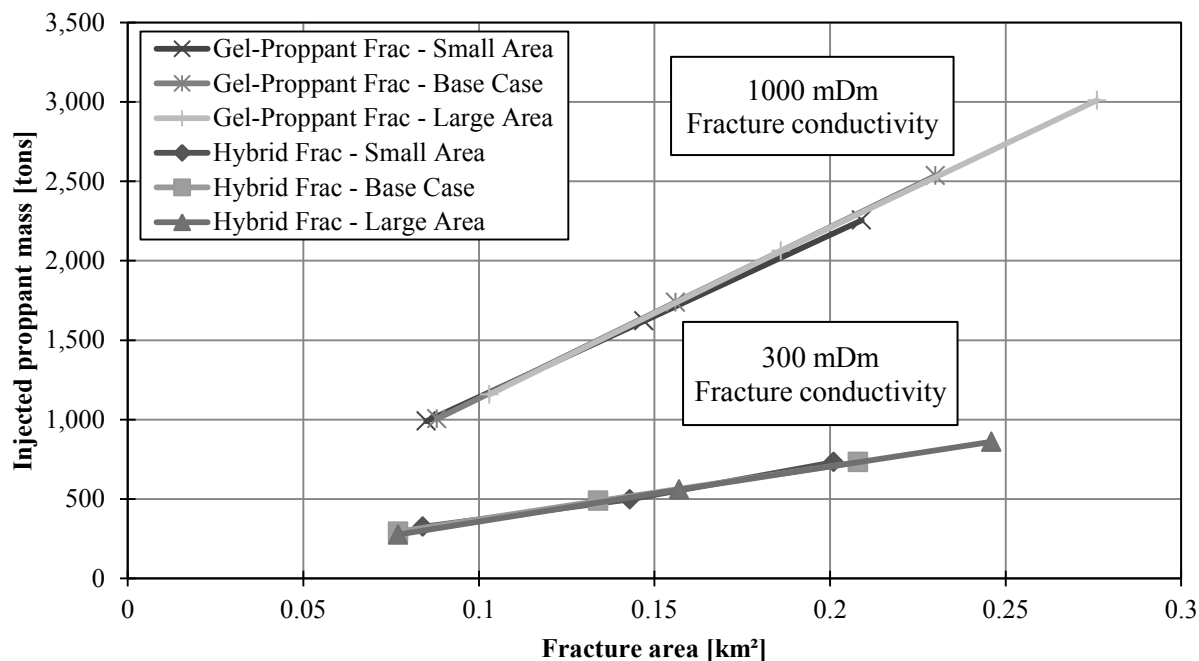


Figure 57: Fracture area vs. proppant mass to create a fracture conductivity of 300 mDm and 1,000 mDm for all three scenarios using gel-proppant, and hybrid fracturing treatments. The target half-lengths were 300 m, 500 m, and 700 m.

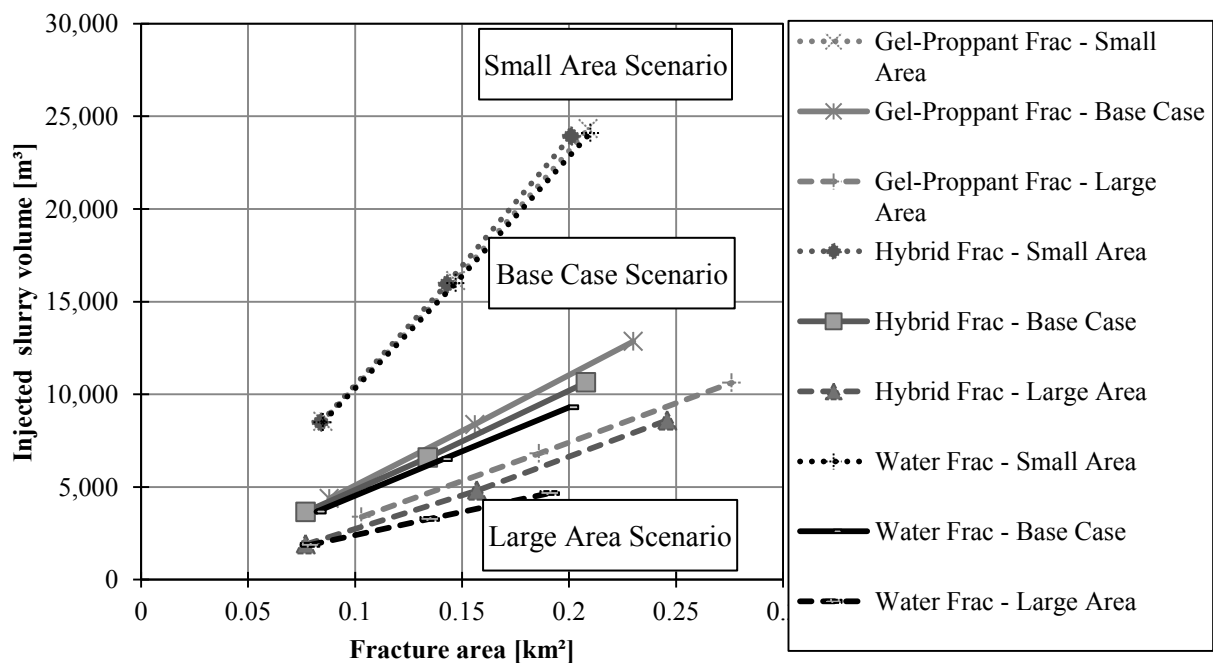


Figure 58: Injected fluid volume vs. fracture area for all three scenarios and all three treatment methods. The target half-lengths were 300, 500, and 700 m.

To achieve a half-length of 700 m, 8602–23929 m³ slurry and 733–860 t proppant were injected. Resulting fracture areas are 0.201–0.246 km² and resulting fracture heights lay between 144 and 175 m.

Conventional gel-proppant treatments were performed using very high viscosity X-linked gel during the entire treatment to transport 20/40 high-strength proppant at a constant injection rate of 100 l/s to develop fractures with a conductivity of 1000 mDm. Treatment parameters and resulting fracture geometries for all conventional gel-proppant treatment simulations are summarized in **Table 24**.

For fracture half-lengths of 300 m, 3394–8547 m³ slurry and 990–1159 t proppant need to be injected. These treatments result in fracture areas between 0.085 and 0.103 km² and fracture heights between 141 and 170 m.

Fracture half-lengths of 500 m can be created using 6815–16146 m³ slurry and 1621–2062 t proppant. Resulting fracture areas are 0.147–0.186 km² and resulting fracture heights are 146–185 m.

To develop fracture half-lengths of 700 m, 10633–24335 m³ slurry and 2255–3009 t proppant needs to be injected. A total fracture area of 0.209–0.276 km² and a total fracture height of 149–195 m results from these treatments.

For all treatments, the injected fluid volume decreases from the Small Area to the Large Area Scenario. The injected proppant mass decreases for lower viscosity fluids and increases for higher viscosity fluids from the Small Area to the Large Area Scenario due to a decrease in fracture area and height for lower viscosity fluids, and an increase in area and height for higher viscosity fluids. Longer target fracture half-lengths lead to higher fractures with a larger area resulting in more injected fluid volume and proppant mass.

Figure 57 shows that for all three scenarios, the injected proppant mass needed to develop a certain average fracture conductivity increases linearly with the created fracture area.

However, the minimum horizontal stress has a significant influence on the fracture conductivity as well. A minimum horizontal stress of 83.7 MPa leads to a fracture conductivity of only about

780 mDm and a minimum horizontal stress of 58 MPa to a fracture conductivity of about 1200 mDm for all gel-proppant fracturing scenarios as compared to the Base Case Scenario with 1000 mDm fracture conductivity.

The relationships between fracture area and injected fluid volume for all simulated scenarios are shown in **Figure 58**. The injected fluid volume increases linearly with the created fracture area. For the Small Area Scenario the largest fluid volumes are needed and for the Large Area Scenario the lowest amounts of fluid are needed due to their different leak-off behavior.

4.4.4.2 Naturally fractured rock

Influence of natural fractures on conventional treatment designs

The influence of natural fracture systems on conventional treatment design results were studied for the Base Case Scenario with a target fracture conductivity of 1000 mDm and a target (main) fracture half-length of 500 m using the same gel-proppant fracturing treatment as derived for the intact rock (**Table 24, center**). The stress difference between the two principle horizontal stresses was set to 0 MPa and the fracture spacing was set to 5 m and 50 m. In addition, the proppant distribution was assumed to be uniform for one case and dominantly distributed in the main fracture for another case. In situ apertures were set to 0.5 mm.

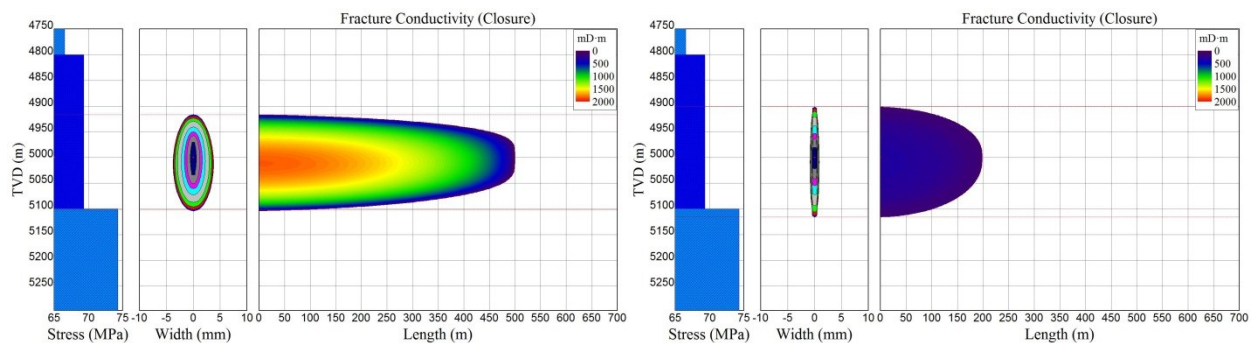


Figure 59: Comparison of the properties of the main fracture resulting from the same treatment (designed for intact rock) for the Base Case Scenario with intact rock (left) and with a natural fracture system of 50 m spacing (right).

The conventional gel-proppant treatment results in an early screen out for a fracture spacing of 5 m with uniform proppant distribution and with proppant distribution mainly in the main fracture.

The same happens for a 50 m fracture spacing and dominant proppant distribution in the main fracture. Only for the case with fracture spacing of 50 m and uniform proppant distribution no screen out is observed for the treatment that was designed for intact rock.

The half-length of the main fracture decreases from 500 m to 199 m, but an additional secondary fracture half-length of 2523 m is created. The fracture height increases from 156 m to 166 m for the main fracture. The secondary fracture network has an average height of 139 m. The fracture area of the main fracture decreases from 0.156 km² to 0.068 km², however a significantly larger secondary fracture network with an area of 0.723 km² is created. The conductivity of the main fracture decreases from 1000 mDm to 173 mDm. The fracture conductivity of the secondary network is 151 mDm. **Figure 59** visually compares the properties of the main fracture resulting from the same treatment (designed for intact rock) without fracture network (left) and with fracture network (right).

Adapted treatment designs for naturally fractured rock

For four cases a conventional gel-proppant treatment was designed using X-linked gel and 20/40 HSP. The results are summarized in **Table 25**. Visually, the resulting fracture networks for 5 m fracture spacing and 50 m fracture spacing are compared in **Figure 60**. The target fracture half-length of 500 m can be achieved by all scenarios.

However, the fracture height growth is less confined for lower fracture spacings leading to average fracture heights of up to 738 m for 5 m fracture spacing and a proppant transport only in the main fracture compared to 156 m for the unfractured case. Additionally, more fluid and proppant need to be injected for smaller fracture spacings to achieve the same target fracture half-length. For a uniform proppant distribution, the target conductivity can be created for larger (50 m) fracture spacings but not for smaller (5 m) fracture spacings. If the proppant is uniformly distributed within the fracture network, even with very high proppant masses (7830 tons), the target fracture conductivity of 1000 mDm could not be achieved for the whole network.

Table 25: Comparison between optimized intact and fractured rock cases for the Base Case Scenario using conventional gel-proppant treatments with X-linked gel and high strength proppants (L = length, H = height, A = area, K = conductivity, V = injected slurry volume, M = injected proppant mass).

Intact rock	Frac spacing:50m uniform proppant distribution	Frac spacing:50m dominant main proppant distr.	Frac spacing:5m uniform proppant distr.	Frac spacing:5m dominant main proppant distr.
$L_{\text{main}}=1,000\text{m}$	$L_{\text{main}}=993\text{m}$	$L_{\text{main}}=1,000\text{m}$	$L_{\text{main}}=964\text{m}$	$L_{\text{main}}=983\text{m}$
$L_{\text{DFN}}=0\text{m}$	$L_{\text{DFN}}=31,535\text{m}$	$L_{\text{DFN}}=31,527\text{m}$	$L_{\text{DFN}}=302,070\text{m}$	$L_{\text{DFN}}=314,390\text{m}$
$H_{\text{main}}=156\text{m}$	$H_{\text{main}}=220\text{m}$	$H_{\text{main}}=428\text{m}$	$H_{\text{main}}=519\text{m}$	$H_{\text{main}}=738\text{m}$
$H_{\text{DFN}}=0\text{m}$	$H_{\text{DFN}}=187\text{m}$	$H_{\text{DFN}}=360\text{m}$	$H_{\text{DFN}}=434\text{m}$	$H_{\text{DFN}}=617\text{m}$
$A_{\text{main}}=0.16\text{km}^2$	$A_{\text{main}}=0.22\text{km}^2$	$A_{\text{main}}=0.43\text{km}^2$	$A_{\text{main}}=0.50\text{km}^2$	$A_{\text{main}}=0.73\text{km}^2$
$A_{\text{DFN}}=0\text{km}^2$	$A_{\text{DFN}}=5.85\text{km}^2$	$A_{\text{DFN}}=11.35\text{km}^2$	$A_{\text{DFN}}=131.2\text{km}^2$	$A_{\text{DFN}}=190.63\text{km}^2$
$K_{\text{main}}=1,000\text{mDm}$	$K_{\text{main}}=104\text{mDm}$	$K_{\text{main}}=1000\text{mDm}$	$K_{\text{main}}=108\text{mDm}$	$K_{\text{main}}=216\text{mDm}$
$K_{\text{DFN}}=0\text{mDm}$	$K_{\text{DFN}}=90\text{mDm}$	$K_{\text{DFN}}=0\text{mDm}$	$K_{\text{DFN}}=95\text{mDm}$	$K_{\text{DFN}}=0\text{mDm}$
$V=8,372\text{m}^3$	$V=41,240\text{m}^3$	$V=74,650\text{m}^3$	$V=181,939\text{m}^3$	$V=286,032\text{m}^3$
$M=1,739\text{tons}$	$M=1,850\text{tons}$	$M=5,201\text{tons}$	$M=7,830\text{tons}$	$M=2,201\text{tons}$

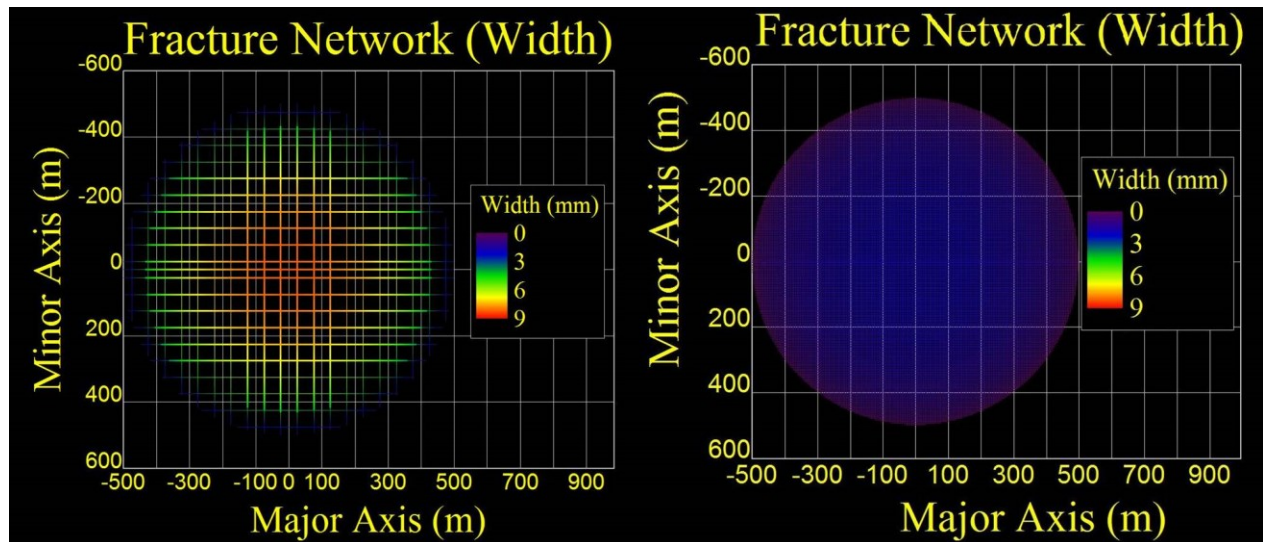


Figure 60: Top view on the fracture network for 50 m fracture spacing (left) and 5 m fracture spacing (right).

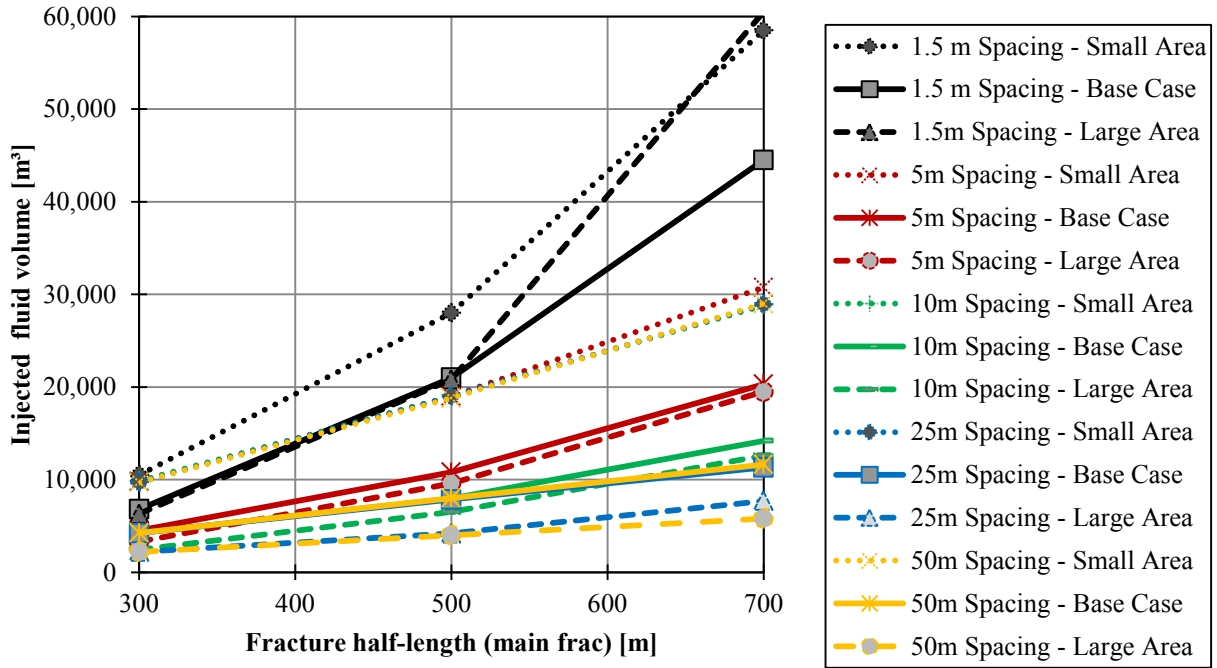


Figure 61: Injected fluid volume needed to achieve a fracture half-length between 300 m and 700 m for fracture spacings between 1.5 m and 50 m.

Because the proppant transport in fracture networks is not well understood and because water fracturing treatments showed the most success in naturally fractured ultra-tight reservoirs [11], we are presenting slickwater volumes needed to create certain fracture networks with different spacings (1.5–50 m) and different lengths of the main fracture (300 m, 500 m, and 700 m) with a stress difference of 0 MPa between the two principal horizontal stresses. **Figure 61** shows that in general about 5,000 m³ of slickwater is sufficient to create a main fracture with a 300 m half-length; about 10,000 m³ of slickwater is needed to create a main fracture with 500 m half-length, and; about 20,000 m³ of slickwater could create a main fracture with a 700 m half-length. This is true for minimum fracture spacings of 5 m and for the Large Area and Base Case Scenarios with low permeability. A fracture spacing of 1.5 m in the Small Area Scenario could result in the need to inject about 10,000 m³ of slickwater to achieve a half-length of 300 m, 30,000 m³ to achieve a half-length of 500 m, and 60,000 m³ to achieve a half-length of 700 m. Main reasons for this increasing water demand are the unconfined fracture height growth for small fracture spacings compared to the confined fracture height growth for larger fracture spacings, and the larger fracture volumes that are created for smaller fracture spacings. The height growth confinement is

worse for the Large Area Scenario due to its higher critical stress (15 MPa compared to 12 MPa for the Base Case and 9 MPa for the Small Area Scenario).

Because water fracturing treatments in naturally fractured rock masses utilize the shear stimulation process, fracture conductivities resulting from these treatments were approximated by the results of flow through experiments on displaced fracture surfaces without proppants and with a small amount of proppants. According to the experimental results of Chen et al. [44], average fracture conductivities of about 10 mDm can be expected for displaced fractures in granites at high (above 40 MPa) confining pressures. However, the conductivity significantly increases with displacement, decreases with confining pressure and varies for different granites [44]. When using a small amount of proppants the conductivity of the displaced shear fractures can increase by a factor of 10 or more [45]. Hence, for the reservoir simulations, we used a fracture conductivity of 10 mDm for water fracturing treatments (shear fractures) without proppants and 100 mDm for water fracturing treatments (shear fractures) with a small amount of proppants.

4.5 RESERVOIR SIMULATIONS

4.5.1 Reservoir simulator

The thermal and hydraulic behavior of the reservoir was modeled using the thermal–hydraulic (TH) finite-difference (FD) reservoir simulator CMG STARS [22]. Fractures were implemented using the single porosity approach and wells were operated at a constant injection/production rate. Wellbore heat losses were simulated without additional insulation. The reservoir model with its initial temperature distribution for an example scenario is shown in **Figure 62**. The parallel wells are shown in gray (I1, P1, P2) with the injection well in the center. Fractures are perpendicular to the wells; their position can be inferred from the local grid refinement around the fractures.

4.5.2 Performance criteria

Certain performance criteria need to be met in order to optimize the thermal and hydraulic performance of different reservoir exploitation scenarios.

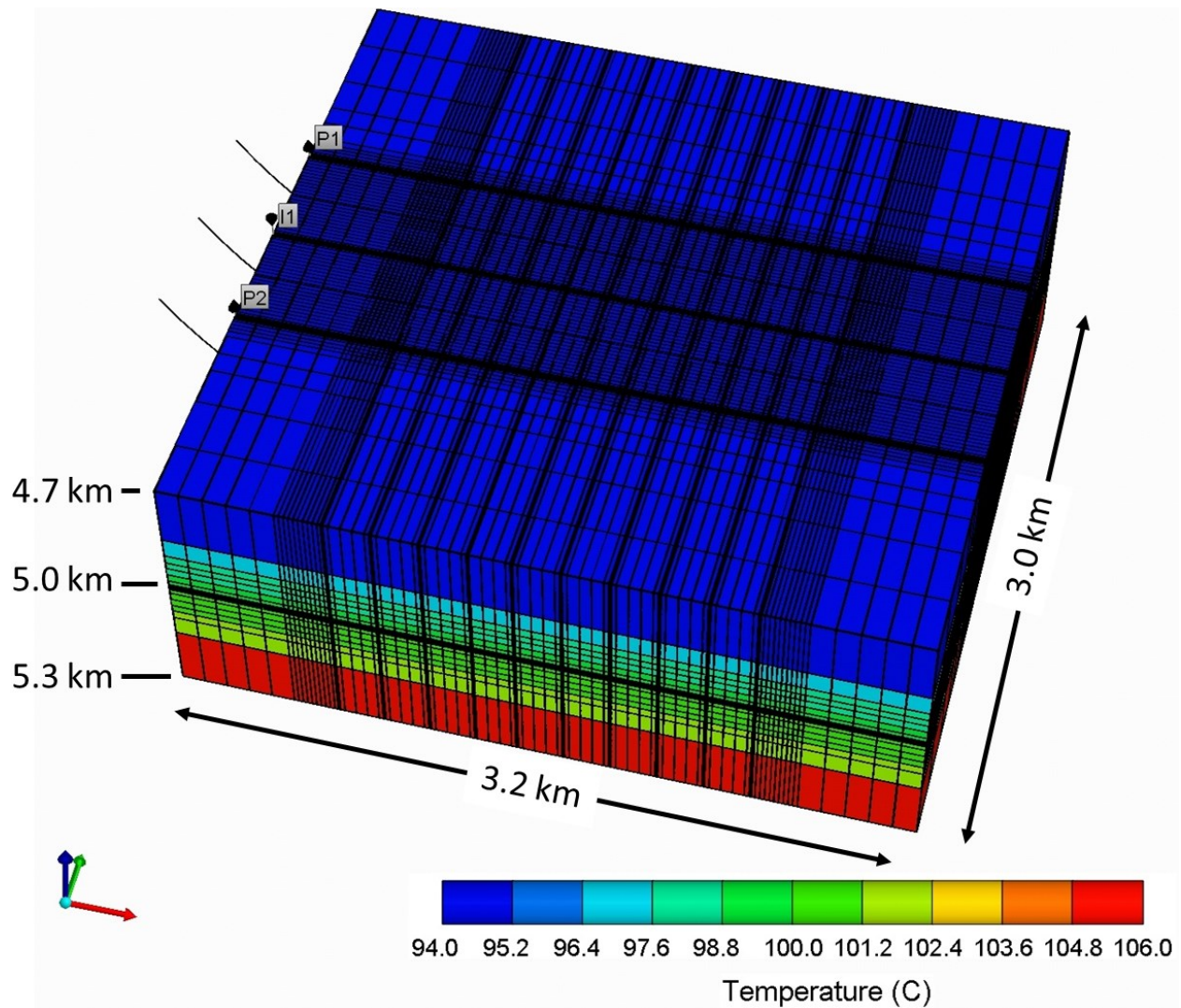


Figure 62: 3-D View of an example reservoir model including initial temperature distribution.

For the processing of mined oil sands in a “warm water process” [2], a temperature of at least 40–50°C is needed [2]. Considering heat losses from the geothermal well to the processing area of 10°C, a wellhead temperature of about 60°C would be a sufficient thermal performance criterion.

The productivity index (PI) is defined as the flow rate divided by the pressure drawdown—the difference between initial bottom hole pressure of a production well and the final bottom hole pressure of a production well. In order to be economic HDR systems generally need a minimum PI of 10 l/s/MPa (or maximum impedance of 0.1 MPa/l/s) [23].

The simulations were performed for a 30-year reservoir lifetime and a total injection/production rate of 60 l/s which is approximately the highest rate so far achieved in HDR systems [46].

4.5.3 Well spacing

We studied the influence of the well spacing on temperature drawdown, productivity index, and extracted thermal energy. Increasing the well spacing for a fixed fracture length results in a decrease of productivity (hydraulic performance), but an increase in extracted energy and well head temperature after 30 years of production (**Figure 63**). Because the productivity can be further increased by subsequent fracturing treatments, we want to increase the extracted energy here. However, we give a safety margin of 100 m from the edge of the created fracture to the position of the production wells. Resulting well spacings are 200 m for a 300 m half-length, 400 m for a 500 m half-length, and 600 m for a 700 m half-length.

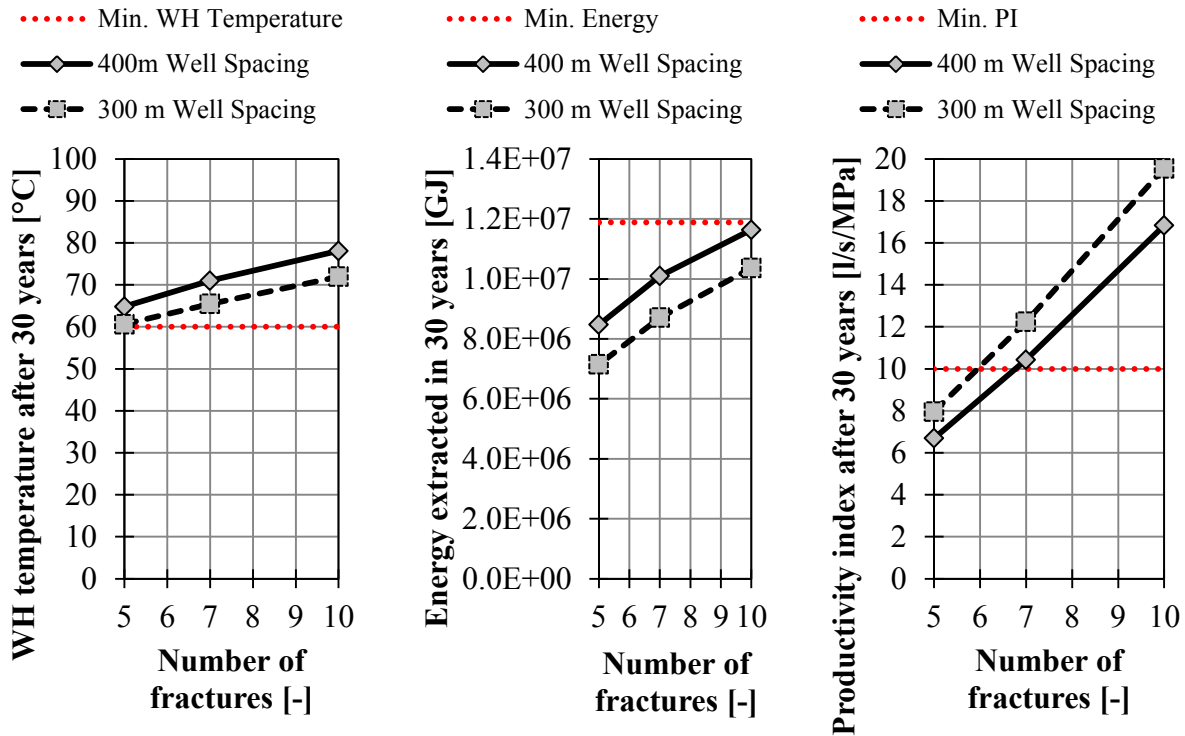


Figure 63: Influence of the number of fractures (treatments) on WH temperature, extracted energy, and productivity index after 30 years of production for the Base Case Scenario (500 m fracture half-length, 400 m well spacing, 1000 mDm fracture conductivity, 100 m fracture spacing).

4.5.4 Number of fracturing treatments

First, the number of treatments (fractures) is found for relatively long fracture spacings of 200 m for the gel-proppant and hybrid fracturing treatments. Because of the significantly larger amount of fractures needed for the two low conductivity (10 mDm and 100 mDm) water fracturing cases, the initial spacing was set to 50 m for 100 mDm and 5 m for 10 mDm to maintain the length of the horizontal well section below 5000 m. Afterwards, the fracture spacing is optimized (reduced).

An increase in fractures (number of treatments) generally leads to an increase in PI (hydraulic performance) and wellhead temperature after 30 years, as well as the extracted amount of heat (**Figure 63**). The number of fractures has the largest impact on the hydraulic and thermal performance.

The minimum number of fracturing treatments (creating one single fracture in intact rock) to achieve the reservoir performance criteria is shown in **Figure 64**. This minimum number increases with decreasing conductivity. In **Section 4.6** we show the minimum number of fracturing treatments needed to achieve the thermal, hydraulic, and economic targets (**Table 26**).

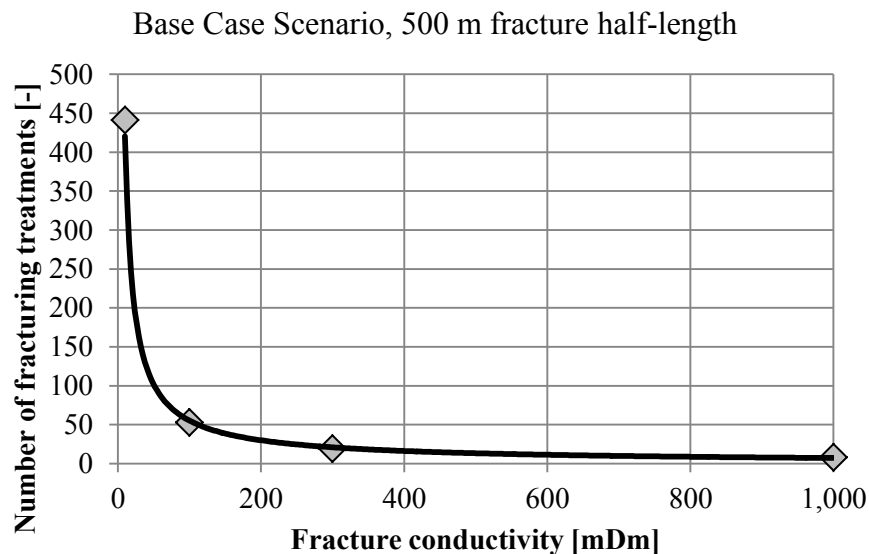


Figure 64: The minimum number of fractures (single fracturing treatments) increases with decreasing fracture conductivity.

Table 26: Reservoir performance criteria.

Thermal performance	
Initial reservoir temperature	100°C
Re-injection temperature	30°C
Minimum well head Temperature	60°C
Hydraulic performance	
Maximum water loss	10 %
Minimum productivity index	10 l/s/MPa
Minimum total circulation rate	60 l/s
Other criteria	
Reservoir lifetime	30 years
Number of wells (inj./prod.)	3 (1/2)
Maximum cost per energy unit	6 \$/GJ

4.5.5 Fracture spacing

The fracture spacing should be chosen such that the fractures do not interfere with each other thermally so that most of the heat can be extracted at a minimum spacing. The spacing should be as small as possible to avoid very long (and hence expensive) horizontal or inclined well sections.

In general, increasing the fracture spacing leads to larger heat amounts that can be extracted from the subsurface and in a larger productivity index (**Figure 65**). However, for a given spacing, both values will stay approximately the same if the spacing is further increased, and if it is decreased the extracted heat and the PI will decrease significantly (**Figure 64**). This optimum (minimum) fracture spacing depends on well spacing, production/injection rate, the fracture conductivity, the fracture area, and the number of fractures.

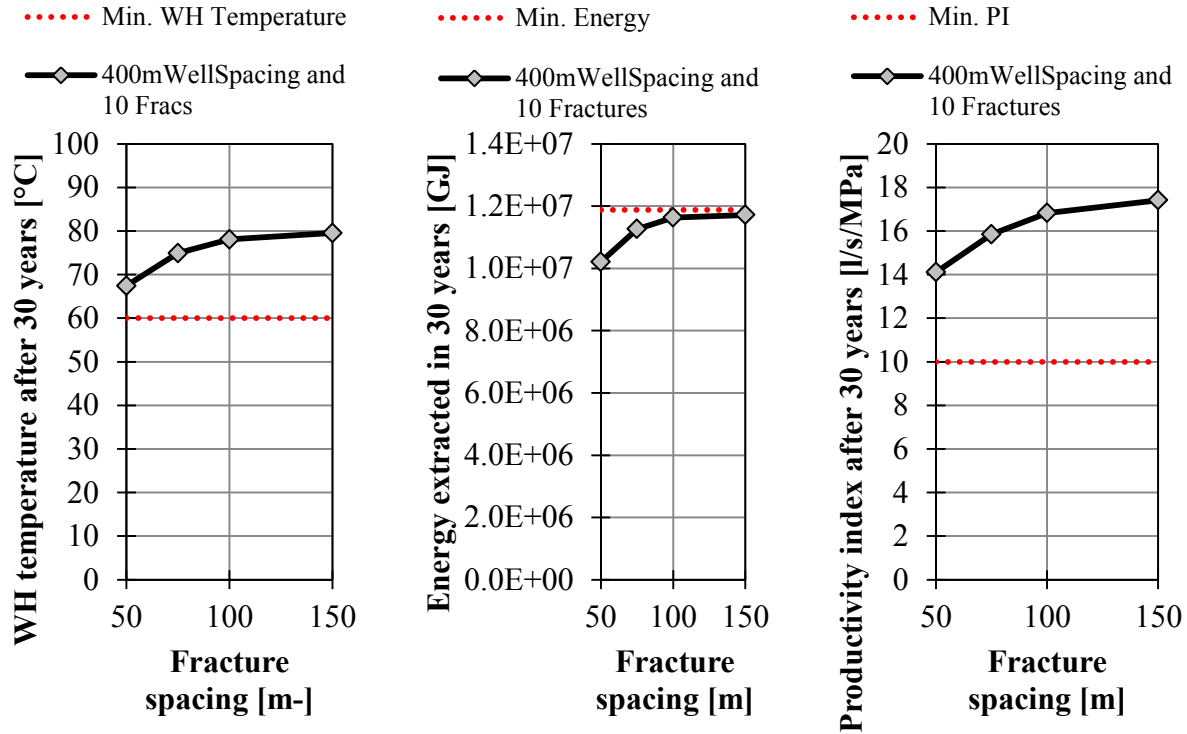


Figure 65: Influence of fracture spacing on WH temperature, extracted energy, and productivity index after 30 years of production for the Base Case Scenario (500 m fracture half-length, 400 m well spacing, 1000 mDm fracture conductivity, 10 fractures).

For our simulations we chose a fracture spacing of 200 m, long enough to avoid thermal and hydraulic interference for scenarios with high fracture conductivity (gel-proppant and hybrid fracturing treatments). For the water fracturing simulations we used a spacing of 50 m (for the 100 mDm case) and of 10 m (for the 10 mDm case) to avoid unrealistically high lengths of the horizontal well section.

4.6 ECONOMIC ANALYSIS

The economic target is set to provide geothermal energy at the same (or lower) price as natural gas. Currently in Alberta the gas price is \$3 per GJ energy [47]. Assuming a gas plant efficiency of 50%, leads to \$6 per GJ as a target value.

Because of the high initial costs, geothermal energy is becoming more competitive with project lifetime. Additionally, higher gas prices and CO₂ certificates would make it even more competitive to the burning of natural gas.

Costs of geothermal projects can vary significantly from site to site mainly depending on the drilling depth [48]. The total costs of the project was subdivided into five categories: (1) Drilling costs, (2) production costs for 30 years, (3) costs for pumps and surface installations, (4) costs of hydraulic stimulations, and (5) other operational costs (**Figure 66**).

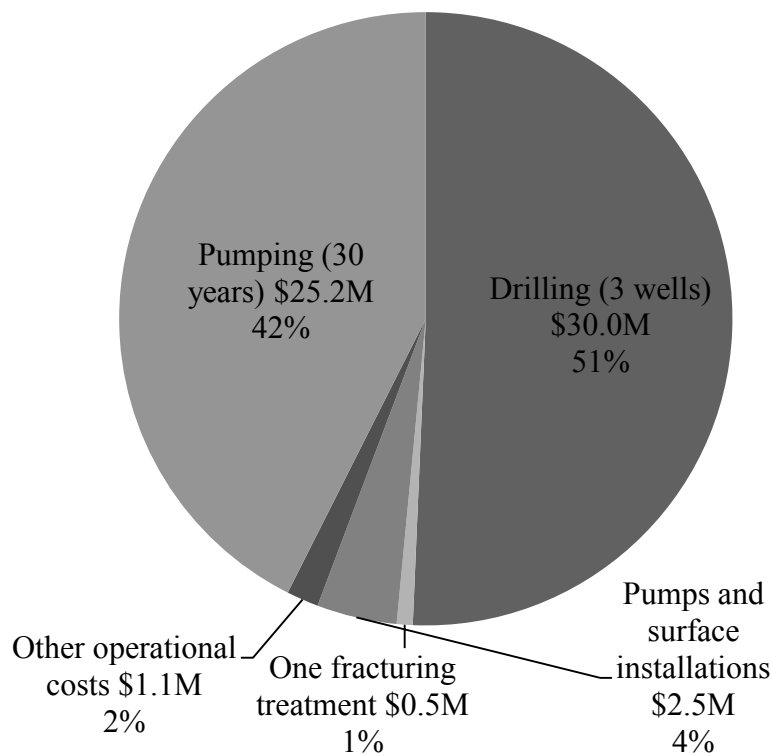


Figure 66: Approximated EGS costs in % and million Canadian dollars.

The expected drilling costs to drill one 5 km deviated well into granitic rock are approximately \$10 million [11]. Thus, the total drilling costs are expected to be \$30 million. The expected production costs for a period of 30 years assuming two production pumps and one injection pump with a total power of 1.2MW and a price of 0.08\$/kW h will be about \$25.2 million. Treatment costs for one well are given by Tester et al. [11] with approximately \$500,000 per well. Gel-proppant and water fracturing treatments in sandstone and volcanic rocks at the geothermal

research site in Groß Schönebeck had approximately the same cost for each treatment. Details about these treatments can be found in Zimmermann et al. [49].

Both stimulation methods had approximately the same costs. For the gel-proppant fractures the cost for gels and proppants are important. Equally important were the costs resulting from the duration of the water fracturing treatment which took place over several days. The labor time and equipment rental (e.g. high pressure pumps) were the cost-driving factors here. Even though the costs of a treatment depend on many parameters and especially on the treatment volume [50] we assumed a cost of \$0.5 million for one hydraulic fracturing treatment (independent of treatment design), and multiplied it by the number of fractures (treatments) needed. All other costs were fixed.

The cost of geothermal energy per GJ was calculated by dividing the total costs of the geothermal project by the (simulated) total heat recovered from the subsurface in 30 years of continuous production.

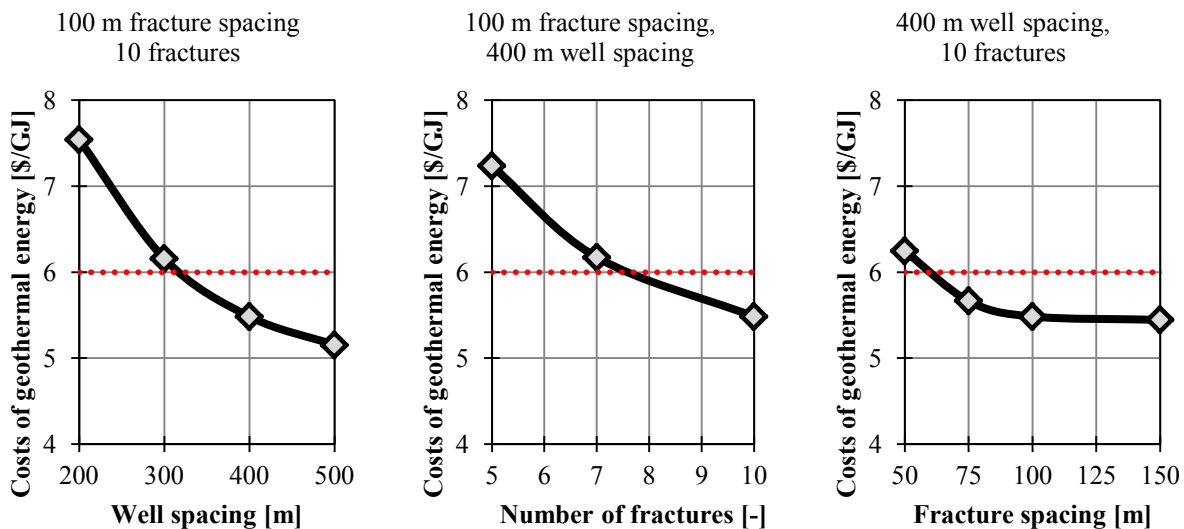


Figure 67: Influence of well spacing, number of fractures, and fracture spacing on the geothermal energy generation costs for one example (Base Case Scenario with 500 m fracture half-length, 1000 mDm fracture conductivity, 400 m well spacing, 10 fractures, and 100 m fracture spacing). The dotted line represents the current costs of generating the same amount of energy with burning natural gas assuming 50% efficiency.

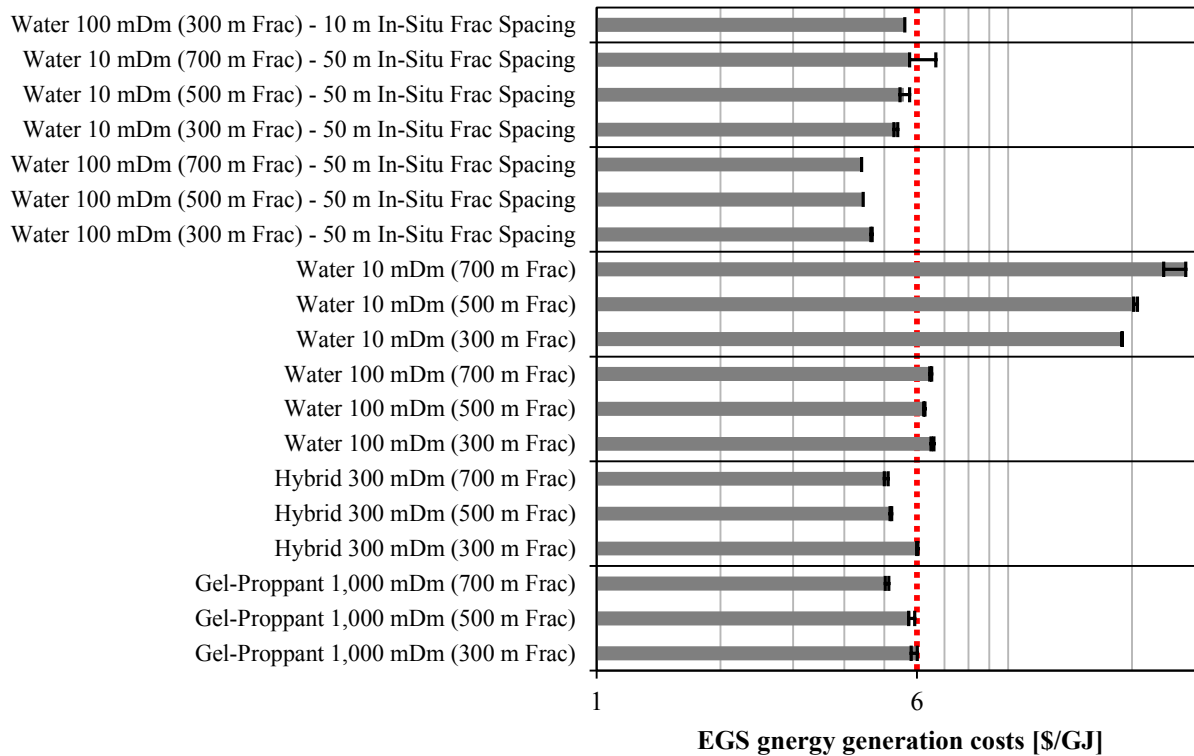


Figure 68: Comparison of the energy generation costs of producing geothermal energy from a 3 well EGS with a lifetime of 30 years for different stimulation types, fracture conductivities, and created fracture half-lengths for intact rock and naturally fractured rock with different in-situ fracture spacings. The presented values are for the Base Case Scenario. The error bars show the variation between all three Scenarios (Small Area, Base Case, and Large Area).

The well spacing was fixed to a value of the half-length minus 100 m as described above. Then the minimum number of fractures to achieve less than 6 \$/GJ was found for a fracture spacing of 200 m (gel-proppant and hybrid fracturing treatments), 50 m (water fracturing treatments with 100 mDm fracture conductivity), and 10 m (water fracturing treatments with 10 mDm fracture conductivity). **Figure 67** shows the influence of well spacing, the number of fractures, and the fracture spacing for an example treatment on the cost per GJ.

For the hydraulic fracturing treatments (for intact rock and fractured rock) presented in **Section 4.4.4**, the costs of geothermal energy generation are presented in **Figure 68**. Because the costs of the stimulations are low (one treatment is about 1% of the total costs) compared to drilling and operational costs, the number of fractures was increased until the economic target of 6\$/GJ was met (if possible) by a higher amount of heat extracted at the same flow rate (due to the longer

production of higher temperature water), and until the productivity index was at least 10 l/s/MPa. Costs could be lower if more than these minimum numbers of fractures are created (see **Figure 67**).

The number of fracturing treatments and the length of the horizontal well section that would be needed to create multiple fractures with spacings of 200 m (gel-proppant and hybrid fracturing treatments), 50 m (water fracturing treatments resulting in 100 mDm fracture conductivity), or 10 m (water fracturing treatments resulting in 10 mDm fracture conductivity) is shown for all simulated cases in **Figure 69**. Additionally, the proppant mass and fluid volume needed to create these multiple fractures and fracture networks are given for all simulated cases in **Figure 70**.

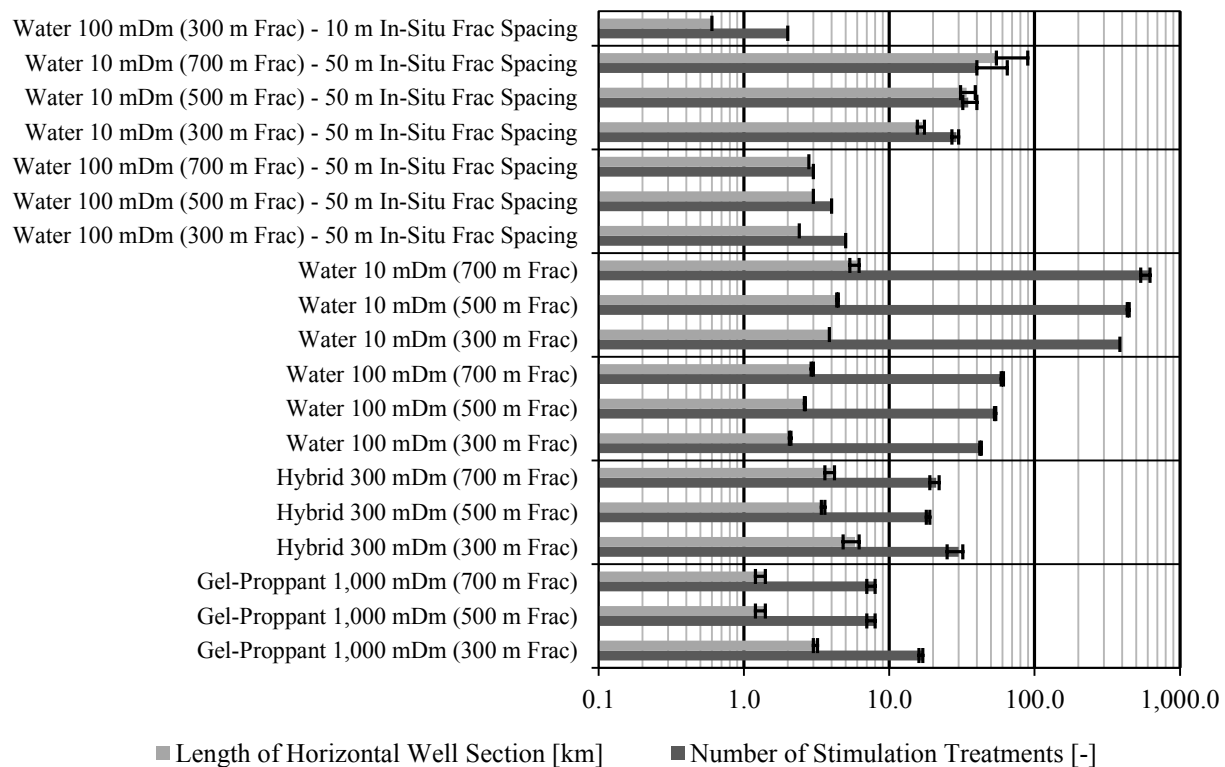


Figure 69: Comparison of the length of the horizontal well section and the number of stimulation treatments needed to fulfill the performance criteria for different stimulation types, fracture conductivities, and created fracture half-lengths for intact rock and naturally fractured rock with different in-situ fracture spacings. The presented values are for the Base Case Scenario. The error bars show the variation between all three Scenarios (Small Area, Base Case, Large Area).

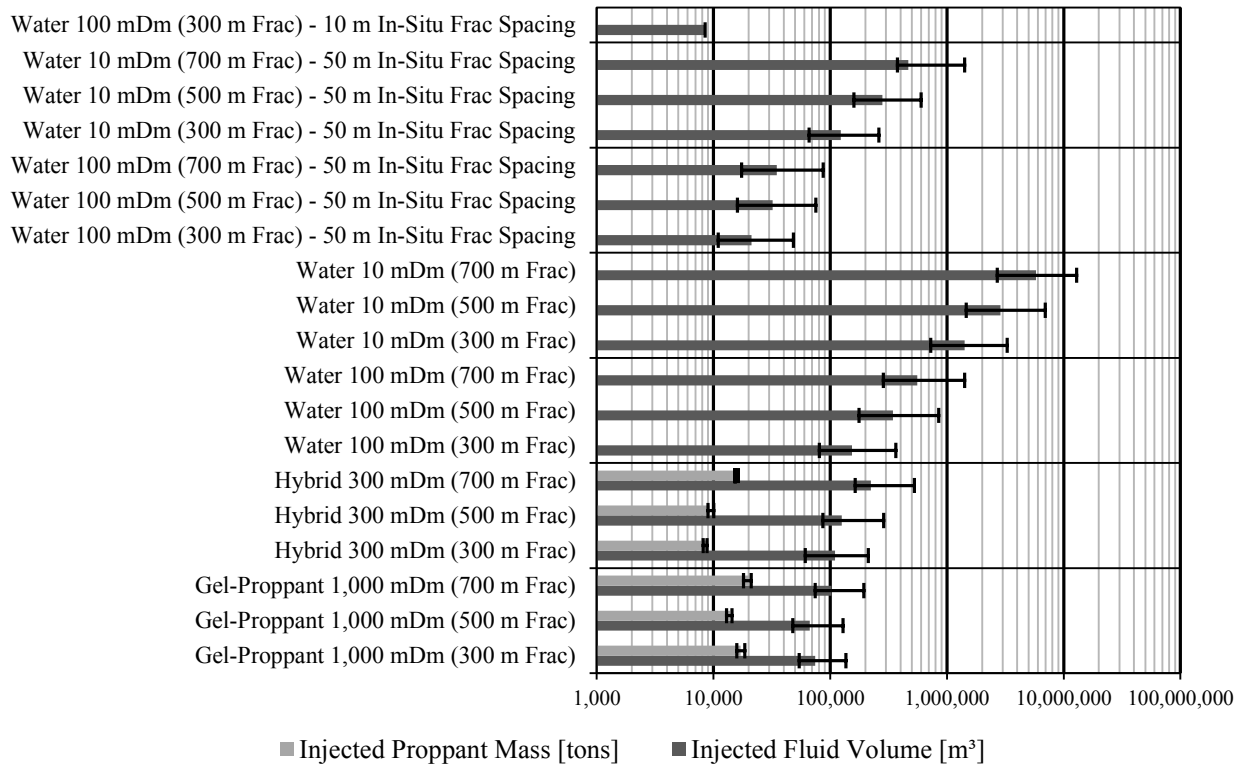


Figure 70: Comparison of the injected proppant mass and fluid volume for different stimulation types, fracture conductivities, and created fracture half-lengths for intact rock and naturally fractured rock with different in-situ fracture spacings. The presented values are for the Base Case Scenario. The error bars show the variation between all three Scenarios (Small Area, Base Case, and Large Area).

For the relatively high conductivity gel-proppant (1000 mDm) and hybrid fracturing (300 mDm) treatments (performed in intact rock) the economic target of 6 \$/GJ can be met for all fracture half-lengths with the appropriate number of treatments. The PI is larger than 10 l/s/MPa here. For the water fracturing treatments with 100 mDm conductivity the costs are slightly higher (6.2–6.5 \$/GJ) because of the much larger amount of fracturing treatments needed (42–60) to achieve a PI of 10 l/s/MPa.

For water fracturing treatments with 10 mDm conductivity, the number of treatments and costs are significantly too high (\$20.4 and 441 treatments for the base case and 500 m half-length) because of the same reasons mentioned above (**Figure 68**). However, this is only true for intact rock (assuming a natural fracture network that is stimulated by water fracturing treatments turns these results upside down). For 50 m in situ fracture spacing only 3 (700 m half-length) to 5 (300 m half-length) treatments are needed to achieve a PI of 10 l/s/MPa (**Figure 69**) leading to costs

between 4.4 \$/GJ and 4.7 \$/GJ, which is well below the target (**Figure 68**). Even fracture conductivities as low as 10 mDm can lead to an economic energy generation, however with a fracture spacing of 50 m, a horizontal well section with a length above 10 km is needed for 10 mDm water fracturing treatments, which is not possible to achieve with the current technology used in granitic rock. The least number of treatments (2) and the shortest horizontal well section (600 m), as well as the lowest amount of fracturing fluid (8500 m³) required to meet all performance criteria was achieved by water fracturing treatments (with a low amount of proppant) generating fractures with a conductivity of 100 mDm within an in situ fracture network with 10 m fracture spacing (**Figure 68 – Figure 70**).

In general, the number of treatments needed to meet the performance criteria increases for shorter fractures and for lower fracture conductivities (**Figure 69**). This is not true for the hybrid fracturing treatments because different fluid types have been used here. Larger fracture half-lengths (areas) and lower fracture conductivities lead to more fracturing fluid that needs to be injected.

In naturally fractured rock, a lower amount of fluid is needed to achieve the performance criteria as compared to treatments performed in intact rock (**Figure 70**). Also, less fracturing treatments need to be performed in naturally fractured rock as compared to intact rock for cases with the same fracture conductivity (**Figure 69**). In all simulations a minimum total fracture area of 1.18 km² is needed to achieve the performance criteria.

4.7 GREENHOUSE GAS EMISSION REDUCTIONS

A major environmental issue in oil sands extraction and processing is the high amount of greenhouse gas (GHG) and especially CO₂ emissions resulting from the combustion of natural gas in order to heat the river water used for these processes. Therefore, we compare the greenhouse gas emissions of the combustion of natural gas with the use of thermal energy from enhanced geothermal systems (**Table 27**).

Howarth et al. [51] published the most comprehensive study on greenhouse gas emissions from shale gas production. According to their study, the combustion of natural gas has 15 gC/MJ (56

gCO₂/MJ) energy greenhouse gas emissions. Using methane and indirect CO₂ emissions for conventional gas they estimated 18–25 gC/MJ (66–92 gCO₂/MJ), and for shale gas, which is the major future gas source, 22–31 gC/MJ (81–114 gCO₂/MJ).

Table 27: Comparison of GHG emissions resulting from burning of natural gas and the production of geothermal energy.

Emissions from natural gas [gCO ₂ -eq./MJ]	Emissions from geothermal energy [gCO ₂ /MJ]	Reduction of GHG emissions with geothermal energy [gCO ₂ /MJ]	Reduction of GHG emissions with geothermal energy [%]
56 - 114	0.2 - 35	21 – 113.8	36 – 99.8

Bloomfield et al. [52] reported 91 gCO₂/kWh emissions for electricity generation from geothermal energy. Frick et al. [53] found in their detailed “life cycle assessment of geothermal binary power plants using enhanced geothermal systems” [53] that the CO₂ emissions of the system depend to a large part on the geological conditions. Values between 5 and 900 CO₂-equivalent g/kWh_{el} are proposed. Goldstein et al. [54] reported four EGS lifecycle greenhouse gas emissions between 25 and 80 gCO₂-equivalent/kWh_{el} from the literature. A survey by Bertani and Thain [55] found that 85% of the geothermal power plant capacity in 2001 shows a weighted average of 122 gCO₂/kWh_{el} and values generally ranging between 60 and 380 gCO₂/kWh_{el} with a total range between 4 and 740 gCO₂/kWh_{el}. These values are all obtained for electricity generation. Assuming a maximum conversion efficiency from thermal to electrical energy of 0.14 for all of these reported values, the CO₂ emissions of the direct use of geothermal energy is between 0.6 gCO₂/kWh_{th} (0.2 gCO₂/MJ) and 126 gCO₂/kWh_{th} (35 gCO₂/MJ) with average values between 11 gCO₂/kWh_{th} (3 gCO₂/MJ) and 17 gCO₂/kWh_{th} (5 gCO₂/MJ).

Our simulation study shows that 1.06E+07 to 1.37E+07 GJ thermal energy can be produced within a 30 years lifetime of a 3-well geothermal system. Resulting savings in CO₂ emissions over a 30 years range are between 0.21 and 0.27 megatonnes (Mt) assuming a minimum reduction of 20 gCO₂/MJ and 0.56 – 0.73 Mt assuming a more likely reduction of 53 gCO₂/MJ.

For comparison, the total amount of CO₂-equivalents emitted in Alberta in 2009 was 113.1 Mt from which 41.9 Mt come from oil sands operation (26.9 Mt from mining and upgrading and 15

Mt from in situ recovery) [4]. To considerably reduce greenhouse gas emissions in the order of thousands of wells need to be drilled. According to these considerations between 1100 and 1440 of the simulated EGS triplets would be needed (at least 3300 wells) to offset all CO₂ emissions from oil sands mining and upgrading assuming a reduction of 53 gCO₂/MJ. Less wells would be needed if a higher heat output can be achieved by optimization.

4.8 SAVINGS OF NATURAL GAS RESOURCES

The second major environmental impact is the huge amount of natural gas that is used to heat up the water for the oil sands extraction and processing. To produce 1 GJ of energy, approximately 26.1 m³ of natural gas needs to be burned [18]. Using the simulated energy extracted in 30 years by the different optimized scenarios, between approximately 406,000 and 525,000 m³ of natural gas can be saved in 30 years of operation of a 3-well EGS system in northern Alberta.

4.9 CONCLUSIONS

The applicability of low enthalpy enhanced geothermal systems for the hot water supply for oil sands processing and extraction in north eastern Alberta was evaluated. For this purpose, hydraulic fracturing treatment and thermal–hydraulic reservoir simulations were performed to compare different reservoir permeability enhancement strategies technically, economically, and environmentally for 5 km deep granitic rocks. The fracturing simulations were performed assuming tensile failure only, neglecting possible shear failure events.

A detailed sensitivity analysis shows the importance of mechanical rock properties, stress confinement (to prevent significant fracture height growth out of the target area), and natural fracture systems and their properties to create large fracture network areas. The strongest variations of created fracture geometries are due to these three parameters.

A 5 km deep enhanced geothermal system can provide hot water at temperatures above 60°C over a period of 30 years (which is sufficient for oil sands mining), at a competitive cost as compared to the burning of natural gas.

The enhanced geothermal system could consist of one deviated (or horizontal) injection well injecting 60 l/s of water with a temperature of 30°C flanked by two deviated (or horizontal) production wells producing 30 l/s of water with a temperature above 60°C. A suitable permeability enhancement is possible by means of different fracturing approaches suitable for different conditions. The creation of large fracture areas seems reasonably possible. However, to maintain a certain fracture conductivity, the generation of complex fracture networks need further investigation and improved physical understanding.

For intact rock, conventional gel-proppant or hybrid fracturing treatments creating high fracture conductivities should be preferred over water fracturing treatments creating lower conductivities without proppants due to the large amount of treatments that would be necessary. However, if natural fracture systems are present the technical feasibility and economic performance of the water fracturing treatments outperform the conventional and hybrid fractures. These water fracturing treatments should be performed with a low amount of high strength light weight proppants.

The most cost effective way to create an EGS in granitic basement rocks was found to be the stimulation of complex natural fracture systems by water fracturing treatments. Additionally, the creation of long fractures (large areas) and high fracture conductivities enhance the overall economics.

Even though no economic EGS for electricity generation could be developed so far, the direct use in areas with a high demand of hot water like the oil sands regions are found to be economically favorable and suitable for a pilot project. Costs of energy generation by EGS can be the same or lower as compared to the burning of natural gas if a complex fracture system can be created and maintained. However, even for non-economic cases, the savings in greenhouse gas emissions (0.56–0.73 Mt of CO₂ in 30 years) and natural gas (406,000–525,000 m³ in 30 years) as compared to the burning of natural gas are enormous and should be motivation enough to establish the EGS technology in Alberta to make the oil sand extraction and processing more environmentally friendly.

REFERENCES

- [1] Government of Alberta. Environmental management of Alberta's oil sands [Internet]. <<http://environment.gov.ab.ca/info/library/8042.pdf>> [19.07.12].
- [2] Long J, Xu Z, Masliyah JH. On the role of temperature in oil sands processing. *Energy Fuels* 2005;19(4):1440–6.
- [3] Majorowicz J, Unsworth M, Chacko T, Gray A, Heaman L, Potter DK, et al. Geothermal energy as a source of heat for oil sands processing in Northern Alberta Canada. In: Hein FJ, Leckie D, Larter S, Suter JR, editors. *Heavy oil and oil sand petroleum systems in Alberta and beyond: AAPG studies in geology*, vol. 64; 2012, AAPG, Canadian Heavy Oil Association and AAPG Energy Minerals Division, p. 725–46.
- [4] Government of Alberta. Facts and statistics – environment [Internet]. <<http://www.energy.alberta.ca/oilsands/791.asp>>.
- [5] Luo F, Xu R-N, Jiang P-X. Numerical investigation of the influence of vertical permeability heterogeneity in stratified formation and of injection/production well perforation placement on CO₂ geological storage with enhanced CH₄ recovery. *Appl Energy* 2013;102:1314–23.
- [6] Procesi M, Cantucci B, Buttinelli M, Armezzani G, Quattrocchi F, Boschi E. Strategic use of the underground in an energy mix plan: synergies among CO₂, CH₄ geological storage and geothermal energy. Latium Region case study (Central Italy). *Appl Energy* 2013;110:104–31.
- [7] Quattrocchi F, Boschi E, Spena A, Buttinelli M, Cantucci B, Procesi M. Synergic and conflicting issues in planning underground use to produce energy in densely populated countries, as Italy Geological storage of CO₂, natural gas, geothermics and nuclear waste disposal. *Appl Energy* 2013;101:393–412.
- [8] Man Y, Yang H, Spitler JD, Fang Z. Feasibility study on novel hybrid ground coupled heat pump system with nocturnal cooling radiator for cooling load dominated buildings. *Appl Energy* 2011;88:4160–71.
- [9] Shengjun Z, Huaixin W, Tao G. Performance comparison and parametric optimization of subcritical Organic Rankine Cycle (ORC) and transcritical power cycle system for low-temperature geothermal power generation. *Appl Energy* 2011;88:2740–54.
- [10] Majorowicz J, Weides S. Is it feasible to use engineered geothermal systems to produce electrical energy in Alberta basin? *CanGEA Rev* 2012;3:2–3.
- [11] Tester JW, Anderson BJ, Batchelor AS, Blackwell DD, DiPippo R, Drake EM, et al. The future of geothermal energy impact of Enhanced Geothermal Systems (EGS) on the United States in the 21st Century. Massachusetts Institute of Technology [Internet]; 2006. <http://www.1eere.energy.gov/geothermal/egs_technology.html>.
- [12] Kitsou OJ, Herzog, H and Tester JW, Economic Modeling of HDR Enhanced Geothermal Systems, Proceedings World Geothermal Congress, 2000 May 28 – June 10, Japan: Beppu-Morioka; 2000. p. 3779–84.
- [13] Tenzer H. Development of hot dry rock technology. *Geo-heat Center bulletin. Oreg Inst Technol* 2001;22(4):14–22.

- [14] Huenges E. and Ledru P. Geothermal energy systems: exploration, development and utilization. Wiley-VCH; 2010. p. 463.
- [15] Economides MJ, Nolte KG. Reservoir stimulation. 3rd ed. Wiley; 2000. p. 856.
- [16] McClure M, Horne R. The effect of fault zone development on induced seismicity. In: Proceedings of the 37th workshop on geothermal reservoir engineering, 2012 January 30–February 1, Stanford University, Stanford, California; 2012.
- [17] McClure M, Horne R. Is pure shear stimulation always the mechanism of stimulation in EGS? In: Proceedings of the 38th workshop on geothermal reservoir engineering, 2012 February 11–13, Stanford University, Stanford, California; 2013.
- [18] Pathak V, Babadagli T, Majorowicz J, Unsworth MJ. Evaluation of engineered geothermal systems as a heat source for oil sands production in Northern Alberta. *Nat Resour Res* 2014;23:247-265.
- [19] Hofmann H, Babadagli T, Zimmermann G. Hydraulic fracturing scenarios for low temperature EGS heat generation from the Precambrian basement in northern Alberta. *GRC Trans* 2012;36:459–67.
- [20] Van der Hoorn K, Heijnen LJ, Gankema ME, Nitters G. Hydraulic fracturing in limestone: a case study of two EGS projects in the Netherlands. In: Proceedings of the 37th workshop on geothermal reservoir engineering, 2012 January 30–February 1, Stanford University, Stanford, California; 2012.
- [21] Meyer & Associates. Mayer fracturing simulators. User's guide meyer fracturing simulators. USA: Unicode Inc.; 2011.
- [22] Computer Modeling Group Ltd. 2011. User's guide STARS advanced process and thermal reservoir simulator; 2009. p. 1120.
- [23] Baria R, Baumgaertner J, Rummel F, Pine RJ, Sato Y. HDR/HWR reservoirs: concepts. *Understand Creat Geotherm* 1999;28:533–52.
- [24] Kalinina E, McKenna, SA, Hadgu T, Lowry T. Analysis of the effects of heterogeneity on heat extraction in an EGS represented with the continuum fracture model. In: Proceedings of the 37th workshop on geothermal reservoir engineering, 2012 January 30–February 1, Stanford University, Stanford, California; 2012.
- [25] Zoback MD. Reservoir geomechanics. 1st ed. Cambridge, United Kingdom and New York, NY, USA: Cambridge University Press; 2007. p. 464.
- [26] Heidbach O, Tingay M, Barth A, Reinecker J, Kurfeß D, Müller B. The world stress map database release; 2008. doi: 10.1594/GFZ.WSM.Rel2008.
- [27] Valley B, Evans KF. Strength and elastic properties of the Soultz granite. 2nd year report. In: Proceedings at the EHDRA scientific conference, 2006 June 15–16; Soultz-sous-Forets, France.
- [28] Kumar J. The effect of Poisson's ratio on rock properties. SPE6094. In: Proceedings at the SPE annual fall technical conference and exhibition, 1976 October 3–6, New Orleans, Louisiana; 1976. p. 12.

- [29] Selvadurai APS, Boulon MJ, Nguyen TS. The permeability of an intact granite. *Pure Appl Geophys* 2005; 162:373–407.
- [30] Sun Z, Ouchterlony F. Fracture toughness of stripa granite cores. *Int J Rock Mech Min Sci Geomech Abstr* 1986:399–409.
- [31] Dai F, Xia K. Tensile strength anisotropy of Barre Granite. In: *Proceedings of the 3rd CANUS rock mechanics symposium*, 2009 May; Toronto, Canada; 2009. p. 15.
- [32] Alehossein H, Boland JN. Strength, toughness, damage and fatigue of rock. *Structural Integrity and Fracture*; 2004.
- [33] Clauser C. Permeability of crystalline rocks. *Eos Trans Am Geophys Union* 1992;73(21):233–40.
- [34] Geraud Y, Rosener M, Surma F, Place J, Le Garzic E, Diraison M. Physical properties of fault zones within a granite body: Example of the Soultz-sous-Forêts geothermal site. *Geoscience* 2010; 342:566–74.
- [35] Petrov VA, Poluektov VV, Zharikov AV, Nasimov RM, Diaur NI, Terentiev VA, et al. Microstructure, filtration, elastic and thermal properties of granite rock samples: implication for HLW disposal. In: Harvey PK, Brewer TS, Pezard PA, Petrov VA, editors. *Petrophysical properties of crystalline rocks*, vol. 240. London: Geological Society of London, Special Publications; 2005. p. 237–53.
- [36] Lemmon EW, Huber ML, McLinden MO. NIST standard reference database 23, NIST reference fluid thermodynamic and transport properties – REFPROP 2010; version 9.0. Standard Reference Data Program, National Institute of Standards and Technology; 2010.
- [37] Knödel K, Lange G, Voigt HJ. *Environmental geology: handbook of field methods and case studies*. Berlin, Heidelberg, New York: Heidelberg; 2007. p. 1357.
- [38] Yew CH. *Mechanics of hydraulic fracturing*. Houston, TX: Gulf Publishing Company; 1997. p. 183.
- [39] Rankin R, Thibodeau M, Vincent MC. Improved production and profitability achieved with superior completions in horizontal wells: a Bakken/three forks case history. Paper SPE 134595. In: *Proceedings of the SPE annual technical conference and exhibition*, 2010 September 19–22, Florence, Italy; 2010. p. 22.
- [40] Meyer BR, Bazan LW. A discrete fracture network model for hydraulically induced fractures: theory, parametric and case studies. SPE 140514. In: *Proceedings of the SPE hydraulic fracturing technology conference*, 2011 January 24–26, The Woodlands, Texas; 2011. p. 36.
- [41] Vasconcelos G, Lourenco PB, Alves CAS, Pamplona J, Miranda T. Relation between tensile and compressive engineering properties of granites. In: Qian Q, Zhou X, editors. *Harmonising rock engineering and the environment: proceedings of the 12th ISRM international congress on rock mechanics*; 2010. p. 380–1.
- [42] Hofmann H, Babadagli T, Zimmermann G. Numerical simulation of complex fracture network development by hydraulic fracturing in naturally fractured ultratight formations. In: *Proceedings of the ASME 2013 32nd international conference on ocean, offshore and arctic engineering*; 2013 June 9–14, Nantes, France, 2013.

- [43] Rickards AR, Brannon HD, Wood WD, Stephenson CJ. High strength, ultra lightweight proppant lends new dimensions to hydraulic fracturing applications. *SPE Prod Oper* 2009;21(2):212–21.
- [44] Chen Z, Narayan SP, Yang Z, Rahman SS. An experimental investigation of hydraulic behavior of fractures and joints in granitic rock. *Int J Rock Mech Miner Sci* 2000;37:1061–71.
- [45] Fredd CN, McConnel SB, Boney CL, England KW. Experimental study of hydraulic fracture conductivity demonstrates the benefits of using proppants. Paper SPE 60326. In: *Proceedings of the SPE rocky mountain regional/low permeability reservoirs symposium*, 2000 March 12–15, Denver, Colorado; 2000. p. 14.
- [46] Majorowicz J, Grasby SE. High potential regions for enhanced geothermal systems in Canada. *Nat Resour Res* 2010;19(3):177–88.
- [47] Government of Alberta. Monthly reference price calculations. Alberta gas reference prices for 2012 [Internet]. <<http://www.energy.alberta.ca/NaturalGas/1316.asp>>.
- [48] World Energy Council. London, UK: *Survey of Energy Resources*; 2010. p. 608.
- [49] Zimmermann G, Blöcher G, Reinicke A, Brandt W. Rock specific hydraulic fracturing and matrix acidizing to enhance a geothermal system – concepts and field results. *Tectonophysics* 2011;503(1–2):146–54.
- [50] Veatch RW. Economics of fracturing: some methods, examples, and case studies. Paper SPE 15509. In: *Proceeding of the SPE annual technical conference and exhibition*, 1986 October 5–8, New Orleans, Louisiana; 1986. p. 16.
- [51] Howarth RW, Santoro R, Ingraffea A. Methane and the greenhouse-gas footprint of natural gas from shale formations. *Clim Change* 2011;106:679–90.
- [52] Bloomfield KK, Moore JN, Neilson Jr RM. Geothermal energy reduces greenhouse gases. *Geotherm Resour Coun Bull* 2003;32:77–9.
- [53] Frick S, Kaltschmitt M, Schröder G. Life cycle assessment of geothermal binary power plants using enhanced low-temperature reservoirs. *Energy* 2010;35:2281–94.
- [54] Goldstein B, Hiriart G, Bertani R, Bromley C, Gutiérrez-Negrín L, Huenges E, et al. *Geothermal energy 2011*. In: Edenhofer O, Pichs-Madruga R, Sokona Y, Seyboth K, Matschoss P, Kadner S, et al., editors. *IPCC special report on renewable energy sources and climate change mitigation*. United Kingdom: Cambridge University Press; 2011.
- [55] Bertani R, Thain I. Geothermal power generating plant CO₂ emission survey. *IGA News* 2002;49:1–3.

CHAPTER 5: NUMERICAL SIMULATION OF COMPLEX FRACTURE NETWORK DEVELOPMENT BY HYDRAULIC FRACTURING IN NATURALLY FRACTURED ULTRATIGHT FORMATIONS

A version of this chapter was published in *Journal of Energy Resources Technology* (2014) **136**: 042907 (9 pages).

The creation of large complex fracture networks by hydraulic fracturing is imperative for enhanced oil recovery from tight sand or shale reservoirs, tight gas extraction, and hot-dry-rock (HDR) geothermal systems to improve the contact area to the rock matrix. Although conventional fracturing treatments may result in biwing fractures, there is evidence by microseismic mapping that fracture networks can develop in many unconventional reservoirs, especially when natural fracture systems are present and the differences between the principle stresses are low. However, not much insight is gained about fracture development as well as fluid and proppant transport in naturally fractured tight formations. In order to clarify the relationship between rock and treatment parameters, and resulting fracture properties, numerical simulations were performed using a commercial discrete fracture network (DFN) simulator.

A comprehensive sensitivity analysis is presented to identify typical fracture network patterns resulting from massive water fracturing treatments in different geological conditions. It is shown how the treatment parameters influence the fracture development and what type of fracture patterns may result from different treatment designs. The focus of this study is on complex fracture network development in different natural fracture systems. Additionally, the applicability of the DFN simulator for modeling shale gas stimulation and HDR stimulation is critically discussed. The approach stated above gives an insight into the relationships between rock properties (specifically matrix properties and characteristics of natural fracture systems) and the properties of developed fracture networks. Various simulated scenarios show typical conditions

under which different complex fracture patterns can develop and prescribe efficient treatment designs to generate these fracture systems.

Hydraulic stimulation is essential for the production of oil, gas, or heat from ultratight formations like shales and basement rocks (mainly granite). If natural fracture systems are present, the fracturing process becomes more complex to simulate. Our simulations suggest that stress state, in situ fracture networks, and fluid type are the main parameters influencing hydraulic fracture network development. Major factors leading to more complex fracture networks are an extensive pre-existing natural fracture network, small fracture spacings, low differences between the principle stresses, well contained formations, high tensile strength, high Young's modulus, low viscosity fracturing fluid, and large fluid volumes. The differences between 5 km deep granitic HDR and 2.5 km deep shale gas stimulations are the following: (1) the reservoir temperature in granites is higher, (2) the pressures and stresses in granites are higher, (3) surface treatment pressures in granites are higher, (4) the fluid leak-off in granites is less, and (5) the mechanical parameters tensile strength and Young's modulus of granites are usually higher than those of shales.

5.1 INTRODUCTION

Shale gas/oil shale reservoirs as well as deep hot low permeability rock have the potential to serve as major energy sources for the growing demand of the 21st century. Both resources are potentially able to supply huge amounts of heat as well as electricity [1–3]. However, it is not possible to exploit low permeability formations bearing oil, gas, or heat without stimulating the reservoir by hydraulic fracturing [4,5]. In the Society of Petroleum Engineers (SPE) media, more than 1400 papers have been published on hydraulic fracturing, the main technology used to stimulate oil, gas, or geothermal reservoir rocks. Most of the studies are based on simplified fracturing models [6–10]. Very recently, it was realized that in many tight oil, gas, and geothermal reservoirs hydraulically induced fracture growth is more complex than conventional models would predict [11]. Hydraulic fractures in naturally fractured tight formations are not simple planar fractures as initially anticipated [6–9] but rather asymmetric [12] complex fracture networks. In most cases, this is due to the interaction between induced fractures, natural fracture network, stress regime, and the difference in the nature of the reservoir rock of interest these days (tight shales or granite) compared to the rock types in conventional reservoirs.

The primary goal of HDR and oil shale/shale gas fracturing is to maximize the fracture area to improve production of heat/oil/gas and economics. For the development of ultralow permeability and naturally fractured shale gas reservoirs multiple fractured horizontal wells are successfully used to improve the well productivities [13,14]. Wu et al. [13] found in a numerical sensitivity analysis that the number and length of the fractures as well as the fairway aspect ratio of the fracture network (permeability anisotropy) have the largest influence on the production rate of these horizontal wells. Especially in ultratight reservoirs the width/conductivity of a fracture is significantly less important [4]. Additionally, for environmental, technical, and economical reasons fracture growth should be contained within the target formation.

Cipolla et al. [15] provided general treatment design guidelines for complex fracture development. Meyer and Bazan [16] presented the mathematical formulation of the reservoir simulator used as well as parametric and case studies. The parametric studies focus on the mechanical interaction, fracture spacing and the number of multiple fractures, fracture efficiency, and the DFN fairway aspect ratio. In the present study, we focus on the verification of the

important findings of Cipolla et al. [15] and extend both studies [15,16] by focusing on stress regime and net frac pressure development. An overview of the simulation process is given in **Figure 71**. It summarizes important treatment parameters, reservoir properties, DFN simulator options, and the resulting complex fracture network properties. The DFN simulator calculates complex fracture network properties for different treatment and reservoir parameters.

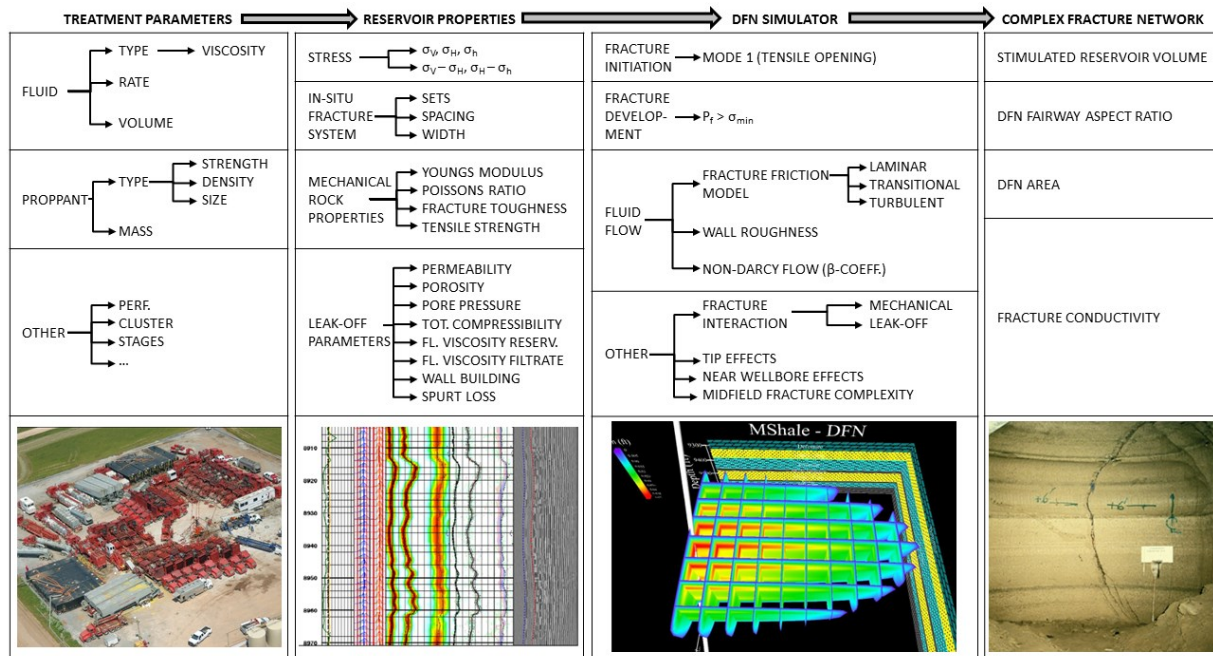


Figure 71: Overview of the main parameters and processes involved in the hydraulic fracturing simulations (graphics taken from Refs. [1–3])

5.2 THE DFN FRACTURING SIMULATOR

For the simulation of fracturing treatments, the commercial DFN simulator MShale [17] was used. The DFN fracturing simulator accounts for a set of primary hydraulic fractures, which are connected to the wellbore and a network of secondary fractures connected to it that can be activated and opened.

Different proppant transport options are available to model the proppant transport in such a network. The fluid flow may be altered by changing fracture friction model parameters and a wall

roughness coefficient. Tip effects may be included as well. The model is based on a methodology which is similar to that presented by Warren and Root [18].

The simulator is based on a network grid system. A single primary fracture or a set of multiple primary fractures is initiated at specified points along the well and develop parallel to the direction of the maximum principle stress. The pressure drop along the fractures is calculated by the Forchheimer equation [17] and depends on the Darcy friction factor, flow rate, and cross sectional area of the fracture [16]. A detailed mathematical description of the model including fluid flow and pressure loss in a single ellipsoidal fracture and mechanical and leak-off interaction between multiple fractures is given by Meyer and Bazan [16]. The net fracture pressure in a primary fracture has to overcome the closure stress perpendicular to the fracture surface of the activated secondary fracture at a point where a secondary fracture intersects a primary fracture.

Thus, secondary fractures are opened if the net fracture pressure reaches above the value of the stress difference between the maximum and minimum horizontal stresses (to open vertical secondary fractures) or between the vertical and minimum horizontal stresses (to open horizontal secondary fractures) at predefined positions where the different fracture sets intersect.

Some of the major assumptions made by the simulator are:

- only Mode 1 fracture initiation (tensile failure)
- natural fracture systems with three perpendicular fracture sets can be implemented
- fracture development only in the three principal planes
- interfacial joint dilatancy is ignored
- primary and secondary fractures have an elliptical shape
- stimulated reservoir volume has an ellipsoidal shape

The calculations are governed by the continuity equation, mass conservation, momentum conservation, and the width-opening pressure equation as described in detail by Meyer and Bazan [16].

5.3 MODEL PARAMETERS

For the fracturing simulations, typical hydraulic and mechanic reservoir properties of granite (reservoir rock bearing heat) and for oil/gas shales were compiled from the literature. All values are summarized in **Table 28**. Besides an average “Base Case” value, the whole possible parameter range for both lithologies is given.

The total compressibility c_t relates permeability and porosity with pressure and time and is defined as: $c_t = S_o c_o + S_w c_w + S_g c_g + c_r$, with the oil saturation S_o , water saturation S_w , gas saturation S_g , oil compressibility c_o , water compressibility c_w , gas compressibility c_g and the bulk rock compressibility c_r [17].

The reservoir fluid viscosity is the viscosity of water/gas at reservoir conditions. The fluid viscosity of the filtrate is the viscosity of water at 20°C.

Table 28: Typical rock properties of granites and shales. Bold numbers show the values used for the base case scenario and numbers in parentheses show parameter ranges.

Property	Granite	Shale
Young's modulus [GPa]	55 (40-70) [19]	30 (10-80) [20-23]
Poisson's ratio [-]	0.2 (0.1-0.3) [24, 25]	0.2 (0.1-0.3) [26, 27]
Fracture toughness [MPa m ^{1/2}]	1.5 (1.3–1.7) [28]	1.5 (1-2) [23]
Tensile strength [MPa]	12 (9-15) [29, 30]	4 (2-6) [31]
Permeability [μD]	0.5 (0.1-1) [25, 32, 33]	0.5 (0.1-1) [23]
Porosity [%]	1 (0.5-1.5) [32]	5 (0-10) [23, 34, 35]
Total compressibility [1/GPa]	0.43 (0.32–0.54) [calculated, no gas]	33 (30-36) [23]
Reservoir fluid viscosity [mPa s]	0.3 (0.2-0.4) [36]	0.02 [23]
Fluid viscosity filtrate [mPa s]	1 [36]	1 [36]

Table 29: Typical fracture network properties for granites and shales. Bold numbers show the values used for the base case scenario and numbers in parentheses show parameter ranges.

Property	Granite	Shale
Fracture sets [-]	≥ 2 sub-vert. [38]	≥ 2 sub-vert. [20]
Fracture spacing [m]	1.5 (0.3-4) [38] 25 (5-300) [assumed]	25 (5-300) [20, 22, 23]
Fracture width [mm]	0 (0.1-1) [38]	0 (0.0001-0.265) [20,35,39]

Besides the rock properties other important reservoir parameters are the natural fracture network properties. Typical fracture network properties and patterns observed in granitic HDR reservoirs and tight gas/oil shales as derived from the literature are given in **Table 29**.

The stress state is the third important parameter influencing the fracture network development. The pore pressure, the minimum horizontal stress (σ_h), and the maximum horizontal stress (σ_H) were calculated based on Ref. [37] for a depth of 2.5 km (typical for shale gas/oil reservoirs) and for a depth of 5 km (typical for HDR reservoirs). While other stress regimes may occur in deep granites or shale gas play only a normal faulting stress regime was considered to keep the extent of this study in a reasonable scope. Reverse faulting and strike slip faulting regimes need to be addressed in separate studies. The maximum horizontal stress was changed between the minimum horizontal and the vertical stress (σ_v). For granite and shale, the calculated stress values are given in **Table 30**. The vertical stress was calculated for a density of the overburden rock of 2650 kg/m³ (2600–2700 kg/m³). The pore pressure was computed for a reservoir fluid density of 1000 kg/m³. The minimum horizontal stress was calculated for a Poisson's ratio of 0.2 (0.1–0.3) and the respective values of vertical stress.

The temperature of the 5 km deep granite is 150°C and for a 2.5 km deep shale it is 75°C assuming a temperature gradient of 30°C/km.

The main differences between granites and shales in terms of simulator input parameters were found to be all the stress values (due to the different depth), Young's modulus, tensile strength, porosity, total compressibility, reservoir fluid viscosity, and fracture aperture.

Table 30: Calculated stress values for a 5 km deep granite and a 2.5km deep shale. Bold numbers show the values used for the base case scenario and numbers in parentheses show parameter ranges. σ_V : vertical stress, σ_H : maximum horizontal stress, σ_h : minimum horizontal stress, and P_p : pore pressure.

Property	Granite (5 km)	Shale (2.5 km)
P_p [MPa]	49	24.5
σ_V [MPa]	130 (128-132)	65 (64-66)
σ_h [MPa]	69 (58-85)	35 (29-42)
σ_H [MPa]	69 (58-132)	65 (29-66)
$\sigma_H - \sigma_h$ [MPa]	0 (0-61)	30 (0 – 30)

In a 2.5 km deep shale the stresses and stress differences are much lower as compared to a 5 km deep granite. Granites are stiffer and stronger than shales and hence have a higher Young's modulus and a higher tensile strength. Shales can have a much higher porosity than granites. However, their permeability is approximately the same. The higher compressibility and lower fluid viscosity in shale gas reservoirs is due to the high compressibility and low viscosity of natural gas contained in the formation.

5.4 METHODOLOGY AND THEORETICAL BACKGROUND

As discussed earlier, for the opening of pre-existing vertical fractures perpendicular to σ_H (secondary vertical fractures) the net fracture pressure has to overcome the difference between σ_H and σ_h . To open pre-existing horizontal secondary fractures, the net fracture pressure has to be greater than the difference between σ_V and σ_h . The primary fractures propagate if the net fracture pressure at the fracture tip becomes larger than the fracture toughness based or a constant critical stress value - whichever is greater (**Figure 72**).

Hence, we studied the effect of the most important model parameters on: (1) the fracture height growth confinement, (2) the final DFN area, (3) the net fracture pressure, and (4) the fairway aspect ratio.

These model parameters are: (a) the variation of stress with depth, (b) the stress contrast between target formation and the underlying formation, (c) the formation height, (d) differences between the three principles stresses ($\sigma_V - \sigma_h$ and $\sigma_H - \sigma_h$) (e) the natural fracture network properties, (f) the injected fluid volume, (g) the injection rate, and (h) the frac fluid type.

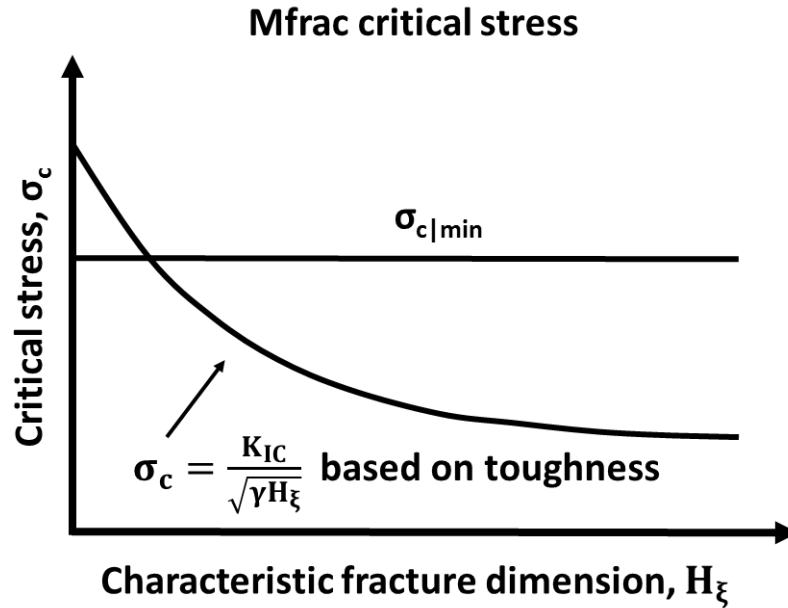


Figure 72: Critical stress for fracture propagation (redrawn from [17]).

The fracture network area is the area of all fracture surfaces generated by the stimulation. Note that this is not a propped fracture area, but rather the area that came into contact with the fracturing fluid during the stimulation.

A fracture was considered confined when the fracture did not grow further in height before the end of the treatment.

The net frac pressure is defined as the difference between the bottom hole fluid pressure within the fracture and the minimum horizontal stress. For single and multiple fractures the given net frac pressure value is given for the tip of the main fracture.

The fairway aspect ratio is the quotient of the fracture-network half-length parallel to σ_H and perpendicular to σ_H .

For both rock types, the simulations were performed using a critical stress value that is either a manually given critical stress value ($\sigma_{c|min}$, equal to the tensile strength) or the fracture toughness based critical stress value, whichever is greater (**Figure 72**).

We studied four different in situ fracture sets. The complete set of results was presented in Ref. [40]. Here, the focus is only on two cases: (1) one fracture set parallel to σ_H (multiple parallel fractures develop perpendicular to the horizontal wellbore) and (2) two perpendicular vertical fracture sets. The horizontal section of the wellbore is 4 km long and parallel to σ_h in all cases. The horizontal model domain is infinite, all layers are horizontal, and the total height of the model is 7 km.

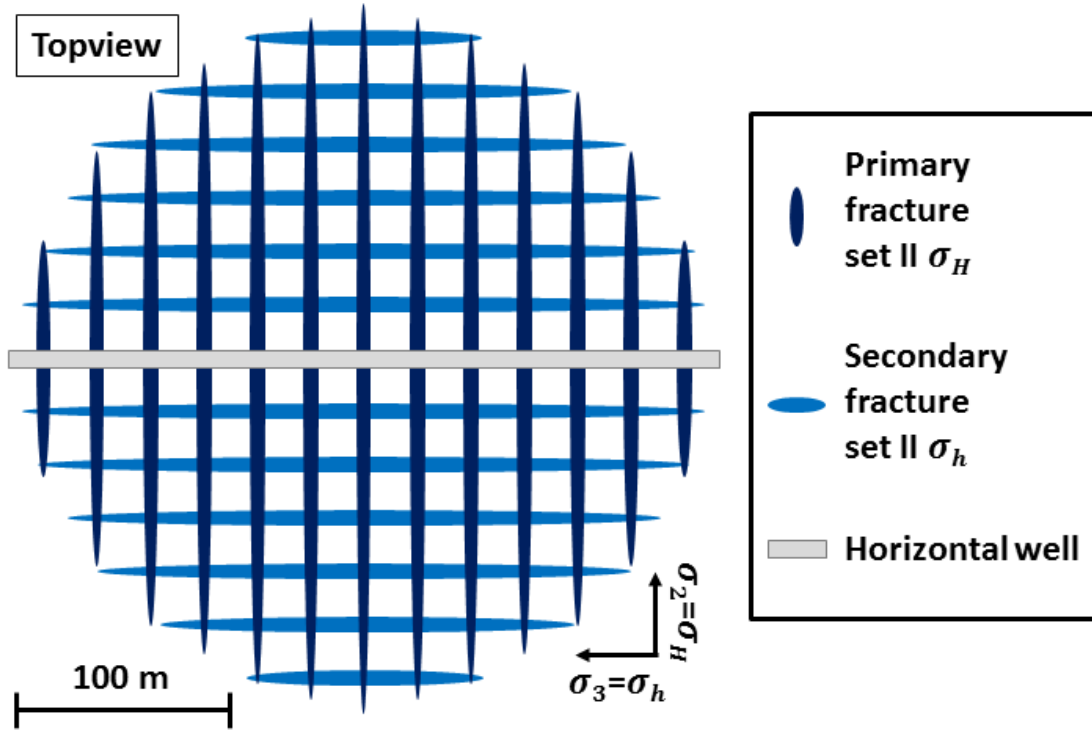


Figure 73: Schematic top view of the base case scenario (two fracture sets, $\sigma_h = \sigma_H$, and 25m fracture spacing). The primary vertical fracture set is parallel to σ_H . The secondary vertical fracture set is perpendicular to the primary fracture set.

In scenario 1 (“1 Set”) only the primary fracture set parallel to σ_H is considered. Scenario 2 (“2 Sets”) is composed of both vertical fracture sets. **Figure 73** shows both fracture sets schematically for the base case scenario. The circular shape of the fracture network results from the equal horizontal stresses. If the difference between σ_H and σ_h increases, the fracture network will have an ellipsoidal shape with the fractures parallel to σ_H being longer. With increasing

horizontal stress difference, the fracture network eventually reduces to one single primary fracture at the center of the model.

The “Base Case” values given in **Section 5.3** are used for all simulations if not indicated differently. Parameters were changed within their expected ranges to evaluate their influence on DFN development and final DFN geometry. The analysis was performed for granites and shales.

For the “Base Case” Scenario, 10,000 m³ of slickwater (water and friction reducers) was injected at a rate of 100 l/s. Slickwater was used because it tends to generate more complex fractures as compared to more viscous oils [41].

5.5 RESULTS

5.5.1 Fracture height growth containment

The variation of stress with depth is the first parameter that was investigated. We distinguished between four different types of stress variation with depth: (1) constant stress, (2) linear stress increase with depth, (3) stepwise stress increase with depth, and (4) a low stress target formation with two adjacent higher stress formations.

In the first and second type of stress variation with depth, the fracture height growth could not be confined. Only if the stress increases stepwise with depth or if the target formation is confined by two adjacent higher stress formations the fracture height growth can be contained within the target formation (**Figure 74**). Both confined cases were used for further simulations. The stress barriers could be the same rock type (a different shale formation or different granitic rock) or a different rock type (for example, metamorphic rocks). Although the stress in shales and granites often is larger than in other formations such as sandstones, field experience shows that fracture height growth is confined in most cases while smaller height growth is observed at shallower depths [42]. Other factors that could confine fracture height growth are interfaces between adjacent formations and different rock properties.

The closer the injection point is to the lower stress barrier (stress scenario 4), the smaller are the stress contrast requirements to contain fracture growth because it is harder for the fracture to overcome the upper stress barrier. After a certain point (below 50 m), a higher stress contrast is

necessary because the net frac pressure is then higher at the lower stress barrier and a stronger stress contrast at the lower boundary is needed (**Figure 75**). The total fracture height increases significantly with the distance of the injection point to the lower stress barrier (above 50 m). Resulting fractures are shorter.

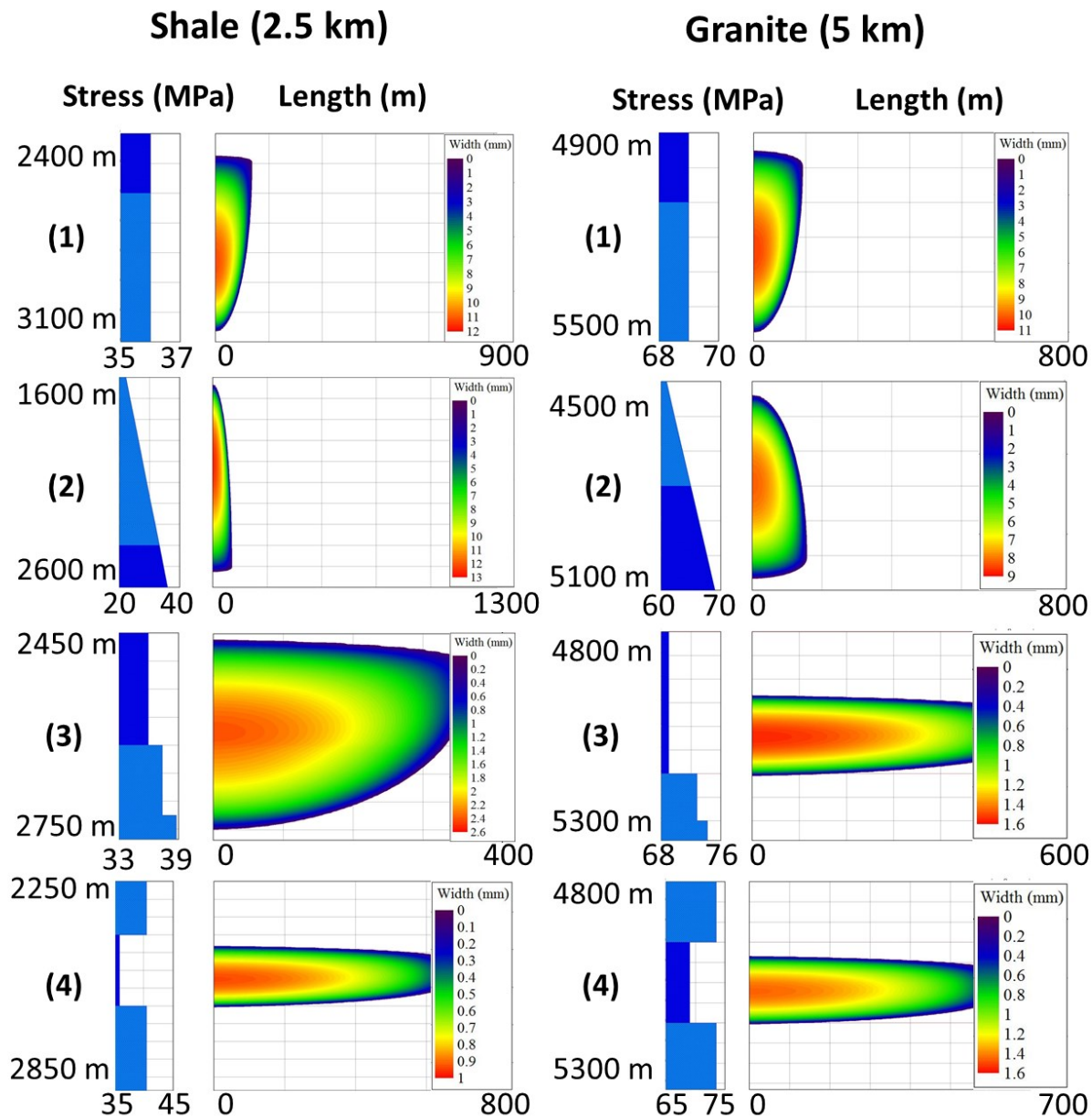


Figure 74: The influence of the stress variation with depth for a 2.5 km deep shale and a 5 km deep granite (1: constant stress, 2: linear stress increase, 3: stepwise stress increase, 4: low stress formation).

To show the influence of in situ fracture network properties on the height growth containment spacing, aperture, and fracture sets were changed and a 100 m thick target formation was

confined by an upper and a lower stress barrier (case 4 - “low stress”). The stress contrast between the target formation and the two adjacent formations was adapted until the height growth was confined. Since the fracture cannot always be confined completely, it was considered as confined if the fracture height growth out of the formation was 10% or less (10 m) of the total height of the formation (100 m).

Figure 76 shows the resulting stress contrast requirements for fracture containment for 2.5 km deep shale and 5 km deep granite, different fracture spacings, and the two fracture sets. Due to the large amount of water that was injected, the required stress contrasts are relatively high. Fracture sets with a smaller fracture spacing generally need a higher stress contrast required for containment because the opening of parallel fractures leads to an additional increase in closure stress for neighboring parallel fractures which in turn increases the net pressure. Below fracture spacings of 25 m, the stress contrast requirements significantly increase. The results for granite and shale are relatively similar indicating that rock properties have less influence on height growth confinement. If only the primary fracture set (parallel to σ_H) is present, the largest stress contrasts are required because there is no additional fluid leak-off into perpendicular secondary fractures. If additionally a secondary system is present, the stress contrast requirements decrease because the net frac pressure decreases.

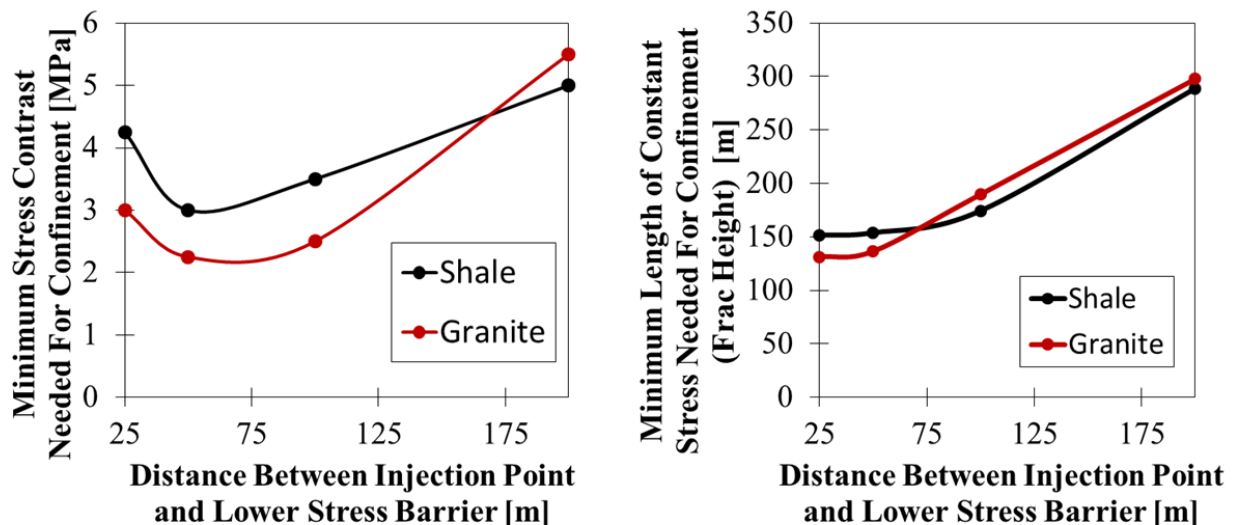


Figure 75: Influence of the distance between injection point and the lower stress barrier on the minimum stress contrast needed for confinement and the minimum formation height (if no upper stress barrier is present).

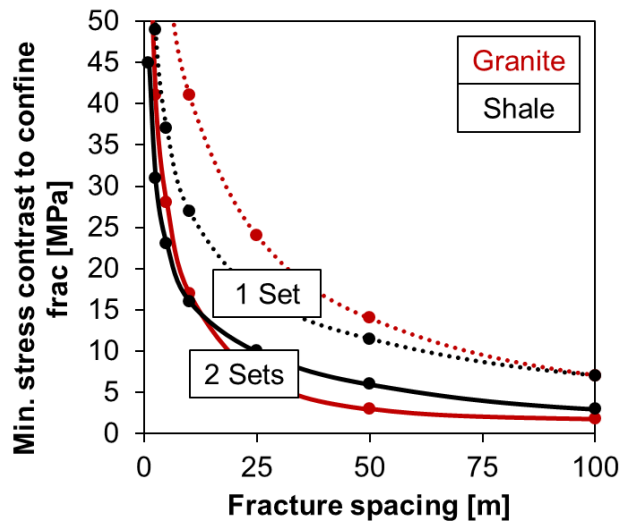


Figure 76: Minimum stress contrast needed to confine fracture height growth for different fracture spacings, fracture sets, and rock types.

Additionally, for the “Base Case” scenario we changed the differences between the two principal horizontal stresses in order to investigate their influence on the stress contrast requirement (**Figure 77**). Overall, the required stress contrast decreases with increasing differences of the principle stresses. For shale, at 4 MPa horizontal stress difference and above only one single primary fracture develops and the required vertical stress contrast is below 1 MPa. For granite, this occurs at 12 MPa. These values equal the critical stress value and the net pressure in an unconfined formation. The relative influence of the fracture sets is the same as described above.

The influence of the initial natural fracture aperture is unimportant as compared to the other factors described.

Longer treatments (larger frac fluid volumes) and higher injection rates lead to higher stress contrast requirements because of the increased net pressure with time (as discussed in **Section 5.5.2**).

Using higher viscosity fluids tremendously alters the confinement requirements. For the “Base Case” scenario shale with 2 MPa stress difference the stress contrast required to confine fracture height growth is 7 MPa when using slickwater and 39 MPa when using a high viscosity crosslinked gel.

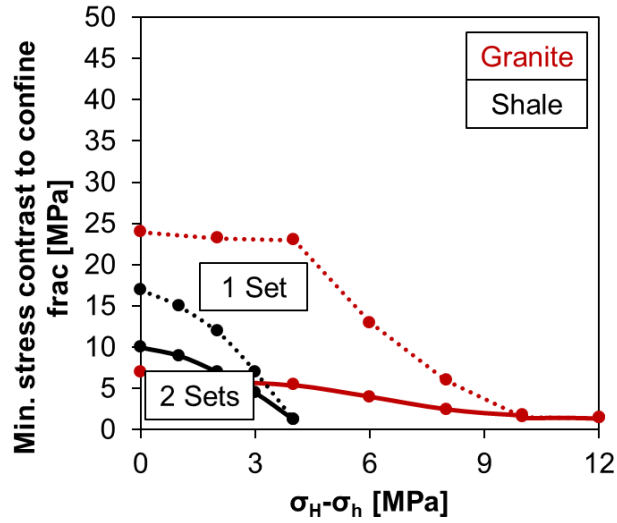


Figure 77: Influence of the differences between vertical and minimum horizontal stress and between maximum and minimum horizontal stress on the minimum stress contrast required to confine fracture height growth.

5.5.2 Net fracture pressure

Higher net pressures generally tend to increase the potential for complex fracture network development because they can overcome higher differences between the three principle stresses that keep the natural fractures closed.

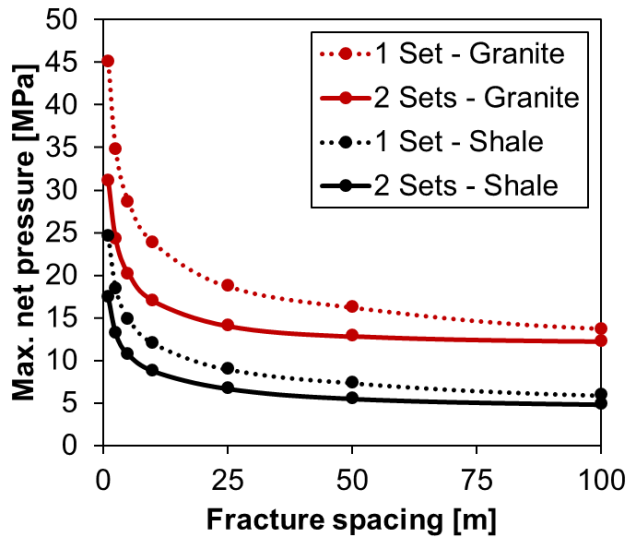


Figure 78: Influence of the fracture spacing on the maximum net pressure observed during stimulation for different rock types and fracture sets.

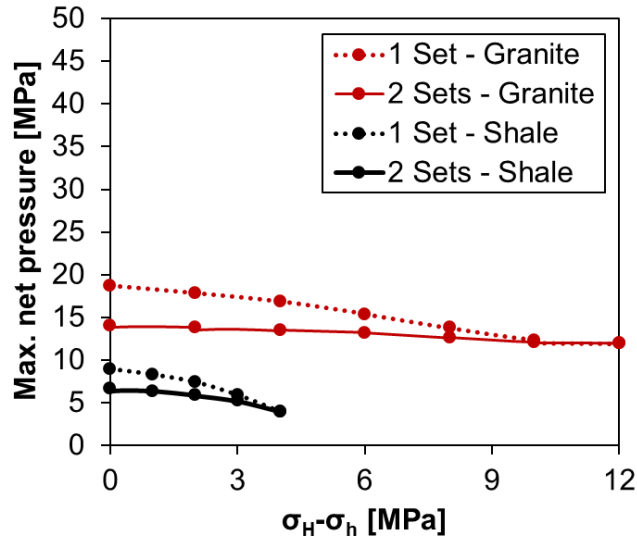


Figure 79: Influence of the differences between the three principle stresses on the maximum net pressure observed during stimulation for different rock types and fracture sets.

The net fracture pressure is influenced by a significant number of parameters. Hence, we only focus on the most important factors here: the critical stress, fracture spacing, fracture sets, and the values of the three principle stresses. Additionally, the influence of the treatment parameters was studied.

For intact rock with one single fracture the maximum net pressure equals to the critical stress (tensile strength) of the formation rock if this is above the fracture toughness based critical stress (**Figure 78**). For shale, this value is 4 MPa and for granite 12 MPa.

For both fracture sets, smaller fracture spacings lead to higher net pressures because the opened fractures increase the closure stress acting on parallel neighboring fractures. Decreasing differences between the three principle stresses significantly increases the net pressure (**Figures 78 and 79**). Also, the primary fracture set parallel to σ_H leads to the highest net pressures and again an addition of a secondary fracture set decreases the net pressure.

In a confined formation, the net pressure increases for higher injection rates (e.g., 6.4 MPa for 200 l/s and 5.9 MPa for 100 l/s for the “Base Case” scenario shale with 2 MPa stress difference) and with time (when injecting at a constant rate). Hence, larger amounts of injected water increase the net pressure in confined formations leading to opening of natural fracture systems even at elevated differences between the principle stresses. Therefore, the fracture network

complexity can potentially increase by increasing fluid volumes and the time of a treatment and injection rates.

However, the net pressure is much more influenced by the fracturing fluid type. For the “Base Case” scenario shale with 2 MPa stress difference the maximum net pressure is 5.9 MPa when using slickwater and 15.2 MPa when using a high viscosity crosslinked gel. However, the resulting fracture network is not necessarily more complex as **Section 5.5.3** will show.

5.5.3 Fracture area

The fracture area needs to be maximized for HDR and shale gas fracturing in order to maintain an economic production.

With one single fracture in an intact rock the total area of the fracture network will be two orders of magnitude smaller as compared to the results of multiple fracture sets. For those, the area significantly increases with decreasing fracture spacing. For example, with 300 m fracture spacing (2 sets, granite) 18 secondary fractures are activated whereas for the 25 m case (2 sets, granite) 190 secondary fractures are activated. The area increases because of higher net pressures and because of a larger amount of fractures. In granites, slightly larger areas can be achieved because the fluid leak-off is slightly lower (**Figure 80**). It also has a minor influence on the total fracture area whether a single fracture system parallel to σ_H or two vertical perpendicular fracture systems are present. This is mainly because the three principle stresses were assumed to be equal and the injected fluid volume was the same for all scenarios.

The fracture area also increases if the differences between the principle stresses decrease (**Figure 81**). The maximum area can be developed if $\sigma_H = \sigma_h$. At larger stress differences (above 4 MPa) the fracture area of the granites is significantly larger as compared to the shale because multiple primary and secondary fractures are still stimulated due to the larger net pressure.

As the net pressure increases with time and fluid volume, obviously the fracture area increases when pumping more fluid. Higher injection rates also lead to slightly larger DFN areas (e.g., 18.18 km² for 200 l/s and 17.99 km² for 100 l/s for the “Base Case” scenario shale with 2 MPa stress difference).

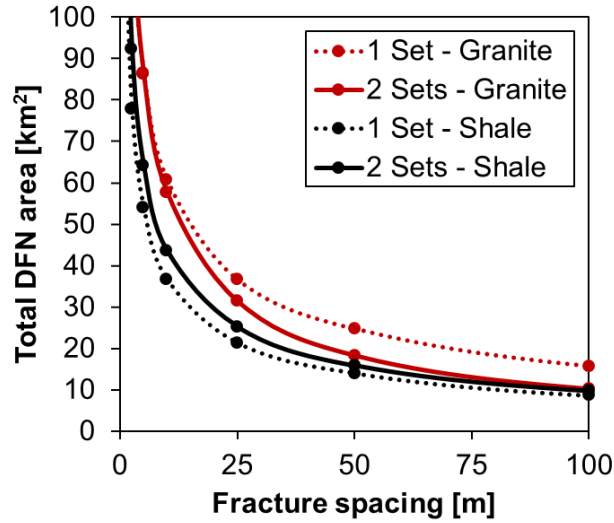


Figure 80: Influence of fracture spacing on the total area of the DFN for different rock types and fracture sets.

The fracturing fluid type has also a strong effect on the fracture area. Higher viscosity fluids generally create smaller (unpropped) fracture areas as compared to lower viscosity fluids. For the “Base Case” scenario shale with 2 MPa stress difference the total DFN area is 6.32 km² when using a high viscosity crosslinked gel and 17.99 km² when using low viscosity slickwater. Slickwater treatments potentially lead to a higher complexity of the generated fracture network because more fractures and larger areas are stimulated.

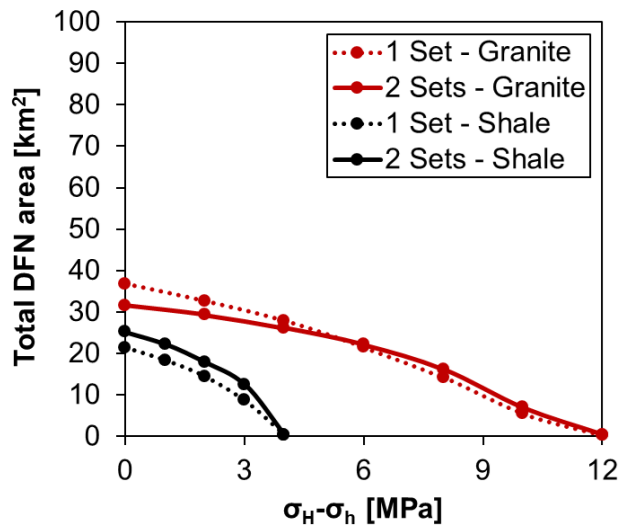


Figure 81: Influence of the differences between the three principle stresses on the total area of the DFN for different rock types and fracture sets.

5.5.4 Fairway aspect ratio

The aspect ratio mainly depends on the differences between the principle stresses as shown in **Figure 82**.

An increase in these stress differences strongly decreases the aspect ratio and hence the “complexity” of the reservoir. The significantly different results between granite and shale also indicate the importance of rock properties such as tensile strength and depth. Differences between the fracture sets are minor.

Additionally, we observed that the injection of larger fluid volumes at the same rate leads to slightly higher aspect ratios (e.g., 0.46 for 10000 m³ and 0.41 for 5000 m³ for the “Base Case” scenario with 2 MPa stress difference).

Using high viscosity gels as fracturing fluid leads to “a more even” fluid distribution and larger aspect ratios as compared to the use of slickwater. For the “Base Case” scenario shale with 2 MPa stress difference the aspect ratio is 0.46 when using slickwater and 0.76 when using a high viscosity crosslinked gel.

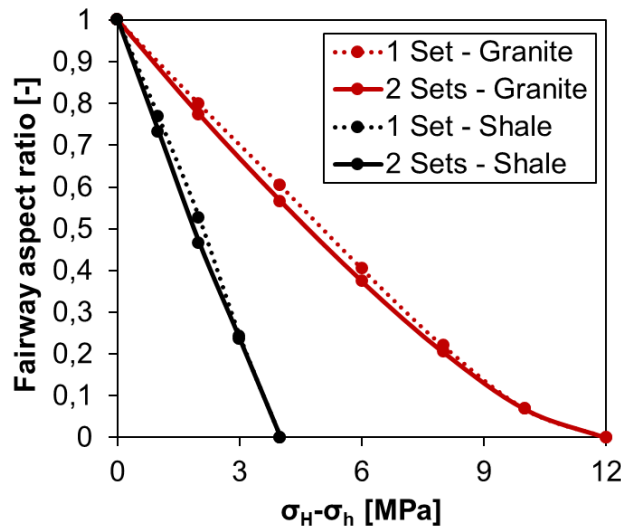


Figure 82: Influence of the differences between the three principle stresses on the aspect ratio of the fracture system for different rock types and fracture sets.

5.6 DISCUSSION

The calculated fracture network properties are the values for the end of the treatment. The fracture geometries (including fracture permeability) after fracture closure should be further investigated.

With the underlying model assumptions (e.g., only tensile failure), multiple secondary fracture networks can only develop if net fracture pressures are high ($\gg 1$ MPa) and/or the differences between the principle stresses are low. The simulations suggest that high net pressures can be achieved, for example, with small fracture spacings and strong stress barriers.

Although natural fractures may be present at great depths [38], not all of these fractures take fluid and may be stimulated simultaneously [5]. Therefore, small fracture spacings might not always be achievable. Pressure losses along the wellbore might also be a problem because more energy is available to stimulate a fracture closer to the wellhead as compared to fractures further away. The same is true for the pressure losses along the fractures. There might be more energy to stimulate secondary fractures closer to the well than further away from the well. This aspect is approximated by the simulator partly by assuming an ellipsoidal shape of the stimulated fracture network and results in a wider fracture opening closer to the injection point.

If the differences between the principle stresses are large (e.g., at the geothermal research site at Soultz-sous-Forêts) and/or dominant fracture zones are present (e.g., Soultz-sous-Forêts) single fractures/fracture zones develop rather than complex fracture networks. Pre-stimulation treatments or multiple simultaneous or subsequent stimulations might be a way to alter the in situ stress field and induce more complex fracture networks in this case.

5.7 SUMMARY AND CONCLUSIONS

Major gas reserves as well as geothermal resources (heat) lie in ultratight shales or granitic rocks with and without natural fractures. These rocks need to be hydraulically stimulated in order for them to be productive. However, a comprehensive simulation of complex fracture network development in ultratight naturally fractured rocks is a challenging problem.

In this study, hydraulic fracturing stimulations in these kinds of environments were simulated with a DFN simulator. Two models were set up: a 2.5 km deep shale formation bearing gas and a 5 km deep granite containing heat. In order to evaluate the influence of rock properties and stimulation parameters on the developed fracture network, a detailed sensitivity analysis was conducted.

In the simulator, a natural fracture opens if the net fracture pressure overcomes the difference between the maximum and the minimum horizontal stress (fractures develop parallel to σ_h), the difference between vertical and minimum horizontal stress (fractures develop in the horizontal plane), or the critical stress (fractures develop parallel to σ_H). Therefore, the net fracture pressure (P_{net}) was of particular importance for us in this study. Other parameters revealing information about the shape of the stimulated fracture network are the total DFN area, the fairway aspect ratio, and fracture height growth containment.

Stress state, in situ fracture network, and the fluid type have the largest influence on all five fracture network properties. Fracturing fluid volume and injection rate were found to be less important.

According to the simulations and for the underlying model assumptions the main factors leading to the development of more complex fracture networks in low permeability rocks are:

- fracture network properties
 - an extensive pre-existing natural fracture network
 - small fracture (natural and hydraulic) spacings
- stress state
 - low differences between principle stresses
 - well contained formations
- rock properties
 - high tensile strength (critical stress)
 - high Young's modulus (stiff rocks)
- stimulation parameters
 - low viscosity fracturing fluid (slickwater)
 - large fluid volumes and high injection rates

Major differences in 5 km deep HDR and 2.5 km deep shale gas reservoirs, which affect treatment designs and results, were found to be:

- The reservoir temperature in granites is significantly larger.
- The pressures and stresses in granites are significantly larger.
- Surface treatment pressures in granites are significantly larger.
- The total reservoir compressibility in granites is significantly lower.
- Due to the low compressibility, the fluid leak-off in granites is significantly lower.
- The mechanical parameters tensile strength and Young's modulus of granites are often much higher as compared to shales.

Results are that for the same treatment design the following differences can be expected between the stimulation of a 2.5 km deep shale and a 5 km deep granite:

- For granite, the net pressure is higher.
- For granite, the total DFN area is larger.
- For granite, the aspect ratio is larger.
- For granite, the stimulated fracture network can hence be expected to be more complex.

However, even though the simulations revealed valuable insights in complex fracture network development, it lacks of a solid mechanical description of the fracturing process itself. The main assumption of MShale is tensile opening of fractures (mode 1). This is not believed to be the only failure mechanism that takes place in geothermal and shale gas reservoirs, where indications for shear failure (modes 2 and 3) are observed as well. Also, natural fracture systems are mostly not perpendicular to each other, but rather intersect each other by an angle. In MShale software, the fractures can only develop in three principle planes perpendicular to each other. Modes 2 and 3 fracture opening as well as arbitrary fracture growth directions and fracture shapes should be additionally taken into account for a better conceptual description of the fracturing process.

REFERENCES

- [1] Economides, M. J., and Wood, D. A., 2009, "The State of Natural Gas," *J. Nat. Gas Sci. Eng.*, 1(1–2), pp. 1–13.
- [2] Goldstein, B. A., Hiriart, G., Tester, J., Bertani, B., Bromley, R., Gutierrez-Negrin, L., Huenges, E., Ragnarsson, H., Mongillo, A., Muraoka, M. A., and Zui, V. I., 2011, "Great Expectations for Geothermal Energy to 2100," *Proceedings, Thirty-Sixth Workshop on Geothermal Reservoir Engineering*, Stanford University, Stanford, CA, Jan. 31–Feb. 2, Paper No. SGP-TR-191.
- [3] Vidhi, R., Kuravi, S., Goswami, D. Y., Stefanakos, E., and Sabau, A. S., 2013, "Organic Fluids in a Supercritical Rankine Cycle for Low Temperature Power Generation," *ASME J. Energy Resour. Technol.*, 135(4), p. 042002.
- [4] Economides, M. J., and Martin, T., 2007, *Modern Fracturing, Enhancing Natural Gas Production*, 1st ed., Energy Tribune Publishing Inc., Houston, TX, p. 531.
- [5] Tester, J., 2006, *The Future of Geothermal Energy, Impact of Enhanced Geothermal Systems (EGS) on the United States in the 21st Century*, Massachusetts Institute of Technology, Cambridge, MA, p. 372.
- [6] Perkins, T., and Kern, L., 1961, "Widths of Hydraulic Fractures," *J. Pet. Technol.*, 13(9), pp. 937–949.
- [7] Nodgren, R., 1972, "Propagation of Vertical Hydraulic Fracture," *Soc. Petrol. Eng. J.*, 12(4), pp. 306–314.
- [8] Khristianovich, S. A., and Zheltov, Y. P., 1955, "Formation of Vertical Fractures by Means of Highly Viscous Fluids," *Proceedings, Fourth World Petroleum Congress*, Rome, Italy, June 6–15, pp. 579–586.
- [9] Geertsma, J., and de Klerk, F., 1969, "A Rapid Method of Predicting Width and Extent of Hydraulically Induced Fractures," *J. Pet. Technol.*, 21(12), pp. 1571–1581.
- [10] Cleary, M. P., 1980, "Analysis of Mechanisms and Procedures for Producing Favourable Shapes of Hydraulic Fractures," *SPE Paper No. 9260*.
- [11] Cipolla, C. L., Warpinski, N. R., and Mayerhofer, M. J., 2008, "Hydraulic Fracture Complexity: Diagnosis, Remediation, and Exploitation," *SPE Paper No. 115771*.
- [12] Tiab, D., Lu, J., Nguyen, H., and Owayed, J., 2010, "Evaluation of Fracture Asymmetry of Finite-Conductivity Fractured Wells," *ASME J. Energy Resour. Technol.*, 132(1), p. 012901.
- [13] Wu, J., Liu, Y., and Yang, H., 2012, "New Method of Productivity Equation for Multipbranch Horizontal Well in Three-Dimensional Anisotropic Oil Reservoirs," *ASME J. Energy Resour. Technol.*, 134(3), p. 032801.

- [14] Osholake, T., Jr., Wang, J. Y., and Ertekin, T., 2013, "Factors Affecting Hydraulically Fractured Well Performance in the Marcellus Shale Gas Reservoirs," *ASME J. Energy Resour. Technol.*, 135(1), p. 013402.
- [15] Cipolla, C. L., Warpinski, N. R., Mayerhofer, M. J., Lolon, E. P., and Vincent, M. C., 2008, "The Relationship Between Fracture Complexity, Reservoir Properties, and Fracture Treatment Design," SPE Paper No. 115769.
- [16] Meyer, B. R., and Bazan, L. W., 2011, "A Discrete Fracture Network Model for Hydraulically Induced Fractures: Theory, Parametric and Case Studies," SPE Paper No. 140514.
- [17] Meyer & Associates, 2011, "User's Guide Meyer Fracturing Simulators," 9th ed., Meyer & Associates, Natrona Heights, PA.
- [18] Warren, J. E., and Root, J. E., 1963, "The Behavior of Naturally Fractured Reservoirs," SPE, 3(3), pp. 245–255.
- [19] Valley, B., and Evans, K. F., 2006, "Strength and Elastic Properties of the Soultz Granite," EHDRA Scientific Conference, Soultz-sous-Forêts, France, June 15–16, pp. 1–6.
- [20] Gale, J. F. W., Reed, R. M., and Holder, J., 2007, "Natural Fractures in the Barnett Shale and Their Importance for Hydraulic Fracturing Treatments," *Am. Assoc. Pet. Geol. Bull.*, 91(4), pp. 603–622.
- [21] Sondergeld, C. H., Newsham, K. E., Comisky, J. T., Rice, M. C., and Rai, C. S., 2010, "Petrophysical Considerations in Evaluating and Producing Shale Gas Resources," SPE Paper No. 131768.
- [22] Esemé, E., Urai, J. L., Krooss, B. M., and Littke, R., 2007, "Review of Mechanical Properties of Oil Shales: Implications for Exploitation and Basin Modelling," *Oil Shale*, 24(2), pp. 159–174.
- [23] Jacot, R. H., Bazan, L. W., and Meyer, B. R., 2010, "Technology Integration: A Methodology to Enhance Production and Maximize Economics in Horizontal Marcellus Shale Wells," SPE Paper No. 135262.
- [24] Kumar, J., 1976, "The Effect of Poisson's Ratio on Rock Properties," SPE Annual Fall Technical Conference and Exhibition, New Orleans, LA, Oct. 3–6, p. 6, SPE 6094.
- [25] Selvadurai, A. P. S., Boulon, M. J., and Nguyen, T. S., 2005, "The Permeability of an Intact Granite," *Pure Appl. Geophys.*, 162(2), pp. 373–407.
- [26] Hill, R. E., 1992, "Analysis of Natural and Induced Fractures in the Barnett Shale," RI Report No. 92/0094.
- [27] Agapito, J., and Hardy, M., 1982, "Induced Horizontal Stress Method of Pillar Design in Oil Shale," *Proceedings of 15th Oil Shale Symposium*, Colorado School of Mines, Golden, CO, Apr. 28–30, pp. 191–197.

- [28] Sun, Z., and Ouchterlony, F., 1986, “Fracture Toughness of Stripa Granite Cores,” *Int. J. Rock Mech. Min. Sci. Geomech.*, 23(6), pp. 399–409.
- [29] Dai, F., and Xia, K., 2009, “Tensile Strength Anisotropy of Barre Granite,” *Proceedings of the 3rd CANUS Rock Mechanics Symposium*, Toronto, ON, Canada, May 9–15, paper 4012, p. 15.
- [30] Alehossein, H., and Boland, J. N., 2004, “Strength, Toughness, Damage and Fatigue of Rock,” *Structural Integrity and Fracture*, http://espace.library.uq.edu.au/eserv/UQ:10122/Alehossein_sif04.pdf
- [31] Beard, T., 2011, “Fracture Design in Horizontal Shale Wells—Data Gathering to Implementation,” *EPA Hydraulic Fracturing Workshop*, Arlington, VA, Mar. 10–11, p. 8.
- [32] Geraud, Y., Rosener, M., Surma, F., Place, J., Le Garzic, E., and Diraison, M., 2010, “Physical Properties of Fault Zones Within a Granite Body: Example of the Soultz-sous-Forêts Geothermal Site,” *Geoscience*, 342(7–8), pp. 566–574.
- [33] Petrov, V. A., Poluektov, V. V., Zharikov, A. V., Nasimov, R. M., Diaur, N. I., Terentiev, V. A., Burmistrov, A. A., Petrunin, G. I., Popov, V. G., Sibgatulin, V. G., Lind, E. N., Grafchikov, A. A., and Shmonov, V. M., 2005, “Microstructure, Filtration, Elastic and Thermal Properties of Granite Rock Samples: Implication for HLW Disposal,” *Petrophysical Properties of Crystalline Rocks*, P. K. Harvey, T. S. Brewer, P. A. Pezard, and V. A. Petrov, eds., *Geolog. Soc. London UK, Special Publications*, 240, pp. 237–253.
- [34] Sone, H., 2012, “Mechanical Properties of Shale Gas Reservoir Rocks and Its Relation to the In-Situ Stress Variation Observed in Shale Gas Reservoirs,” *Ph.D. thesis*, Stanford University, Stanford, CA.
- [35] Ning, X., Fan, J., Holditch, S. A., and Lee, W. J., 1993, “Property Measurement in Naturally Fractured Devonian Shale Cores Using a New Pressure Pulse Method,” *SCA Conference Paper No. 9301*.
- [36] Lemmon, E. W., Huber, M. L., and McLinden, M. O., 2010, “NIST Standard Reference Database 23,” *NIST Reference Fluid Thermodynamic and Transport Properties—REFPROP*, version 9.0, Standard Reference Data Program, National Institute of Standards and Technology, Gaithersburg, MD, p. 55.
- [37] Zoback, M. D., 2007, *Reservoir Geomechanics*, Cambridge University, Cambridge, MA.
- [38] Kalinina, E., McKenna, S. A., Hadgu, T., and Lowry, T., 2012, “Analysis of the Effects of Heterogeneity on Heat Extraction in an EGS Represented With the Continuum Fracture Model,” *Proceedings of 37th Workshop on Geothermal Reservoir Engineering*, Stanford University, Stanford, CA, Jan. 30–Feb. 1.
- [39] Gale, J. F. W., and Holder, J., 2012, “Natural Fractures in Some US Shales and Their Importance for Gas Production,” *Pet. Geol. Conf. Ser.* 2010, 7, pp. 1131–1140.

- [40] Hofmann, H., Babadagli, T., and Zimmermann, G., 2013, “Numerical Simulation of Complex Fracture Network Development by Hydraulic Fracturing in Naturally Fractured Ultratight Formations,” ASME Paper No. OMAE2013-11084.
- [41] Ishida, T., Chen, Q., Mizuta, Y., and Roegiers, J.-C., 2004, “Influence of Fluid Viscosity on the Hydraulic Fracturing Mechanism,” ASME J. Energy Resour. Technol., 126(3), pp. 190–200.
- [42] Fisher, K., and Warpinski, N., 2012, “Hydraulic-Fracture-Height Growth: Real Data,” SPE Paper No. 145949.

CHAPTER 6: A GRAIN-BASED MODELING STUDY OF MINERALOGICAL FACTORS AFFECTING STRENGTH, ELASTIC BEHAVIOUR AND MICRO FRACTURE DEVELOPMENT DURING COMPRESSION TESTS IN GRANITES

A version of this chapter was submitted to *Journal of Engineering Fracture Mechanics*.

The influence of mineral size, mineral size distribution, and model discretization on elastic rock properties, rock strength, and types and amounts of micro cracks was studied numerically using a two-dimensional discrete element grain-based modeling (GBM) approach. The model was calibrated to unconfined and confined compression tests and Brazilian tensile tests performed on Aue granite. Additionally, confined asymmetric compression tests (CAT) were simulated for the same rock and compared to physical fracture paths for further validation.

The GBM approach is able to reproduce all major laboratory observations from Aue granite including the correct ratio between compression strength and Brazilian tensile strength that could not be captured with earlier contact models. While a good match for the Aue granite was achieved using the same calibrated micro properties but updated mineralogy, the results of the same tests on three other granites could not be matched to the experimental data. This is due to the different stress concentrations within the minerals when the mineral size is changed, but the same particles are overlaid over this mineral geometry. Besides strength and elastic properties, micro fracture development is strongly influenced by the particle size and mineral size distribution.

6.1 INTRODUCTION

Strength, elasticity, and fracture development in granitic basement rocks are critical to a variety of applications such as the stability of surface or subsurface structures, radioactive waste storage,^[1] or heat extraction from impermeable deep basements by developing enhanced geothermal systems.^[2,3] Common rock mechanic tests to identify rock strength, elastic parameters, and fracture patterns in tension and compression are the Brazilian tensile tests, unconfined compression tests (UCS tests), and confined compression tests at different confining pressures. Additionally, less common tests such as asymmetric compression tests by Zang et al.^[4] were performed to study the fracture process zone development under different conditions.

The results of these tests were governed by a variety of factors. At micro scale, mineral composition,^[5] mineral size distribution,^[6] mineral shape,^[7] micro defects,^[8] and resulting rock mechanics properties^[5] were observed to govern the failure process in standard rock mechanics tests (e.g. unconfined compression tests, confined compression tests, and Brazilian tensile tests). Microstructure was generally found to be more important than mechanical or empirical rock properties.^[9] Similar to field scale results, in laboratory hydraulic fracturing experiments it is also observed that discontinuities and stress differences significantly influence the hydraulic fracture complexity.^[10]

Both laboratory and field test results show similar complex fracture or crack networks. To understand the details of failure and fracture development, besides experimental data, a sound numerical tool is needed to sufficiently describe the major observations from the rock mechanical experiments. While there is a variety of different numerical methods available to study rock mechanics,^[11] most of these methods have problems with large complex fracture networks.^[12] Discrete element methods (DEM) are one promising approach to study rock mechanics tests and fracturing processes numerically.^[13,14]

DEM codes like UDEC^[15]/3DEC^[16] and PFC2D^[17]/PFC3D^[18] have been increasingly used in the past years even to investigate water fracturing treatments performed in geothermal settings in two- and three-dimensions including coupled fluid-mechanical behaviour, fracture initiation and propagation of new fractures and slip and opening along joints in a pre-existing DFN.^[19-23]

Particle-based distinct element methods have the advantage of being able to handle arbitrary rock properties and to being able to avoid discretization around fractures. The macroscopic properties (e.g. Young's modulus, Poisson's ratio, strength) are the emergent properties of the model and the model input (e.g. bond strengths and particle size) has to be calibrated with trial and error to match the desired behaviour.^[12,24,25]

A variation of the particle-based distinct element method, called the grain-based modeling (GBM) approach, was used in this study. Details about this approach and the motivation for using it are described in detail in **Section 6.2**. After a description of the grain-based modeling approach and the modeling procedure, the model calibration results are presented. Based on the calibrated GBM, the influence of mineral size, mineral size distribution, and model discretization on the simulation results was investigated and these results are presented and discussed.

6.2 PFC2D GRAIN-BASED MODELING (GBM) OF BRITTLE FAILURE OF GRANITES

The two-dimensional distinct element method (DEM) Particle Flow Code (PFC2D) has recently been used extensively to study different rock mechanical problems.^[14,26,27] It was found, however, that the ratio between the tensile strength and compressive strength is significantly greater in the model than observed in experiments and the failure envelope of the particle model is linear and gives a much lower friction angle as compared to laboratory results.^[28] These deficiencies could be reduced by introducing a clumped particle model, where several particles are clumped together to any arbitrary shape that results in a better calibration of tension versus compressional strength, stress-strain behaviour, non-linear failure envelope, as well as crack distribution and rupture path.^[28,29] However, these clumped particles, representing the minerals, are rigid bodies that cannot break. In laboratory studies it was found that fractures follow not only mineral boundaries, but also intersect minerals and grain crushing occurs.^[30] Hence, the grain-based modeling (GBM) approach was developed, which extends the bonded-particle model (BPM^[31]) by using the smooth-joint logic^[32] to mimic a grain-based material.^[33]

PFC2D GBMs simulate deformable, breakable, polygonal grains. This mimics the real microstructure of crystalline rocks more closely and allows matching the ratio between

unconfined-compressive strength and direct-tension strength more closely, as well.^[34] Recent PFC2D GBM studies have been conducted,^[35-38] however, while the ratio between direct tensile strength and unconfined compressive strength could be matched by the GBM approach, the Brazilian tensile tests and unconfined compression test results can still not be reproduced with the same model when only one mineral type is considered in the model.^[38] Therefore, four different mineral types are explicitly modeled in this study. A GBM modeling approach also exists for UDEC^[39] but in this approach the grains are unbreakable such as in PFC2D clumped particle models.

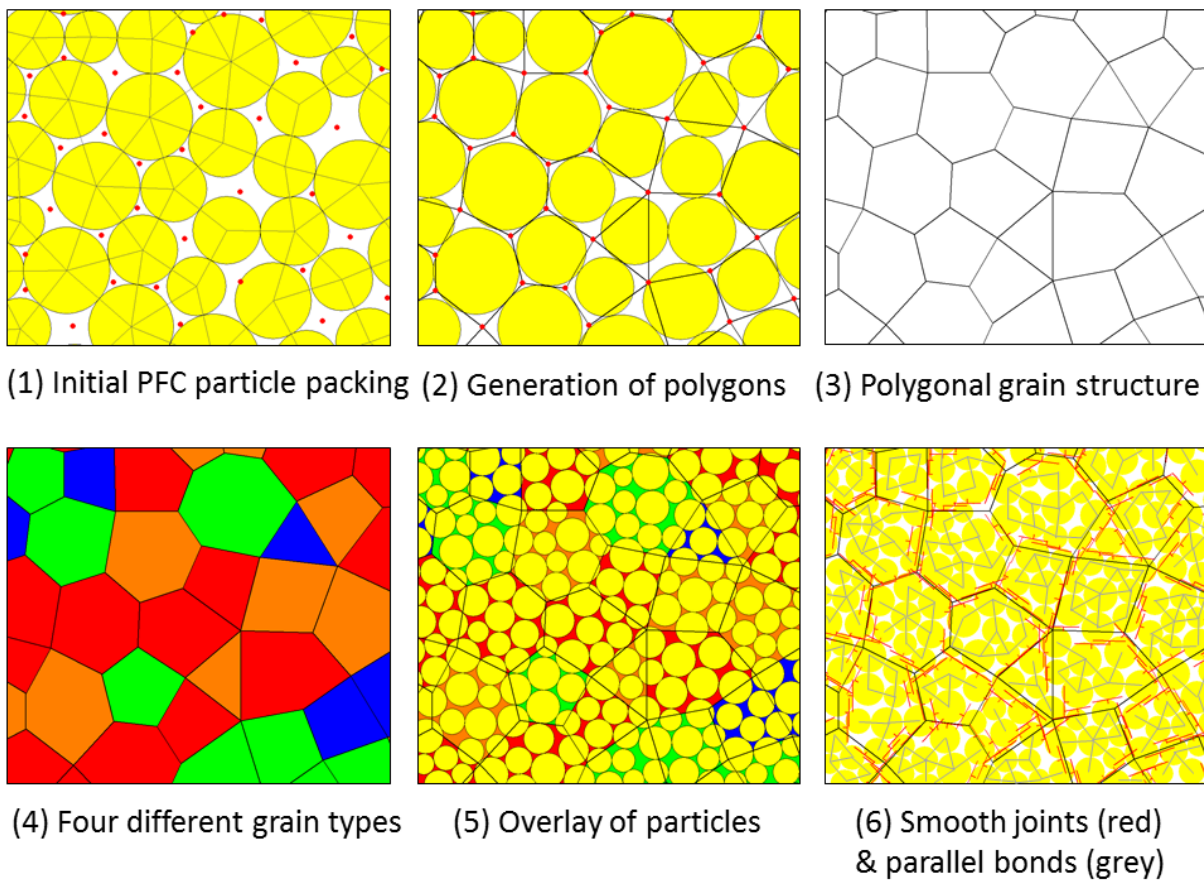


Figure 83: Generation of a grain-based model (GBM) with different grain types based on an initial particle packing (1-4), (5) bonded particle model overlaid on the grain structure, and (6) GBM consisting of grains or minerals (parallel-bonded disks) and interfaces between the grains (smooth-joint contacts).

PFC2D grain-based models are constructed by (1) generating a polygonal mineral structure, which has similar statistical properties as real rock using a disk-packing scheme within PFC2D (**Figure 83 images 1-4**), (2) constructing the parallel-bonded material using the procedure

described in Potyondy and Cundall,^[31] (3) overlaying the mineral structure on the base material and modifying particles and contact properties to correspond with the minerals (**Figure 83, image 5**), and (4) associating each polygon edge with an interface consisting of smooth-joint contacts (**Figure 83, image 6**). By introducing these smooth joint contacts, the artificial roughness resulting from the model discretization is suppressed (**Figure 84**) and specific smooth joint contact properties are assigned to these mineral boundaries. While the geometrical roughness is gone, a smooth joint “dilation angle” may be specified to represent fracture roughness. Strength properties (normal strength, cohesion, friction angle) are given explicitly and stiffness properties are calculated from the smooth joint contact and the two contacting particles and a multiplication factor (refer to Bahrani et al.)^[38]. The mineral structure generation procedure and the grain-based modeling procedure are described in detail in Potyondy’s work.^[40-42]

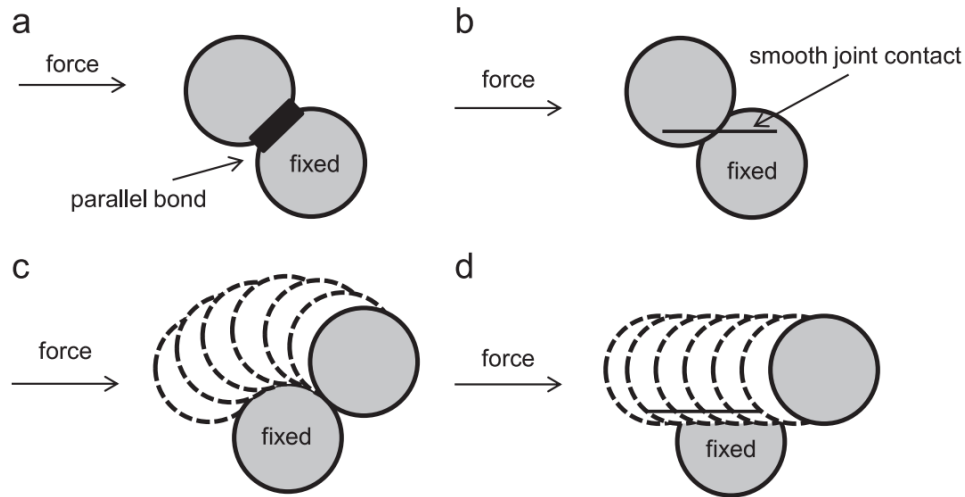


Figure 84: Parallel-bond (a) and smooth-joint contact (b) and particle movement after bond/contact breakage (c and d).^[37]

The minerals (grains) consist of circular particles, which are bonded at their contacts. Such a contact bond consists of two elastic springs with specific tensile strength, shear strength, normal stiffness, and shear stiffness. Bond micro-failure is defined by the force-displacement laws, which relate the normal and shear contact forces to the displacement of particles.

Tensile failure occurs if the tensile normal contact force equals the contact bond tensile strength. After, de-bonding the normal and shear contact forces are set to zero. Contacts fail in shear if the shear contact force equals the contact bond shear strength. In this case the shear contact force is

reduced to a residual level that equals the friction coefficient times the normal compressive contact force. Force-displacement behaviour and strength envelope of parallel bonds and smooth joint contacts are shown in **Figure 85**.

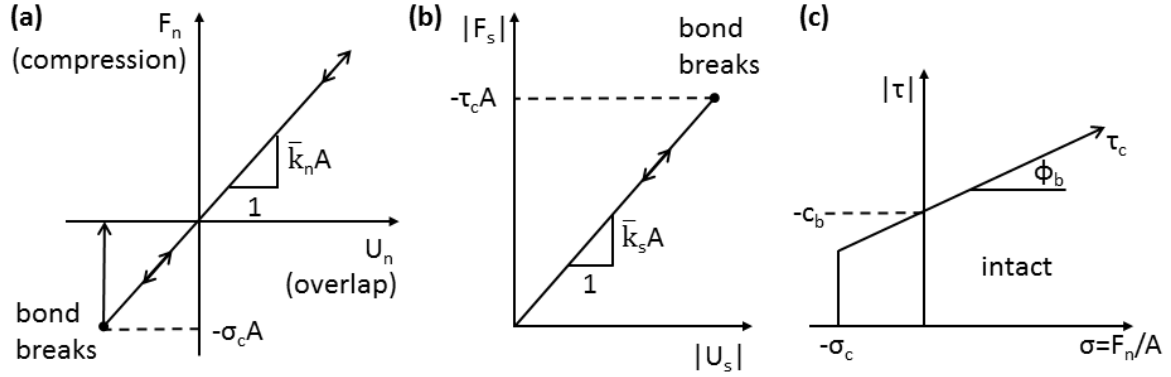


Figure 85: Force-displacement behaviour for bonded particles and smooth joints: (a) normal force versus normal displacement, (b) shear force versus shear displacement, and (c) strength envelope (redrawn from Itasca)^[18]. F_n =normal force, F_s =shear force, $-\sigma_c$ =tensile strength, U_n =normal displacement, U_s =shear displacement, k_n =normal stiffness, k_s =shear stiffness, c_b =cohesion, Φ_b =friction angle, τ_c =shear strength, A =contact area between two particles).

6.3 MODELING PROCEDURE

6.3.1 Model Setup and Calibration

Laboratory test results from four different granites were used for the setup and calibration of the PFC2D GBM. The red Aue granite from Blauenthal/Germany (syeno-monzo-granite) was the focus of the investigation (benchmark experiments) and the Eibenstock I, Eibenstock II, and Kirchberg II granites were used to get further insight. The following assumptions were made: 1) All smooth-joint contacts were assigned the same parameters such that the strength of all smooth-joint contacts were defined by the same tensile strength, cohesion and friction angle before failure and by the same friction coefficient after failure. 2) The peak strength envelope of the parallel bonds is defined by tensile strength, cohesion and friction angle. The friction coefficient at particle-particle contacts and the particle geometry, which causes local dilation, govern the residual strength of broken bonds. Different properties were assigned to the four different mineral

types. 3) Parallel bonds and particles have the same Young's modulus, which is different for each mineral type. 4) Parallel bonds and particle contacts have the same normal-to-shear stiffness ratio, which is different for each mineral type. The normal and shear stiffnesses of the smooth-joint contacts were set independently to a fraction of the values of the grains. 5) The grain micro-properties and the grain-boundary micro-properties for all four granites were the same. Different geomechanical behaviour results from differences in the mineralogy and mineral size distribution only.

For the Aue granite, a Brazilian tensile test, symmetrical biaxial unconfined and confined compression tests with 10 MPa and 40 MPa confining pressure and asymmetrical biaxial unconfined and confined compression tests with 10 MPa and 40 MPa confining pressure were simulated and calibrated against laboratory data (i.e., tensile strength, uniaxial compressive strength, compressive strength at 10 MPa confining pressure, compressive strength at 40 MPa confining pressure, Young's modulus, Poisson's ratio, failure patterns, and failure types). All compression tests were initially performed with constant displacement and additionally with crack rate controlled displacement to evaluate the effect of continuous versus stepwise displacement on the fracture patterns in compression tests.

For additional verification, Brazilian tensile test and symmetrical biaxial compression tests (unconfined, 10 MPa, 20 MPa and 30 MPa confining pressure) were simulated for three other granites (Eibenstock I, Eibenstock II, and Kirchberg II) and compared with the physical test results. Hence, a total of 31 actual laboratory tests were simulated with the GBM approach and used for model calibration. Photographs of some of the intact rocks and pictures of the mineral distributions of the DEM model are given in **Figure 86**. Schematic test setups are shown in **Figure 87**.

Performing a Brazilian tensile test, an unconfined compression test, and confined compression tests for each model, the following procedure was used for model calibration: 1) The mineralogy and mineral size distribution for the Aue granite model was set according to **Table 31**. 2) The Young's modulus of Aue granite was matched by performing a UCS test with high normal strengths and cohesions and changing parallel bond modulus and particle modulus, parallel bond shear to normal stiffness and particle shear to normal stiffness, and the smooth joint shear stiffness and normal stiffness multipliers. 3) Then, the Poisson's ratio of Aue granite was

matched by performing a UCS test and varying the shear to normal stiffness ratios of the particle contacts and the parallel bonds and the smooth joint stiffness multipliers. 4) After the successful calibration of the elastic rock properties the tensile strength of Aue granite was matched by performing a Brazilian tensile test and reducing the smooth-joint normal (tensile) strength. 5) The UCS of Aue granite was calibrated by varying parallel bond normal strength and cohesion and smooth joint normal strength and cohesion. 6) Finally, the confined compression strengths with 10 MPa and 40 MPa confining pressure (cohesion, friction angle) were calibrated by changing parallel bond normal strengths, parallel bond and smooth joint cohesions, and particle and smooth joint friction angles. 7) Because some model parameters influence multiple rock properties, several iterations between steps 1-6 were necessary to obtain a satisfying calibration of all of the above rock properties. 8) The qualitative observations from thin sections (fracture patterns) and the quantitative observations of failure type (by acoustic emission source type) were then compared with the asymmetrical confined compression test simulations of the Aue granite. 9) After this comprehensive calibration of the Aue granite model, Brazilian tensile tests, unconfined compression tests and confined compression tests with 10 MPa, 20 MPa and 30 MPa confining pressure were simulated for the three remaining granites (Eibenstock I, Eibenstock II, Kirchberg II) using the same calibrated set of micro parameters to evaluate whether the found micro properties of the minerals and mineral boundaries hold true for multiple rocks or only the calibrated granite.

The sample dimensions for the physical compression tests were 10 cm (height) x 5 cm (diameter). The rock disk for the Brazilian tensile test had a diameter of 5 cm as well. To reduce the computational time, a 5 cm (height) x 2.5 cm (diameter) sample was simulated, which was a reasonable step as shown in **Section 6.4.1** where the results for the 10 cm x 5 cm model are compared to the 5 cm x 2.5 cm model. Here, it was found that this reduction in model size had no significant influence on the results but significantly reduced computational time.

The mineral content and mineral sizes of the investigated granites are given in **Table 31**. For Aue granite, for each mineral type the average mineral size given in Zang^[44] was used. The mineral size varies from 0.9 to 1.8 mm;^[45] hence, the standard deviation of mineral size for each grain type was chosen within this spectrum. The limited number of larger grains as observed by Zang^[44] was neglected. Mineral content and size of the Aue granite can also be found in Yoon et

al.^[28] and Zang et al.^[46] For the other three granites, the geomechanical tests were performed by Xin^[43] and the mineral content and average mineral size was determined by the authors.

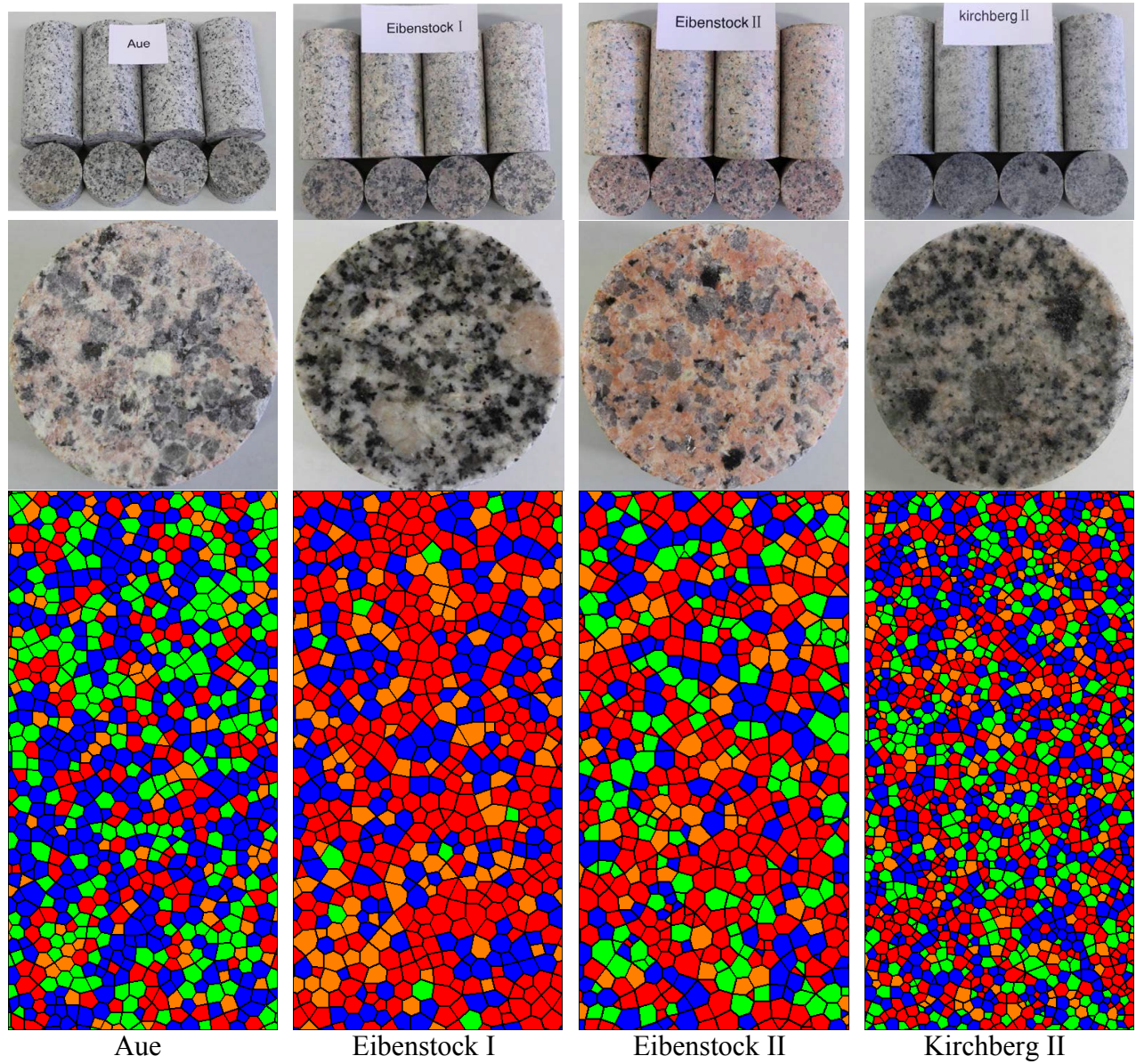


Figure 86: Photographs of the tested intact granite samples (height = 10 cm, diameter = 5 cm)^[43] and grain-based model representation (height = 5 cm, width = 2.5 cm). Note that no photograph was available for the Aue granite that was used for calibration and the picture shown is also taken from Xin).^[43] The colors indicate different mineral types (red=quartz, blue=plagioclase, green=orthoclase, orange=mica).

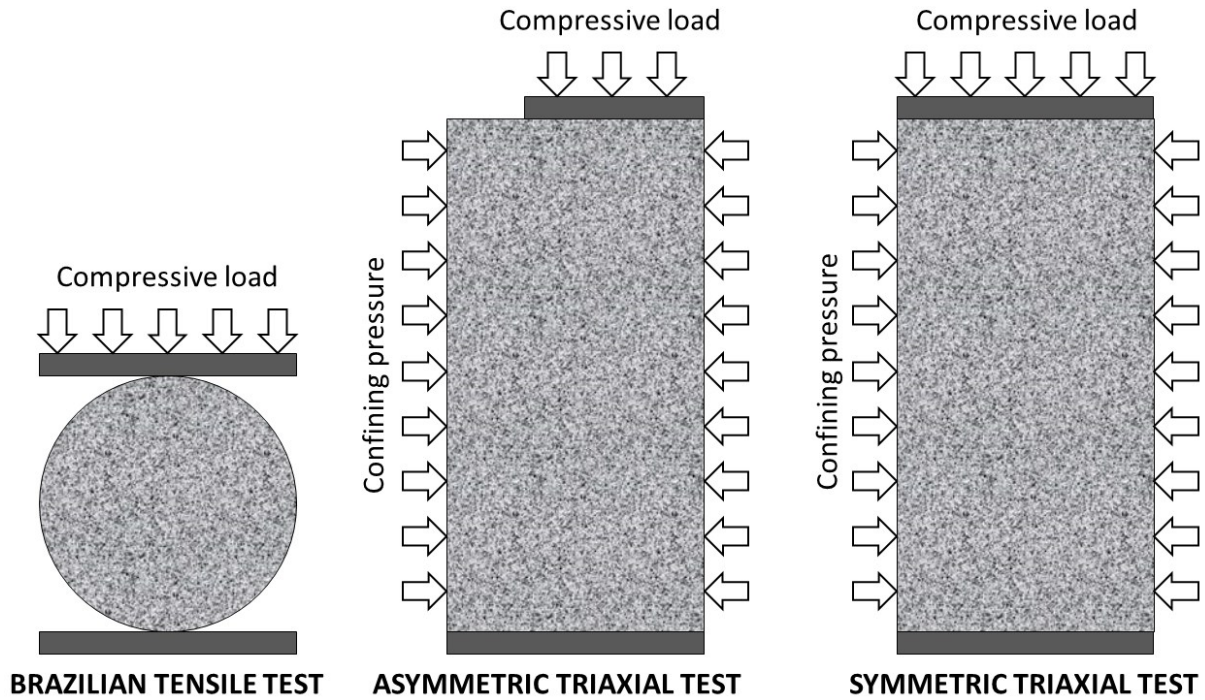


Figure 87: Schematics of the three laboratory test setups.

Table 31: Measured mineral content and size of all four studied granites.

	Mineral content				Average mineral size (diameter)			
	Quarz (%)	Plagio (%)	Ortho (%)	Mica (%)	Quarz (mm)	Plagioclase (mm)	Orthoclase (mm)	Mica (mm)
Aue ^[28,46]	30	40	20	10	1.45±0.35	1.35±0.45	1.35±0.45	1.20±0.30
Eib. I	49	33	2	15	1.56±0.59	1.56±0.59	1.56±0.59	1.56±0.59
Eib. II	44	24	21	11	1.14±0.65	1.14±0.65	1.14±0.65	1.14±0.65
Kirch. II	37	30	23	10	0.72±0.26	0.72±0.26	0.72±0.26	0.72±0.26

After model calibration, the effect of mineral size, mineral size distribution, and model discretization on compressive strength (unconfined, 10MPa and 40 MPa confinement pressure), tensile strength, elastic rock properties, amount of cracks, and crack types were studied using the calibrated PFC2D GBM as the base case model. A similar sensitivity analysis with a procedure that included the application of experimental design and optimization was performed by Yoon et

al.^[25] for the PFC2D bonded-particle model. The exact procedure of the sensitivity analysis performed in the present study is described in the following sections.

6.3.2 Sensitivity Analysis

6.3.2.1 Mineral Size

On the calibrated model, the influence of different aspects of the mineral size was studied. The influence of the average mineral (grain) size was studied by simultaneously changing the grain radius of all minerals between 0.5 mm and 3.0 mm (0.5 mm, 1 mm, 1.5 mm, 2 mm, 2.5 mm, and 3.0 mm) without standard deviation in the size distribution. For smaller minerals, the particle sizes would have to be decreased otherwise there would be less than two particles in one mineral. For larger minerals, the model size would need to be increased because with 3 mm long minerals, there are already less than five minerals along the shorter model dimension.

Table 32: Overview of three scenarios with different mineral sizes to study the influence of heterogeneity on the simulation results.

	Average mineral diameter			
	Quartz (mm)	Plagioclase (mm)	Orthoclase (mm)	Mica (mm)
Scenario 1	1.35	1.35	1.35	1.35
Scenario 2	5	3	2	0.5
Scenario 3	5 ± 2.5	3 ± 1.5	2 ± 1	0.5 ± 0.25

Additionally, the grain size distribution was studied by specifying different standard deviations (the same for all mineral types) using the average mineral size given for Aue granite in **Table 31**. The standard deviation of the mineral diameter was changed from ± 0 mm to ± 0.5 mm (0 mm, 0.25 mm, 0.5 mm). Larger standard deviations could not be implemented with the given average mineral sizes of the calibrated Aue granite model.

In the end, three scenarios were compared: 1) a homogeneous mineral size distribution (all minerals have the same size) and 2) a heterogeneous mineral size distribution without standard deviation, and 3) a heterogeneous mineral size distribution with standard deviation. Hence, the complexity of the mineral distribution increases with scenario number. The properties of these three scenarios are given in **Table 32**.

6.3.2.2 Random distribution of minerals and particles

Each model consists of a random distribution of minerals and particles. By using the same seed numbers for mineral distribution and particle distribution, the same model with the same minerals and particles at exactly the same positions will be generated and the result will be exactly the same. When the seed number is changed, this mineral or particle distribution is different, but fulfills the same statistical parameters (i.e., mean and standard deviation of mineral percentages and mineral and particle sizes). To evaluate the effect of these random distributions on the simulation results, seven different random distributions with different seed numbers for the mineral distribution and the particle distribution were simulated and the results were compared to the calibrated model to see the variability of the modeling results caused by this.

6.4 RESULTS

6.4.1 Model calibration

It was possible to calibrate the 5 cm (height) x 2.5 cm (diameter) Aue granite model against laboratory strength data and elastic properties as shown in **Table 33 and Figure 88** using the approach described in **Section 6.3.1**. This model was used as the base model for all subsequent simulations described in the following sections. As **Table 33** shows, the model results of the calibrated Aue granite model are very close to the measured experimental values. The calibrated model micro properties are summarized in **Tables 34 and 35**. The values are the result of the calibration keeping in mind the differences in strength and elastic properties of the different minerals (**Table 35**). While the tensile strength of the parallel bonds is much higher than the tensile strength of the smooth joint contacts, the cohesions of parallel bonds and smooth joint

contacts are relatively similar and the friction angles are the same for the parallel bonds of all minerals and the smooth joint contacts. The model values are different from the measured values for the minerals because these modeled values do not represent the whole mineral but one single parallel-bond or particle within the mineral. And since the geomechanical properties of the model depend on the particle sizes and particle packing, these parallel bond and particle properties will be different for each model depending on the particle size distribution (**Table 35**). For example, the reason for the higher tensile strength of the parallel bond contacts compared to a whole mineral is the stress concentration on the contacts between the particles resulting from the particle geometries (and different for each particle size distribution and particle packing). When a mineral consists of more particles, the stress is distributed over more contacts and the strength of each contact must be smaller to match the “macroscopic” strength of a mineral.

Table 33: Laboratory test results (10x5cm specimen) compared to the GBM results for the calibrated Aue granite model (5x2.5cm model), the 10x5cm Aue granite model and the 5x2.5 cm models of the other three granites. The calibration was only done for the Aue granite.

	T_o (MPa)	UCS (MPa)	$\sigma_{1@10MPa}$ (MPa)	$\sigma_{1@20MPa}$ (MPa)	$\sigma_{1@30MPa}$ (MPa)	$\sigma_{1@40MPa}$ (MPa)	E (GPa)	ν (-)
Aue ^[28, 45]	8.0	134	256	-	-	456	48	0.19
GBM 5x2.5cm	8.3	134	258	-	-	457	47	0.21
GBM 10x5cm	6.5	132	258	-	-	453	48	0.22
Eibenstock I ^[43]	6.5	98	173	229	277	-	35	0.25 [*]
GBM	8.1	145	270	348	409	-	61	0.23
Eibenstock II ^[43]	7.0	121	256	347	422	-	31	0.26 [*]
GBM	6.6	133	248	326	387	-	36	0.27
Kirchberg II ^[43]	12.6	193	297	376	444	-	65	0.22 [*]
GBM	6.9	80	216	294	348	-	25	0.11

^{*}dynamic Poisson's ratio

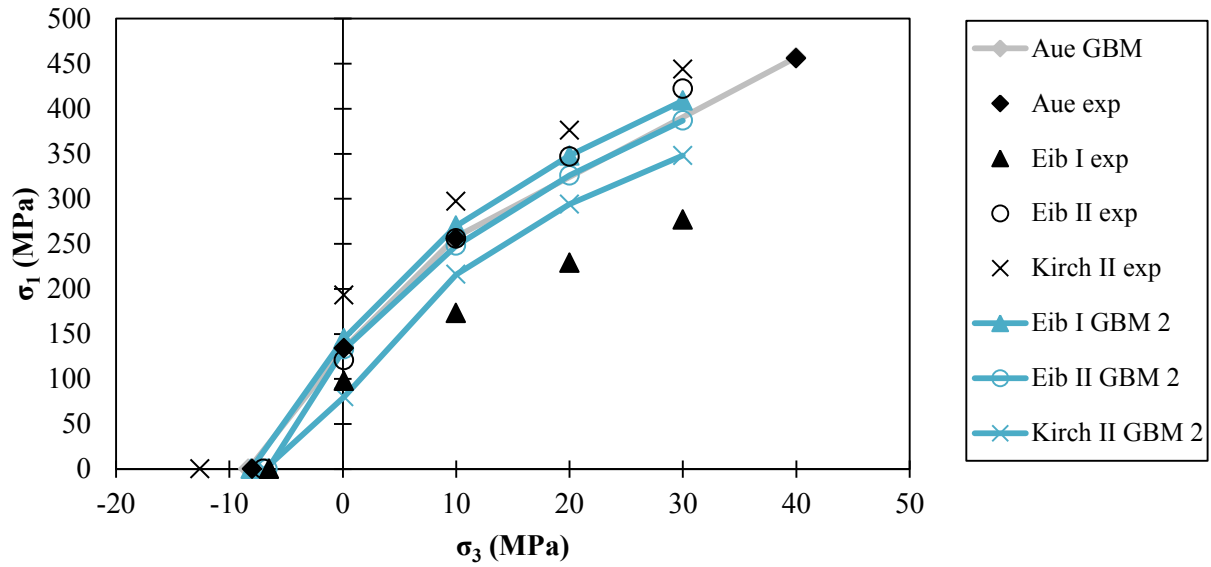


Figure 88: Calibrated Aue granite and Eibenstock I, II, and Kirchberg II GBM results compared to experimental data. While the Aue granite results match the experimental values, simulated failure stresses for the other three granites are different from the experimental ones if the same mineral and mineral boundary properties are used.

For the same reason, using the same calibrated micro properties but different mineralogy and mineral size distribution, the experimental results of the other three granite models vary significantly from the laboratory test results. **Table 33 and Figure 88** indicate this mismatch. Only the results for the Eibenstock II granite simulations are relatively close to the measured values because its mineral size distribution is similar to the calibrated Aue granite. Models with smaller minerals that revealed a higher strength in the laboratory tests actually show a lower strength in the GBM simulations. The same discrepancy was observed for the Young's moduli. As stated above, the reason for this mismatch is a result of the particle sizes and particle size distributions in the model. For example, in the Kirchberg II granite the minerals are smaller than in the Aue granite, which leads to a strength increase in the physical compression tests. However, in the GBM model, the smaller minerals consist of less particles and particle contacts. Therefore, the stress concentration on each contact within a mineral is higher compared to the Aue granite where the stress is distributed over more contacts. Thus, the model with the smaller minerals fails earlier if the contact strengths are the same. Other potential reasons for this mismatch are investigated in **Section 6.4.2** and discussed in **Section 6.5**.

Table 34: Calibrated micro-parameters used for all four granites.

Micro-parameter	Value			
Micro-properties of the minerals	Qz	Plagio	Ortho	Other
Minimum particle radius (mm)	0.2	0.2	0.2	0.2
Particle-size ratio (R_{\max}/R_{\min}) (-)	1.66	1.66	1.66	1.66
Particle-particle contact modulus (GPa)	49	39	29	19
Contact normal to shear stiffness ratio (-)	1.0	2.0	2.0	1.5
Particle friction coefficient (-)	1.2	1.2	1.2	1.2
Particle density (kg/m ³)	2650	2600	2600	2850
PB radius multiplier (-)	1	1	1	1
PB modulus (GPa)	49	39	29	19
PB normal to shear stiffness ratio (-)	1.0	2.0	2.0	1.5
PB tensile strength (mean) (MPa)	610	570	570	540
PB tensile strength (std. dev.) (MPa)	0	0	0	0
PB cohesion (mean) (MPa)	310	300	300	250
PB cohesion (std. dev.) (MPa)	0	0	0	0
PB friction angle (°)	80	80	80	80
Micro-properties of the mineral boundaries (smooth joint contacts)				
SJ contact normal stiffness factor (-)	0.6			
SJ contact shear stiffness factor (-)	0.9			
SJ bond tensile strength (MPa)	9			
SJ bond cohesion (MPa)	300			
SJ bond friction angle (°)	80			
SJ bond friction coefficient (-)	1.2			

Qz = Quartz, Plagio = Plagioclase, Ortho = Orthoclase, PB = parallel bond, SJ = smooth joint

The crack distributions for different tests are compared to photographs of the samples after laboratory testing and measured acoustic emission (AE) events in **Figure 89**. The simulated crack patterns are relatively widely spread throughout the samples. This is similar to the distribution of measured AE events. Macroscopic crack paths are visible by accumulated cracks within the GBMs, but more micro cracks develop in the model than AE observed in the physical experiment. Looking at the distribution of acoustic emission (AE) events that are associated with micro cracking, it can be seen that the simulated crack distribution is fairly close to the experimentally determined AE distribution. This is especially true if it is considered that not all of the grain boundary tensile cracks induce AE events. The displacement fields of the particles in the GBM shown in **Figure 89** match the observed macroscopic crack pattern. The general behaviour of all tests could be captured by the model. It was observed that vertically aligned grain boundary tensile cracks develop (parallel to the loading axis) during UCS tests and shear bands form during confined compression tests. There is no significant difference in the simulation result between the relatively fast and constant displacement controlled load and the relatively slow changing crack rate controlled load; in the physical experiments, a stronger difference was observed.^[47] While mainly grain boundary tensile and grain shear cracks develop during the tests, with increasing confining pressure, mainly the amount of grain shear cracks increases with some additional increase in grain tensile and grain boundary shear cracks.

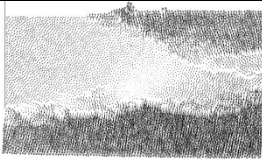
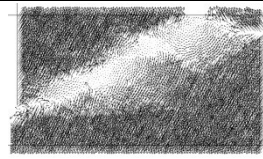
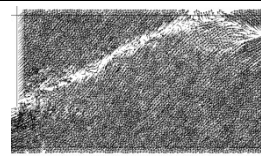
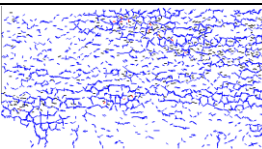
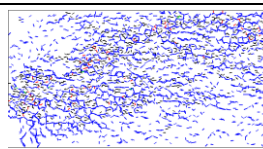
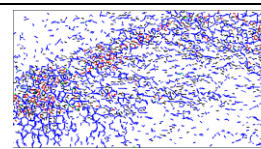

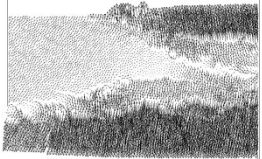
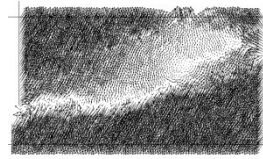
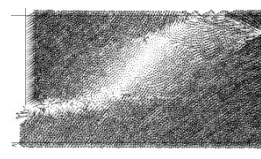
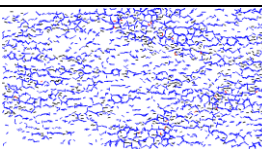
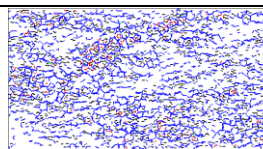
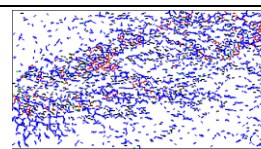
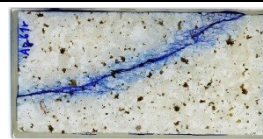


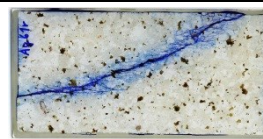

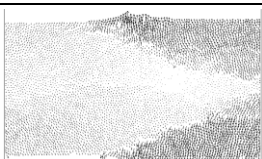
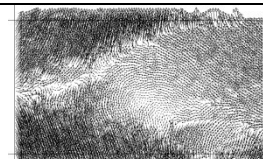
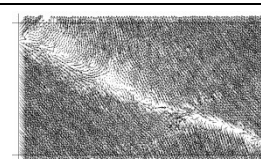
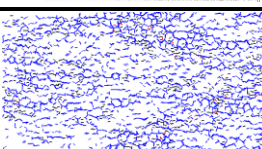
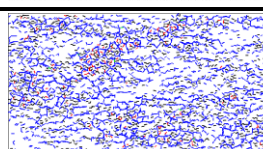
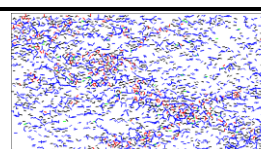
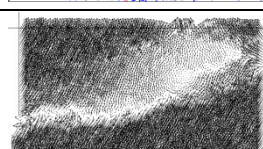
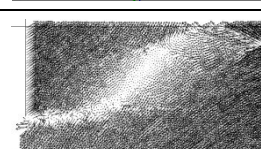
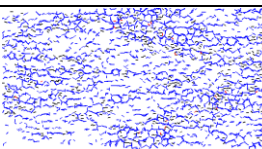
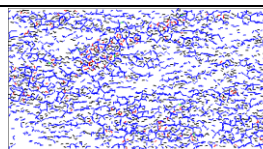
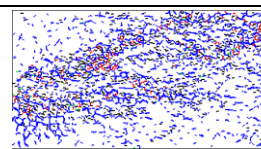
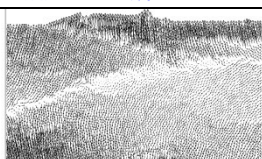
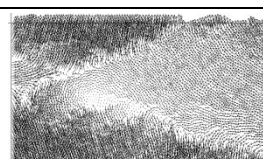
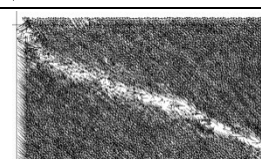
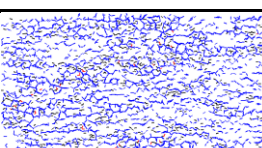
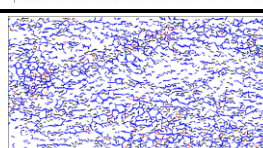
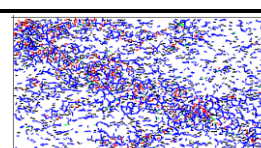
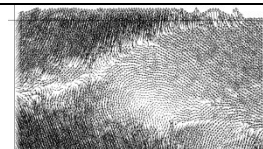
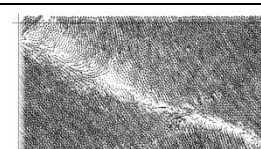
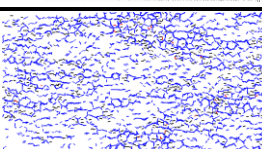
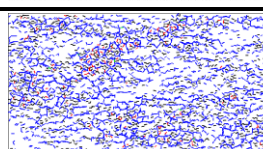
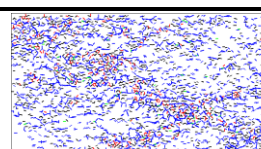
Confining pressure (Pc)		0.1 MPa (unconfined)	10 MPa	40 MPa
Aue, asymmetric, constant displacement controlled load	Displ. vectors (GBM)			
				
		AE events (exp) ^[46]	No data available	No data available
	Crack path (exp)			
Aue, asymmetric, changing rate controlled load	Displ. vectors (GBM)			
				
		Crack path (exp)		
	Micro cracks (GBM)			
Aue, symmetric, displ. Controlled load	Displ. vectors (GBM)			
				
		Micro cracks (GBM)		
	Micro cracks (GBM)			
Aue, symmetric, crack rate controlled load	Displ. vectors (GBM)			
				
		Micro cracks (GBM)		
	Micro cracks (GBM)			

Figure 89: Comparison of the crack paths and AE events of the triaxial tests with the displacement vectors and micro cracks from the GBM simulations (blue=grain boundary tensile, green=grain boundary shear, red=grain shear) at different confining pressures.

Table 35: Comparison between elastic parameters (ranges taken from previous studies)^[48-50] of minerals and their GBM micro-property equivalents (PA=particle, PB=parallel bond) used in the calibrated model.

Property	Quartz	Plagioclase	Orthoclase	Mica
Young's modulus mineral	90 GPa (65-95 GPa)	70 GPa (60-95 GPa)	60 GPa (50-80 GPa)	35 GPa (35-180 GPa)
Young's modulus PA&PB	49 GPa	39 GPa	29 GPa	19 GPa
Tensile strength mineral	50 MPa (30-50 MPa)	35 MPa	35 MPa	20 MPa (5 – 40 MPa)
Tensile strength PB	610 MPa	570 MPa	570 MPa	540 MPa
Internal friction coefficient mineral	0.25 (0.1-0.65)	0.35 (0.1-0.8)	0.35 (0.1-0.8)	0.55 (0.3-0.8)
Internal friction coefficient PA	1.2	1.2	1.2	1.2
Cohesion mineral	110 MPa	100 MPa (80 – 125 MPa)	100 MPa (80 – 125 MPa)	70 MPa (48 – 95 MPa)
Cohesion PB	310 MPa	300 MPa	300 MPa	250 MPa

6.4.2 Sensitivity Analysis of Model Parameters

6.4.2.1 Mineral size

Using the mineral properties of the calibrated Aue granite model, the influence of the mineral size on different test results was investigated by changing the average mineral diameter between 0.5 mm and 2 mm. The mineral size strongly influences number and type of cracks, strength, and elastic behaviour of the rock. With increasing average mineral diameter, the total number of cracks decreases by about 18 - 28% in all three confined and unconfined compression tests when the average mineral diameter is increased by a factor of 4 from 0.5 mm to 2 mm (**Figure 90**).

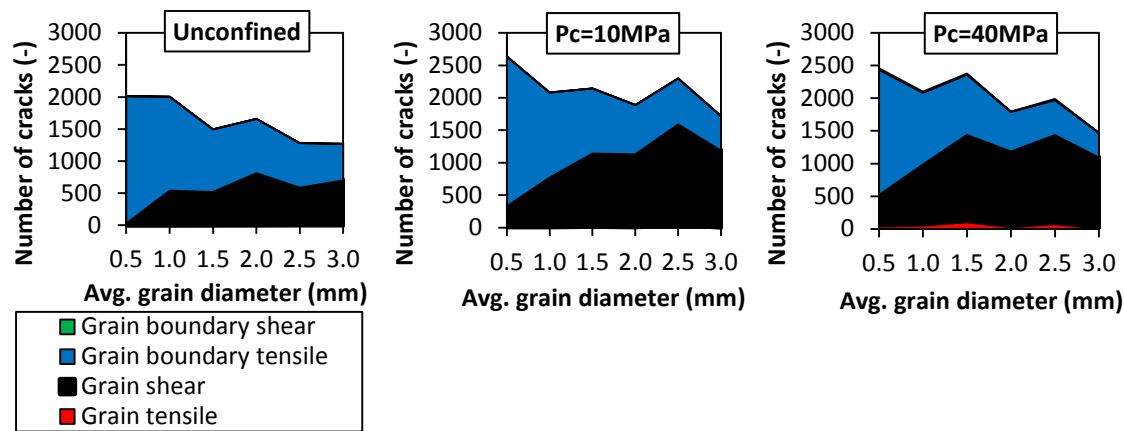


Figure 90: Influence of the average grain diameter on number and type of cracks resulting from an unconfined compression test (left), and biaxial confined compression tests with 10 MPa (center) and 40 MPa (right) confining pressure.

While the number of grain shear cracks is increasing with increasing average mineral diameter, the number of grain boundary tensile cracks is decreasing. This is mainly because larger grains consist of more parallel-bonds which are able to break and the total number of smooth joint contacts (mineral boundary contacts, which are able to break) is reduced.

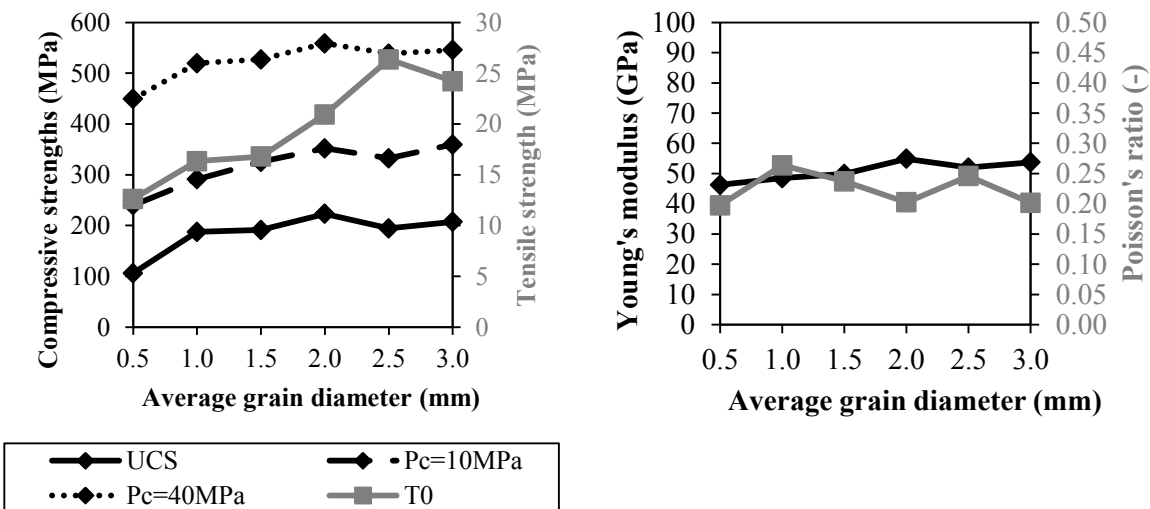


Figure 91: Influence of the average grain diameter on compressive strength with different confining pressures (Pc), tensile strength, and elastic properties.

UCS, confined compressive strengths, and Brazilian tensile strength all increase significantly with increasing mineral diameter (Figure 91, left). In physical experiments, the opposite is observed.^[51] As mentioned in Section 6.4.1, smaller minerals are built up by less particles

leading to a higher stress concentration on these few particles. Since the particle bond strengths are the same but the stress on the bond is higher in smaller minerals, the bond breaks earlier, leading to an overall reduction of the rock strength. The same is true not only for the parallel bonds within the minerals but also for the smooth joint contacts on the mineral boundaries.

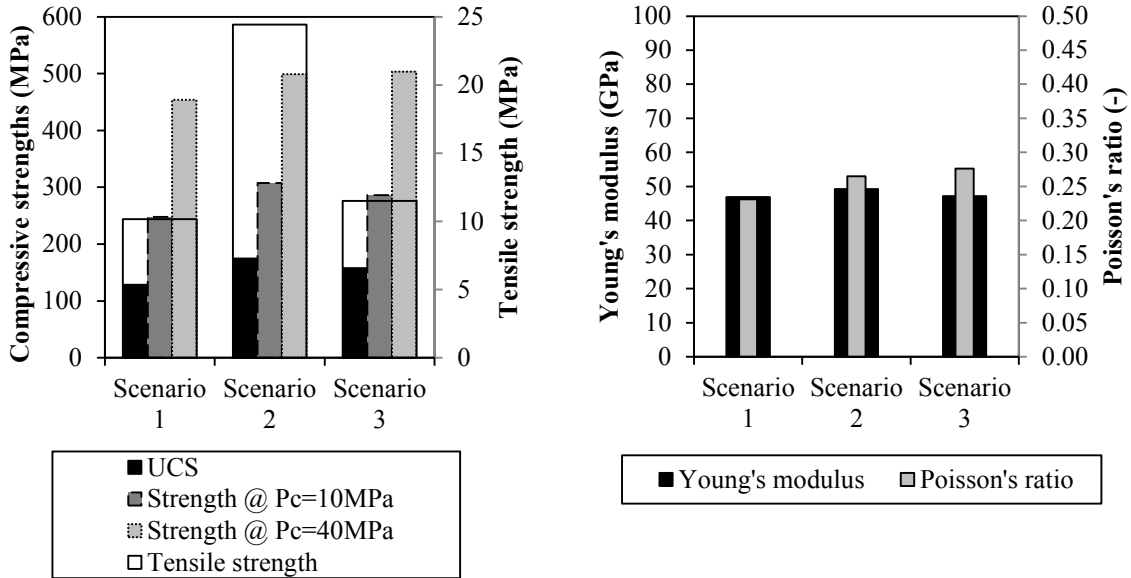


Figure 92: Strength and elastic properties for different mineral size distribution Scenarios. Scenario 1: uniform size of all minerals; Scenario 2: multiple sizes without standard deviation; Scenario 3: multiple sizes with standard deviation.

Young's modulus is slightly increasing with increasing average mineral size. Also, the effect of mineral size on Poisson's ratio was found to be minor (**Figure 91, right**) because both parameters are measured in the elastic range before failure.

Figures 92 and 93 show strengths, elastic properties, and numbers and types of cracks developing in compression tests for three scenarios with different mineral size distributions. In Scenario 1, each mineral has the same size; in Scenario 2, all minerals have different mean sizes and a standard deviation of half the mineral size (mineral sizes are normal distributed), and; in Scenario 3 all minerals have different sizes (diameters) without standard deviation (quartz = 5 mm, plagioclase = 3 mm, orthoclase = 2 mm, mica = 0.5 mm). The strength slightly increases from Scenario 1 to Scenario 3. More complex size distributions, hence, seems to strengthen the rock due to more interlocking between the minerals. Scenario 3, with the standard deviation, has the highest Poisson's ratio. Young's modulus is almost the same for all three scenarios and the

number of cracks decreases from the uniform distribution (Scenario 1) to more complex mineral size distributions (Scenarios 2 and 3).

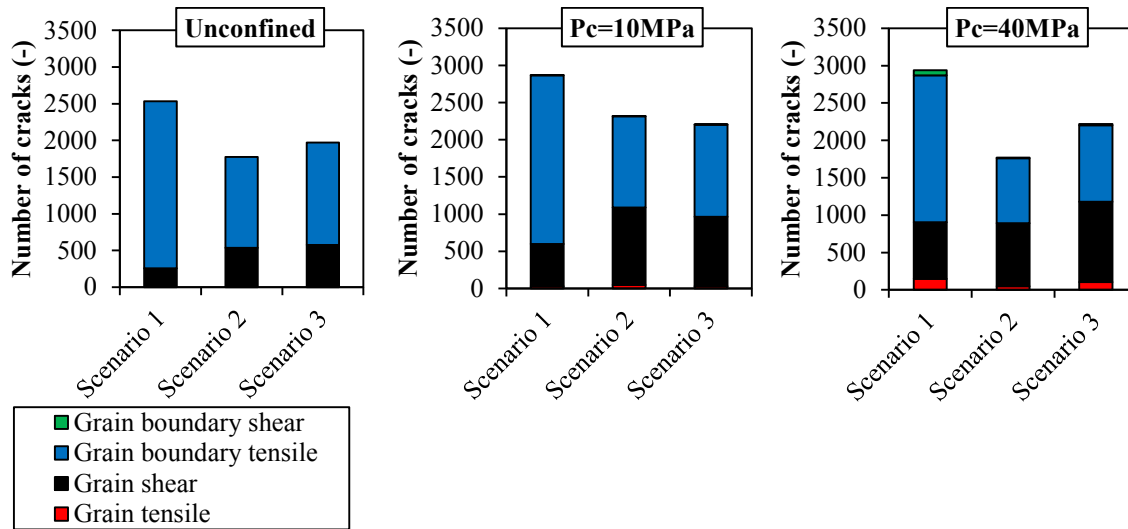


Figure 93: Crack amounts and types developing in compression tests for different mineral size distributions. Scenario 1: uniform size of all minerals; Scenario 2: multiple sizes without normal distribution; Scenario 3: multiple sizes with normal distribution.

6.4.2.2 Random distribution of minerals and particles

To investigate the influence of the randomness of the distribution of the minerals having the same statistical volumetric percentages and size distributions, the calibrated model was run seven more times with a different seed number for the mineral distribution and the particle distribution. The different Mohr-Coulomb failure envelopes for these realizations are compared to the calibrated model and the experimental data in **Figure 94**. The Young's modulus varies only between 45 and 48 MPa, but the Poisson's ratio varies between 0.21 and 0.33 and is, hence, strongly dependent on the mineral distribution. Similarly, with different seed number for the particle distribution, the Young's modulus varies between 47 MPa and 50 MPa and the Poisson's ratio varies between 0.20 and 0.26. The variation of the number of grain tensile cracks, grain shear cracks, grain boundary tensile cracks, and grain boundary shear cracks for the UCS test and the confined compression tests with 10 MPa and 40 MPa confining pressure are shown in **Table 36**. Increasing the confining stress leads to an increase in grain tensile cracks, grain shear cracks and grain boundary shear cracks, and a decrease in grain boundary tensile cracks. Overall, more shear

cracks develop with increasing confining pressure and the tensile-to-shear crack ratio decreases. The variation of the number of cracks with varying seed number for mineral and particle distribution is relatively high, especially for higher crack numbers.

Overall, the random distribution has an insignificant influence on confined compression strengths, tensile strength, and Young's modulus, but Poisson's ratio and numbers of cracks are significantly different for different random distributions of the minerals and particles. This means that the distribution of minerals and particles within a model has a huge impact on fracture development (amount of fractures and fracture types) as a result of inhomogeneities. This represents the expected impact of inhomogeneities on fracture development in laboratory rock samples as well as field scale fracture development.

Table 36: Amount of cracks developing depending on the mineral and particle distributions with different confining pressures compared to the calibrated Aue granite base case model.

	Grain tensile cracks	Grain shear cracks	Grain boundary tensile cracks	Grain boundary shear cracks	Tensile/shear crack ratio
UCS base case (bc)	0	248	2105	0	8.5
UCS mineral	0-3	88-313	1699-2282	0	7.3-19.3
UCS particle	0-12	110-530	1853-2228	0-5	4.2-16.8
Pc=10MPa bc	20	591	2017	3	3.4
Pc=10MPa mineral	3-25	369-738	1792-2211	0-6	3.0-4.9
Pc=10MPa particle	0-20	338-626	1722-2074	1-9	3.3-5.1
Pc=40MPa bc	66	669	1567	33	2.3
Pc=40MPa mineral	28-166	541-858	1500-1998	30-63	2.3-2.7
Pc=40MPa particle	47-122	513-794	1469-1761	28-56	2.2-2.8

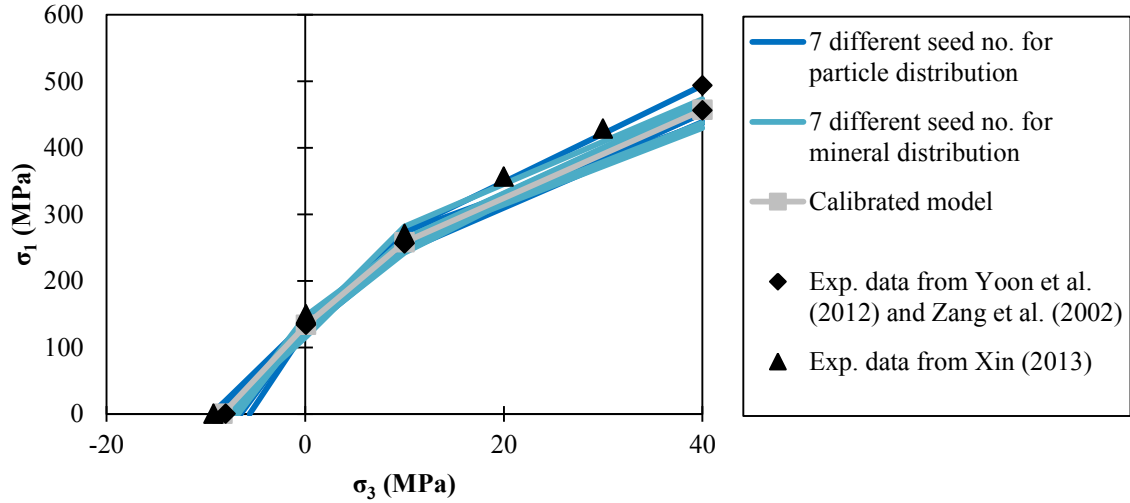


Figure 94: Influence of random distribution of minerals and particles on Mohr-Coulomb failure envelope.

6.5 DISCUSSION

Using the GBM approach presented in this paper, it was shown that it is possible to calibrate compressive strength at different confining pressures, Brazilian tensile strength, and elastic properties of Aue granite derived from unconfined and confined compression tests and Brazilian tensile test results. To match compressive strength and tensile strength at the same time, the smooth joint normal strength (equivalent to mineral boundary tensile strength) needs to be relatively low (i.e. 9 MPa). The result is that only grain boundary tensile cracks develop during the calibrated Brazilian tensile test. If mineral or mineral boundary properties or particle size are changed by $\pm 50\%$, some grain shear cracks may develop but no grain tensile or grain boundary shear cracks formed during Brazilian tensile testing. In the compression tests, mainly grain boundary tensile and grain shear cracks develop but since the calibrated model parameters are not unique and different models may lead to the same result, it would also be possible to develop other crack types, as well, when a calibration with different model properties is achieved.

When comparing the simulated fracture patterns resulting from compression tests with the observed ones in the physical experiments, it seems that more fractures develop and their distribution is more even in the GBM. One reason for this behaviour might be that smaller cracks could not be observed in the physical experiments even though these cracks developed. The simulated micro cracks represent the AE events more closely than the macroscopic fractures do.

Still, there is a discrepancy but the areas with high crack concentrations fit well with the experimentally determined macroscopic fracture patterns. Looking at the displacement field of the simulated particles reveals very similar structures to the actual macroscopic fracture patterns in most of the experiments. Another reason might be the fact that only one set of properties was used for all mineral boundaries (smooth joint contacts). A more sophisticated model where the mineral boundary strength properties follow a statistical distribution or depend on the neighbouring minerals should be developed to test how this changes the fracture patterns. However, in general, the main fracture paths developing in the models match fairly well with the physically observed ones.

Additionally, the calibrated mineral and mineral boundary properties were used to simulate UCS, confined compression tests and Brazilian tensile tests of three other granites by only updating the percentages of the mineral types and the mineral size distribution. No satisfying match could be obtained by this approach for the two granites with significantly different mineralogy and mineral size distribution, which may be for several reasons. First, as mentioned earlier, the calibrated mineral and mineral boundary properties are not unique and there might be a set of properties that matches all four granites. Second, other factors such as initial micro cracks or different properties of mineral boundaries may significantly influence the simulation results. Third, the PFC2D GBM is only a two-dimensional model and three-dimensional effects may be important. Fourth, the shapes of the minerals in the model are based on the structure of circular particles and may therefore not represent the structure of the real minerals well enough. Digitizing and “meshing” of real rock thin sections would be a future way to overcome this limitation. The main reason identified that caused the mismatch for the other granites is the influence of the mineral size distribution on the simulation results. In the physical experiments, rocks with smaller minerals are stronger than those with larger minerals.^[51] In the calibrated GBM, the opposite behaviour was observed. The reason for this is the increased number of parallel bonds within one mineral in larger minerals, leading to a lower stress concentration at the contacts and, in turn, leading to later failure of the specimen.

A proper calibration of all investigated rock types and test types is a very time-consuming process and remains the subject of future research. The presented sensitivity analysis of mineral and mineral boundary properties aims to help achieve this goal. While a simultaneous calibration

of all four models might still be possible with a different combination of micro properties, a variation of particle size distribution, mineral size distribution or a different random distribution of the minerals. Maybe a simultaneous calibration of all four granites is not possible due to the reasons stated above and the particle and parallel bond properties need to be changed for each granite. This would mean that the model results cannot be extended to study the geomechanical behaviour of other granites. This question is beyond the scope of this work and will need to be addressed in a separate study.

The investigation of the influence of mineral size, mineral size distribution, and model discretization show a number of interesting observations. One highlight is that the GBM approach reproduces the strong impact that the heterogeneity (e.g. mineral distribution or different properties of different minerals) of the rock has on microscopic crack development and macroscopic fracturing as well as rock strength. These results may be applicable to field scale problems considering mineral boundaries as pre-existing rock defects (i.e. natural fractures) and minerals as rock matrix. However, to draw solid conclusions from the model results for field scale problems, field scale simulations are necessary.

6.6 CONCLUSIONS

With the grain-based modeling approach, it is possible to calibrate compressive strength at different confining pressures, Brazilian tensile strength, and elastic rock properties of Aue granite. Earlier DEM models, which did not account for (1) mineral structures (particle models),^[28] (2) breakable grains (clumped particle models),^[52] and (3) minerals with different properties (GBM with one mineral type)^[38] were not able to achieve this goal. It was shown that a successful and valid calibration can be achieved in a much shorter time using smaller model dimensions than that of the physical sample dimensions (2.5 cm x 5 cm instead of 5 cm x 10 cm).

Grain boundary tensile and grain shear cracks are the governing fracture types in the simulated compression tests and only grain boundary tensile cracks develop during the simulated Brazilian tensile test. With increasing confining stress the relative amount of grain shear cracks increases and in addition some grain tensile and grain boundary shear cracks develop.

The GBM approach is able to reproduce the strong impact of heterogeneity of rocks on microscopic crack development and macroscopic failure. However, a simultaneous calibration of four different granites with the same mineral and mineral boundary properties was not possible because of the stress concentration in a smaller mineral with fewer particles leading to a decrease in strength. In the physical experiments, smaller minerals lead to a strength increase. Also, some discrepancies between the observed and modeled crack types and fracture patterns were noticed. Even though the stress-strain curve of the calibrated Aue granite model showed the expected behaviour, slight changes in the model may lead to an additional force increase after a short force drop at sample failure. These topics should be addressed in future studies.

The grain-based modeling approach may be improved for these future studies by including actual mineral geometries from thin sections by introducing different properties for the boundaries between different minerals, by using a three-dimensional approach and by calibration against even more test data.^[53]

REFERENCES

- [1] N.G. Witherspoon, N.G.W. Cook, J.E. Gale, *Science* **1981**, 221, 894, doi: 10.1126/science.7466363.
- [2] J.W. Tester, B.J. Anderson, A.S. Batchelor, et al., “The future of geothermal energy impact of enhanced geothermal systems (EGS) on the United States in the 21st century,” *Massachusetts Institute of Technology* **2006** [online], www.1eere.energy.gov/geothermal/egs_technology_html.
- [3] B. Valley, K.F. Evans, Proc. *EHDRA Scientific Conference*, Soultz-sous-Forêts, France, 15–16 June **2006**.
- [4] Zang, C. Wagner, S. Stanchits, et al., *Geophys. J. Int.* **1998**, 135, 1113, doi: 10.1046/j.1365-246X.1998.00706.x.
- [5] L. Ren, J. Zhao, Y. Hu, *The Scientific World Journal* **2014**, 2014, 847107, doi:10.1155/2014/847107.
- [6] M. Nicksair, C.D. Martin, *Rock Mech. Rock Eng.* **2014**, 47, 1165, doi: 10.1007/s00603-013-0451-2.
- [7] G. Rong, G. Liu, D. Hou, et al., *The Scientific World Journal* **2013**, 2013, 589215, doi:10.1155/2013/589215.
- [8] O. Alm, L.-L., Jaktlund, Kuo, S. *Physics of the Earth and Planetary Interiors* **1985**, 40, 161, doi: 10.1016/0031-9201(85)90127-X.
- [9] Y.H. Hatzor, A. Zur, Y. Mimran, *Tectonophysics* **1997**, 281, 141, doi: 10.1016/S0040-1951(97)00073-5.
- [10] L.J.L. Beugelsdijk, C.J. de Pater, K. Kato, Proc. *SPE Asia Pacific Conference on Integrated Modelling for Asset Management*, Yokohama, Japan, 25-26 April **2000**, doi: 10.2118/59419-MS.
- [11] L. Jing, *Int. J. of Rock Mech. and Min. Sci.* **2003**, 40, 283, doi: 10.1016/S1365-1609(03)00013-3.
- [12] M.W. McClure, R.N. Horne, “Discrete Fracture Network Modeling of Hydraulic Stimulation – Coupling Flow and Geomechanics,” in *Springer Briefs in Earth Sciences* **2013**.
- [13] Lisjak, G. Grasselli, *J. of Rock Mech. and Geotech. Eng.* **2014**, 6, 301, doi: 10.1016/j.jrmge.2013.12.007.
- [14] D.O. Potyondy, Proc. *7th Asian Rock Mech. Symp.*, Seoul, South Korea, 15-19 October **2012**, 73.
- [15] Itasca Consulting Group Inc., “UDEEC Universal Distinct Element Code User’s Guide,” Minneapolis, MS, USA **2011**.
- [16] Itasca Consulting Group Inc., “3DEC 3 Dimensional Distinct Element Code User’s Guide,” Minneapolis, MS, USA **2013**.

- [17] Itasca Consulting Group Inc., “PFC2D Particle Flow Code in 2 Dimensions User’s Guide,” Minneapolis, MS, USA **2008a**.
- [18] Itasca Consulting Group Inc., “PFC3D Particle Flow Code in 3 Dimensions User’s Guide,” Minneapolis, MS, USA **2008b**.
- [19] Riahi, B. Damjanac, Proc. *38th Workshop on Geothermal Reservoir Engineering*, Stanford University, Stanford, CA, USA, February 11-13 **2013**.
- [20] Riahi, B. Damjanac, J. Furtney, Proc. *39th Workshop on Geothermal Reservoir Engineering*, Stanford University, Stanford, CA, USA 24-26 February **2014**.
- [21] J.F. Hazzard, R.P. Young, S.J. Oates, Proc. *5th North American Rock Mech. Symp., Mining and Tunnel Innovation and Opportunity*, Toronto, Ontario, Canada, 7-10 July **2002**, 1023.
- [22] J.S. Yoon, A. Zang, O. Stephansson, Proc. *38th Workshop on Geothermal Reservoir Engineering*, Stanford University, Stanford, CA, 11–13 February **2013**.
- [23] J.S. Yoon, A. Zang, O. Stephansson, *Geothermics* **2014**, 52, 165, doi: 10.1016/j.geothermics.2014.01.009.
- [24] P.A. Cundall, *Geotech. Eng.* **2001**, 149, 41, doi: 10.1680/geng.2001.149.1.41.
- [25] J.S. Yoon, *Int. J. of Rock Mech. & Min. Sci.* **2007**, 44, 871, doi: 10.1016/j.ijrmms.2007.01.004.
- [26] D.O. Potyondy, J.F. Hazzard, Proc. *1st Int. FLAC/DEM Symp.*, Minneapolis, MS, USA, 25–27 August **2008**.
- [27] N. Cho, C.D. Martin, D.C. Segro, *Int. J. of Rock Mech. and Min. Sci.* **2007**, 44, 997, doi: 10.1016/j.ijrmms.2007.02.002.
- [28] J.S. Yoon, A. Zang, O. Stephansson, *Int. J. of Rock Mech. & Min. Sci.* **2012**, 49, 68, doi: 10.1016/j.ijrmms.2011.11.004.
- [29] S. Mosher S, R.L. Berger, D.E. Anderson, *Rock Mech.* **1975**, 7, 167, doi: 10.1007/BF01246723.
- [30] N. Erarsalan, D.J. Williams, *Rock Mech. and Rock Eng.* **2012**, 45, 327, doi: 10.1007/s00603-011-0209-7.
- [31] D.O. Potyondy, P.A. Cundall, *Int. J. of Rock Mech. & Min. Sci.* **2004**, 41, 1329, doi: 10.1016/j.ijrmms.2004.09.011.
- [32] D. Mas Ivars, D.O. Potyondy, M. Pierce, et al., Proc. *8th World Congress on Computational Mechanics/5th European Congress on Computational Methods in Applied Sciences and Engineering*, Venice, Italy, 30 June–5 July **2008**.
- [33] D.O. Potyondy, Proc. *4th Int. Conf. on Discrete Element Methods*, Brisbane, Australia, 27–29 August **2007**.
- [34] N. Bahrani, B. Valley, P.K. Kaiser, et al., Proc. *45th US Rock Mech. Symp.*, San Francisco, CA, USA, 26–29 June **2011**.
- [35] R.P. Bewick, P.K. Kaiser, W.F. Bawden, et al., *Rock Mech. Rock Eng.* **2013a**, 47, 1647, doi: 10.1007/s00603-013-0490-8.

- [36] R.P. Bewick, P.K. Kaiser, W.F. Bawden, *Rock Mech. Rock Eng.* **2013b**, 47, 1673, doi: 10.1007/s00603-013-0494-4.
- [37] N. Bahrani, P.K. Kaiser, B. Valley, *Int. J. of Rock Mech. & Min. Sci.* **2014**, 71, 117, doi: 10.1016/j.ijrmms.2014.07.005.
- [38] N. Bahrani, D.O. Potyondy, M. Pierce, Proc. 21st Canadian Rock Mech. Symp., Edmonton, Alberta, Canada, 5–9 May **2012**.
- [39] H. Lan, C.D. Martin, B. Hu, *J. of Geophysical Research* **2010**, 115, B01201, doi: 10.1029/2009JB006496.
- [40] D.O. Potyondy, Proc. *Rock Mech. in the Nordic Countries*, Kongsberg, Norway, 9–12 June **2010a**.
- [41] D.O. Potyondy, *Technical Memorandum*, Itasca Consulting Group Inc., Minneapolis, MS, USA, May 28 **2010b**.
- [42] D.O. Potyondy, *Technical Memorandum*, Itasca Consulting Group Inc., Minneapolis, MS, USA, 28 May **2010c**.
- [43] T. Xin, “Hydro-Mechanical Coupled Behaviour of Brittle Rocks – Laboratory Experiments and Numerical Simulations,” *Dissertation*, TU Bergakademie Freiberg, Germany **2013**.
- [44] Zang, *Scientific Technical Report STR97/19* **1997**, DOI: 10.2312/GFZ.b103-97192.
- [45] Zang, S. Stanchits, G. Dresen, “Acoustic Emission Controlled Triaxial Rock Fracture and Friction tests,” In: Dyskin, A.V., Hu, X. & Sahouryeh, E. (eds.), *Structural Integrity and Fracture* **2002**, Swets & Zeitlinger, Lisse, 289.
- [46] Zang, F.C. Wagner, S. Stanchits, et al., *J. of Geophysical Research* **2000**, 105, 651, doi: 10.1029/2000JB900239.
- [47] Zang, J.S. Yoon, O. Stephansson, et al., *Geophys. J. Int.* **2013**, 195, 1282, doi: 10.1093/gji/ggt301.
- [48] M.C. Villeneuve, M.S. Diederichs, P.K. Kaiser, et al., Proc. 3rd CANUS Rock Mechanics Symposium, Toronto, Ontario, Canada, May **2009**.
- [49] G. Simmons, H. Wang, “Single Crystal Elastic Constants and Calculated Aggregate Properties: A Handbook,” in *The M.I.T. Press*, Cambridge, London **1971**.
- [50] W. Chen, H. Konietzky, *Tectonophysics* **2014**, 633, 164, doi: 10.1016/j.tecto.2014.06.033.
- [51] A. Togrul, I.H. Zarif, *Eng. Geology* **1999**, 51, 303, doi: 10.1016/S0013-7952(98)00071-4.
- [52] A. Zang, J.S. Yoon, S. Jeon, O. Stephansson, Proc. 18th European Conference on Fracture – ECF, Dresden, Germany, 30 August–3 September **2010**.
- [53] G.A. Savanick, D.I. Johnson, *Int. J. Rock Mech. Min. Sci. & Geomech. Abstr.* **1974**, 11, 173, doi: 10.1016/0148-9062(74)90884-5.

CHAPTER 7: A GRAIN BASED MODELING STUDY OF FRACTURE BRANCHING DURING COMPRESSION TESTS IN GRANITES

A version of this chapter was accepted for publication in *International Journal of Rock Mechanics and Mining Sciences*.

Macroscopic fracture and microscopic crack patterns resulting from compression tests change according to confining pressure and microscopic rock properties such as mineralogy and mineral size. However, a proper correlation between these parameters is missing. Since fracture development in granites are of major interest for different kinds of engineering applications and studies on fracture growth mechanism at micro (mineral) scale are limited, attention was given to this type of rock in this paper. Previous observation indicated that the grain-based modeling (GBM) approach may be a suitable numerical tool to obtain a further insight into fracture development and growth processes at the micro scale. The aim of this study is to clarify which parameters used in GBMs systematically influence fracture patterns resulting from compression tests.

In a previous study we showed the calibration of Aue Granite and a sensitivity analysis of mineral size and random distribution of minerals and particles and their influence on elastic properties, strength and fracture types. In this study the same calibrated model is used to further evaluate the influence of these parameters as well as the particle, parallel-bond, and smooth joint properties of the model on the resulting fracture patterns. It was found that complex crack networks always develop in heterogeneous GBMs and crack network complexity increases with increasing heterogeneity. While each of the particles, parallel bond, and smooth joint properties govern the development of a specific crack type, no obvious relations between these properties and the total number of cracks and the resulting crack network complexity were found.

7.1 INTRODUCTION

Understanding the hydraulic fracturing process in granitic rocks is critical for the development of enhanced geothermal systems (EGS) [1]. One major factor for the success of EGS projects in these environments is the ability to create complex (branched) fracture networks with a high enough overall fracture network permeability (to allow the production of sufficient fluid flow rates) and total fracture surface area (heat exchange area), but at the same time low enough single fracture permeability to prevent early breakthrough of the cold water front from the injection well(s) at the production well(s).

Although a single fracture can already follow a complex (irregular) path (e.g. due to interaction with discontinuities in the rock and the stress field), one also has to focus on the complexity of a whole fracture network and its dependency on the applied conditions and existing characteristics of the rock. Besides other measures, this fracture network complexity is considered as the number of individual fractures that build up a fracture network. In this study, the amounts and types of individual cracks and qualitative fracture patterns are considered.

The development of complex fracture patterns was observed in different rock types at scales from micrometers (e.g. grain crushing) [2] over hundreds of meters (e.g. hydraulic fracturing) [3] to kilometers (e.g. mid-oceanic ridges) [4]. Ren et al. [5] provided a review of factors and mechanisms of complex fracture development in shales. Hofmann et al. [6] compared complex fracture development in shales and granite at macro scale.

Even though hydraulic fracturing treatments are still often assumed to result in simple shaped bi-wing fractures, early mineback experiments of hydraulic fracturing treatments (direct fracture examination through excavation of the rock) already led to the conclusion that even in homogeneous formations fractures are more complex [3]. Besides direct observations in neighboring wells [12], microseismicity [7-11], tilt mapping [7,12], treatment pressure analysis [7,12], production data [12], and reservoir modeling [13] from hydraulic fracturing treatments in many geological environments also support the observation of complex fracture network development at macro scale. The most important natural factors triggering hydraulic fracture complexity were found to be discontinuities (joints, faults, bedding planes) and heterogeneities within the rock mass [3] in conjunction with the in-situ stress field [14]. Environments where

complex fracture networks may be formed include shale formations such as the Barnett shale [11,12] and granitic basement rock [13].

Since field scale data is very limited and mostly non-unique, this study focusses on laboratory (micro) scale. To be able to draw conclusions from the fracture complexity resulting from laboratory tests to the field scale, the following two assumptions are made: (1) micro scale grain boundaries of granitic laboratory specimens are considered to represent pre-existing discontinuities (fracture networks), and (2) the grains represent the intact rock mass. Even though extensive experimental laboratory and numerical studies have been performed to investigate tensile, compressive, and shear failure processes in granitic rocks, little of the data was actually used to study the influence of the mineralogy on fracture complexity.

The grain-based modeling (GBM) approach [15] is used to study these problems. In an earlier study, a GBM for Aue granite was calibrated and investigated the influence of mineral size and random distribution of minerals and particles, which makes up the minerals on elastic properties, strength, and amounts and types of micro cracks during compression tests with 0.1 – 40 MPa confining pressure [16]. The same calibrated model is used in this study. The results from the previous study are re-interpreted in terms of fracture growth and the current study additionally adds an investigation of the mineralogy, mineral properties, and mineral boundary properties on the development of specific crack types and fracture patterns.

7.2 CALIBRATED PFC2D GRAIN-BASED MODEL OF AUE GRANITE

An already calibrated GBM was used to investigate the effects of GBM model parameters on crack patterns resulting from compression tests. More details such as the calibration procedure can be found in Hofmann et al. [16]. Details about the discrete element Particle Flow Code 2D (PFC2D) are given elsewhere [17]. A segment from the calibrated model (**Figure 95**) shows the composition of the GBM. Circular particles are overlaid on the grain structure consisting of three different grain types. The particles within the grains are bonded together by parallel-bonds [18], which may fail in tensile or shear mode. Each grain type has different particle and smooth joint properties. Grain boundaries are represented by smooth joint contacts, which may also fail in

tensile or shear mode and are yet described by another set of parameters. A description of the smooth joint contact logic is given by Mas Ivars et al. [19].

Table 37: Calibrated micro-parameters for the Aue granite [16]. These parameters were used for the base case model.

Micro-parameter	Value			
Micro-properties of the minerals	Qz	Plagio	Ortho	Other
Minimum particle radius (mm)	0.2	0.2	0.2	0.2
Particle-size ratio (R_{\max}/R_{\min}) (-)	1.66	1.66	1.66	1.66
Particle-particle contact modulus (GPa)	49	39	29	19
Contact normal to shear stiffness ratio (-)	1.0	2.0	2.0	1.5
Particle friction coefficient (-)	1.2	1.2	1.2	1.2
Particle density (kg/m ³)	2650	2600	2600	2850
PB radius multiplier (-)	1	1	1	1
PB modulus (GPa)	49	39	29	19
PB normal to shear stiffness ratio (-)	1.0	2.0	2.0	1.5
PB tensile strength (mean) (MPa)	610	570	570	540
PB tensile strength (std. dev.) (MPa)	0	0	0	0
PB cohesion (mean) (MPa)	310	300	300	250
PB cohesion (std. dev.) (MPa)	0	0	0	0
PB friction angle (°)	80	80	80	80
Micro-properties of the mineral boundaries (smooth joint contacts)				
SJ contact normal stiffness factor (-)	0.6			
SJ contact shear stiffness factor (-)	0.9			
SJ bond tensile strength (MPa)	9			
SJ bond cohesion (MPa)	300			
SJ bond friction angle (°)	80			
SJ bond friction coefficient (-)	1.2			

The calibrated suite of parameters of the model is summarized in **Table 37**. **Table 38** shows the good agreement between strengths and elastic parameters of the laboratory tests and the

numerical model. Photographs of Aue granite samples and the GBM model representation are shown in Hofmann et al. [16]. Note that the physical model size was 10 cm x 5 cm and the numerical model size is only 5 cm x 2.5 cm to reduce computational time while no significant difference in the model results were observed [16]. The mineral content and sizes of Aue granite are as follows: 30% quartz ($d=1.45 \pm 0.35$ mm), 40% plagioclase ($d=1.35 \pm 0.45$ mm), 20% orthoclase ($d=1.35 \pm 0.45$ mm) and 10% mica ($d=1.20 \pm 0.30$ mm) [20-22].

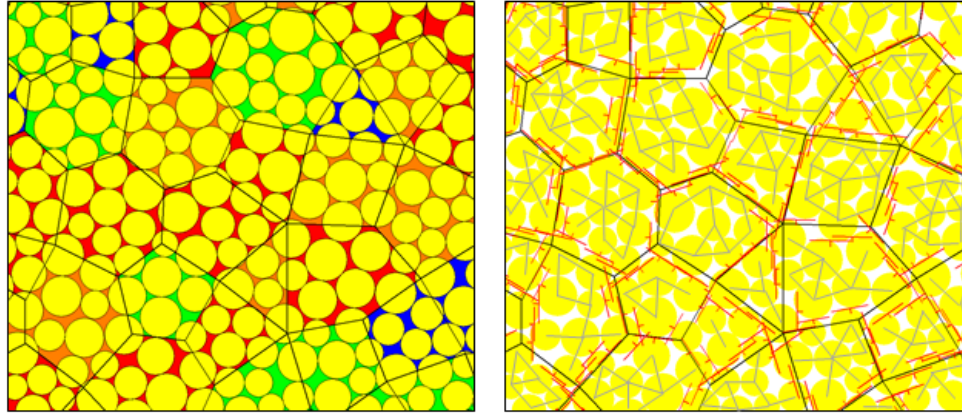


Figure 95: Bonded particles (yellow) overlaid on the grain structure (left) and parallel bonds (grey) between particles representing the intact minerals and smooth joint contacts (red) representing the grain interfaces (right).

Table 38: Laboratory test results compared to calibrated GBM results for Aue granite [16].

	T_o (MPa)	UCS (MPa)	$\sigma_{1@10MPa}$ (MPa)	$\sigma_{1@40MPa}$ (MPa)	E (GPa)	ν (-)
Laboratory [20,23]	8.0	134	256	456	48	0.19
GBM	8.3	134	258	457	47	0.21

7.3 MODELING PROCEDURE

This study focuses on the investigation of GBM model parameters that influence the crack patterns resulting from unconfined and confined compression tests with 10 MPa and 40 MPa

confining pressure. For a better interpretation of the simulation results, additionally the influence of the investigated parameters on strength and elastic parameters is deemed necessary.

First, the results of the sensitivity analysis in the previous study [16] were re-investigated to evaluate the influence of mineral size and distribution of minerals and particles on the resulting fracture patterns. The mineral micro properties (parallel-bond and particle properties) and the mineral boundary micro properties (smooth joint properties) of the calibrated model, which are given in **Table 38**, were then varied separately between $\pm 50\%$ of the values of the calibrated Aue granite model to investigate their sensitivity on the fracture patterns. Additionally, the influence of mineralogy on fracture development was investigated. Therefore, 17 different Scenarios were simulated with different mineral contents (quartz, alkali feldspar, and plagioclase). In the end, the effect of model size on the simulation results was studied to show whether it is possible to use a smaller model to decrease computational time. The model size was changed between 3.125 cm^2 ($1.25 \text{ cm} \times 2.5 \text{ cm}$) and 112.5 cm^2 ($7.5 \text{ cm} \times 15 \text{ cm}$).

7.4 RESULTS AND DISCUSSION

7.4.1 Calibrated Aue granite model

The temporal crack development of the calibrated Aue granite model during the confined compression test with 40 MPa confining pressure is shown in **Figure 96**. Grain boundary tensile cracks form from the beginning of the experiment because the grain boundary tensile strength was very low (9 MPa) compared to the tensile strength of grains (540 – 610 MPa) and the shear strength of grains and grain boundaries (250 - 310 MPa). The low value for the grain boundary tensile strength was needed to calibrate the model against Brazilian tensile test results. The high values of the grain tensile strengths and grain and grain boundary cohesions were needed to match the failure stresses at higher confining pressures.

With vertical stresses above the cohesion of most mineral grains (above 300 MPa), the number of grain shear cracks starts to increase significantly with the same slope as the grain boundary tensile cracks. Grain tensile cracks start to develop when the peak stress is reached because the relatively high local normal stresses required to break parallel bonds in the grains ($>540 \text{ MPa}$) are

not reached before large displacements occurs due to macroscopic shear failure. This is also why at the onset of the vertical stress decrease, the amounts of all crack types start to increase significantly. The amount of grain boundary shear cracks is the lowest because most grain boundaries fail in tensile mode (due to the low tensile strength) before local shear stresses are high enough to overcome the shear strength of grain boundaries.

Figure 97 shows the resulting crack patterns at a stress level of 50% of the failure stress after failure for different confining pressures (unconfined, $P_c=10$ MPa, $P_c=40$ MPa). Qualitatively, it can be seen that grain boundary tensile cracks dominated at all confining pressures because the grain boundary tensile strength of the calibrated model was relatively low compared to the tensile strength of the grains and the cohesion of the grains and grain boundaries. In the unconfined case, the least amount of grain shear, grain tensile, and grain boundary shear cracks developed because most tensile fractures open in the direction perpendicular to the axial load and there was no confining pressure to reduce the local tensile stress that was developing in the direction perpendicular to the axial load.

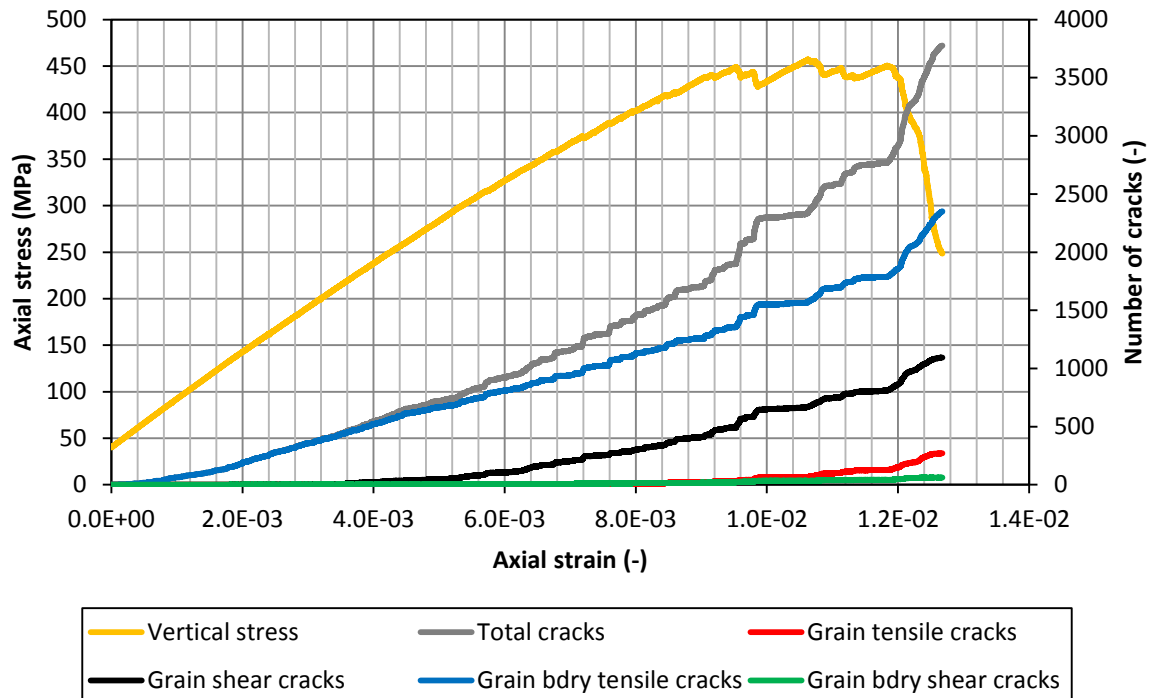


Figure 96: Evolution of vertical stress and amounts of micro cracks with 40 MPa confining pressure (calibrated Aue granite model).

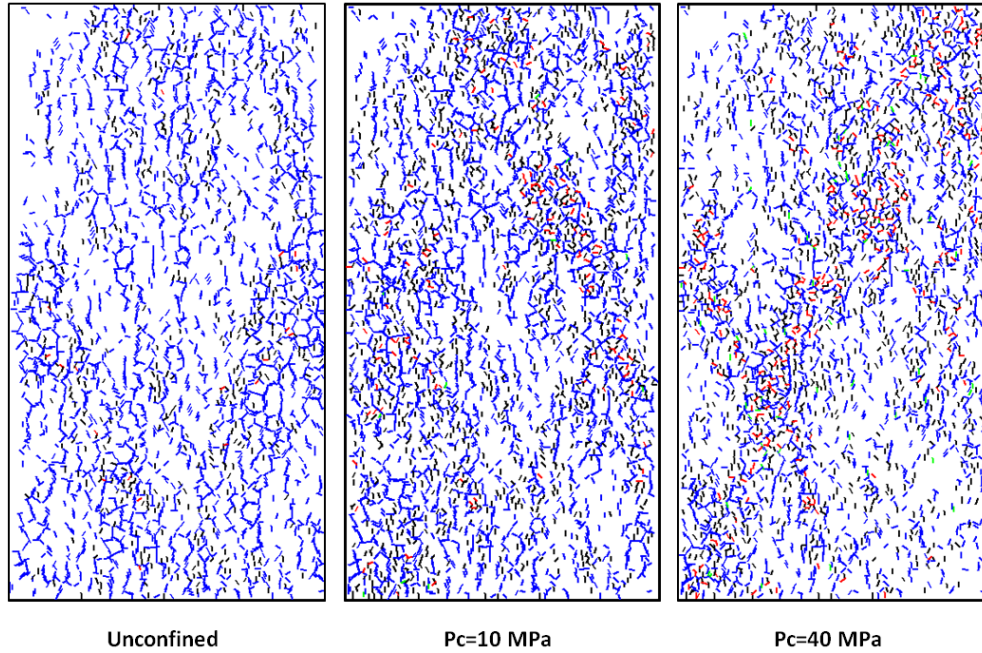


Figure 97: Fracture patterns resulting from compression tests with different confining pressures (P_c) at 50% below failure stress (blue = grain boundary tensile cracks, green = grain boundary shear cracks, red = grain tensile cracks, black = grain shear cracks).

With increasing confining pressure, these local tensile stresses were reduced. This is why higher local grain tensile, grain shear, and grain tensile stresses can develop and more grain tensile, grain shear cracks, and grain boundary shear cracks form. As a result of this, in the confined cases, macroscopic shear fractures with about 30° deviation from the vertical compression axis developed with a stronger crack accumulation in these shear bands with increasing confining pressure, whereas most of the cracks were aligned parallel to the axis of compression in the unconfined test. With increasing confining pressure, more deviated cracks were observed.

Overall, a low confining pressure led to a more even crack distribution of mainly grain boundary tensile cracks throughout the sample and higher confining pressures led to the formation of more distinct fracture paths that consisted of all crack types.

7.4.2 Mineral size and randomness of mineral and particle distribution

In the previous study [16], the average mineral diameter was changed between 0.5 and 3.0 mm. It was observed that the total number of cracks decreased with increasing grain diameter. While the

number of grain boundary tensile cracks decreased with increasing grain diameter, the number of grain shear cracks increased. Also, the ratio of tensile-to-shear cracks decreased with increasing grain size (**Figure 98**). With larger minerals, most grain boundaries still failed in tensile mode, but the amount of smooth joint contacts representing the grain boundaries was much lower compared to the much larger amount of the parallel bonds representing the grains. Since these parallel bonds had a higher tensile strength than the mineral boundaries, fewer cracks developed. Because the model was set up by more parallel bonds, which frequently fail in shear, the tensile-to-shear crack ratio decreased.

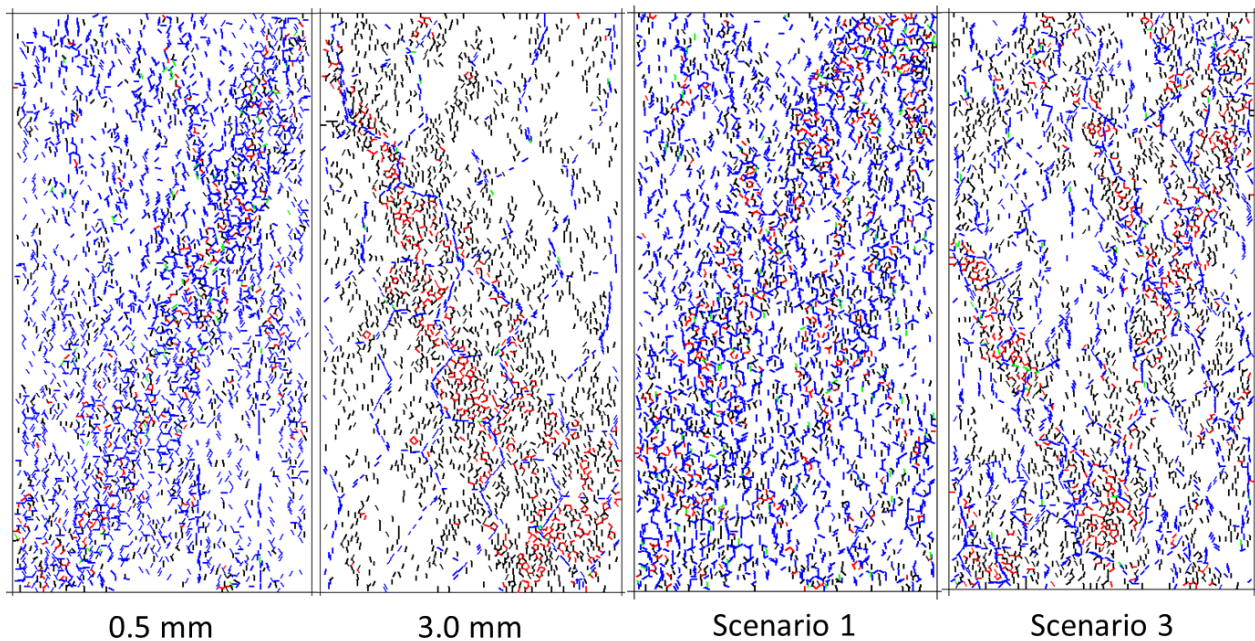


Figure 98: Influence of mineral size on crack patterns for different average mineral diameters (0.5 mm and 3 mm) and different mineral size distributions (Scenario 1 = all minerals have the same diameter of 1.35 mm and Scenario 3 = all minerals have different sizes: quartz = 5 ± 2.5 mm, plagioclase = 3 ± 1.5 mm, orthoclase = 2 ± 1 mm, mica = 0.5 ± 0.25 mm).

Additionally, three different Scenarios were modeled: In Scenario 1, all minerals had a uniform size; in Scenario 2 each mineral type had a different size, and; in Scenario 3, each mineral type had a different average size and a normal distribution. It was observed that in the more heterogeneous models (Scenarios 2 and 3), less total cracks were induced while the relative amounts of grain shear cracks were higher and the relative amounts of grain boundary tensile cracks were lower in these more heterogeneous models. It was also observed in Scenario 3 that the fractures form preferentially along agglomerations of smaller minerals and some larger

minerals were less fractured (**Figure 98**). As stated above, the reason for this behavior is the effect that the larger minerals have on crack development.

The seed numbers (random distribution) for the mineral distribution and the particle distribution of the model were changed seven times each. It was shown in the previous study that this had a relatively low influence on the strength envelope. The crack amounts, however, were significantly affected by both random distributions. For example, the amount of grain shear cracks varies between 88 and 313 if the seed number of the mineral distribution is changed and it varies between 110 and 530 if the seed number of the particle distribution is changed. It can be seen that the macroscopic rupture paths were different for each random distribution but the relative amounts of the different crack types stayed approximately the same (**Figure 99**). Grain boundary tensile cracks were distributed throughout the sample and grain tensile and shear cracks were localized at macroscopic rupture paths.

Overall, the effect of heterogeneity (mineral sizes, mineral distribution, and particle distribution) had a strong effect on the crack patterns and types and amounts of cracks due to the different local stress concentrations resulting from the different geometries.

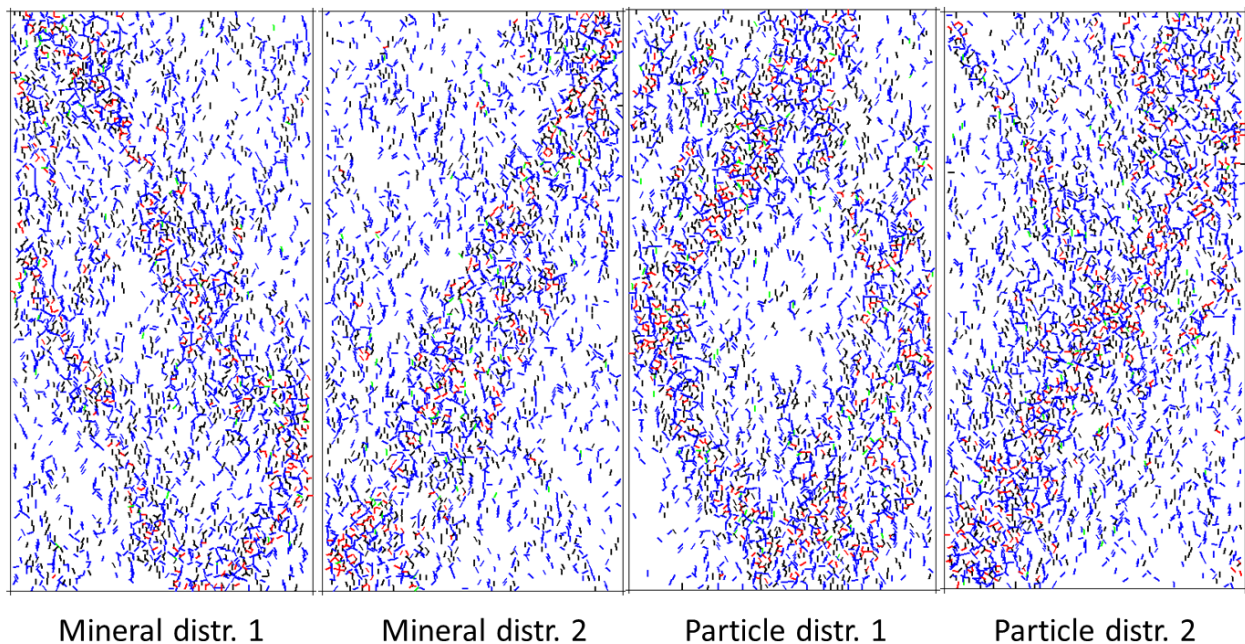


Figure 99: Influence of mineral and particle random distribution on crack pattern after a confined compression test with 40 MPa confining pressure. The macroscopic rupture paths change with mineral and particle distribution, but the relative amounts of each crack type stays the same.

7.4.3 Mineral and mineral boundary micro properties

The effect of mineral and mineral boundary micro properties on strength and amount, type and pattern of micro cracks was studied by increasing and decreasing the value of each micro property from its calibrated value (given in **Table 37**) by 50% while all other properties were kept constant. The parallel bond and smooth joint friction angles were only increased from 80° to 85° because 90° is the maximum angle, and since the standard deviations of normal strength and cohesion are 0 for the calibrated base model, this value could not be decreased by 50%.

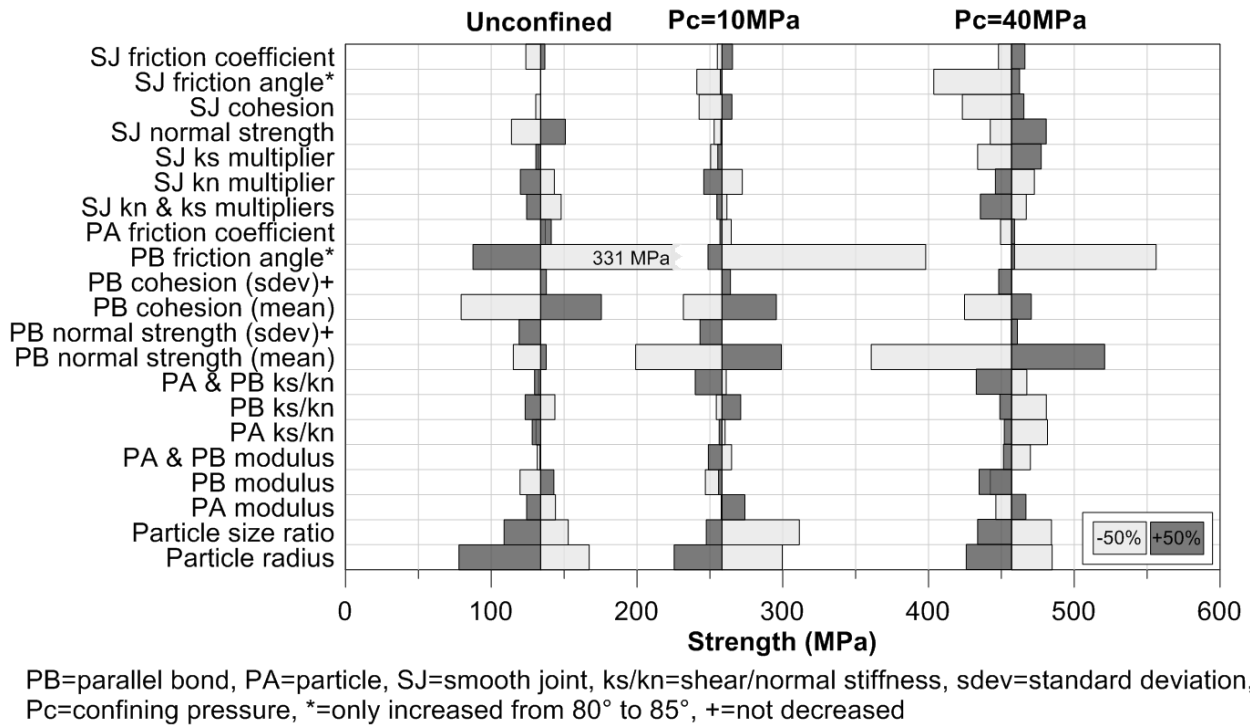


Figure 100: Influence of mineral and mineral boundary micro properties on unconfined (left) and confined strength with 10 MPa (center) and 40 MPa (right) confining pressure. Each property was set separately to a value of +50 % above (dark grey) and -50% below (light grey) the calibrated base case value.

Figure 100 shows that the UCS and the strengths with 10 MPa and 40 MPa confining pressure are obviously mostly influenced by the strength of the parallel bonds (PB normal strength, PB cohesion, and PB friction angle) and the smooth joints (SJ normal strength, SJ cohesion, and SJ friction angle). Other important parameters are the discretization (particle radius and particle size ratio) and the stiffnesses (ratio between shear and normal stiffness and shear and normal stiffness

multipliers). Details about each parameter are discussed below together with their influence on crack development.

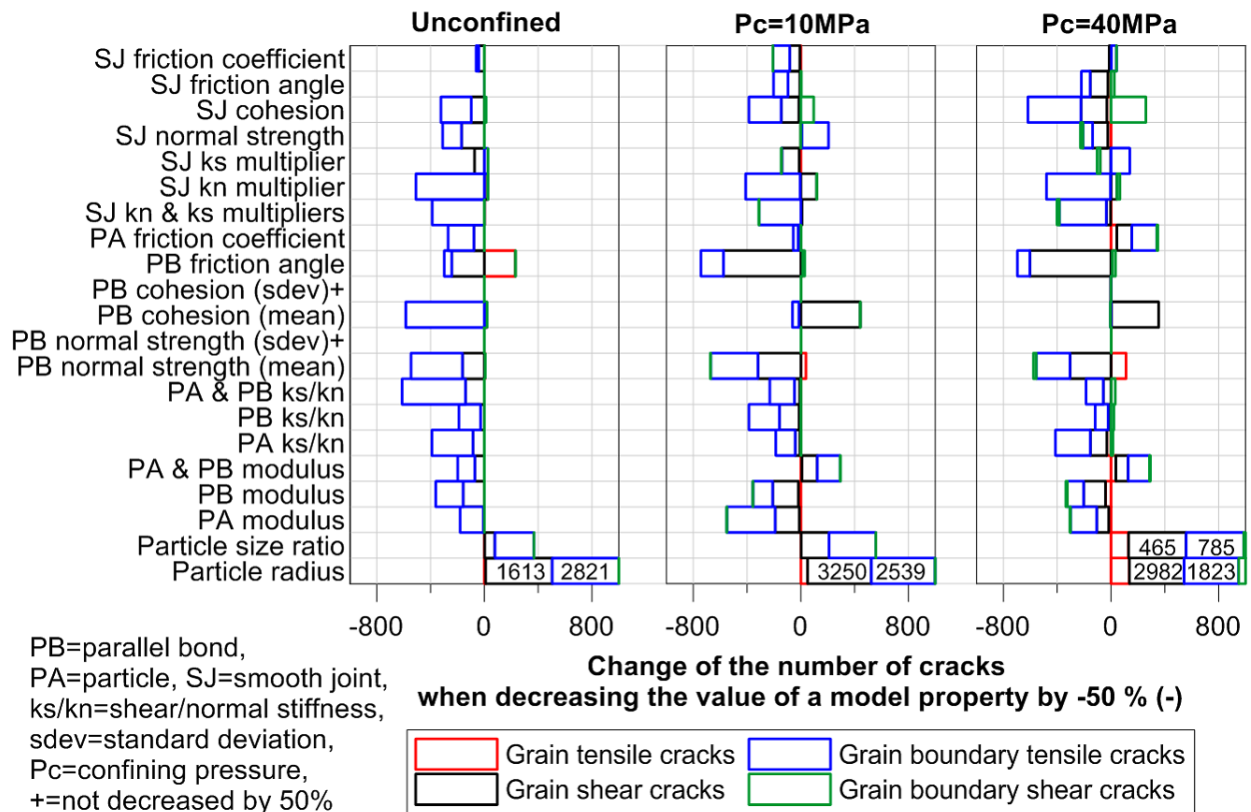


Figure 101: Influence of mineral and mineral boundary micro properties on amount and type of micro cracks at peak load during compression tests.

For each crack type, **Figures 101 and 102** show how many more or less micro cracks develop during an unconfined and a confined compression test with 10 MPa and 40 MPa confining pressure if a mineral or mineral boundary micro property is decreased by 50% (**Figure 101**) or increased by 50% (**Figure 102**). All of the investigated mineral and mineral boundary micro properties had a relatively strong influence on the number of cracks induced by the three tests. The effect of each parameter on crack development is discussed separately now.

The model discretization (minimum size and the ratio of maximum to minimum size of the particles that make up the minerals) had a very strong effect on compressive strength and number of micro cracks. Smaller particles increased the strength while larger particles and fewer particles within a mineral led to a strength reduction. This occurs because the same load applied to the

model was concentrated on fewer particle contacts, which led to higher local stress concentrations on these contacts.

The particle size also had the strongest effect on the amount of micro cracks and on the percentage of different types of micro cracks. More small particles resulted in more cracks and relatively more grain cracks as compared to grain boundary cracks because the amount of parallel bonds within the minerals increased more than the amount of smooth joint contacts between the minerals when the particle size is decreased, but the types of cracks that were dominant stayed the same. When the number of cracks was normalized to the number of contacts, the same behavior was observed for the relative number of cracks. The relative number of total cracks increased by 13% (UCS) to 19% ($P_c=10\text{MPa}$) if smaller particles were used and the relative number of total cracks was decreased by 3% ($P_c=10\text{MPa}$) to 6% ($P_c=40\text{MPa}$) if larger particles were used. This increase or decrease was most significant for the relative amounts of grain shear cracks and grain boundary tensile cracks.

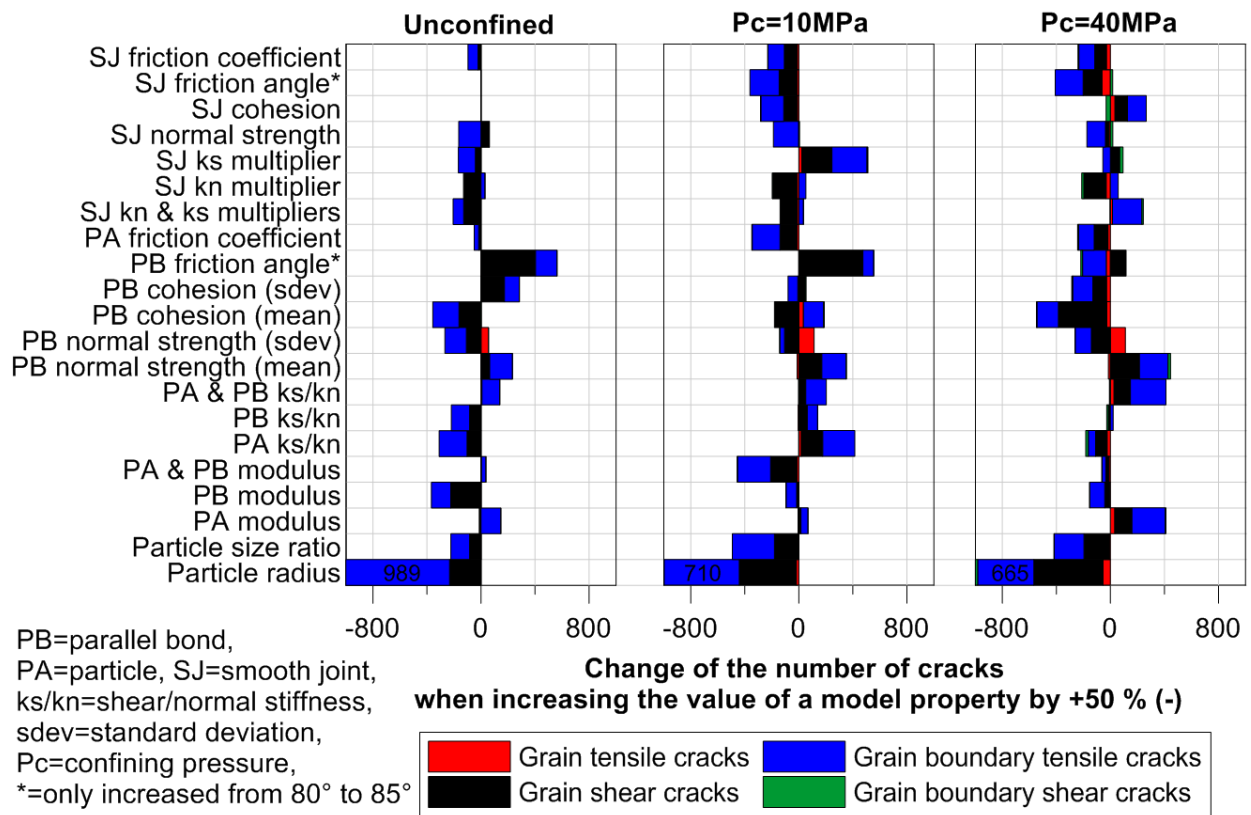


Figure 102: Influence of mineral and mineral boundary micro properties on amount and type of micro cracks at peak load during compression tests.

Overall, choosing the particle size for a model is very important since all other model properties need to be calibrated for this one particle distribution. Enough particles should be chosen that each mineral consists of multiple particles, but too many particles would significantly increase computational time. **Figure 103** shows the increased coarseness of the fracture pattern with increased particle size. Major observations like the concentration of grain cracks along macroscopic rupture paths, however, remained the same.

The mean parallel bond (PB) normal strength governs the tensile strength of the minerals; hence, an increase in the mean parallel bond normal strength increases the samples' compressive strengths. Due to the higher tensile strength, less grain tensile cracks develop if the PB normal strength is increased. At the same time, the numbers of all other crack types increase because higher local normal and shear stresses form when parallel bonds fail at higher local stresses. This can be observed quantitatively in **Figures 101 and 102** and qualitatively in the fracture pattern shown in **Figure 104**. An increase in the standard deviation of the parallel bond normal strength reduced the samples' compressive strength and the number of grain shear and grain boundary tensile cracks, while the number of grain tensile cracks was increased because more weak parallel bonds exist within the grains than without using a standard deviation for this value.

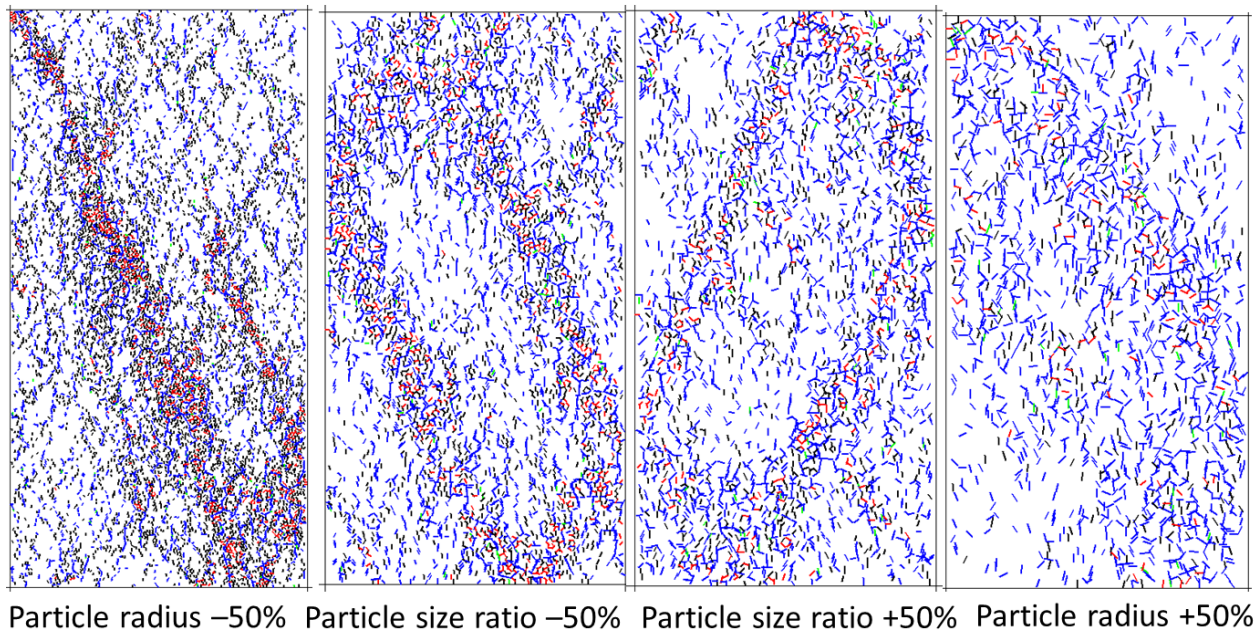


Figure 103: Fracture patterns resulting from a confined compression test with 40 MPa confining pressure for different particle sizes.

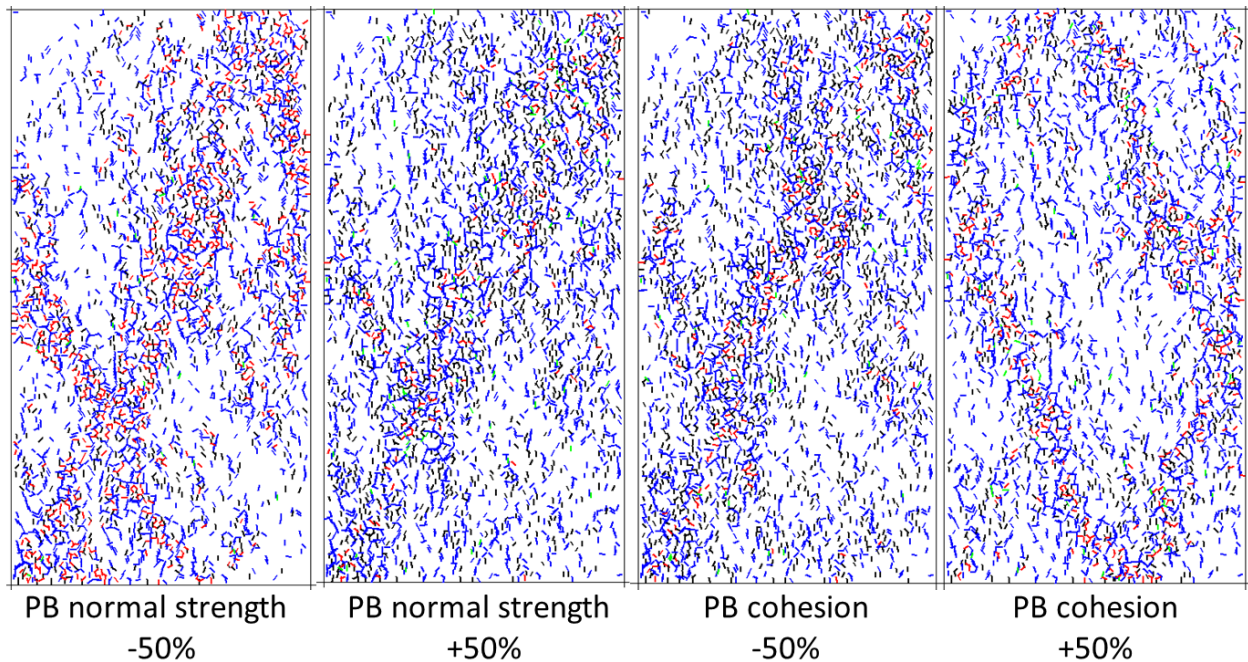


Figure 104: Fracture patterns resulting from confined compression tests with 40 MPa confining pressure for increased/decreased parallel bond normal strengths and parallel bond cohesions by 50%.

An increase in smooth joint normal strength leads to an increase in compressive strengths and less grain boundary tensile cracks because the smooth joint contacts (mineral boundaries) can resist a higher normal stress, pulling two particles apart. At the same time, more of the other crack types are able to form due to elevated local stresses.

The mean parallel bond cohesion and the parallel bond friction angle govern the shear strength of the minerals and the smooth joint cohesion, and the smooth joint friction angle governs the shear strength of the mineral boundaries. Therefore, an increase in cohesion leads to an increase in the macroscopic compressive strengths of the sample. With a lower SJ cohesion, more grain boundary shear cracks form because their shear strength is reduced. Because the critical stress levels for the other three crack types are reached in less particle contacts, the number of all other crack types is less when the SJ cohesion is reduced (**Figure 105**). For the UCS test, the number of cracks did not change when increasing the cohesion because, for the base case, no shear cracks developed in the UCS test. Analogues to the SJ cohesion, a lower PB cohesion leads to the development of more grain shear cracks.

An increase in the smooth joint friction angle increases the macroscopic compressive strengths due to a higher resistance of grain boundaries to shear stresses. A higher SJ friction angle

increases the slope of the Mohr-Coulomb failure envelope of the SJ contacts. Therefore, a higher SJ friction angle increases the shear strength of the grain boundaries more for higher confining stresses and a change in this parameter, therefore, has an increasing impact on confined compressive strength with increasing confinement. This is also why, with smaller friction angle, more grain boundary shear cracks and fewer cracks of the other three types develop. The unconfined compressive strength and the cracks that develop in the UCS test are not influenced by the smooth joint friction angle because, without confining pressure, only the cohesion defines the shear strength.

Figure 106 shows the increasing total number of cracks and, specifically, the development of more grain shear cracks with increasing PB friction angle. Therefore, an increase in the parallel bond friction angle reduces the compressive strength while this effect is less pronounced with increasing confinement.

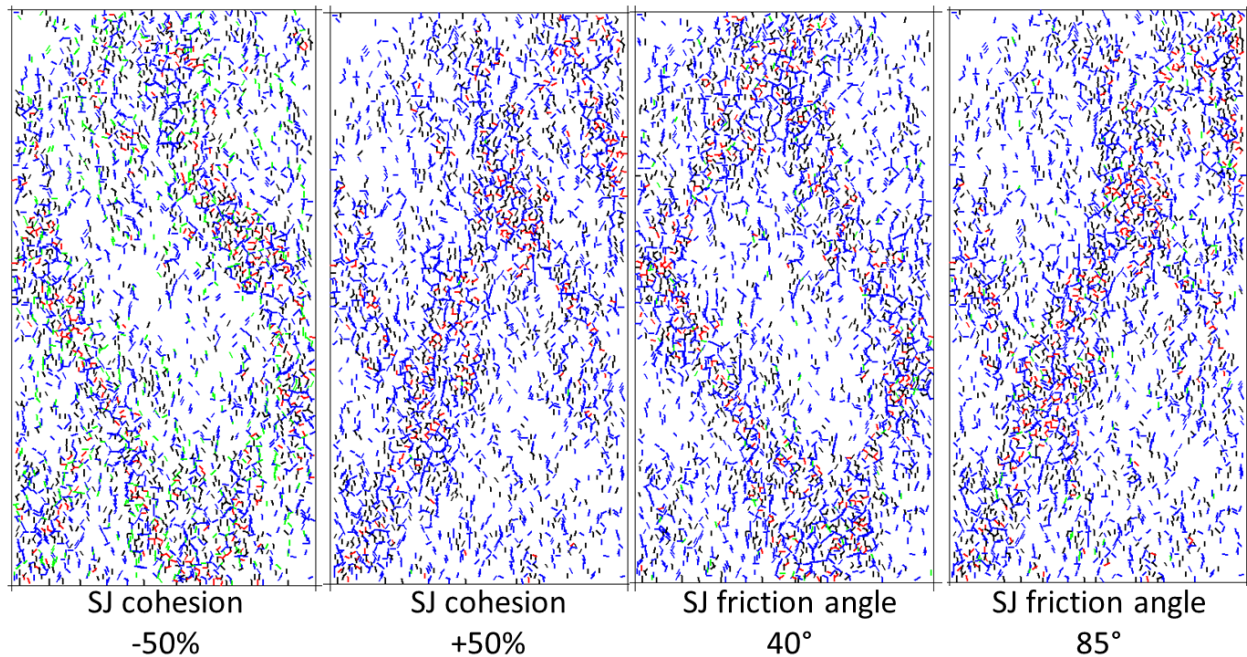


Figure 105: Fracture patterns resulting from confined compression tests with 40 MPa confining pressure for increased/decreased values of the smooth joint cohesion and friction angle.

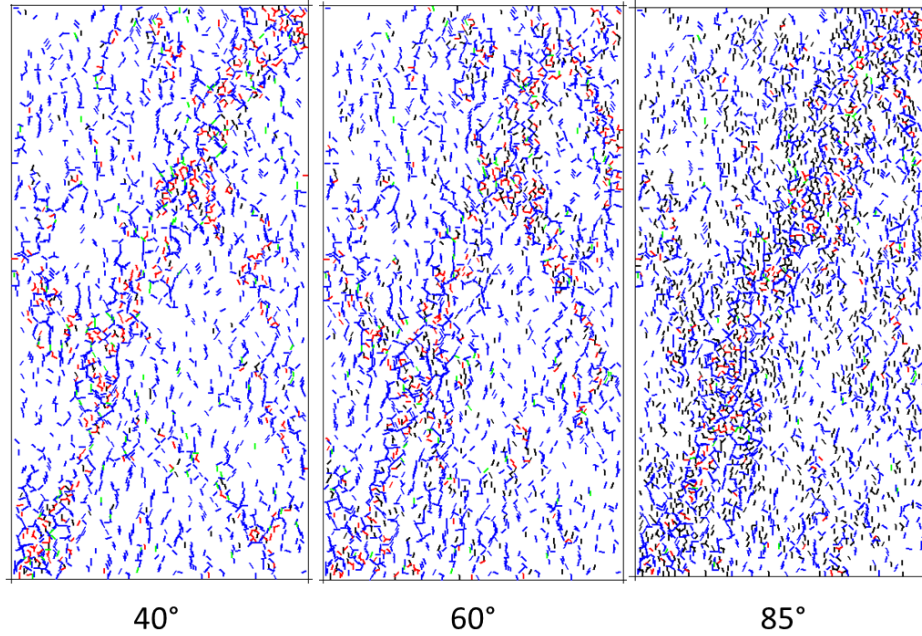


Figure 106: Fracture patterns resulting from confined compression tests with 40 MPa confining pressure for different parallel bond friction angles.

Except for the steeper slope of the Mohr-Coulomb failure envelope with increasing PB friction angle, this behavior is opposed to the behavior observed for the SJ friction angle and is also different from what is intuitively expected because, according to the Mohr-Coulomb failure criteria, higher PB friction angles lead to higher PB shear strengths. In an attempt to explain this behavior, it is important to keep in mind that parallel bonds are not idealized smooth joints with a specified roughness where particles are displaced along a straight line independent of the geometry of neighboring particles. When a parallel bond fails in shear, the particles connected by this contact have to move around neighboring particles. The higher friction angle and the resulting PB shear strength increase leads to more shear displacement when a particle breaks, which, in turn, induces higher local stresses to neighboring contacts. This results in the development of more cracks and hence the overall strength is reduced. On the other hand, lower PB friction angles lead to less shear displacements and, therefore, smaller local stresses, which increases the overall compressive strength of the material.

Normal and shear stiffnesses of smooth joints, parallel bonds, and particles influence the compressive strength and fracture development of a material because they relate the applied

stress to the resulting particle displacements. A higher stiffness means particles are displaced less when a certain stress is applied and vice versa.

A reduction of the ratio between shear and normal stiffness (k_s/k_n) of the particles and the parallel bonds leads to a lower shear stiffness compared to the normal stiffness. Lower shear stiffness leads to larger shear displacements due to the applied shear stress. This larger displacement increases the local stress concentrations at neighboring contacts before the parallel bond fails in shear, which, in turn, leads to failure of more surrounding contacts. A higher normal stiffness leads to less normal displacements due to normal stress before failure and, therefore, lower local stress concentrations, which leads to failure of less surrounding contacts. Overall, the compressive strength increases. Because of the complex geometry of the particle assembly, the number of cracks varied for different confining pressures. If particle and parallel bond stiffness ratios are increased simultaneously, the number of cracks increases, and if both ratios are increased separately, the number of cracks may increase or decrease depending on the confining pressure.

The normal and shear stiffness multipliers have a similar influence on strength and micro cracking. If the normal stiffness multiplier is increased, the normal displacement is less (mostly in lateral direction because most SJ contacts fail in tensile mode and open parallel to the lateral direction). Therefore, less additional confining stress is induced in the lateral direction due to tensile displacement of neighboring contacts and hence these SJ contacts can fail easier in tension and the compressive strength is reduced. This leads to the development of more grain boundary tensile cracks and a lower amount of all other crack types.

If the shear stiffness multiplier is reduced, then more shear displacement occurs due to the applied shear stress before a SJ contact fails in shear. Therefore, less grain boundary shear cracks develop, which increases the strength for experiments with confining pressure. The UCS is unaffected by this change because no grain boundary shear cracks developed in the base case model and hence the number of grain boundary shear cracks cannot be reduced for this case.

If SJ normal and shear stiffness multiplier are increased simultaneously less, normal and shear displacements develop on SJ contacts. Therefore more grain boundary tensile and shear cracks develop and the compressive strength is reduced.

The moduli of particles and parallel bonds govern the sample's Young's modulus. Poisson's ratio is also slightly increased if the parallel bond moduli of the minerals are lowered. Changing only particle or parallel bond modulus also slightly changes the compressive strength of the sample while a simultaneous change of both moduli does not significantly affect the compressive strength. Reduction in particle and/or PB modulus leads to the development of fewer cracks (grain shear and grain boundary tensile) in the unconfined compression test. In the confined compression tests, the number of cracks decreases when particle or PB moduli are reduced separately, but increases when both moduli are reduced together. When both moduli are increased together, the result is different for different confining pressures. If only the particle modulus is increased, more cracks develop, and when only the PB modulus is increased, fewer cracks develop. While overall a higher particle Young's modulus leads to the development of more cracks, the influence on strength and crack development is relatively small.

The particle and smooth joint friction coefficients have an insignificant effect on the simulation results considered in this study because it describes the frictional sliding of particles after their bonds are broken and, thus, mainly affect the post-peak behavior of the tests. An increase of SJ or PB friction coefficient reduces the number of all crack types because there is more resistance to particle displacement.

7.4.4 Mineralogy

Using the mineral size distribution of the calibrated Aue granite model but changing the mineralogy of the model, the influence of mineralogy on the simulation results was investigated. Due to the small difference in strength of the different minerals, the mineralogy had no significant influence on the rock strength (**Figure 107**). The influence of mineralogy on number and type of cracks at failure for the unconfined compression test is shown in **Figure 108**.

General trends that can be observed are: (1) a decrease of cracks with decreasing Quartz content, and (2) with the same Quartz content, a higher Na-Fsp content and lower K-Fsp content led to more cracks while the maximum number of cracks was reached when Na-Fsp and K-Fsp content were the same (Quartz Monzonite). No such trends can be identified for the confined

compression tests with 10 MPa and 40 MPa confining pressure. These values are within the deviation resulting from different random distributions of particles or minerals [16].

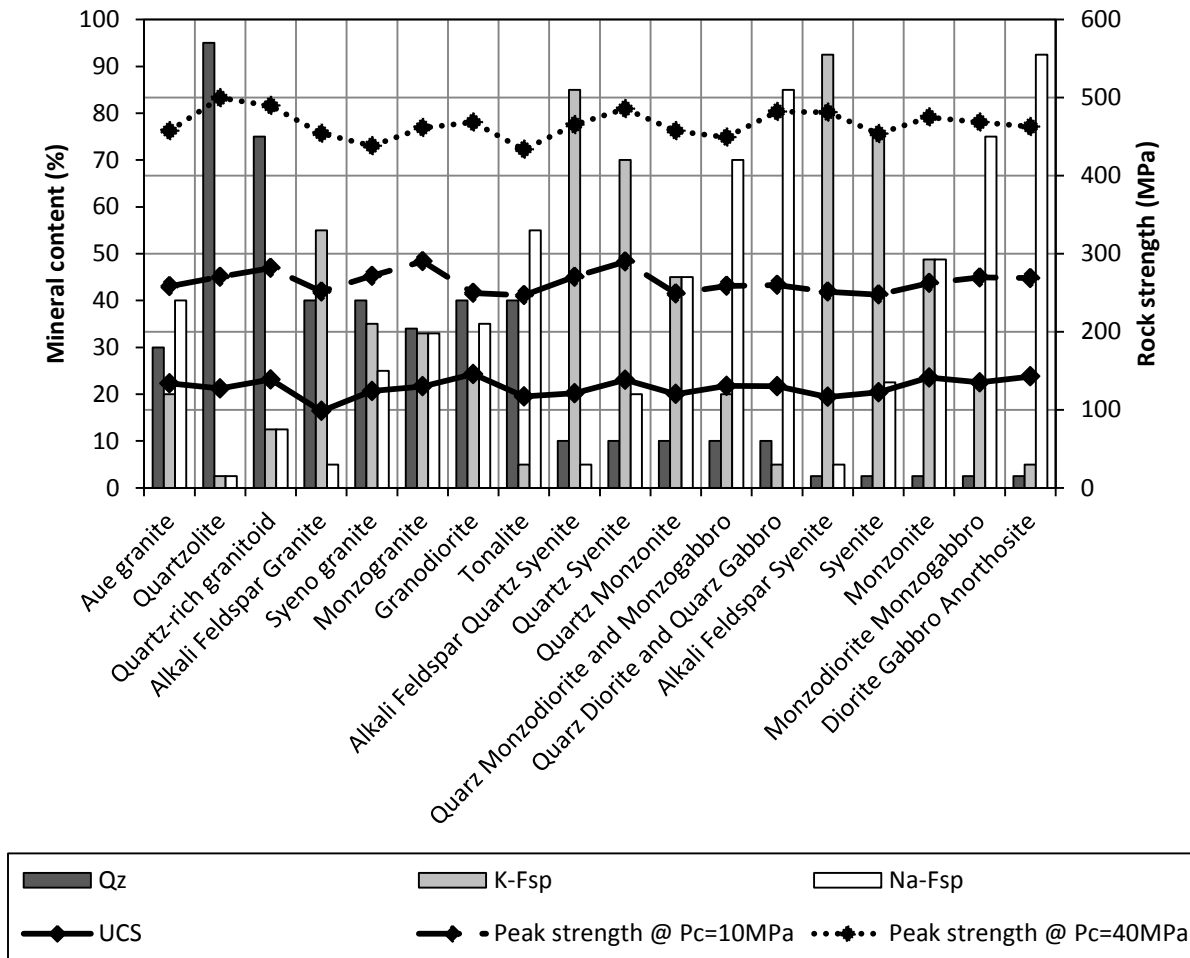


Figure 107: Influence of mineralogy on compressive strengths.

No significant trend in the number of total cracks was observed with increasing confining pressure. Only very few grain boundary shear cracks and grain tensile cracks were induced in all tests. The amount of grain boundary shear cracks and grain tensile cracks increased with increasing confining pressure. Overall, this shows that models consisting of minerals with similar strength values result in (1) similar macroscopic strengths and (2) similar amounts crack types. Fracture patterns are not shown here but are also similar for these cases.

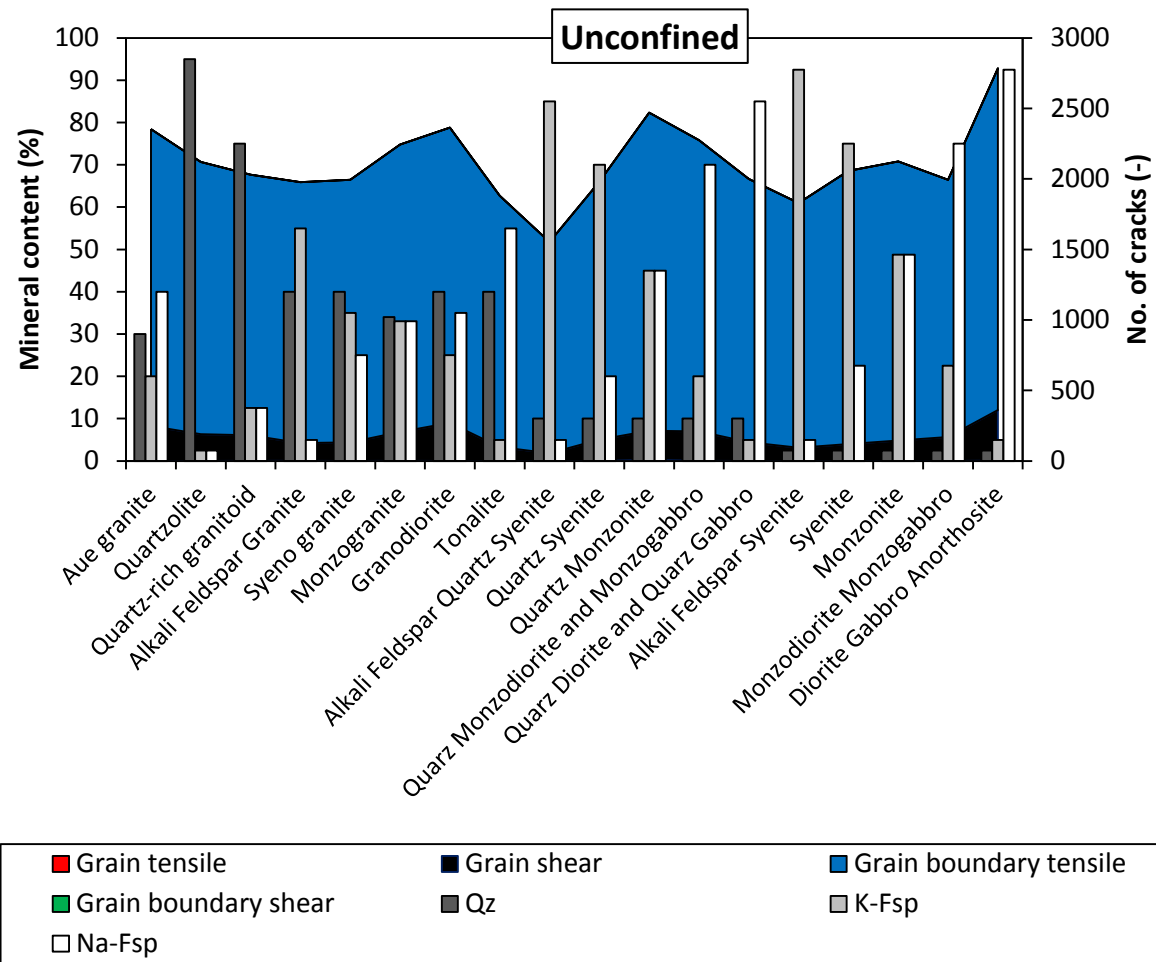


Figure 108: Influence of mineralogy on number and type of cracks at failure of an unconfined compression test.

7.4.5 Model Size

The measured strengths are not significantly affected by the model size; hence, the relative amount of each crack type is also independent of model size. The total number of cracks increases with increasing model size, which means that observations made in smaller GBMs will also be made in larger GBMs. Hence, model size can be reduced to reduce computational times and conclusions may be drawn for larger GBMs without actually executing the simulations. The fractured model after a confined compression test with 40 MPa confining pressure is shown in **Figure 109**.

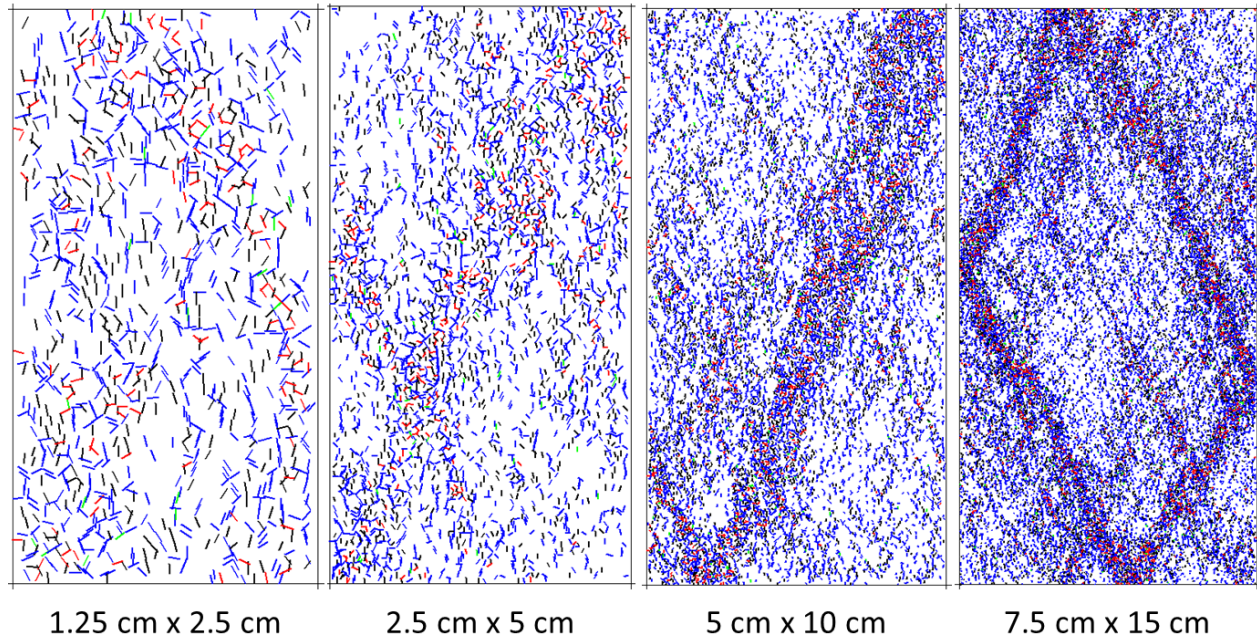


Figure 109: Crack patterns resulting from a confined compression test with 40 MPa confining pressure for different model sizes (width x height). Increasing the model size gives more distinct rupture paths, but the relative amounts of micro cracks are the same.

7.5 CONCLUSIONS

GBMs micro crack development during simulated compression tests was influenced by almost all of the investigated parameters. The most important parameters were particle size and distribution, mineral size and distribution, and grain and grain boundary strength properties (normal strength, cohesion, friction angle). Only the mineralogy had no significant influence on crack amounts, types, and distributions because the strength properties used for all mineral types were relatively close to each other. Additionally, it was found that increasing the model size did not change the relative amounts of each crack type.

Overall, fracture branching in GBMs was governed by heterogeneities and model discretization. While the GBM approach was able to reproduce the strong impact of heterogeneity of rock and rock masses on microscopic crack development and macroscopic failure, in heterogeneous GBMs, complex crack networks always developed when a sample was compressed.

Fracture complexity in the GBM increased with increasing heterogeneity. The influence of micro properties of grains and grain boundaries on the development of specific crack types was explained in detail. However, no obvious relation between any of these properties and the total number of cracks and the resulting fracture complexity were found. Depending on the shear and tensile strength of minerals and mineral boundaries, different amounts of grain tensile, grain shear, grain boundary tensile, and grain boundary shear cracks developed.

REFERENCES

- [1] Tester JW, Anderson BJ, Batchelor AS, et al. The future of geothermal energy impact of enhanced geothermal systems (EGS) on the United States in the 21st century. Massachusetts Institute of Technology 2006 [online]. www.1eere.energy.gov/geothermal/egs_technology_.html.
- [2] Zhao Y, Huang J, Wang R. Real-time SEM observations of the microfracturing process in rock during a compression test. *Int J Rock Mech Min Sci & Geomech Abstr* 1993; 30: 643.
- [3] Warpinski NR, Teufel LW. Influence of geologic discontinuities on hydraulic fracture propagation. *Journal of Petroleum Technology* 1987: 209.
- [4] Weiland CM, Macdonald KC, Grindlay NR. Ridge segmentation and the magnetic structure of the Southern Mid-Atlantic Ridge 26°S and 31°-35°S: Implications for magnetic processes at slow spreading centers. *Journal of Geophysical Research* 1996; 101: 8055.
- [5] Ren L, Zhao J, Hu Y. Hydraulic fracture extending into network in shale: Reviewing influence factors and their mechanism. *The Scientific World Journal* 2014: 847107.[http://doi: 10.1155/2014/847107](http://doi:10.1155/2014/847107).
- [6] Hofmann H, Babadagli T, Zimmermann G. Numerical simulation of complex fracture network development by hydraulic fracturing in naturally fractured ultratight formations. *Journal of Energy Resources Technology* 2014: 136. [http://doi: 10.1115/1.4028690](http://doi:10.1115/1.4028690).
- [7] Fisher MK, Wright CA, Davidson BM, et al. Integrating fracture mapping technologies to optimize stimulations in the Barnett shale. *Proc. SPE Annual Technical Conference and Exhibition, San Antonio, Texas, USA, 29 September – 2 October 2002; SPE 77441*.
- [8] Cipolla CL, Warpinski NR, Mayerhofer MJ, et al. The relationship between fracture complexity, reservoir properties, and fracture treatment design. *Proc. SPE Annual Technical Conference and Exhibition, Denver, Colorado, USA, 21-24 September 2008; SPE 115769*.
- [9] Warpinski NR, Mayerhofer MJ, Vincent MC, et al. Stimulating unconventional reservoirs: maximizing network growth while optimizing fracture conductivity. *Proc. SPE Unconventional Reservoirs Conference, February 2008; 237*.
- [10] Warpinski NR, Kramm RC, Heinze JR, et al. Comparison of single- and dual-array microseismic mapping techniques in the Barnett shale. *Proc. SPE Annual Technical Conference and Exhibition, Dallas, Texas, October 2005; SPE 95568*.
- [11] Maxwell SC, Urbancic TI, Steinsberger N, et al. Microseismic imaging of hydraulic fracture complexity in the Barnett shale. *Proc. SPE Annual Technical Conference and Exhibition October 2002: 965*.

- [12] Fisher MK, Wright CA, Davidson MB, et al. Integrating fracture mapping technologies to optimize stimulations in the Barnett shale. Proc. SPE Annual Technical Conference and Exhibition, San Antonio, Texas, USA, 29 September – 2 October 2002; SPE 77441.
- [13] Xu C, Dowd PA, Mohais R. Connectivity analysis of the Habanero enhanced geothermal system,” Proc. 37th Workshop on Geothermal Reservoir Engineering, Stanford, California, January 30 – 1 February 2012; SGP-TR-194.
- [14] Chen M, Zhou J, Jin Y, et al. Experimental study on fracturing features in naturally fractured reservoir. *Acta Petrolei Sinica* 2008: 431.
- [15] Potyondy DO. A grain-based model for rock: Approaching the true microstructure. Proc. Rock Mech. in the Nordic Countries, Kongsberg, Norway, 9–12 June 2010.
- [16] Hofmann H, Babadagli T, Yoon, JS, et al. A grain-based modeling study of mineralogical factors affecting strength, elastic behavior and micro fracture development during compression tests in granites, submitted to *J. Frac. Mech.* 2015.
- [17] Itasca Consulting Group Inc. PFC2D Particle Flow Code in 2 Dimensions User’s Guide. Minneapolis, MS, USA 2008.
- [18] Potyondy DO, Cundall PA. A bonded-particle model for rock. *Int. J. of Rock Mech. & Min. Sci.* 2004; 41: 1329–1364. <http://doi: 10.1016/j.ijrmms.2004.09.011>.
- [19] Mas Ivars D, Pierce ME, Darcel C, Reyes-Montes J, et al. The synthetic rock mass approach for jointed rock mass modeling. *Int. J. Rock Mech. & Min. Sci.* 2011; 48: 219-244.
- [20] Yoon JS, Zang A, Stephansson O. Simulating fracture and friction of Aue granite under confined asymmetric compressive test using clumped particle model. *Int. J. of Rock Mech. & Min. Sci.* 2012; 49: 68–83. <http://doi: 10.1016/j.ijrmms.2011.11.004>.
- [21] Zang A, Wagner FC, Stanchits S, et al. Fracture process zone in granite. *J. of Geophysical Research* 2000; 105: 651. doi: 10.1029/2000JB900239.
- [22] Zang A. Scientific Technical Report STR97/19 1997. <http://doi:10.2312/GFZ.b103-97192>.
- [23] Zang A, Stanchits S, Dresen G. Acoustic Emission Controlled Triaxial Rock Fracture and Friction tests. In: Dyskin AV, Hu X, Sahouryeh E, editors. *Structural Integrity and Fracture*: Swets & Zeitlinger; 2002, p. 289.

CHAPTER 8: CONTINUOUS MEASUREMENT OF TIME AND PRESSURE DEPENDENT FRACTURE PERMEABILITY OF ALIGNED AND DISPLACED TENSILE FRACTURES IN GRANITIC ROCKS DURING CYCLIC LOADING

A version of this chapter was submitted to *Geophysical Journal International*.

The pressure dependent fracture permeability of four granitic rock samples was determined in a triaxial test cell under hydrostatic loading conditions. Tensile fractures were generated in the cylindrical samples by Brazilian tests. Confining pressures were cycled twice between 2 MPa and 50 MPa. Permeability and strain responses were determined for one intact rock, for two samples with aligned fracture surfaces and for two samples with a shear displacement of 1 mm. Additionally, the fracture apertures were determined optically before and after testing and the fracture surfaces were scanned after testing. The results were compared to published data from fractured granitic and sedimentary rocks and to permeability requirements for fractures of enhanced geothermal systems in granitic basement rocks.

Intact rock permeability is below $1\text{e-}18\text{ m}^2$. It was found that without shear displacement the fracture permeability decreases logarithmically from initial values of about $1\text{e-}10\text{ m}^2$ at a constant confining pressure of only 2 MPa. However, with increasing confining pressure the sample permeability is still ten times larger than in intact rock. With shear displacement, the fracture permeability remains unchanged at $2\text{e-}9\text{ m}^2$ at constant confining pressure of 2 MPa and is reduced significantly less with increasing confining pressure.

In typical conventional and unconventional oil and gas reservoir rocks such as sandstones and shales, the aligned and displaced fracture permeability significantly decreases with increasing confining pressure and time if no proppants are used. To a lesser extent, this is also true for aligned fractures in granitic rock. Therefore, typically proppants need to be used to increase the

fracture conductivity in these rocks. Whereas in granitic rocks with displaced fracture surfaces, the fracture conductivity can be similar without the use of propping agents due to an effective self-propping effect.

The results of this study also lead to the conclusion that the development of complex fracture networks is a more promising concept for the development of an enhanced geothermal system (EGS) in granitic basement rock compared to the development of some large single fractures.

8.1 INTRODUCTION

For the utilization of geothermal energy, large amounts of fluids need to be circulated through a hot rock mass. While this is successfully done in conventional geothermal reservoirs, the major potential in geothermal energy development lies in the use of deep and hot but low permeable granitic basement rock (Tester et al. 2006) where fracture networks need to be hydraulically stimulated to achieve the desired flow rates. In these enhanced geothermal systems (EGS), fluid flows mainly through natural or induced fractures, and, therefore, the permeability of these fractures is the most crucial parameter governing the hydraulic and thermal performance of an EGS in granitic basement rock.

Fracture permeability and hydraulic aperture strongly depends on the rock (e.g. mineralogy) and fracture properties (e.g. fracture surface roughness) and the effective stresses acting on the fracture surfaces. Pressure dependent fracture permeability of granites has been studied over decades (Detournay 1980; Elliott & Brown 1988; Zhao & Brown 1992; Chen et al. 2000; Watanabe et al. 2008; Watanabe et al. 2009). The reported values vary depending on effective closure stress (Pyrak-Nolte & Morris 2000), sample size (Raven & Gale 1985), fracture type (Iwano & Einstein 1995), shear displacement (Lee & Cho 2002), number of pressure cycles (Gale 1982), and time (Morrow et al. 2001). In these tests the fractures were either natural (Hakami et al. 1996) or artificially created by different methods: saw cut (Iwano & Einstein 1995), tensile splitting using a wedge (Watanabe et al. 2011), splitting along preexisting veins (Chen et al. 2000), (modified) Brazilian tensile testing (Watanabe et al. 2008) and shear with different normal loads (Watanabe et al. 2009). The tests were performed with aligned fracture surfaces (Watanabe et al. 2008) and shear displacements from as low as 0.07 mm (Chen et al. 2000) up to 15 mm (Lee et al. 2002). Effective closure pressures mostly range between 0 MPa and 50 MPa, but some tests were performed up to 100 MPa (Watanabe et al. 2008, 2009). Additionally, fluid flow through fractures was visualized (Raimbay et al., 2014) and surface scanning measurements were performed (Develi & Babadagli 2015) to further characterize this process. Some pressure dependent permeability data is also available from in-situ tests (Pratt et al. 1977). To the knowledge of the authors, no pressure dependent fracture permeability measurements were performed on fractures in granitic rock using proppants.

Similar experimental schemes were applied to measure fracture permeabilities for oil and gas bearing sedimentary rocks (sandstones, limestones, shales) with proppants (Briggs et al. 2014; Zhang et al. 2014; Fredd et al. 2000) and without proppants (Fredd et al. 2000; Gutierrez et al. 2000; Cho et al. 2012; Briggs et al. 2014; Zhang et al. 2014; Haifeng et al. 2015). Fractures in sedimentary rocks were also tested for geothermal applications with proppants (Reinicke et al. 2013).

Major consistent findings from all these reported experiments may be summarized as follows:

- (1) With increasing effective closure stress, fracture permeability is reduced for all fracture types.
- (2) With increasing time, fracture permeability is reduced for all fracture types due to asperity degradation and gouge production (Morrow *et al.* 2001; Dempsey *et al.* 2013).
- (3) With increasing number of closure stress cycles, fracture permeability is reduced. At least 2 to 3 cycles are needed before hysteresis effects become negligible.
- (4) Saw-cut samples show the lowest permeability values. Aligned natural, tensile, and shear fractures tend to have a slightly higher permeability. Gale (1982) observed that induced fractures gave lower permeability than natural fractures.
- (5) Displaced fractures have a higher permeability than aligned fractures because of the self-propping effect.
- (6) A larger shear displacement leads to a higher fracture permeability. After a certain threshold value, the fracture permeability does not further increase with additional shear displacement (Watanabe *et al.* 2009; Lee & Cho 2002).
- (7) Dilation and gouge production are the two factors governing the hydraulic behavior of shear fractures. Shear failure erodes fracture surface asperities. Therefore, a displaced shear fracture has a lower fracture permeability than a manually displaced rough tensile fracture. This effect increases with increasing normal stress on the fracture plane during shearing (Watanabe *et al.* 2009; Lee & Cho 2002).
- (8) Adding proppants always increases the fracture permeability compared to fractures without proppants (if no significant proppant crushing or chemical effects occur).
- (9) Findings about the effect of sample size are inconsistent (Raven & Gale 1985). However, in-situ tests show similar permeability values as laboratory tests (Pratt *et al.* 1977).

More data is needed to evaluate and extend these results from earlier studies. The data can then be used to determine the feasibility of an EGS and to set up numerical models to obtain a deeper insight into the processes governing these systems. During the development and operation of an EGS, new fractures might be developing and existing fractures open and probably slip due to elevated pore pressure during stimulation and injection, while new and existing fractures tend to close again during production in the surrounding of the production wells. In addition to the effect of pore pressure, the stress shadow effect (Yoon et al. 2014) resulting from the opening of fractures may lead to the increase of normal stress on neighboring fractures.

In this study, the pressure dependent fracture permeability of four different granites was determined. In addition to the parameters studied in most of the experiments described above, the effect of cyclic loading was studied. Also, the fracture permeability was determined continuously and not only for single effective closure stress levels.

8.2 SAMPLE MATERIALS AND EXPERIMENTAL PROCEDURES

Permeability and strain response to cyclic changes in hydrostatic confining pressure (2–50 MPa) were measured on four different granitic rock samples. These samples were either intact, fractured with aligned fracture surfaces, or fractured with displaced fracture surfaces (**Figure 110**). Additionally, the time dependent permeability and strain behavior under a constant confining pressure of 2 and 50 MPa over the course of several hours was determined.

8.2.1 Sample materials

Four different granitic rocks were used as sample materials. Three of these rocks are granodiorites from outcrops in the Annabel Lake shear zone in Saskatchewan, Canada (Cholach *et al.* 2005). Additionally, a Sierra granite from a quarry in California was tested. An overview of some properties of the tested rocks is given in **Table 39**. Each sample was drilled to a cylinder of 10 cm in length and 5 cm in diameter. Finally, surface grinding was performed on both ends of the sample.

Table 39: Some properties of the four tested granitic rocks.

Sample ID	SG	34	31	32
Rock type	Sierra granite (“Sierra white”)	Granodioritic pluton	Granodioritic pluton	Granodioritic pluton
Origin	California, USA	Annabel Lake shear zone	Annabel Lake shear zone	Annabel Lake shear zone
Mineralogy	-	34.9% QZ, 52% PL, 8.2% BIO, 2.3% HBD ⁽³⁾	-	2.5% QZ, 61.8% PL, 27.3% HBD, 5.2% KF, 2.0% ACS ⁽³⁾
Tensile strength ⁽²⁾	11.7 MPa	12.7 MPa	15.7 MPa	13.5 MPa
Porosity	0.9% ⁽¹⁾	-	-	-
Permeability	1e-18 m ² ⁽¹⁾	<1e-18 m ² ⁽⁴⁾	-	-
Displacement	aligned	aligned, intact	1 mm	1 mm
Comments	Fracture faces initially connected	Fracture faces initially not connected	Test stopped at Pc=38 MPa due to leakage in jacket	Unexpected permeability jumps observed

⁽¹⁾Moore & Glaser (2007), ⁽²⁾derived from Brazilian tensile tests that were performed for fracture generation, ⁽³⁾Cholach *et al.* (2005), ⁽⁴⁾determined in this study; QZ: quartz, PL: plagioclase, BIO: biotite, HBD: hornblende, KF: K-feldspar, ACS: accessory

8.2.2 Fracture generation

Tensile fractures were induced at the center of intact samples along the axial sample direction. Fracture generation was achieved by Brazilian tensile testing. The test was performed with a constant displacement of 0.0003 mm/s. The slow displacement rate was needed to be able to create a single defined fracture in the sample and to avoid other sample disturbances. During the tests, the samples were kept in a heat-shrinkable tube to avoid any breakouts. The fracture surfaces of the Sierra Granite Sample remained stuck together whereas, for Sample 34, both sample halves were separated. Thus, the Sierra Granite sample had a significantly smaller initial fracture aperture compared to Sample 34.

Since the force was measured during the Brazilian tensile tests, the Brazilian tensile strength of all rocks was calculated and is given in **Table 41**.

8.2.3 Fracture displacement

A fracture displacement was achieved for Samples 31 and 32 by manually taking the two halves of the sample apart and placing them together with 1 mm displacement in axial direction. This displacement was maintained by putting two sheets of heat shrinking tube (0.5 mm thickness each) on top and bottom of the sample to fill the gap (**Figure 110**). The material was cut along the outer sample boundary and along the fracture. To make sure fluid flow in the fracture is not disturbed, the sheets were cut in half-moon shape on the fracture side. Additionally, holes were punched through the sheets to allow fluid flow through the rock matrix (**Figure 111, left**). Since the experiment with Sample 31 had to be stopped at an effective confining pressure of 38 MPa due to a hole developed in the shrink tube, a metal stripe was placed over the fracture contact with the surrounding wall in Sample 32 as shown in **Figure 111 (right)**.

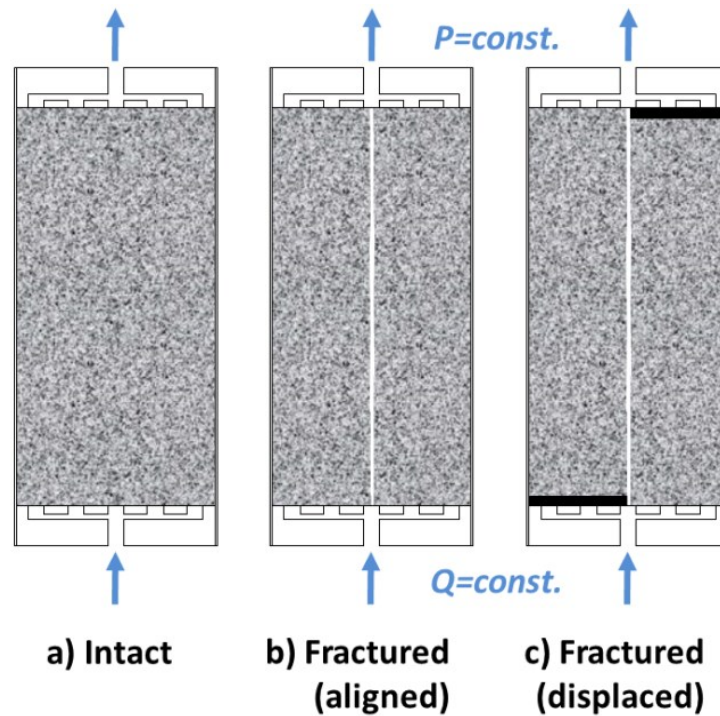


Figure 110: Intact (a), aligned fractured (b) and displaced fractured (c) samples were tested in the triaxial cell. A displacement of 1 mm was maintained by putting two layers of heat shrink tube (with 0.5 mm thickness each) on half of the samples cross-sections as indicated by the black bars.

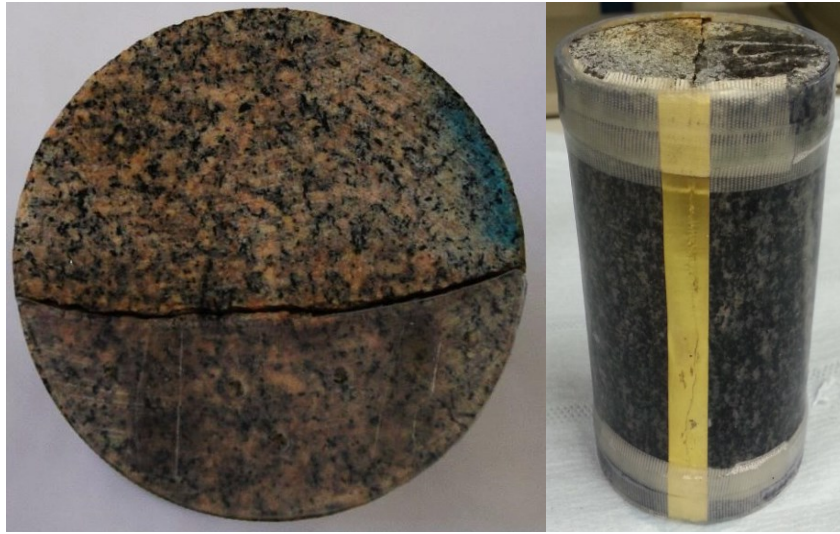


Figure 111: Top view of Sample 31 (left) and side view of Sample 34 (right).

8.2.4 Pressure dependent fracture permeability measurements

Before testing, all samples were cleaned in an ultra-sonic bath and dried in an oven at a temperature of 60°C for more than one day. The actual pressure dependent fracture permeability tests were performed at a temperature of 30°C in the triaxial test cell shown in **Figure 112**, which was connected to two Quizix pump systems. The pumps flow distilled water through the end caps on top and bottom of the sample and maintain the fluid pressure difference between upstream and downstream of the sample. During all tests, axial and lateral strain was measured with two axial strain gauges and one circumferential strain gauge.

The following testing procedure was used for all samples: (1) Before testing, a vacuum was generated within the system. (2) Then, the confining pressure was increased from 0 MPa to 2 MPa at a rate of 5 MPa/hr without fluid flow through the sample. At this stage, only the strain was measured. (3) Once a confining pressure level of 2 MPa was reached, the sample was saturated by flowing distilled water through the sample. (4) Downstream of the sample, a constant pressure of 0.5 MPa was held while upstream, a constant flow rate (between 0.0001 and 35 ml/min) was used to create a pressure difference of 0.02 MPa – 0.5 MPa between both sides. (5) Flow rates were chosen according to the sample permeability and were adapted during the tests according to permeability changes. (6) The differential pressure was measured with a differential pressure gauge. Due to the fluid pressure, the effective confining pressure at this stage

was about 1.5 MPa. (7) Strain and differential pressure were then measured over 20–90 hours (depending on the sample) at the effective confining pressure of 1.5 MPa to constrain if there is a permeability reduction with time at constant pressure. (8) After this stage, the first confining pressure cycle was started by increasing the confining pressure from 2 MPa to 50 MPa at a rate of 5 MPa/hr. (9) After holding the confining pressure of 50 MPa for 1 to 19 hours (different for each sample and cycle), the pressure was decreased again from 50 MPa to 2 MPa. (10) The second cycle then started by holding confining pressure at 2 MPa for 10 to 14 hours (different for each sample and cycle) and repeating the same procedure as for the first cycle. (11) At the end of the second cycle, the confining pressure was reduced to ambient pressure. Absolute confining pressure change with time is shown exemplary for the Sierra granite sample in **Figure 113**.

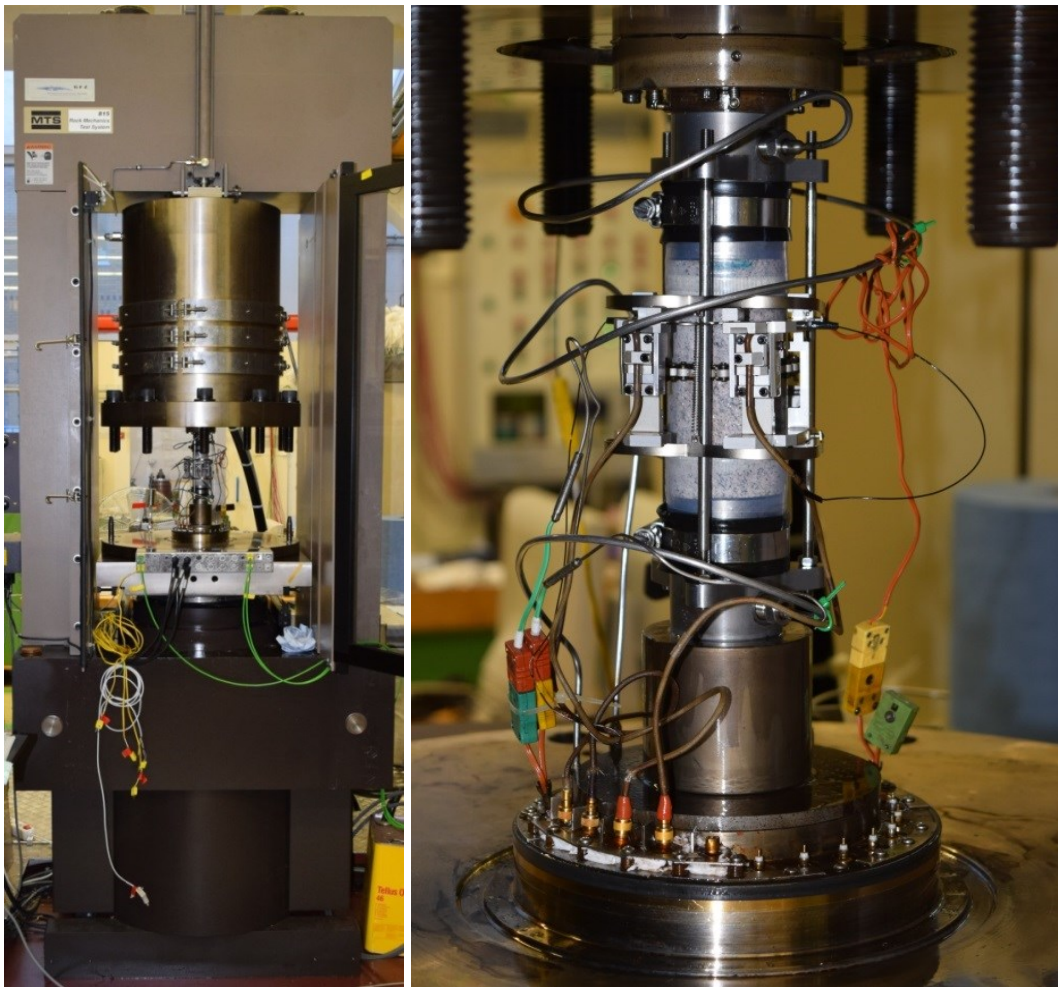


Figure 112: Triaxial test cell with sample (left) and close-up on a sample installed in the triaxial test cell (right). The sample is equipped with one circular and two axial strain gauges. Additionally, the temperature is measured on top and bottom of the sample.

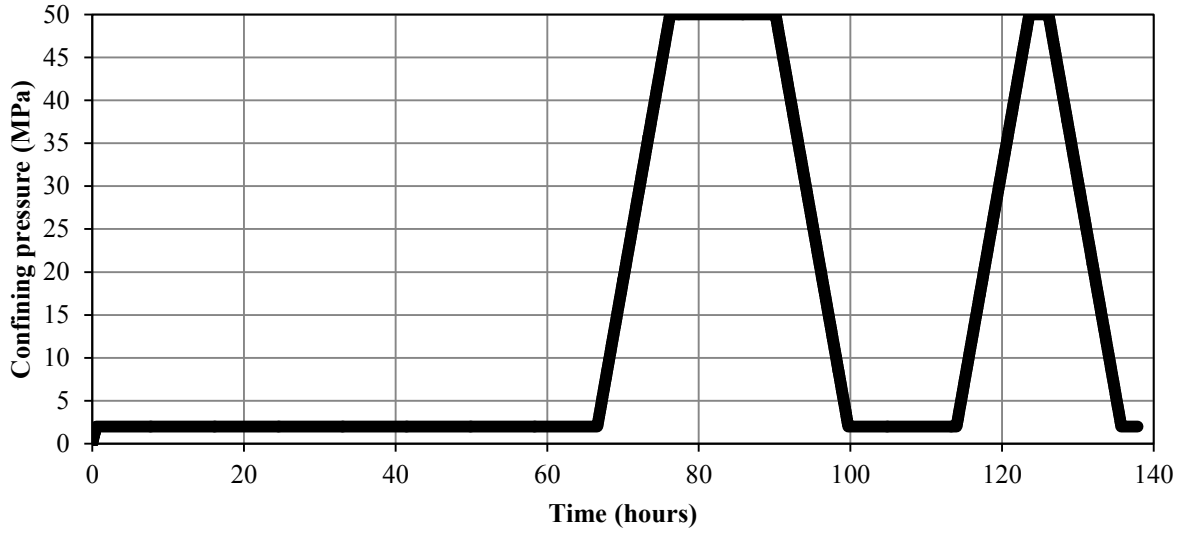


Figure 113: Confining pressure change with time for the Sierra granite sample.

The effective confining pressure P_{ceff} (Terzaghi 1925) is the difference between the confining pressure P_c and the absolute fluid pressure at the center of the sample P_f , which is the sum of the outlet pressure P_{out} and half of the differential pressure ΔP (**Equations 6 and 7**). The differential pressure is the difference between outlet and inlet pressure.

$$P_{ceff} = P_c - P_f \quad (6)$$

$$P_f = P_{out} + \frac{\Delta P}{2} \quad (7)$$

8.2.4.1 Determination of hydraulic aperture and fracture permeability

The permeability of the tested sample k_{sample} is calculated using Darcy's law (**Equation 8**):

$$k_{sample} = -\frac{\dot{V}\mu L}{A\Delta P} \quad (8)$$

Where \dot{V} is the fluid flow rate, which was held constant during an experiment, pressure and temperature dependent fluid viscosity μ is taken from the NIST database (Lemmon *et al.* 2013), L is the sample length, A ($A = \pi R^2 + 2a_h R$) is the cross-sectional area of the sample, which was

calculated based on the measured diameter perpendicular to the fracture, R is the radius of the sample, a_h is the hydraulic fracture aperture and ΔP is the differential pressure across the sample, which was directly measured using a differential pressure gauge.

This sample permeability times A is the sum of the matrix permeability k_{matrix} times the cross-sectional area of the matrix A_{matrix} ($A_{matrix} = \pi R^2$) and the fracture permeability k_f times the cross-sectional area of the fracture A_f ($A_f = 2a_h R$) assuming a rectangular fracture shape (**Equation 9**).

$$Ak_{sample} = A_{matrix}k_{matrix} + A_fk_f \quad (9)$$

Equation 9 reduces to **Equation 10** (which is equal to **Equation 11**) assuming k_{matrix} to be negligible (e.g. k_{matrix} of Sierra Granite is $1e-18 \text{ m}^2$).

$$Ak_{sample} = A_fk_f \quad (10)$$

$$(\pi R^2 + 2a_h R)k_{sample} = (2a_h R)k_f \quad (11)$$

Assuming laminar fluid flow between smooth parallel plates (“cubic law”), fracture permeability and hydraulic aperture are related by **Equation 12**, which was used to calculate the fracture permeability.

$$k_f = \frac{a_h^2}{12} \quad (12)$$

By substituting **Equation 12** into **Equation 11**, the hydraulic fracture aperture was calculated using **Equation 13**.

$$a_h = \sqrt[3]{6\pi k_{sample} R} \quad (13)$$

8.2.4.2 Determination of ductile and elastic response

Due to increasing confining pressure, the samples deformed elastically in the axial and lateral directions. Also, irreversible fracture closure caused an additional contribution to deformation

occurring in the lateral direction. Since there was no ductile strain in the vertical direction, it was assumed that the measured axial strain was equal to the elastic axial strain and the elastic portion of the lateral strain.

The irreversible lateral strain $\varepsilon_{c-non-elastic}$ due to fracture closure is hence the difference between lateral strain ε_c and axial strain ε_a (**Equation 14**).

$$\varepsilon_{c-non-elastic} = \varepsilon_c - \varepsilon_a \quad (14)$$

8.2.4.3 Determination of mechanical fracture aperture based on optical and strain measurements

Before and after the cyclic loading tests the aperture was directly measured optically on top and bottom of the sample using a stereo microscope. From all manually measured aperture values, the mean and median were taken.

During the tests, the fracture aperture was indirectly calculated by the following procedure. First, the non-elastic lateral strain $\varepsilon_{c-non-elastic}$ was determined by subtracting the axial strain ε_a from the total measured lateral strain ε_c as described above. This part of the strain was attributed to the deformation of the fracture. Then, the change in non-elastic lateral extension $\Delta ext_{c-non-elastic}$ was determined by multiplying the circumference u of the sample with the non-elastic lateral strain (**Equation 15**). Half of the change in non-elastic circumferential extension then equals the change in fracture aperture Δa .

$$\Delta ext_{c-non-elastic} = u * \Delta \varepsilon_{c-non-elastic} = 2\Delta a \rightarrow \Delta a = \frac{\Delta ext_{c-non-elastic}}{2} \quad (15)$$

8.2.5 Fracture surface scanning

After testing in the triaxial cell, fracture surfaces of three of the tested samples (Sierra granite, Sample 34 and Sample 31) were scanned. For comparison, the fracture surface of an untested Granodioritic pluton from the Annabel shear zone (Sample 16) was also scanned. The sample

consisted of 17.6% quartz, 69% plagioclase, 8% hornblende, and 2.3% accessory minerals (Cholach *et al.* 2005). The fracture generation procedure of Sample 16 was the same as for all other samples.

A 40 x 90 mm² rectangular portion in the middle of each fracture surface was scanned by taking its geometrical center as a reference point. Elevations Z on these rectangular portions of the surfaces were automatically digitized with a sampling interval of 1 mm in the horizontal X and Y axes. The measurement resolution in the vertical Z axis was 1/10 mm. Thus, for each surface, a two dimensional data set consisting of 40 x 90 data points, 1 mm apart, was collected and logged into the computer. Details about the surface scanning device are described in Develi *et al.* (2001).

From these measurements, the ratio between the total fracture surface area A_T and the planar fracture surface area A_P was determined as a surface roughness parameter. The total fracture surface area takes into account the asperities while the planar fracture surface area is the product of the length of the fracture surface and the width of the fracture surface. Larger values indicate a higher roughness.

In order to calculate the variogram fractal dimension values of the fracture surfaces, the variogram analysis method was applied to all 40 profiles parallel to the axial direction of the surfaces. Details about this method can be found in Develi & Babadagli (2015). For each fracture surface, the variogram fractal dimension values of 40 profiles, each of which consists of 90 data points, were computed by taking the maximum lag distance as 10% of the maximum profile length (Babadagli & Develi 2001; Huang *et al.* 1992; Kulatilake & Um 1998). For each fracture surface, the arithmetic mean of the 40 fractal dimension values was calculated and assigned as surface fractal dimension values.

8.3 EXPERIMENTAL RESULTS

8.3.1 Hydraulic and strain response of an intact sample

For Sample 34, the intact rock permeability was determined. As seen in **Figure 114**, it took about 75–100 hours to reach a relatively constant permeability of approximately $1\text{e-}18\text{ m}^2$ before

pressure cycling and a further reduction to values between $2\text{e-}19$ and $3\text{e-}19$ m^2 . Small drops in the permeability curve are due to decreasing flow rate. After reaching an effective confining pressure of 10 MPa, the test was changed from flow rate control to pressure control because the pumps did not allow a further decrease of flow rate. Therefore, permeability determination was less accurate from this stage on, but one can observe that it remains below $1\text{e-}18$ m^2 .

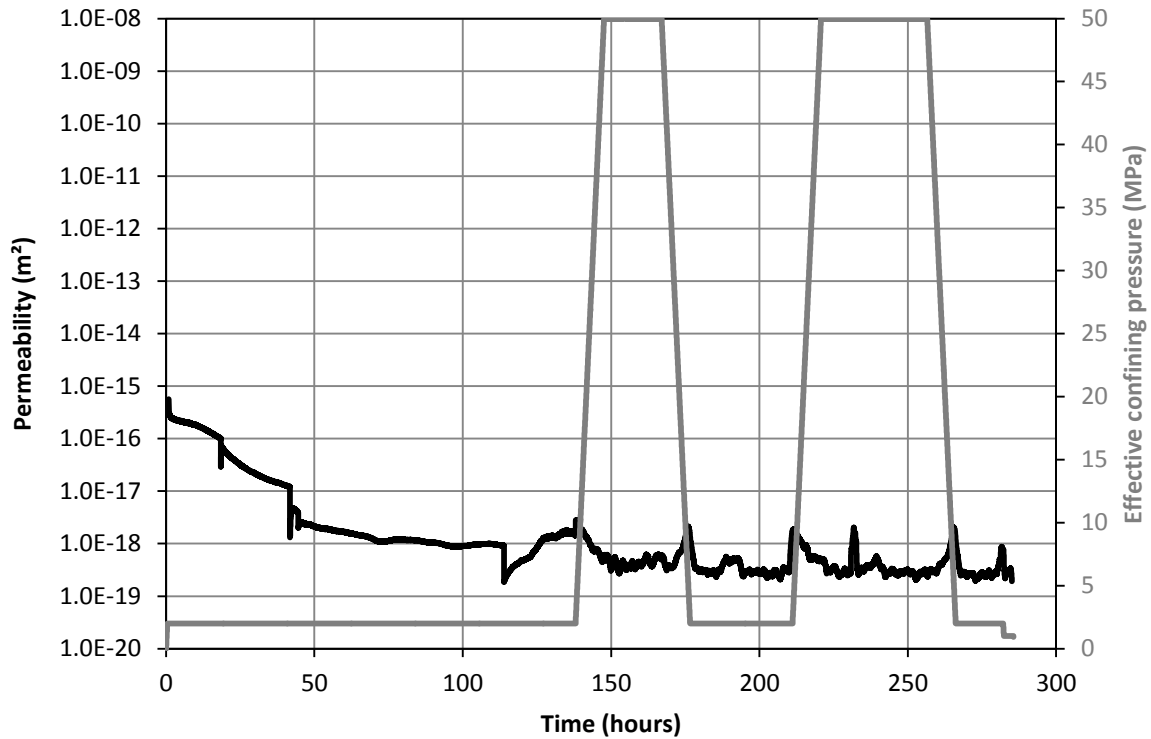


Figure 114: Sample permeability over time and effective confining pressure cycles for the intact Sample 34.

The maximum measured sample permeability of a fractured sample is $1\text{e-}12$ m^2 (both displaced samples at 2 MPa confining pressure before cycling) and the minimum measured sample permeability is $1\text{e-}17$ m^2 (Sierra granite at 50 MPa confining pressure at the second cycle). Since the Sierra Granite sample and Sample 34 both have a matrix permeability of $1\text{e-}18$ m^2 or less, it is reasonable to assume the matrix to be impermeable and neglect in the calculations for determining the fracture permeabilities.

Figure 115 shows the circumferential strain development with cycling effective confining pressure and time. A positive circumferential strain indicates a reduction of the samples

circumference. During the initial constant confining pressure phase of 136 hours, the circumferential strain increased and did not reach a constant level. At the following constant pressure stages, the circumferential strain reached a constant level after an initial increase/decrease. After the first confining pressure cycle, the circumferential strain was not fully recovered. The second confining pressure cycle showed almost no hysteresis effect anymore and the sample behaved elastic.

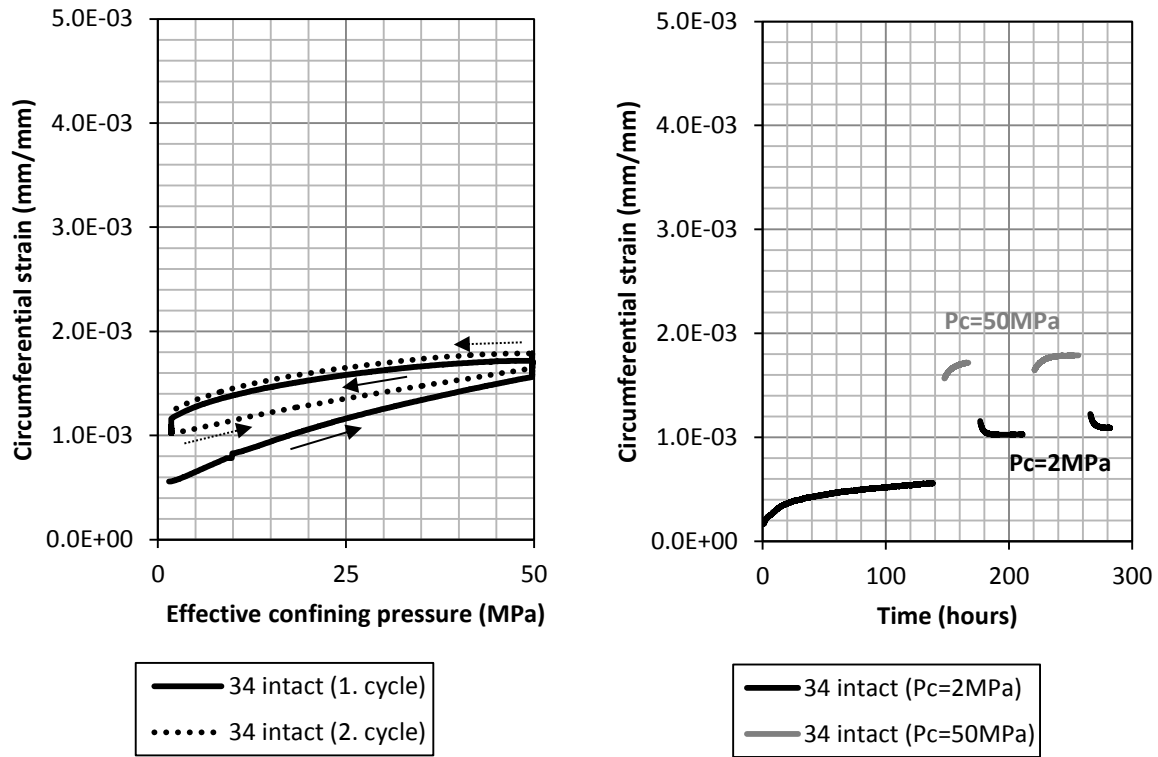


Figure 115: Circumferential strain of the intact Sample 34 changing with effective confining pressure (left) and time (right). Only the periods with constant confining pressure (2 MPa and 50 MPa) are shown on the right.

8.3.2 Confining pressure dependent hydraulic and strain response of fractured samples

8.3.2.1 Aligned fracture surfaces

Fracture permeability changes of the two samples with aligned fracture surfaces resulting from the two confining pressure cycles are shown in **Figure 116**. Both samples exhibited a significant fracture permeability reduction of almost two orders of magnitude with an increase of effective

confining pressure from 1.5 MPa to 49.5 MPa. The difference between the initial fracture permeability at 1.5 MPa effective confining pressure and the fracture permeability after one confining pressure cycle was approximately one order of magnitude for both samples. The second cycle did not significantly further reduce the fracture permeability. The fracture permeability of Sample 34 was initially higher than for the Sierra granite sample because the initial optically determined aperture of Sample 34 was more than twice the aperture of the Sierra granite (**Table 41**). After cycling, both fracture permeabilities were approximately the same.

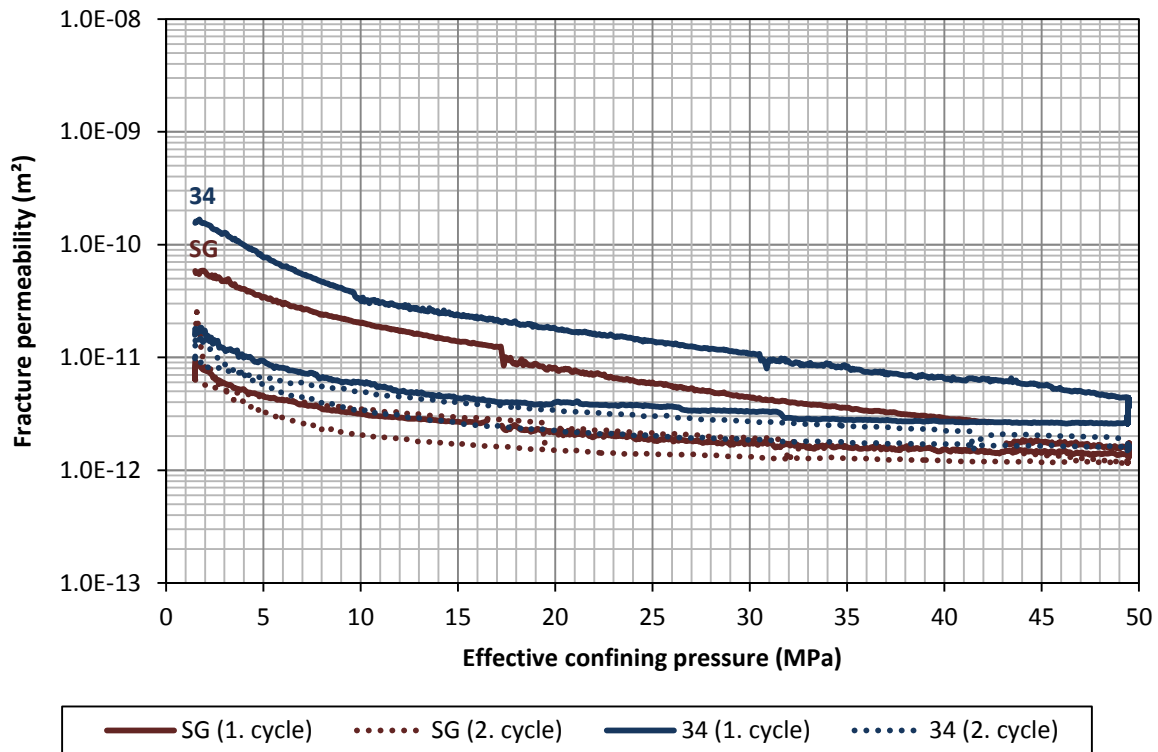


Figure 116: Permeability development of samples with aligned fracture surfaces under cyclic loading conditions.

Different from the intact sample where the circumferential strain is elastic, the circumferential strain of the fractured samples resulted partly from the elastic deformation of the rock and partly from fracture closure. **Figure 117** shows how the circumferential strain of the samples with aligned fracture surfaces changes during confining pressure cycling. For the Sierra Granite sample, only a slightly higher circumferential strain was measured compared to the intact Sample 34. Both samples showed relatively similar behavior. For example, the intact Sample 34 and the Sierra Granite sample both did not yield a significant hysteresis at the second confining pressure

cycle anymore. The reason for this similar behavior is that the two fracture surfaces of the Sierra Granite were still connected to each other before testing and the fracture can be considered as a hair crack. Due to the closure of this crack, the circumferential strain was still larger in the Sierra Granite sample. For the fractured Sample 34 a significantly larger circumferential strain and a significantly larger hysteresis between the two confining pressure cycles was observed because the fracture faces did not stick together before the test and hence the initial optically determined fracture aperture was more than two times larger (**Table 41**).

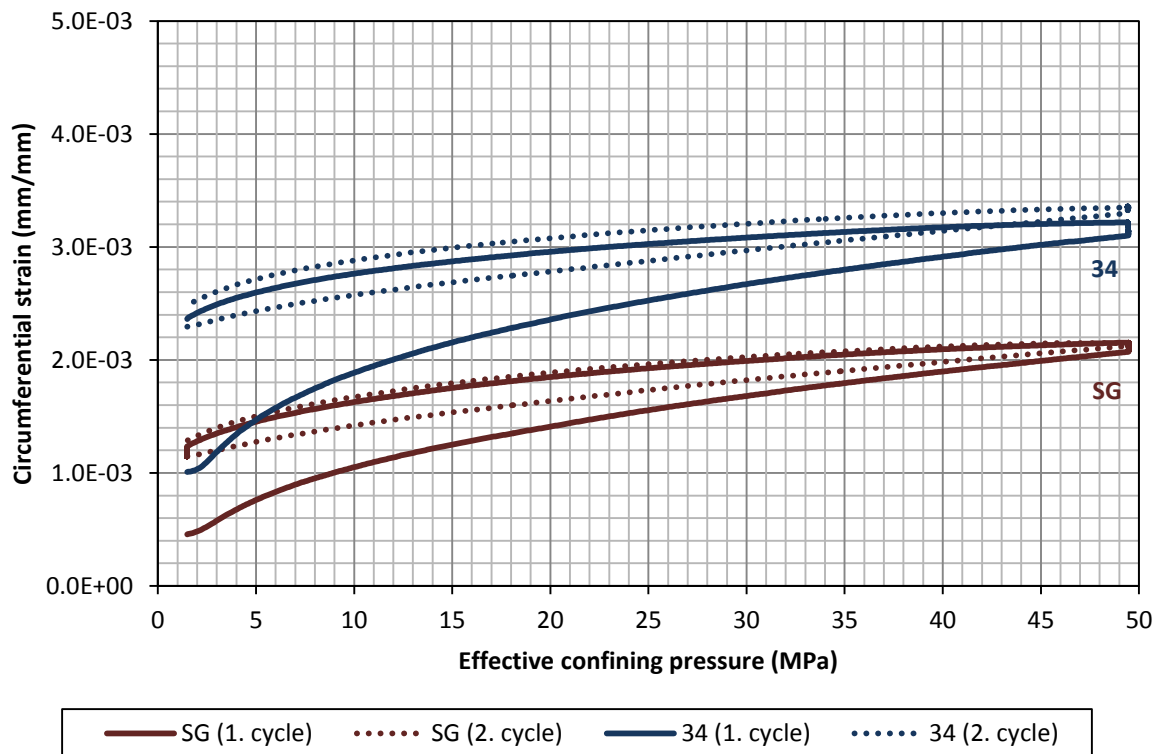


Figure 117: Variation of circumferential and axial strain of samples with aligned fracture surfaces with effective confining pressure.

Confining pressure dependent changes in hydraulic aperture, which was calculated based on the hydraulic data (**Equation 13**), and mechanical aperture, which was calculated based on the strain data (**Equation 15**), for the samples with aligned fracture surfaces are given in **Figure 118**. The hydraulic apertures were significantly less than the mechanical apertures due to rough fracture surfaces and tortuous fluid flow. Hence, the changes in hydraulic apertures were also less than the changes in mechanical aperture. Hydraulic apertures change only by 10 μm during pressure increase or reduction after the first pressure cycle. The mechanical aperture change of Sample 34

was significantly larger than the aperture change of the Sierra Granite sample. This is because Sample 34 had a larger initial aperture and hence the applied confining pressure led to a larger aperture reduction.

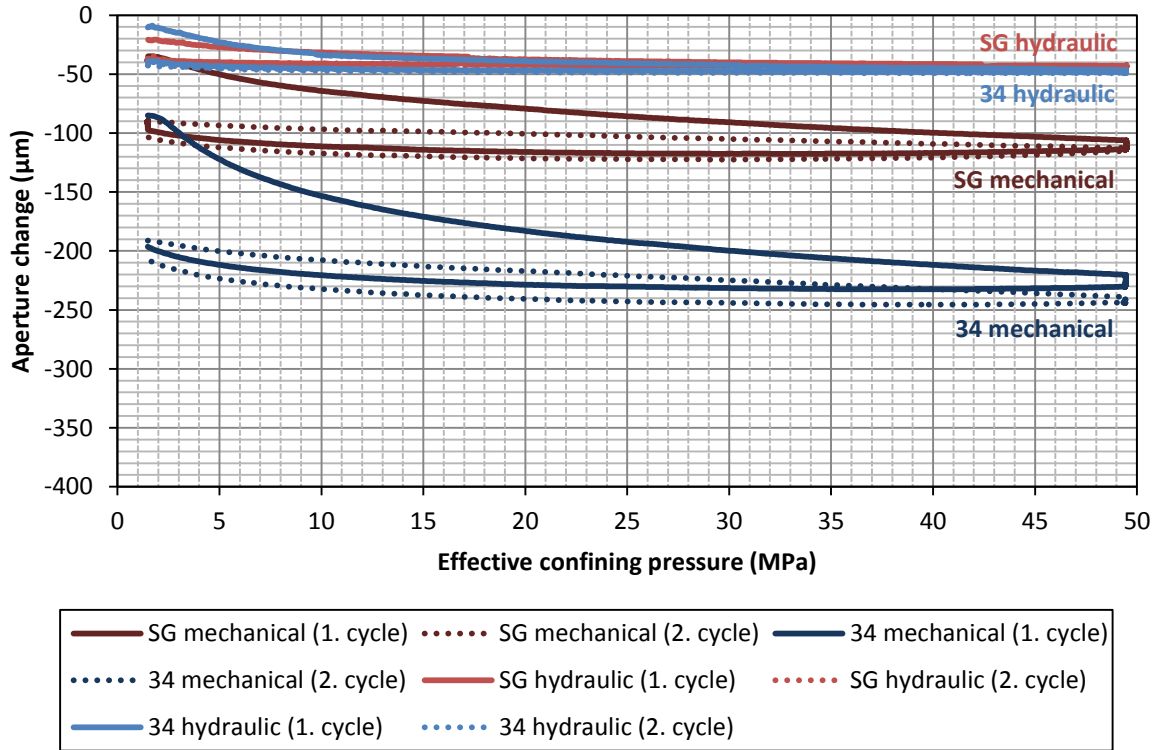


Figure 118: Variation of mechanical and hydraulic apertures of samples with aligned fracture surfaces with effective confining pressure.

8.3.2.2 Displaced fracture surfaces

As opposed to the samples with aligned fracture surfaces, both samples with displaced fracture surfaces showed a relatively constant permeability with minor permeability decrease up to an effective confining pressure of 15 MPa (**Figure 119**). The trend held on for Sample 31 until the shrinkable tube had a hole at the point of the widest fracture opening at about 38 MPa and the test needed to be stopped.

The permeability of Sample 32 showed a different behavior and was reduced by one order of magnitude if the initial fracture permeability at 2 MPa confining pressure was compared with the final fracture permeability after 2 confining pressure cycles at 2 MPa confining pressure. This

may be explained by the following: (1) fracture displacement and re-alignment of the fracture surfaces, (2) significant asperity degradation or (3) fines transportation and plugging of the fracture aperture. The same process may be the reason for jumps in the permeability, which were partly triggered by changes in flow rate. These factors are discussed in more detail in **Section 8.5**. Overall, the fracture permeability of the samples with displaced fracture surfaces were about ten times higher as compared to the samples with aligned fracture surfaces. For Sample 31, the fracture permeability at higher confining pressures was even larger.

The circumferential strain of the samples with displaced fracture surfaces (**Figure 120**) was also larger compared to the samples with aligned fracture surfaces (**Figure 117**). The inelastic part of this strain was significant for Sample 32 as can be inferred from the offset between initial circumferential strain and final circumferential strain after cycling. The circumferential strain for Sample 31 was larger compared to Sample 32 because of a larger initial aperture.

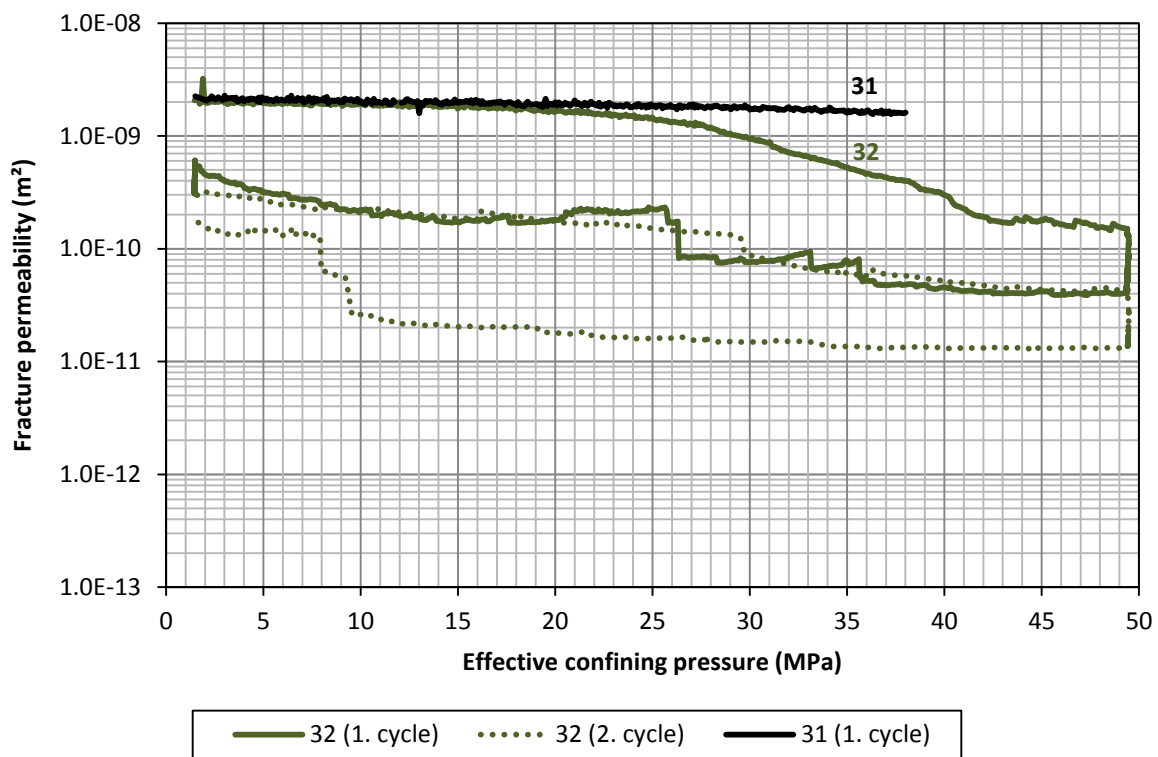


Figure 119: Permeability development of samples with displaced fracture surfaces under cyclic loading conditions.

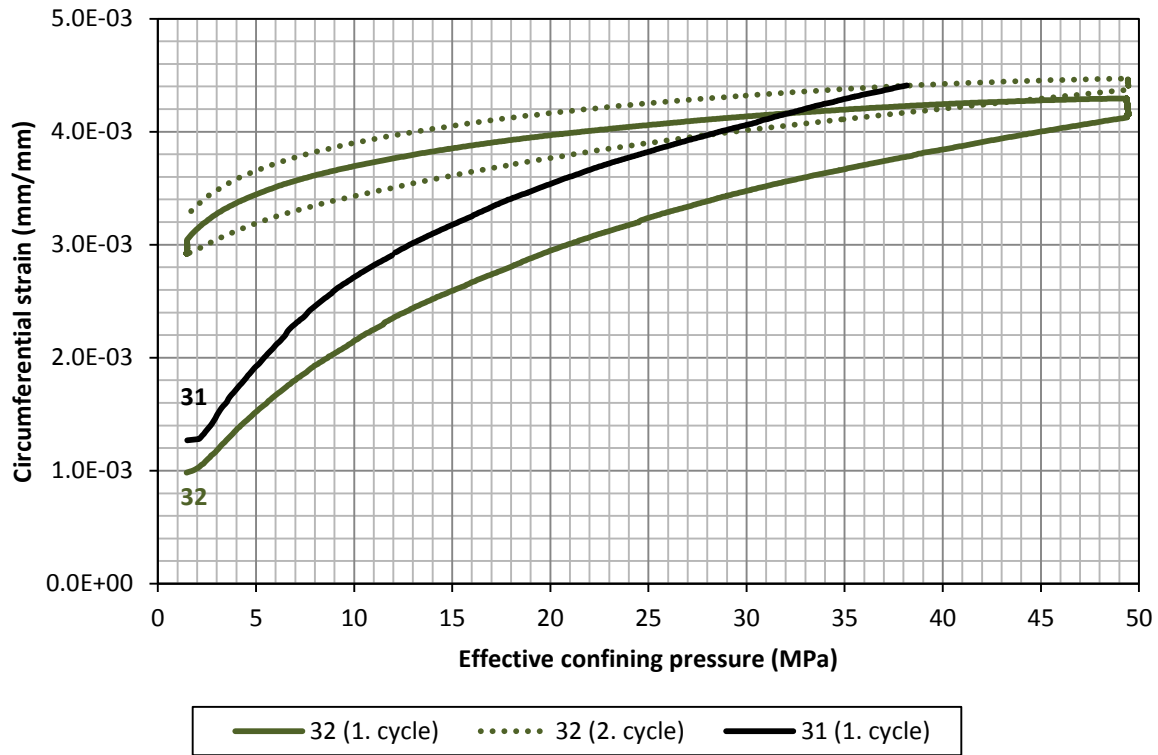


Figure 120: Variation of circumferential strain with effective confining pressure for the samples with displaced fracture surfaces.

The changes in hydraulic and mechanical apertures displayed the same behavior as the permeability and strain respectively (**Figure 121**). While Samples 31, 32, and 34 had a similar initial aperture change of about 100 μm resulting from the constant 1.5 MPa effective confining pressure phase, the initial aperture of the Sierra Granite sample was only reduced by 40 μm before the first pressure cycle. This is because the Sierra Granite had a significantly lower initial fracture aperture (**Table 41**). The further aperture change with increasing confining pressure was larger and almost identical for the displaced samples compared to the two aligned samples, which showed a much lower aperture reduction with effective confining pressure.

The hydraulic aperture of the displaced Sample 32 changed by about 110 μm while the mechanical aperture changed by 300 μm . Between 20 and 38 MPa, the hydraulic aperture change differed significantly for both samples with displaced fracture surfaces. At the same time, the mechanical aperture changes were almost the same. Therefore, the permeability reduction in Sample 32 might not be due to fracture closure but rather due to a different reason, such as fines

migration and resulting plugging of the fracture. Possible reasons for this behavior are discussed in **Section 8.5**.

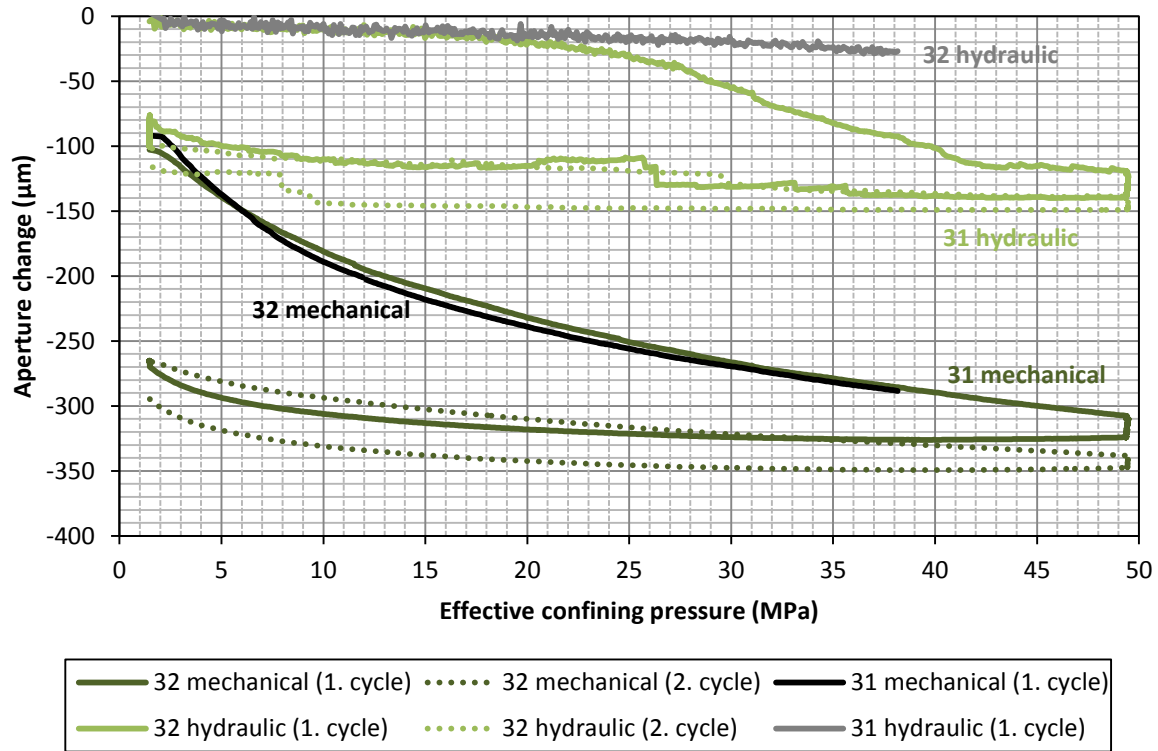


Figure 121: Variation of calculated mechanical and hydraulic apertures with effective confining pressure.

8.3.3 Confining pressure dependent hydraulic and strain response of fractured samples

8.3.3.1 Aligned fracture surfaces

The fracture permeability reduction with time at constant confining pressure stages is shown in **Figure 122** for the samples with aligned fracture surfaces. At the initial phase, the behavior under 1.5 MPa effective confining pressure indicates that the permeability falls with time in a logarithmic manner at this constant confining pressure. During constant confining pressure at later stages (1.5 MPa and 49.5 MPa effective confining pressures), the rate of permeability reduction was slightly reduced with increasing number of cycles. At the last stage (1.5 MPa effective confining pressure after two pressure cycles), the fracture permeability stayed almost constant.

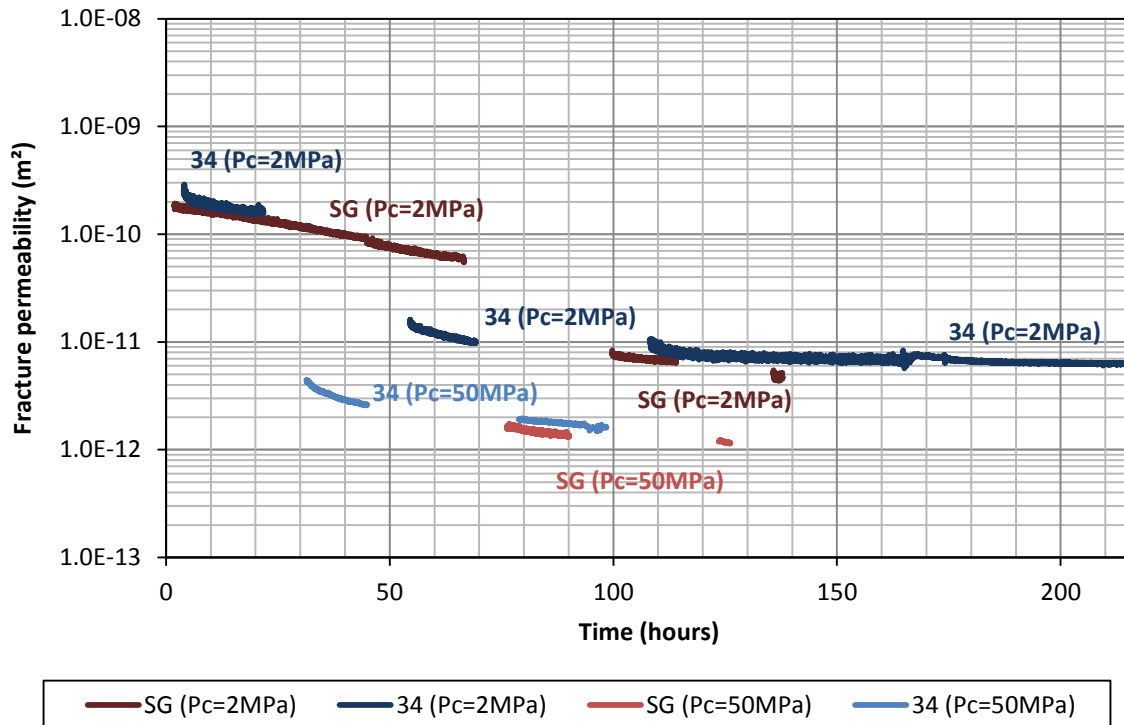


Figure 122: Fracture permeability development of samples with aligned fracture surfaces over time.

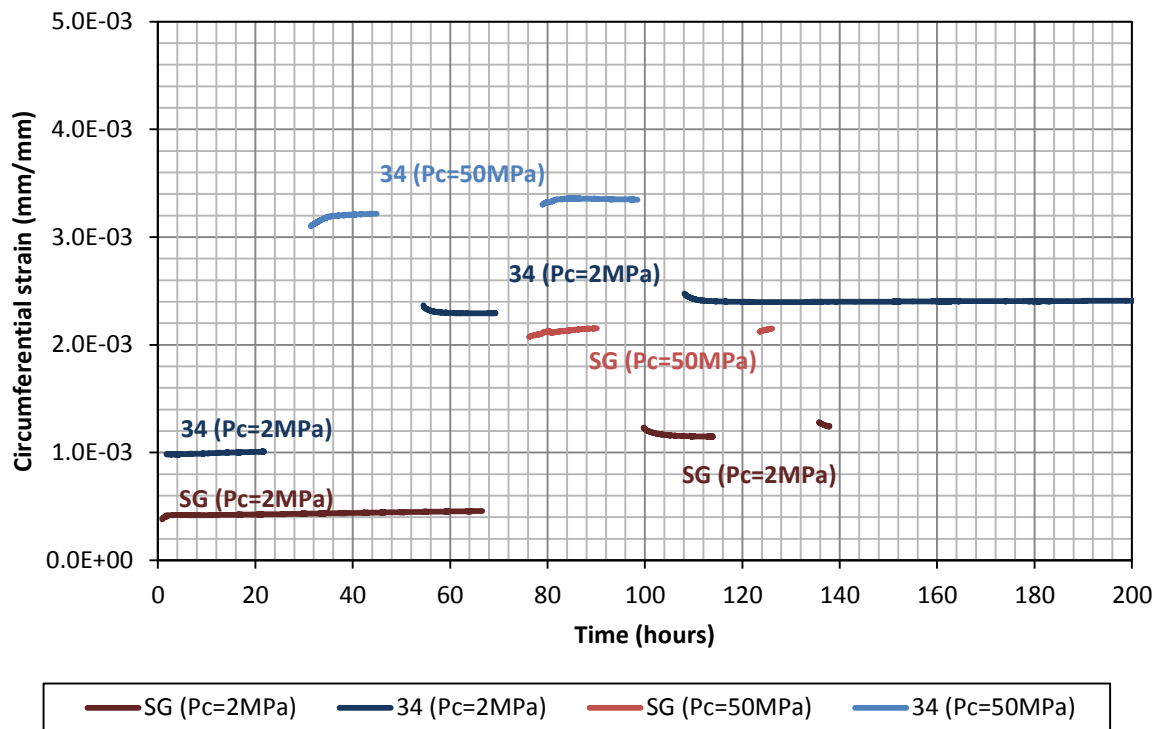


Figure 123: Variation of circumferential strain with time during periods of constant effective confining pressure for samples with aligned fracture surfaces.

Figure 123 shows the strain development of these samples during periods with constant confining pressure. In the initial phase, the strain increased slightly while it was relatively constant at later stages. After cycling, the circumferential strain of Sample 34 stayed constant over a period of more than 80 hours at 1.5 MPa effective confining pressure.

The same observations can be made for the hydraulic aperture (same behavior as permeability) and the mechanical aperture (same behavior as circumferential strain). Both apertures are shown for the two samples in **Figure 124**.

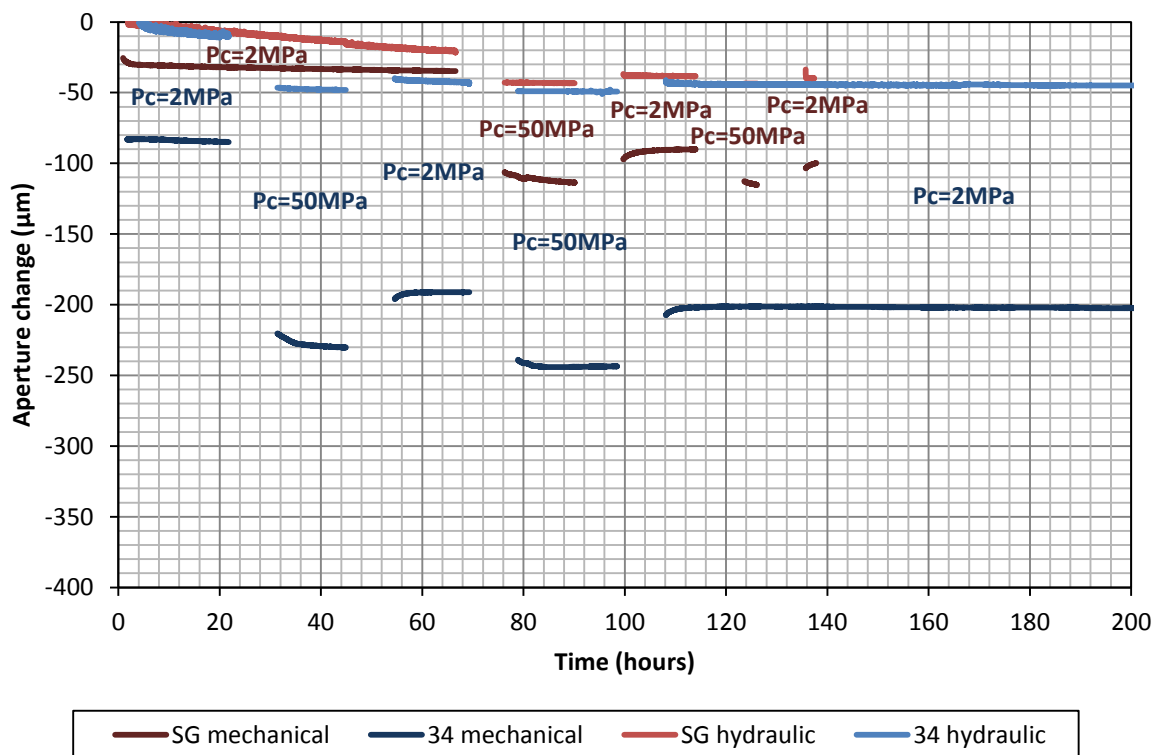


Figure 124: Variation of calculated mechanical and hydraulic apertures with time for samples with aligned fracture surfaces.

8.3.3.2 Displaced fracture surfaces

The permeability reduction for the two rocks with displaced fracture surfaces was insignificant during the initial 65 hours (Sample 31) and 86 hours (Sample 32) with constant effective confining pressure of 1.5 MPa (**Figure 125**). There were no other periods with constant pressure for Sample 31 because the test was stopped after about 77 hours due to a leakage of confining oil

into the sample as a result of a hole in the heat shrinkable tube. The permeability of Sample 32 was significantly reduced at later stages. Potential reasons for are discussed in **Section 8.5**.

The circumferential strain variations with time for these two tests are given in **Figure 126**. Before cycling, the circumferential strain slightly increased, which is attributed to a creeping fracture closure in addition to elastic behavior. Later stages showed a relatively constant strain after about 10 hours.

The mechanical and hydraulic behavior discussed above can be interpreted in terms of fracture aperture change (**Figure 127**). The curves followed the trend of the data given in **Figures 125 and 126**. Hydraulic aperture did not change in the initial phase while some creeping behavior of the mechanical aperture was observed.

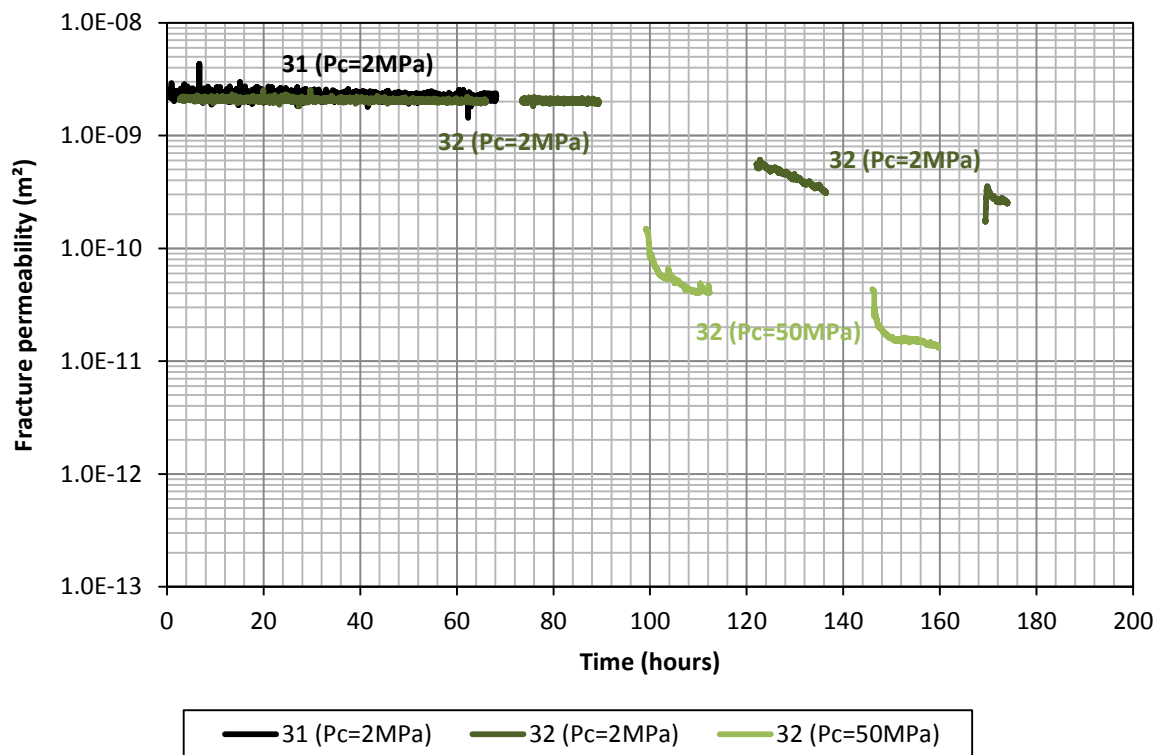


Figure 125: Fracture permeability development of all fractured samples over time.

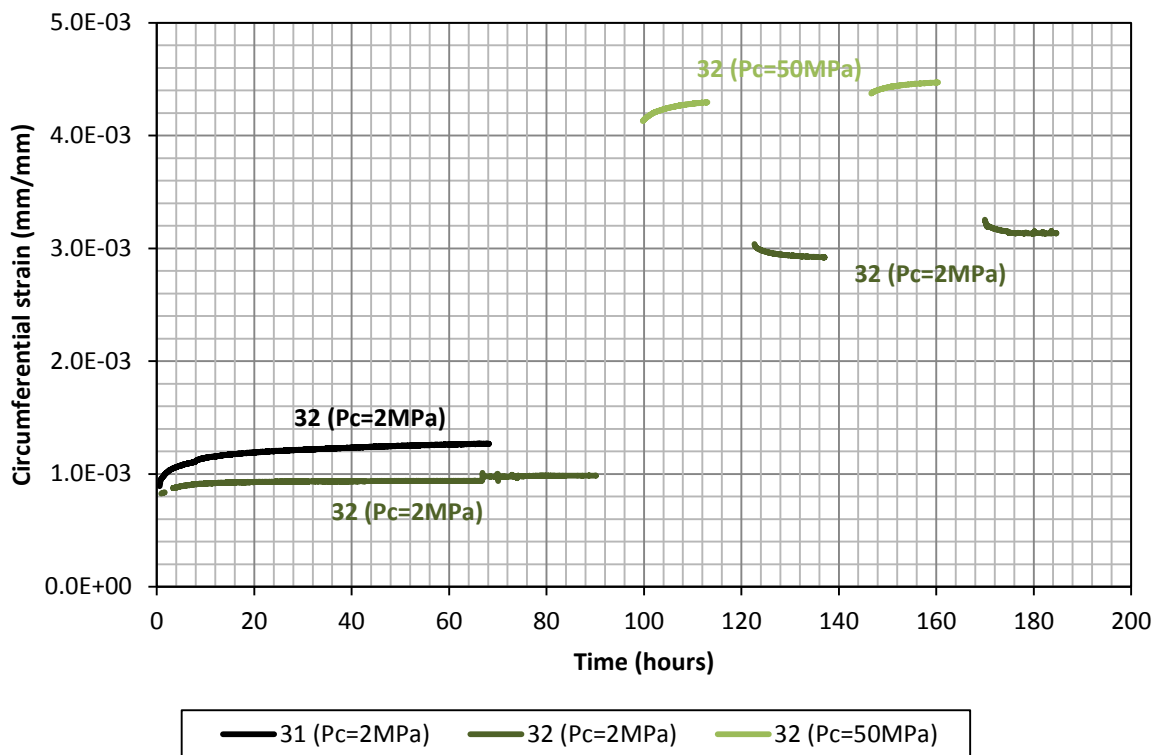


Figure 126: Variation of circumferential strain with time for samples with displaced fracture surfaces.

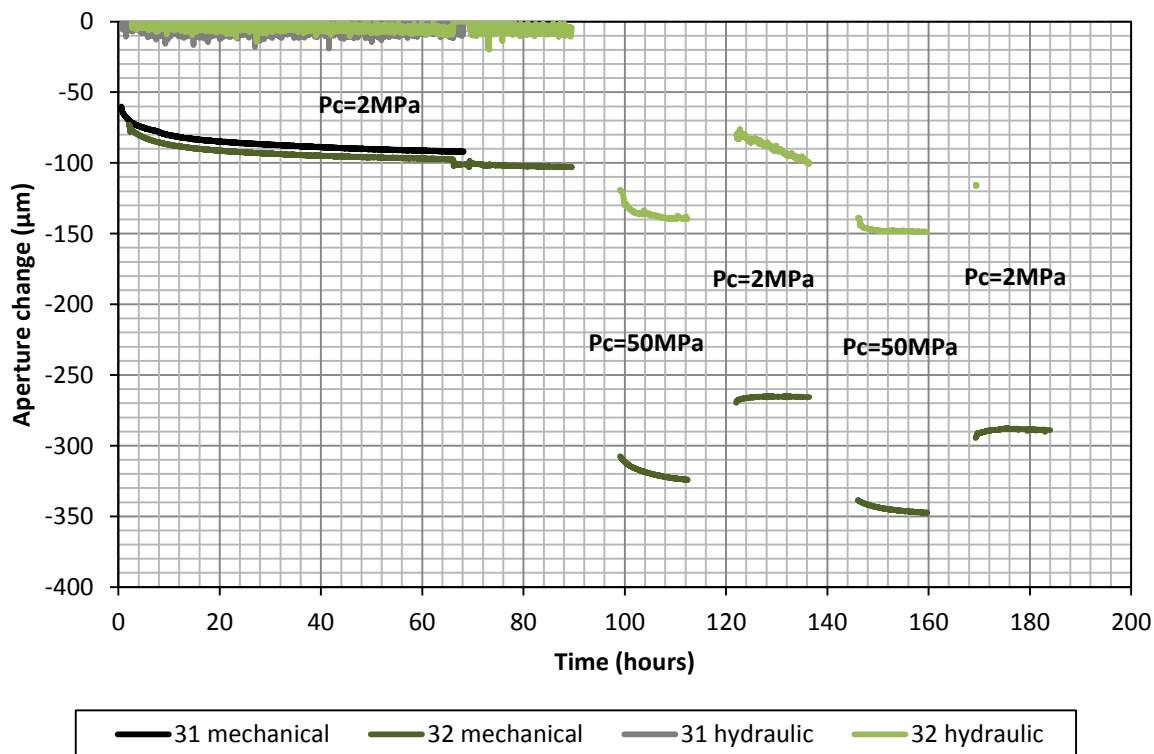


Figure 127: Variation of calculated mechanical and hydraulic apertures with time.

8.3.4 Fracture surface scanning results after testing

Figure 128 shows a 3D view of the scanned fracture surfaces of the three samples subject to elevated confining pressure (34, SG, and 31) and a reference sample (Sample 16). The variogram fractal dimensions over a profile number for each fracture surface are displayed in **Figure 129**. The average of these values along with another surface roughness indicator is given in **Table 40**. The details of the measurements of these parameters can be found in Babadagli & Develi (2001) and Develi & Babadagli (2015).

The surface scanning measurements showed that the two samples with aligned fracture surfaces (Sample 34 and Sierra granite) had the largest ratios of total (A_T) to planar (A_P) fracture surface area and may therefore be described as rougher. These two samples were both subject to two confining pressure cycles up to 50 MPa. The duration of the permeability test was about 80 hours longer for Sample 34 (with the higher A_T/A_P ratio after testing) than for the Sierra granite (with the lower A_T/A_P ratio after testing).

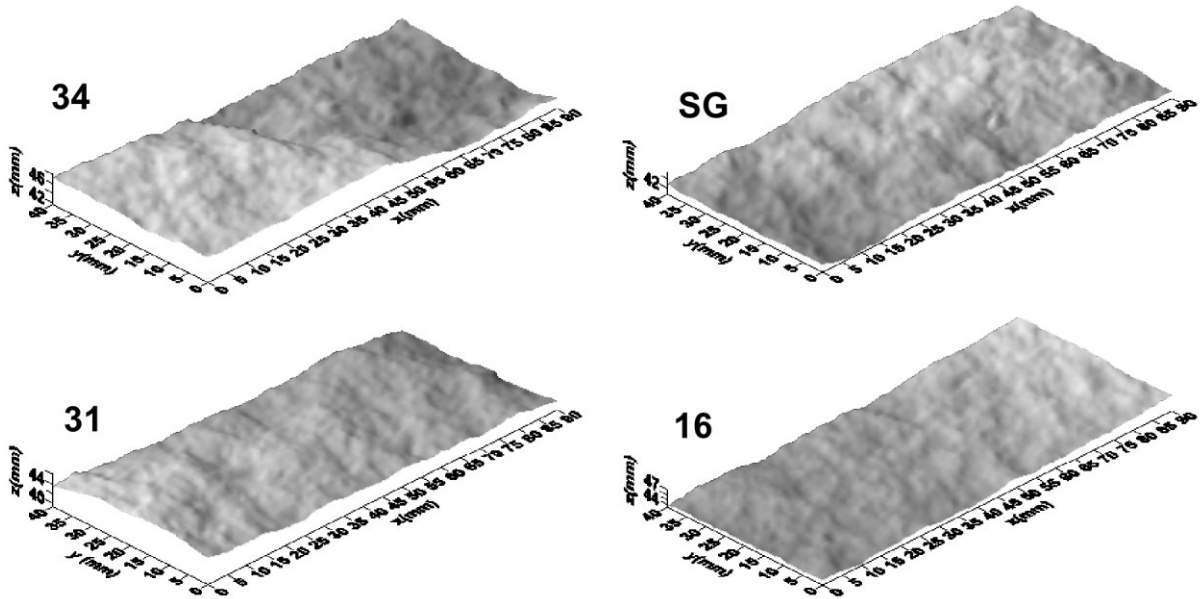


Figure 128: 3D view of the scanned fracture surfaces.

Table 40: Ratio of total (A_T) to planar fracture surface area (A_P) and variogram fractal dimensions (D_{va}) for three samples subject to elevated confining pressure (SG, 31, 31) and one sample that was not subject to confining pressure (16).

Sample	A_T/A_P	D_{va}	Comments
34	1.0394	1.326	Aligned fracture, 2 pressure cycles to 50 MPa, 216 hr experiment
SG	1.0334	1.424	Aligned fracture, 2 pressure cycles to 50 MPa, 136 hr experiment
31	1.0318	1.359	Displaced fracture, 1 pressure ramp to 38 MPa, 70 hr experiment
16	1.0209	1.489	Reference sample, no experiment

Sample 31 (with displaced fracture surfaces and the shortest permeability test duration) had a lower A_T/A_P ratio and the untested reference sample that was not subject to any confining pressure (Sample 16) showed by far the lowest A_T/A_P ratio and had therefore the smoothest fracture walls.

The limited data suggests an increase in A_T/A_P ratio (and hence an increase in fracture surface roughness) if a sample is subject to longer periods of confining pressure or higher confining pressures. However, this may also be the result of different mineralogical properties. No obvious correlation between variogram fractal dimension (D_{va}) and confining pressure was found.

The fracture surfaces of Sample 31 were displaced by 1 mm; therefore, even an average roughness (A_T/A_P ratio and D_{va}) led to the largest measured aperture and permeability. Fracture surfaces of Samples 34 and Sierra granite were not displaced. Sample 34 with the lower variogram fractal dimension (lower roughness) had the larger aperture and permeability of the two samples. This behavior was also observed, for example, by Develi & Babadagli (2015).

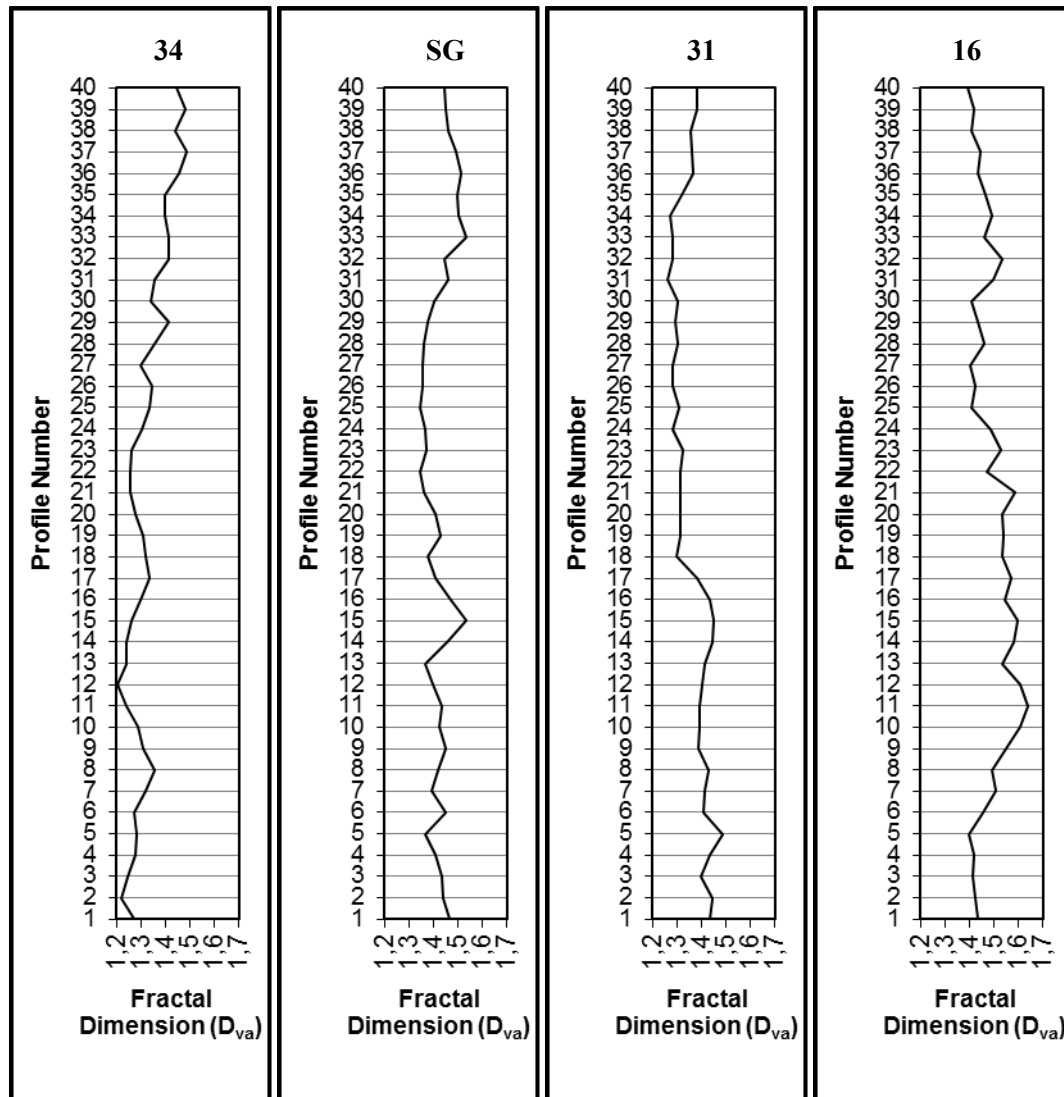


Figure 129: Variation of the variogram fractal dimensions (D_{va}) with the profiles parallel to the x-axis of the digitized fracture surfaces shown in **Figure 128**.

8.4 COMPARISON WITH LITERATURE DATA AND RELEVANCE FOR EGS DEVELOPMENT

Several conclusions from previous literature studies are already summarized in the introduction. Selected effective closure stress (stress acting on the fracture surface in the direction perpendicular to this surface) dependent fracture permeability values from granitic rocks (e.g. granites and granodiorites), which were derived from the literature, are given in **Figure 130**. These literature values include fracture permeabilities of aligned and displaced tensile fractures,

aligned and displaced shear fractures, aligned and displaced natural fractures, saw-cut fractures, and in-situ fractures from different authors. To keep the diagram readable, only aligned fractures and displaced fractures are distinguished. Depending on rock type, shear displacement, sample size, closure pressure, and failure type, permeabilities of shear fractures range between $4\text{e-}9$ and $1\text{e-}12$ m^2 . Fracture permeabilities of aligned fractures are less compared to displaced fractures and range between $1\text{e-}9$ and $3\text{e-}13$ m^2 depending on the same parameters (except for shear displacement).

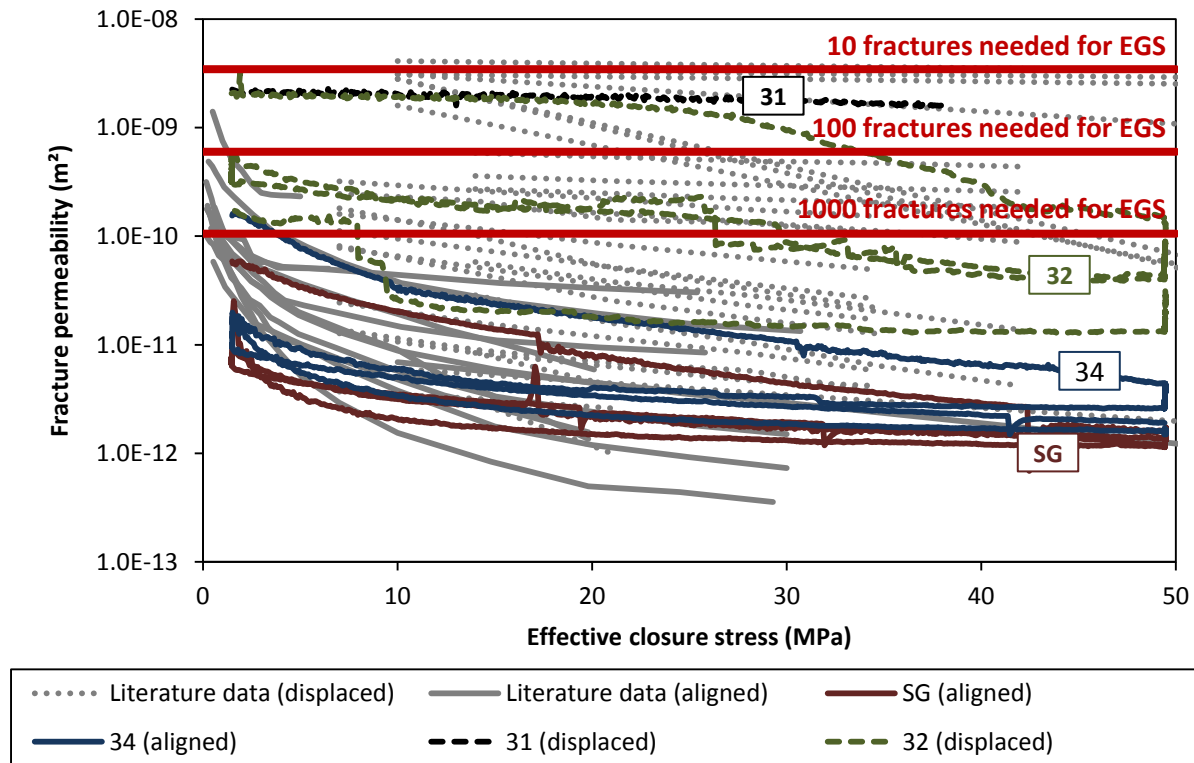


Figure 130: Comparison of measured fracture permeabilities to selected literature data from fractures in granitic rocks (Pratt *et al.* 1977; Gale 1982; Iwano *et al.* 1995; Hakami *et al.* 1996; Chen *et al.* 2000; Lee *et al.* 2002; Watanabe *et al.* 2008; Watanabe *et al.* 2009). The red lines indicate how many fractures are needed with the specific fracture permeability to achieve the design goals of an EGS project in a basement rock for a case study presented in Hofmann *et al.* (2014; data from Fig. 27).

These data are compared with the measurements from the current study. The presented measurements are in good agreement with the previously published literature data. The result of Sample 31 with displaced fracture surfaces follows the trend of other data from displaced tensile fractures where the permeability is significantly higher compared to samples with aligned fracture surfaces and the permeability is not significantly reduced with increasing closure stress.

On the other hand, displaced shear fractures are subject to a significant permeability reduction with increasing closure stress, which was also observed in Sample 32.

Aligned fractures (Samples 34 and Sierra Granite) also show the same behavior as the aligned fractures from the literature data where permeability reduction with increasing closure stress is more pronounced and overall permeabilities are up to three orders of magnitude smaller compared to displaced tensile fractures.

Figure 130 also shows how many large fractures (500 m half-length, 141 m average height) are needed to be developed for different fracture permeabilities for economical heat extraction from a proposed EGS well triplet in 5 km deep granitic basement rock in northern Alberta (Hofmann *et al.* 2014). The system consists of one horizontal injection well flanked by two parallel horizontal production wells separated by 400 m. Hydraulic stimulation treatments are only performed in the injection well. From the data collection it can be seen that more than 10 of these fractures are needed in any case – even if a sustainable shear displacement of tensile fractures could be achieved. With the fracture permeability determined for some displaced tensile fractures and all displaced shear fractures, more than 100 fractures are needed and, in many cases, even more than 1000 fractures are needed. With the development of aligned tensile fractures, much more than 1000 fractures would be needed to meet the design goals of this simulated system. In the light of this data, the development of a sustainable EGS in granitic basement rock consisting of some individual large single displaced fractures needs to be questioned. A complex fracture network consisting of at least 100s of branching self-propping fractures would be the most promising option to efficiently develop such a system. Besides the fracture types, number of fractures, and single fracture permeability, the interconnectivity between the fractures also plays a crucial role in determining the permeability of the whole reservoir (Jafari & Babadagli 2011). A well connected fracture network has a much larger permeability compared to a network of poorly connected fractures. In the above considerations, idealized parallel fractures connected to the bore holes are considered.

To classify this data with other rock types, in **Figure 131**, fracture permeabilities determined in this study are compared to literature data from sedimentary rocks (sandstones and shales) with and without proppants. Again, literature data from aligned and displaced natural, shear, and tensile fractures as well as saw cut fractures were collected. While all previous data was without

proppants, here fractures with and without proppants are compared. The range of fracture permeabilities is similar to the ones determined for granitic rocks (**Figure 130**). On the other hand, to reach the high fracture permeabilities of displaced fractures in granitic rocks, high strength proppants (e.g. ceramics) need to be used in aligned and displaced fractures. Displaced fractures in shales and sandstones have a similar or a slightly higher permeability as compared to aligned fracture faces in granites. Aligned fracture faces of shales and sandstones are subject to a significant reduction of fracture permeability already at relatively low effective closure stresses (<20 MPa). This was not observed for the aligned fractures in granitic rocks. In general, the fracture permeability of shales seems to be reduced stronger with increasing closure stress as compared to sandstones.

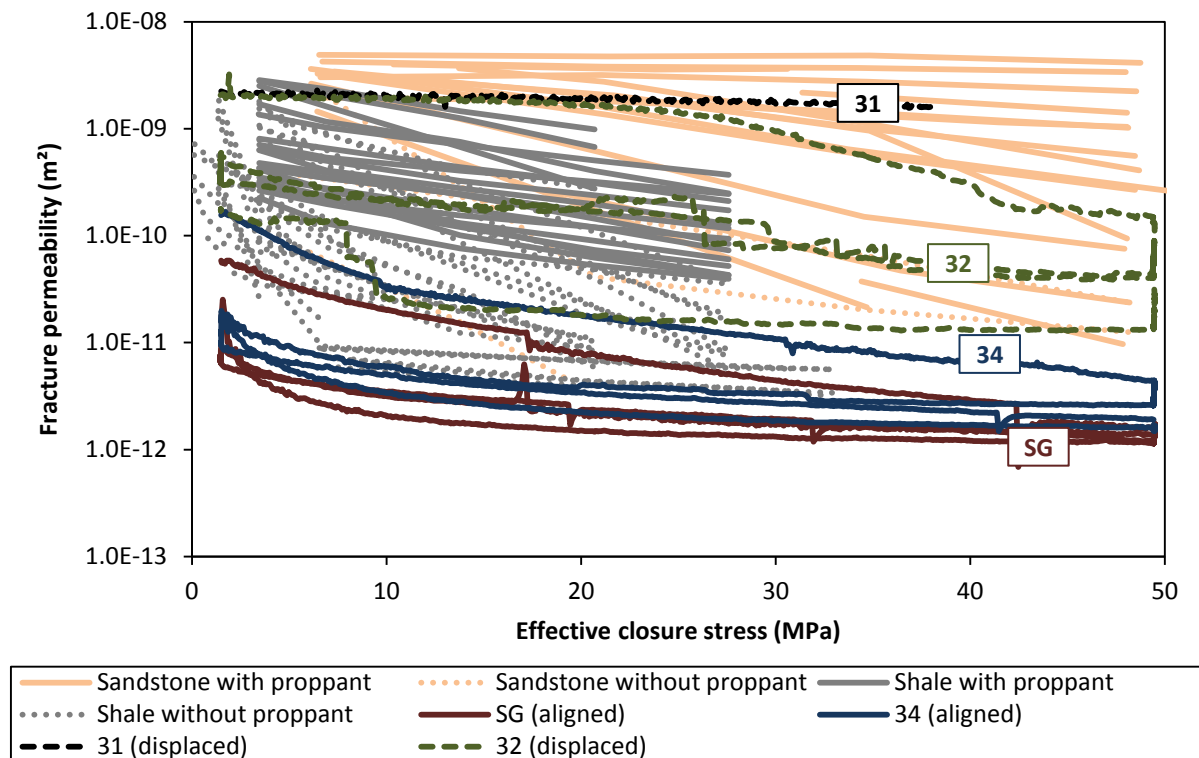


Figure 131: Comparison of measured fracture permeabilities to selected literature data (Fredd *et al.* 2000; Guiterrez *et al.* 2000; Cho *et al.* 2012; Briggs *et al.* 2014; Zhang *et al.* 2014) from sedimentary rocks (sandstones and shales).

Overall, because the short term (hours - days) fracture permeability of self-propping displaced tensile fractures are similar to those of propped fractures in sandstones, it seems reasonable to perform hydraulic stimulation treatments for the development of EGS without the use of

proppants if complex fracture networks can be developed. On the other hand, proppants should be used if shale or sandstone formations are to be developed as EGS.

The use of proppants for the stimulation of granitic rocks may lead to a further fracture permeability increase. Additional experiments with proppants in granitic rocks are therefore needed.

8.5 DISCUSSION

As shown in the previous section, the fracture permeability results are in good agreement with literature data. Hence, the presented experimental approach is deemed adequate to measure aligned and displaced fracture conductivities of granitic rocks.

The mechanical aperture change calculated from the strain data is in fair agreement with the aperture reduction measured before and after the test with the microscope (**Table 41**). This comparison can only be made for the two Samples with aligned fracture surfaces due to the lack of data for the two tests with displaced fracture surfaces. The optically determined change of the maximum aperture is 77 μm , the change of the mean aperture is 40 μm and the change of the median aperture is 34 μm . Compared to this, the aperture calculated from the strain measurements and extrapolated to 0 MPa confining pressure is about 80 μm , which is about equal to the change in optically determined maximum aperture. For Sample 34, a maximum aperture change of 142 μm , a mean aperture change of 153 μm , and a median aperture change of 120 μm were optically measured. The strain based aperture change extrapolated to 0 MPa is about 190 μm . The cause of the discrepancy is that the sample was able to relax after it was taken out of the triaxial test cell and before the aperture could be measured optically. An overestimation of the strain based aperture values might also be due to the heat shrink tube around the sample, which might be subject to a small part of deformation as well. Therefore, the mechanical behavior of the shrink tube needs further investigation. Absolute strain based mechanical aperture values are not given because there was no reliable method available to quantify the exact initial mechanical aperture for the samples.

Table 41: Apertures measured with a stereo microscope before and after the experiments.

Sample	Sierra granite (aligned)		34 (aligned)		31 (1 mm displacement)		32 (1 mm displacement)	
	before	after	before	after	before	after	before	after
No. of data points	129	201	61	182	119	99	108	-
Maximum aperture (μm)	248	171	426	284	492	434	485	-
Minimum aperture (μm)	0	0	0	0	0	0	0	-
Mean aperture (μm)	71	31	212	59	284	168	217	-
Standard deviation (μm)	46	24	110	52	85	82	65	-
Median (μm)	59	25	167	47	271	149	219	-

In all tests, mechanical apertures derived from strain and optical measurements and hydraulic apertures derived from permeability measurements were significantly different. Reasons for this discrepancy lie in the assumptions of the hydraulic model (cubic law). Fracture surfaces are rough and not smooth parallel plates, channeling may occur, fluid flow is tortuous and may be turbulent and not laminar at high flow rates. A reduction in mechanical fracture aperture may also increase these effects due to fracture surface roughness as stated by Develi & Babadagli (2015). All of these factors reduce the hydraulic aperture. Different fluid flow model assumptions would lead to different hydraulic apertures for the specific models.

Several relationships between mechanical and hydraulic apertures were proposed in the literature, which consider factors such as absolute and average asperity height, variation coefficient of the mechanical aperture, joint roughness coefficient, and shear displacement (Chen & Zhou 2011 and references therein). Based on these relationships, hydraulic apertures can be estimated for specific fluid flow models based on mechanical apertures if the mechanical aperture can be estimated. This is important since the hydraulic aperture is the value needed for flow calculations and numerical modeling.

Samples 31 and 32 (both with displaced fracture surfaces) both show a similar reduction of mechanical aperture with increasing confining pressure; however, the hydraulic aperture changes

only in Sample 32 and not in Sample 31. One explanation for this behavior is that the weaker Sample 32 (see tensile strengths in **Table 39**) was subject to significant asperity degradation at elevated confining pressures. This might lead to fracture closure and/or fines migration. The abrasion from the fracture surface might plug the fracture without significantly reducing the mechanical fracture aperture. Another possibility is fracture displacement, which could result in partial re-alignment of the fracture surfaces reducing the effective (hydraulic) aperture of the fracture but still keeping the same mechanical aperture.

Both factors might also be responsible for some permeability jumps that occurred during confining pressure cycling in Sample 32. While the global trend of the permeability development in this sample is reasonable, the reason for these permeability jumps remains unclear. Another explanation might be that the pressure fluctuations are the result of multiphase flow (e.g. air in the system). In that case the pressure drops and increases because gas flow paths are broken or reformed. Such a behavior was observed by Diomampo (2001).

8.6 CONCLUSIONS

In this study, the effective confining pressure dependent fracture permeabilities and hydraulic apertures of two aligned fractures and two displaced fractures in different granitic rocks were continuously measured during two subsequent confining pressure cycles from 2 MPa to 50 MPa. Additionally, the axial and lateral strain was measured to infer the mechanical aperture change of the fractures. Permeability and elastic behavior of one intact granitic rock sample during cyclic loading were also determined.

The fracture permeabilities of the tested granitic rocks lie between $1\text{e-}12\text{ m}^2$ (aligned fracture surfaces after 2 pressure cycles) and $2\text{e-}9\text{ m}^2$ (initial permeability with displaced fracture surfaces). Displaced fracture surfaces have significantly higher and more sustainable fracture permeabilities compared to aligned fracture surfaces. Aligned fractures were subject to permeability decrease even at 2 MPa constant confining pressure. However, samples with aligned fracture surfaces under 50 MPa confining pressure after two pressure cycles still had a 10 times higher sample permeability compared to the intact rock sample. These results are in general

agreement with fracture permeability data presented in the literature, which range between $3\text{e-}13\text{ m}^2$ (aligned fracture surfaces) and $4\text{e-}9\text{ m}^2$ (initial permeability of displaced tensile fractures).

Additionally, the data for fractures in granitic rocks was compared to fractures in sedimentary rocks. In general, aligned and displaced fractures in granitic rocks are more resistant to closure stress increase than similar fractures in sedimentary rocks. Displaced tensile fractures in granitic rocks have a similar permeability than fractures in sedimentary rocks, which are propped open by high strength proppants.

Comparison of the presented data and literature data with earlier simulation results lead to the conclusion that the development of complex fracture networks consisting of at least 100s of single fractures is a more promising concept for the development of an EGS in granitic basement rock than the development of some large single displaced fractures.

Overall, fractures developed for enhanced geothermal heat extraction from basement rocks by hydraulic stimulation treatments are more sustainable if the stimulated rock is stronger and a shear offset can be achieved. Proppants are not needed to maintain reasonably high fracture permeability for a short term (hours–days) in displaced tensile fractures in granites but they would be needed for a similar system in sedimentary rock (i.e. sandstones and shales). However, long term (months–years) permeability development at constant and cyclic changes of pressure and temperature as they occur in EGS especially of displaced fracture surfaces remains subject to further research.

REFERENCES

- Babadagli, T. & Develi, K., 2001. On the application of methods used to calculate fractal dimension of fracture surfaces, *Fractals*, 9, 105–28.
- Briggs, K., Hill, A.D., & Zhu, D., 2014. The relationship between rock properties and fracture conductivity in the Fayetteville Shale, SPE 170790, Annual Technical Conference and Exhibition, Amsterdam, The Netherlands, 27-29 October.
- Chen, Y. & Zhou, C., 2011. Stress/Strain-Dependent Properties of Hydraulic Conductivity for Fractured Rocks, In *Developments in Hydraulic Conductivity Research*, Dikinya O (Ed.), InTech. www.intechopen.com/books/developments-in-hydraulic-conductivityresearch/stress-strain-dependent-properties-of-hydraulic-conductivity-for-fractured-rocks
- Chen, Z., Narayan, S.P., Yang, Z., & Rahman, S.S., 2000. An experimental investigation of hydraulic behavior of fractures and joints in granitic rock. *Int. J. of Rock Mech. & Min. Sci.*, 37, 1061-1071.
- Cho, Y., Apaydin, O.G., & Ozkan, E., 2012. Pressure-dependent natural-fracture permeability in shale and its effect on shale-gas well production, SPE 159801, SPE Annual Technical Conference and Exhibition, San Antonio, TX, USA, 8-10 October..
- Cholach, P.Y., Molyneux, J.B., & Schmitt, D.R., 2005. Flin Flon Belt seismic anisotropy: elastic symmetry, heterogeneity, and shear-wave splitting, *Can. J. Earth Sci.*, 42, 533-554. doi: 10.1139/E04-094.
- Dempsey, D., Kelkar, S., Lewis, K., *et al.*, 2013. Modeling Shear Stimulation of the Desert Peak EGS Well 27-15 Using a Coupled Thermal-Hydrological-Mechanical Simulator, Proc. 47th US Rock Mechanics/Geomechanics Symposium, San Francisco, CA, USA, 23-26 June.
- Detournay, E., 1980. Hydraulic conductivity of closed rock fractures: an experimental and analytical study. Proc. 13th Canadian Rock Mechanics Symposium on Underground Rock Engineering, Montreal, Canada, 168-173.
- Develi, K., Babadagli, T., & Comlekci, C., 2001. A new computer controlled surface scanning device for measurement of fracture surface roughness, *Comput. Geosci.*, 27, 265–277. doi: 10.1016/j.ijrmms.2014.11.002.
- Develi, K. & Babadagli, T., 2015. Experimental and visual analysis of single-phase flow through rough fracture replicas, *Int. J. of Rock Mech. & Min. Sci.*, 73, 139-155. doi: 10.1016/j.ijrmms.2014.11.002.
- Diomampo, G.P., 2001. Relative permeability through fractures. *Technical report Stanford Geothermal Program*, SGP-TR-170. <https://pangea.stanford.edu/ERE/research/geoth/publications/techreports/SGP-TR-170.pdf>
- Elliott, G.M. & Brown E.T., 1988. Laboratory measurement of the thermos-hydro-mechanical properties of rock, *Quarterly Journal of Engineering Geology*, 21, 299-314.
- Fredd, C.N., McConnel, S.B., Boney, C.L., & England, K.W., 2000. Experimental study of hydraulic fracture conductivity demonstrates the benefits of using proppants. SPE 60326, Rocky Mountain Regional Low Permeability Reservoirs Symposium, Denver, CO, USA, 12-15 March.

- Gale, J.E., 1982. The effects of fracture type (induced versus natural) on the stress-fracture closure-fracture permeability relationships, Proc. 23rd U.S. Symposium on Rock Mechanics (USRMS), Berkeley, CA, USA, 25-27 August.
- Guitierrez, M., Oino, L.E., & Nygard, R., 2000. Stress-dependent permeability of a de-mineralised fracture in shale, *Marine and Petroleum Geology*, 17, 895-907.
- Haifeng, Z., Jun, S., Erfei, M., Hang, C., & Guohua, L., 2015. Scale model of stress sensitivity for fractured low-permeability reservoirs, Proc. 39th Workshop on Geothermal Reservoir Engineering, Stanford, California, 26-28 January, SGP-TR-204.
- Hakami, E. & Larsson, E., 1996. Aperture measurements and flow experiments on a single natural fracture, *Int. J. Rock Mech. Min. Sci. & Geomech. Abstr.*, 33, 395-404.
- Hofmann, H., Babadagli, T., & Zimmermann, G., 2014. Hot water generation for oil sands processing from enhanced geothermal systems: Process simulation for different hydraulic fracturing scenarios, *Applied Energy*, 113, 524-547.
- Huang, S.L., Oelfke, S.M., & Speck, R.C., 1992. Applicability of fractal characterization and modeling to rock joint profiles, *Int. J. Rock Mech. Min. Sci. Geomech. Abstr.*, 29, 89-98.
- Iwano, M. & Einstein, H.H., 1995. Laboratory experiments on geometric and hydromechanical characteristics of three different fractures in granodiorite, Proc. 8th ISRM Congress, Tokyo, Japan, 25-29 September.
- Jafari, A. & Babadagli, T., 2011. Generating 3D permeability map of fracture networks using well, outcrop, and pressure-transient data. *SPE Reservoir Evaluation & Engineering*, 14, 215-224. SPE 124077, doi: 10.2118/124077-PA.
- Kulatilake, P.H.S.W. & Um, J., 1998. Requirements for accurate quantification of self-affine roughness using the variogram method, *Int. J. Solids Struct.*, 35, 4167-89.
- Lee, H. & Cho, T., 2002. Hydraulic Characteristics of Rough Fractures in Linear Flow under Normal and Shear Load, *Rock Mech. and Rock Eng.*, 35, 299-318.
- Lemmon, E.W., Huber, M.L., & McLinden, M.O., 2013. NIST Standard Reference Database 23: Reference Fluid Thermodynamic and Transport Properties-REFPROP, Version 9.1, *National Institute of Standards and Technology, Standard Reference Data Program*, Gaithersburg 2013.
- Moore, J.R. & Glaser, S.D., 2007. Self-potential observations during hydraulic fracturing, *Journal of Geophysical Research*, 112, B02204.
- Morrow, C.A., Moore, D.E., & Lockner, D.A., 2001. Permeability reduction in granite under hydrothermal conditions, *Journal of Geophysical Research*, 106, 551-560.
- Pratt, H.R., Swolfs, H.S., Brace, W.F., *et al.*, 1977. Elastic and transport properties of an in situ jointed granite. *Int. J. Rock Mech. Min. Sci. & Geomech. Abstr.* 14, 35-45.
- Pyrak-Nolte, L.J. & Morris, J.P., 2000. Single fractures under normal stress: The relation between fracture specific stiffness and fluid flow. *Int. J. of Rock Mech. & Min. Sci.*, 37, 245-262.
- Raimbay, A., Babadagli, T., Kuru, E., & Develi, K., 2014. Effect of fracture surface roughness and shear displacement on permeability and proppant transportation in a single fracture,

Proc. SPE/CSUR Unconventional Resources Conference, Calgary, Alberta, Canada, September 30–October 2. doi: 10.2118/171577-MS.

Raven, K.G. & Gale, J.E., 1985. Water flow in a natural rock fracture as a function of stress and sample size, *Int. J. Rock Mech. Min. Sci. & Geomech. Abstr.*, 22, 251-261.

Reinicke, A., Blöcher, G., Zimmermann, G., *et al.*, 2013. Mechanically induced fracture-face skin: Insights from laboratory testing and modeling approaches, *SPE Production & Operations*, 28, 26-35.

Terzaghi, C., 1925. Principles of Soil Mechanics, *Engineering News-Record*, 95, 19-27.

Tester, J.W., Anderson, B.J., Batchelor, A.S., *et al.*, 2006. The future of geothermal energy impact of enhanced geothermal systems (EGS) on the United States in the 21st century, Massachusetts Institute of Technology [online]. www.leere.energy.gov/geothermal/egs_technology_html.

Watanabe, N., Hirano, N., & Tsuchiya, N., 2008. Determination of aperture structure and fluid flow in a rock fracture by high-resolution numerical modeling on the basis of a flow-through experiment under confining pressure, *Water Resour. Res.*, 44, W06412. doi:10.1029/2006WR005411.

Watanabe, N., Hirano, N., & Tsuchiya, N., 2009. Diversity of channeling flow in heterogeneous aperture distribution inferred from integrated experimental-numerical analysis on flow through shear fracture in granite, *J. of Geophysical Research*, 114, B04208.

Watanabe, N., Ishibashi, T., Ohsaki, Y., *et al.*, 2011. X-ray CT based numerical analysis of fracture flow for core samples under various confining pressures, *Engineering Geology*, 123, 338-346. doi:10.1016/j.enggeo.2011.09.010.

Yoon, J.S., Zimmermann, G., & Zang, A., 2014. Numerical investigation on stress shadowing in fluid injection-induced fracture propagation in naturally fractured geothermal reservoirs, *Rock Mech. Rock Eng.* Doi: 10.1007/s00603-014-0695-5.

Zhang, J., Kamenov, A., Zhu, D., *et al.*, 2014. Laboratory measurement of hydraulic-fracture conductivities in the Barnett Shale, *SPE Production & Operations*, August 2014, 216-227, SPE 163839.

Zhao, J. & Brown, E.T., 1992. Hydro-thermo-mechanical properties of joints in the Carnmenellis granite, *Quarterly Journal of Engineering Geology*, 25, 279-290.

CHAPTER 9: A HYBRID DISCRETE/FINITE ELEMENT MODELING STUDY OF COMPLEX HYDRAULIC FRACTURE DEVELOPMENT FOR ENHANCED GEOTHERMAL SYSTEMS (EGS) IN GRANITIC BASEMENTS

A version of this chapter was submitted to *International Journal of Fracture*.

The technical and economic success of enhanced geothermal systems (EGS) in granitic basement rocks depends on the ability to effectively develop complex fracture networks by hydraulic stimulation treatments. To study hydraulic fracture growth, horizontal two dimensional discrete element models were set up for the conditions expected in Precambrian basement rocks in Northern Alberta. The simulated fracture networks were then transferred to a finite element reservoir model to investigate the thermal and hydraulic efficiencies of the fracture networks. Natural and engineering factors influencing stimulated fracture network complexity are summarized and their significance is discussed based on the simulation results. The numerical results fit reasonably well to major field observations and led to a proposed reservoir stimulation guideline. This guideline involves drilling wells with a horizontal segment at reservoir depth, performing multiple sequential stimulation treatments alternating between two wells with an offset between the stages in both wells, and a long continuous injection of low viscosity fluid at a high rate without proppants. Favorable drilling targets for the development of complex fracture networks are brittle rocks in complex tectonic settings that are characterized by at least two intersecting natural fracture sets that are favorably oriented to the in-situ stress field, a low difference between the major principle stresses, and a low reservoir permeability. The reservoir simulations show the benefit of developing well connected complex fracture networks compared to single parallel hydraulic fractures.

9.1 INTRODUCTION

The largest potential for geothermal energy lies within deep and hot low permeability granitic basement rocks [Tester *et al.*, 2006]. However, the energy stored in these rocks cannot be utilized with conventional techniques. These systems need additional engineering to access the stored heat and are hence commonly referred to as engineered or enhanced geothermal systems (EGS). Such a system typically consists of at least one production well through which the hot fluid is produced, at least one injection well through which the colder fluid from the surface is re-injected to the reservoir, and a fracture network that hydraulically connects production and injection wells.

The major challenge in EGS reservoir engineering is the development of a suitable fracture network that acts as subsurface heat exchanger and fluid pathway. A suitable fracture network must fulfill two requirements. First, the fluid flow rate through the fracture network and the productivity of a production well has to be high enough to extract enough heat energy to be economical. Second, the residence time of the re-injected cold fluid must be long enough to be able to heat up before it reaches the production well and to avoid early breakthrough of the cold water plume at the production well, which can be achieved by large enough heat exchanger (fracture) surface areas. Additionally, a large enough rock mass volume needs to be accessed to exploit the required amounts of heat.

The development of a complex (branched) fracture network, rather than creating single high permeability fractures, was proposed as the key for economical EGS energy extraction [Hofmann *et al.*, 2014a]. This is because complex fracture networks with relatively low permeable single fractures can have the same overall hydraulic conductivity as a single high permeable fracture to allow the production of a sufficient amounts of fluid, but with the advantage that the heat exchanger area (fracture surface area) is significantly increased and single fracture permeability is low enough to prevent early breakthrough of the cold water front from the injection well(s) at the production well(s).

Although a single fracture can already follow a complex (irregular) path (e.g. due to interaction with discontinuities in the rock and the stress field and anisotropic rock properties), the focus in this study is on the complexity of a whole fracture network. Besides other measures such as the

fairway aspect ratio (fracture network width divided by fracture network length; [Hofmann *et al.*, 2014b]), this fracture network complexity may be considered as the number of individual fractures that build up a fracture network. In this study, the influence of the investigated model parameters on the amount and type of individual cracks that develop during hydraulic stimulation treatments are studied together with the fracture network patterns.

Even though hydraulic fracturing treatments are still often assumed to result in simple shaped bi-wing fractures, early mineback experiments of hydraulic fracturing treatments (direct fracture examination through excavation of the rock) already led to the conclusion that even in homogeneous formations fractures are more complex [Warpinski and Teufel, 1987].

The development of complex fracture patterns was observed in different rock types at scales from micrometers (e.g. grain crushing [Haimson and Chang, 2005]) over hundreds of meters (e.g. hydraulic fracturing [Warpinski and Teufel, 1987]) to kilometers (e.g. mid-oceanic ridges [Weiland *et al.*, 1996]). Besides direct observations in neighboring wells [Fisher *et al.*, 2002], microseismicity [Cipolla *et al.*, 2008a; Warpinski *et al.*, 2008; Warpinski *et al.*, 2005; Maxwell *et al.*, 2002], tilt mapping [Fisher *et al.*, 2002], treatment pressure analysis [Fisher *et al.*, 2002], production data [Fisher *et al.*, 2002], and reservoir modeling [Xu *et al.*, 2012] also support the observation of complex fracture network development resulting from hydraulic stimulation treatments in various geological environments. The most important natural factors triggering hydraulic fracture complexity were found to be discontinuities (joints, faults, bedding planes) and heterogeneities within the rock mass (e.g. Warpinski and Teufel [1987]) in conjunction with the in-situ stress field (e.g. Chen *et al.* [2008]; Cipolla *et al.* [2008b]). Environments where complex fracture networks may be formed include shale formations such as the Barnett shale [Fisher *et al.*, 2002; Maxwell *et al.*, 2002] and granitic basement rock [Xu *et al.*, 2012].

In previous studies, some factors affecting complex fracture network development were already identified and investigated. For example, Kan and Olson [2015] investigated complex fracture development in naturally fractured reservoirs using a displacement discontinuity method; Ren *et al.* [2014] provide a review of factors and mechanisms of complex fracture development in shales; Pearson *et al.* [2013] presented completion and stimulation designs that increase fracture complexity in the Bakken shale; Nagel *et al.* [2013] evaluated completion techniques for their influence on shale fracture complexity using a 2D discrete element model, and; Cipolla *et al.*

[2008b] presented relationships between reservoir properties, treatment design, and fracture complexity in shales. *Hofmann et al.* [2014b] compared complex fracture development in shales and granite using the software MShale, but most of the factors are not sufficiently understood and most of the work was done for shales only. To the authors' knowledge, recommendations on methods to increase fracture network complexity for EGS development in granitic basement rocks were not yet presented in previous literature.

Therefore, this study systematically summarizes and investigates major engineering practices that aim to increase the stimulated hydraulic fracture network complexity by hydro-mechanical distinct element modeling. Similar horizontal 2D reservoir scale hydraulic stimulation models were set up in previous studies to investigate the effect of different parameters and effects, such as injection scheme and the stress shadowing effect on induced seismicity [*Yoon et al.*, 2014a-b, 2015].

To evaluate the efficiency of the stimulation treatments, the resulting fracture networks are exported to the reservoir simulator OpenGeoSys [*Kolditz et al.*, 2012] using a recently developed interface [*Hofmann et al.*, 2015a]. With this finite element code the hydraulic and thermal efficiencies of the developed fracture networks are investigated and compared. The numerical study is done for a hypothetical EGS project in Fort McMurray (Northern Alberta, Canada) where geothermal energy from deep Precambrian basement rocks could be used as alternative heat source for oil sands processing [*Hofmann et al.*, 2014a]. Previous studies done for this location [*Hofmann et al.*, 2014a-b] lack of some important aspects of fracture development such as the possibility of shear failure, arbitrary fracture shapes and heterogeneity of the rock mass. These features are all included in the model presented in this study, which can therefore be seen as a supplement of the previous studies.

First, natural and engineering factors are reviewed that potentially alter fracture network complexity. Then, the distinct element model is explained and the model setup is presented. In the end, the modeling results are presented and discussed.

9.2 POTENTIAL FACTORS GOVERNING FRACTURE NETWORK COMPLEXITY

The following review of factors governing the complexity of engineered fracture networks in low permeability rocks summarizes mostly laboratory and field scale work done on shales, but the qualitative statements should also be valid for other rock types such as granites. More detailed explanations of these factors are given in *Ren et al.* [2014] and *Cipolla et al.* [2008b].

9.2.1 Natural factors

The **tectonic setting** and the **geological history** are the first order controls on fracture network complexity in low permeability rocks because they control the three second order natural factors that are presented below [*Potocki*, 2012]. Rocks in more complex tectonic settings (e.g. strike-slip/thrust regimes) are subject to additional tectonic stress and are intervened by more natural discontinuities as compared to more simple tectonic settings (e.g. passive margins). Fluid injection into these systems leads to a more complex interaction between induced fractures and discontinuities [*Potocki*, 2012] and hence the resulting fracture network is more complex.

Natural discontinuities such as faults, natural fractures, and bedding planes are a major factor governing fracture complexity. Field tests and mineback observations show the development of complex branching fractures in fractured formations [*Warpinski and Teufel*, 1987]. The importance of natural discontinuities results from several aspects. First, developing hydraulic fractures might intersect a natural discontinuity, follow it, or die out due to fluid leak-off into the natural fracture depending on the local in-situ stresses and the geometry of the natural and induced fracture (especially the approach angle) and fracture properties [*Chuprakov et al.*, 2011]. Additionally, it was observed that fluid injected into a long open hole section mainly flows into one or a few pre-existing fractures (e.g. at Soultz-sous-Forêts *Michelet and Toksöz* [2007]). Another important aspect is that critically oriented fractures seem to be the major fluid conduits in fractured reservoirs [*Barton et al.*, 1995] and injected fluid might follow these critically stressed pre-existing fractures, which generally are not perpendicular to the minimum principle stress and hence the fluid flow path would be more complex than in an induced tensile fracture in an intact rock mass. *Kan and Olson* [2015] found in a numerical modeling study that the fracture

propagation path is dominated by the longest natural fractures and by natural fractures that make a small angle with approaching hydraulic fractures.

The in-situ stress is another major parameter governing fracture complexity. As mentioned earlier, the stress field needs to be seen in conjunction with pre-existing discontinuities in the rock mass, but in general small differences between the principle stresses tend to increase fracture network complexity [Chen *et al.*, 2008]. Local stresses changed due to stimulation treatments are more likely to change the directions of the principle stresses if the difference between them is smaller.

Rock mechanics properties are the third important factor influencing fracture complexity [Ren *et al.*, 2014]. Rickman *et al.* [2008] proposed that rock **brittleness** (which combines Poisson's ratio and Young's modulus and depends on the mineralogy of the rock) influences fracture complexity. A more brittle rock with a higher Young's modulus and a lower Poisson's ratio has a higher tendency to develop complex fracture networks. Layered rock and anisotropic minerals within the granite also influence the fracture development.

Hydraulic reservoir properties are the forth factor that govern fracture development. In higher permeable formations, fluid leak-off results in lower fluid pressures inside the fracture network during stimulation treatments. Hence, fracture patterns are less complex in higher permeable formations (e.g. sandstones) compared to lower permeable formations (e.g. shales and granites).

9.2.2 Engineering factors

From the natural factors summarized above, only local stress fields may be changed and the natural fracture network may be stimulated and extended by engineering measures. The general geology and rock mechanics properties cannot be changed. Some treatment design parameters that have the potential to increase fracture network complexity are summarized now.

For example, higher fracture complexity is observed in water fracturing treatments using low viscosity slickwater as **fracturing fluid type** as compared to cross-linked gel treatments using higher viscosity gels [Cipolla *et al.*, 2008a].

Larger **fluid volumes and treatment durations** also help to increase complexity by simply covering a larger area that is contacted by the injected fluid [Ren *et al.*, 2014]. This increases the chance to connect more natural fractures to the fracture network.

High **flow rates** [Pearson *et al.*, 2013] and therefore high net pressures [Ren *et al.*, 2014] may also be used to increase fracture complexity. This is because increasing the bottom hole pressure above the minimum principle stress forces the tensile opening of new (and existing) fractures in addition to shear of existing fractures [McClure and Horne, 2014], which potentially results in a more complex fracture network.

For the **injection scheme**, numerical investigations show that continuous fluid injection may lead to more complex fracture networks compared to cyclic rate injections [Yoon *et al.*, 2015]. This is because in cyclic injection schemes, there is time for the rock mass to relax and reduce the net pressure in the developing network. On the other hand, Safari *et al.* [2013] pointed out that pulsed fracturing (creating bottom hole pressure above the minimum and maximum principle stresses for short periods of time) has the potential to force fracture propagation in multiple directions.

The well locations and **well paths** can be used to alter fracture network complexity by vertical deviation and by deviation from the minimum and maximum principle horizontal stress directions. Additionally, the distance to neighboring wells might be important if they are also stimulated.

Multiple stimulation treatments (i.e., pre-stimulation treatments, re-stimulation treatments, multi-stage treatments) are thought to be the major and most promising methods to develop complex fracture networks. Because there are always discontinuities in the subsurface with different orientations, altering the local stress field (e.g. by pre- or re-stimulation treatments and utilizing the stress shadow effect) will induce shear failure in different fracture sets and, hence, increase overall fracture network complexity. An opened fracture exerts additional compressive stress in the direction normal to the fracture [Warpinski and Branagan, 1989]. The stress shadow resulting from the opening of a pre-existing or new fracture due to fluid injection therefore changes the local stresses surrounding the stimulated area, which in turn alters the fracture paths from neighboring stimulation stages. That is why multi-stage stimulations, stimulations in

neighboring wells, re-stimulation treatments, and pre-stimulation treatments might be performed to make use of the stress shadow effect to increase fracture network complexity. An earlier DEM study on stress shadowing performed by *Yoon et al.* [2014b] reveals that the stress shadow effect leads to deviated fracture growth paths in such a model.

The **completion design** is another important factor that has an impact on the fracture network pattern resulting from hydraulic stimulation treatments. Main aspects are the distance between several stimulation stages and the order in which these treatments are performed (e.g. at the same time in two neighboring wells, at the same time in one well, subsequently, etc.). As explained above, this is mainly due to changes in the local stress field resulting from earlier stimulation stages [*Nagel et al.*, 2013]. As part of the well completion there are also an optimum number of fractures per stage to maximize total fracture surface area [*Kan and Olson*, 2015].

Whether (and how) the above summarized factors influence stimulated fracture network complexity and what would be the effect on thermal and hydraulic reservoir performance is investigated further in this study by DEM and FEM simulations.

9.3 DISCRETE ELEMENT FRACTURE MODEL

9.3.1 Particle flow code 2D

The two dimensional version of the discrete element model Particle Flow Code (PFC2D, *Itasca* [2008]) was used to simulate complex fracture development in low permeable basement rocks. The model consists of discrete non-deformable cylindrical particles with unit thickness.

Particles are connected at their contact points by parallel bonds of finite strength, which may break in tensile mode (Mode I failure) and in shear mode (Mode II failure) as a result of applied loads following the Mohr-Coulomb failure criterion. Each broken bond is assumed to be an individual fracture. More details about the parallel bond contact model are given in *Potyondy and Cundall* [2004].

Pre-existing fractures are represented by the smooth joint contact logic [*Mas Ivars et al.*, 2011]. These contacts suppress the geometric roughness that would result from the model discretization.

Instead a smooth joint dilation angle is specified to model fracture roughness independent of the model discretization. The smooth joint contacts are characterized by a separate set of parameters for each fracture set.

For the simulation of hydraulic stimulation treatments, a fluid flow algorithm and a hydro-mechanical coupling scheme are used and are summarized below, but are explained in detail in *Yoon et al.* [2014a]. By assuming bonded particle contacts to be fluid flow channels viscous fluid flow through the particle assembly is simulated. The spaces between the particles are polygonal pore spaces, which are connected by the flow channels and in which fluid is stored. The volume of these pore spaces equals to the mechanical apertures of the connected flow channels multiplied the reservoir thickness and a multiplication factor. Pressure differences between two neighboring pore spaces cause fluid flow through the connecting flow channel. The rate at which the fluid flows from one to another pore space is governed by the cubic law by assuming laminar flow between two smooth parallel plates (**Equation 16**).

$$q = \frac{Ha^3\Delta P_f}{12\mu L} \quad (16)$$

H is the hydraulic reservoir thickness, a is the hydraulic aperture of the flow channel, ΔP_f is the fluid pressure difference between two neighboring pore spaces, L is the length of the flow channel connecting these pore spaces, and μ is the fluid viscosity.

For each time step the fluid pressure change in a pore space is calculated by **Equation 17** as a function of fluid bulk modulus K_f , pore space volume V_d , net sum of the flow volume entering and leaving the pore space, and the change of pore space volume ΔV_d resulting from mechanical loading [*Yoon et al.*, 2014a].

$$\Delta P_f = \frac{K_f}{V_d} \left(\sum q \Delta t - \Delta V_d \right) \quad (17)$$

The resulting force exerted by the fluid pressure causes deformations on the surrounding particles, which in turn changes stress states at the surrounding areas and results in aperture changes in surrounding flow channels. Fluid volume and pressure increase due to fluid injection

therefore leads to bond breakages in the particle assembly. Once a parallel bond is broken fracture aperture is set to the aperture at zero normal stress a_0 .

For intact bonds the hydraulic aperture a of the flow channel changes as a function of the hydraulic aperture at infinite normal stress a_i , the hydraulic aperture at zero normal stress a_0 , the normal stress at the particle contact σ_n and a coefficient of decay α according to **Equation 18** [Hökmark *et al.*, 2010].

$$a = a_i + (a_0 - a_i) \exp(-\alpha \sigma_n) \quad (18)$$

If a bond between two particles is broken the pressure at both domains connected by this contact is the average pressure between the two domains.

9.3.2 Model setup

The horizontal two dimensional 3 km x 3 km model is aligned with the main principle stress axes S_h and S_H . Particle diameters range between 40 m and 60 m which is approximately twice the size of particles in previous studies [Hazzard *et al.*, 2002; Yoon *et al.*, 2015] and allows sufficient resolution at reasonable simulation times. The model is surrounded by a 100 m wide zone of larger particles. Fluid is injected at ten different points in each model along two lines that represent horizontal wells, which are each stimulated five times. The hydraulic behavior of the well is not explicitly modeled. The base case model is set up of 2 x 5 injection points representing 10 fracturing stages in two parallel horizontal wells. Stage spacing is 300 m and well spacing is 400 m. In the base case scenario, water injection is performed subsequently for one hour at each stage at a constant rate of 100 l/s and the model is run for another hour after the last stage is finished, leading to a total simulation time of 11 hours. The total injected fluid for all scenarios is the same (3600 m³) unless otherwise stated. The model setup of the base case model is shown in **Figure 132**. Variations of this base case model are explained in **Section 9.5**.

Model properties were taken from a previous study on hydraulic stimulation treatments in 5 km deep granitic basement rock in Northern Alberta [Hofmann *et al.*, 2014a]. Since this previous study only accounted for tensile failure, shear failure criteria are taken from different sources. Pre-existing fracture properties were partly taken from Yoon *et al.* [2015]. Apertures at zero and

infinite normal stress and the correlation coefficient α were estimated based on previous laboratory studies of pressure dependent fracture permeability measurements on Granites [Hofmann *et al.*, 2015b]. A summary of all parameters specified for the DEM model is given in **Table 42**. Since the fluid properties are constant fluid viscosity and isothermal bulk modulus were used for water with a temperature of 30°C and a pressure of 49 MPa, which are assumed to be the conditions for a short term injection (hours) where the injected water does not have enough time to heat up significantly.

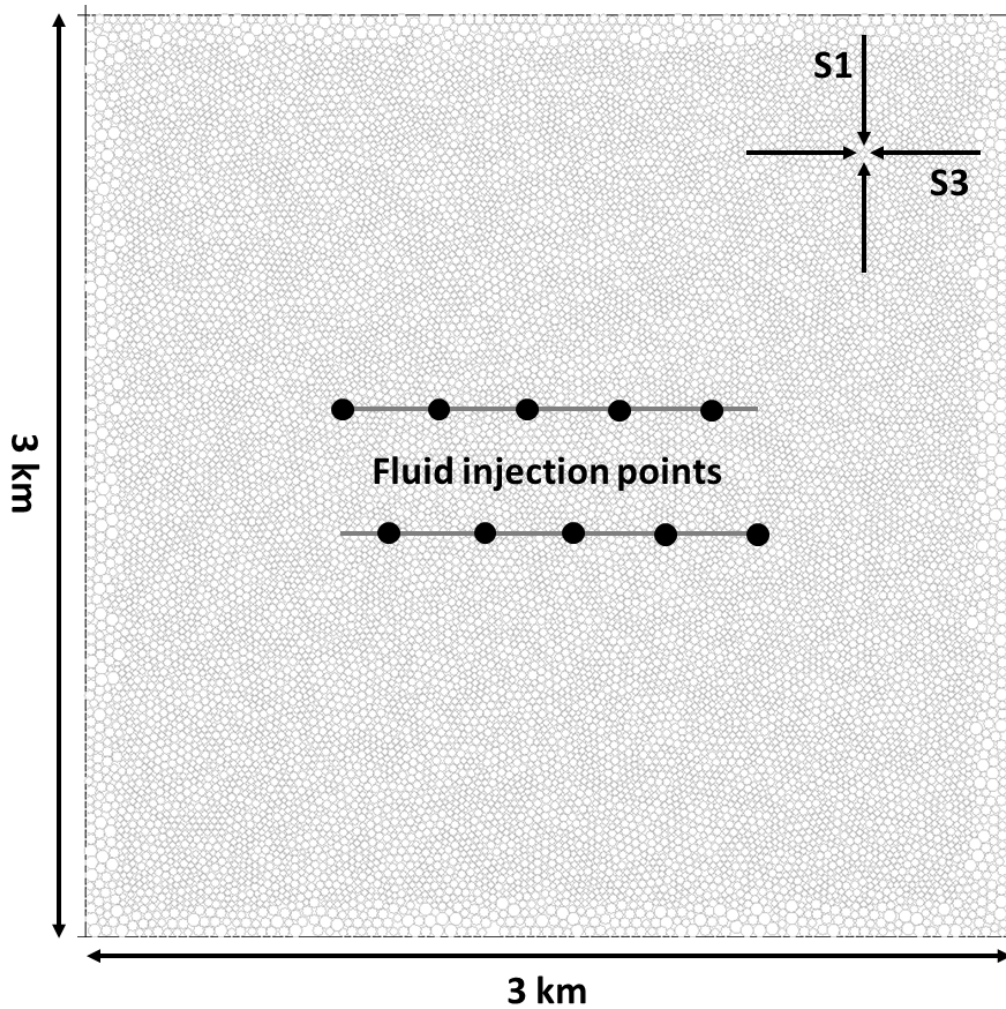


Figure 132: The two dimensional horizontal discrete element hydraulic fracturing model showing the particles, the principle stress directions and the injection point locations for the base case model.

Table 42: Model parameters of the discrete element fracture model.

DEM Model Property	Value	References & Remarks
Model size	3 x 3 km	100 m layer with coarser particles around the model
Particle diameter range	40 - 60 m	
Time step	1.5 s	
Effective maximum horizontal stress S_H'	40 MPa	At 5 km depth, 20–56 MPa [Hofmann et al., 2014a]
Effective minimum horizontal stress S_h'	20 MPa	At 5 km depth [Hofmann et al., 2014a]
Rock matrix		Parallel bond model [Potyondy and Cundall, 2004]
Tensile strength	12 MPa	Hofmann et al. [2014a]
Cohesion	23 MPa	Aue granite [Yoon et al., 2012]
Friction angle	52°	Aue granite [Yoon et al., 2012]
Friction coefficient	0.9	Cornet et al. [2007]
Young's modulus	55 GPa	Hofmann et al. [2014a]
Poisson's ratio	0.2	Hofmann et al. [2014a]
Normal to shear stiffness ratio	2.5	Yoon et al. [2012]
Density	2650 kg/m ³	Hofmann et al. [2015a]
Pre-existing fractures		Smooth joint model [Mas Ivars et al., 2011]
Tensile strength	0.0 MPa	Yoon et al. [2015]
Cohesion	0.5 MPa	Yoon et al. [2015]
Friction angle	30°	Yoon et al. [2015]
Dilation angle	3°	Yoon et al. [2015]
Normal stiffness	20 GPa/m	assumed
Shear stiffness	5 GPa/m	assumed
Fluid flow model		Cubic law
Fluid viscosity	0.8 mPa s	Water at 30 °C & 49 MPa [Lemmon et al., 2013]
Fluid bulk modulus	2.5 GPa	Water at 30 °C & 49 MPa [Lemmon et al., 2013]
Initial reservoir pressure	0 MPa	Saturated, but 0 MPa pressure [Yoon et al., 2015]
Aperture at zero normal stress a_0	200 μ m	Hofmann et al. [2015b], displaced tensile fractures
Aperture at infinite normal stress a_i	5 μ m	Hofmann et al. [2015b], aligned tensile fractures
Coefficient of decay α	1.0	So closed cracks behave like aligned tensile fractures and open cracks like displ. tensile fractures

9.4 FINITE ELEMENT RESERVOIR MODEL

9.4.1 OpenGeoSys

The thermal and hydraulic behavior of the fracture networks developed with the DEM model is simulated using the open source finite element based open source code OpenGeoSys (OGS, *Kolditz et al.* [2012]). The fracture network geometry and fracture properties (i.e. aperture) were exported to OGS using a recently developed interface [*Hofmann et al.*, 2015a]. The flow pipe geometry, which connects the hydraulic domains in PFC, was exported to OGS using a modified version of the meshing tool MeshIt [*Blöcher et al.*, 2010; *Blöcher et al.*, 2015; *Cacace and Blöcher*, 2015]. A FE mesh was generated around the cracked elements, which were included as discrete elements in the FE model. Hydraulic fracture apertures and fracture lengths L were converted to fracture permeabilities k_f (**Equation 19**) and cross-sectional areas A (**Equation 20**).

$$k_f = \frac{a^2}{12} \quad (19)$$

$$A = La \quad (20)$$

OGS is capable of calculating fluid flow and heat transport through a porous media, which may be intersected by a network of discrete fractures with arbitrary shape [*Cacace et al.*, 2013; *Cherubini et al.*, 2013]. Similar to the DEM model, fluid flow through fractures is calculated using the cubic law assuming laminar flow between smooth parallel plates. The authors refer to *Watanabe et al.* [2010] and *Watanabe et al.* [2012] for a more detailed description of governing equations and numerical schemes.

9.4.2 Model setup

In the current study the two dimensional DEM model was converted to a two dimensional FEM model (**Figure 133**) with the interface described in *Hofmann et al.* [2015a]. Model size and model properties were the same; only the matrix between the fractures was given a permeability of $0.5\text{e-}18 \text{ m}^2$ and porosity of 0.5%. Additionally, thermal properties of the reservoir model were specified. These properties were also taken from *Hofmann et al.* [2014a].

Initial conditions were a homogeneous reservoir pressure of 49 MPa and a homogeneous temperature of 100°C. Outer model boundaries were given a no flux boundary condition. The FE mesh was refined around wells and fractures with a minimum edge length of 2 m. The maximum edge length away from these line elements was 50 m. Wells were represented as linear elements with 100% porosity and properties of water. Water properties (density, viscosity, heat capacity, and thermal conductivity) were pressure and temperature dependent.

For simplicity, a pressure dependent fracture conductivity relation was not specified because only the relative amounts of productivity and temperature development in the production wells were of concern for this study. Parameters of the FEM model are given in **Table 43**.

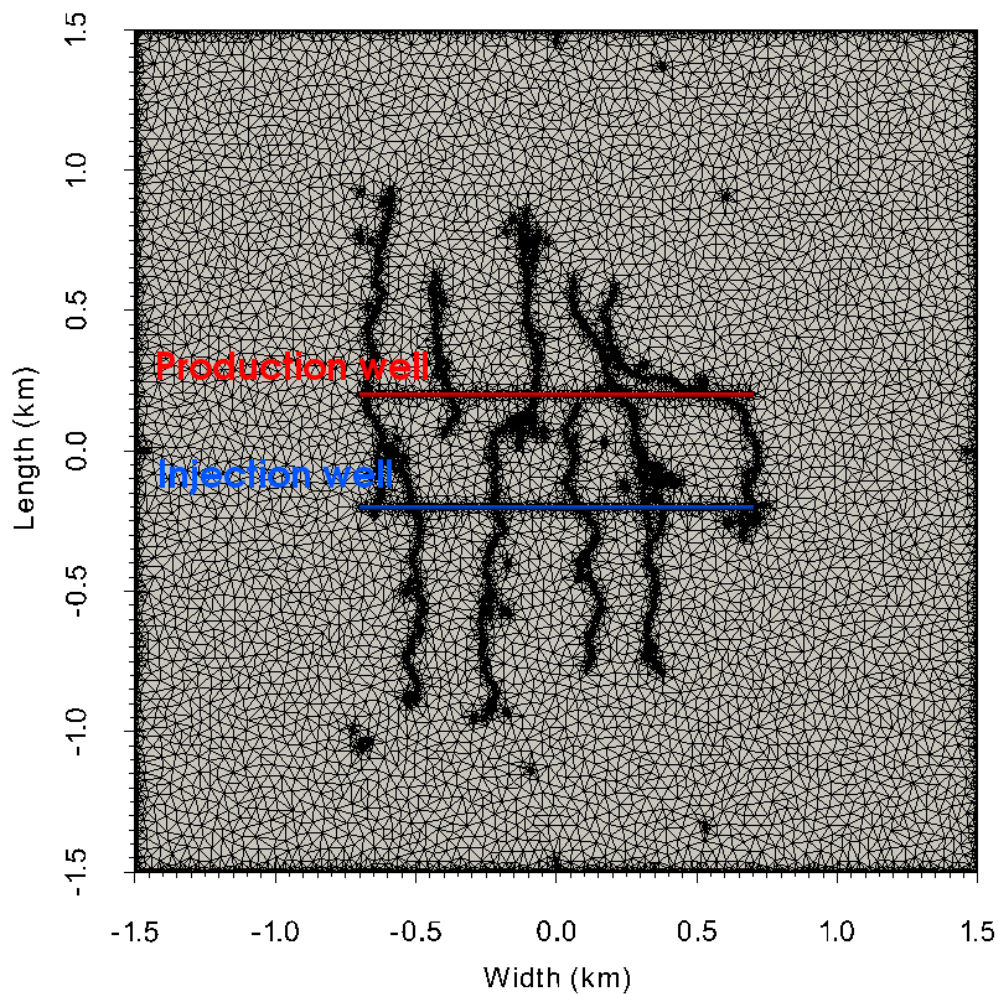


Figure 133: Setup of an exemplary FEM model including the two horizontal wells. The FE mesh is refined around wells and fractures.

Table 43: Model parameters of the finite element reservoir model.

FEM Model Property	Value	References & Remarks
Boundary conditions (.bc)		
(Re-)Injection temperature	30 °C	<i>Hofmann et al.</i> [2014a]
Outer model boundaries	No flux	adiabatic
Initial conditions (.ic)		
Domain pressure	49 MPa	<i>Hofmann et al.</i> [2014a]
Domain temperature	100 °C	<i>Hofmann et al.</i> [2014a]
Temperature in injection well	30 °C	<i>Hofmann et al.</i> [2014a]
Fluid properties (.mfp)		
Density water	$f(P,T)$ kg/m ³	Helmholtz free energy model
Viscosity water	$f(P,T)$ Pa s	IAPWS-2008 model
Heat capacity water	$f(P,T)$ J/kg/K	IAPWS-IF97 model
Thermal conductivity water	$f(P,T)$ W/m/K	IAPWS-2008 model
Medium properties (.mmp)		
Formation thickness/fracture area	200 m / $f(a)$	Avg. frac heights from <i>Hofmann et al.</i> [2014a] / Eq. 20
Matrix/fracture porosity	0.5% / 100%	<i>Hofmann et al.</i> [2014a] / open fracture
Matrix/fracture tortuosity	1 / 1	Assuming flow through parallel plates
Matrix/fracture storage	1e-10 / 4.6e-10	For solid rock / property of water
Matrix/fracture permeability	0.5e-18 m ² / $f(a)$	<i>Hofmann et al.</i> [2014a] / Eq. 19
Solid properties (.msp)		
Density	2650 kg/m ³	<i>Hofmann et al.</i> [2014a]
Heat capacity	900 J/kg/K	<i>Hofmann et al.</i> [2014a]
Thermal conductivity	2.7 W/m/K	<i>Hofmann et al.</i> [2014a]
Source terms (.st)		
Injection rate	10 l/s	To avoid excessive pressure buildup in low PI scenarios
Production rates	10 l/s	To avoid excessive pressure drawdown in low PI scenarios
Time discretization (.tim)		
Minimum time step size	1 s	
Maximum time step size	1 year	
Total simulation time	30 years	

9.5 MODELING PROCEDURE

First, hydraulic stimulation simulations were performed using the DEM base case model. The results of this base case model were first compared to the results of a classical hydraulic fracturing model. Based on the governing factors identified in **Section 9.2**, the base case model was altered to see the effect of different parameters on the developed fracture patterns. These parameters specifically include completion design, stage spacing, well spacing, well azimuth, and treatment design as engineering factors and stress field, pre-existing fractures, and permeability as natural factors. For each scenario, the fracture pattern is shown and the changes in the patterns are identified. To evaluate the thermal and hydraulic efficiency of each treatment, the fracture patterns were exported to OGS and a 2D thermal-hydraulic reservoir model was run for 30 years. Productivity indices (production rate divided by the pressure drawdown in the production well) and temperature drawdowns in the production wells are therefore compared to each other and to the number of broken bonds (cracks) and major flow paths that developed between the two wells. In the end, suggestions are made on how to increase fracture network complexity in Northern Alberta Precambrian basement rocks by means of different engineering measures and under which reservoir conditions it is more likely to be able to develop such a system.

9.6 HYDRAULIC FRACTURING SIMULATION RESULTS

9.6.1 Base case model

The base case modeling results were compared to the classical two dimensional PKN model for hydraulic fracture development [Perkins and Kern, 1961; Nodgren, 1972]. The PKN fracture aperture w on the position x along the hydraulic fracture length L was calculated with **Equation 21** using the fluid viscosity μ and elastic properties (ν and E) from **Table 42**.

$$w(x) = 3 \left[\frac{\mu q (1 - \nu^2) (L - x)}{E} L \right]^{1/4} \quad (21)$$

Based on the average PKN fracture aperture, the fluid volume was calculated to develop a hydraulic fracture with a certain length and height. The PKN model predicts the development of

an 850 m long and 200 m high hydraulic fracture with an injection of 358 m³ of water within one hour at a rate of 100 l/s. In the first stage of the base case DEM model a fracture with 878 m length (distance between the two broken bonds at the two ends of the fracture) and 200 m height was developed due to an injection of 360 m³ of water within one hour at a rate of 100 l/s. The difference in the predicted length was 28 m, which was below the resolution of the model (particle diameters range between 40 and 60 m) and were therefore judged as insignificant. Both fracture wings did not have the same length in the DEM model because of the inhomogeneous structure of the model.

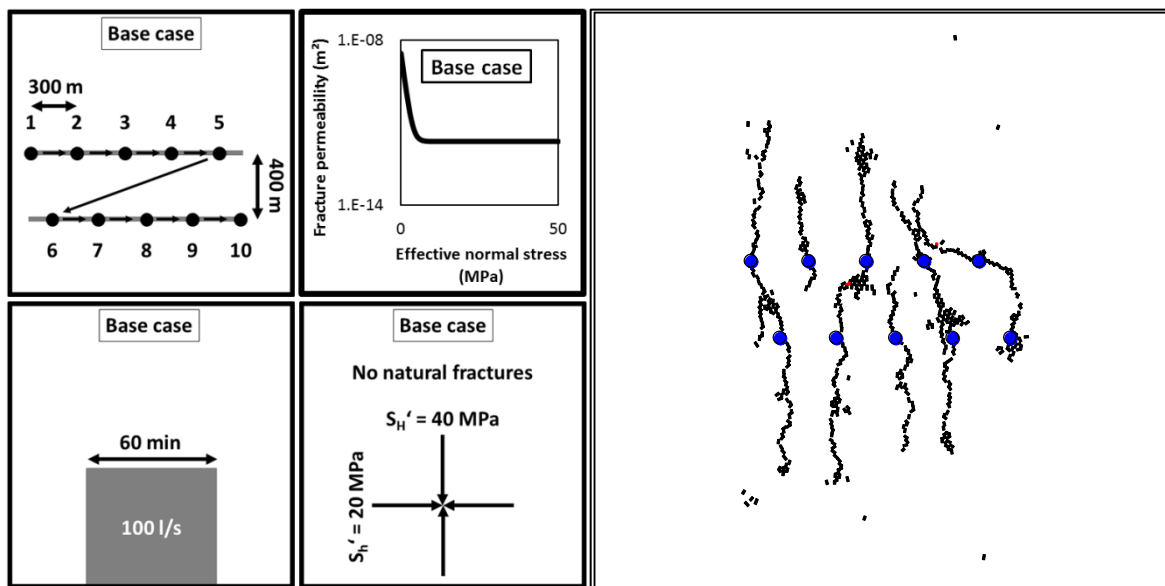


Figure 134: Base case completion design, treatment design, fracture permeability and stress (left) and simulated fracture network (right).

Figure 134 shows the model setup and the final developed fracture network for this calibrated base case model after ten subsequent stimulation stages of 360 m³ each. Stage spacing was 300 m and the stages between the wells were shifted by 150 m. In **Figure 135**, the fluid pressures in the injection domains of all stages are given, and in **Figure 136**, the average minimum and maximum effective horizontal stresses in a 200 m diameter circle around each stage are displayed. In the first three stages, relatively straight parallel fractures were developed perpendicular to S_h (**Figure 134**). Because the fluid pressure increased for each stage within one well (**Figure 135**) due to the stress shadow effect, S_h' increased from initially 20 MPa to values close to S_H' of almost 40 MPa. Since S_H' remained relatively unchanged (**Figure 136**) the developed fractures in the fourth and fifth stage grew in a different direction than the first three fractures.

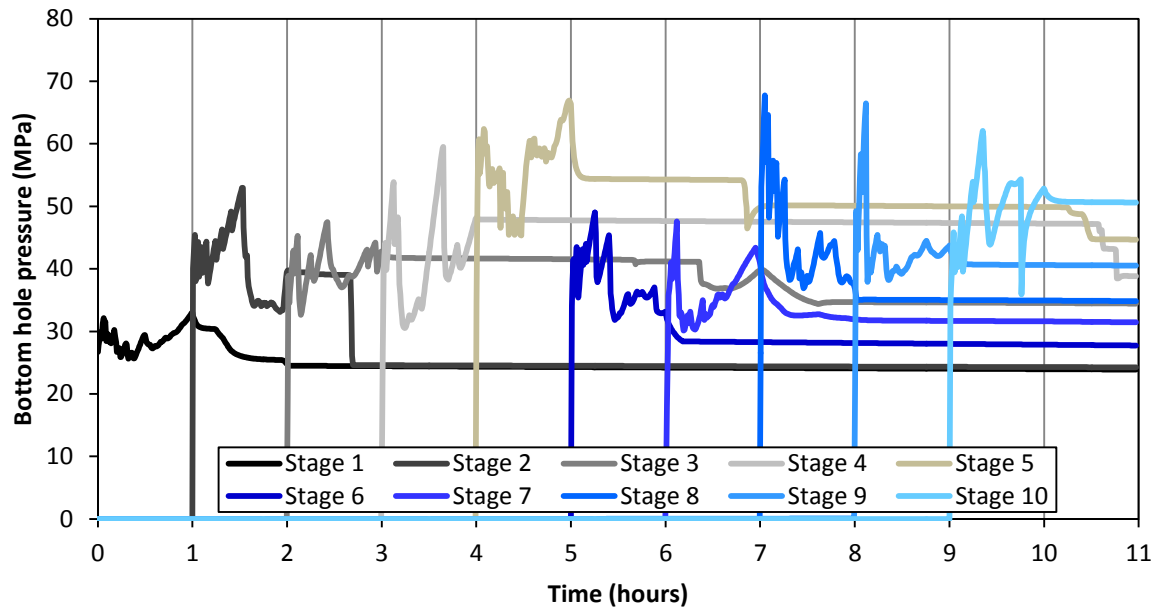


Figure 135: Fluid pressure at each injection domain during the treatment. In each stage 360 m³ of water was injected at 100 l/s in one hour.

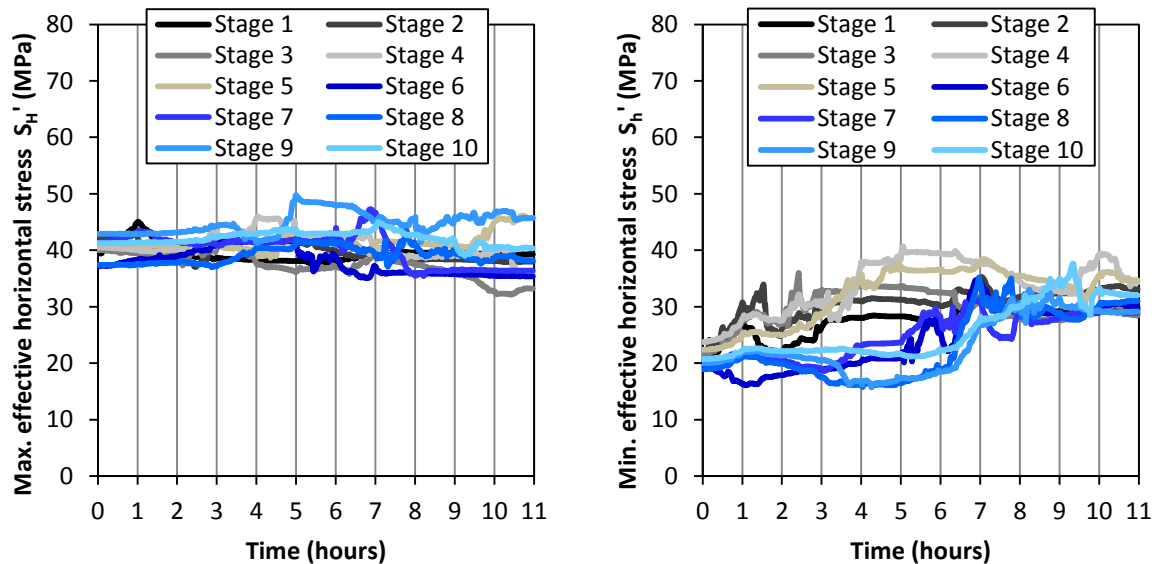


Figure 136: Maximum (left) and minimum (right) horizontal stress measured within a circle of 100 m radius around each injection point.

For the five stages in the second well, the same increase of fluid pressure with stage number was observed. Fractures grew parallel to each other and three of the five fractures linked up with the previously developed fractures from the first five stages, which led to a more complex fracture network geometry between the wells.

9.6.2 Effect of engineering factors on fracture pattern

9.6.2.1 Completion design

16 different completion design scenarios were simulated to evaluate how the completion design alters fracture network development. The results and sketches of each scenario are given in **Figures 137 and 138**. Each number stands for the stage number and in each stage 360 m³ of water were again injected at 100 l/s in one hour. Two same stage numbers mean they were stimulated at the same time.

In the first seven scenarios, the stage positions in the second well were shifted in between the stages of the first well like in the Base Case Scenario. All of these seven scenarios resulted in a relatively similar fracture network compared to the Base Case Scenario. However, some differences should be pointed out. Alternating stimulations between the two wells led to a deviation of fracture growth paths in both wells and not only in the first well as shown by Scenario 1. Additionally, some crack accumulations can be observed in this scenario and the last two stages are not connected to the fracture network. The simultaneous stimulation of two opposite stages in both wells in Scenario 2 led to the connection of the fractures of both stages but no connection with subsequent fractures was achieved. The resulting fracture network consists of five parallel fractures, which were deviated between the wells.

In Scenario 3 all stages in a well were stimulated simultaneously. This led to the development of mainly parallel fractures, which were barely connected due to the spacing between the stages. A similar behavior was observed in Scenario 4 where all stages of both wells were stimulated simultaneously. A better connection between fractures from one stage in one well and the two opposite stages in the other well were achieved by simultaneously stimulating these two stages after the first stage (Scenario 5), and by simultaneously stimulating all three stages (Scenario 6). By stimulating simultaneously in both wells, the outer stages first, then the center stages and finally the stages between the outer ones and the center (Scenario 7), some crack accumulation was achieved between the wells. Additionally, a long fracture was developed in the center and fracture length growth was suppressed in the last stage, which was located between the first two stages due to elevated stresses resulting from the earlier stages.

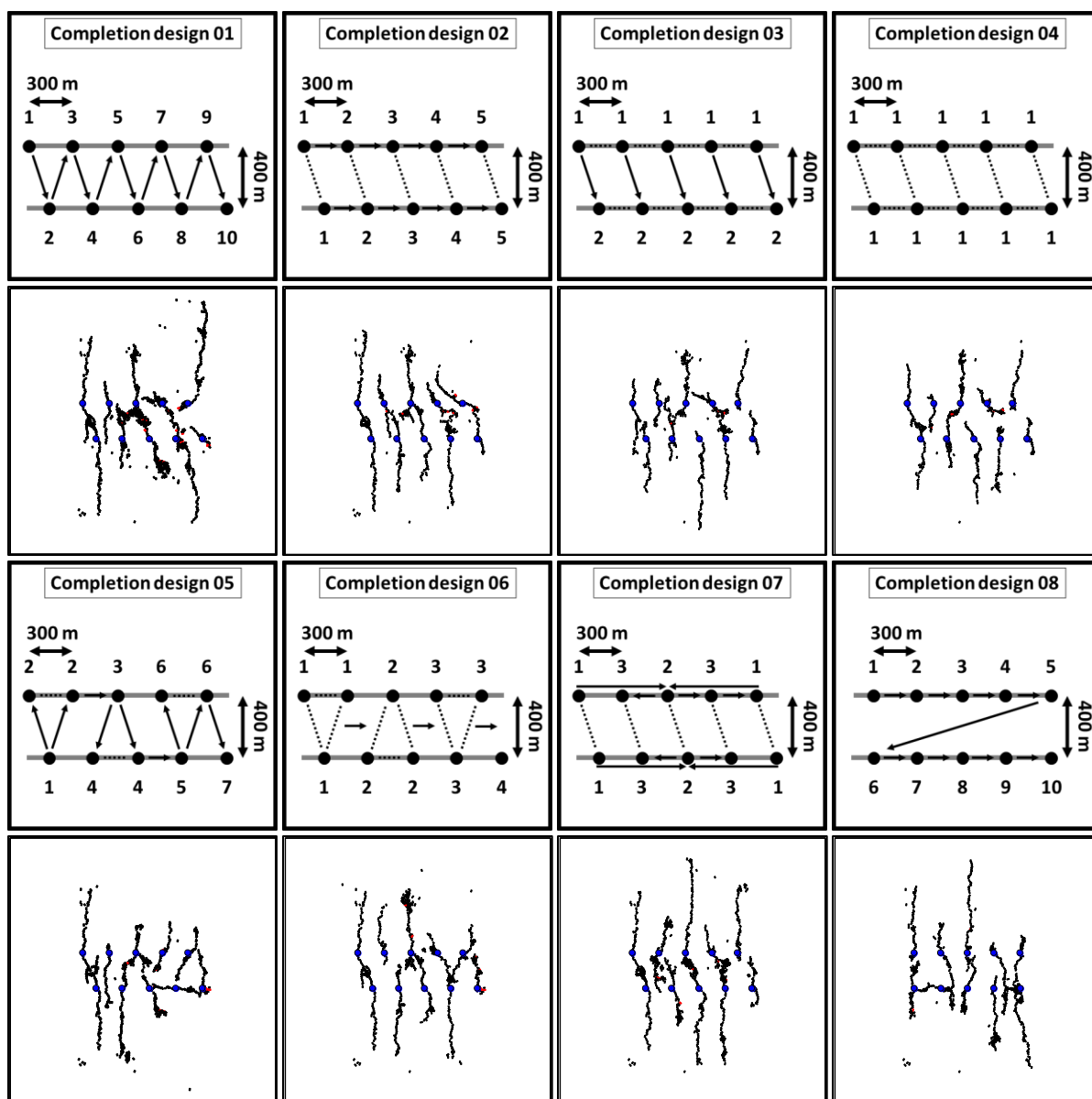


Figure 137: Effect of completion designs 1 - 8 on fracture pattern (blue= injection points, black=tensile fractures, red=shear fractures). For each scenario the schematic completion design and the resulting fracture pattern are shown.

In Scenarios 8 to 12, the injection stage locations in both wells were exactly opposite to each other. Otherwise some of the same completion designs as before were tested. Due to fracture growth from stages in the first well, which was often very close to subsequent stages in the second well, the local stress state at these points changed, which led to the development of new fractures perpendicular to existing fractures (Scenario 8). Alternate stimulation between both wells led to connections between opposite fractures (Scenario 9) while simultaneous stimulation

of opposing stages did not achieve the same degree of connectivity (Scenario 10). Flow paths between the wells were shorter in Scenarios 8 to 12 compared to Scenarios 1 to 7.

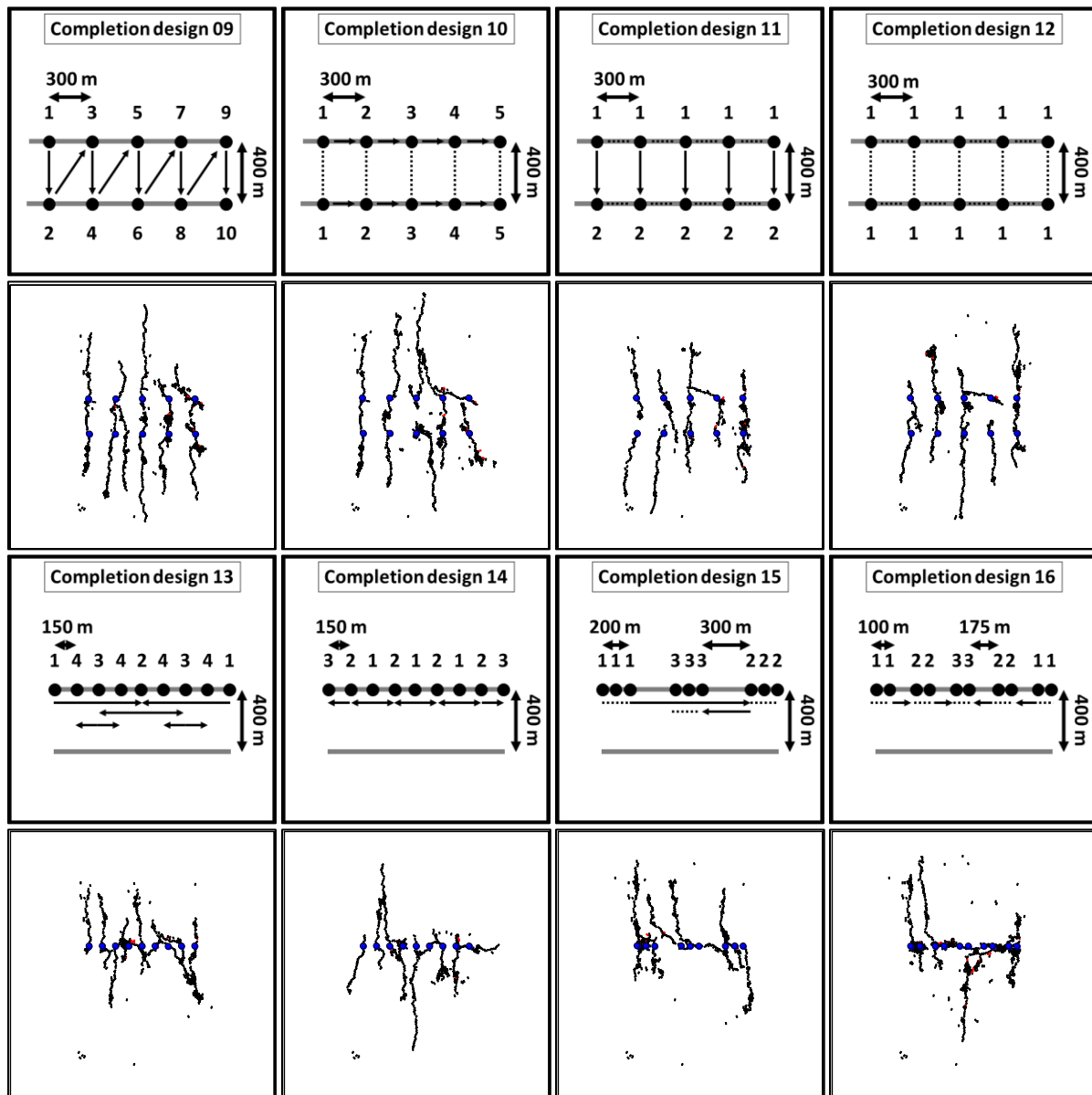


Figure 138: Effect of completion designs 9 - 16 on fracture pattern (blue= injection points, black=tensile fractures, red=shear fractures). For each scenario the schematic completion design and the resulting fracture pattern are shown.

In the last four scenarios (13 to 16), only one well was stimulated by 9 or 10 treatments. More treatments, which were closer together, led to a higher degree of interaction between the individual stages. Fractures of stages as close as 100 m apart from each other linked up to one individual fracture (Completion design 16) and fractures were highly deviated from the

maximum horizontal stress direction (Completion designs 15 and 16). The fracture network developed by Completion designs 13 and 14, where first the ends of the horizontal section of the well and later the center parts and vice versa were stimulated, resulted in less deviation of fracture growth from the maximum horizontal stress direction.

Overall, (1) an offset between stages in both wells, (2) alternate stimulation between both wells, and (3) special stage clusters led to more complex and better connected fracture networks.

9.6.2.2 Stage spacing

As part of the completion design the spacing between the stimulation stages had a large influence on the resulting fracture pattern (**Figure 139**). With smaller spacing, more fractures can be developed within a given area, leading to a complex fracture network between the wells.

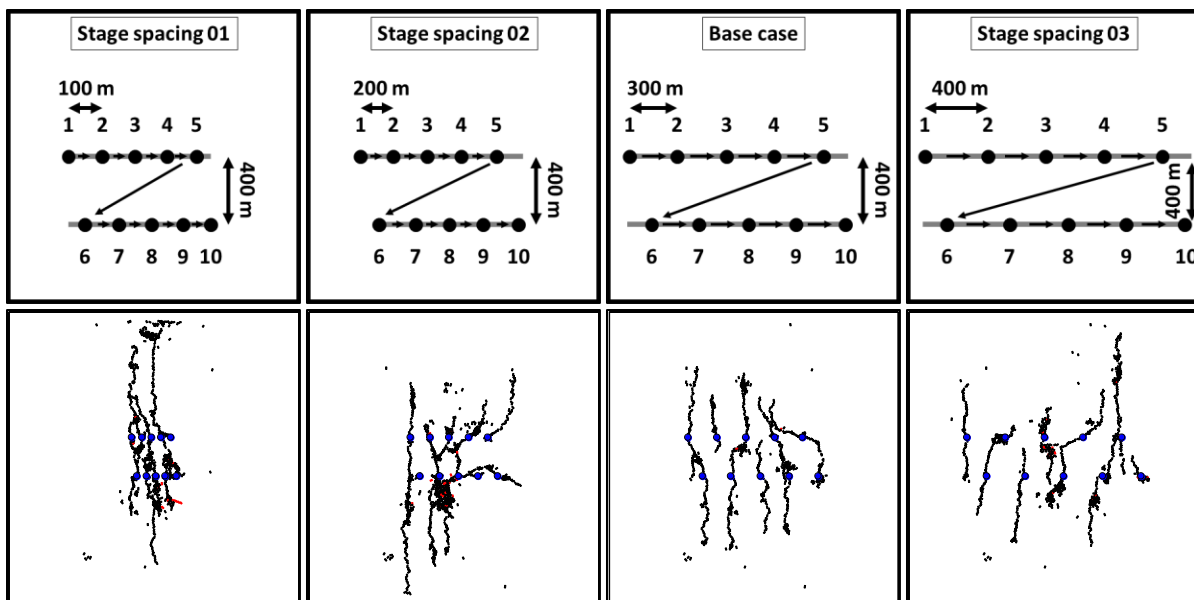


Figure 139: Effect of stage spacing on fracture pattern (black=tensile fractures, red=shear fractures).

However, in this case neighboring fractures also link up and grow far away from the target area between the wells as one or two single fractures (Stage spacing 1). On the other hand, a larger spacing reduces fracture lengths and in each stage a single fracture is developed, which does not link up with fractures from neighboring stages anymore if the fracture spacing is large enough

(Stage spacing 3). Overall, this shows that an optimum stage spacing exists. This aspect should be investigated in detail in future studies.

9.6.2.3 Well azimuth

In the previous examples the wells were drilled parallel to the minimum horizontal stress direction to allow fracture growth perpendicular to these wells. Three different scenarios with wells deviated 30°, 45° and 60° from S_h were simulated (**Figure 140**). A larger deviation resulted in the development of parallel fractures with a longer flow path between the wells. With 60° deviation from S_h , most of the area between the wells was stimulated, which makes it a valid option to drill wells strongly deviated from the minimum horizontal stress direction.

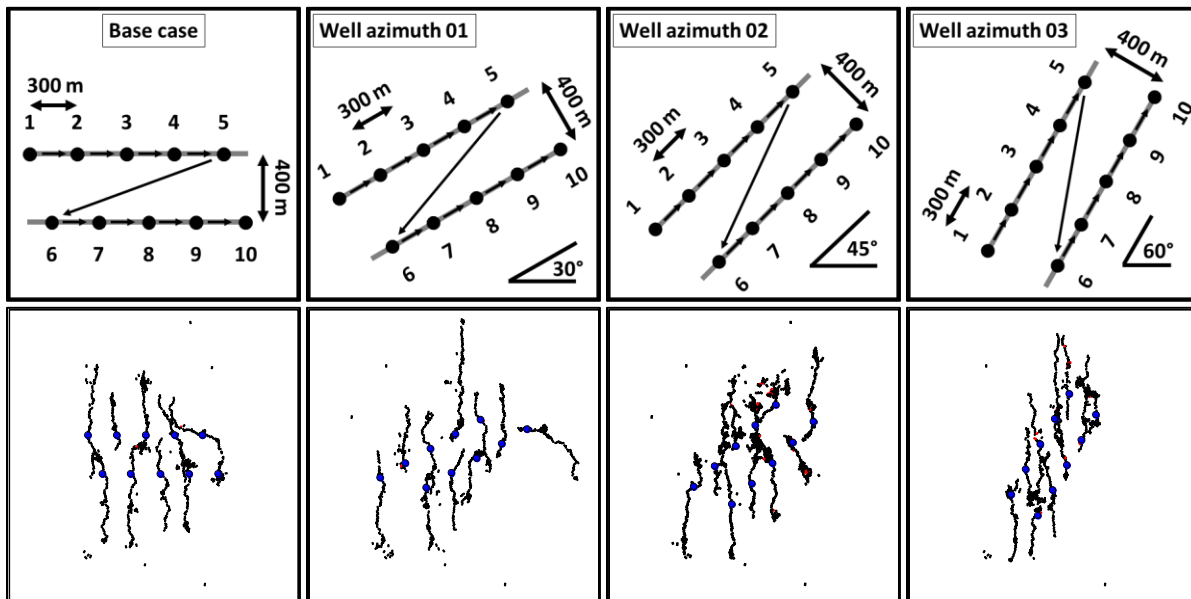


Figure 140: Effect of well deviation on fracture pattern (black=tensile fractures, red=shear fractures).

9.6.2.4 Well spacing

Next, the effect of well spacing on fracture development was studied between 200 m and 600 m (**Figure 141**). Fractures developed in the second well tended to grow away from the area between the wells because of the elevated stress caused by the fractures from the first well. If the wells were too close (e.g. 200 m in Well Spacing 2) with the tested completion design, the fractures

from the first well grew next to the stimulation locations of the second well. The elevated stresses resulting from these first fractures hindered the fractures from the second well to grow towards the first well and forced them to grow out of the target area. When the wells were set further away from each other (e.g. 600 m in Well Spacing 1), some fractures from the first stage did not grow far enough to intersect the other well. In this case, fractures from the second well were also hindered to grow towards the first well. An optimum well spacing was achieved when both wells were connected by the fractures developed in each well.

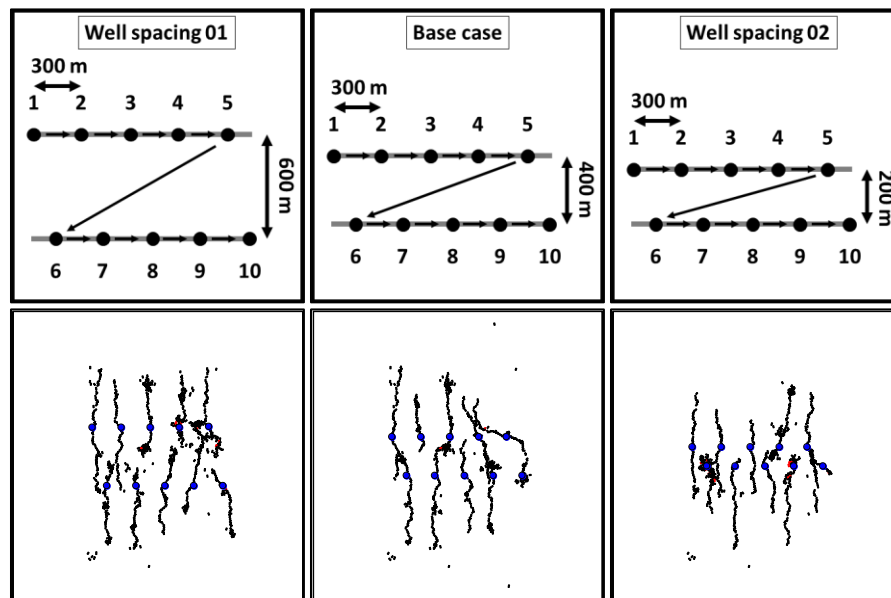


Figure 141: Effect of well spacing on fracture pattern (black=tensile fractures, red=shear fractures).

9.6.2.5 Treatment design

The effect of the stimulation treatment design of each stage was also investigated and the results are shown in **Figure 142**. In all cases, 360 m³ was injected in each stage except for Treatment design 6 where only 180 m³ was injected to see the effect of injected fluid volume. Shorter treatments with a higher flow rate led to the development of longer fractures (Treatment Design 3). Longer treatments with a lower flow rate (Treatment Designs 1 and 2) led to a higher fracture accumulation in the target area between the two wells. The reason for this seems to be the increase treatment time, while the reason for an increased crack accumulation in Treatment Design 2 is the higher flow rate. Staged flow rate increase with time (Treatment Design 4) resulted in a fracture network similar to using a constant 150 l/s flow rate (Treatment Design 3).

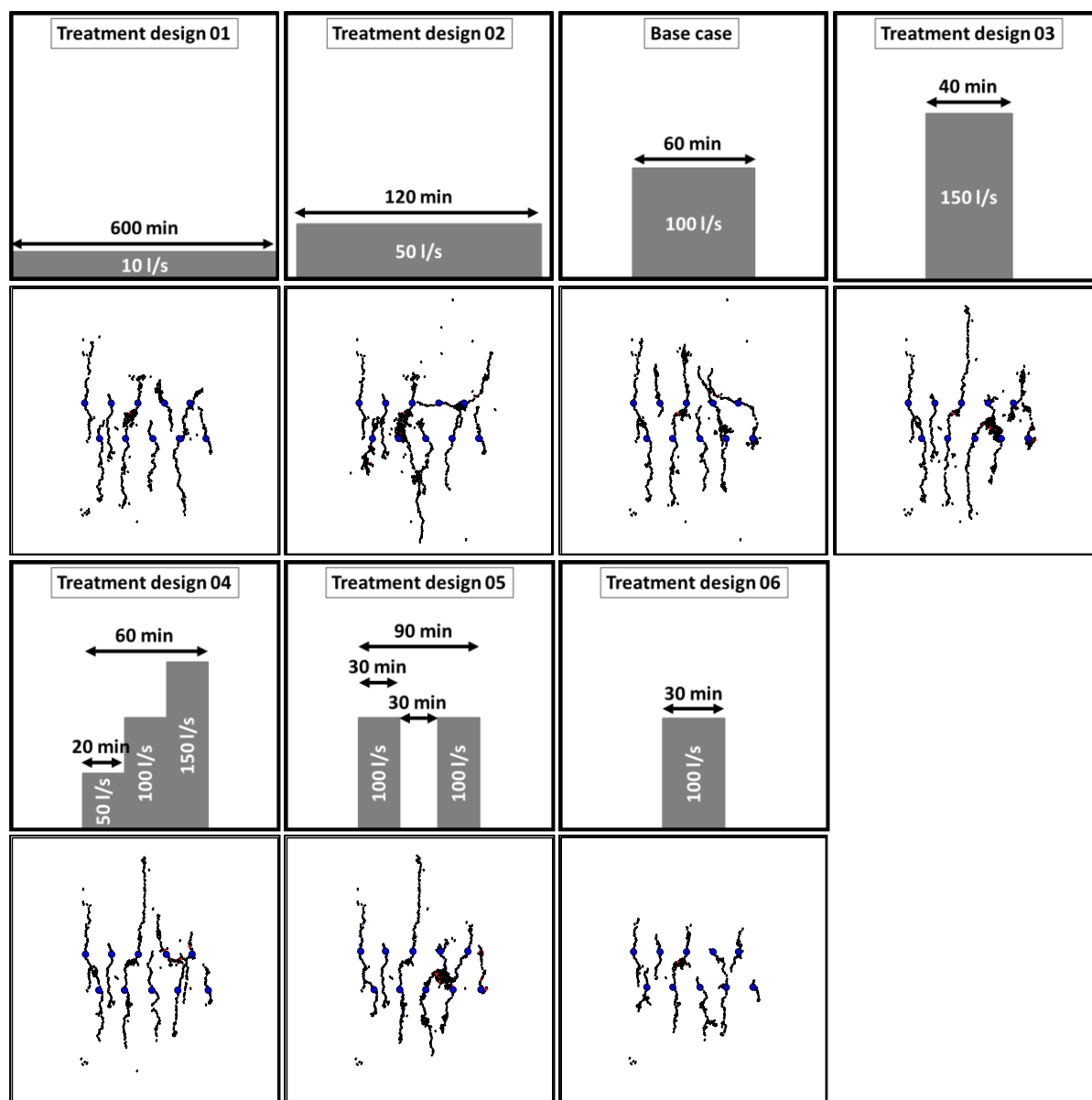


Figure 142: Effect of treatment design on fracture pattern (black=tensile fractures, red=shear fractures).

Also using discontinuous injection (Treatment Design 5) does not change the simulation results significantly because fluid leak-off into the matrix is so low. In Treatment Design 6, only half of the fluid volume was injected, which led to insufficient fracture-well connectivity.

Overall, continuous injection, longer treatments, higher flow rates, and larger injected fluid volumes led to a more complex and better connected fracture network.

9.6.2.6 Fluid viscosity

The last engineering factor that was investigated was the viscosity of the injected fluid. Two additional scenarios were set up (**Figure 143**). Fluid viscosity 1 equaled the viscosity of water at 100°C and 49 MPa, Fluid viscosity 2 was typical for intermediate viscosity water based fracturing fluids. It can be seen that lower viscosity fluids led to longer and more parallel fractures, which were less connected because the local stresses around the fractures were less affected. Hence, the benefit of lower viscosity fluids is the development of longer fractures. It may have additional advantages for naturally fractured formations. Higher viscosity fluid seems to be an option to stronger deviate fracture growth paths in subsequent fracturing stages.

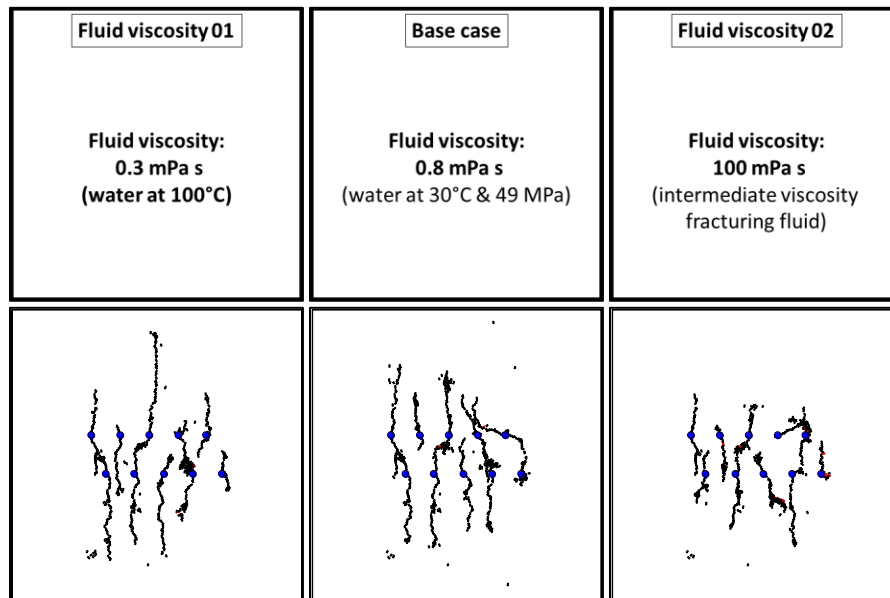


Figure 143: Effect of fracturing fluid viscosity on the resulting fracture pattern (black=tensile fractures, red=shear fractures).

9.6.3 Effect of natural factors on fracture pattern

9.6.3.1 Stress field

The difference between the maximum and the minimum horizontal stress was changed from 10 MPa to 30 MPa. As expected, a lower stress anisotropy (difference between S_H' and S_h') led to

the development of more deviated fractures and hence a better connected fracture network (Figure 144).

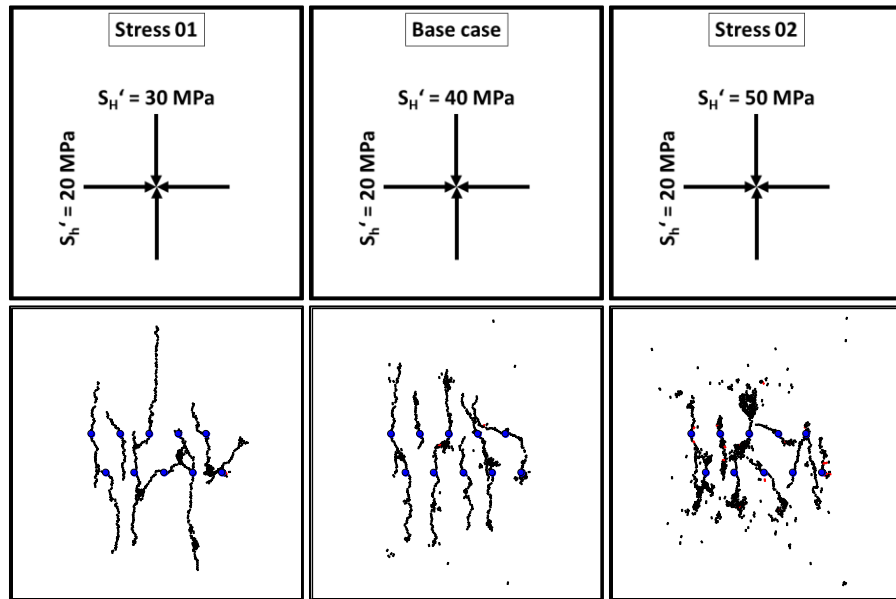


Figure 144: Influence of in-situ stress field on hydraulic fracture development (black=tensile fractures, red=shear fractures).

9.6.3.2 Pre-existing fractures

Different random distributions of natural fracture networks were simulated while either the number of fracture sets, the number of fractures, the azimuth of the fractures or the length of the fractures was changed in the different scenarios (Figures 145 and 146).

In the first four scenarios, the angle between the fracture orientation and the minimum horizontal stress direction was changed. A higher variation in the possible angles (e.g. 0° - 90° in Fracture network 4) led to a higher interconnectivity between the natural fractures and consequently to a more complex network of sheared pre-existing fractures and new tensile and shear fractures. If fracture sets are favorably oriented to the in-situ stress field and new tensile fractures approach a natural fracture at a low angle, natural fractures fail in shear. If a new tensile fracture grows perpendicular to a pre-existing fracture, it is either arrested or it intersects the natural fracture (e.g. Fracture network 1).

In Scenarios 6 to 8, the length of the fractures was changed. In Scenario 6, with the shortest fractures, only a limited number of sheared natural fractures were observed. In Scenario 7, only long fractures between 300 m and 500 m were present. In Scenario 8, fracture lengths ranged between 5 m and 500 m. The stimulated fracture pattern was very similar in both cases, suggesting that the longer fractures govern fracture growth.

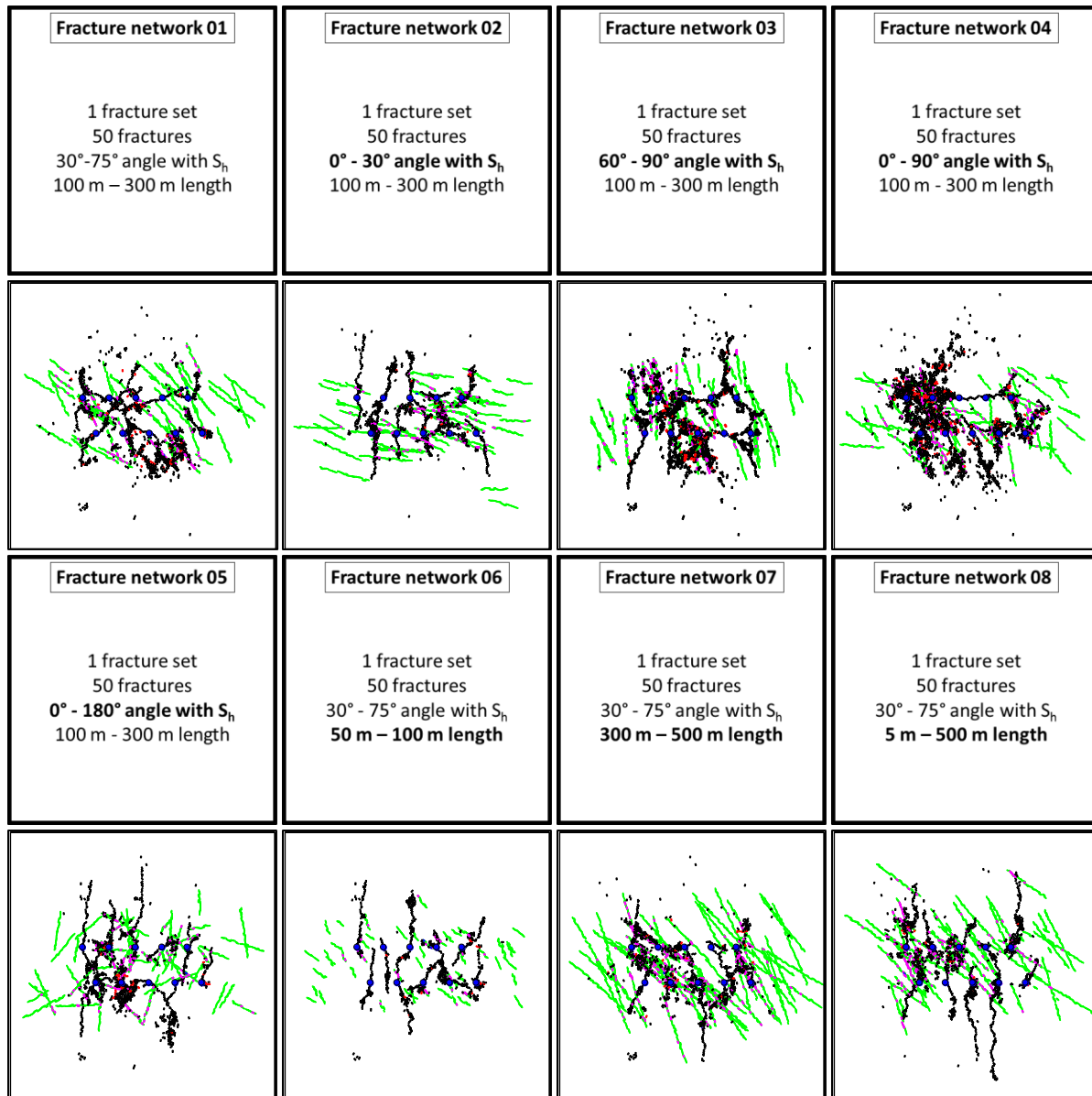


Figure 145: Influence of randomly distributed natural fracture networks 1-8 on hydraulic fracture development (green=pre-existing fractures, black=tensile fractures, red=shear fractures, blue=tensile failure of pre-existing fracture, magenta=shear failure of pre-existing fracture).

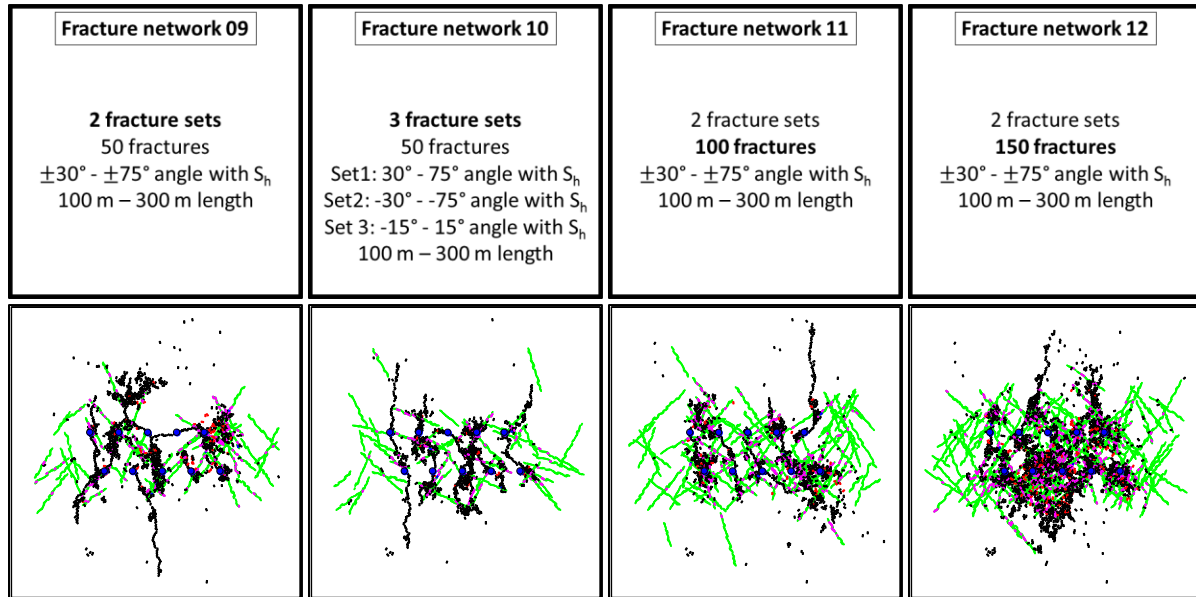


Figure 146: Influence of randomly distributed natural fracture networks 9-12 on hydraulic fracture development (green=pre-existing fractures, black=tensile fractures, red=shear fractures, blue=tensile failure of pre-existing fracture, magenta=shear failure of pre-existing fracture).

In Scenarios 9 to 12, the number of fracture sets and the number of fractures was increased. The result was an increased number of broken bonds with increasing fracture density.

9.6.3.3 Permeability

Finally, the permeability of the flow channels as function of effective normal stress acting on each flow channel was studied (**Figure 147**). Four scenarios were set up.

Permeability 1 had a fracture aperture of $0.5 \mu\text{m}$ at infinite stress and $200 \mu\text{m}$ at zero stress with a significant jump in permeability at low effective normal stresses. The resulting fractures were relatively similar to the Base Case Scenario where the fracture aperture at infinite stress was $5 \mu\text{m}$. Permeability 2 had an aperture of $50 \mu\text{m}$ at infinite stress, which resulted in significant fluid leak-off into surrounding domains and very short fractures.

Permeability 3 equaled the Base Case Scenario with the difference being that the transition from low permeability at high stresses to high permeability at low stresses was smoother ($\alpha=0.3$). The fracture pattern is similar to the Base Case Scenario except that neighboring fractures were less subject to elevated stresses and hence all fractures were parallel.

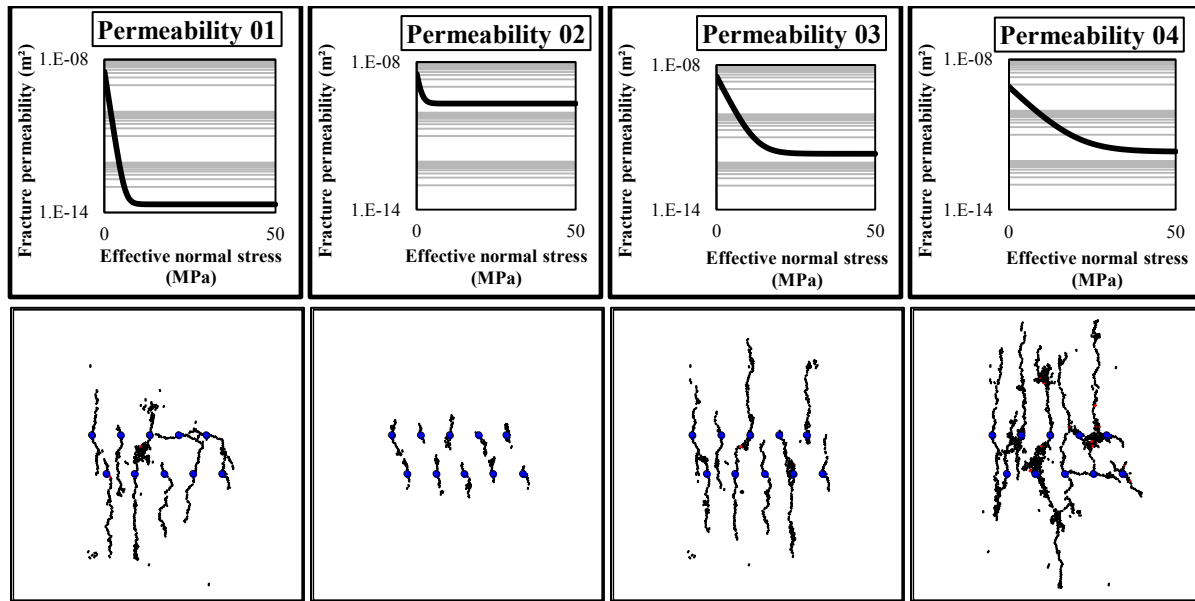


Figure 147: Influence of flow channel permeability (as a function of normal stress) on hydraulic fracture development.

Scenario Permeability 4 was the same as Permeability 3 except for a reduced aperture of 100 μm at zero normal stress. As a result, the longest fractures and the most complex fracture network of these four scenarios developed.

Overall, a lower permeability at infinite normal stress (Permeability 1) and a lower permeability at zero normal stress (Permeability 4) both led to more complex fracture networks compared to scenarios with higher permeabilities (Permeability 2 and 3).

9.7 RESERVOIR SIMULATION RESULTS

9.7.1 Base case model

For each Scenario given in **Section 9.6**, the thermal and hydraulic behavior of the fractured reservoir was simulated. **Figure 148** shows the exemplary pressure and temperature field that developed after 30 years of operation of the EGS. The total number of individual cracks was 644. One can see that a hydraulic and thermal connection between both wells was achieved through 4 major flow paths. Two of the major fractures did not intersect both wells and were therefore not contributing to the system. This connectivity governed the thermal and hydraulic performance of

the system. In the following two sections, the temperature of the produced water after 30 years and the productivity index PI (ratio of flow rate and pressure decline) of the production well is presented for all simulated scenarios. The PI of the Base Case Scenario is 5.3 l/s/MPa and the temperature at the production point after 30 years is 93°C.

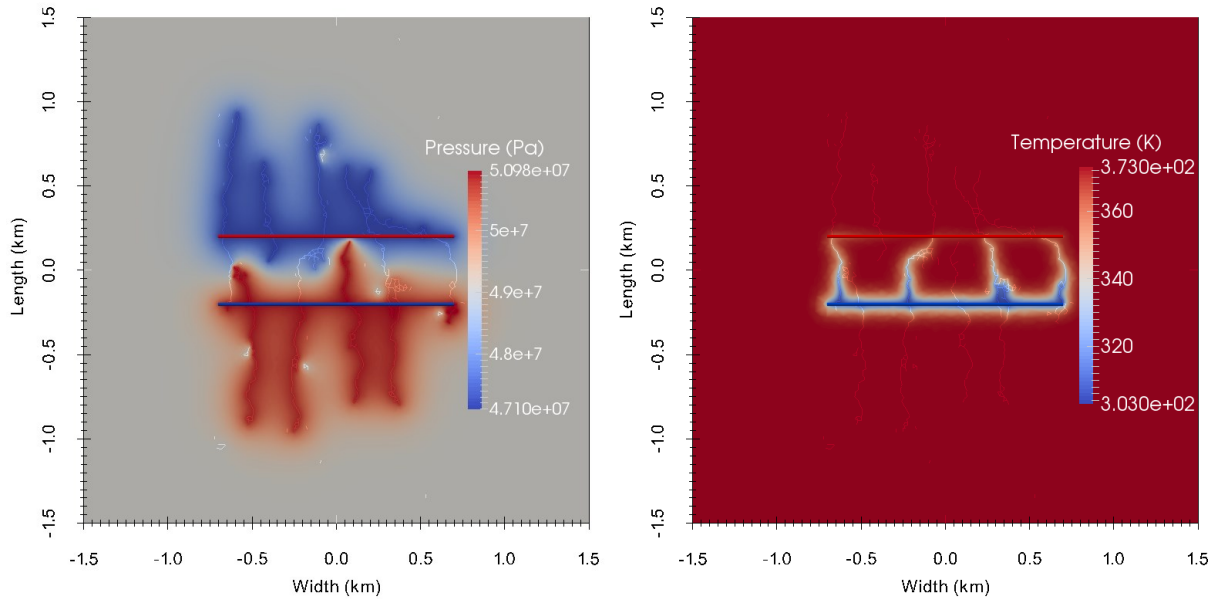


Figure 148: Pressure (left) and temperature (right) distribution of the base case model after 30 years of production.

9.7.2 Influence of engineering factors on hydraulic and thermal performance

Figure 149 shows the influence of the different engineering factors on the number of broken bonds and major flow paths between the two wells and the resulting produced water temperature and the productivity index. The number of cracks varied between 430 and 895 and the number of major flow paths lied between 1 and 5. The productivity index achieved with these fracture networks was between 0.9 l/s/MPa and 10.3 l/s/MPa and the temperature of the produced water was between 48°C and 99°C, depending on the scenario.

Completion design had the strongest influence on the productivity index. Completion design 14, where only one well was stimulated, had the highest PI even though only 9 stimulation stages were performed and therefore 360 m³ less water was injected, which led to the development of only 525 cracks. Except for Completion design 15 (with three stimulation clusters), where only

one flow path connected the two wells because most fractures grew away from the injection well, the other two cases where all treatments were performed in the production well only (Completion designs 13 and 16) also had a high PI. This is because more fractures intersected this well (9-10) compared to the other cases even though only 2 to 4 of them also intersected the injection well. Therefore the focus should be on the stimulation of production wells.

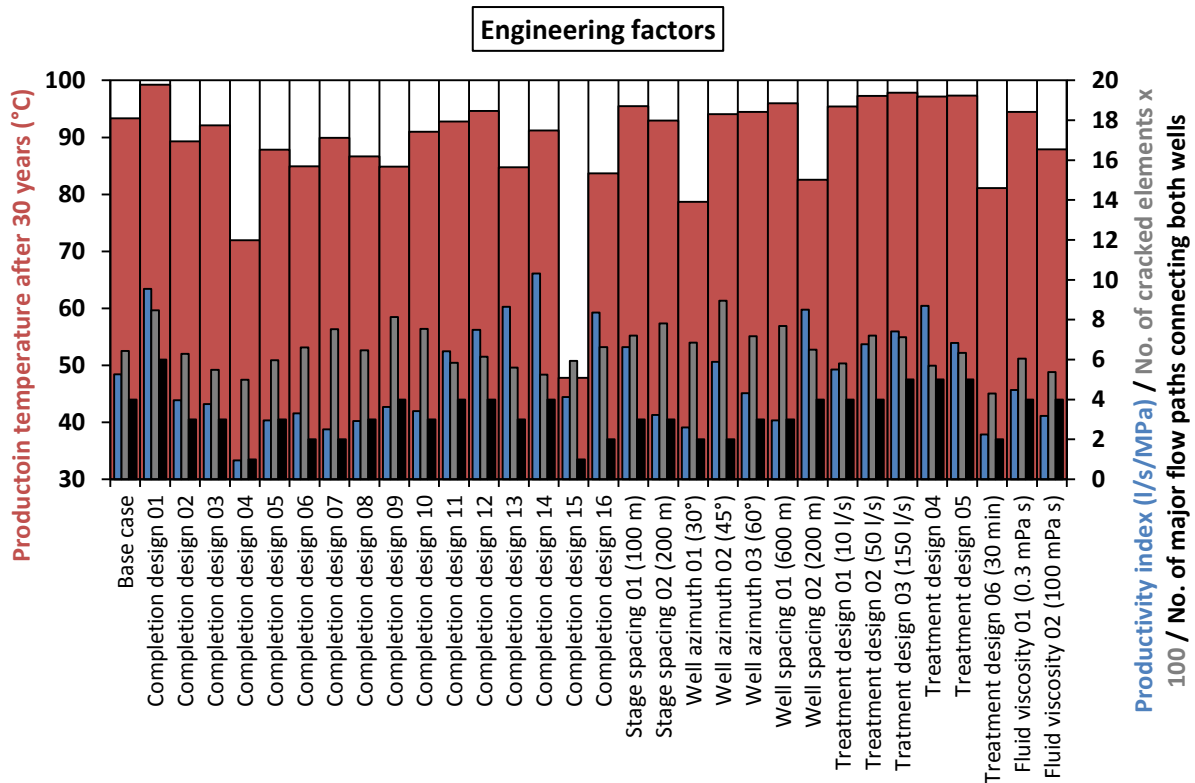


Figure 149: Influence of engineering factors on number of individual broken bonds (cracks), number of major flow paths between both wells, productivity index and production temperature after 30 years.

Another case where a PI of 10 l/s/MPa was achieved is Completion design 1. Here, the alternate stimulation between the two wells led to the development of 6 major flow paths, which all intersected both wells and where 4 of them intersected each other. The result of this complex flow path was the lowest temperature drawdown of all scenarios. Therefore, Completion design 1 had the best combined thermal and hydraulic performance of all scenarios and was the preferred stimulation design while more stimulations performed in one well obviously increases its productivity. The lowest PI was achieved with Completion design 4 where both wells and all stages were stimulated simultaneously and the stages between the wells had an offset, which

resulted in only one major flow path. Also, the temperature drawdown in this scenario was significant because of the limited heat exchanger area.

The smaller Stage spacing 1 (100 m) led to longer fractures and a more complex fracture network between the wells and hence to a higher productivity and a higher temperature compared to the Base Case Scenario (200 m) and Stage spacing 2 (300 m). Small stage spacings should therefore be preferred over larger spacings within the investigated range. However, care should be taken about excessive fracture length growth out of the reservoir and potential fluid loss through these fractures. There might be an optimum spacing, which needs further investigation.

Drilling the well in a direction deviated from the minimum horizontal stress direction can be beneficial. With 45° deviation (Scenario Well azimuth 2), a higher PI and a higher temperature were achieved compared to the Base Case and the other deviations (30° and 60°). This is because almost 900 cracks formed in this scenario. A further performance increase would be achieved if the length of the wells would be increased until they intersect the two major fractures from the first and the last treatment.

An increase in the well spacing (e.g. 600 m) led to a worse hydraulic connection between the two wells and therefore decreased the PI. At the same time, the final temperature was higher due to the longer flow paths between the wells and the resulting longer residence time of the injected water in the reservoir before reaching the production well. For Well spacing 2 with 200 m distance between the wells, the opposite effect was observed. Connectivity was increased, the productivity was significantly higher, and the temperature drawdown was significantly lower compared to a larger well spacing. An optimum spacing existed for each fracture network. The base case scenario with 400 m spacing was considered a good compromise with average PI and temperature drawdown.

Higher flow rates resulted in the formation of more cracks and a better connectivity and therefore in an increase of the productivity and the produced temperature. A longer treatment time (Treatment design 1) also increased PI and produced temperature compared to the Base Case because more complex crack patterns formed between the wells even though less cracks developed in total. In Treatment design 6 only half of the fluid was injected compared to all other scenarios, which resulted in the development of only 2 large fractures intersecting both wells and

a reduction in number of cracks, productivity and produced temperature. Increasing the flow rate with time (Treatment design 4) and discontinuous injection (Treatment design 5) develop fewer cracks but show a better thermal and hydraulic performance than continuous injection. Overall, the continuous injection of larger volumes of fluid at high flow rates can be suggested.

Injecting a lower viscosity fluid (Fluid viscosity 1) led to the development of more cracks and hence a higher PI and temperature compared to the injection of higher viscosity fluid (Fluid viscosity 2) and should therefore be preferred.

Stage spacing 3 is not shown in **Figure 149** because the well would need to be longer than in the other cases.

9.7.3 Influence of natural factors on hydraulic and thermal performance

The influence of the fracture patterns developed by different stress states, natural fracture networks, and permeabilities on number of cracks, number of major flow paths between the wells, produced water temperature, and productivity index is shown in **Figure 150**. Depending on the scenario, the number of cracks varied between 541 and 2506 and the number of major flow paths lied between 1 and 5. The productivity index achieved with these fracture networks was between 1.2 l/s/MPa and 12.8 l/s/MPa and the temperature of the produced water was between 80°C and 99°C, depending on the scenario.

Even though an increased difference between the principle horizontal stresses to 30 MPa led to the formation of more cracks, the productivity and produced temperature for this case were less compared to the Base case Scenario with 20 MPa stress difference and Scenario Stress 1 with 10 MPa stress difference. This is because with lower stress difference, fractures can easier grow in different directions, which leads to a better interconnectivity of the individual fractures and therefore a better hydraulic connection between the wells.

In all simulations with fracture network, significantly more cracks (up to 2506) were formed compared to the intact cases (up to 895) because the fractures represented by smooth joint contacts have a lower tensile and shear strength than the intact rock represented by the parallel bonds. However, the number of major flow paths through the system was often less compared to

the intact rock and hence productivities and production temperatures were less for 8 from the 12 fractured cases.

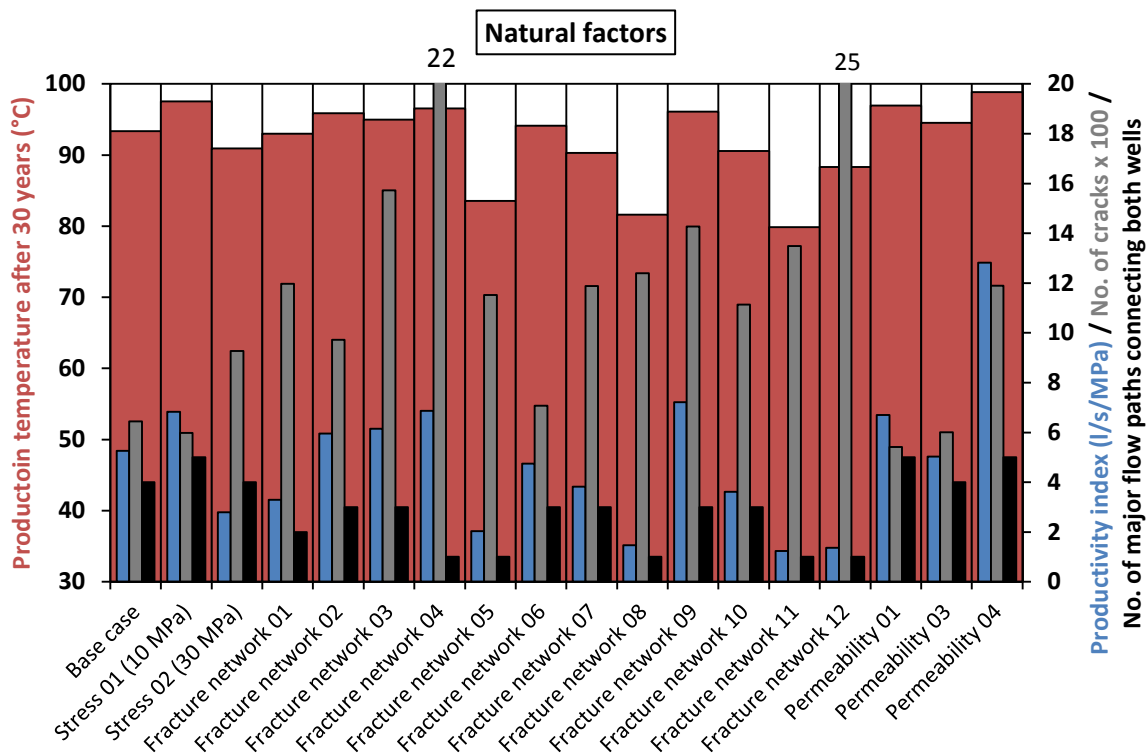


Figure 150: Influence of natural factors on number of individual broken bonds (cracks), number of major flow paths between both wells, productivity index and production temperature after 30 years.

Cases with natural fracture orientations closer to the maximum horizontal stress direction (which was the preferred direction of fracture growth in intact rock) led to the development of more cracks (Fracture network 3) compared to cases where natural fractures were oriented closer to the minimum horizontal stress direction (Fracture network 2). Since the number of major flow paths in both cases was the same, the PI and temperature were similar.

Shorter fractures led to the development of less cracks (Fracture network 6) compared to long fractures (Fracture network 7) but, again, the PI and temperature were similar because only two major flow paths developed in both cases.

In Fracture network 8, the natural fracture lengths varied between 5 m and 500 m, which resulted in similar number of cracks but only one flow path developed and hence the PI and temperature were less.

Having two fracture sets (Fracture network 9) increased the number of cracks and also the productivity and temperature. When a third fracture set was added in the direction close to the minimum horizontal stress direction (Fracture network 10), fluid flow paths were partly blocked and productivity and temperature decreased.

Increasing the number of pre-existing fractures to 100 (Fracture network 11) and 150 (Fracture network 12) significantly increased the number of cracks, but there was only one flow path developing in these two scenarios and hence the productivity and temperature were lower compared to the cases with 50 fractures.

Overall, 2 fracture sets close to the maximum horizontal stress direction and long natural fractures increased the productivity index and reduced the temperature drawdown.

In the scenario with the lowest flow channel permeability at zero normal stress (Permeability 4), more cracks developed compared to higher permeability cases and the productivity index was the highest of all natural factor scenarios. Also, the lowest temperature drawdown of all natural fracture scenarios was observed for this case. In the scenario with lower permeability at infinite normal stress (Permeability 1), also 5 major flow paths developed and productivity and temperature were higher compared to the higher permeability case (Permeability 3) where only 4 major flow paths developed.

9.8 DISCUSSION

The particle based DEM is a fairly suitable approach to model the effect of different natural factors and engineering parameters on fracture growth because the DEM produced plausible fracture network geometries and simulation results match qualitatively with previous studies. However, conclusions from the simulations can only be qualitative at this stage. One reason for this is the dependence of the simulation results on the heterogeneity of the model resulting from the unique particle size distribution. While this resembles the reservoir specific heterogeneous distribution of rock properties and discontinuities in real reservoirs, the presented results only show one out of many realizations.

What is not explicitly shown in the paper is that qualitatively the same results were found independent of the particle size distribution. Other restrictions are the two-dimensionality of the model, the relatively large particles used, and a missing wellbore model. The fluid flow model may be improved by using different stress dependent hydraulic aperture relationships for flow channels through intact particle contacts and the different kinds of broken bonds (tensile and shear failure of parallel bonds and tensile and shear failure of smooth joint contacts). Also, the influence of natural fracture systems and their properties on fracture development needs to be studied in more detailed.

Since the simulation results are only for an artificial model, a validation with field data would be beneficial. This should be done using hydraulic and microseismic data. One major factor to be considered for this validation is the stress dependent fluid flow law through the flow channels between the domains.

The reservoir simulations also produced plausible results. While for this study only the unbonded (cracked) flow channels were considered in the model, all other flow channels can also be exported and incorporated in the reservoir model. However, this is significantly more time-consuming. Each fracture of the reservoir model had a constant hydraulic fracture aperture of 200 μm , which equals the DEM flow channel aperture at zero effective normal stress. This assumption is reasonable because even particles adjacent to tensile fractures were subject to some displacement and laboratory tests show that the hydraulic aperture of displaced tensile fractures in granitic rock is about 200 μm and is not significantly reduced with increasing normal stress [Watanabe *et al.*, 2008]. Alternatively, a pressure dependent fracture permeability relationship can also be used in the reservoir model in future studies, if deemed necessary.

Water was circulated through the well doublet only at a rate of 10 l/s, which is too low for an economical operation. However, this low flow rate was necessary to be able to compare all scenarios to each other and avoid excessive pressure buildup and drawdown in the wells in low productive scenarios. The reservoir simulation results therefore show qualitatively which fracture network has the best thermal and hydraulic performance.

The extension of the interface by an iterative transfer of pressures and temperatures from FEM to DEM and fracture geometries from DEM to FEM after each calculation step would be beneficial

for future studies. This way further fracture development resulting from pressure changes during operation conditions can be accounted for, as well.

9.9 CONCLUSIONS

This study shows the first comprehensive application of the newly developed interface combining a particle based DEM and an open source FEM code, which was originally presented in *Hofmann et al.* [2015a]. Complex hydraulic fracture development by hydraulic stimulation treatments and the subsequent thermal and hydraulic behavior during operation of the developed enhanced geothermal system was modeled over 30 years. This approach makes it possible to simultaneously evaluate the influence of reservoir engineering and natural factors on fracture growth patterns and thermal and hydraulic reservoir performance.

The influence of several natural and engineering factors on fracture network complexity resulting from hydraulic stimulation treatments were reviewed and systematically analyzed using the discrete element model. Properties expected in a 5 km deep granitic Precambrian basement rocks in Northern Alberta (Canada) were used for this case study.

Subsequent reservoir modeling showed the benefits for the thermal and hydraulic performance of an enhanced geothermal system if complex fracture networks with multiple flow paths and large fracture areas can be developed rather than single fractures.

Based on the presented literature review and the numerical simulations, the following reservoir engineering concepts are proposed to develop a complex fracture network in granitic basement rock with a good thermal and hydraulic performance in Northern Alberta and similar reservoirs:

- Horizontal wells with long laterals need to be drilled and multiple stimulation stages need to be performed to access sufficient reservoir volume.
- While the focus should be on the productivity improvement of the production well, both wells should be stimulated to achieve a better hydraulic connection between them.
- Alternating stimulation treatments between wells and an offset between the stage locations of the wells are also beneficial to connect fractures to both wells.

- A small stage spacing (e.g. 100 m) should be used to increase fracture network complexity between the wells. However, excessive fracture growth out of the target zone might be a problem when performing multiple stimulation treatments too close to each other.
- The thermal and hydraulic performance of wells drilled at an angle of 45° to the minimum horizontal stress direction was better compared to drilling parallel to the minimum horizontal stress direction.
- Large volumes of low viscosity fluid (e.g. water) should be injected continuously at a high rate in each stage until the target fracture length is reached.
- Well spacing is a compromise between higher productivity and earlier thermal breakthrough with smaller spacings and lower productivity and later thermal breakthrough with larger spacings. Intermediate spacings of approximately 400 m seems reasonable.

In reservoirs with the following properties, it is more likely to be able to develop complex fracture networks with a good thermal and hydraulic performance:

- Complex tectonic setting and geologic history;
- Low difference between the magnitudes of the principle stresses;
- Two intersecting natural fracture sets close to the maximum horizontal stress direction consisting of long natural fractures;
- Hard and brittle rock (high Young's modulus and low Poisson's ratio);
- Low permeability.

One problematic issue when performing multiple stimulation treatments that was identified by the presented simulations is the formation of dominant single fracture paths when individual fractures link up with a fracture from a previous treatment. It was also found that the stress shadow effect can be used to change fracture geometries in subsequent or simultaneous fracturing stages.

Even though the modeling results are qualitatively in good agreement with previous studies and the relative influence of important factors could be illustrated, the following model improvements are suggested for future studies:

- Different fluid flow relations for different fracture types (intact flow channels, tensile fractures, shear fractures, open pre-existing fractures, sheared pre-existing fractures);
- Temperature dependent fluid viscosity for long term treatments;
- Implementation of wellbore hydraulics into the model;
- Extension of the interface to three dimensional models;
- Iterative coupling between DEM and FEM after each time step.

More research is needed to investigate the effect of natural fracture systems on fracture development in particle based DEM models. A model calibration on appropriate field scale data is also suggested.

REFERENCES

- Barton, C.A., M.D. Zoback, and D. Moos (1995), Fluid flow along potentially active faults in crystalline rock, *Geology*, 23(8):683-686, doi: 10.1130/0091-7613(1995)023<0683:FFAPAF>2.3.CO;2.
- Blöcher, G., M. Cacace, B. Lewerenz, G. Zimmermann (2010), Three dimensional modelling of fractured and faulted reservoirs: Framework and implementation, *Chemie der Erde – Geochemistry*, 70(3):145-153, doi: 10.1016/j.chemer.2010.05.014.
- Blöcher, G., M. Cacace, T. Reinsch, and N. Watanabe (2015), Exploitation concepts for a deep geothermal system in the North German Basin, submitted to *Computers & Geosciences*.
- Cacace, M., and G. Blöcher (2015), MeshIt – a software for three dimensional geometric modelling of faulted reservoirs, submitted to *Computers and Geosciences*.
- Cacace, M., G. Blöcher, N. Watanabe, I. Moeck, N. Börsing, M. Scheck-Wenderoth, O. Kolditz, and E. Huenges. Modelling of fractured carbonate reservoirs: outline of a novel technique via a case study from the Molasse Basin, southern Bavaria, Germany, *Environ Earth Sci.*, 70(8):3585-3602, doi: 10.1007/s12665-013-2402-3.
- Chen, M., J. Zhou, Y. Jin, and G. Zhang (2008), Experimental study on fracturing features in naturally fractured reservoirs, *Acta Petrolei Sinica*, 29(3):431-434, doi: 10.7623/syxb200803023.
- Cherubini, Y., M. Cacace, G. Blöcher, and M. Scheck-Wenderoth (2013), Impact of single inclined faults on the fluid flow and heat trans-port: results from 3-D finite element simulations, *Environ. Earth Sci.*, 70(8):3603-3618, doi: 10.1007/s12665-012-2212-z.
- Chuprakov, D.A., A.V. Akulich, E. Siebrits, and M. Thiercelin (2011), Hydraulic-fracture propagation in a naturally fractured reservoir, *SPE Prod. & Oper.*, 26(1):88-97, SPE 128715, doi: 10.2118/128715-PA.
- Cipolla, C.L., N.R. Warpinski, and M.J. Mayerhofer (2008a), Hydraulic fracture complexity: Diagnosis, remediation, and exploitation, paper presented at SPE Asia Pacific Oil & Gas Conference and Exhibition, Perth, Australia, SPE 115771.
- Cipolla, C.L., N.R. Warpinski, M.J. Mayerhofer, E.P. Lolon, M.C. Vincent (2008b), The relationship between fracture complexity, reservoir properties, and fracture treatment design, paper presented at SPE Annual Technical Conference and Exhibition, Denver, CO, USA, SPE 115769.
- Cornet, F.H., T.H. Bérard, and S. Bourouis. How close to failure is a granitic rock mass at a 5 km depth? *Int. J. Rock Mech. Min. Sci.*, 44(1):47-66, doi: 10.1016/j.ijrmms.2006.04.008.
- Fisher, M.K., B.M. Davidson, A.K. Goodwin, E.O. Fielder, W.S. Buckler, and N.P. Steinberger (2002), Integrating fracture mapping technologies to optimize stimulations in the Barnett shale, paper presented at SPE Annual Technical Conference and Exhibition, San Antonio, TX, USA, SPE 77441.
- Haimson, B., and C. Chang (2005), Brittle fracture in two crystalline rocks under true triaxial compressive stresses, *Geological Society London Special Publications*, 240(1):47-59, doi: 10.1144/GSL.SP.2005.240.01.05.

- Hofmann, H., G. Blöcher, H. Milsch, T. Babadagli, and G. Zimmermann (2015b), Continuous measurement of time and pressure dependent fracture permeability of aligned and displaced tensile fractures in granitic rocks during cyclic loading, submitted to *Geophys. J. Int.*
- Hofmann, H., J.S. Yoon, A. Zang, G. Blöcher, G. Zimmermann, and T. Babadagli (2015a), A new hybrid simulation approach to evaluate the efficiency of hydraulic stimulation treatments, paper presented at World Geothermal Congress, Melbourne, Australia.
- Hofmann, H., T. Babadagli, and G. Zimmermann (2014a), Hot water generation for oil sands processing from enhanced geothermal systems: Process simulation for different hydraulic fracturing scenarios, *Appl. Energy*, 113:524-547, doi: 10.1016/j.apenergy.2013.07.060.
- Hofmann, H., T. Babadagli, and G. Zimmermann (2014b), Numerical simulation of complex fracture network development by hydraulic fracturing in naturally fractured ultratight formations, *J. Energy Resour. Tech.*, 136(4):042907 (9 pages), doi: 10.1115/1.4028690.
- Hökmark, H., M. Lönnqvist, and B. Fälth (2010), THM-issues in repository rock – thermal, mechanical, thermos-mechanical and hydromechanical evolution of the rock at the Forsmark and Laxemar sites, Technical Report TR-10-23, Swedish Nuclear Fuel and Waste Management Co, Sweden.
- Itasca Consulting Group Inc. (2008), PFC2D Particle Flow Code in 2 Dimensions User's Guide, Minneapolis, MS, USA.
- Kan, W., and J.E. Olson (2015), Numerical investigation of complex hydraulic fracture development in naturally fractured reservoirs, paper presented at SPE Hydraulic Fracturing Technology Conference, The Woodlands, TX, USA, SPE 173326.
- Kolditz, O., S. Bauer, L. Bilke, N. Böttcher, et al. (2012), OpenGeoSys: an open-source initiative for numerical simulation of thermo-hydro-mechanical/chemical (THM/C) processes in porous media, *Env. Earth Sci.*, 67(2):589-599.
- Lemmon, E. W., M.L. Huber, and M.O. McLinden (2013), NIST Standard Reference Database 23: Reference Fluid Thermodynamic and Transport Properties-REFPROP, Version 9.1, National Institute of Standards and Technology, Standard Reference Data Program, Gaithersburg.
- Mas Ivars, D., M.E. Pierce, C. Darcel, J. Reyes-Montes, et al. (2011), The synthetic rock mass approach for jointed rock mass modeling. *Int. J. Rock Mech. Min. Sci.*, 48(2):219-244, doi: 10.1016/j.ijrmms.2010.11.014.
- Maxwell, S.C., T.I. Urbancik, N.P. Steinsberger, and R. Zinno (2002), Microseismic imaging of hydraulic fracture complexity in the Barnett shale, paper presented at SPE Annual Technical Conference and Exhibition, San Antonio, TX, USA, SPE 77440.
- McClure, M.W., and Horne, R.N. (2014), An investigation of stimulation mechanisms in enhanced geothermal systems, *Int. J. Rock Mech. Min. Sci.*, 72:242-260, doi: 10.1016/j.ijrmms.2014.07.011.
- Michelet, S., and M.N. Toksöz (2007), Fracture mapping in the Soultz-sous-Forêts geothermal field using microearthquake locations, *J. Geophys. Res.*, 112(B7):B07315 (14 pages), doi: 10.1029/2006JB004442.

- Nagel, N., F. Zhang, M. Sanchez-Nagel, and B. Lee (2013), Quantitative evaluation of completion techniques on influencing shale fracture complexity, in: Bunger, A.P., J. McLennan, and R. Jeffrey (ed.), *Effective and Sustainable Hydraulic Fracturing*, InTech, 513-546, doi: 10.5772/56304.
- Nodgren, R. (1972), Propagation of vertical hydraulic fractures, *J. Petrol. Tech.*, 12(4):306-314, doi: 10.2118/3009-PA.
- Pearson, C.M., L. Griffin, C. Wright, and L. Weijers (2013), Breaking up is hard to do: creating hydraulic fracture complexity in the Bakken Central Basin, paper presented at SPE Hydraulic Fracturing Technology Conference, The Woodlands, TX, USA, SPE 163827.
- Perkins, T. and L. Kern (1961), Widths of hydraulic fractures, *J. Petrol. Tech.*, 13(9):937-949, doi: 10.2118/89-PA.
- Potocki, D. (2012), Understanding induced fracture complexity in different geological settings using DFIT net fracture pressure, paper presented at SPE Canadian Unconventional Resources Conferences, Calgary, Canada, SPE 162814.
- Potyondy, D.O., and P.A. Cundall (2004), A bonded-particle model for rock, *Int. J. Rock Mech. Min. Sci.*, 41(8):1329-1364, doi: 10.1016/j.ijrmms.2004.09.011.
- Ren, L., J. Zhao, and Y. Hu (2014), Hydraulic fracture extending into network in shale: Reviewing influence factors and their mechanism, *The Scientific World Journal*, 2014:847107 (9 pages), doi: 10.1155/2014/847107.
- Rickman, R., M. Mullen, E. Petre, B. Grieser, and D. Kundert (2008), A practical use of shale petrophysics for stimulation design optimization: all shale plays are not clones of the Barnett shale, paper presented at SPE Annual Technical Conference and Exhibition, Denver, CO, USA, SPE 115258.
- Safari, M.R., R. Gandikota, U. Mutlu, M. Ji, J. Glanville, and H. Abass (2013), Pulsed fracturing in shale reservoirs: Geomechanical aspects, ductile-brittle transition and field implications, paper presented at Unconventional Resources Technology Conference, Denver, CO, USA, SPE 168759.
- Tester, J.W., B.J. Anderson, A.S. Batchelor, D.D. Blackwell, et al. (2006), The future of geothermal energy – Impact of enhanced geothermal systems (EGS) on the United States in the 21st Century, Massachusetts Institute of Technology, Available from: <www.1eere.energy.gov/geothermal/egs_technology_html>.
- Warpinski, N.R., and P.T. Branagan (1989), Altered-stress fracturing, *J. of Petrol. Tech.* 41(9):990-997, SPE 17533, doi: 10.2118/17533-PA.
- Warpinski, N.R., R.C. Kramm, J.R. Heinze, C.K. Waltman, and S.R. Machovoe (2005), Comparison of single- and dual-array micro-seismic mapping techniques in the Barnett shale, paper presented at SPE Annual Technical Conference and Exhibition, Dallas, TX, USA, SPE 95568.
- Warpinski, N.R., and T.W. Teufel (1987), Influence of geologic discontinuities on hydraulic fracture propagation, *J. Petrol. Technol.*, 39(2):209-220, doi: 10.2118/13224-PA.
- Watanabe, N., N. Hirano, and N. Tsuchiya (2008), Determination of aperture structure and fluid flow in a rock fracture by high-resolution numerical modeling on the basis of a flow-

through experiment under confining pressure, *Water Resour. Res.*, 44(6):W06412, doi:10.1029/2006WR005411.

- Watanabe, N., W. Wang, C.I. McDermott, T. Taniguchi, and O. Kolditz (2010), Uncertainty analysis of thermo-hydro-mechanical coupled processes in heterogeneous porous media, *Comput. Mech.* 45(4):263-280, doi: 10.1007/s00466-009-0445-9.
- Watanabe, N., W. Wang, J. Taron, U.J. Görke, and O. Kolditz (2012), Lower-dimensional interface elements with local enrichment: application to coupled hydro-mechanical problems in discretely fractured porous media, *Int. J. Numer. Meth. Engng*, 90(8):1010-1034, doi: 10.1002/nme.3353.
- Weiland, C.M., K.C. Macdonald, and N.R. Grindlay (1996), Ridge segmentation and the magnetic structure of the Southern Mid-Atlantic Ridge 26° S and 31°-35° S: Implications for magmatic processes at slow spreading centers, *J. Geophys. Res.*, 101(B4):8055-8073, doi: 10.1029/95JB03535.
- Xu, C., P.A. Dowd, and R. Mohais (2012), Connectivity analysis of the Habanero enhanced geothermal system, paper presented at 37th Workshop on Geothermal Reservoir Engineering, Stanford, CA, USA.
- Yoon, J.S., A. Zang, and O. Stephansson (2012), Simulating fracture and friction of Aue granite under confined asymmetric compressive test using clumped particle model, *Int. J. Rock Mech. Min. Sci.*, 49:68-83, doi: 10.1016/j.ijrmms.2011.11.004.
- Yoon, J.S., A. Zang, and O. Stephansson (2014a), Numerical investigation on optimized stimulation of intact and naturally fractured deep geothermal reservoirs using hydro-mechanical coupled discrete particles joints model, *Geothermics* 52:165-184, doi: 10.1016/j.geothermics.2014.01.009.
- Yoon, J.S., G. Zimmermann, and A. Zang (2014b), Numerical investigation on stress shadowing in fluid injection-induced fracture propagation in naturally fractured geothermal reservoirs, *Rock Mech. Rock Eng.*, December 2014, 16 pages, doi: 10.1007/s00603-014-0695-5.
- Yoon, J.S., G. Zimmermann, and A. Zang (2015), Discrete element modeling of cyclic rate fluid injection at multiple locations in naturally fractured reservoirs, *Int. J. Rock Mech. Min. Sci.*, 74:15-23, doi: 10.1016/j.ijrmms.2014.12.003.

CHAPTER 10: OVERVIEW OF THE RESEARCH, CONTRIBUTIONS AND RECOMMENDATIONS

10.1 CRITICAL DISCUSSION OF SIMULATION APPROACHES

Hydraulic stimulation treatments and fluid circulation through a fractured inhomogeneous rock mass are very complex processes and information about rock properties and their distribution is very limited. Additionally, no EGS has been developed before in Alberta. These are some reasons why the presented numerical simulation studies and numerical models in general are subject to assumptions and limitations. Also, the accurate estimation of the costs of such projects is quite challenging. For example, surface facilities, such as a district heating, system or interest rates were not included in the calculation and the costs for each stimulation treatment were assumed to be the same.

To overcome the restriction of limited information about rock properties and geological data and missing field data a broad variety of cases was considered and different sensitivity analyses were performed for each modeling approach. Especially data about stresses and fracture networks were not available at all for deep granitic basement rocks in Northern Alberta. To get an idea about the stress at depth a simplified assumption had to be made (Equation 3) which was shown to be inadequate when compared to many field cases. However, due to missing data there was no other option to approximate the stresses at depth.

The work was divided into three phases with increasing model complexity to account for different aspects of EGS development and operation. However, all results are still idealized and only valid for the inherent assumptions.

All models had in common that flow in fractures was assumed to be laminar between two parallel plates. Any effects of friction, turbulence or channeling were neglected. Considering these effects would lead to higher pressure losses during stimulation and therefore yield underdeveloped fracture networks with shorter fractures. These effects would decrease the productivity index of the wells. Channeling fluid flow in fractures would reduce the effective fracture surface area that is in contact with the fluid and therefore reduce the heat output.

Additionally, no chemical effects were considered in this study, that could improve or hinder fluid flow due to solution and precipitation. Thermal stresses, which could induce additional thermal fractures, were also not included in this study.

For the reservoir simulations no pressure dependent fracture permeability function was applied in both models because no mechanical processes were investigated during reservoir operation simulations. Such a function would reduce fracture permeability at higher effective normal stresses on the fracture walls resulting from pressure depletion around production wells and it would increase fracture permeability at lower effective normal stresses due to higher fluid pressures around injection wells. In this case productivities would be lower and injectivities would be higher.

Some model specific assumptions, advantages, and disadvantages are given below:

1. In the conventional hydraulic fracturing simulator MFrac and the DFN model MShale fractures initiate and develop in tensile mode only. A fracture initiates or propagates if the net fracture pressure is above the critical stress, which can be specified as a constant value equal to the formations tensile strength (**Chapters 4 and 5**) or which is calculated based on the fracture toughness leading to a decrease in critical stress with increasing fracture length (**Chapter 3**). If a constant critical stress value is used the resulting fracture apertures are larger and hence larger amounts of fluid need to be injected to reach the same length as compared to the case when the critical stress decreases with fracture length.
2. Both models do not account for shear failure and idealize fracture geometries as ellipsoidal symmetrical fracture half-wings with a continuous aperture and permeability distribution. Since the model does not account for shear displacements, the developed fracture closes completely after the treatment if no proppants were injected. Also, the proppant distribution in a real fracture is most likely heterogeneous which leads to lower fracture permeabilities in parts of the fracture. Long term fluid circulation may also degrade proppants due to chemical reactions and proppant crushing and reduce fracture permeability with time. Gel residuals as well may plug flow paths.
3. Different layers were specified in these two models, but model properties are homogeneous in each layer, which has an infinite extension. In real reservoirs, the rock mass is expected to be more heterogeneous with a possible heterogeneous or anisotropic property distributions and discontinuities such as fracture networks or major fault zones intersecting the reservoir. This would deviate fracture growth paths and fracture

geometries from the idealized ellipsoidal shape and lead to irregular and branching fractures. While new tensile fractures may cross natural fractures and further develop in the same direction, it could also be arrested or follow the path of the natural fracture. In any case the fluid leak-off along the natural fracture would increase the required fluid volume to develop a fracture with a certain length.

4. The results from the studies performed with MFrac are still valuable because this code is routinely used for prediction, real-time analysis and evaluation of hydraulic fracturing treatments and proppant transport, and fluid flow and heat transport are fully coupled with fracture propagation. Additionally, the influence of different proppants and fracturing fluids on fracture development and proppant transport could be evaluated due to an extensive fluid and proppant property database.
5. MShale has the same advantages. The difference between the two models is that MShale also includes natural fracture networks and mechanical and hydraulic interaction between different fracture sets. However, natural fractures and newly developed fractures are limited to the extension within the three principle planes and the stimulated fracture network volume has an ellipsoidal shape. As stated above, this is a strong limitation, especially since fractures do not tend to develop perpendicular to each other because the resistance to fracture opening is strongest if fractures grow perpendicular to the maximum horizontal stress direction. However, using MShale, the additional volume needed to develop a network of fractures could be estimated.
6. The resulting fracture networks of these two models were exported to the finite difference reservoir simulator CMG STARS. The fractures were modeled as high permeable rectangular elements with an average height of the cylindrical shaped fracturing model output with an average fracture permeability. This leads to an overestimation of the fracture height at the fracture tip and an underestimation of the fracture height at the stimulated well. Additionally, the fracture permeability at the stimulated well is underestimated and the fracture permeability at the fracture tip is overestimated. Overall, the hydraulic performance of wells drilled close to a fracture tip is overestimated and the hydraulic performance of the stimulated well is underestimated with this simplification.
7. Using the grain-based modeling (GBM) approach mineral grains were modeled as a deformable, breakable assembly of particles bonded together by parallel bonds with high

strength, whereas the mineral boundaries were mimicked by smooth joint contacts with lower strength. While both types of contacts can fail in tensile and shear mode according to the Mohr-Coulomb failure criteria the mineral shapes are limited to polygons resulting from the shapes of particle assemblies. Real mineral shapes, e.g. of mica, could be different, which would change the simulation results because it was found that heterogeneity and size distributions play an important role in micro crack development. Since there is no space between the grains, it is assumed that the rock has no porosity. Due to the large amounts of different parameters the GBM modeling results are not unique, which means that a different set of parameters could also lead to a calibration of the same model. Additionally, all models need to be calibrated separately as it was shown that the calibrated model did not reproduce the triaxial test results from different granites using the same micro properties but different amounts and sizes of the minerals. The advantage of GBMs is that the modeled geometry comes close to the real microstructure of crystalline rocks.

8. The hydraulic model used for the PFC2D field scale simulations is subject to some limitations. The flow of a viscous fluid is simulated by assuming that each bonded particle contact is a flow channel which connects two fluid reservoirs that can store fluid. The fluid pressure in such a polygonal reservoir adds to the forces acting on the surrounding particles. For all contacts the same normal stress dependent fracture aperture law was used which changes the aperture between a minimum value at infinite normal stress and a maximum value at zero normal stress. Using different relationships for the different flow channel types (intact, tensile fracture, shear fracture) would be a next step to improve the model. Advantages of the model are that tensile and shear failure is possible, rock properties are inhomogeneous and arbitrary complex fracture geometries can develop. Additionally, microseismicity can be calculated and fluid leak-off through flow channels is possible, whereas there is no fluid leak-off through particles. While this approach is able to give an insight in fracture development from a new perspective, the long simulation times make it inappropriate for real time analysis of hydraulic stimulation treatments.
9. Both GBM and PFC2D field scale models were set up in two dimensions, which has the major limitation that fracture growth in a third dimension is not possible and a specific

fracture height needs to be assumed. A final limitation of the GBM model and the PFC2D field scale model are that fractures can only develop between grains and relatively large particles need to be used to allow calculation in reasonable time.

10. The resulting fracture networks from the DEM simulations were exported to the open source finite element reservoir simulator OpenGeoSys with a newly developed interface. Flow channels from intact particle contacts were not exported. For the reservoir simulations it was assumed that all fractures have the permeability at zero normal stress, which does not change as a function of normal stress on the fracture walls. This was done because it was assumed that all fractures were subject to some degree of displacement and the laboratory experiments showed that permeability reduction with increasing normal stress for displaced fracture surfaces is only minor. This is obviously a best case scenario. Lower fracture permeabilities and a higher degree of permeability reduction with increasing normal stress would reduce the calculated well productivities. The FEM model was used because it has the advantage that the complex fracture geometries from the DEM model could be directly exported to the FEM model, which is not possible with the FDM model used for the fracturing models with simple geometries. An additional advantage is that it was possible to use pressure and temperature dependent fluid properties and that the model can be extended by including coupled mechanical and chemical processes as well.
11. In all cases, the fracture networks, developed by hydro-mechanical fracturing models, were exported to a hydro-thermal reservoir model. During operation this fracture network was not changed anymore. However, pressure changes due to injection and production change effective stresses in the reservoir, which may result in additional fracture opening, growth, and closure after the actual stimulation treatment, which might lead to varying hydraulic performance or excessive fluid leak-off through fractures developing away from the reservoir.

Restricted by the above stated model assumptions and limitations some scientific and practical conclusions are presented in the following sections. Suggested model improvements are discussed afterwards.

10.2 SCIENTIFIC CONTRIBUTIONS

1. A range of hydraulic, thermal, mechanical, and geological reservoir parameters for the deep Precambrian basement underneath Fort McMurray and sedimentary rocks below Edmonton was collected and can be the basis for future studies.
2. The relative influence of a variety of parameters on fracture development and heat output within their expected data range was investigated for the first time for the Precambrian basement rocks beneath Fort McMurray and selected sedimentary formations below Edmonton using different simulation approaches. It was shown how the most important parameters, the in-situ stress field, natural fracture networks, and initial reservoir permeability influence stimulated fracture network geometries.
3. Also, some differences between DFN model properties and DFN simulation results of 2.5 km deep shales and 5 km deep granites were identified and the granites tend to develop larger and more complex fracture networks in the DFN model due to higher net pressures.
4. These are the first numerical simulation studies for EGS development in Alberta that incorporate hydraulic stimulations, reservoir behavior, economic viability, and environmental aspects.
5. To evaluate the hydraulic and thermal efficiency of hydraulic stimulation treatments simulated with the particle based DEM code PFC2D, a new interface between PFC2D and the FEM reservoir simulator OpenGeoSys was developed.
6. Two grain-based modeling studies contributed to a further understanding of the influence of different micro scale model properties on micro and macro scale fracture growth and macro scale strength and elastic properties. It was found that heterogeneities govern fracture growth and complexity and micro parameters govern the development of different micro fracture types.
7. New laboratory experimental results increased the data- and knowledgebase of pressure dependent fracture permeability, which is essential for numerical modeling and development of EGS. Displaced tensile fractures in granites can have a similar permeability without proppants as propped fractures in sedimentary rocks while the permeability of unpropped aligned tensile fractures is insufficient for EGS except more than thousands of individual large fractures can be developed.

10.3 PRACTICAL CONTRIBUTIONS

Overall, the development of EGS for oil sands processing in Fort McMurray and district heating in Edmonton significantly reduces GHG emissions and saves natural gas resources. However, economically it can only compete with natural gas if the system is optimally engineered or natural gas prices increase significantly. Technically, EGS development for both applications is challenging. Therefore new reservoir engineering concepts were proposed for both applications based on the numerical simulation results.

For the development of EGS from sedimentary rocks in the Edmonton area the simulation results lead to the following recommendations:

- The Basal Sandstone unit and the Cooking Lake formation (limestone) were found to be able to provide the highest heat output of all four investigated sedimentary layers below Edmonton, whereas the Wabamun group is not viable for geothermal energy extraction.
- Productivity improvement by multi stage stimulation treatments is necessary in all formations.
- Horizontal wells outperform vertical wells and well triplets are more economic than well doublets.
- In the low permeability Basal Sandstone Unit fractures should connect the wells directly.
- In the higher permeability Cooking Lake and Nisku formations fluid should flow between the fractures through the matrix.
- Conventional gel-proppant fracturing treatments are suitable for the hydraulic stimulation of the investigated rock types.
- EGS should be operated for at least 20 – 30 years to be economical.

1140 houses can be heated with geothermal energy from the most promising simulated three-well system in the Basal Sandstone Unit with a re-injection temperature of 70°C. 517 of these well triplets would be needed to replace natural gas for residential, commercial, and institutional buildings in Edmonton. Energy generation costs vary between 6.4 \$/GJ and 15.1 \$/GJ and can be further reduced by reducing the injection temperature, optimization, and combined use for multiple applications. Large amounts of GHG emissions can be reduced and natural gas can be saved.

Based on the simulation results, a new reservoir engineering concept is proposed for EGS in granitic basement rock that has not been tested in the field yet. This concept involves the following key points:

- In Fort McMurray, wells need to be drilled to 5 km depth through mainly granitic basement rock to reach temperatures of about 100°C.
- At least two or three long (e.g. 2 km) relatively closely-spaced (e.g. 400 m) parallel horizontal or highly deviated wells should be drilled to improve the chance of hydraulic connectivity between the fracture network and the wells, to reduce water losses, to allow for multiple stimulation treatments, and to access sufficient reservoir volume.
- Performing multi stage stimulations aims to increase fracture network complexity, develop multiple low conductivity individual flow paths, but with a high total fracture network hydraulic conductivity while maximizing the fracture network area to create sufficient heat exchanger area ($> 1 \text{ km}^2$).
- The simulation results also suggest a continuous injection of large amounts of low viscosity fluid (e.g. water) at a high rate in each stage.
- While the focus should be on the productivity enhancement of the production well, alternating stimulation treatments between wells and an offset between the stage locations of the wells are also suggested to improve the hydraulic connection between neighboring wells.
- A small stage spacing (e.g. 100 m) should be used to increase fracture network complexity between the wells. However, excessive fracture growth out of the target zone might be a problem when performing multiple stimulation treatments too close to each other because individual fractures can link up and form one long fracture.
- Wells should be drilled at an angle of 45° to the minimum horizontal stress direction because it led to longer fluid pathways and a better connection between the wells in the DEM simulations compared to wells aligned with the minimum horizontal stress direction.
- The stress shadow effect resulting from one stimulation treatment should be utilized to change fracture growth directions of subsequent treatments such that fractures intersect and build a complex network.

The required temperatures and economic targets for heat provision for oil sands processing were achieved for a stimulated well triplet consisting of one injection well injecting 60 l/s of water at 30°C flanked by two production wells producing 30 l/s of water each at temperatures above 60°C over a period of 30 years.

The actual reservoir engineering concepts and treatment designs are site-specific and need to be updated when new information is available. The most important reservoir characteristics that should be sufficiently explored are natural fracture systems and the principle in-situ stresses in, below, and above the target formation. Potential drilling targets are confined, heterogeneous, naturally fractured formations with a low stress anisotropy.

The pressure dependent fracture permeability from laboratory experiments in conjunction with a literature survey and the simulation results showed that displaced self-propping fractures in granites have a large enough permeability to allow similar fluid flow as achieved by using proppants in sedimentary rocks. In this case only 10s of large scale (e.g. 500 m half-length, 150 m height) fractures would need to be developed. For the sedimentary rocks (e.g. Basal Sandstone Unit) the use of proppants is imperative.

An EGS for oil sands processing in Alberta would be the first attempt to utilize low enthalpy granitic basement rocks for heat extraction in an area with low tectonic activity. However, since most of the earth's heat is stored in low permeable basement rocks, the improved understanding of EGS development in general and hydraulic fracture development specifically resulting from this study can potentially find application in the improvement of EGS development all over the world.

10.4 SUGGESTED FUTURE WORK

While the presented results give an overview of important processes, lead to a proposed reservoir engineering concept, and approximate the environmental benefits and economics of EGS, several issues can be identified that would improve the numerical models and that could confirm, refine and optimize the found results.

1. In the presented study, the hydraulic stimulation treatments and the reservoir operation were simulated separately. Since fracture growth may also occur during reservoir operation and the reservoir pressures may be changed during stimulation, a single model should be developed that is able to adequately handle all major processes, which govern both reservoir stimulation and operation. Alternatively, the current DEM – FEM interface could be extended to a fully coupled model where pressures, temperatures, and fracture permeabilities are exchanged after each time step.
2. The particle based DEM simulations can most significantly be improved by using a 3D model, including micro seismicity and a well bore model in the analysis, and defining different flow laws for different fracture types. The GBM approach may be improved by mapping the actual mineral geometries from thin sections and assigning different properties for boundaries between different mineral types.
3. While the investigated parameter range shows the potential range of model outputs for granitic rocks in general, using rock samples from the Hunt well to refine the knowledge about rock properties in the Fort McMurray area would narrow down the predicted modeling results. The same is true for the Basal Sandstone unit in the basin where only limited data was available. The presented reservoir engineering concepts and numerical models should be updated as soon as more data is available.
4. The permeability of fractures under elevated effective confining pressures should be further investigated. The largest scientific benefit would be gained from long term fracture experiments of all fracture types, investigating the permeability improvement by proppants in fractures in granites, and fracture creation under in-situ conditions within the triaxial cell.
5. Other potential areas in Alberta with a high demand of heat and above average temperature gradients such as the Edson – Hinton area or the northwest part of the province should be investigated for their potential to exploit geothermal energy as well.
6. As an alternative approach to provide heat for oil sands processing, the technical and economical aspects of utilizing lower temperature water from shallower formations for preheating should be assessed.
7. Since the minor success of EGS so far is mainly due to the very limited field experience, the proposed reservoir engineering concept should be tested in the field with detailed

scientific support, documentation, and analysis. This would help proving the viability of the concept and identifying practical problems associated with it. The data can be used to validate and update the numerical models and the system understanding could be significantly improved. The results of such a study would be applicable to many similar granitic basement rocks.

BIBLIOGRAPHY

- Adachi, J., Siebrits, E., Peirce, A., and Desroches, J. (2007). Computer simulation of hydraulic fractures. *International Journal of Rock Mechanics & Mining Sciences*, **44**:739-757.
- Agapito, J., and Hardy, M. (1982). Induced Horizontal Stress Method of Pillar Design in Oil Shale. *Proceedings of the 15th Oil Shale Symposium*, Golden, CO, USA, April 28–30, 191–197.
- Aggour, T.M. and Economides, M.J. (1999). Impact of fluid selection on high-permeability fracturing. *SPE Production & Facilities*, **14**:72-76, SPE 54536.
- Alberta Energy (2014). Monthly reference price calculations, Alberta gas reference prices. Available from: <www.energy.alberta.ca/NaturalGas/1316.asp> [retrieved April 25, 2014].
- Alehossein H., Boland J.N. (2004). Strength, toughness, damage and fatigue of rock. *Proceedings of Structural Integrity and Fracture*, Brisbane, Australia, September 26-29.
- Alm, O., Jaktlund, L.-L., Kuo, S. (1985). The influence of microcrack density on the elastic and fracture mechanical properties of Stripa granite. *Physics of the Earth and Planetary Interiors*, **40**:161-179.
- Augustine, C., Tester, J.W., Anderson, B. (2006). A comparison of geothermal with oil and gas well drilling costs. *Proceedings of the 31st Workshop on Geothermal Reservoir Engineering*, Stanford, CA, USA, January 30-February 1.
- Babadagli, T. and Develi, K., (2001). On the application of methods used to calculate fractal dimension of fracture surfaces. *Fractals*, **9**:105–128.
- Bahrani, N., Valley, B., Kaiser, P.K., Pierce, M. (2011). Evaluation of PFC2D grain-based model for simulation of confinement-dependent rock strength degradation and failure processes. *Proceedings of the 45th US Rock Mechanics Symposium*, San Francisco, CA, USA, June 26-29, ARMA 11-156.
- Bahrani, N., Potyondy, D.O., Pierce, M. (2012). Simulation of Brazilian test using PFC2D grain-based model. *Proceedings of the 21st Canadian Rock Mechanics Symposium*, Edmonton, Alberta, Canada, May 5-9.
- Bahrani, N., Kaiser, P.K., Valley, B. (2014). Distinct element method simulation of an analogue for a highly interlocked, non-persistently jointed rockmass. *International Journal of Rock Mechanics & Mining Sciences*, **71**:117-130

- Baisch, S., Vörös, R., Rothert, E., Stang, H., Jung, R., and Schellschmidt, R. (2010). A numerical model for fluid injection induced seismicity at Soultz-sous-Forêts. *International Journal of Rock Mechanics and Mining Sciences*, **47**:405-413.
- Baria, R., Baumgaertner, J., Rummel, F., Pine, R.J., and Sato, Y. (1999). HDR/HWR reservoirs: Concepts, understanding and creation. *Geothermics*, **28**:533-552.
- Barree, R.D. (1983). A Practical Numerical simulator for three-dimensional fracture propagation in heterogeneous media. *Proceedings of the SPE Reservoir Simulation Symposium*, San Francisco, CA, USA, November 15-18, SPE 12273.
- Barton, C.A., Zoback, M.D., and Moos, D. (1995). Fluid flow along potentially active faults in crystalline rock. *Geology*, **23**:683-686.
- Batycky, J.P., Leaute, R.P., and Dawe, B.A. (1997). A mechanistic model of cyclic steam stimulation. *Proceedings of the International Thermal Operations and Heavy Oil Symposium*, Bakersfield, CA, USA, February 10-12, SPE 37550.
- Beard, T. (2011). Fracture Design in Horizontal Shale Wells—Data Gathering to Implementation. *Proceedings of the EPA Hydraulic Fracturing Workshop*, Arlington, VA, March 10–11.
- Beckwith, R. (2010). Hydraulic Fracturing: The Fuss, The Facts, The Future. *Journal of Petroleum Technology*, **62**:34-41.
- Bertani, R. and Thain, I. (2002). Geothermal power generating plant CO2 emission survey. *IGA News*, **49**:1-3.
- Beugelsdijk, L.J.L., de Pater, C.J., Kato, K. (2000). Experimental hydraulic fracture propagation in a multi-fractured medium. *Proceedings of the SPE Asia Pacific Conference on Integrated Modelling for Asset Management*, Yokohama, Japan, April 25-26.
- Bewick, R.P., Kaiser, P.K., Bawden, W.F., Bahrani, N. (2013a). DEM simulation of direct shear: 1. Rupture under constant normal stress boundary conditions. *Rock Mechanics and Rock Engineering*, **47**:1647-1671.
- Bewick, R.P., Kaiser, P.K., and Bawden, W.F. (2013b). DEM simulation of direct shear: 2. Grain boundary and mineral grain strength component influence on shear rupture. *Rock Mechanics and Rock Engineering*, **47**:1673-1692.
- Bioenergy Feedstock Information Network – BFIN (2013). Quick-reference of conversion factors used by the bioenergy feedstock development programs at ORNL. Available from: <bioenergy.ornl.gov/papers/misc/energy_conv.html> [retrieved October 12, 2013].
- Blöcher, G., Cacace, M., Lewerenz, B., and Zimmermann, G. (2010). Three dimensional modelling of fractured and faulted reservoirs: Framework and implementation. *Chemie der Erde – Geochemistry*, **70**:145-153.
- Blöcher, G., Cacace, M., Reinsch, T., and Watanabe, N. (2015). Exploitation concepts for a deep geothermal system in the North German Basin. *Submitted to Computers & Geosciences*.
- Bloomfield, K.K., Moore, J.N., Neilson Jr, R.M. (2003). Geothermal energy reduces greenhouse gases. *Geothermal Resources Council Bulletin*, **32**:77–79.

- Breede, K., Dzebisashvili, K., Liu, X., and Falcone, G. (2013). A systematic review of enhanced (or engineered) geothermal systems: past, present and future. *Geothermal Energy*, **1**:4 (27 pages).
- Briggs, K., Hill, A.D., and Zhu, D. (2014). The relationship between rock properties and fracture conductivity in the Fayetteville Shale. *Proceedings of the Annual Technical Conference and Exhibition*, Amsterdam, The Netherlands, October 27-29, SPE 170790.
- Brown, D.W. 2009. Hot Dry Rock Geothermal Energy: Important Lessons From Fenton Hill. *Proceedings of the 34th Workshop on Geothermal Reservoir Engineering*, Stanford, CA, USA, February 9-11.
- Bruel, D. (2007). Using the migration of the induced seismicity as a constraint for fractured Hot Dry Rock reservoir modelling. *International Journal of Rock Mechanics and Mining Sciences*, **44**:1106-1117.
- Butler, R.M., McNab, G.S., and Lo, H.Y. (1981). Theoretical studies on the gravity drainage of heavy oil during in-situ steam heating. *The Canadian Journal of Chemical Engineering*, **59**:455-460.
- Cacace, M., Blöcher, G., Watanabe, N., Moeck, I., Börsing, N., Scheck-Wenderoth, M., Kolditz, O., and Huenges, E. (2013). Modelling of fractured carbonate reservoirs: outline of a novel technique via a case study from the Molasse Basin, southern Bavaria, Germany. *Environmental Earth Sciences*, **70**:3585-3602.
- Cacace, M., and Blöcher, G. (2015). MeshIt – a software for three dimensional geometric modelling of faulted reservoirs. *Submitted to Computers and Geosciences*.
- Canadian Association of Petroleum Producers – CAPP (2014). The facts on: Oil sands. Available from: <www.capp.ca/UpstreamDialogue/OilSands/Pages/default.aspx> [retrieved April 24, 2014].
- Canadian Association of Petroleum Producers – CAPP (2012). Water use in Canada's oil sands. Available from: <www.capp.ca/getdoc.aspx?DocId=193756&DT=NTV> [retrieved April 24, 2014].
- Chan, J. (2013). Subsurface geophysical characterization of the crystalline Canadian shield in Northeastern Alberta: Implications for geothermal development. M.Sc. thesis, Department of Physics, University of Alberta.
- Chen, Z., Narayan, S.P., Yang, Z., and Rahman, S.S. (2000). An experimental investigation of hydraulic behavior of fractures and joints in granitic rock. *International Journal of Rock Mechanics and Mining Sciences*, **37**:1061–1071.
- Chen, M., Zhou, J., Jin, Y., Zhang, G. (2008). Experimental study on fracturing features in naturally fractured reservoir. *Acta Petrolei Sinica*, **29**:431-434.
- Chen, Y. and Zhou, C. (2011). Stress/Strain-Dependent Properties of Hydraulic Conductivity for Fractured Rocks. In: *Developments in Hydraulic Conductivity Research*. Dikinya, O. (editor), InTech. Available from: <www.intechopen.com/books/developments-in-hydraulic-conductivityresearch/stress-strain-dependent-properties-of-hydraulic-conductivity-for-fractured-rocks>

- Cheng, Y. (2009). Boundary element analysis of the stress distribution around multiple fractures: Implications for the spacing of perforation clusters of hydraulically fractured horizontal wells. *Proceedings of the SPE Eastern Regional Meeting*, Charleston, USA, September 23-25, SPE 125769.
- Chen, W. and Konietzky, H. (2014). Simulation of heterogeneity, creep, damage and lifetime for loaded brittle rocks. *Tectonophysics*, **633**:164-175.
- Cherubini, Y., Cacace, M., Blöcher, G., and Scheck-Wenderoth, M. (2013). Impact of single inclined faults on the fluid flow and heat transport: results from 3-D finite element simulations. *Environmental Earth Sciences*, **70**:3603-3618.
- Cho, N., Martin, C.D., and Sego, D.C. (2007). A clumped particle model for rock. *International Journal of Rock Mechanics and Mining Sciences*, **44**:997-1010.
- Cho, Y., Apaydin, O.G., and Ozkan, E. (2012). Pressure-dependent natural-fracture permeability in shale and its effect on shale-gas well production. *Proceedings of the SPE Annual Technical Conference and Exhibition*, San Antonio, TX, USA, October 8-10, SPE 159801.
- Cholach, P.Y., Molyneux, J.B., and Schmitt, D.R. (2005). Flin Flon Belt seismic anisotropy: elastic symmetry, heterogeneity, and shear-wave splitting. *Canadian Journal of Earth Science*, **42**:533-554.
- Chuprakov, D.A., Akulich, A.V., Siebrits, E., and Thiercelin, M.J. (2011). Hydraulic-fracture propagation in a naturally fractured reservoir. *SPE Production & Operations*, **26**:88-97, SPE 128715.
- Cipolla, C.L., Warpinski, N.R., Mayerhofer, M.J., Lonon, E.P., and Vincent, M.C. (2008). The relationship between fracture complexity, reservoir properties, and fracture treatment design. *Proceedings of the SPE Annual Technical Conference and Exhibition*, Denver, CO, USA, September 21-24, SPE 115769.
- Cipolla, C. L., Warpinski, N. R., and Mayerhofer, M. J. (2008). Hydraulic Fracture Complexity: Diagnosis, Remediation, and Exploitation. *Proceedings of the SPE Asia Pacific Oil and Gas Conference and Exhibition*, Perth, Australia, October 20-22, SPE 115771.
- Clauser, C. (1992). Permeability of crystalline rocks. *Eos Transactions American Geophysical Union*, **73**:233-40.
- Cleary, M.P. (1994). Discussion of comparison study of hydraulic fracturing models – test case: GRI staged field experiment No. 3. *SPE Production and Facilities*, **9**:17-18, SPE 28158.
- Cleary, M. P. (1980). Analysis of Mechanisms and Procedures for Producing Favourable Shapes of Hydraulic Fractures. *Proceedings of the Annual Technical Conference and Exhibition*, Dallas, TX, USA, September 21-24, SPE 9260.
- Computer Modeling Group Ltd. (2011). User's guide STARS advanced process and thermal reservoir simulator, 1120 pages.
- Conolly, C.A., Walter, L.M., Baadsgaard, H., and Longstaffe, F.J. (1990). Origin and evolution of formation waters, Alberta Basin, western Canada sedimentary basin. I. Chemistry. *Applied Geochemistry*, **5**:375-395.
- Cornet, F.H., Bérard, T.H., and Bourouis, S. (2007). How close to failure is a granitic rock mass at a 5 km depth? *International Journal of Rock Mechanics and Mining Sciences*, **44**:47-66.

- Cundall, P.A. (2001). A discontinuous future for numerical modelling in geomechanics? *Geotechnical Engineering*, **149**:41-47.
- Dahi-Taleghani, A. and Olson, J. (2011). Numerical modeling of multistranded-hydraulic-fracture propagation: accounting for the interaction between induced and natural fractures. *Society of Petroleum Engineering Journal*, **16**:575-581, SPE 124884.
- Dai, F., Xia, K. (2009). Tensile strength anisotropy of Barre Granite. *Proceedings of the 3rd CANUS Rock Mechanics Symposium*, Toronto, ON, Canada, May 9-15, paper 4012.
- Damjanac, B., Gil, I., Pierce, M., and Sanchez, M. (2010). A new approach to hydraulic fracturing modeling in naturally fractured reservoirs. *Proceedings of the 44th U.S. Rock Mechanics Symposium and 5th U.S.-Canada Rock Mechanics Symposium*, Salt Lake City, UT, USA, June 27-30.
- Dempsey, D., Kelkar, S., Lewis, K., Hickman, S., Davatzes, N., Moos, D., and Zemach, E. (2013). Modeling Shear Stimulation of the Desert Peak EGS Well 27-15 Using a Coupled Thermal-Hydrological-Mechanical Simulator. *Proceedings of the 47th US Rock Mechanics/Geomechanics Symposium*, San Francisco, CA, USA, June 23-26.
- Deng, S., Podgorney, R., and Huang, H. (2011). Discrete element modeling of rock deformation, fracture network development and permeability evolution under hydraulic stimulation. *Proceedings of the 36th Workshop on Geothermal Reservoir Engineering*, Stanford, CA, USA, January 31-February 3.
- Dershowitz, W.S., Cottrell, M.G., Lim, D.H., and Doe, T.W. (2010). A discrete fracture network approach for evaluation of hydraulic fracture stimulation of naturally fractured reservoirs. *Proceedings of the 44th U.S. Rock Mechanics Symposium and 5th U.S.-Canada Rock Mechanics Symposium*, Salt Lake City, UT, USA, June 27-30.
- Detournay, E. (1980). Hydraulic conductivity of closed rock fractures: an experimental and analytical study. *Proceedings of the 13th Canadian Rock Mechanics Symposium on Underground Rock Engineering*, Montreal, Canada, May 28-29.
- Develi, K., Babadagli, T., and Comlekci, C. (2001). A new computer controlled surface scanning device for measurement of fracture surface roughness. *Computers and Geosciences*, **27**:265-277.
- Develi, K. and Babadagli, T. (2015). Experimental and visual analysis of single-phase flow through rough fracture replicas. *International Journal of Rock Mechanics and Mining Sciences*, **73**:139-155.
- Dickson, M.H. and Fanelli, M. (2005). Geothermal energy: utilization and technology. Taylor and Francis, New York, USA, 224 pages.
- Dietrich, P., Helmig, R., Sauter, M., Hötzel, H., Köngeter, J., and Teutsch, G. (2005). Flow and transport in fractured porous media, Springer, Berlin, Germany, 447 pages.
- Diomampo, G.P. (2001). Relative permeability through fractures. *Technical report Stanford Geothermal Program*, SGP-TR-170, Available from: pangea.stanford.edu/ERE/research/geoth/publications/techreports/SGP-TR-170.pdf
- DiPippo, R. (2012). Geothermal power plants – principles, applications, case studies and environmental impact. 3rd edition, Butterworth-Heinemann, Oxford, UK, 600 pages.

- Schlumberger (2006). Eclipse 100 Reference Manual.
- Economides, M. J., and Wood, D. A. (2009). The State of Natural Gas. *Journal of Natural Gas Science Engineering*, **1**:1-13.
- Economides, M.J. and Martin, T. (2007). Modern Fracturing – Enhancing natural gas production. 1st edition, Energy Tribune Publishing, Houston, TX, USA, 531 pages.
- Economides, M.J. and Nolte, K.G. (2000). Reservoir Stimulation. 3rd edition, John Wiley & Sons Ltd., UK, 856 pages.
- Elliott, G.M. and Brown E.T. (1988). Laboratory measurement of the thermos-hydro-mechanical properties of rock. *Quarterly Journal of Engineering Geology*, **21**:299-314.
- Energy Resources Conservation Board – ERCB (2013). Alberta's energy reserves 2012 and supply/demand outlook 2013-2022. Statistical report ST98-2013, Available from: <www.aer.ca/documents/sts/ST98/ST98-2013.pdf> [retrieved April 24, 2014].
- Environment Canada (2013). Canada's emissions trends. Available from: <www.ec.gc.ca/ges-ghg/985F05FB-4744-4269-8C1A-D443F8A86814/1001-Canada's%20Emissions%20Trends%202013_e.pdf> [retrieved April 24, 2014].
- Erarsalan, N. and Williams, D.J. (2012). Investigating the effect of cyclic loading on the indirect tensile strength of rocks. *Rock Mechanics and Rock Engineering*, **45**:327-340.
- Eseme, E., Urai, J. L., Krooss, B. M., and Littke, R. (2007). Review of Mechanical Properties of Oil Shales: Implications for Exploitation and Basin Modelling. *Oil Shale*, **24**:159–174.
- Evans, K.F., Zappone, A., Kraft, T., Deichmann, N. and Moia, F. (2012). A survey of the induced seismic response to fluid injection in geothermal and CO₂ reservoirs in europe. *Geothermics*, **41**:30-54.
- Fisher, M.K., Wright, C.A., Davidson, B.M., Goodwin, A.K., Fielder, E.O., Buckler, W.S., and Steinsberger, N.P. (2002). Integrating fracture mapping technologies to optimize stimulations in the Barnett shale. *Proceedings of the SPE Annual Technical Conference and Exhibition*, San Antonio, TX, USA, September 29-October 2, SPE 77441.
- Fisher, K., and Warpinski, N. (2012). Hydraulic-Fracture-Height Growth: Real Data. *SPE Productions & Operations*, **27**:8-19, SPE 145949.
- Fredd, C.N., McConnell, S.B., Boney, C.L., and England, K.W. (2000). Experimental study of hydraulic fracture conductivity demonstrates the benefits of using proppants. *Proceedings of the SPE Rocky Mountain Regional/Low Permeability Reservoirs Symposium*, Denver, CO, USA, March 12-15, SPE 60326.
- Frick, S., Kaltschmitt, M., Schröder, G. (2010). Life cycle assessment of geothermal binary power plants using enhanced low-temperature reservoirs. *Energy*, **35**:2281–2294.
- Fu, P., Johnson, S.M., and Carrigan, C.R. (2013). An explicitly coupled hydro-geomechanical model for simulating hydraulic fracturing in arbitrary discrete fracture networks. *International Journal of Numerical and Analytical Methods in Geomechanics*, **37**:2278-2300.

- Gale, J.E. (1982). The effects of fracture type (induced versus natural) on the stress-fracture closure-fracture permeability relationships. *Proceedings of the 23rd U.S. Symposium on Rock Mechanics (USRMS)*, Berkeley, CA, USA, August 25-27.
- Gale, J.F.W., Reed, R.M., and Holder, J. (2007). Natural Fractures in the Barnett Shale and Their Importance for Hydraulic Fracturing Treatments. *American Association of Petroleum Geology Bulletin*, **91**:603–622.
- Gale, J.F.W., and Holder, J. (2010). Natural Fractures in Some US Shales and Their Importance for Gas Production. *Petroleum Geology Conference Series*, **7**:1131–1140.
- Geertsma, J. and de Klerk, F. (1969). A Rapid method of predicting width and extent of hydraulic induced fractures. *Journal of Petroleum Technology*, **21**:1571-1581, SPE 2458.
- Geraud, Y., Rosener, M., Surma, F., Place, J., Le Garzic, E. and Diraison, M. (2010). Physical properties of fault zones within a granite body: Example of the Soultz-sous-Forêts geothermal site. *Geoscience*, **342**:566-574.
- Goldstein, B., Hiriart, G., Bertani, R., Bromley, C., Gutiérrez-Negrín, L., Huenges, E., et al. (2011). Geothermal energy. In: Edenhofer O, Pichs-Madruga R, Sokona Y, Seyboth K, Matschoss P, Kadner S, et al., (editors). IPCC special report on renewable energy sources and climate change mitigation. Cambridge University Press, UK, 401-436.
- Goldstein, B.A., Hiriart, G., Tester, J., Bertani, B., Bromley, R., Gutierrez-Negrin, L., Huenges, E., Ragnarsson, H., Mongillo, A., Muraoka, M. A., and Zui, V. I., (2011). Great Expectations for Geothermal Energy to 2100. *Proceedings of the 36th Workshop on Geothermal Reservoir Engineering*, Stanford, CA, USA January 31–February 2.
- Government of Alberta (2014). Facts and statistics – environment. Available from: <www.energy.alberta.ca/OilSands/791.asp> [retrieved April 4, 2014].
- Government of Alberta (2012a). Environmental management of Alberta’s oil sands. Available from: <<http://environment.gov.ab.ca/info/library/8042.pdf>> [retrieved July 19, 2012].
- Government of Alberta (2012b). Monthly reference price calculations. Alberta gas reference prices for 2012. Available from: <<http://www.energy.alberta.ca/NaturalGas/1316.asp>> [retrieved July 19, 2012].
- Grant, M.A. and Bixley, P.F. (2011). Geothermal reservoir engineering. 2nd edition, Academic Press, Burlington, USA, 378 pages.
- Guitierrez, M., Oino, L.E., and Nygard, R. (2000). Stress-dependent permeability of a de-mineralised fracture in shale. *Marine and Petroleum Geology*, **17**:895-907.
- Gupta, H. and Roy, S. (2007). Geothermal energy: An alternative resource for the 21st century. 1st edition, Elsevier, Amsterdam, The Netherlands, 292 pages.
- Haifeng, Z., Jun, S., Erfei, M., Hang, C., and Guohua, L. (2015). Scale model of stress sensitivity for fractured low-permeability reservoirs. *Proceedings of the 39th Workshop on Geothermal Reservoir Engineering*, Stanford, CA, USA, January, 26-28.
- Haimson, B. and Chang, C. (2005). Brittle fracture in two crystalline rocks under true triaxial compressive stresses. *Geological Society London Special Publications*, **240**:47-59.

- Hakami, E. and Larsson, E. (1996). Aperture measurements and flow experiments on a single natural fracture. *International Journal of Rock Mechanics, Mining Sciences and Geomechanics Abstracts*, **33**:395-404.
- Hanova, J., Dowlatabadi, H., Mueller, L. (2007). Ground source heat pump systems in Canada: economics and GHG reduction potential. Discussion paper, RFF DP 07-18, Resources for the future. Available from: <www.green-erg.com/documents/Canada_GSHP.pdf> [retrieved November 15, 2013].
- Hatzor, Y.H., Zur, A., Mimran, Y. (1997). Microstructure effects on microcracking and brittle failure of dolomites. *Tectonophysics*, **281**:141-161.
- Haug, K., Nygaard, R., Keith, D. (2007). Evaluation of stress and geomechanical characteristics of a potential site for CO₂ geological storage in Central Alberta, Canada. Available from: <www.keith.seas.harvard.edu/papers/109.Haug.2007.EvalofStress&GeomChar.e.pdf>.
- Hawkes, C.D., Bachu, S., Haug, K., Thompson, A.W. (2005). Analysis of in-situ stress regime in the Alberta Basin, Canada, for performance assessment of CO₂ geological sequestration sites. *Proceedings of the 4th Annual Conference on Carbon Capture and Sequestration*, Alexandria, VA, USA, May 2-5.
- Hazzard, J.F., Young, R.P., and Oates, S.J. (2002). Numerical modeling of seismicity induced by fluid injection in a fractured reservoir. *Proceedings of the 5th North American Rock Mechanics Symposium, Mining and Tunnel Innovation and Opportunity*, Toronto, Canada, 7-10 July, 1023-1030.
- Heidbach, O., Tingay, M., Barth, A., Reinecker, J., Kurfess, D., Mueller, B. (2008). The world stress map database release 2008. doi: 10.1594/GFZ.WSM.Rel2008.
- Hein, F.J., Leckie, D., Larter, S., and Suter, J.R.: Heavy oil and bitumen petroleum systems in Alberta and beyond: the future is nonconventional and the future is now. In: Hein, F.J., Leckie, D., Larter, S., and Suter, J.R., (eds.). Heavy-oil and oil-sand petroleum systems in Alberta and beyond: *AAPG Studies in Geology*, **64**:1-21.
- Helms L. (2008). Horizontal drilling. *North Dakota Department of Mineral Resources (DMR) News*, **35**:1-3.
- Hicks, T.W., Pine, R.J., Willis-Richards, J., Xu, S., Jupe, A.J., and Rodrigues, N.E.V. (1996). A hydro-thermo-mechanical numerical model for HDR geothermal reservoir evaluation. *International Journal of Rock Mechanics and Mining Sciences Geomechanics Abstracts*, **33**:499-511.
- Hill, R.E. (1992). Analysis of Natural and Induced Fractures in the Barnett Shale. RI Report No. 92/0094.
- Hökmark, H., Lönnqvist, M., and Fälth, B. (2010). THM-issues in repository rock – thermal, mechanical, thermos-mechanical and hydromechanical evolution of the rock at the Forsmark and Laxemar sites. Technical Report TR-10-23, Swedish Nuclear Fuel and Waste Management Co, Sweden.
- Hofmann, H., Babadagli, T., and Zimmermann, G. (2012a). Hydraulic fracturing scenarios for low temperature EGS heat generation from the Precambrian basement in Northern Alberta. *GRC Transactions*, **36**:459-467.

- Hofmann, H., Babadagli, T., and Zimmermann, G. (2012b). Conception and simulation of hydraulic fracturing treatments for the development of enhanced geothermal systems (EGS) in the Precambrian basement rocks in Northern Alberta. 3rd HAI Annual Meeting, Edmonton, AB, Canada, May 10.
- Hofmann, H., Babadagli, T., and Zimmermann, G. (2012c). Hot water generation for oilsands processing from Hot-Dry-Rocks: process simulation for different hydraulic fracturing scenarios. 2nd HAI Science Forum, Potsdam, Germany, September 10.
- Hofmann, H., Weides, S., Babadagli, T., Zimmermann, G., Moeck, I., Majorowicz, J., and Unsworth, M. (2013a). Integrated reservoir modeling for enhanced geothermal energy systems in Central Alberta, Canada. *Proceedings of the 38th Workshop on Geothermal Reservoir Engineering*, Stanford, CA, USA, February 11-13.
- Hofmann, H., Babadagli, T., and Zimmermann, G. (2013b). Numerical simulation of complex fracture network development by hydraulic fracturing in naturally fractured ultratight formations. *Proceedings of the 32nd International Conference on Ocean, Offshore and Arctic Engineering*, Nantes, France, June 9-14, OMAE2013-11084.
- Hofmann, H., Babadagli, T., and Zimmermann, G. (2013c). Hydraulic fracture development for EGS heat generation for oil sands processing in northern Alberta, Canada. 3rd HAI Science Forum, Edmonton, Canada, September 19.
- Hofmann, H., Weides, S., Babadagli, T., Zimmermann, G., Moeck, I., Majorowicz, J., and Unsworth, M. (2014a). Potential for enhanced geothermal systems in Alberta, Canada. *Energy*, **69**:578-591.
- Hofmann, H., Blöcher, G., Börsing, N., Maronde, N., Pastrok, N., and Zimmermann, G. (2014b). Potential for enhanced geothermal systems in low permeability limestones – stimulation strategies for the Western Malm karst (Bavaria), *Geothermics*, **51**:351-367.
- Hofmann, H., Babadagli, T., and Zimmermann, G. (2014c). Hot water generation for oil sands processing from enhanced geothermal systems: process simulation for different hydraulic fracturing scenarios, *Applied Energy*, **113**:524-547.
- Hofmann, H., Babadagli, T., and Zimmermann, G. (2014d). Numerical simulation of complex fracture network development by hydraulic fracturing in naturally fractured ultratight formations. *Journal of Energy Resources Technology*, **136**:042907 (9 pages).
- Hofmann, H., Babadagli, T., and Zimmermann, G. (2014e). Development of complex fracture networks for enhanced geothermal systems. 4th HAI-E&E Science Forum, Edmonton, Canada, September 29.
- Hofmann, H., Yoon, J.S., Zang, A., Blöcher, G., Zimmermann, G., and Babadagli, T. (2015a). A new hybrid simulation approach to evaluate the efficiency of hydraulic stimulation treatments. *Proceedings of the World Geothermal Congress*, Melbourne, Australia, April 19-24.
- Hofmann, H., Babadagli, T., Yoon, J.S., Zang, A., and Zimmermann, G. (2015b). A grain-based modeling study of mineralogical factors affecting strength, elastic behaviour and micro fracture development during compression tests in granites. *Submitted to Engineering Fracture Mechanics (under review)*.

- Hofmann, H., Babadagli, T., and Zimmermann, G. (2015c). A grain based modeling study of fracture branching during compression tests in granites. *Accepted for publication in International Journal of Rock Mechanics and Mining Sciences*.
- Hofmann, H., Blöcher, G., Milsch, H., Babadagli, T., and Zimmermann, G. (2015d). Continuous measurement of time and pressure dependent fracture permeability of aligned and displaced tensile fractures in granitic rock during cyclic loading. *Submitted to Geophysical Journal International (under review)*.
- Hofmann, H., Babadagli, T., Yoon, J.S., and Zimmermann, G. (2015e). A hybrid discrete/finite element modeling study of complex hydraulic fracture development for enhanced geothermal systems (EGS) in granitic basements. *Submitted to International Journal of Fracture (under review)*.
- Howarth, R.W., Santoro, R., Ingraffea, A. (2011). Methane and the greenhouse-gas footprint of natural gas from shale formations. *Climate Change*, **106**:679–90.
- Huang, S.L., Oelfke, S.M., and Speck, R.C. (1992). Applicability of fractal characterization and modeling to rock joint profiles. *International Journal of Rock Mechanics, Mining Sciences and Geomechanics Abstracts*, **29**:89–98.
- Huenges, E. and Ledru, P. (2010). Geothermal energy systems: exploration, development, and utilization, John Wiley & Sons, Weinheim, Germany, 486 pages.
- Ishida, T., Chen, Q., Mizuta, Y., and Roegiers, J.-C. (2004). Influence of Fluid Viscosity on the Hydraulic Fracturing Mechanism. *Journal of Energy Resources Technology*, **126**:190–200.
- Itasca Consulting Group Inc. (2008). PFC2D – Particle flow code in 2 dimensions, Version 4.0, Minneapolis, USA.
- Itasca Consulting Group Inc. (2011). UDEC – Universal distinct element code, Version 5.0, Minneapolis, USA.
- Itasca Consulting Group Inc. (2013). 3DEC – 3 dimensional distinct element code, Version 5.0, Minneapolis, USA.
- Itasca Consulting Group Inc. (2014). PFC3D – Particle flow code in 3 dimensions, Version 6.0, Minneapolis, USA.
- Iwano, M. and Einstein, H.H., 1995. Laboratory experiments on geometric and hydromechanical characteristics of three different fractures in granodiorite. *Proceedings of the 8th ISRM Congress, Tokyo, Japan, September 25-29*.
- Jacot, R.H., Bazan, L.W., and Meyer, B.R. (2010). Technology Integration: A Methodology to Enhance Production and Maximize Economics in Horizontal Marcellus Shale Wells. *Proceedings of the SPE Annual Technical Conference and Exhibition, Florence, Italy, 19-22 September, SPE 135262*.
- Jafari, A. and Babadagli, T. (2011). Generating 3D permeability map of fracture networks using well, outcrop, and pressure-transient data. *SPE Reservoir Evaluation & Engineering*, **14**:215-224, SPE 124077.
- Jeffrey, R., Wu, B., and Zhang, X. (2012). The effect of thermoelastic stress change in the near wellbore region on hydraulic fracture growth. *Proceedings of the 37th Workshop on Geothermal Reservoir Engineering, Stanford, CA, USA, January 30-February 1*.

- Jing, Z., Willis-Richards, J., Watanabe, K., and Hashida, T. (2000). A three-dimensional stochastic rock mechanics model of engineered geothermal systems in fractured crystalline rock. *Journal of Geophysical Research*, **105**:23663-23679.
- Jing, L. (2003). A review of techniques, advances and outstanding issues in numerical modelling for rock mechanics and rock engineering. *International Journal of Rock Mechanics and Mining Sciences*, **40**:283-353.
- Johansen, K., Jensen, L.J.K., Marsden, C., and Bakshi, S. (2013). Optimizing water injection in a mature chalk field by application of streamline simulation. *Proceedings of the SPE Annual Technical Conference and Exhibition*, New Orleans, LS, USA, September 30-October 2, SPE 166336.
- Jung, R. (2013). EGS – Goodbye or Back to the Future. *In*: Bunger, A.P., McLennan, J., and Jeffrey, R. (editors). *Effective and sustainable hydraulic fracturing*, inTech, 95-121.
- Kalinina, E., McKenna, S.A., Hadgu, T., and Lowry, T. (2012). Analysis of the effects of heterogeneity on heat extraction in an EGS represented with the continuum fracture model. *Proceedings of the 37th Workshop on Geothermal Reservoir Engineering*, Stanford, CA, USA, January 30-February 1.
- Kan, W., Olson, J.E. (2015). Numerical investigation of complex hydraulic fracture development in naturally fractured reservoirs. *Proceedings of the SPE Hydraulic Fracturing Technology Conference*, The Woodlands, TX, USA, February 3-5, SPE 173326.
- Karner, S.L. (2005). Stimulation techniques used in enhanced geothermal systems: perspectives from geomechanics and rock physics. *Proceedings of the 30th Workshop on Geothermal Reservoir Engineering*, Stanford, CA, January 31-February 2.
- Kelkar, S., Lewis, K., Hickman, S., Davatzes, N.C., Moos, D., and Zyvoloski, G. (2012). Modeling coupled thermal-hydrological-mechanical processes during shear stimulation of an EGS well. *Proceedings of the 37th Workshop on Geothermal Reservoir Engineering*, Stanford, CA, USA, January 30-February 1.
- Keshavarzi, R. and Mohammadi, S. (2012). A new approach for numerical modeling of hydraulic fracture propagation in naturally fractured reservoirs. *Proceedings of the SPE/EAGE European Unconventional Resources Conference and Exhibition*, Vienna, Austria, March 20-22, SPE 152509.
- Khristianovich, S.A., and Zheltov, Y.P. (1955). Formation of Vertical Fractures by Means of Highly Viscous Fluids. *Proceedings of the 4th World Petroleum Congress*, Rome, Italy, June 6–15, 579–586.
- Knödel, K., Lange, G., and Voigt, H.J. (2007). *Environmental geology: handbook of field methods and case studies*. Berlin, Heidelberg, New York, 1357 pages.
- Kitsou, O.J., Herzog, H. and Tester, J.W. (2000). Economic Modeling of HDR Enhanced Geothermal Systems. *Proceedings of the World Geothermal Congress*, Beppu-Morioka, Japan, May 28 – June 10, 3779–3384.
- Kohl, T. and Mégel, T. (2007). Predictive modeling of reservoir response to hydraulic stimulations at the European EGS site Soultz-sous-Forêts. *International Journal of Rock Mechanics and Mining Sciences*, **44**:1118-1131.

- Kolditz, O., Bauer, S., Bilke, L., Böttcher, N., Delfs, J.O., Fischer, T., Görke, U.J., Kalbacher, T., Kosakowski, G., McDermott, C.I., Park, C.H., Radu, F., Rink, K., Shao, H., Shao, H.B., Sun, F., Sun, Y.Y., Singh, A.K., Taron, J., Walther, M., Wang, W., Watanabe, N., Wu, Y., Xie, M., Xu, W., Zehner, B. (2012). OpenGeoSys: an open-source initiative for numerical simulation of thermo-hydro-mechanical/chemical (THM/C) processes in porous media. *Environmental Earth Sciences*, **67**:589-599.
- Kulatilake, P.H.S.W. and Um, J. (1998). Requirements for accurate quantification of self-affine roughness using the variogram method. *International Journal of Solids and Structures*, **35**:4167–4189.
- Kumar, J. (1976). The effect of Poisson's ratio on rock properties. *Proceedings of the SPE Annual Fall Technical Conference and Exhibition* New Orleans, LS, USA, October 3–6, SPE 6094.
- Lan, H., Martin, C.D., and Hu, B. (2010). Effect of heterogeneity of brittle rock on micromechanical extensile behavior during compression loading. *Journal of Geophysical Research*, **115**:B01201 (14 pages).
- Last, N.C. and Harper, T.R. (1990). Response of fractured rock subject to fluid injection. Part I. Development of a numerical model. *Tectonophysics*, **172**:1-31.
- Lee, H. and Cho, T. (2002). Hydraulic Characteristics of Rough Fractures in Linear Flow under Normal and Shear Load. *Rock Mechanics and Rock Engineering*, **35**:299-318.
- Lee, S.H. and Ghassemi, A. (2011). Three-dimensional thermo-poro-mechanical modeling of reservoir stimulation and induced seismicity in geothermal reservoir. *Proceedings of the 36th Workshop on Geothermal Reservoir Engineering*, Stanford, CA, USA, January 31-February 3.
- Lemmon, E.W., Huber, M.L., and McLinden, M.O. (2010). NIST standard reference database 23: reference fluid thermodynamic and transport properties-REFPROP, version 9.0, National Institute of Standards and Technology, Standard Reference Data Program, Gaithersburg.
- Lemmon, E.W., Huber, M.L., and McLinden, M.O. (2013). NIST Standard Reference Database 23: reference fluid thermodynamic and transport properties-REFPROP, version 9.1, National Institute of Standards and Technology, Standard Reference Data Program, Gaithersburg.
- Lindal, B. (1973). Industrial and other applications of geothermal energy (except power production and district heating). In: Christopher, H. and Armstead, H. (editors). *Geothermal Energy: Review of Research and Development*, LC No. 72-97138, UNESCO, Paris, France, 135-148.
- Lisjak, A. Grasselli, G. (2014). A review of discrete modeling techniques for fracturing processes in discontinuous rock masses. *Journal of Rock Mechanics and Geotechnical Engineering*, **6**:301-314.
- Long, J., Xu, Z., Masliyah, J.H. (2005). On the role of temperature in oil sands processing. *Energy Fuels*, **19**:1440–1446.
- Luo, F., Xu, R.-N., Jiang, P.-X. (2013). Numerical investigation of the influence of vertical permeability heterogeneity in stratified formation and of injection/production well

perforation placement on CO₂ geological storage with enhanced CH₄ recovery. *Applied Energy*, **102**:1314–1323.

Majorowicz, J. and Moore, M.C. (2008). Enhanced Geothermal Systems (EGS) Potential in the Alberta Basin. ISEEE Research Paper, University of Calgary.

Majorowicz, J., and Grasby, S.E. (2010). High potential regions for enhanced geothermal systems in Canada. *Natural Resources Research*, **19**:177-188.

Majorowicz, J.A., Unsworth, M.J., Babadagli, T., Chacko, T., Currie, C.A., Grobe, M., Heaman, L.M., Heidbach, O., Huenges, E., Moeck, I., Ritter, O., Rostron, B.J., Schmitt, D., van der Baarn, M., and Weides, S. (2010). Investigation of geothermal energy as a heat source for oilsands extraction in northern Alberta. *Proceedings of the AGU Fall Meeting*, San Francisco, CA, USA, December 13-17.

Majorowicz, J., Unsworth, M., Chacko, T., Gray, A., Heaman, L., Potter, D.K., Schmitt, D., and Babadagli, T. (2012). Geothermal energy as a source of heat for oil sands processing in Northern Alberta, Canada. *In*: Hein, F.J., Leckie, D., Larter, S., and Suter, J.R. (editors), Heavy Oil and Oil Sand Petroleum Systems in Alberta and Beyond: *AAPG Studies in Geology*, **64**:725-46.

Majorowicz, J., Hofmann, H., and Babadagli, T. (2013). Deep geothermal heat storage under oilsands - can we use it to help oilsands industry? New EGS concept proposed. *GRC Transactions*, **37**:173-178.

Majorowicz, J., Chan, J., Crowell, J., Gosnold, W., Heaman, L.M., Kück, J., Niewenhuis, G., Schmitt, D.R., Unsworth, M., Walsh, N., and Weides, S. (2014). The first deep heat flow determination in crystalline basement rocks beneath the Western Canadian Sedimentary Basin. *Geophysical Journal International*, advance access.

Majorowicz, J. and Grasby, S.E. (2014). Geothermal energy for Northern Canada: Is it economical? *Natural Resources Research*, **23**:159-173.

Man, Y., Yang, H., Spitler, J.D., and Fang, Z. (2011). Feasibility study on novel hybrid ground coupled heat pump system with nocturnal cooling radiator for cooling load dominated buildings. *Applied Energy*, **88**:4160–4171.

Mas Ivars, D., Potyondy, D.O., Pierce, M., and Cundall, P.A. (2008). The smooth-joint contact model. *Proceedings of the 8th World Congress on Computational Mechanics/5th European Congress on Computational Methods in Applied Sciences and Engineering*, Venice, Italy, June 30-July 5.

Mas Ivars, D., Pierce, M.E., Darcel, C., Reyes-Montes, J., Potyondy, D.O., Young, R.P., and Cundall P.A. (2011). The synthetic rock mass approach for jointed rock mass modeling. *International Journal of Rock Mechanics and Mining Sciences*, **48**:219-244.

Maxwell, S.C., Urbancic, T.I., Steinsberger, N., Zinno, R. (2002). Microseismic imaging of hydraulic fracture complexity in the Barnett shale. *Proceedings of the SPE Annual Technical Conference and Exhibition*, San Antonio, TX, USA, September 29-October 2, SPE 77440.

- McClure, M. and Horne, R. (2012a). The effect of fault zone development on induced seismicity. *Proceedings of the 37th workshop on geothermal reservoir engineering*, Stanford, CA, USA, January 30–February 1.
- McClure, M. and Horne, R. (2012b). Opening mode stimulation or shear stimulation? *GRC Transactions*, **36**:515-522.
- McClure, M. and Horne, R. (2013a). Is pure shear stimulation always the mechanism of stimulation in EGS? *Proceedings of the 38th Workshop on Geothermal Reservoir Engineering*, Stanford, CA, USA, February 11-13.
- McClure, M.W. and Horne, R.N. (2013b). Discrete fracture network modeling of hydraulic stimulation – coupling flow and geomechanics. *Springer briefs in earth sciences*, Springer, Cham, Heidelberg, New York, Dordrecht, London, 96 pages.
- McClure, M.W., and Horne, R.N. (2014). An investigation of stimulation mechanisms in enhanced geothermal systems. *International Journal of Rock Mechanics and Mining Sciences*, **72**:242-260.
- Meyer & Associates (2011). User's guide Meyer fracturing simulators, 9th edition, Unicode Inc., Natrona Heights, PA, USA.
- Meyer, B.R. and Bazan, L.W. (2011). A discrete fracture network model for hydraulically induced fractures: theory, parametric and case studies. *Proceedings of the SPE Hydraulic Fracturing Technology Conference*, The Woodlands, TX, USA, January 24-26, SPE 140514.
- Michelet, S., Toksöz, M.N. (2007). Fracture mapping in the Soultz-sous-Forêts geothermal field using microearthquake locations. *Journal of Geophysical Research*, **112**:B07315 (14 pages).
- Min, K.S., Zhang, Z., and Ghassemi, A. (2010). Hydraulic fracturing propagation in heterogeneous rock using the VMIB method. *Proceedings of the 35th Workshop on Geothermal Reservoir Engineering*, Stanford, CA, USA, February 1-3.
- Montgomery, C.T. and Smith, M.B. (2010). Hydraulic fracturing: history of an enduring technology. *Journal of Petroleum Technology*, **62**:26-32.
- Moore, J.R. and Glaser, S.D. (2007). Self-potential observations during hydraulic fracturing, *Journal of Geophysical Research*, **112**:B02204 (17 pages).
- Morrow, C.A., Moore, D.E., and Lockner, D.A. (2001). Permeability reduction in granite under hydrothermal conditions. *Journal of Geophysical Research*, **106**:551-560.
- Mosher, S., Berger, R.L., and Anderson, D.E. (1975). Fracture characteristics of two granites. *Rock Mechanics*, **7**:167-176.
- Nagel, N., Gil, I., Sanchez-Nagel, M., and Damjanac, B. (2011). Simulating hydraulic fracturing in real fractured rocks – overcoming the limits of pseudo3d models. *Proceedings of the SPE Hydraulic Fracturing Technology Conference*, The Woodlands, TX, USA, January 24-25.
- Nagel, N., Zhang, F., Sanchez-Nagel, M., and Lee, B. (2013). Quantitative evaluation of completion techniques on influencing shale fracture ,complexity'. *In*: Bunger, A.P.,

- McLennan, J., Jeffrey, R. (editors). Effective and Sustainable Hydraulic Fracturing, 513-546, doi: 10.5772/56304.
- National Energy Board (2013). Natural gas. Available from: <www.neb-one.gc.ca/clf-nsi/rnrgynfmitn/nrgyrprt/nrgytlk/tlksmmr2013/ntrlgs-eng.html#s2> [retrieved September 25, 2013].
- Natural Resources Canada – NRC (2008). CO2 emission factors. Available from: <oee.nrcan.gc.ca/industrial/technical-info/benchmarking/canadian-steel-industry/6602> [retrieved November 19, 2013].
- Natural Resources Canada – NRC (2010). Comprehensive energy use database, 1990 to 2010. Available from: <oee.nrcan.gc.ca/corporate/statistics/neud/dpa/comprehensive_tables/index.cfm> [retrieved January 28, 2013].
- Nicksair, M. and Martin, C.D. (2014). Factors affecting crack initiation in low porosity crystalline rocks. *Rock Mechanics and Rock Engineering*, **47**:1165-1181.
- Ning, X., Fan, J., Holditch, S. A., and Lee, W. J. (1993). Property Measurement in Naturally Fractured Devonian Shale Cores Using a New Pressure Pulse Method. *Proceedings of the SCA Conference*, Paper No. 9301.
- Nodgren, R. (1972). Propagation of Vertical Hydraulic Fracture. *Society of Petroleum Engineering Journal*, **12**:306–314.
- Orzol, J., Jung, R., Jatho, R., Tischner, T., and Kehrner, P. (2005). The GeneSys-Project: extraction of geothermal heat from tight sandstones. *Proceedings of the World Geothermal Congress*, Antalya, Turkey, April 24-29.
- Osholake, T., Jr., Wang, J. Y., and Ertekin, T. (2013). Factors Affecting Hydraulically Fractured Well Performance in the Marcellus Shale Gas Reservoirs. *Journal of Energy Resources Technology*, **135**:013402 (10 pages).
- Palmer, I., Moschovidis, Z., and Cameron, J. (2007). Modeling shear failure and stimulation of the Barnett shale after hydraulic fracturing. *Proceedings of the SPE Hydraulic Fracturing Technology Conference*, College Station, TX, USA, January 29-31, SPE 106113.
- Parker, R. (1999). The Rosemanowes HDR project 1983-1991. *Geothermics*, **28**:603-615.
- Pathak, V., Babadagli, T., Majorowicz, J.A., and Unsworth, M.J. (2014). Evaluation of engineered geothermal systems as a heat source for oil sands production in Northern Alberta. *Natural Resources Research*, **23**:247-265.
- Pearson, C.M., Griffin, L., Wright, C., Weijers, L. (2013). Breaking up is hard to do: creating hydraulic fracture complexity in the Bakken Central Basin. *Proceedings of the SPE Hydraulic Fracturing Technology Conference*, The Woodlands, TX, USA, February 4-6, SPE 163827.
- Pembina Institute. (2013). Edmonton's energy transition. Discussion paper. Available from: <www.pembina.org/pub/2391> [retrieved October 9, 2013].
- Perkins, T. and Kern, L. (1961). Widths of hydraulic fractures. *Journal of Petroleum Technology*, **13**:937-949.

- Petrov, V.A., Poluektov, V.V., Zharikov, A.V., Nasimov, R.M., Diaur, N.I., Terentiev, V.A., Burmistrov, A.A., Petrunin, G.I., Popov, V.G., Sibgatulin, V.G., Lind, E.N., Grafchikov, A.A., and Shmonov, V.M. (2005). Microstructure, filtration, elastic and thermal properties of granite rock samples: implication for HLW disposal. *Geological Society of London Special Publications*, **240**:237–53.
- Pine, R.J. and Cundall, P.A. (1985). Applications of the fluid-rock interaction program (FRIP) to the modelling of hot dry rock geothermal energy systems. *In*: Stephansson, O. (editor). *Proceedings of the International Symposium on Fundamentals of Rock Joints*, Bjorkliden, Sweden.
- Potocki, D. (2012). Understanding induced fracture complexity in different geological settings using DFIT net fracture pressure. *Proceedings of the SPE Canadian Unconventional Resources Conferences*, Calgary, AB, Canada, October 30–November 1, SPE 162814.
- Potyondy, D.O. and Cundall, P.A. (2004) A bonded-particle model for rock. *International Journal of Rock Mechanics & Mining Sciences*, **41**:1329-1364.
- Potyondy, D.O. (2007). The effect of voids on the mechanical properties of rock. *Proceedings of the 4th International Conference on Discrete Element Methods*, Brisbane, Australia, August 27-29.
- Potyondy, D.O. and Hazzard, J.F. (2008). Effects of stress and induced cracking on the static and dynamic moduli of rock. *Proceedings of the 1st International FLAC/DEM Symposium*, Minneapolis, MS, USA, August 25-27.
- Potyondy, D.O. (2010a). A grain-based model for rock: Approaching the true microstructure. *Proceedings of Rock Mechanics in Nordic Countries*, Kongsberg, Norway, June 9-12.
- Potyondy, D.O. (2010b). PFC2D Grain-based models. Technical Memorandum, Itasca Consulting Group Inc., Minneapolis, MS, USA, May 28.
- Potyondy, D.O. (2010c). PFC2D Grain-structure generator, Technical Memorandum, Itasca Consulting Group Inc., Minneapolis, MS, USA, May 28.
- Potyondy, D.O. (2012). The bonded-particle model as a tool for rock mechanics research and application: current trends and future directions. *Proceedings of the 7th Asian Rock Mech. Symp.*, Seoul, South Korea, October 15-19.
- Pratt, H.R., Swolfs, H.S., Brace, W.F., Black, A.D., and Handin, J.W. (1977). Elastic and transport properties of an in situ jointed granite. *International Journal of Rock Mechanics, Mining Sciences and Geomechanics Abstracts*, **14**:35-45.
- Procesi, M., Cantucci, B., Buttinelli, M., Armezzani, G., Quattrocchi, F., Boschi, E. (2013). Strategic use of the underground in an energy mix plan: synergies among CO₂, CH₄ geological storage and geothermal energy. Latium Region case study (Central Italy). *Applied Energy*, **110**:104–131.
- Pruess, K. (1991). TOUGH2: A general-purpose numerical simulator for multiphase fluid and heat flow. Technical Report, LBL-29400, Lawrence Berkeley Laboratory, CA, USA.
- Pyrak-Nolte, L.J. and Morris, J.P. (2000). Single fractures under normal stress: The relation between fracture specific stiffness and fluid flow. *International Journal of Rock Mechanics and Mining Sciences*, **37**:245-262.

- Quattrocchi, F., Boschi, E., Spena, A., Buttinelli, M., Cantucci, B., Procesi, M. (2013). Synergic and conflicting issues in planning underground use to produce energy in densely populated countries, as Italy Geological storage of CO₂, natural gas, geothermics and nuclear waste disposal. *Applied Energy*, **101**:393–412.
- Rachez, X. and Gentier, S. (2010). 3D-hydromechanical behavior of a stimulated fractured rock mass. *Proceedings of the World Geothermal Congress*, Bali, Indonesia, April 25-30.
- Ragnarsson, A. (2005). Geothermal Development in Iceland 2000-2004. *Proceedings of the World Geothermal Congress*, Antalya, Turkey, 24-29 April.
- Rahman, M. and Rahman, M. (2009). A fully coupled numerical poroelastic model to investigate interaction between induced hydraulic fracture and pre-existing natural fracture in a naturally fractured reservoir: potential application in tight gas and geothermal reservoirs. *Proceedings of the SPE Annual Technical Conference and Exhibition*, New Orleans, LS, USA, October 4-7, SPE 124269.
- Rahnama, F., Marsh, R.A., and Philip, L. (2013). The Alberta oil sands: Reserves and long-term supply outlook. In: Hein, F.J., Leckie, D., Larter, S., and Suter, J.R., (editors), Heavy-oil and oil-sand petroleum systems in Alberta and beyond: *AAPG Studies in Geology*, **64**:133-144.
- Raimbay, A., Babadagli, T., Kuru, E., and Develi, K., 2014. Effect of fracture surface roughness and shear displacement on permeability and proppant transportation in a single fracture. *Proceedings of the SPE/CSUR Unconventional Resources Conference*, Calgary, AB, Canada, September 30–October 2, SPE 171577.
- Rankin, R., Thibodeau, M., and Vincent, M.C. (2010). Improved production and profitability achieved with superior completions in horizontal wells: a Bakken/three forks case history. *Proceedings of the SPE Annual Technical Conference and Exhibition*, Florence, Italy, September 19–22, SPE 134595.
- Raven, K.G. and Gale, J.E. (1985). Water flow in a natural rock fracture as a function of stress and sample size. *International Journal of Rock Mechanics, Mining Science & Geomechanics Abstracts*, **22**:251-261.
- Reinicke, A. (2009). Mechanical and Hydraulic Aspects of Rock-Proppant Systems: Laboratory Experiments and Modelling Approaches. Dissertation, University of Potsdam.
- Reinicke, A., Blöcher, G., Zimmermann, G., Huenges, E., Dresen, G., Stanchits, S., Legarth, B.A., and Makurat, A. (2013). Mechanically induced fracture-face skin: Insights from laboratory testing and modeling approaches. *SPE Production & Operations*, **28**:26-35.
- Ren, L., Zhao, J., and Hu, Y. (2014). Hydraulic fracture extending into network in shale: Reviewing influence factors and their mechanism. *The Scientific World Journal*, **2014**:847107 (9 pages).
- Riahi, A. and Damjanac, B. (2013). Numerical study of hydro-shearing in geothermal reservoirs with a pre-existing discrete fracture network. *Proceedings of the 38th Workshop on Geothermal Reservoir Engineering*, Stanford, CA, USA, February 11-13.

- Riahi, A., Damjanac, B., and Furtney, J. (2014). Discrete element modeling of thermo-hydro-mechanical coupling in enhanced geothermal reservoirs. *Proceedings of the 39th Workshop on Geothermal Reservoir Engineering*, Stanford, CA, USA, February 24-26.
- Rickards, A.R., Brannon, H.D., Wood, W.D., and Stephenson, C.J. (2009). High strength, ultra lightweight proppant lends new dimensions to hydraulic fracturing applications. *SPE Productions & Operations*, **21**:212–221.
- Rickman, R., Mullen, M., Petre, E., Grieser, B., Kundert, D. (2008). A practical use of shale petrophysics for stimulation design optimization: all shale plays are not clones of the Barnett shale. *Proceedings of the SPE Annual Technical Conference and Exhibition*, Denver, CO, USA, September 21-24, SPE 115258.
- Rodríguez, J.A. and Herrera, A. (2003). Geothermal El Salvador. *GRC Bulletin*, **July/August 2003**:159-162.
- Rogers, S., Elmo, D., Dunphy, R., and Bearinger, D. (2010). Understanding hydraulic fracture geometry and interactions in the Horn River Basin through DFN and numerical modeling. *Proceedings of the Canadian Unconventional Resources and International Petroleum Conference*, Calgary, AB, Canada, October 19-21.
- Rong, G., Liu, G. Hou, D., and Zhou, C.-B. (2013). *The Scientific World Journal* **2013**:589215 (12 pages).
- Roussel, N. and Sharma, M. (2011). Strategies to minimize frac spacing and stimulate natural fractures in horizontal completions. *Proceedings of the SPE Annual Technical Conference and Exhibition*, Denver, USA, October 30-November 2, SPE 146104.
- Rushing, J.A. and Sullivan, R.B. (2003). Evaluation of a Hybrid Water-Frac Stimulation Technology in the Bossier Tight Gas Sand Play. *Proceedings of the SPE Annual Technical Conference and Exhibition*, Denver, CO, USA, October 5-8, SPE 84394.
- Rutqvist, J. and Tsang, C.-F. (2003) Tough-Flac: A numerical simulator for analysis of coupled thermal-hydrological-mechanical processes in fractured and porous geological media under multi-phase flow conditions. *Proceedings of the TOUGH Symposium*, Lawrence Berkeley National Laboratory, Berkeley, CA, USA, May 12-14.
- Rutqvist, J., Dobson, P.F., Garcia, J., Hartline, C., Jeanne, P., Oldenburg, C.M., Vasco, D.W., and Walters, M. (2015). The northwest Geysers EGS Demonstration Project, California: Pre-stimulation modeling and interpretation of the stimulation. *Mathematical Geosciences*, **47**:3-29.
- Safari, M.R., Gandikota, R., Mutlu, U., Ji, M., Glanville, J., and Abass, H. (2013). Pulsed fracturing in shale reservoirs: Geomechanical aspects, ductile-brittle transition and field implications. *Proceedings of the Unconventional Resources Technology Conference*, Denver, CO, USA, August 12-14, SPE 168759.
- Sanyal, S.K., Butler, S.J., Swenson, D., and Hardeman, B. (2000). Review of the state-of-the-art of numerical simulation of enhanced geothermal systems. *Proceedings of the World Geothermal Congress*, Kyushu – Tohoku, Japan, May 28-June 10.
- Sausse, J., Dezayes, C., Genter, A., and Bisset, A. (2008). Characterization of fracture connectivity and fluid flow pathways derived from geological interpretation and 3D

- modelling of the deep seated EGS reservoir of Soultz (France). *Proceedings of the 33rd Workshop on Geothermal Reservoir Engineering*, Stanford, CA, USA, January 28-30.
- Savanick, G.A., and Johnson, D.I. (1974). Measurements of the strength of grain boundaries in rock. *International Journal of Rock Mechanics, Mining Sciences and Geomechanics Abstracts*, **11**:173-180.
- Schindler, M., Nami, P., Schellschmidt, R., Teza, D., and Tischner, T. (2008). Summary of hydraulic stimulation operations in the 5 km deep crystalline HDR/EGS reservoir at Soultz-sous-Forêts. *Proceedings of the 33rd Workshop on Geothermal Reservoir Engineering*, Stanford, CA, USA, January 28-30.
- Schulte, T., Zimmermann, G., Vuataz, F., Portier, S., Tischner, T., Junker, R., Jatho, R., Huenges, E. (2010). Enhancing geothermal reservoirs. In: Huenges, E. and Ledru, P., (editors), *Geothermal energy systems: exploration, development, and utilization*, John Wiley & Sons, Weinheim, 173-244.
- Segura, J.M., and Carol, I. (2004). On zero-thickness interface elements for diffusion problems. *International Journal of Numerical and Analytical Methods in Geomechanics*, **28**:947-962.
- Selvadurai, A.P.S., Boulon, M.J., and Nguyen, T.S. (2005). The permeability of an intact granite. *Pure and Applied Geophysics*, **162**:373-407.
- Sesetty, V. and Ghassemi, A. (2012). Modeling and analysis of stimulation for fracture network generation. *Proceedings of the 37th Workshop on Geothermal Reservoir Engineering*, Stanford, CA, USA, January 30-February 1.
- Shakib, J.T. and Jalalifar, H. (2013). Hydraulic fracturing growth in fracture reservoirs using analytical and numerical simulation: T-type intersections. *Journal of Chemical and Petroleum Engineering*, **47**:129-138.
- Shengjun, Z., Huaixin, W., and Tao, G. (2011). Performance comparison and parametric optimization of subcritical Organic Rankine Cycle (ORC) and transcritical power cycle system for low-temperature geothermal power generation. *Applied Energy*, **88**:2740-2754.
- Simmons, G. and Wang, H. (1971). *Single Crystal Elastic Constants and Calculated Aggregate Properties: A Handbook*. 2nd edition, The M.I.T. Press, Cambridge, London, UK, 370 pages.
- Sondergeld, C.H., Newsham, K.E., Comisky, J.T., Rice, M.C., and Rai, C.S. (2010). Petrophysical Considerations in Evaluating and Producing Shale Gas Resources. *Proceedings of the SPE Unconventional Gas Conference*, Pittsburgh, PS, USA, February 23-25, SPE 131768.
- Sone, H. (2012). *Mechanical Properties of Shale Gas Reservoir Rocks and Its Relation to the In-Situ Stress Variation Observed in Shale Gas Reservoirs*. Ph.D. thesis, Stanford University, Stanford, CA, USA.
- Statistics Canada (2012). *The Canadian population in 2011: population counts and growth*. Ottawa, Ministry of Industry, Catalogue no. 98-310-X2011001.
- Stober, I. and Bucher, K. (2013). *Geothermal energy – from theoretical models to exploration and development*. Springer, Berlin, Heidelberg, Germany, 291 pages.

- Sun, Z. and Ouchterlony, F. (1986). Fracture Toughness of Stripa Granite Cores. *International Journal of Rock Mechanics, Mining Science and Geomechanics Abstracts*, **23**:399-409.
- Taron, J. and Elsworth, D. (2009). Thermal-hydrologic-mechanical-chemical processes in the evolution of engineered geothermal reservoirs. *International Journal of Rock Mechanics and Mining Sciences*, **46**:855-864.
- Tenzer, H. (2001). Development of hot dry rock technology. *GHC Bulletin*, **December 2001**:14-22.
- Terzaghi, C. (1925). Principles of Soil Mechanics. *Engineering News-Record*, **95**:19-27.
- Tester, J.W., Anderson, B.J., Batchelor, A.S., Blackwell, D.D., DiPippo, R., Drake, E.M., Garnish, J., Livesay, B., Moore, M.C., Nichols, K., Petty, S., Toksoez, M.N., Veatch Jr., R.W., Baria, R., Augustine, C., Murphy, E., Negaru, P., and Richards, M. (2006). The future of geothermal energy – Impact of enhanced geothermal systems (EGS) on the United States in the 21st Century. Massachusetts Institute of Technology. Available from: <www.1eere.energy.gov/geothermal/egs_technology_html>.
- Thiele, M.R., Batycky, R.P., and Blunt, M.J. (1997). A streamline-based 3D field-scale compositional reservoir simulator. *Proceedings of the SPE Annual Technical Conference and Exhibition*, San Antonio, TX, USA, October 5-8, SPE 38889.
- Tiab, D., Lu, J., Nguyen, H., and Owayed, J. (2010). Evaluation of Fracture Asymmetry of Finite-Conductivity Fractured Wells. *Journal of Energy Resources Technology*, **132**:012901 (7 pages).
- Togrul, A. and Zarif, I.H. (1999). Correlation of mineralogical and textural characteristics with engineering properties of selected granitic rocks from Turkey. *Engineering Geology*, **51**:303-317.
- Valley, B., and Evans, K.F. (2006). Strength and elastic properties of the Soultz granite. 2nd year report. *Proceedings of the the EHDRA Scientific Conference*, Soultz-sous-Forêts, France, June 15-16.
- Van der Hoorn, K., Heijnen, L.J., Gankema, M.E., and Nitters, G. (2012). Hydraulic fracturing in limestone: a case study of two EGS projects in the Netherlands. *Proceedings of the 37th Workshop on Geothermal Reservoir Engineering*, Stanford, CA, USA, January 30-February 1.
- Vasconcelos, G., Lourenco, P.B., Alves, C.A.S., Pamplona, J., and Miranda, T. (2010). Relation between tensile and compressive engineering properties of granites. *In*: Qian, Q. and Zhou, X. (editors). Harmonising rock engineering and the environment: Proceedings of the 12th ISRM international congress on rock mechanics, 380–381.
- Vassilellis, G.D., Bust, V.K., Li, C., Cade, R., and Moos, D. (2011). Shale engineering application: The MAL-145 project in West Virginia. *Proceedings of the Canadian Unconventional Resources Conference*, Calgary, AB, Canada, November 15-17, SPE 146912.
- Veatch, R.W. (1986). Economics of fracturing: some methods, examples, and case studies. *Proceedings of the SPE Annual Technical Conference and Exhibition*, New Orleans, LS, USA, October 5–8, SPE 15509.

- Vidhi, R., Kuravi, S., Goswami, D. Y., Stefanakos, E., and Sabau, A. S. (2013). Organic Fluids in a Supercritical Rankine Cycle for Low Temperature Power Generation. *Journal of Energy Resources Technology*, **135**:042002 (9 pages).
- Villeneuve, M.C. Diederichs, M.S., Kaiser, P.K., Frenzel, C. (2009). Constitutive model for numerical modelling of highly stressed heterogeneous massive rocks at excavation boundaries. *Proceedings of the 3rd CANUS Rock Mechanics Symposium*, Toronto, ON, Canada, May 11-13.
- Walsh, N. (2013). Geochemistry and geochronology of the Precambrian basement domains in the vicinity of Fort McMurray, Alberta: A geothermal perspective. M.Sc. Thesis, Department of Earth and Atmospheric Sciences, University of Alberta.
- Wang, W., and Kolditz, O. (2007). Object-oriented finite element analysis of thermo-hydro-mechanical (THM) problems in porous media. *International Journal of Numerical Methods in Engineering*, **69**:162-201.
- Wang, X. and Ghassemi, A. (2012). A 3D thermal-poroelastic model for geothermal reservoir stimulation. *Proceedings of the 37th Workshop on Geothermal Reservoir Engineering*, Stanford, CA, USA, January 30-February 1.
- Warpinski, N.R., and Teufel, L.W. (1987). Influence of geologic discontinuities on hydraulic fracture propagation. *Journal of Petroleum Technology* **39**:209-220.
- Warpinski, N.R., and Branagan, P.T. (1989). Altered-stress fracturing. *Journal of Petroleum Technology*, **49**:990-997.
- Warpinski, N.R., Moschovidis, Z.A., Parker, C.D., and Abou-Sayed, I.S. (1994). Comparison study of hydraulic fracturing models – test case: GRI staged field experiment no. 3. *SPE Production & Facilities*, **9**:7-16.
- Warpinski, N.R., Kramm, R.C., Heinze, J.R., and Waltman C.K. (2005). Comparison of single- and dual-array microseismic mapping techniques in the Barnett shale. *Proceedings of the SPE Annual Technical Conference and Exhibition*, Dallas, TX, USA, October 9-12, SPE 95568.
- Warpinski, N.R., Mayerhofer, M.J., Vincent, M.C., Cipolla, C.L., and Lonon, E. (2008). Stimulating unconventional reservoirs: maximizing network growth while optimizing fracture conductivity. *Proceedings of the SPE Unconventional Reservoirs Conference*, Keytone, CO, USA, February 10-12, SPE 114173.
- Warpinski, N.R. (2009). Stress amplification and arch dimension in proppant beds deposited by waterfracs. *SPE Production & Operations*, **25**:461-471.
- Warren, J.E. and Root, P.J. (1963). The behavior of naturally fractured reservoirs. *Society of Petroleum Engineers Journal*, **3**:245-255.
- Watanabe, N., Hirano, N., and Tsuchiya, N. (2008). Determination of aperture structure and fluid flow in a rock fracture by high-resolution numerical modeling on the basis of a flow-through experiment under confining pressure. *Water Resources Research*, **44**:W06412 (11 pages).
- Watanabe, N., Hirano, N., and Tsuchiya, N. (2009). Diversity of channeling flow in heterogeneous aperture distribution inferred from integrated experimental-numerical

- analysis on flow through shear fracture in granite. *Journal of Geophysical Research*, **114**:B04208 (17 pages).
- Watanabe, N., Wang, W., McDermott, C.I., Taniguchi, T., and Kolditz, O. (2010). Uncertainty analysis of thermo-hydro-mechanical coupled processes in heterogeneous porous media. *Computational Mechanics*, **45**:263-280.
- Watanabe, N., Ishibashi, T., Ohsaki, Y., Tsuchiya, Y., Tamagawa, T., Hirano, N., Okabe, H., and Tsuchiya, N. (2011). X-ray CT based numerical analysis of fracture flow for core samples under various confining pressures. *Engineering Geology*, **123**:338-346.
- Watanabe, N., Wang, W., Taron, J., Görke, U.J., and Kolditz, O. (2012). Lower-dimensional interface elements with local enrichment: application to coupled hydro-mechanical problems in discretely fractured porous media. *International Journal of Numerical Methods in Engineering*, **90**:1010-1034.
- Waters, G.A., Dean, B.K., Downie, R.C., Kerrihard, K.J., and McPherson, B. (2009). Simultaneous hydraulic fracturing of adjacent horizontal wells in the woodford shale. *Proceedings of the SPE Hydraulic Fracturing Technology Conference*, The Woodlands, TX, USA, January 19-21, SPE 119635.
- Watson, A. (2014). *Geothermal energy – fundamentals and applications*, Springer.
- Weides, S., Moeck, I., Majorowicz, J., Palombi, D., and Grobe, M. (2013). Geothermal exploration of Paleozoic formations in Central Alberta. *Canadian Journal of Earth Sciences* **50**:519-534.
- Weides, S. and Majorowicz, J. (2014). Implications of spatial variability in heat flow for geothermal resource evaluation in large foreland basins: the case of the Western Canada Sedimentary Basin, *Energies*, **7**:2573-2594.
- Weides, S., Moeck, I., Majorowicz, J., and Grobe, M. (2014). The Cambrian Basal Sandstone Unit in Central Alberta – an investigation of temperature distribution, petrography, and hydraulic and geomechanical properties of a deep saline aquifer. *Canadian Journal of Earth Sciences*, **51**:783-796.
- Weijers, L., Wright, C., Mayerhofer, M., and Cipolla, C. (2005). Developing calibrated fracture growth models for various formations and regions across the United States. *Proceedings of the SPE Annual Technical Conference and Exhibition*, Dallas, TX, USA, October 9-12, SPE 96080.
- Weiland, C.M., Macdonald, K.C., and Grindlay, N.R. (1996). Ridge segmentation and the magnetic structure of the Southern Mid-Atlantic Ridge 26°S and 31°-35°S: Implications for magnetic processes at slow spreading centers. *Journal of Geophysical Research*, **101**:8055-8073.
- Weng, X., Kresse, O., Cohen, C.-E., Wu, R., and Gu, H. (2011). Modeling of hydraulic-fracture-network propagation in a naturally fractured formation. *SPE Productions and Operations*, **26**:368-380.
- Willis-Richards, J., Watanabe, K., and Takahashi, H. (1996). Progress toward a stochastic rock mechanics model of engineered geothermal systems, *Journal of Geophysical Research*, **101**:17481-17496.

- Witherspoon, N.G., Cook, N.G.W., and Gale, J.E. (1981). Geologic storage of radioactive waste: field studies in Sweden. *Science*, **221**:894-900.
- World Energy Council (2010). Survey of Energy Resources. London, UK, 608 pages.
- Wu, J., Liu, Y., and Yang, H. (2012). New Method of Productivity Equation for Multiphase Horizontal Well in Three-Dimensional Anisotropic Oil Reservoirs. *Journal of Energy Resources Technology*, **134**:032801.
- Wyborn, D., Graaf, L., Davidson, S., and Hann, S. (2005). Development of Australia's first hot fractured rock (HFR) underground heat exchanger, Cooper Basin, South Australia. *Proceedings of the World Geothermal Congress, Antalya, Turkey*, 24-29 April.
- Wyborn, D. (2011). Hydraulic stimulation of the Habanero enhanced geothermal system (EGS), South Australia. 5th BC unconventional gas technical forum. Available from: datafind.gov.bc.ca/query.html?qp=&style=ener&qt=mayet&Submit.x=0&Submit.y=0 [retrieved April 27, 2014].
- Xin, T. (2013). Hydro-Mechanical Coupled Behaviour of Brittle Rocks – Laboratory Experiments and Numerical Simulations. Dissertation, TU Bergakademie Freiberg, Germany.
- Xu, W., Thiercelin, M., Ganguly, U., Weng, X., Gu, H., Onda, H., Sun, J., and Le Calvez, J. (2010). Wiremesh: a novel shale fracturing simulator. *Proceedings of the International Oil and Gas Conference and Exhibition, Beijing, China*, June 8-10, SPE 132218.
- Xu, C., Dowd, P.A., Mohais, R. (2012). Connectivity analysis of the Habanero enhanced geothermal system. *Proceedings of the 37th Workshop on Geothermal Reservoir Engineering, Stanford, CA, USA*, January 30-1 February.
- Yew, C.H. (1997). Mechanics of hydraulic fracturing, Gulf Publishing Company, Houston, 183 pages.
- Yoon, J.S. (2007). Application of experimental design and optimization to PFC model calibration in uniaxial compression simulation. *International Journal of Rock Mechanics and Mining Sciences*, **44**:871-889.
- Yoon, J.S., Zang, A., and Stephansson, O. (2012). Simulating fracture and friction of Aue granite under confined asymmetric compressive test using clumped particle model. *International Journal of Rock Mechanics and Mining Sciences*, **49**:68-83.
- Yoon, J.S., Zang, A., and Stephansson, O. (2013). Simulation of hydraulic stimulation of fractured reservoir and induced seismicity using discrete element-fracture network model. *Proceedings of the 38th Workshop on Geothermal Reservoir Engineering, Stanford, CA, USA*, February 11-13.
- Yoon, J.S., Zang, A., and Stephansson, O. (2014a). Numerical investigation on optimized stimulation of intact and naturally fractured deep geothermal reservoirs using hydro-mechanical coupled discrete particles joints model. *Geothermics*, **52**:165-184.
- Yoon, J.S., Zimmermann, G., and Zang, A. (2014b). Numerical investigation on stress shadowing in fluid injection-induced fracture propagation in naturally fractured geothermal reservoirs. *Rock Mechanics and Rock Engineering*, December 2014, doi: 10.1007/s00603-014-0695-5.

- Yoon, J.S., Zimmermann, G., and Zang, A. (2015). Discrete element modeling of cyclic rate fluid injection at multiple locations in naturally fractured reservoirs. Technical Note, *International Journal of Rock Mechanics and Mining Sciences*, **74**:15-23.
- Zang, A. (1997). Akustische Emissionen beim Spröbruch von Gestein. Scientific Technical Report STR97/19, doi: 10.2312/GFZ.b103-97192.
- Zang, C. Wagner, S. Stanchits, Dresen, G., Andresen, R., and Haidekker, M.A. (1998). *Geophysical Journal International*, **135**:1113-1130.
- Zang, A., Wagner, F.C., Stanchits, S., Janssen, C., and Dresen, G. (2000). Fracture process zone in granite. *Journal of Geophysical Research*, **105**:651-623.
- Zang, A., Stanchits, S., and Dresen, G. (2002). Acoustic Emission Controlled Triaxial Rock Fracture and Friction tests. In: Dyskin, A.V., Hu, X., and Sahouryeh, E., (editors). Structural Integrity and Fracture, Swets & Zeitlinger, 289 pages.
- Zang, A., Yoon, J.S., Jeon, S., and Stephansson, O. (2010). Testing of clumped particle models in simulation of laboratory rock fractures in compression. *Proceedings of the 18th European Conference on Fracture – ECF*, Dresden, Germany, August30-September 3.
- Zang, A., Yoon, J.S., Stephansson, O., and Heidbach, O. (2013). *Geophysical Journal International*, **195**:1282-1287.
- Zhang, J., Kamenov, A., Zhu, D., and Hill, D. (2014). Laboratory measurement of hydraulic-fracture conductivities in the Barnett Shale. *SPE Production & Operations*, **29**:216-227, SPE 163839.
- Zhao, J. and Brown, E.T. (1992). Hydro-thermo-mechanical properties of joints in the Carnmenellis granite. *Quarterly Journal of Engineering Geology*, **25**:279-290.
- Zhao, X. and Young, R.P. (2011). Numerical modeling of seismicity induced by fluid injection in naturally fractured reservoirs. *Geophysics*, **76**:WC167-WC180.
- Zhao, Y., Huang, J., and Wang, R. (1993). Real-time SEM observations of the microfracturing process in rock during a compression test. *International Journal of Rock Mechanics, Mining Science & Geomechanics Abstracts*, **30**:643-652.
- Zimmermann, G. and Reinicke, A. (2010). Hydraulic Stimulation of a deep sandstone reservoir to develop an Enhanced Geothermal System: Laboratory and field experiments. *Geothermics*, **39**:70-77.
- Zimmermann, G., Blöcher, G., Reinicke, A., and Brandt, W. (2011). Rock specific hydraulic fracturing and matrix acidizing to enhance a geothermal system – concepts and field results. *Tectonophysics*, **503**:146-154.
- Zimmermann, G., Hofmann, H., Babadagli, T., Yoon, J.S., Zang, A., Deon, F., Urpi, L., Blöcher, G., Hassanzadegan, A., and Huenges, E. (2015). Multi-fracturing and cyclic hydraulic stimulation scenarios to develop Enhanced Geothermal Systems – Feasibility and mitigation strategies to reduce seismic risk. *Proceedings of the World Geothermal Congress*, Melbourne, Australia, April 19-25.
- Zoback, M.D. (2007). Reservoir geomechanics. Cambridge University Press, Cambridge, UK and New York, NY, USA, 464 pages.